https://theses.gla.ac.uk/

Theses Digitisation:

https://www.gla.ac.uk/myglasgow/research/enlighten/theses/digitisation/

This is a digitised version of the original print thesis.

Copyright and moral rights for this work are retained by the author

A copy can be downloaded for personal non-commercial research or study, without prior permission or charge

This work cannot be reproduced or quoted extensively from without first obtaining permission in writing from the author

The content must not be changed in any way or sold commercially in any format or medium without the formal permission of the author

When referring to this work, full bibliographic details including the author, title, awarding institution and date of the thesis must be given

Enlighten: Theses
https://theses.gla.ac.uk/
research-enlighten@glasgow.ac.uk

DESIGN OF SHEAR WALL– FLOOR SLAB CONNECTIONS USING SHEAR REINFORCEMENT

by

MUHAMMAD SHAFIUL BARI

A Thesis submitted for the degree of
Doctor of Philosophy

Department of Civil Engineering
University of Glasgow

© M.S. Bari, 1987

October, 1987.

ProQuest Number: 10997384

All rights reserved

INFORMATION TO ALL USERS
The quality of this reproduction is dependent upon the quality of the copy submitted.

In the unlikely event that the author did not send a complete manuscript
and there are missing pages, these will be noted. Also, if material had to be removed,
a note will indicate the deletion.

ProQuest 10997384

Published by ProQuest LLC (2018). Copyright of the Dissertation is held by the Author.

All rights reserved.
This work is protected against unauthorized copying under Title 17, United States Code
Microform Edition © ProQuest LLC.

ProQuest LLC.
789 East Eisenhower Parkway
P.O. Box 1346
Ann Arbor, MI 48106 – 1346

SUMMARY

This thesis presents an experimental and theoretical study of the ultimate strength of shear wall– floor slab junctions reinforced for flexure and shear subjected to monotonic and reversed cyclic loading.

The experiments were done on reinforced concrete models designed to represent the local stress state at the junctions. The floor slabs were approximately one meter square and 100 to 150 mm thick. The slab was cast monolithic with a short height of the wall. In all fifteen models were tested. Eleven models had a rectangular shear wall, while the remaining four had a T– section shearwall. The main parameters investigated were:

a. Shear reinforcement
b. Ratio of (moment / shear) due to "wind"
c. Length of the wall– slab junction
d. Ratio of Flange width of wall / Bay width of slab
e. Ratio of (moment / shear) due to gravity load
f. Strength and stiffness degradation due to cyclic loading.

A theoretical investigation was conducted using a specially developed three dimensional nonlinear finite element programme. The twenty node isoparametric brick element was adopted. Nonlinear effects due to the yielding of steel, cracking and crushing of concrete were included. The current constitutive laws for cyclic loading behaviour of concrete was investigated.

Finally, in order to assist the designers, empirical formulae have been developed to calculate the ultimate strength of junctions without shear reinforcement subjected to monotonic loading only. If the designer discovers that the joint is not capable of resisting the design loads, then it is suggested to use shear reinforcement according to BS 8110 in the slab in the form of closed vertical stirrup, where the shear stress exceeds allowable concrete shear stress.

ACKNOWLEDGEMENTS

The work presented in this thesis was carried out in the department of Civil Engineering at Glasgow University under the general direction of Professor A. Coull whose help and encouragement is gratefully acknowledged.

I wish to express my thanks to Dr. D. R. Green, Head of the Department of Civil Engineering for making the facilities available.

I wish to express my indebtedness to my supervisor, Dr. P. Bhatt for his valuable guidance, advice and constant encouragement throughout the work.

Many thanks are also due to:

- The teaching staff of Civil Engineering Department, in particular, Dr. D. V. Phillips, Dr. P. D. Arthur and Mr. G. Irving for their interest and useful discussions.

- My colleages in the Department of Civil Engineering, in particular, Dr. G. F. Elnounu, Dr. L. Abd El-Hafiz, Dr. M. S. Mohamed and Mr. I. A. Khaliq for their useful discussions.

- The staff of the Concrete Laboratory, in particular, Mr. A. Burnett, Mr. R. McCaskie, Mr. J. Thomson, Mr. I. Todd and Mr. A. Gray for their assistance in preparing and testing the models.

- The Association of Commonwealth Universities for awarding a postgraduate scholarship.

- The British Council who looked after me and my family during the full tenure of the scholarship.

- SERC for part of the financial support.

– My wife for her moral support and assistance in typing the manuscript.

– Finally, my thanks are reserved for my parents for their boundless patience, continual encouragement and moral support throughout the years.

CONTENTS

NOTATIONS

Symbols used in the text are defined where they appear. For convenience, a summary of those symbols is presented below chapterwise.

CHAPTER - TWO

A	Cross sectional area of the wall
A_{cp}	Area of critical cross section for shear punching failure
A_s	Area of steel reinforcement.
A_w	Cross sectional area of vertical stirrup.
b	Width of a section.
b_1	Width of the critical shear perimeter measured parallel to the direction of M.
b_0	Perimeter of the column.
C	Side length of square column.
C_1, C_2	Dimensions of the column.
d	Effective depth of slab.
e	Eccentricity, M/V.
f'_c	Cylinder compressive strength of concrete.
f_{cu}	Cube compressive strength of concrete.
h	Distance between the centre lines of the connecting beams, OR, overall slab thickness.
I	Second moment of area.
J	Property of the critical perimeter analogous to the polar moment of inertia.
K.M	A portion of the unbalanced moment transferred by torsion
L	Corridor opening width.

ℓ	Distance between the centroids of the coupled walls
M	Amount of unbalanced moment.
M_o	Capacity of the critical section for moment transfer only
P_k	Characteristic punching resistance.
q	Shear force per unit height of the coupled wall.
$R_{\ell s}$	Ratio of long side to short side of a rectangular column
s	Spacing of the stirrup
T	Integral shear force in the wall = $\int q\, dx$
u	Length of critical shear perimeter.
V	Applied shear force.
V_0	Capacity of the critical section for shear transfer only
V_d	Design shear strength.
$V_{d,ACI}$	Ultimate shear strength predicted by ACI Code
$V_{d,BS}$	Ultimate shear strength predicted by British Code
V_u	Ultimate shear strength
v	Shear stress
v_c	Allowable shear stress in concrete.
v_{shear}	Shear stress due to direct shear.
$v_{torsion}$	Shear stress due to torsion.
v_{eff}	Effective shear stress at the perimeter.
W	Length of the web of the wall.
X	Total slab length.
X_1	Length of the side of perimeter considered parallel to the axis.
x	Abscissa measured from the top of the wall, OR x - axis
Y	Total slab width.

Y_e	Effective width of slab
y	Distance of any section from the centroid, OR y - axis
Z	Flange width of the wall.
α, β, γ	Coefficients in continuum connection method
γ_m	Partial safety factor

CHAPTER - THREE

A_w	Cross sectional area of vertical stirrup.
b	Width of a section.
f_{cu}	Cube compressive strength of concrete.
L	Corridor opening.
M_x, M_y, M_{xy}	Moment triad at the centre of element
M^*_x, M^*_y	Design moments in x,y directions respectively.
Q_x, Q_y	Shear forces at the centre of element
s	Spacing of the stirrup
t_f	Thickness of the flange of the wall.
t_w	Thickness of the web of the wall.
v	Shear stress
v_c	Allowable shear stress in concrete.
W	Length of the web of the wall.
w	Displacement in z - direction
$\partial w/\partial x$	Rotation about y - axis
$\partial w/\partial y$	Rotation about x - axis
θ	Angle of the yield line to the x-axis
X	Total slab length.
x,y	Rectangular coordinate system
Y	Total slab width.
Z	Flange width of the wall.

CHAPTER - FOUR

$[B]$	Strain matrix.
$[D]$	Rigidity matrix.
$[D]_c$	Rigidity matrix for cracked concrete.
$[D]_{x,y,z}$	Rigidity matrix in x,y,z space.
E	Young's modulus.
f'_c	Cylinder compressive strength of concrete.
f_{cu}	Cube compressive strength of concrete.
$[F^e]$	Vector of nodal forces.
$[F_u]$	Vector of residual forces
G_0	Initial value of shear modulus
G_s	Secant shear modulus.
I_1	First stress invariant.
I_2	Second stress invariant.
I_3	Third stress invariant.
J_2	Second deviatoric stress invariant.
J_3	Third deviatoric stress invariant.
$[J]$	Jacobian matrix.
K_0	Initial value of bulk modulus
K_s	Secant bulk modulus.
$[K]$	Stiffness matrix.
ℓ,m,n	The direction cosines of a principal stress.
$[N]$	Shape functions.
$[P]$	Body force per unit volume.
$[P_i]$	Total Equivalent nodal forces.
$[P_i]$conc	Equivalent nodal forces contributed by concrete.
$[P_i]$steel	Equivalent nodal forces contributed by steel.
$[q]$	Applied surface tractions.

q,r,θ	Cylindrical coordinate system.
[R]	Rotation matrix; or vector of external nodal forces.
S	Loaded surface area.
[T]	Transformation matrix.
u,v,w	Components of displacement in x, y, z directions respectively.
V	Volume of the structure.
x,y	Rectangular coordinate system
β	Shear retention factor.
γ_{oct}	Octahedral shear strain.
$\gamma_{xy},\gamma_{yz},\gamma_{zx}$	Shear strain components.
ξ, η, ζ	Local coordinate axes.
ϵ_1, ϵ_2, ϵ_3	Principal strains.
ϵ_{oct}	Octahedral normal strain.
ϵ_{od}, ϵ_{oh}	Volumetric strain, deviatoric and hydrostatic
ϵ_{to}	Cracking tensile strain
ϵ_x, ϵ_y, ϵ_z	Components of normal strains.
$[\epsilon]$	Vector of normal and shear strain components.
$[\epsilon_o]$	Vector of initial strains.
ν	Poisson's ratio.
π	Total potential
$\sigma_1,\sigma_2,\sigma_3$	Principal stresses
σ_{int}	Internal stresses.
σ_{oct}	Octahedral normal stresses.
σ_x, σ_y, σ_z	Normal stress components.
$[\sigma]$	Vector of normal and shear stress components.
$[\sigma_0]$	Vector of initial stresses.
τ_{oct}	Octahedral shear stress.

τ_{oc} The value of τ_{oct} at ultimate strength level of concrete for θ = 60 degrees.

τ_{oe} The value of τ_{oct} at ultimate strength level of concrete for θ = 0 degrees.

τ_{of} The value of τ_{oct} at ultimate strength level of concrete for $0 < \theta < 60$ degrees.

CHAPTER - FIVE

f_{cu} Cube compressive strength of concrete.

f_y Yield stress of steel.

LVDT Linear voltage displacement transducer

CHAPTER - SIX

A_s Area of steel reinforcement.

A_{sv} Cross sectional area of vertical stirrup.

b Width of a section.

C_1, C_2 Dimensions of the column.

d Effective depth of slab.

E Young's modulus.

f'_c Cylinder compressive strength of concrete.

f_{cu} Cube compressive strength of concrete.

f_y Yield stress of steel.

f_{yw} Yield strength of web steel.

K_{cr} Cracked section stiffness

K_0 Pre-cracking stiffness

L Corridor opening.

M_f Ultimate flexural capacity of slab section

M_g Moment due to gravity loads.

M_o Experimental unbalanced moment at the onset of steel yielding

t_f	Thickness of the flange of the wall.
t_w	Thickness of the web of the wall.
u	Length of critical shear perimeter.
V_{design}	Design lateral load.
V_d	Design shear strength.
V_{exp}	Experimental failure load
V_g	Ultimate gravity load.
V_w	Amount of lateral (wind) load.
v	Shear stress
v_c	Allowable shear stress in concrete.
W	Length of the web of the wall.
X	Total slab length.
x	Depth of the rectangular stress block, OR x - axis
Y	Total slab width.
y	y - axis
Z	Flange width of the wall.
γ_m	Partial safety factor
γ_f	A fraction of the unbalanced moment transferred by flexure.
ϵ_1, ϵ_2	Measured strains in the wall.
λ	Efficiency of closed vertical stirrups
ρ	Percentage of flexural steel

CHAPTER - SEVEN

A_{cp}	Area of critical cross section for shear punching failure
b	Width of a section.
b_p	Length of the critical Perimeter.
d	Effective depth of slab.

f_{cu}	Cube compressive strength of concrete.
f_y	Yield stress of steel.
J	Property of the critical perimeter analogous to the polar moment of inertia.
L	Corridor opening width.
R_f	Rectangularity factor of the junction
t_f	Thickness of the flange of the wall.
t_w	Thickness of the web of the wall.
V_{cal}	Calculated failure load
V_{design}	Design lateral load.
V_{exp}	Experimental failure load
V_g	Ultimate gravity load.
$V_{L.Y}$	Lateral load at which steel yielding was first observed
V_{theo}	Theoretical failure load
v_c	Allowable shear stress in concrete.
W	Length of the web of the wall.
X	Total slab length.
x	Distance behind flange up to which the critical section extends, OR x - axis
Y	Total slab width.
y	y - axis
Z	Flange width of the wall.
β	Shear retention factor.
ϵ_m	Average of the three principal strains
ϵ_{to}	Cracking tensile strain
σ_x, σ_y, σ_z	Normal stress components.
$\tau_{xy}, \tau_{yz}, \tau_{zx}$	Shear stress components
$[\sigma]$	Vector of normal and shear stress components.

CHAPTER - EIGHT

$[C]$	Material compliance matrix.
d	Distance of the current stress point from the bounding surface along direction of $d\sigma_{ij}$
d_{max}	Value of d at the beginning of the current loading process
$d\epsilon_{kk}$	Volumetric strain increment
$[D]$	Rigidity matrix.
E	Young's modulus
e_{ij}, de_{ij}	Deviatoric strain tensor and its increment
f'_c	Cylinder compressive strength of concrete.
F_{cd}	Shear compaction/dilatancy factor
H	Generalized plastic shear modulus
I_1, dI_1	First stress invariant and its increment.
i,j,k,m	Indices with values 1,2,3 .
J_2	Second deviatoric stress invariant.
J_3	Third deviatoric stress invariant.
K_t, K_0	Tangent bulk modulus and its initial value
S_{ij}	Deviatoric stress tensor.
$\gamma_o, d\gamma_o$	Octahedral shear strain and its increment.
δ_{ij}	Kronecker delta.
$\epsilon_{ij}, d\epsilon_{ij}$	Strain tensor and its increment.
ϵ_{max}	Maximum principal compressive strain ever experienced by the material.
ν	Poisson's ratio.
θ	Angle between projection of positive vector of σ_{ij} and that of any tensile semi-axis on deviatoric plane, OR rotation of the slab relative to the wall

θ_y	Yield rotation i.e. rotation of the slab at the onset of steel yielding
μ_d	Rotational ductility factor (θ/θ_y)
φ	Damping coefficient
$\sigma_{ij}, d\sigma_{ij}$	Stress tensor and its increment
$\tau_o, d\tau_o$	Octahedral shear stress and its increment

CHAPTER ONE

INTRODUCTION

1.1 Shear Wall Structures

A popular form of high rise structure, especially for hotel and apartment use, is a slab–coupled shear wall structure. The reason for this is economy resulting from reduced floor heights and simplified formwork. From the constructional and architectural view points, it is relatively easy to make the final structure aesthetically pleasing.

Figure 1.1(a) shows a pictorial view of a shear wall structure and Figure 1.1(b) shows a typical (idealised) floor plan of an apartment building in which self–contained units are arranged side by side along the length of the building. This arrangement naturally results in parallel assemblies of division walls running perpendicular to the face of the building, with intersecting longitudinal walls along the corridor and facade. The cross–walls are employed not only as division walls but also as load bearing walls. The longitudinal corridor and facade walls are provided with openings for access to the living areas and balconies and for window framing. If they are also designed to be load bearing, these longitudinal walls act effectively as flanges for the primary cross–walls. In addition to its use as structural partition walls, shear walls are used to enclose lift shafts and stair wells to form partially open box structures which act as strong points in the building. Thus, in practice, shear walls of various shapes such as planar, flanged or box–shaped, may be coupled together in cross–wall structures (Figure 1.2).

1.2 Behaviour of Shearwall subjected to Lateral Load

In designing tall buildings, special considerations must be given to provide sufficient stiffness in all directions against lateral loads. The lateral loads may arise due to wind, earthquake or perhaps even blast effect. When subjected to

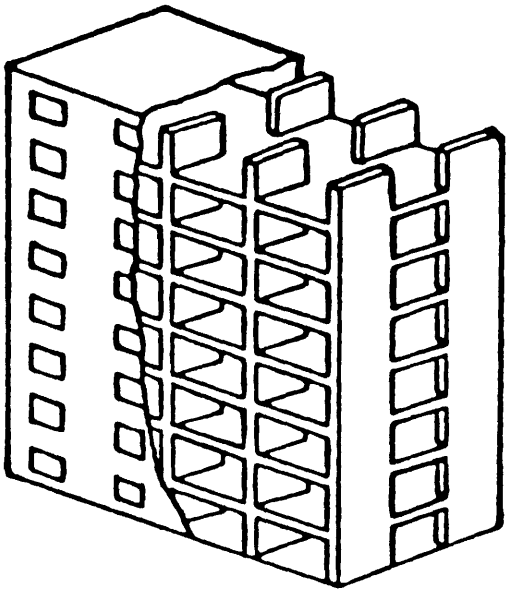

(a) Perspective view of a shear wall building.

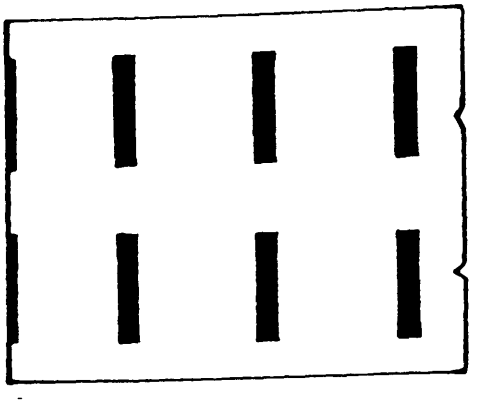

(b) Plan of a typical shear wall building.

Figure (1.1)

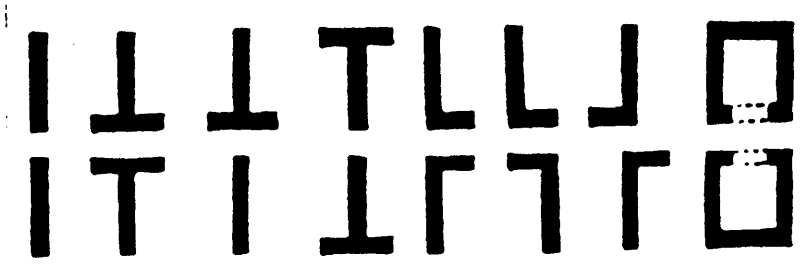

Figure (1.2) : Different wall configurations.

lateral forces, the shear wall is dominated by its flexural behaviour and shearing effects are insignificant. The shear walls resist the lateral loads on the structure by rigid frame action, with floor slabs acting as girders and shear walls acting as columns. Apart from stress considerations, attention has to be given to vibrations and lateral sway of the building to ensure the comfort of the occupants.

1.3 Purpose of This Study

When a shear wall structure is subjected to gravity and lateral loads, substantial bending moment, twisting moment and shear force are transferred at the slab– wall junction. Previous work has been concerned with the study of slab– wall junction when only 'flexural' reinforcement has been used. To the author's knowledge, no information is available on the strength of connection when shear reinforcement is used in addition to 'flexural' reinforcement. During an earthquake, the slab– wall junctions of a shear wall structure will be subjected to repeated reversals of loads. This may lead to a shear failure in the slab around the wall due to degradation of shear strength. There is a lack of information on the behaviour and performance of slab– wall junctions under seismic loading conditions. The object of the work, reported in this thesis are:

a) Conduct an experimental and theoretical study of the influence of shear reinforcement on the strength of slab– wall junction. The basic aim is to develop a general design procedure for the slab– coupled shear wall structures including check for shear strength and design for shear steel using BS 8110 rule. 'Large scale' reinforced concrete models will be tested under monotonic loading to failure. A three dimensional non– linear finite element method is used for theoretical study.

b) Some cyclic load test on models to get more informations on the deformations that may safely occur and the deterioration of load– carrying capacity of wall– slab connections subjected to seismic type loading. Parallel theoretical work will be conducted to investigate the relevance of the current constitutive laws for cyclic loading behaviour of concrete.

CHAPTER TWO

LITERATURE REVIEW

2.1 General

The structural analysis and design of a slab–coupled shear wall system can be conveniently performed using the techniques developed for beam–coupled shear wall systems provided the effective width of the slab can be established. In a coupled–wall system, the stresses are not uniform across the width of the slab. In order to design the slab safely, it is necessary to know the magnitude and distribution of the stresses developed through the coupling action. It is also essential to determine accurately the interactive forces developed at the slab–wall junction.

In this chapter, a brief critical review of previous experimental and analytical research work done in the following fields is given:

a) Analysis of shear wall structures to determine the stresses due to lateral loads

b) Effective stiffness of slabs coupling shear walls

c) Design of slab–wall junction using shear reinforcement

2.2 Analysis of Shear Wall

The analysis of uniform walls pierced with regular sets of similar openings i.e. coupled shear walls, has attracted several investigators. A simplified analysis has been produced by assuming that the discrete system of connections, formed by lintel beams or floor slabs as shown in Figure (2.1), may be replaced by an equivalent continuous medium, as shown in Figure (2.2). By assuming that the axially rigid lintel beams have a point of contraflexure at mid–span, the behaviour of the system can be defined by a single second order differential equation. A general closed form solution of the problem can be obtained.

Using the above simplified approach, Rosman[1] first derived solutions for a wall with one or two symmetric bands of openings, with various conditions of

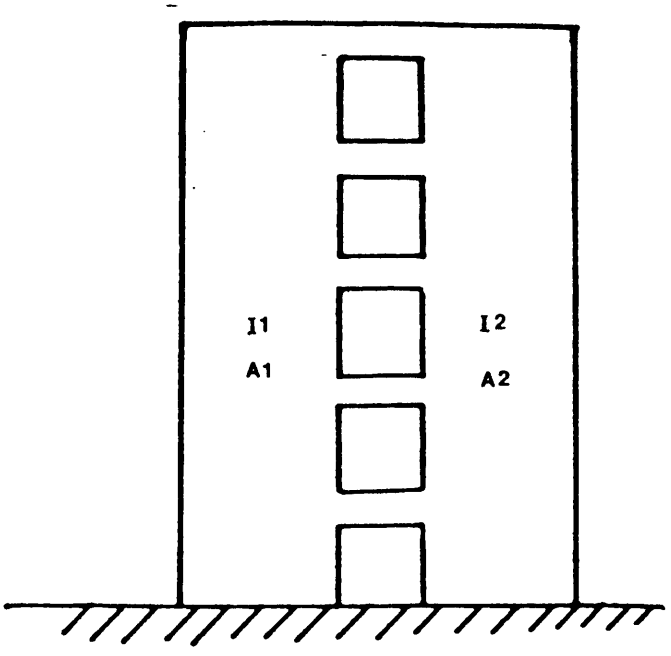

Figure (2.1) : A typical shear wall with openings.

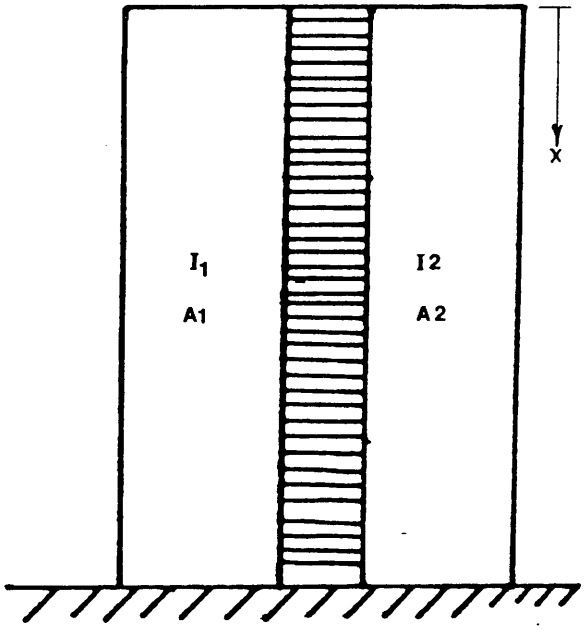

Figure (2.2) : Shear wall with idealized continuous connection of laminae.

support at the lower end (piers on rigid basement, on separate foundations, and on various forms of column supports). Deformations due to bending moment and normal forces in the walls and flexural and shear deformations in the connecting beam were also taken into account. The axial force in the walls was chosen as the statically redundant function. So, if q is the shear force related to the unit length, the axial force in the wall is

$$T = \int_0^x q.dx \qquad (2.1)$$

where x is the abscissa, measured from the top of the wall as shown in Figure (2.2). Making use of certain simplifying assumptions, the governing differential equation takes the form

$$d^2T / dx^2 - \alpha^2 T = - \gamma x \qquad (2.2)$$

A direct mathematical solution of above equation can be obtained for any loading case. Equations (2.3) and (2.4) show the general solutions of above differential equation for the case of concentrated lateral load at the top and uniformly distributed lateral load respectively.

$$T = C_1 \sinh \alpha x - (\gamma / \alpha^2)\, x \qquad (2.3)$$

$$T = C_1 \sinh \alpha x - (2\beta/\alpha^4)(\cosh \alpha x - 1) + (\beta/\alpha^2)\, x^2 \qquad (2.4)$$

The co-efficients α, β and γ depend on the load and the geometrical properties of the shear wall. Once the value of T is known, the shear force and bending moment in the connecting beams can be easily calculated using equilibrium considerations.

2.3 Effective Width of Floor Slabs

The aforementioned theory in section (2.2) is concerned with shear walls interconnected by beams only. The structural analysis and design of a slab-coupled

shear wall system may readily be performed using existing techniques of beam–coupled shear wall structures, provided that the equivalent width of the slab which acts effectively as a wide coupling beam, or its corresponding structural stiffness, can be assessed.

The effective width of slabs coupling walls of different shapes was investigated theoretically by Tso and Mahmoud[2] and Coull and Wong[3]. They[3] produced design curves suitable for use in an engineering office. The curves generally show the variation of the effective slab width or stiffness with different geometrical parameters. Typical nondimensional design curves for the effective width of slab between plane shear walls and T–section coupled walls, are shown in Figure (2.3).

2.4 Design of Slab–Wall Junction

The region of a slab in the vicinity of a support could fail in shear by developing a failure surface in the form of a truncated cone or pyramid. This type of failure, called a 'punching shear failure', is usually the source of collapse of flat slab and slab–coupled shear wall structures. Design of this region of slab is therefore of paramount importance. Comprehensive test data and reliable design criteria exist to estimate shear strength of slabs at interior slab–column junctions loaded by reasonably concentric loads. In contrast, limited experimental results are available regarding shear strength of slabs at exterior column junctions and shear wall junctions. Failures at slab to column connections in the 1964 Alaska, 1967 Venezuela, 1971 San Fernando and 1985 Mexico earthquakes have shown the need for caution in the calculation of shear strength at slab to column connections under cyclic loading condition. In recent years, some form of shear reinforcement is used in the slab to increase the punching shear strength of the connection. But detailed design methods are not available for proportioning shear reinforcement around the slab–column connections where both shear and moment are transferred.

In the following, major publications on the shear strength of slab–column

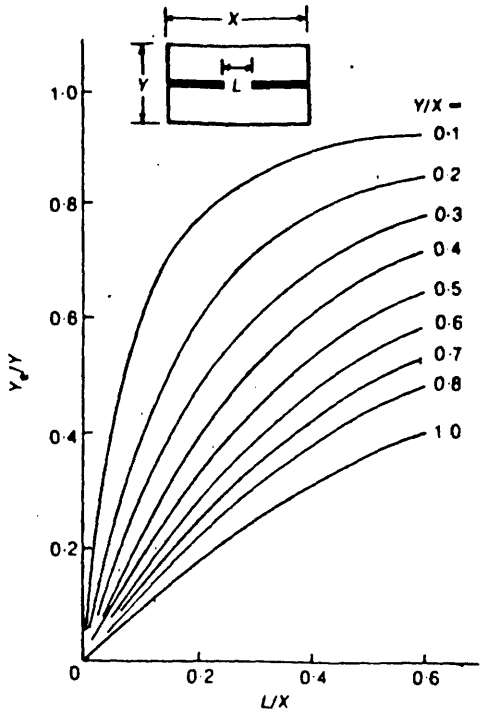

Figure (2.3-a) : Design curves for effective width of slab (planar walls).

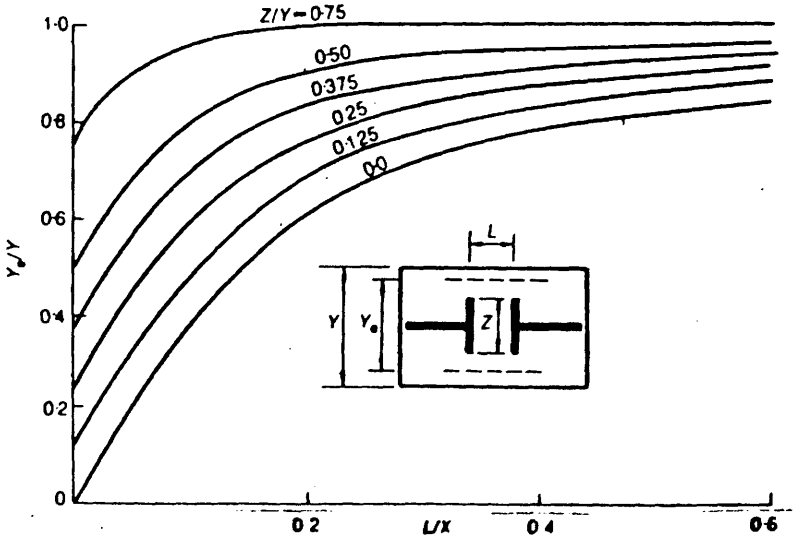

Figure (2.3-b) : Design curves for effective slab width (Flanged wall).

connection with or without shear reinforcement, transferring both shear and moment or shear only to columns will be critically reviewed. This will be followed by an examination of the work on shear wall – slab junction.

2.4.1 Strength of Slab–Column Connections with Shear Reinforcement Transferring Shear only.

A large number of tests have been carried out on slabs with shear reinforcement subjected to shearing action only i.e. when the load is considered to be applied without eccentricity with respect to the critical section of the slab. These tests have led to several semiemperical design procedures. An extensive review of the available data concerning the shearing strength of slabs with shear reinforcement in the form of structural steel sections, bent up bars, stirrups, prefabricated wire cages etc. was made by Hawkins[4]. He concluded that for slabs with properly detailed bent up bars or stirrups and transferring shear only, the shear capacity equals the lesser of the following strengths:

(a) the shear strength for a slab without shear reinforcement calculated on the basis of ACI Code 318–71 for a critical section located d/2 beyond the end of the stirrups or the bend in the bent–up bars, where d is the effective depth of the slab

(b) half the shear capacity for a slab without shear reinforcement for a critical section at a distance d/2 from the column perimeter plus the vertical component of the yield strength of the shear reinforcement intersected by a crack inclined at 45 degrees to the horizontal.

It was apparent from the observed behaviours of tested specimens that adequate anchorage for the shear reinforcement is essential to obtain sufficient ductility. Shear reinforcement, where needed, must extend to a distance of at least 1.5 d from the column perimeter. Bars must be bent down within a distance 0.5 d of the column at an angle not less than 30^0 to the horizontal. The maximum

spacing between vertical stirrups should be 0.5 d.

2.4.2 Shear Strength of Slabs with Moments Transferred to columns.

The state of knowledge about the strength of column–slab connections transferring moments, that increase monotonically to failure, has been summarized by ACI–ASCE Committee 426[5]. Available methods for predicting the ultimate strength of such connections can be divided into four groups :

(1) Analysis based on a linear variation in shear stress,

(2) Analysis based on thin plate theory

(3) Beam analogies, and

(4) Finite Element based procedures

For comparison, a summary of the essential features of the four methods is presented here. Much less research has been done on defining the stiffness of connections transferring moment than on defining their strength. Available information is limited to either elastic definitions of stiffness or the beam type model developed by Hawkins[6].

2.4.2.1 Linear Variation in Shear Stress Methods

The ACI Code 318 and Commentary [7] specify the use of a linear variation in shear stress approach for predicting the limiting shear capacity of connections transferring shear and moment. This procedure was first proposed as a working stress method by Di Stasio and Van Buren[8] in 1960. Figure (2.4) shows the model proposed by them. They divided the resisting mechanism of the connection into two parts. As shown in Figure (2.4– b), one part was an uniform shear field that resisted the shear force. The other part was a linear shear field, Figure (2.4– c), which resisted the torsion part of the applied bending moment. This approach was subsequently utilised by Moe[9], and Hanson and Hanson [10] whose procedure was first incorporated into the ACI Building Code in 1963 and carried over essentially unchanged into ACI Codes 318–71, 318–77 and 318–83.

For an interior slab– to– column connection, as shown in Figure (2.4– a), it is assumed in this approach that around the column periphery, at some distance from it, there exists a pseudo– critical section. ACI Code specifies this critical perimeter at a distance d/2 from the column periphery, where d is the effective depth of the slab. The resultant forces acting on this perimeter is due to the axial force and bending moment in column. The axial force, V, is transmitted to the column by uniform shear along the perimeter as shown in Figure (2.4– b). The resultant moment , M, in column is transferred partly by bending of slab (normal frame action) and partly by linear shear stress distribution (torsion) at the perimeter as shown in Figure (2.4– c). Therefore, the maximum shear stress according to Figure (2.4– d) will be

$$v_{AB} = v_{shear} + v_{torsion}$$
$$= V/A_{cp} + K.M\ C_{AB}/J \qquad (2.5)$$

where A_{cp} = area of the critical perimeter

J = a property of the critical perimeter analogous to the polar moment of inertia.

K.M = is the fraction of the total moment, M, transferred by torsion, and

C_{AB} = is the distance from the centre of rotation to the section AB.

ACI Code 318– 83 specifies that the fraction , K, of the total moment M, transferred by shear across the critical perimeter is given by

$$K = 1 - \frac{1}{1 + 2/3\ \sqrt{(C_1 + d)/(C_2 + d)}} \qquad (2.6)$$

where C_1, C_2 = dimensions of the column as shown in Figure 2.4.

The remaining fraction of unbalanced moment (1– K).M must be transferred by reinforcement within lines 1.5h, where h is the slab thickness on either side of the column. For ACI Code 318– 83 the maximum value of shear stress is limited to

$$v_c = 0.17(1+2/R_{\varrho s})\ \sqrt{f_{cu}}\ N/mm^2 \qquad (2.7)$$

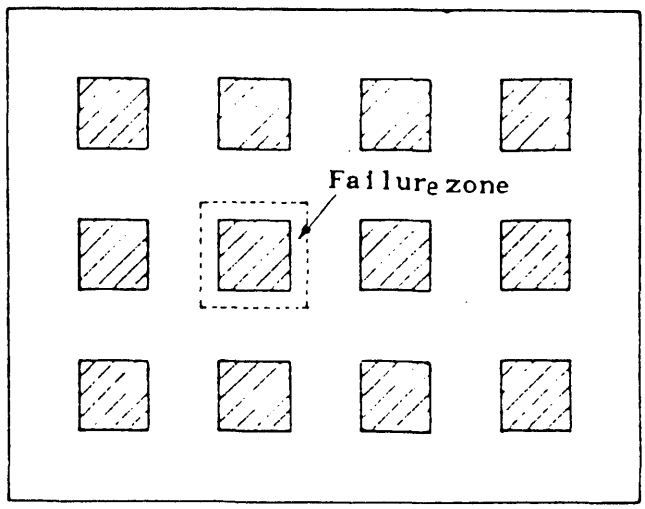

(a) Plan of a typical flat-slab column structure

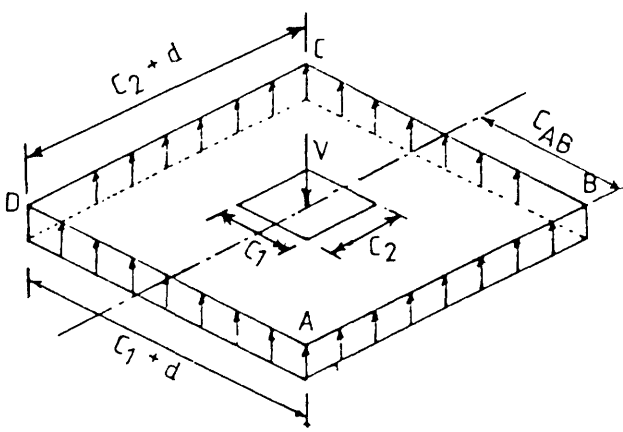

(b) Uniform shear stress due to axial force, V

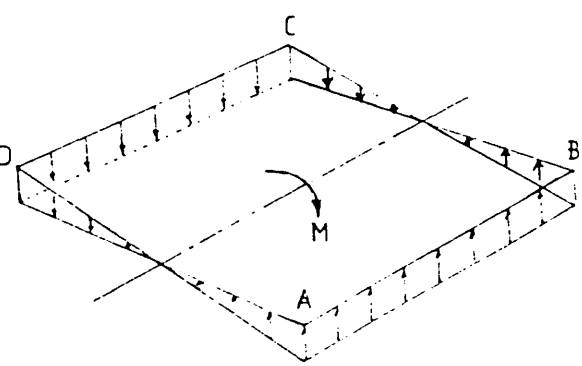

(c) shear stress (torsional) due to applied bending moment, M

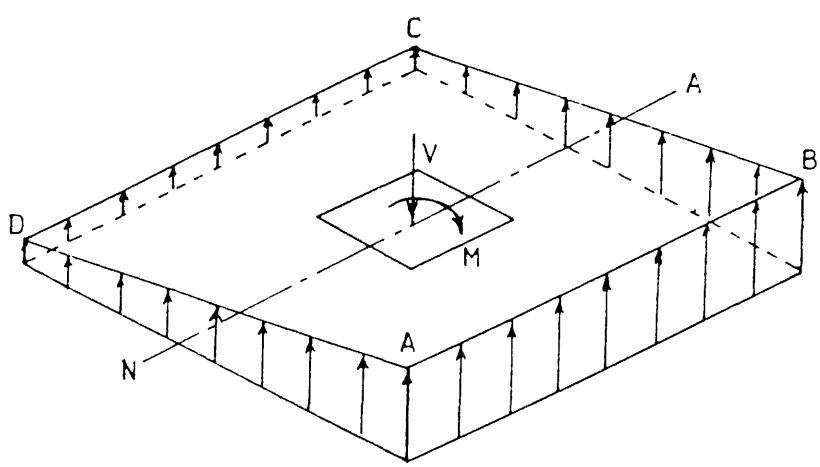

(d) Net shear stress around the critical perimeter

Figure (2.4) : Theory of linear variation in shear stress.

but not greater than 0.33 $\sqrt{f_{cu}}$ N/mm^2. $R_{\ell s}$ is the ratio of long side to short side of a rectangular column and f_{cu} is the cube crushing strength of concrete.

The moment–shear interaction relationship predicted by the ACI Code procedure is shown in Figure (2.5) for an interior column connection. Ordinate, V/V_o, are ratios of the direct shear transferred to the column to the capacity of the section for shear transfer only. Abscissa, $K.M/M_o$, are ratios of the moment transferred by shear to the same capacity for moment transfer only. V_o and M_o are calculated from equations (2.8) :

$$V_o = v_c.A_{cp} \qquad (2.8-a)$$

$$M_o = v_c.J/C_{AB} \qquad (2.8-b)$$

Line ab on Figure (2.5) represents the condition for which the maximum shear stress is limited to v_c. Diagrams on Figure (2.5) indicate idealized shear stress distributions for different points along line ab. Line cd represents the possible limitation imposed by the flexural reinforcement which must transfer the moment $(1 - K).M$.

The geometric properties of the connection and the concrete strength are the factors dictating the position of the line ab. The amount of reinforcement within lines 1.5h either side of the column affects only the position of line cd. Test results [5] indicate a behaviour not far from that idealization. Hawkins et. el.[6] have shown that measured ultimate shear strengths of the specimens, when converted to the shear stress lie along curve such as amn, for a 21 N/mm^2 (3000 psi) concrete. That curve lies progressively further outside the envelope acd as the reinforcement ratio within lines 1.5h either side of the column increases above 0.8%. The reverse is true as ratios decrease below 0.8%.

Regan[11] proposed a simple modified linear shear stress approach which was incorporated in the British Code CP 110[12] and carried over with slight modification into BS 8110[13]. The British Code BS 8110 specifies the critical

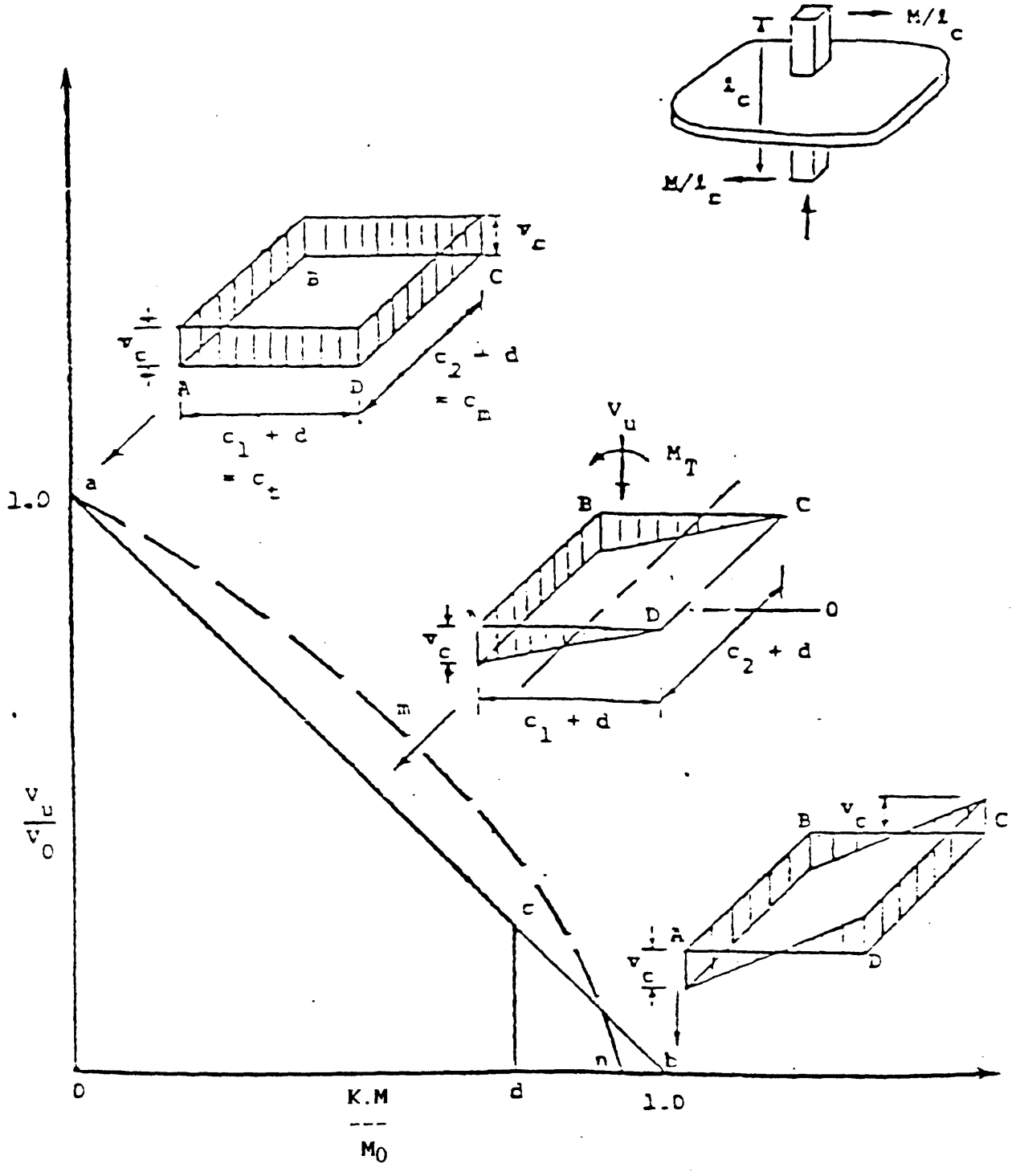

Figure (2.5) : Moment-shear Interaction Relationship for Interior Column connection

section at a distance 1.5d from the column perimeter and it has square corners whether the column is square or circular. The treatment of moment transfer accounted in this code is also different from that in ACI Code. The bending moment is assumed to be carried entirely by uneven shear along the critical perimeter. In the presence of unbalanced moment, M, the effective shear stress at the critical perimeter of internal column connection is taken as:

$$v_{eff} = (V/A_{cp}) \left(1 + \frac{1.5\ M}{V\ X_1} \right) \qquad (2.9)$$

where X_1 is the length of the side of perimeter considered parallel to the axis of bending. According to Figure (2.4) X_1 is equal to $(C_2 + 3d)$. The maximum value of shear stress for British Code BS 8110 is limited to

$$v_c = 0.27(f_{cu})^{1/3}(100As/bd)^{1/3}(400/d)^{1/4} / \gamma_m \qquad (2.10)$$

where values of (100As/bd) are calculated for widths equal to those of the column plus 1.5d of slab to either side of it. Further $0.15 \leq (100As/bd) \leq 3.0$ and $(400/d) \geq 1$ and γ_m is the partial factor of safety. For the purpose of making comparisons between the shear strengths predicted by Codes of practice, equations (2.5) and (2.9) can be written in the form of design equations as follows:

$$V_{d,ACI} = v_c . A_{cp} / \left[1 + M/Vd \left(\frac{K . C_{AB} . A_{cp} . d}{J} \right) \right] \qquad (2.11)$$

$$V_{d,BS} = v_c . A_{cp} / \left[1 + M/Vd \left(\frac{1.5\ d}{X_1} \right) \right] \qquad (2.12)$$

where permissible maximum shear stress, v_c, is given by equation (2.7) for ACI Code and by equation (2.10) for British Code. Although the design equations look different from one another, the shear strength predictions is not widely different as is evident from Figures (2.15) to (2.28). The maximum variation from one another

is within 15%. The effect of various parameters e.g. C_1/C_2 ratio (i.e. ratio of side lengths of column) , C/d ratio (i.e. ratio of side length of column to the effective depth of slab), M/Vd ratio , compressive strength of concrete, percentage of flexural steel etc. on ultimate shear strength predicted by above design equations will be discussed in details in section 2.4.4.

2.4.2.2 Thin Plate Methods

Methods of analysis based on elastic thin plate theory have been proposed by Mast et al[14,15]. While such approaches assume linear behaviour, they allow also consideration of the effects of dimensions and boundary conditions for the plate as well as different aspect ratio for the column. The loading and boundary conditions of the flat plate used by Mast is shown in Figure (2.6). Shear and moment distribution predicted for the above plate at a section 0.05 L, where L is the span, are compared in Figure (2.7) with the distributions appropriate for equation (2.5). Mast's distribution both transverse and parallel to the direction of the applied moment, are markedly non−linear. One can see that the flexural moments M_x are much higher as calculated from equation (2.5) than given by thin plate method and the contribution of the torsional moments M_{yx} is underestimated by the straight−line shear distribution hypothesis (where the combined effect of q_y and M_{yx} is only shown in Figure 2.7−a).

Mast found that in contrast, to the assumptions made in the ACI Code 318−71 formulation, the relative participation of the torsional, flexural and shear stresses to moment transfer varied with the shape and size of the column and the dimensions and boundary conditions for the plate. He also found that the stresses computed by his theory and the values predicted by equation (2.5) was in good agreement for columns in which the C_2 face, transverse to the direction of the applied moment, was wider than the C_1 face, parallel to the direction of moment. The stresses were in poor agreement for columns in which the C_1 face was wider than C_2.

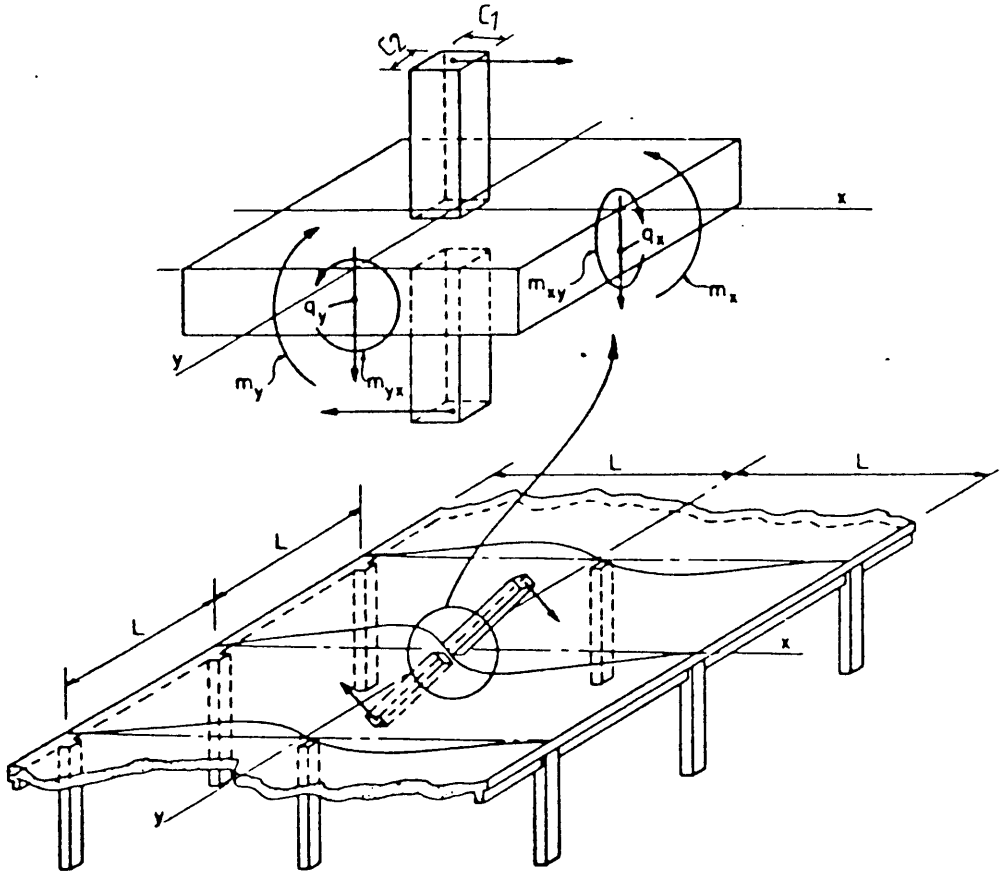

Figure (2.6) : Loading and boundary conditions for flat plate.

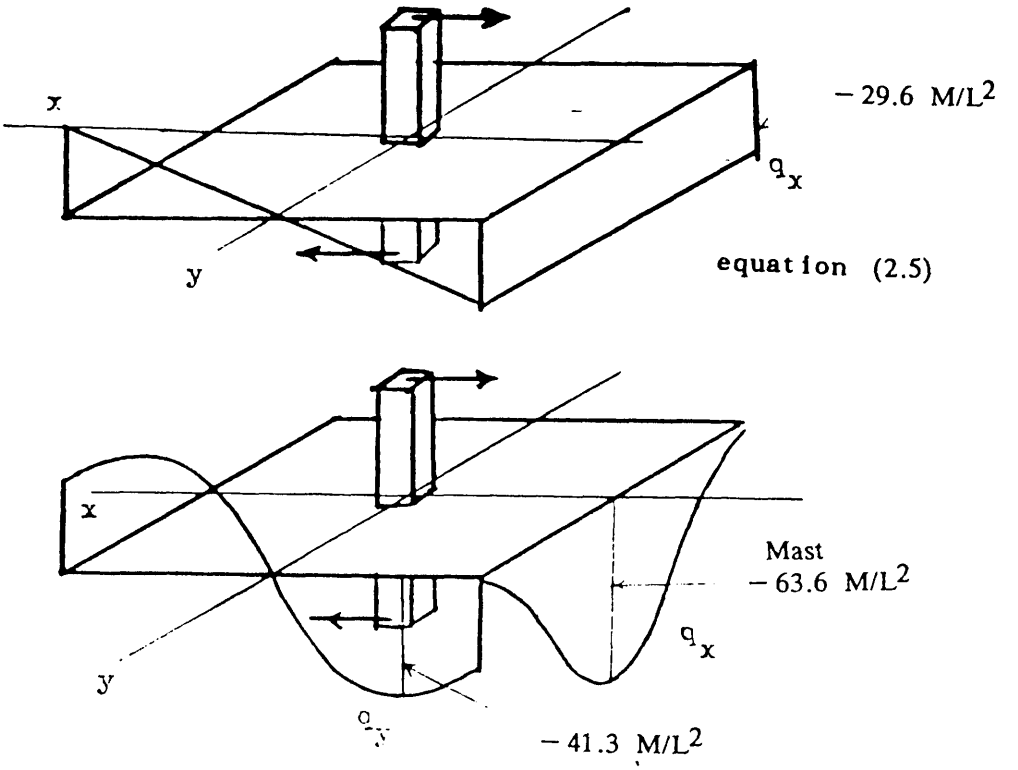

(a) Distribution of shear forcees.

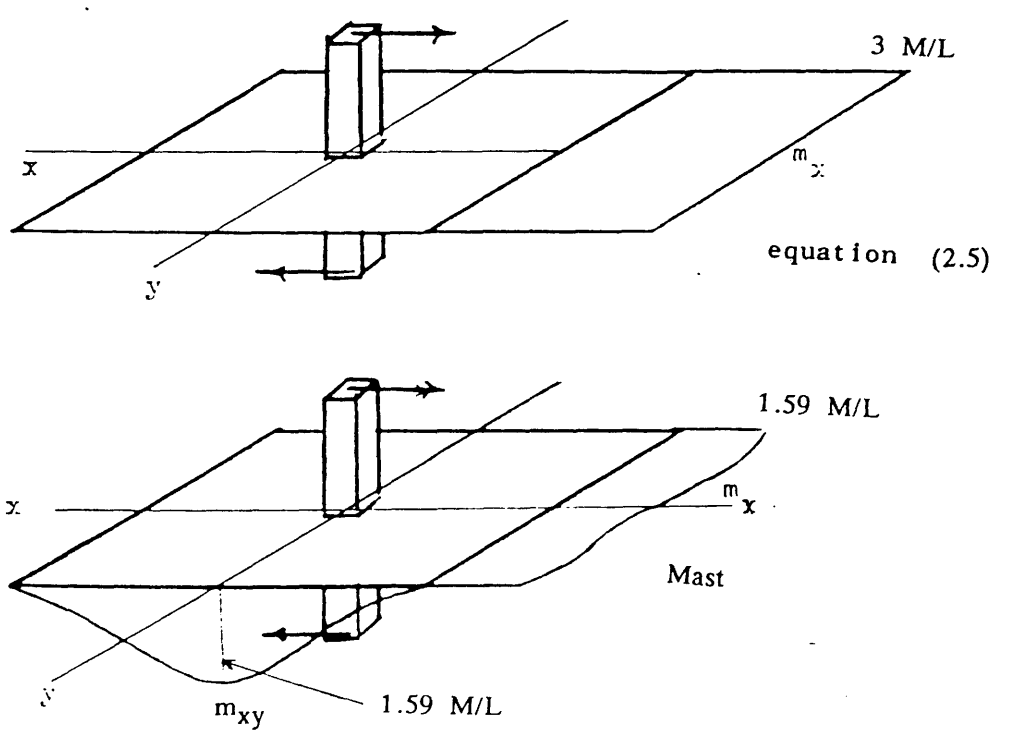

(b) Distribution of moments.

Figure (2.7) : Comparison between the linear distribution and the elastic theory[14,15] at a section 0.05 L from the centre of an interior column (L is the span).

Long [16,17] developed an elastic–partially plastic method of analysis. They idealized the problem as an axi–symmetric slab–column specimen spanning between lines of contraflexure and having a column radius equal to 0.6 times the side length of a square column. Radial and tangential moments for moment transfer were obtained by superposing solutions for shear loading only and moment loading only. Account was taken of the changes in moment caused by cracking around the column perimeter. Stresses computed from these moments were limited to appropriate ultimate values. There were three governing criteria. First, the stress in the compression zone adjacent to the column could reach the strength of the concrete in biaxial compression prior to yielding of the reinforcement. Second, shear effects could cause the octahedral stress on an inclined plane passing through the slab–column junction to reach the limiting stress predicted by an octahedral stress criterion for failure[18]. This limiting stress could be reached prior to or after the radial moment reached its yield value. Third, the strength could be governed by failure of the concrete in biaxial compression after both the radial and tangential moments reached their yield values. Correction factors were applied for support conditions and dowel effects. Their procedure gave good predictions of the strengths measured by Moe[10] and poorer agreement with the strengths measured by Hanson and Hanson[11]. He attributed the lack of agreement in the later case to differences in boundary conditions for the test specimens and the analytical model.

In his study, Yamazaki[19] used an incremental procedure to extend finite element plate bending analysis into the inelastic range. He concluded that capacities of slab–column connections transferring moment could not be determined by extrapolating results predicted by elastic finite element analysis. Because, in the inelastic range, there is considerable redistribution of moments and shears between the column faces as the stiffness of each face changes with loading. He found that the ACI 318–71 procedure provides a realistic measure of shear stresses on the front column face but underestimates shear stress on the side column face. He also

found significant influences on ultimate capacity of the twisting moment and of bond slip of the reinforcing bars passing through the column.

The nature of the punching failure in slabs does not require the flexural capacity of the slabs to be exhausted. In other words, complete redistribution of stresses in the slab in the post-elastic stage may not occur prior to punching. This means that adopting the elastic theory to estimate punching failure load may not be unreasonable.

2.4.2.3 Beam Analogy

In ACI Code, it is assumed that moment is transferred to a column by a combination of flexure and torsion and shear stresses at the column interface. The ACI method ignores the influence of slab reinforcements at the side faces but compensates for this by making the width of the slab effective for moment transfer, $(C_1 + 3h)$, greater than that for shear transfer, $(C_1 + d)$. Kanoh[20], for example, showed in his tests that the moment which can be transferred by torsion, when converted into a torsional shear stress by the full plastic formula, equals about 9.8 N/mm^2 (1400 psi). This means that the ultimate torsional shear stress of slabs tested in that manner is much larger than that specified by ACI 318-71 Code for beams which ranges from 2 to 5 N/mm^2 (280 to 700 psi). The main difference between the ACI Code method and beam analogies exists in the treatment of torsional effects at the side faces of column. Many investigators have proposed beam type analogies to predict the strength of connections transferring moments. The accuracy of such procedures is improved as the number of test results is increased. In general, it has been found that beam analogies give better agreement with test data than the ACI Code method. Further, beam analogies predict that for all conditions, the capacity of a connection can be increased up to a certain point, by increasing the reinforcement ratio in the region of the connection. Such an approach is very useful to a designer who might otherwise be forced to alter the geometry of his structure.

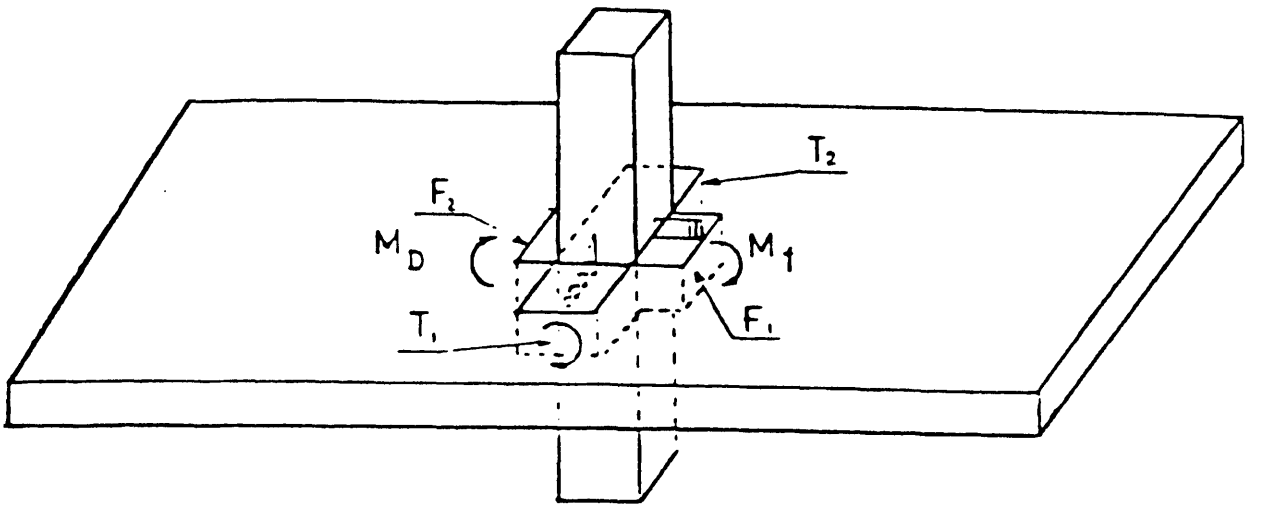

(a) general view.

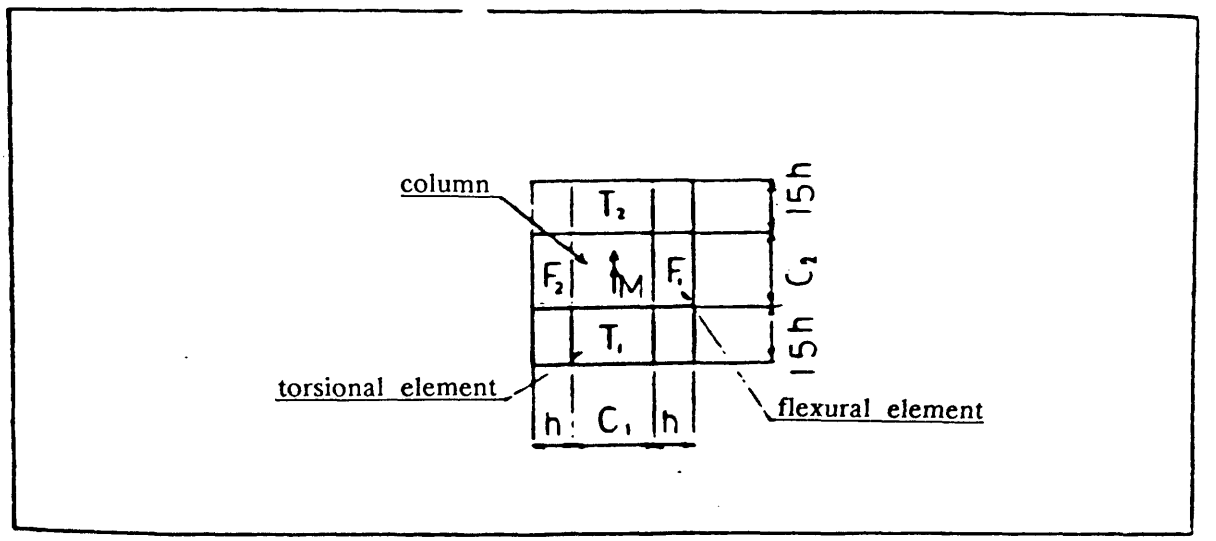

(b) Plan view.

Fig (2.8) : Stiffness model for interior column connection.

The analogy proposed by Hawkins[21] for interior column connection is shown in Figure (2.8). The slab is assumed to be attached to the column through front and back flexural beams F_1 and F_2 and side face torsional beams T_1 and T_2. Each beam is presumed capable of developing at its junction with the column the ultimate bending moment, torque and shear forces and the combinations of these quantities predicted by the ACI Code. The ultimate strength combinations of the model are based on a limiting value of $0.67\sqrt{f_{cu}}$ in N/mm^2 for the maximum torsional stress that can be applied without shear and the limiting value of $0.83\sqrt{f_{cu}}$ in N/mm^2 for the maximum shear stress that can be provided without torsion. In the analysis of a given slab–column connection using the strength equations, it is assumed that some redistribution of actions between critical faces can occur. For the case of an interior slab–column connection transferring unbalanced bending moment in one direction, the suggested beam analogy[21] results in the eight possible limiting strength combinations shown in Figure (2.9–a). These various combinations arise because of the possibility that the deformations at failure are insufficient to permit the simultaneous development of the ultimate capacities of all beam sections. Two possible modes of failures were considered. The first "moment–torsion" involves failure on all four column faces. This mode places a limit on the moment transferred to the column rather than limiting the shear. The ultimate torsional strength is reached on side faces AC and BD at the same time the flexural strength is reached on faces AB and CD (cases 1, 2 and 3). The second mode, referred to as 'shear–torsion' requires failure on three faces only. This mode dominates when the shear transferred is significant. For moderate values of shear the ultimate torsional strength is reached on the side faces and the ultimate shear strength on face AB (cases 4 , 5 and 6). For high shears the ultimate shear strength is also reached on the face CD (cases 7 and 8). For an edge connection transferring unbalanced bending moment in one direction, the number of possible limiting strength combinations is two, as shown in Figure (2.9–b). For a corner connection transferring unbalanced bending moment in two

directions, the number of possible limiting strength combinations is three, as shown in Figure (2.9– c). For the limiting combinations shown in Figures (2.9) the arrows indicate development of the limiting capacity in bending, shear or combined shear and torsion. Where moments or shears are not indicated on a given face, their values are taken as those required for static equillibrium of the applied forces on the connection.

The eight possible limiting strength combinations shown in Figure (2.9– a) for interior connections makes the application of that procedure relatively difficult because of the large number of failure cases to be considered. A simpler beam analogy has been developed by Park and Islam[22]. They, in fact, assumed that, case 6 of Figure (2.9– a) is the critical limiting case. That assumption provides a lower bound to the moment capacity and presumes considerable ductility in bending, torsion and shear. In the case of connections with shear reinforcement it was shown by Hawkins[21] that if the total shear strength is assumed to be made from concrete and shear steel, then the contribution from concrete is only half its theoretically calculated strength. Park and Islam[22] also allowed 50% reduction in accordance with the previous findings in the concrete shear resisting mechanism to the strength of slab– column connections with shear reinforcement. The unbalanced moment strengths calculated by this simplified beam analogy have been shown to be 33% conservative when compared with test results[22]. Better agreement (5% conservatism) was reported when 50% reduction in the concrete shear resisting mechanism was ignored.

2.4.2.4 Finite Element Based Procedures

The strength of slab– column connections can be more accurately assessed by finite element procedure. A two dimensional plate bending layered finite element computer program was used by Memon[23] to analyse elongated edge column– slab connection. The predicted ultimate loads were in general higher than the experimental load. Later, Elnounu[24] developed a three dimensional finite element

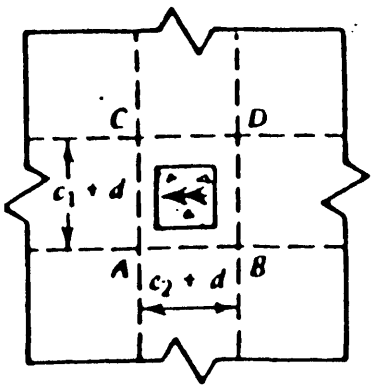

Plan of connection

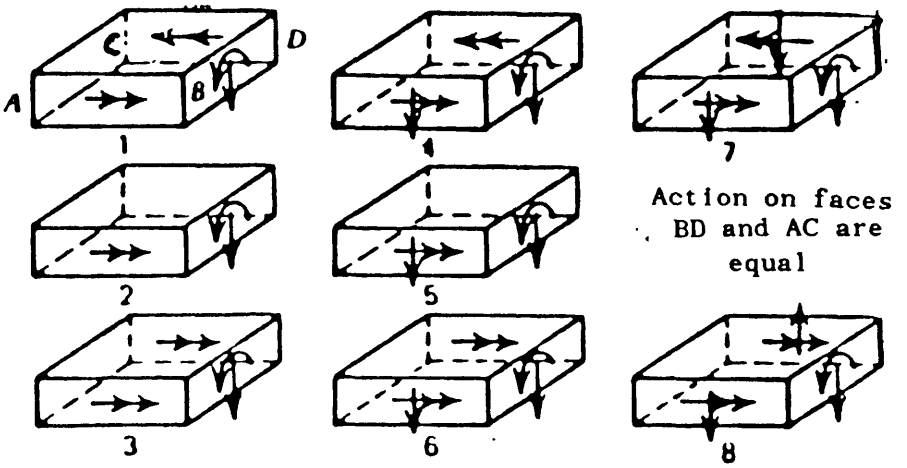

Failure conditions at faces AB, BD, CD and AC

Cases 1,4,7 low M/V ratio, cases 3,6,8 high M/V ratio
cases 1,2,3 likely for low ρ and high c/d, cases 7,8 likely for high ρ and low c/d.

(a)

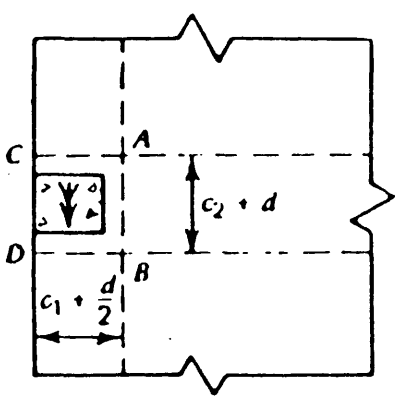

Plan of connection

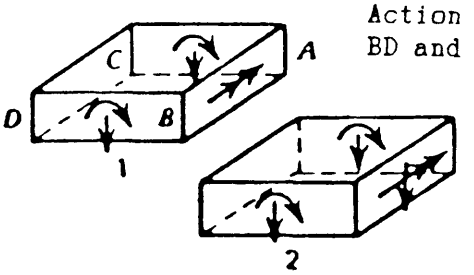

Action on faces
BD and AC are equal

Failure conditions at faces AB, BD and AD.

(b)

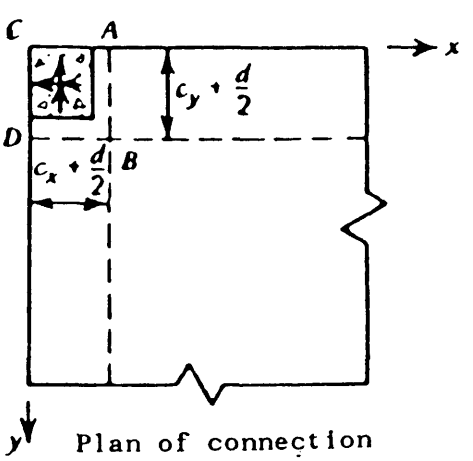

Plan of connection

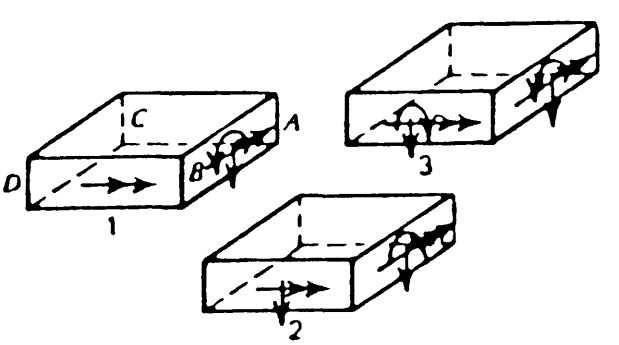

Failure conditions at faces AB and BD.

(c)

Note : Arrows indicate development of limiting capacity : shear↓, torsion↺, bending↠.

Figure (2.9) : Limiting strength combinations for beam analogy for slab-column connections. (a) Interior connection. (b) Edge connection. (c) Corner connection

method for nonlinear stress analysis of reinforced concrete structures. The computer programme was used to predict the ultimate loads of rectangular and flanged shear wall– floor slab connections with or without shear reinforcement. The results showed good agreement with the experimental values. The detailed description of the finite element method will be given in chapter four.

2.4.2.5 Summary

From the sub– sections of 2.4.2, it appears that extensive work has been done to study the transfer of moments and shears from flat slabs to columns. Basically, three methods to estimate the strength of the slab– column connections were used, viz. theory of linear variation in shear stress, elastic theory of plates, and beam analogies. Although empirical, the first method (ie., theory of linear variation in shear stress) was of wider acceptability for practical design purposes. This is reflected in the recommendations of the current codes of practice. Although the other two methods were implemented by some investigators, they lead to rather difficult design equations. Due to the development of the high– speed digital computers, finite element method is also used in the analysis/design of slab– column connections.

2.4.3 Design of Flat Slabs for Punching Shear Using Shear Reinforcement

When the punching resistance of a given connection is inadequate, the design can be improved in the following ways :

(1) *By increasing the concrete strength.*

The codes of practice assume that punching resistance is equal to the nth root of concrete strength. BS 8110, ACI and CEB assume that n = 1/3, 1/2 and 2/3 respectively. Further BS 8110 limits $f_{cu} \geq 40$ N/mm^2. Figures (2.24) to (2.27) show the effect of variation of concrete strength on punching shear resistance.

(2) *By increasing the quantity of flexural reinforcement*

Flexural reinforcement influence punching resistance in so many ways. An increase of flexural steel increases the depth of the compression zone and thus the area of uncracked concrete available to support shear. It reduces the widths of cracks, thus improving the transfer of forces by aggregate interlock, and also provides an increased dowel action. Viewed in terms of a failure mechanism involving a vertical displacement at an inclined fracture surface, an increase of reinforcement enhances the restraint available in the plane of the slab.

(3) *By increasing the effective size of the column*, either by enlarging the whole column or by adding a capital.

(4) *By increasing the thickness of the slab*, either throughout the panels in question or locally by the introduction of a drop panel.

(5) *By providing shear reinforcement*.

In many circumstances, the use of shear reinforcement is the most attractive solution. If shear reinforcement is placed in the slab, apart from flexural failure, the following modes of failure shown in Figure (2.10) are possible :

(a) Punching on a surface crossed by shear reinforcement.

(b) Punching outside the reinforced zone.

(c) Punching between the innermost reinforcement and the column faces.

(d) Wide– beam shear failure.

Numerous tests have been carried out to evaluate the punching shear strength of slabs where the moment transfer is zero. In recent years, a significant amount of test data has also become available for the case where both shear and moment are transferred. Shear reinforcement in the form of stirrups, bent– up bars, shear combs or structural shearhead etc., has been used in the slab to avoid punching shear failure and to increase the ductility of the connection. Several theories have been put forward to predict the strengths observed in these tests.

Islam and Park[25,26] conducted tests on eight half– scale models of reinforced concrete interior flat plate square column specimens under combined gravity and seismic type loading. Shear reinforcement and slow cyclic loading were considered in some of the models. The test specimens were designed to assess the effect of various types of shear reinforcement on the strength and ductility of slab–column connections in the presence of shear and unbalanced moment. They reported that slab–column connections without any shear reinforcement had little ductility, and failure occured suddenly by diagonal tension cracking and splitting on the top of the slab along the bars on the critical side of the column. The use of closed stirrups resulted in a more ductile behaviour at large deflections when bent up bars or structural steel shearheads[25] were used as shear reinforcement. The success of the closed stirrups in producing a relatively ductile connection can be attributed not only to the stirrups providing torsional and flexural shear resistance at large deformations, but also to the stirrups holding the top and bottom slab reinforcement together in the vicinity of the column. This holding action prevented the top slab bars from splitting off the cover concrete, and prevented the slab from moving down the column on the critical side. They concluded[26] that the ACI 318–71 approach for strength of slab column connections without shear reinforcement is safe but in some cases it is extremely conservative, and that a better indication of the strength may be obtained from the beam analogy[22] proposed by them.

Rangan and Hall[27,28] carried out tests on four half scale models of edge panels of a flat plate floor. In a recent paper[29], with the aid of a physical model, Rangan explained the behaviour of the slab and the punching shear failure mechanism. A punching shear failure is initiated either by the failure of the slab at the side face of the critical section in combined torsion and shear or by the failure of the slab at the front face (and the back face if any) in shear (cases 4 to 8 in Figure (2.9–a). Based on the observations obtained from tests, Rangan derived expressions for the calculation of punching shear strength of reinforced

concrete slabs in the presence of an unbalanced bending moment. The expressions cover flat plate floors with or without edge beams as well as slabs with or without shear reinforcement. The following recommendations were made by him[29] for the design of slabs without edge beams against punching shear failure. The equations suggested by him are arranged in the form of design equations.

a. Where unbalanced moment, M, transferred to the column centre is zero (see Figure 2.4), the design shear strength is taken as

$$V_d = 0.7\ v_c\ A_{cp} \qquad (2.13)$$

where v_c is defined in equation (2.7) and

A_{cp} is the area of critical perimeter at a distance d/2 from the column face.

b. Where there are no beams at the side faces of the column parallel to the direction of M and where M is less than or equal to M_o, given by equation (2.15), the moment transfer is considered to be adequate. The design shear strength in this case shall be taken as

$$V_d = 0.7\ v_c\ A_{cp} / \left[\ 1 + M/Vd\ \left(\frac{u}{8\ b_1}\right)\right] \qquad (2.14)$$

$$M_o = 8\ d\ (\ b_1/u\ )\ (\ 0.7\ v_c\ A_{cp} - V\ ) \qquad (2.15)$$

where V = shear force transferred to the column centre

u = length of critical shear perimeter,
= $2(C_1 + C_2 + 2d)$ (See Figure 2.4)

b_1 = width of critical perimeter measured parallel to the direction of M.
= $(C_1 + d)$

c. When M is greater than M_o, the moment transfer is considered to be large and the slab width equal to b_1, shall be provided with shear reinforcement.

d. Where shear reinforcements are required, they recommended closed ties as shear reinforcement and the spacing, s, of closed ties shall not exceed the

lesser of h and 300 mm, where h is the thickness of the slab.

The punching shear strength predicted by the above design equations were compared with 88 available test results of slabs containing corner, edge and interior columns. The average ratio of test strength to calculated strength was 1.60, with a coefficient of variation of 25 percent. The design equations appear to be rather over-conservative. The reasons put forward by him[29] for the conservative predictions are some factors such as, average ratio of tensile reinforcement provided in the slab, depth of slab, boundary restraint and size of the column etc. which have not been taken into consideration in the design equation (2.14)

After testing 40 concrete slabs containing corner, edge and interior columns with the object of investigating the interaction of shear and unbalanced moment at the slab-column connection, Regan[30] proposed an approach to calculate the punching shear stresses referred to a realistic failure surface. Although emperical, the proposed treatment of punching differs from that of current codes of practice in that the area of concrete by which the punching force is divided to give a nominal stress is approximately that of the true failure surface and not the product of the slab depth and a notional 'critical perimeter'. Figure (2.11) illustrates the surfaces considered and gives expressions for the surface area, A_{cp}, in common circumstances.

At an internal slab-column connection subjected to eccentric loading, the punching strength in a dense concrete slab without shear reinforcement in the form of design equation is[30] :

$$V_d = v_c A_{cp} / \left[1 + M/Vd \left(\frac{1.5\ d}{\sqrt{(C_1+2d)\ (C_2+2d)}} \right) \right] \qquad (2.16)$$

where,

$$v_c = 0.13\ K_{sc}\ (f_{cu})^{1/3}\ (100As/bd)^{1/3}\ (300/d)^{1/4} \qquad (2.17)$$

$$K_{sc} = 1.15\ \ (4\pi \times \text{Column area}) / (\text{Column perimeter})^2$$

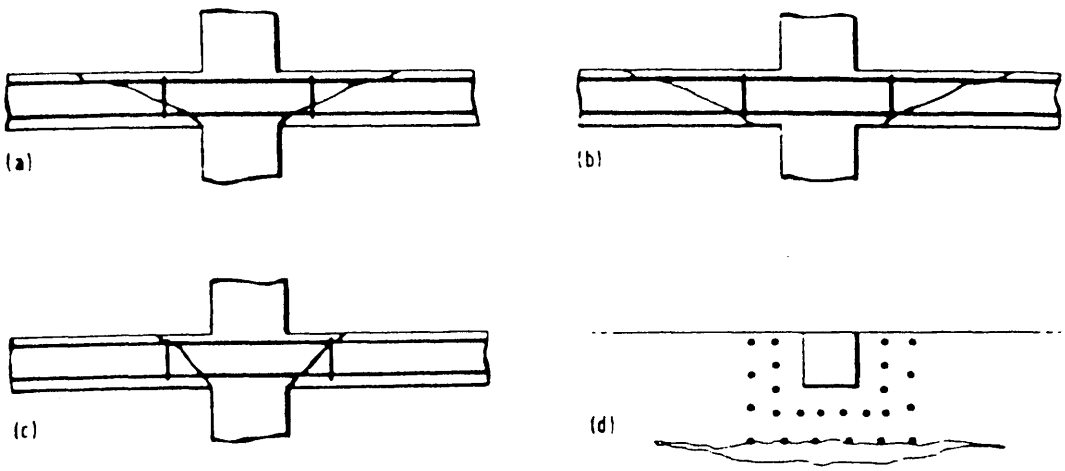

Figure (2.10) : Possible modes of shear failures for slabs with shear reinforcement.

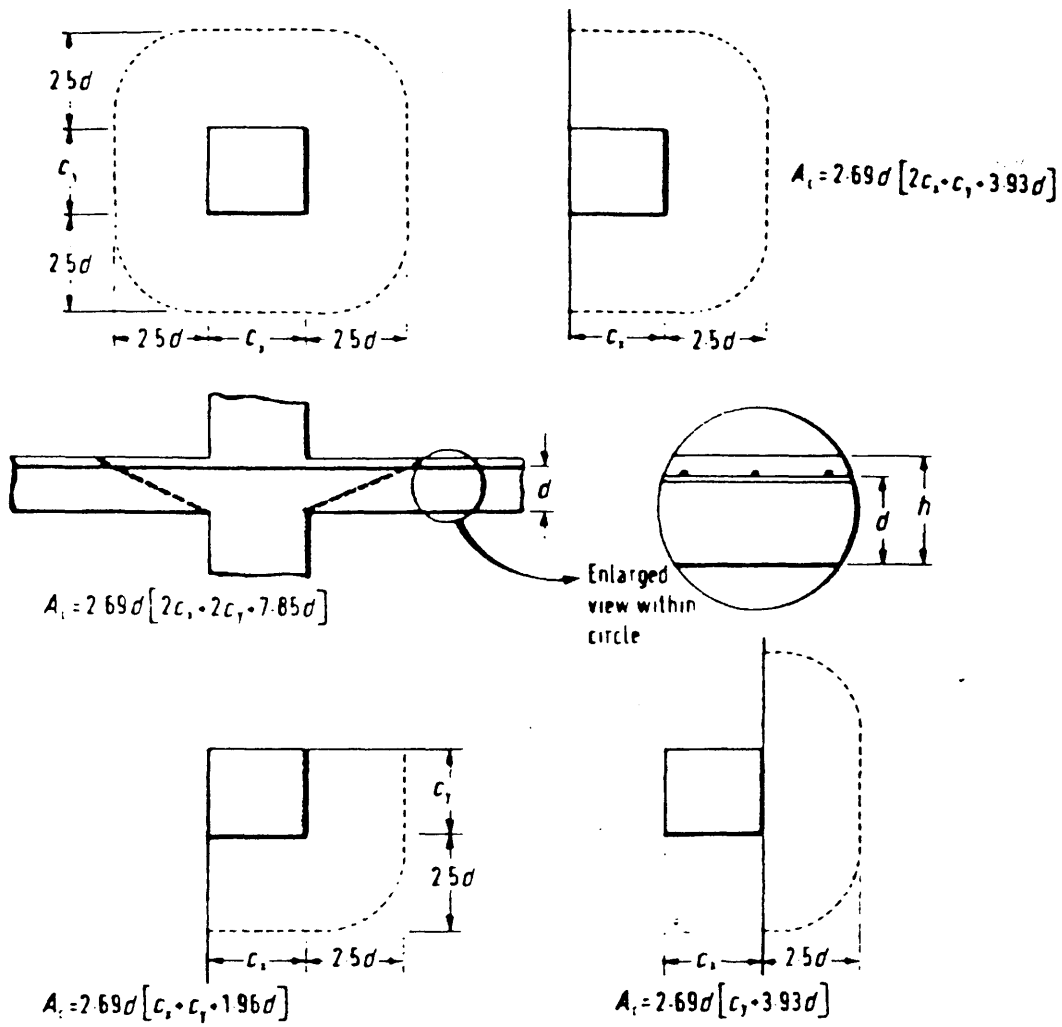

Figure (2.11) : Concrete areas used in punching calculation [29]

He considered the eccentricity of load (M/V) in both x and y directions in equation (2.16). At edge and corner columns, the design ultimate punching resistance was approximated by the following equations:

$$V_{d,edge} = v_c A_{cp} / [\ 1.25 + M/Vd\ (\frac{1.5\ d}{(C + 2d)})] \qquad (2.18)$$

$$V_{d,corner} = 0.8\ v_c\ A_{cp} \qquad (2.19)$$

where the appropriate A_{cp} values are as indicated by Figure (2.11), and values of (100As/bd) are calculated for widths equal to those of the columns plus 2.5d of slab at each face. e and C refer to the load eccentricity and column width parallel to the slab edge.

Figure (2.12) shows a comparison between calculated punching strength and relevent test data from his work[30] and other published results for internal slab–column connections under concentric load. It can be seen from Figure (2.12) that the expression proposed for concentric loading is practically a lower bound to the test results. Figure (2.13) presents a comparison between equation (2.16) and test results from the CIRIA work and other published results for slabs with overall depths in the range 75 to 175 mm. The agreement between the predicted punching strength and experimental failure load is fairly good.

A relatively new form of shear reinforcement, known as "shear combs", is used to increase the punching resistance of reinforced concrete slabs. The commonest sort of comb is a unit of reinforcement comprising a number of vertical studs anchored at one end by enlarged heads and at the other by welded connections to a common 'rail' or steel plate. The units are arranged around a column, frequently in a radial pattern.

The first use of individual bar shear reinforcement with end anchorage was reported by Ghali[31] who made tests on slab–column connections with the slabs strengthened by prestressed bolts. This was followed by further work[32,33] using

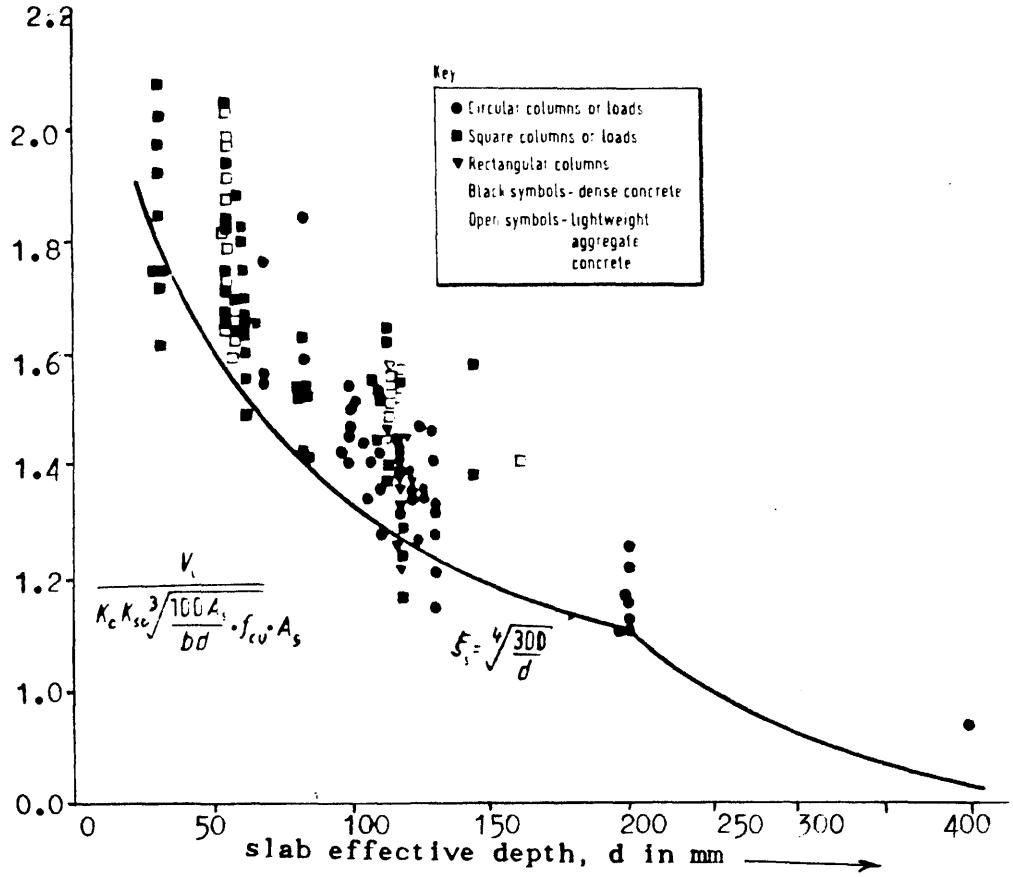

Figure (2.12) : Punching shear test results for internal slab-column connections under concentric load

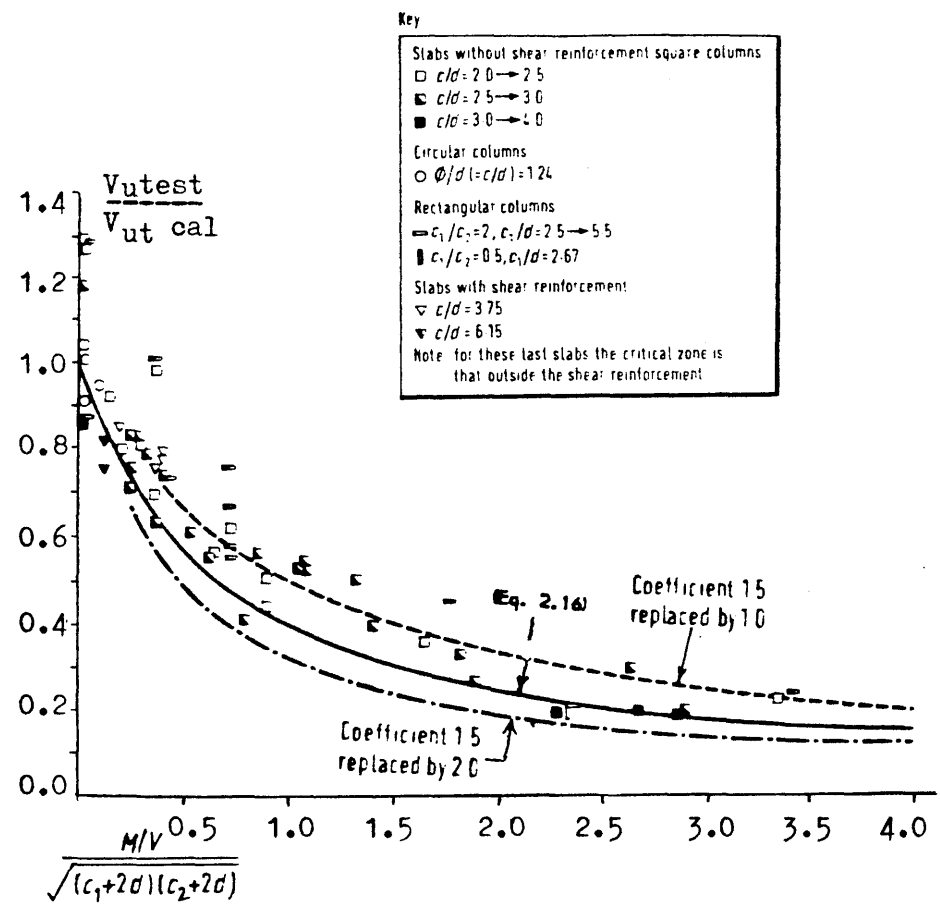

Figure (2.13) : Test results for internal slab-column connections under eccentric loading

short off–cuts of steel I–sections as shear reinforcement. In the paper[33] they concluded that for the test specimens with a reinforcement ratio of 1.0 percent or more, this special shear reinforcement increased significantly both the strength and ductility of the connection. Most of the shear elements had yielded extensively thus demonstrating efficient anchorage. Using stud as shear reinforcement for flat concrete plates, as shown in Figure (2.14), Mokhtar[34] found that a smaller amount of flexural and shear reinforcement is required than using closed stirrups as shear reinforcement. This is because for efficient anchorage, the stirrups must enclose the flexural reinforcement and the concrete cover specified by the codes must be measured above the stirrups and not the flexural steel. With shear studs, the top of the anchor plates can be located at the same level as the top of the uppermost flexural reinforcement and the cover is measured from that level. The other advantages of the studs are:

i) they are easy to install, even in thin slabs,

ii) they do not interfere with flexural reinforcement,

The test series[34] confirm the previous results[32,33] that the use of shear stud reinforcement greatly increases the ultimate strength and the ductility of the slab–column connections. Regan[35] in a paper reviewed all the information available on shear combs and the criteria for their design in the context of current knowledge of punching and proposed a method of design using shear combs to prevent punching failure of slabs.

Hawkins et al[36,37] reported results and analysis of tests to failure conducted on more than 80 full–scale slab–column subassemblages simulating conditions associated with the transfer of moments between flat plates and interior, edge and corner columns. Several parameters were considered in the experiments, viz. slab thickness, concrete strength, concrete type, integral beam stirrup reinforcement, flexural reinforcement pattern and ratio of reinforcement, column rectangularity and the ratio of moment transferred to the column to the shear. It was found[37] that

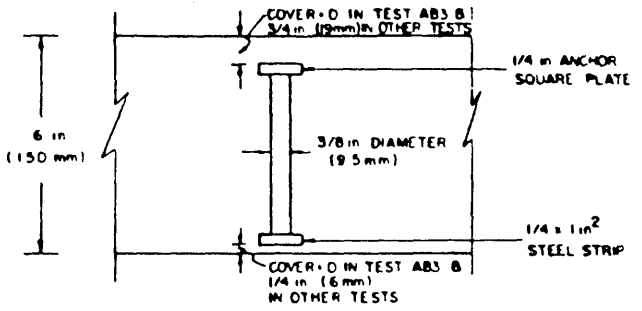

SECTION A – A

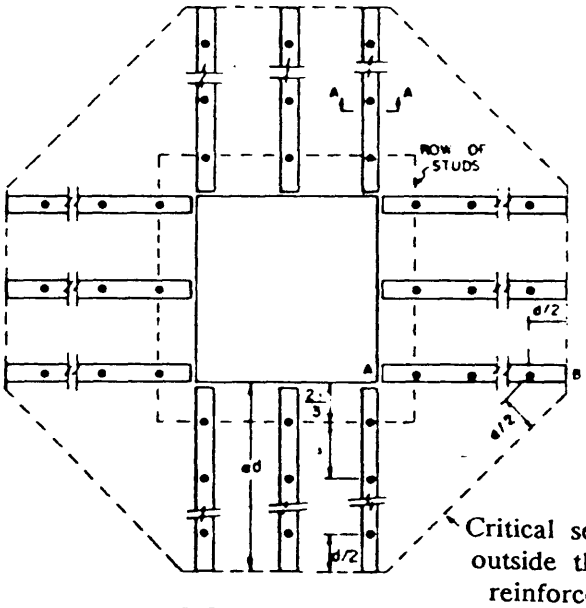

TOP VIEW

Figure (2.14) : Typical arrangement of shear studs in Cal-gary tests(34)

with adequate amounts of properly distributed and proportioned shear reinforcement elasto–plastic behaviour can be obtained. Test results also showed that shear reinforcement increases the cracked section stiffness. They developed an ultimate strength procedure for interior and exterior column–slab connections based on beam analogy. The slab framing into each column face was idealized as beams running in two directions at right angles. The ultimate capacity of the connection was obtained by summing the ultimate bending moment, torsional moment and shear forces of the beams, as discussed in section 2.4.2.3. It was concluded[37] that the ACI Code 318–77 provisions for determining the strength of slab to interior column connections transferring moment are reasonable for design. The strength predictions are conservative when the value of the reinforcement ratio, ρ, within lines 1.5 slab thickness on either side of the column exceeds 0.8% . That conservatism increases as ρ value increases and the warning of impending failure decreases. They added that the provision may be non–conservative for ρ value less than 0.8%, but the flexural capacity of the reinforcement in the column region then controls and significant deformations occur before any punching failure.

2.4.4 Comparative Study of Different Design Equations

Punching shear failure is a subject on which there is no consensus on a theoretical level and there are rather wide divergencies between different empérical treatments. Code recommendations are also empirical and expressed in terms of purely nominal shear stresses. Codes differ in the definitions of critical perimeters, and in the expressions used to define the limiting value of the shear stress, v_c. In this section, the variation in the prediction of ultimate shear strength by different design equations, varying one parameter in those design equations and keeping all other constant, will be studied (see table 2.1 for details). Four design equations, (2.11), (2.12), (2.14) and (2.16) have been considered in this comparative study. The materials safety factor was assumed to be unity in the design equations. Limits on the ranges of parameters covered by the Code formulae have been ignored, but

this has litlle effect on the comparisons.

From Figure (2.15) it is clear that M/Vd ratio, varying from 1.0 to 4.0 , has no effect on the ultimate shear strength. The variation in ultimate shear strength by different design equations is due to other parameters which are assumed a certain constant value in this study. The maximum variation is within 15%.

An increase in C/d ratio (the ratio of the side length of the column to the effective depth of the slab) results in an increase in punching shear strength, as shown in Figures (2.16) to (2.19). The rate of increase in shear strength due to increase in C/d ratio is highest in ACI Code equation (2.11), but the predicted strength is not always greater than the strength predicted by British Code. However as d increases the strength prediction by ACI becomes greater than that predicted by BS 8110. The shear strength predicted by design equations (2.14) and (2.16) are roughly similar over the range of C/d variation.

The curves predicted by the design equations and showing the effect of C_1/C_2 ratio (the ratio of the side lengths of the column) on the ultimate punching shear strength are presented in Figures (2.20) to (2.23). Generally the predicted shear strength by ACI and Rangan are similar. Regan generally predicts much lower values than others.

Figures (2.24) to (2.27) show the effect of compressive strength of concrete on punching shear strength for different effective depth of slab. ACI and Rangan predict the same strength, whereas strengths predicted by equations BS 8110 and Regan differ by a constant amount. British Code predicts around 15% higher strength than ACI for smaller depth of slab, but it predicts slightly lower strength than ACI for higher 'd' values and concrete strength greater than 45 N/mm^2.

Figure (2.28) shows the effect of percentage of steel, ρ , on punching shear strength. Percentage of steel has no effect on ACI Code equation (2.11) and equation (2.14) proposed by Rangan. British Code predicts lower strength than ACI

TABLE (2.1)

Figures	Main parameters studied	Other parameters kept constant
2.15	M / Vd	ρ = 1.0 ; f_{cu} = 40 N/mm^2 C_1/C_2 = 1.25 ; d = 250 mm C_2/d = 1.25
2.16 to 2.19	C_2/d ratio for d = 100, 150, 200 and 250 mm	ρ = 1.0 ; f_{cu} = 40 N/mm^2 M/Vd = 1.0 ; C_1/C_2 = 1.0
2.20 to 2.23	C_1/C_2 ratio for d = 100, 150, 200 and 250 mm	ρ = 1.0 ; f_{cu} = 40 N/mm^2 M/Vd = 1.0 ; C_2/d = 1.0
2.24 to 2.27	f_{cu} for d = 100, 150, 200 and 250 mm	ρ = 1.0 ; C_1/C_2 = 1.25 M/Vd = 1.0 ; C_2/d = 1.25
2.28	ρ	f_{cu} = 40 N/mm^2 ; d = 200 mm M/Vd = 1.0 ; C_2/d = 1.25 C_1/C_2 = 1.0

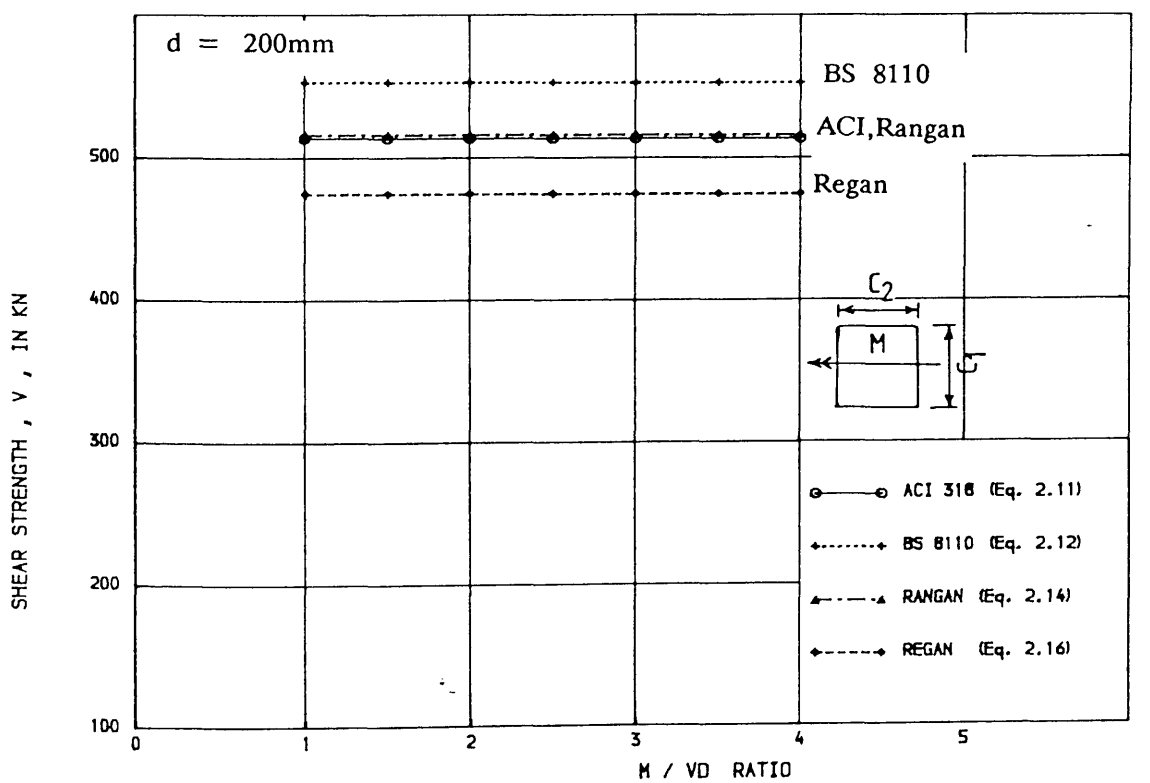

FIGURE (2.15) , CURVES SHOWING THE EFFECT OF M/VD RATIO ON THE PUNCHING SHEAR STRENGTH , FCU=40N/mm2 , C2/D=1.25, C1/C2=1.25, D=200MM, ROV=1.0

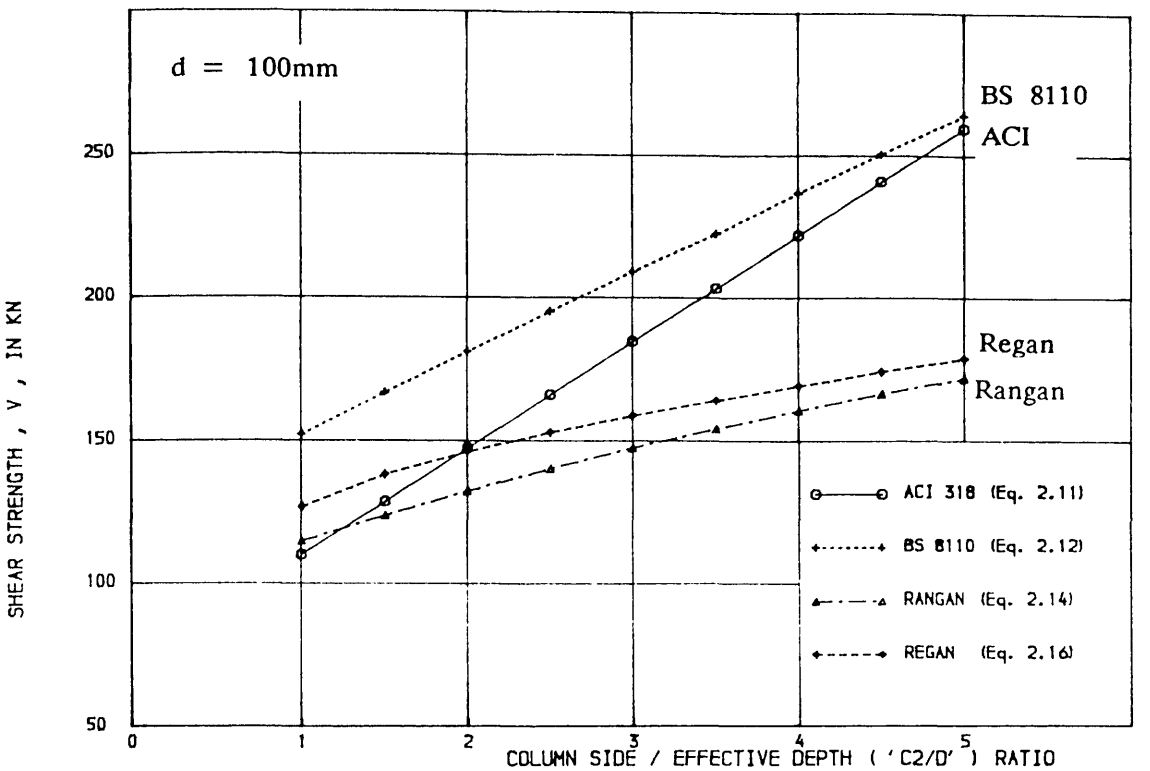

FIGURE (2.16) , CURVES SHOWING THE EFFECT OF ' C2/D ' RATIO ON THE PUNCHING SHEAR STRENGTH , FCU=40N/mm2 , C1/C2=1, M/VD=1.0, D=100MM, ROV=1.0

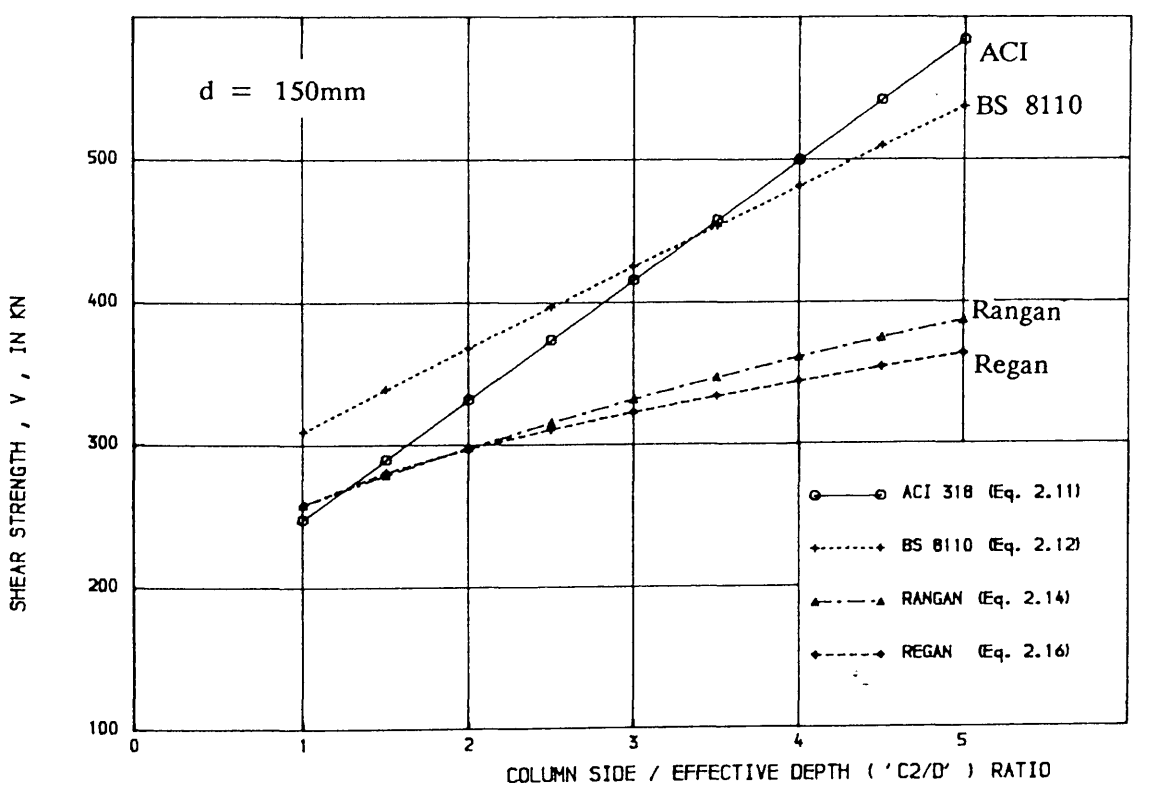

FIGURE (2.17) , CURVES SHOWING THE EFFECT OF ' C2/D ' RATIO ON THE PUNCHING SHEAR STRENGTH , FCU=40N/mm2 , C1/C2=1, M/VD=1.0, D=150MM, ROV=1.0

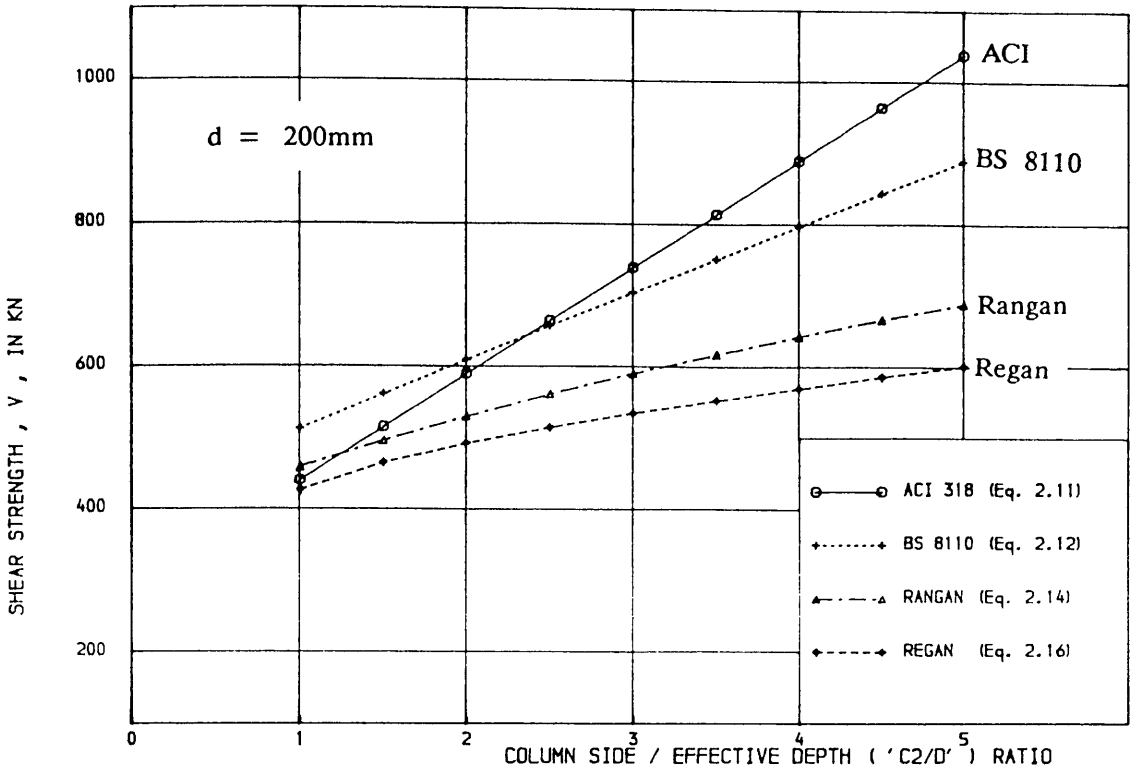

FIGURE (2.18) , CURVES SHOWING THE EFFECT OF ' C2/D' RATIO ON THE PUNCHING SHEAR STRENGTH , FCU=40N/mm2 , C1/C2=1, M/VD=1.0, D=200MM, ROV=1.0

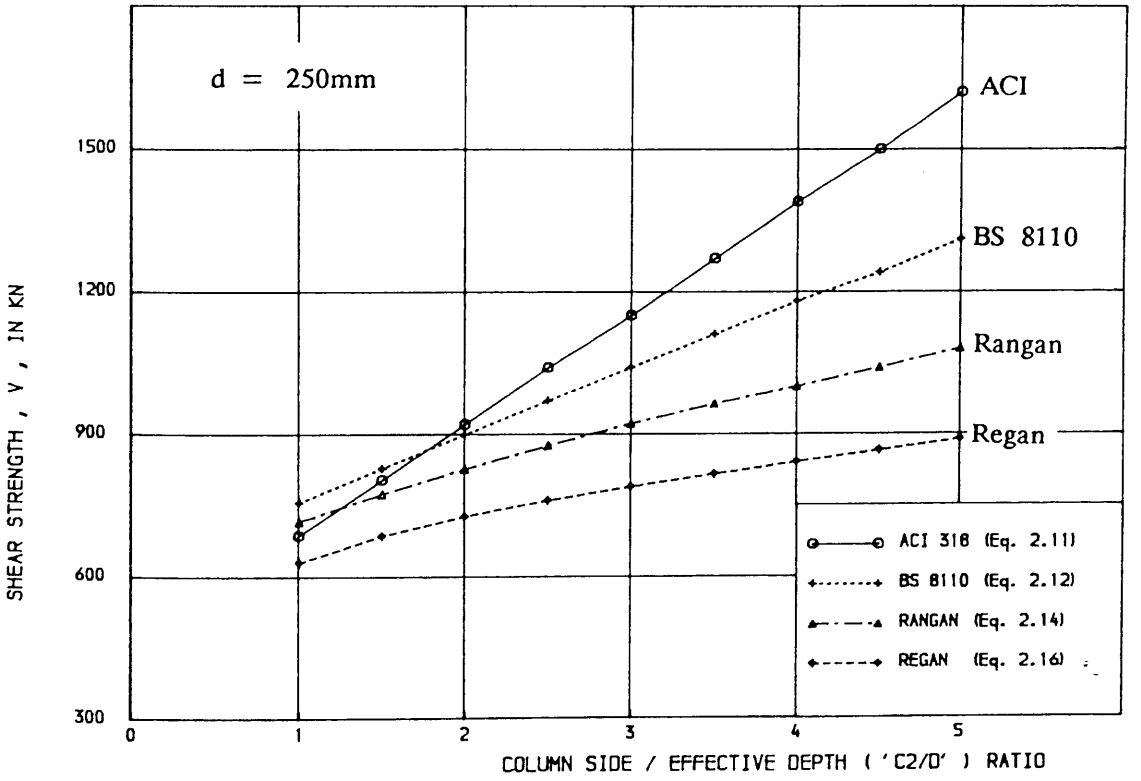

FIGURE (2.19) , CURVES SHOWING THE EFFECT OF ' C2/D ' RATIO ON THE PUNCHING SHEAR STRENGTH , FCU=40N/mm2 , C1/C2=1, M/VD=1.0, D=250MM, ROV=1.0

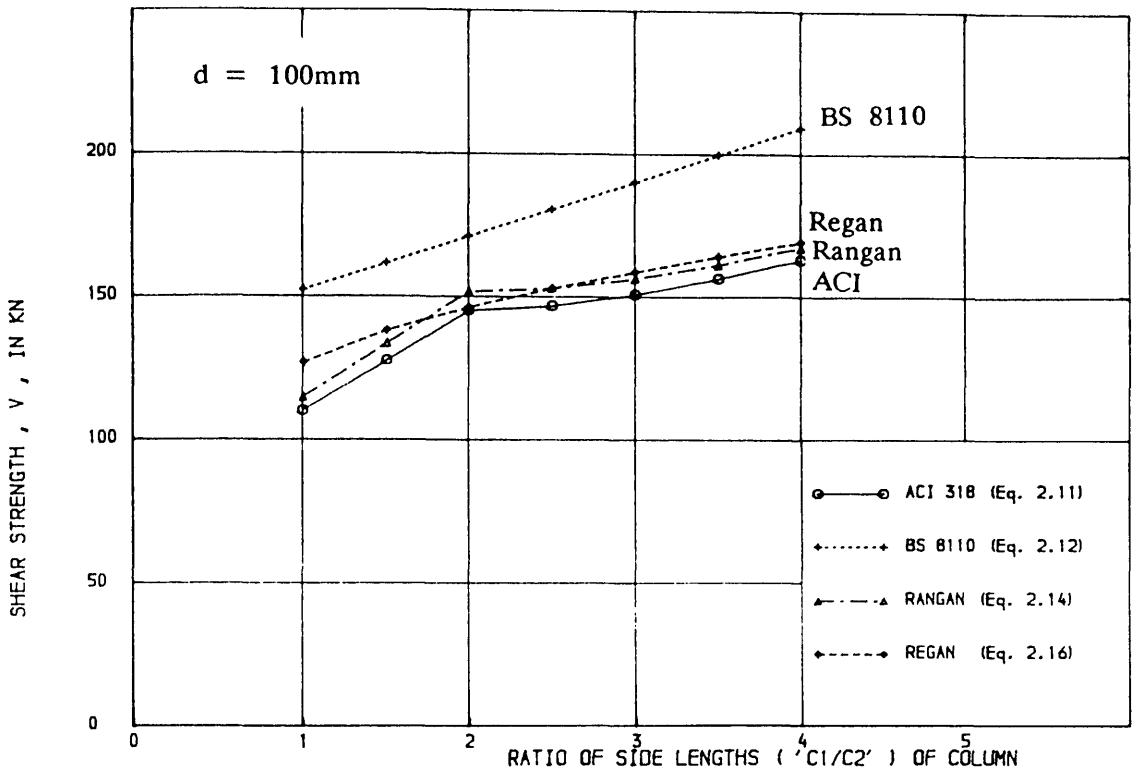

FIGURE (2.20) , CURVES SHOWING THE EFFECT OF ' C1/C2 ' RATIO ON THE PUNCHING SHEAR STRENGTH , FCU=40N/mm2 , C2/D=1, M/VD=1.0, D=100MM, ROV=1.0

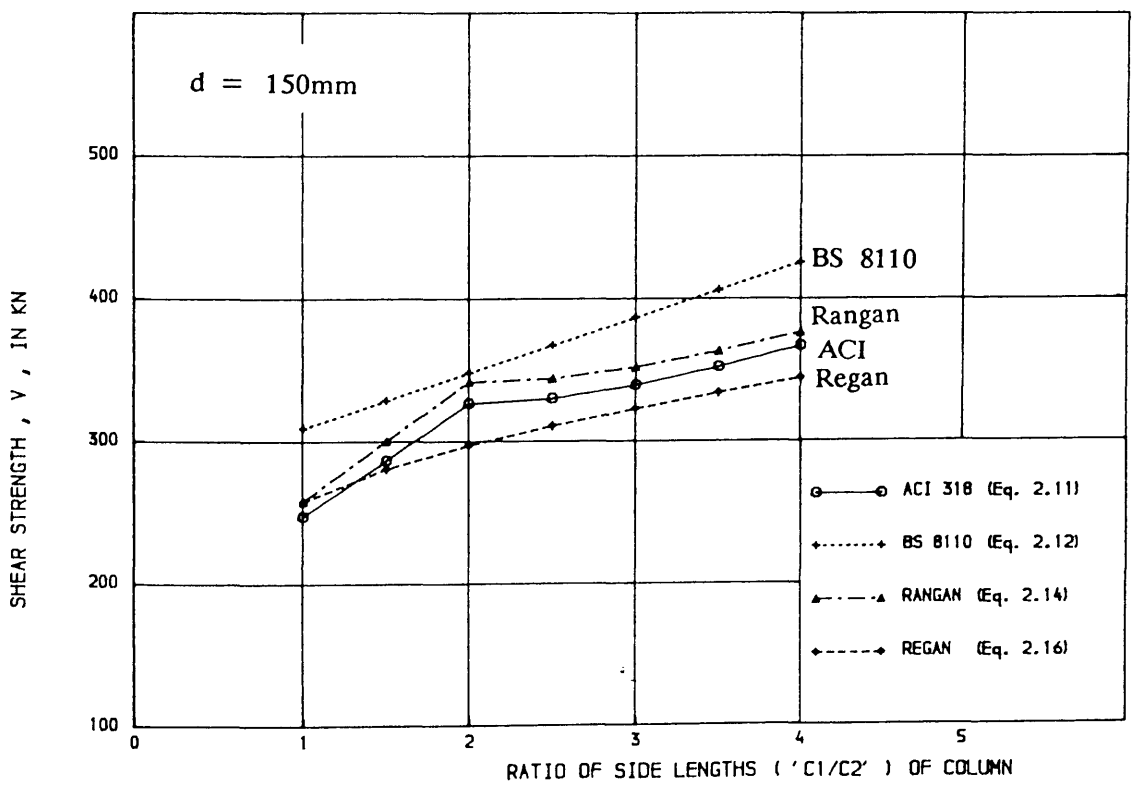

FIGURE (2.21) , CURVES SHOWING THE EFFECT OF ' C1/C2 ' RATIO ON THE PUNCHING SHEAR STRENGTH , FCU=40N/mm2 , C2/D=1, M/VD=1.0, D=150MM, ROV=1.0

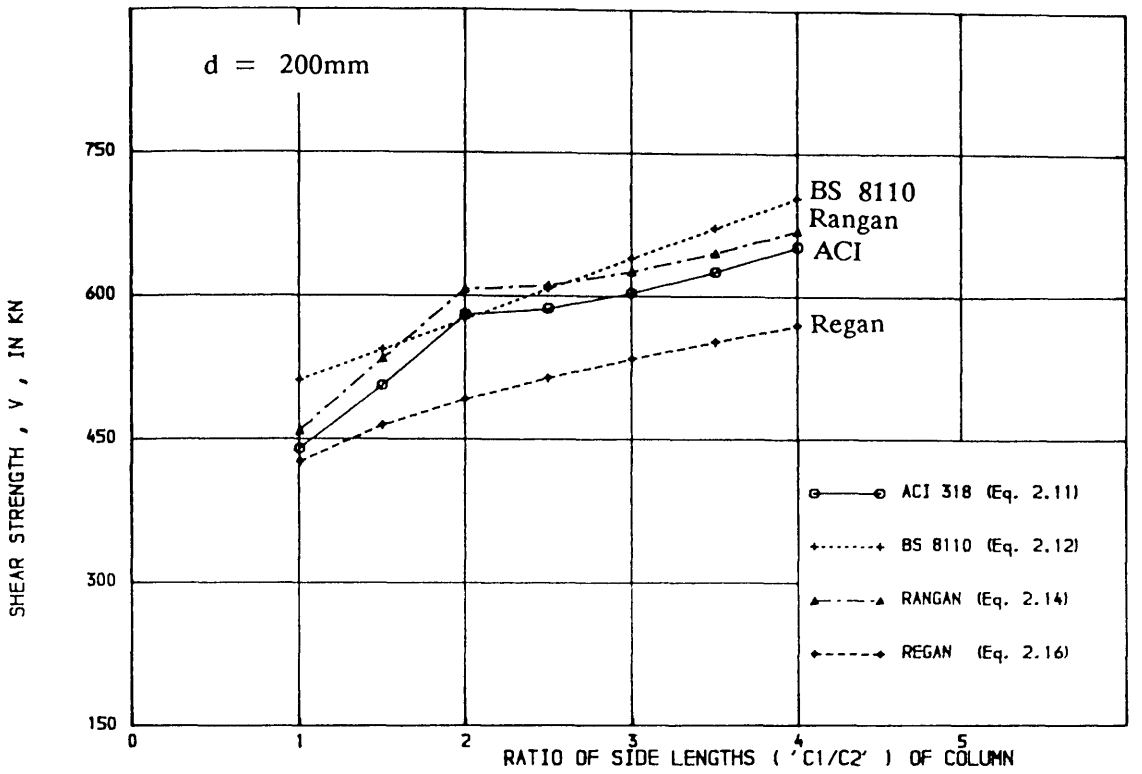

FIGURE (2.22) , CURVES SHOWING THE EFFECT OF ' C1/C2 ' RATIO ON THE PUNCHING SHEAR STRENGTH , FCU=40N/mm2 , C2/D=1, M/VD=1.0, D=200MM, ROV=1.0

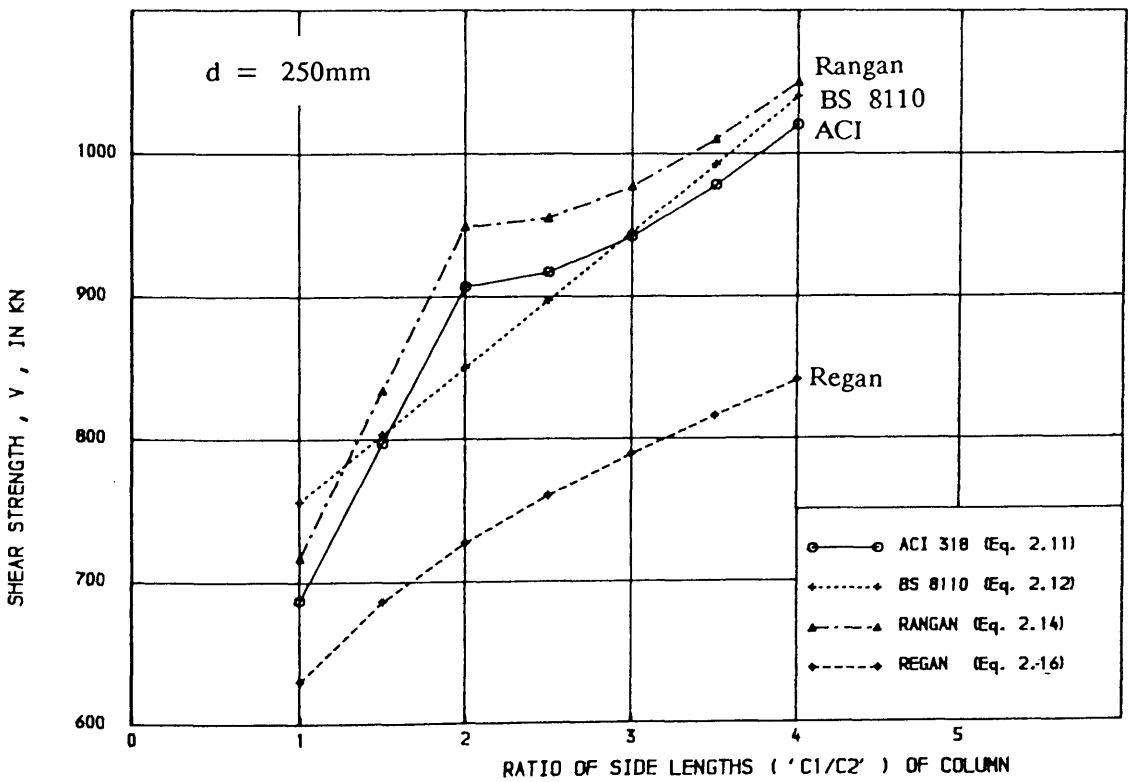

FIGURE (2.23) , CURVES SHOWING THE EFFECT OF ' C1/C2 ' RATIO ON THE PUNCHING SHEAR STRENGTH , FCU=40N/mm2 , C2/D=1, M/VD=1.0, D=250MM, ROV=1.0

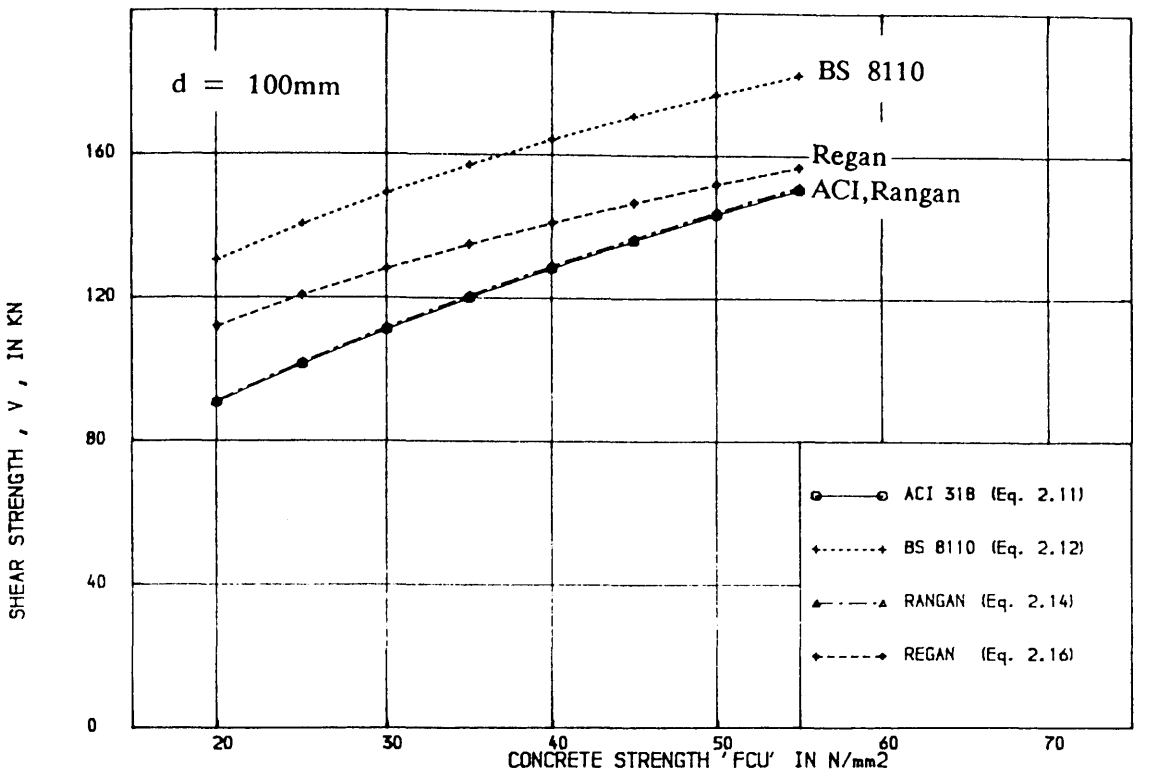

FIGURE (2.24) , CURVES SHOWING THE EFFECT OF VARIATION OF FCU ON THE PUNCHING SHEAR STRENGTH , C1/C2=1.25 , C2/D=1.25, M/VD=1.0, D=100MM, ROV=1.0

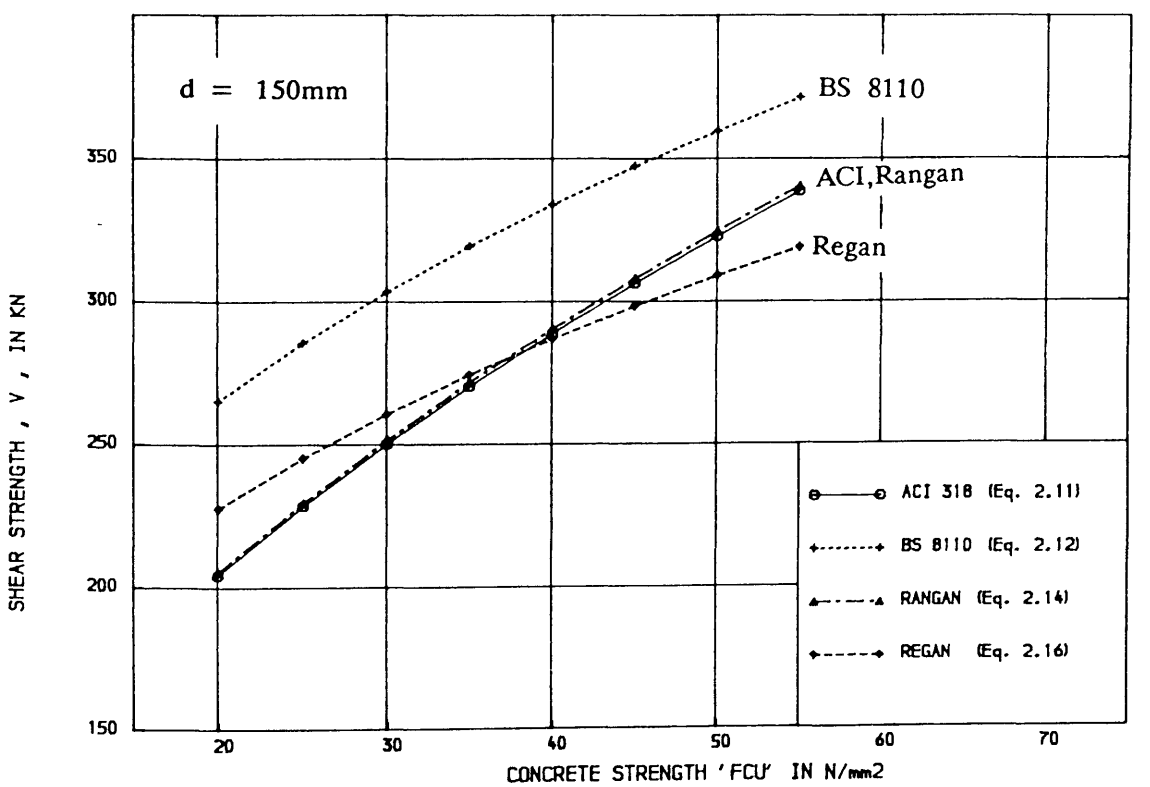

FIGURE (2.25) , CURVES SHOWING THE EFFECT OF VARIATION OF FCU ON THE PUNCHING SHEAR STRENGTH , C1/C2=1.25 , C2/D=1.25, M/VD=1.0, D=150MM, ROV=1.0

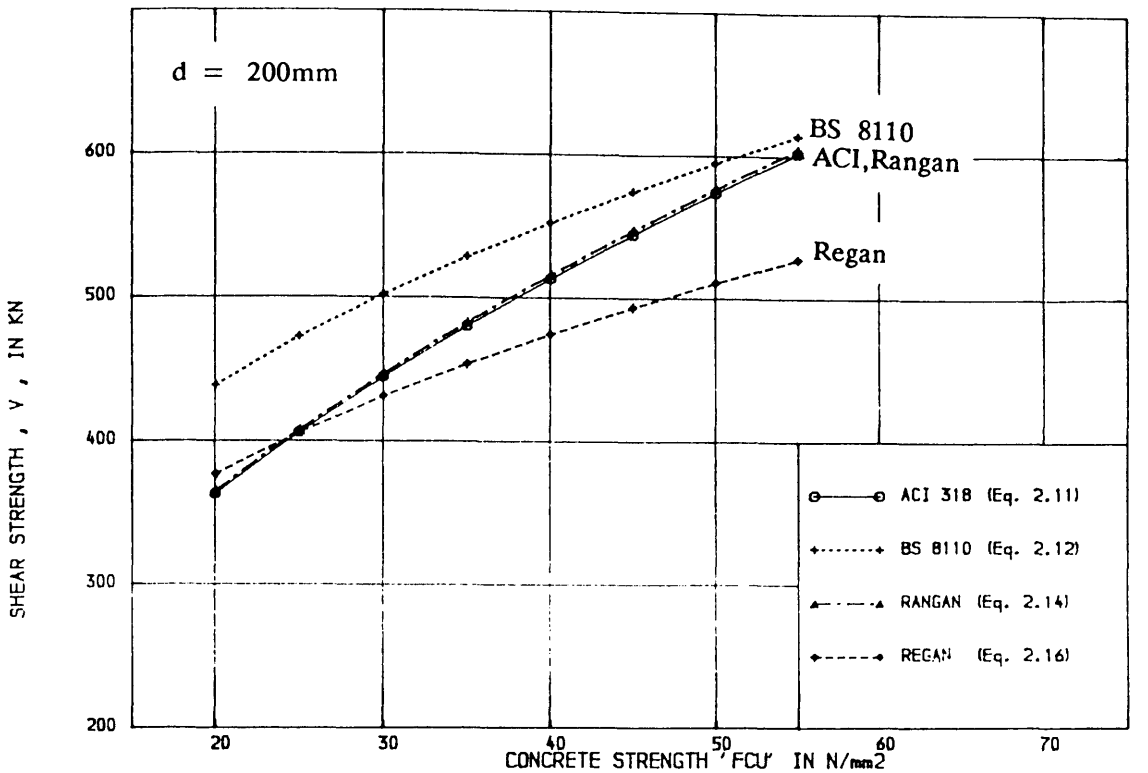

FIGURE (2.26) , CURVES SHOWING THE EFFECT OF VARIATION OF FCU ON THE PUNCHING SHEAR STRENGTH , C1/C2=1.25 , C2/D=1.25, M/VD=1.0, D=200MM, ROV=1.0

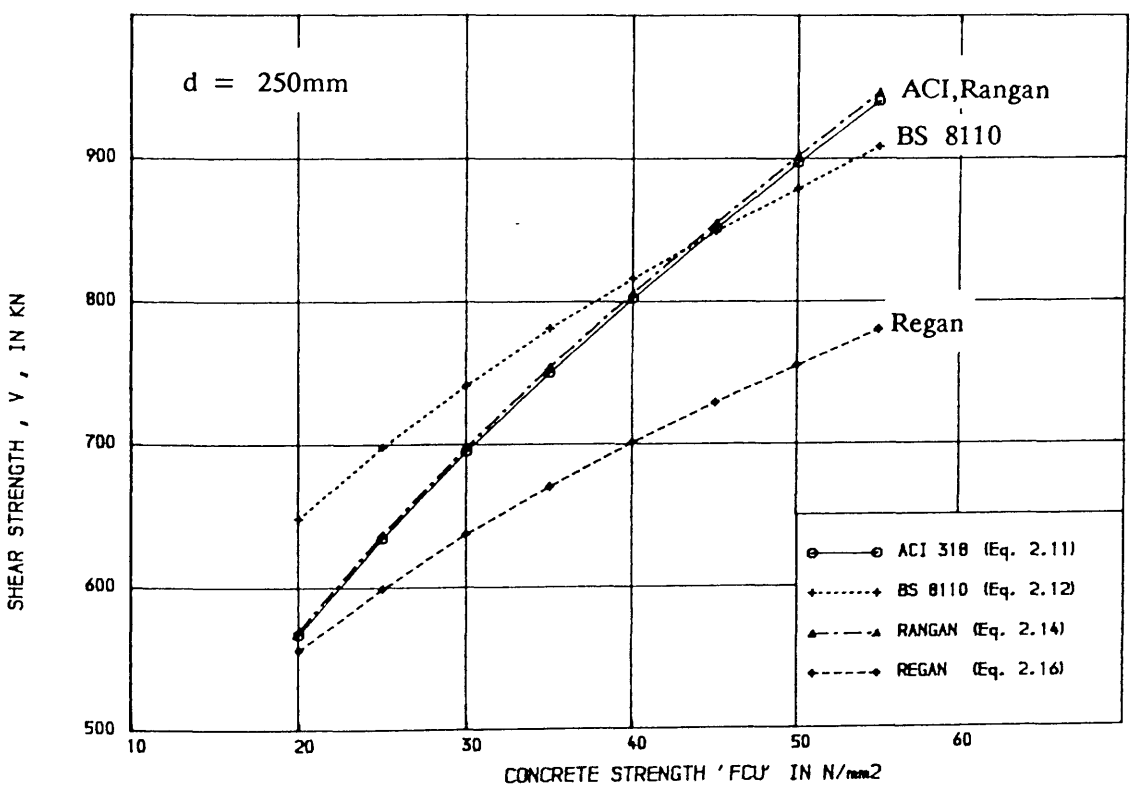

FIGURE (2.27) , CURVES SHOWING THE EFFECT OF VARIATION OF FCU ON THE PUNCHING SHEAR STRENGTH , C1/C2=1.25 , C2/D=1.25, M/VD=1.0, D=250MM, ROV=1.0

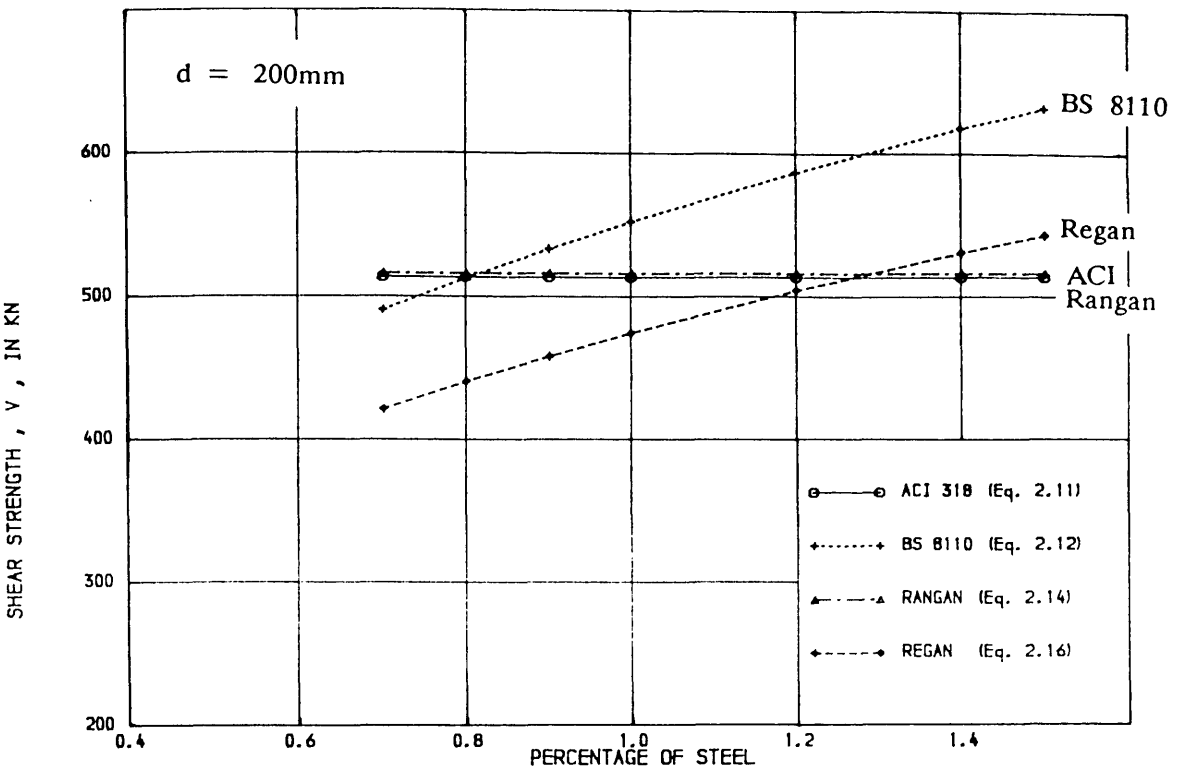

FIGURE (2.28) , CURVES SHOWING THE EFFECT OF PERCENTAGE OF STEEL ON THE PUNCHING SHEAR STRENGTH , FCU=40N/mm2 , C2/D=1.25, M/VD=1.0, D=200MM, C1/C2=1.

for ρ less than 0.8% and higher strength for ρ greater than 0.8%. This limit may vary for different column shapes, concrete strength and effective depth of slab. The values predicted by equations (2.16) and (2.12) proposed by Regan and British Code again differ by a constant amount with Regan predicting lower values. Equation (2.16) predicts approximately 12% lower strength than equation (2.12) for different percentage of steel.

2.4.5 Code Rules For Shear Reinforcement

The Code provisions for evaluating shear strength of slabs with moments transferred to the columns was discussed in section 2.4.2. In the following sub-sections code rules for the use of shear reinforcement in the slab around the connection will be discussed.

2.4.5.1 British Code : BS 8110

No shear reinforcement is required when the shear stress v is less than v_c, calculated by equation (2.10). When v exceeds v_c, shear reinforcement should be provided in slabs over 200 mm deep to increase the shear resistance in accordance with the following equation :

$$\Sigma A_w \sin\alpha \geq \frac{(v - v_c)\, u\, d}{f_{yw}} \qquad (2.20)$$

where u = critical shear perimeter, $2(C_1 + C_2 + 6d)$,

fyw = characteristic strength of shear reinforcement

A_w = area of two legs of the link

α = angle between the shear reinforcement and the plane of the slab

In equation (2.20), $(v - v_c)$ should not be taken less than 0.4 N/mm^2. The shear reinforcement should be distributed evenly around the zone on at least two perimeters. The spacing around the perimeter should not exceed 1.5d. In assessing the reinforcement required, shear reinforcement within the zone provided to reinforce other zones may be taken into account.

The zone immediately adjacent to the column (i.e., the zone whose inner perimeter touches the column and whose outer perimeter is 1.5d from the column) is checked first. If this zone does not require reinforcement then no further checks are required. If shear reinforcement is required, then successive zones are checked as shown in Figure (2.29), until a zone is reached which does not require reinforcement.

The maximum shear for which a slab–column connection may be designed is limited by the requirement that the nominal shear stress, v, should not exceed a design value equal to 0.8 $\sqrt{f_{cu}}$ or 5 N/mm^2, whichever is less.

2.4.5.2 American Code : ACI 318–77 and 318–83

In ACI Codes 318–77 and 318–83, sec. 11.12.1.4, it is specified that maximum shear stress due to factored shear forces and moments shall not exceed v_c, where v_c is defined in equation (2.7) and be not greater than $0.33\sqrt{f_{cu}}$. For slabs with shear reinforcement, the shear stress, v , on any column face must not exceed the larger of the values given by equations (2.7) and (2.21).

$$v_n = \frac{v_c}{2} + \frac{A_w\ f_{yw}}{u\ s} \qquad (2.21)$$

In other words, the amount of shear reinforcement needed to increase the shear resistance against punching type of failure is

$$\frac{A_w}{s} = \frac{(v_n - v_c/2)\ u}{f_{yw}} \qquad (2.22)$$

where $A_w f_{yw}$ = yield strength of stirrups crossing a potential inclined crack extending at 45 degrees from the compressive surface of the slab and a perimeter located d/2 closer to the loaded area than the critical section under consideration.

u = perimeter of critical section under consideration

= $2(C_1 + C_2 + 2d)$, according to Figure (2.4)

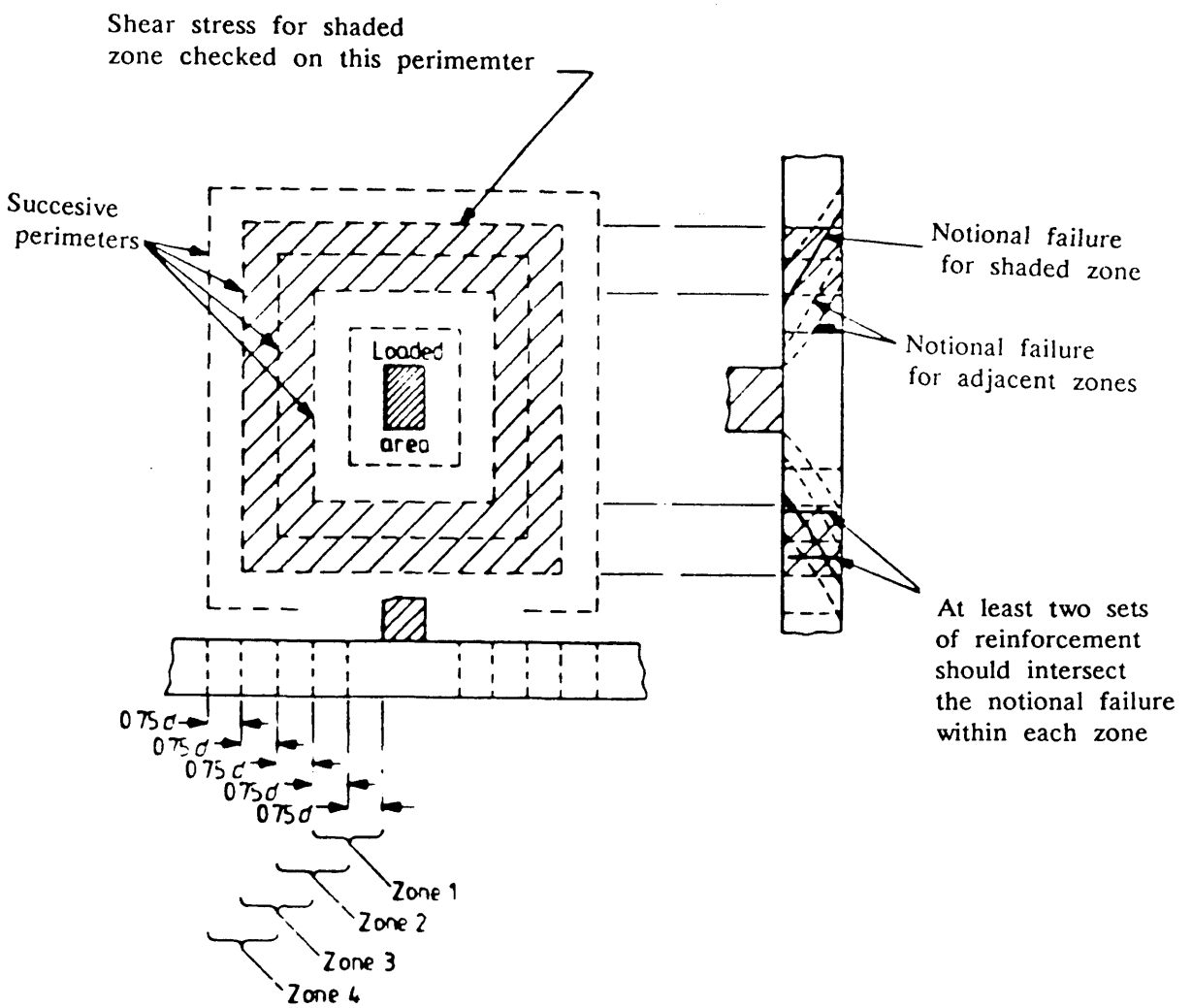

The figures show the location of successive perimeters and and failure zones. A typical failure zone (zone 3) is shown shaded together with the notional failure associated with the zone.

Figure (2.29) : Punching shear zones according to BS 8110.

s = spacings of stirups in direction perpendicular to perimeter of critical section

2.4.6 Strength of Slab– Column Connections Under Reversed Cyclic Loading.

Tsuboi and Kawaguchi[38] studied experimentally the behaviour of flat slabs under repeated monotonic loadings. Their 1000mm square and 300mm thick slabs contained centrally located 200mm. square column stubs. Monotonically increasing and reverse cyclic loadings were applied through the column stub while two opposite slab edges were supported and the other two edges left free. Three of the nine specimens were made of plain mortar and the other six slabs had varied distribution of reinforcement, the total amount of which was same in all the six specimens. They found that[38] the distribution of longitudinal reinforcement affected the punching shear resistance around the column and repeated load reduced the punching shear resistance. The concept of effective width was found to be useful for the practical design of flat slabs and from test results they obtained the effective width to be equal to 0.58 to 0.61 of the side dimension of the square slabs in the elastic state.

None of their specimens contained any form of shear reinforcement. They did not propose any theoretical procedure for calculating the ultimate strength of slab– column connections.

Four of the eight specimens, tested by Islam and Park[25], were subjected to several cycles of bending moment reversals. The loading cycle used for specimens is shown in Figures (2.30) and (2.31). This loading sequence was not intended to simulate any particular earthquake but it was rather regulated by the edge displacements to generate elastic and post– elastic loading history. Edge displacements imposed on the specimens with shear reinforcement were considerably larger than those used for the specimen without shear reinforcement. Static cyclic loading was used by them[25] because of the convenience of applying that type of

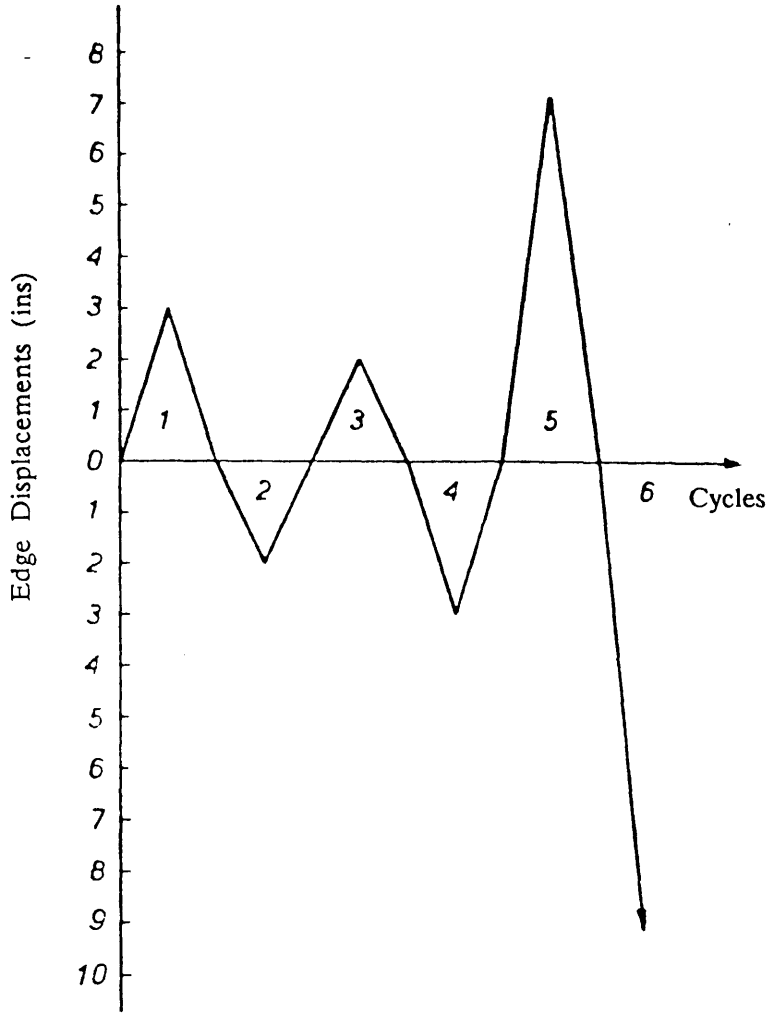

Figure (2.30) : Loading cycles for specimens 6CS, 7CS and 8CS.

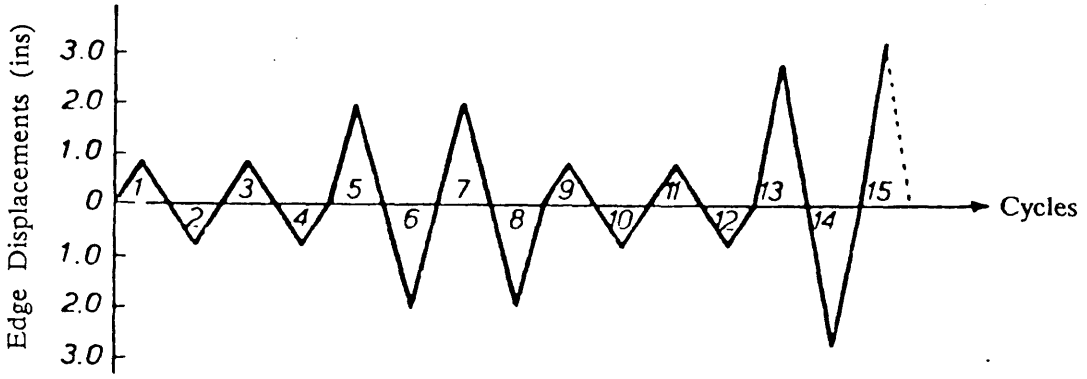

Figure (2.31) : Loading cycles for specimen 3C.

loading. The use of slow reversals of load to represent dynamic loading was thought to be conservative because the strength of concrete and steel increases with increasing rates of strain due to work–hardening. It was found that the load carrying capacity with cyclic loading deteriorated by about 50% at final cycle but that was accompanied by very large cyclic deformations. The series of tests showed that flat–plate column junctions reinforced with shearheads and closed stirrups as shear reinforcement behave in a satisfactory manner as earthquake resistant connections.

Hawkins et. al[39,40] conducted tests on ten full scale models. Specimen dimensions were chosen so as to permit a realistic examination of the behaviour of slab–column connections under constant dead load coupled with reversed cyclic lateral loads. Five out of ten specimens contained integral beam stirrup reinforcement. The main variables in Reference (40) were the amount and distribution of the flexural reinforcement and the size, spacing, detailing and length of the closed stirrup reinforcement. From the test results of specimens containing shear reinforcement[40] and compared with the results of tests on similar specimens without shear reinforcement[39], the following beneficial effects of providing properly designed and detailed integral beam stirrup reinforcement are reported :

(a) an increase in the ductility of the connection at ultimate load,

(b) an increase in the energy absorption of the connection,

(c) an increase in the strength particularly for low reinforcement ratios, and

(d) a change in the hysteretic behaviour of connections with low reinforcement ratios from a shear to a moment type of energy dissipation mechanism,

In order for the stirrups to be fully effective, they suggested that the stirrups must be detailed such that

(i) they are closed hoops with a longitudinal reinforcing bar in each corner,

(ii) they are anchored by 45^0 standard bends around one or more longitudinal bars, and

(iii) they extend far enough out from the column face into each column strip so that the wide beam shear force V_n on the shear periphery shown in Figure (2.32) does not result in a shear stress V_n/bd exceeding $0.53\sqrt{f'c}$ where f'c is expressed in N/mm^2 and that perimeter does not approach closer than 1.5h to the column perimeter, where h is the overall thickness of the slab. For reversed cyclic loading they[40] concluded that both the ACI procedure and the Beam analogy are slightly nonconservative for evaluating the ultimate strength of connections for low reinforcement ratios (reinforcement ratios less than about 0.8%).

2.4.7 Analytical Model for Cyclic loading Behaviour of Slab–Column Connections

The seismic analysis of reinforced concrete structures requires a realistic conceptual model which recognizes the continually varying stiffness and energy–absorbing characteristics of the structures. To set up an analytical model in a form appropriate for seismic analysis, the hysteresis loops must be defined for cyclic force–displacement relationships. The variations which occur in the relationship with load level and history must be considered in detail. Since there are many possible alternatives at each point in the loading history, it is not convenient to provide a continuous description of the moment–rotation curve. Therefore, a series of rules were first proposed by Takeda et. al[41] for constructing the moment curvature curve for load reversals.

The rules given for loading and unloading for different conditions are shown in Figure (2.33). The Takeda model has a bilinear envelope which allows for only one stiffness value prior to yield. Further, the Takeda model assumes equal yield moments and stiffness for positive and negative moments. The Takeda model was later modified by Akiyama and Hawkins[6] so that the envelope could recognize both uncracked and cracked stiffness prior to yielding, as well as different yield moments and cracked section stiffness for positive and negative moments. The Takeda results were developed for beam sections. The modified unloading –

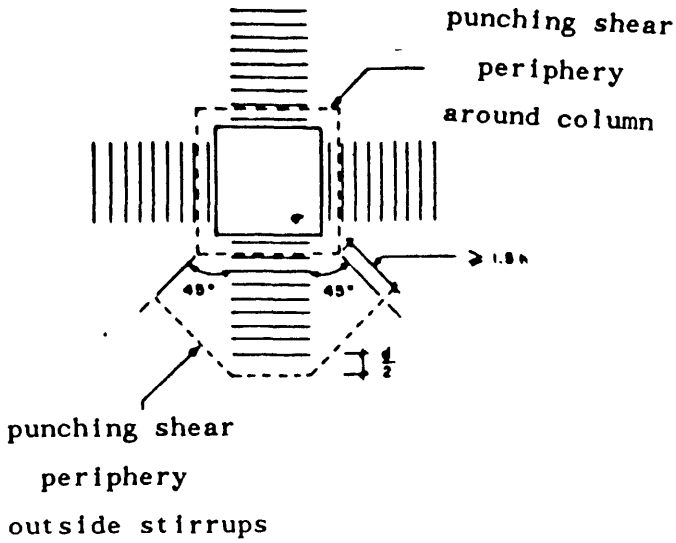

Figure (2.32) : Critical punching shear peripheries

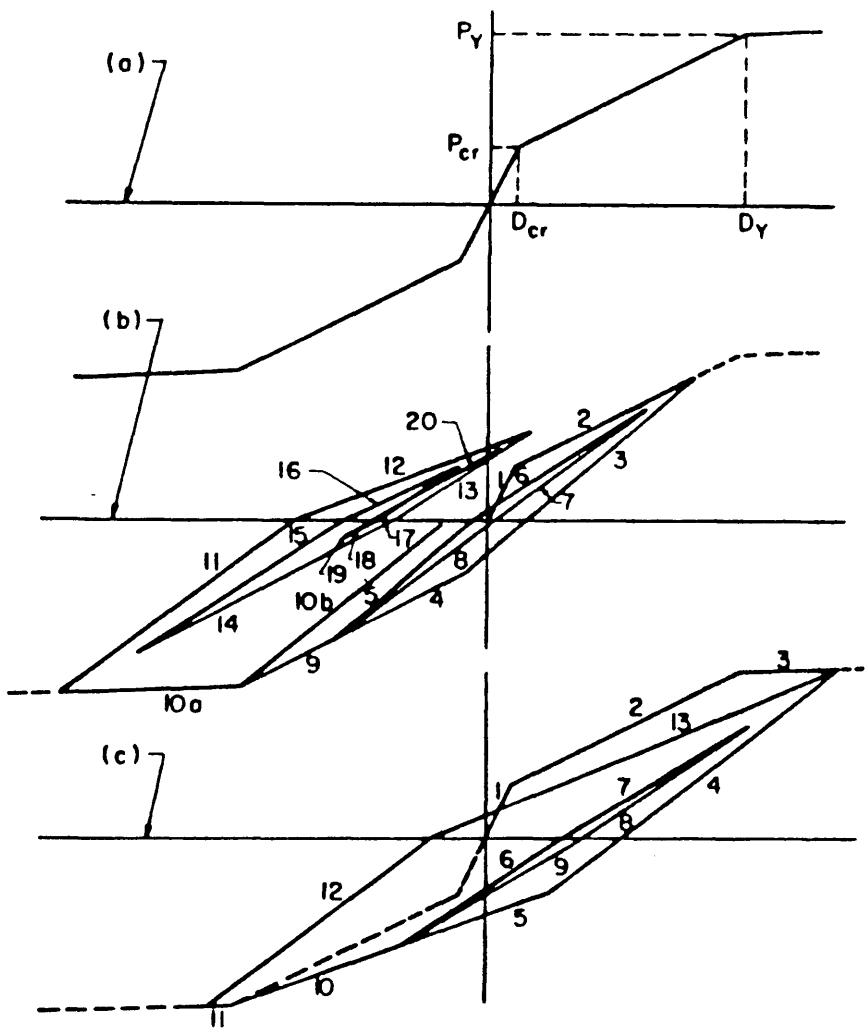

Figure (2.33) : Examples of assumed static load-deflection relationship

reloading rules of the Takeda model was used to predict cyclic loading results of slab–column connections. The details of the cyclic loading rules can be found in References (6) and (41).

The seismic response characteristics of slab–column connections[6] was predicted by a two–dimensional beam analogy model, using the modified unloading–reloading rules of the Takeda model. The model was calibrated through comparisons with the experimental results for nine interior column–slab subassemblages tested at the University of Washington. Average ratio of the predicted moment transfer capacity to the test results is shown in Table (2.2). Predictions are very good for the series without shear reinforcement and comparatively good for the series with shear reinforcement. The stiffness predicted for test specimens were compared with the test results as characterized by the relation between the slab's edge deformation and the applied lateral load. The stiffness prediction was in comparatively good agreement with test results.

2.4.8 Shear and Moment Transfer From Slabs to Shear Walls

Schwaighofer and Collins[42] reported one adhoc test on a pair of one–third scale reinforced concrete shearwalls coupled by a slab. The layout of the model is shown in Figure (2.34). It represents three pairs of planar coupled shearwalls. Lateral loading was simulated by applying relative displacements in the longitudinal direction of the walls by means of six hydraulic jacks as shown in Figure (2.35). From the observations and results obtained from the test, they[42] recommended that the shear force transferred from wall to wall by the coupling slab at punching shear failure of the slab may be assumed to act uniformly over a specified critical section. Thus, the ultimate shear force V_u, Figure (2.36–a) is given by assuming a uniform ultimate shear stress of $0.33\sqrt{f'c}$ N/mm^2 acting over the U–shaped critical section at d/2 from the faces of the wall so that the three faces of the U are of approximately the same length, where d is the effective depth of the slab. The assumed critical section is shown in Figure (2.36–b). The design equation for

TABLE 2,2

No.of tests	Type of slab-column connection	Shear reinforcement used	predicted moment transfer capacity/ Test results	
			mean	standard deviation
7	Interior	No	1.00	0.07
8	Interior	Yes	1.12	0.07
2	Exterior: moment parallel to the edge	No	0.99	0.06
3	Exterior: moment parallel to the edge	Yes	1.07	0.05
3	Exterior: moment normal to the edge	No	1.00	0.09
5	Exterior: moment normal to the edge	Yes	1.03	0.07
3	corner	No	0.99	0.07
2	corner	Yes	0.91	0.00

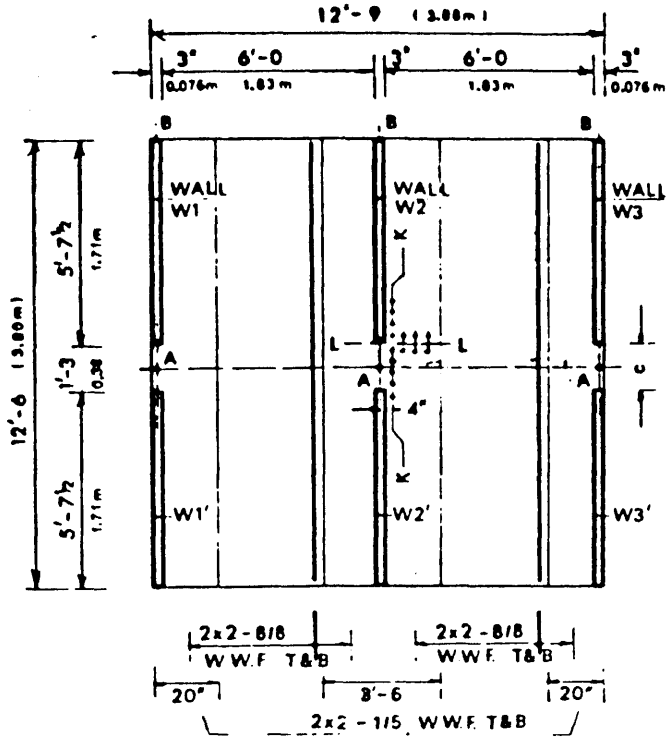

Figure (2.34) : Plan of model tested by Schwalghofer and Collins[42].

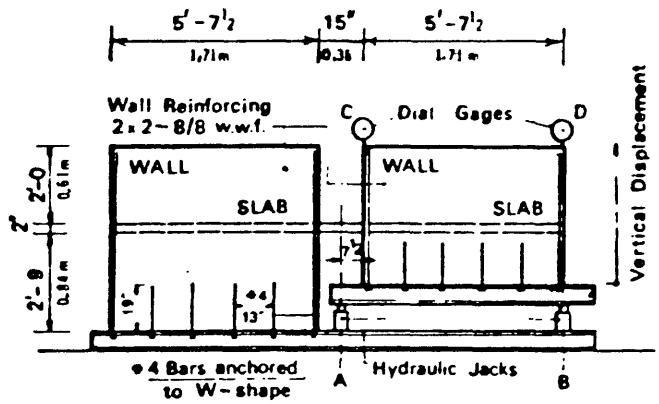

Figure (2.35) : Elevation of model tested by Schwalghofer and Collins[42].

ultimate shear force is given by

$$V_u = (0.33 \sqrt{fcu}) \{3(t_w + d)d\} \quad (2.23)$$

where t_w is the thickness of the wall. Based on these assumptions, their calculated failure load was about 80% of the experimental one. The flexural strength of the coupling slab was suggested to be predicted by using a slab width equals to the corridor opening plus the wall thickness because beyond that, insignificant values of strains in the reinforcement were recorded. No shear reinforcement was used in the test specimen.

In a recent study, Memon[23] conducted tests on fourteen 'large scale' models of reinforced concrete plane shearwall–slab junction and Elnounu[24] tested sixteen 'large scale' models of flanged shearwall–slab junction. None of their[23,24] models contained any form of shear reinforcement. The model represents part of a floor plan (the shaded area in Figure (2.37)). Since they were interested in the local behaviour of the slab–wall junction, the exact boundary conditions of the real structure were disregarded in the models adopted in their study. The wall which extended above and below the slab level was clamped to the floor of the laboratory in a manner which will be described later in this thesis. Both gravity (super imposed) loads and lateral (wind) loads were considered. The lateral loads were simulated by a prescribed uniform displacement along the transverse edge of the slab. The final failure in the case of all the models was brittle.

Observing the location of failure surface of the models, critical perimeter shown in Figure (2.38) was suggested. Adopting the ACI 318–77 approach of allowable shear strength in concrete (i.e., $v_c = 0.33\sqrt{f'c}$) the estimated failure load was 25% conservative as compared with the experimental one. Comparing his experimental results with other approaches, Memon showed that Coull and Wong[43]'s elastic analysis based approach yields underestimation of the strength while Schwaighofer and Collins' approach[42] is unconservative in some cases. A two dimensional plate bending layered finite element computer programme was used

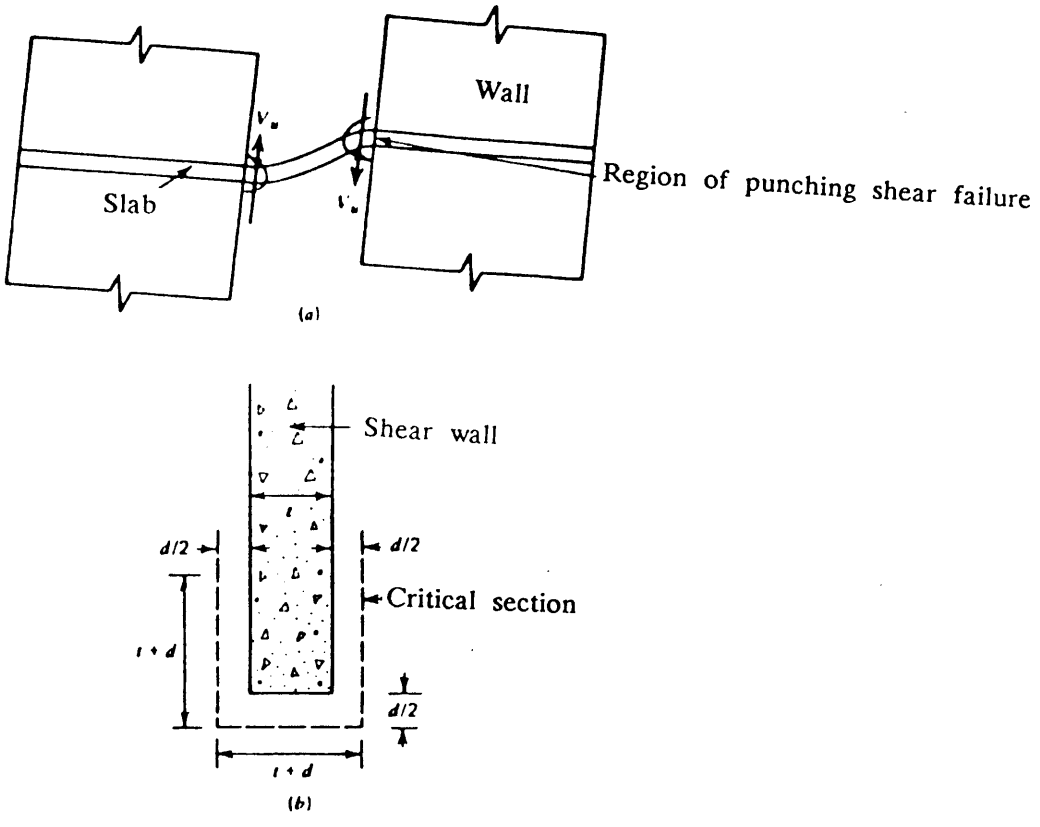

Figure (2.36) : Shear strength of slab-wall connection.
(a) Displacement of coupled walls and slab.
(b) Critical section of slab for shear strength

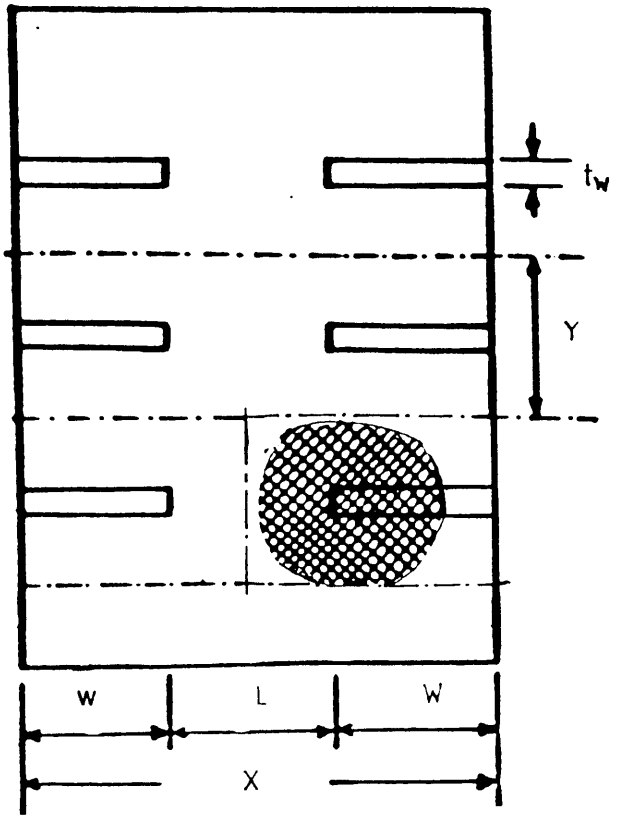

Figure (2.37-a) : Plan of a typical shear wall-slab building

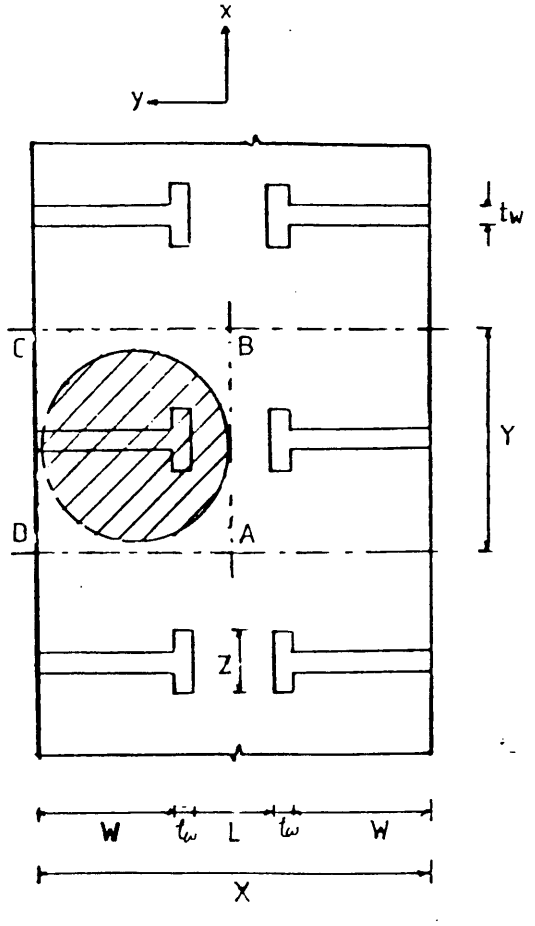

Figure (2.37-b) : Floor-plan of a typical shear wall structure

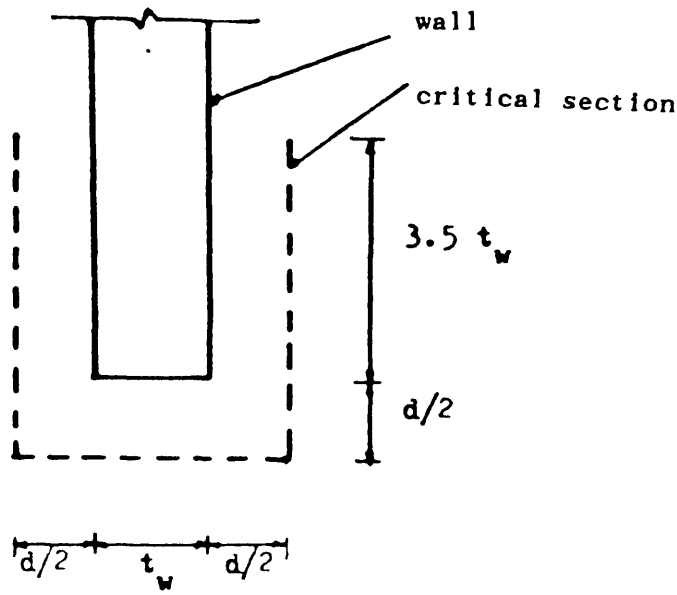

(a) Location of proposed critical section.

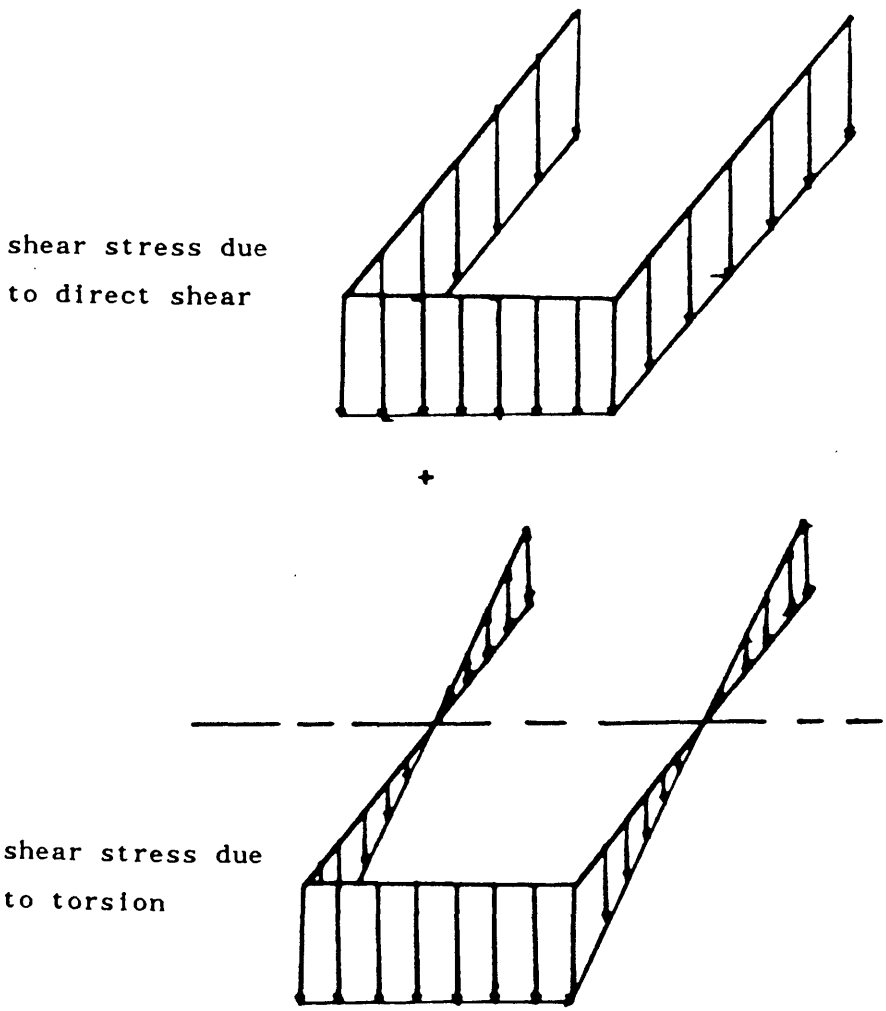

(b) Shear stress distribution along the critical section.

Figure (2.38) : Memon's [23] recommendations for planar shear walls.

for theoretical analysis. The predicted ultimate loads were in general 36% higher than the experimental load. Later, a 3−D nonlinear finite element programme specially written for the purpose[24] was used to carryout the theoretical studies. The results[44] showed good agreement (average V_{cal}/V_{exp} = 1.04, S.D = 0.13) with the experimental values.

Only T−section shear walls with flanges along the corridor were considered by Elnounu[24]. The major parameters included were : wall flange width, bay width ratio, gravity load/lateral load ratio, web length of wall and flexural reinforcement ratio. The final failure in the case of all the models except those which failed in flexure was brittle. Nonlinear three dimensional stress analysis, using the finite element method as described in chapter four was used for theoretical investigation. The twenty node isoparametric brick element was employed. The nonlinear response caused by concrete cracking, nonlinear triaxial stress−strain relations, and the yielding of steel reinforcement was investigated. In general good agreement was obtained between the experimental and theoretical values for deflections and strains. It was shown[23] that the theoretical analysis by nonlinear finite element method is capable of predicting to good accuracy the ultimate loads and the general behaviour of the shearwall−floor slab junction.

Finally, based on the results of the study, a critical section as shown in Figure (2.39) was suggested. The properties of the critical section were clearly defined. Adopting the ACI 318−83 approach of allowable shear strength in concrete (i.e., $v_c = 0.33\sqrt{f'c}$) the estimated failure load was 6% conservative as compared with the experimental one. No partial safety factors were incorporated in the failure load calculation and he concluded that the proposed method can be used safely with the relevant safety factors.

2.5 General Discussion

A wide range of experimental and theoretical investigations have been

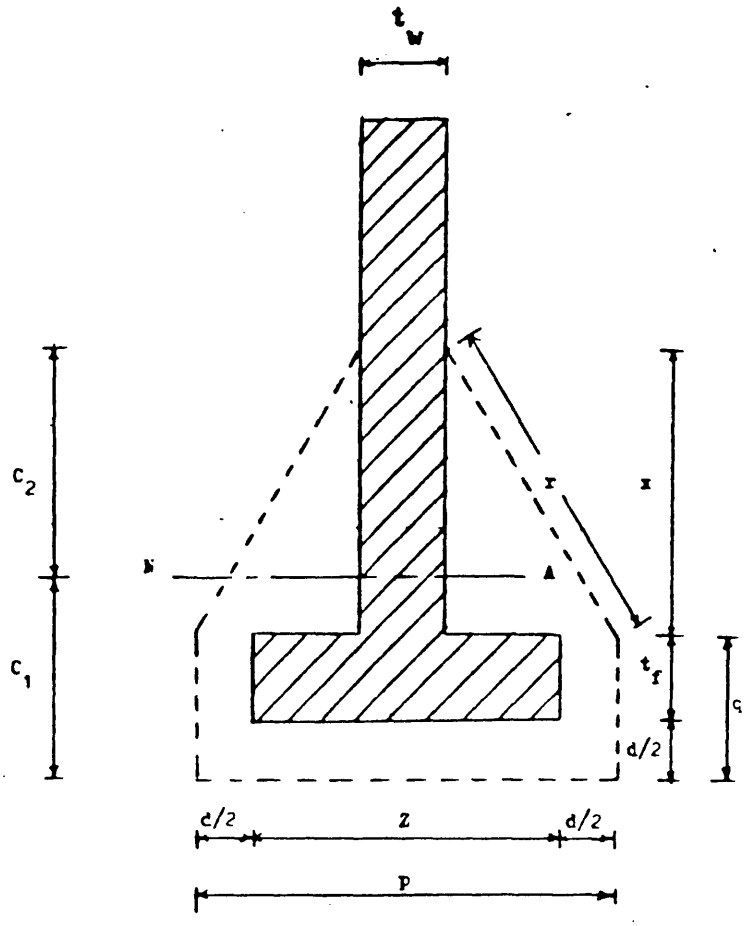

$$x/Z = 5.189\ e^{-0.513(Z/t)}$$

r = length of inclined portion of the section

$$= \sqrt{x^2 + (p - t_w)^2/4}$$

$$C_1 = [\ q^2 + r\ (x + 2q)\ ] / [\ p + 2(q + r)\ ]$$

$$C_2 = q + x - C_1$$

$$b_p = p + 2\ (r + q)$$

$$A_{cp} = d\ .\ b_p$$

$$J / C_1 = d.\ \left[\ p.C_1 + q(C_1 - q/3) + \frac{3xrq(C_1-q)(C_1-2q/3)+2r^2((C_1-q)^3+C_2^3)}{3x(xq+r(C_1-q))}\ \right]$$

Figure (2.39) : Proposed critical section for Flaged shear walls [24] with section properties.

conducted on flat plate structures. When flat plates have been tested to destruction[5], it has been found that shear conditions at the slab–to–column connection, rather than flexural conditions, have generally controlled the system's ultimate strength. Further, tests of flat slab structures have shown that unless shear reinforcement is provided at a slab–column connection the combination of excessive unbalanced moments and high shear forces invariably cause punching failure. Incorporating shear reinforcement in a slab–column connection substantially improves the connection's ductility and eliminates punching failure. It has been found that only integral beam stirrup reinforcement ensured satisfactory performance for reversed cyclic loading.

The analysis of the coupled shear wall type structures has also been thoroughly investigated. In slab–coupled shear walls, it was shown that both the gravity load and wind load have to be finally transmitted to the walls at the wall–slab junction. The junction is therefore very heavily stressed and is a critical region as far as punching failure is concerned. Codes of practice have dealt with such a problem for slab–exterior column connections. The validity of such information for the case of walls is questionable for the reason that the wall has a much greater width than the column, thus it is capable of resisting much greater torsional and shear stresses.

Experimental as well as theoretical work have been reported on slab–wall junctions for shear walls with and without flanges. The results of prior investigations demonstrate that it is difficult to avoid brittle failure in the slab without using any form of shear reinforcement in the slab. To the best of the author's knowledge, no experimental and theoretical work have been done on slab–wall junctions for shear walls using shear reinforcement in the slab. In addition, very little is known about the seismic resistance of shear wall to slab junction, which needs to be examined in respect of ductility available at the junctions and loss in load–carrying capacity due to reversal of applied loadings. It is for this reason that the present work reported in this thesis was undertaken.

CHAPTER THREE

DESIGN OF REINFORCED CONCRETE SLABS

3.1 Introduction

There are a number of possible approaches to the analysis and design of reinforced concrete slab systems. The various approaches available are elastic theory, limit analysis theory and modifications to them. Such methods can be used to analyze a given slab system to determine either the stresses in the slabs and the supporting system or the load–carrying capacity. The methods can also be used to determine the distribution of moments and shears to allow the reinforcing steel and concrete sections to be designed. The philosophy behind different approaches is to find a suitable slab design method such that,

(a) the slabs can sustain all loads and deformations liable to occur during construction, with an appropriate degree of safety,
(b) they can perform their intended functions adequately, in service, and
(c) they can possess an appropriate factor of safety against failure.

3.2 Theory of Elasticity in Slab Design

Classical elastic theory of analysis applies to slabs which are sufficiently thin for shear deformations to be insignificant and sufficiently thick for in–plane forces to be unimportant. The distribution of moments and shears found by elastic theory is such that :

(1) The equilibrium conditions are satisfied at every point in the slab.
(2) The boundary conditions are complied with, and
(3) Stress is proportional to strain; that is, bending moments are proportional to curvature.

The governing equation is a fourth–order partial differential equation in terms

of the deflection of the slab at general point (x,y) on the slab, the loading on the slab, and the flexural rigidities of the slab section. The solution of the equation gives the distributions of bending and torsional moments and shear forces throughout the slab.

3.3 Theory of Plasticity in Slab Design

This theory recognizes that because of plasticity, redistribution of moments and shears away from the elastic distribution can occur before the ultimate load is reached. Any solution to the ultimate load has to satisfy the following conditions of classical plasticity which assumes unlimited ductility :

1 – The Equilibrium Condition : The internal stresses must be in equilibrium with the externally applied loads

2 – The Yield Condition : The yield criteria defining the strength of the slab sections must nowhere be exceeded.

3 – The Mechanism Condition : Under the ultimate load, sufficient plastic regions must exist to transform the structure into a mechanism.

If conditions (1) and (2) are satisfied we get a lower– bound solution. While on the other hand, if condition (3) is used in conjunction with virtual work, then we get an upper– bound solution.

3.4 The Yield Criterion

The yield condition defines the combination of stresses necessary to cause plastic flow at a point. Consider the slab element shown in Figure (3.1) under the moment field M_x, M_y and M_{xy}. The sign convention adopted here is such that all moments acting on the element are positive as shown in the Figure. The following simplifying assumptions are made in order to derive the yield criterion in terms of three moment components :

1. The concrete is assumed to have a zero tensile strength.

2. Bar diameters are small in comparison with slab depth, and that they can carry stresses only in their original direction. Accordingly, kinking of bars across a yield line is not considered.
3. The slab element is lightly reinforced, so that compression failure are not permissible and only ductile failures are allowed. This is necessary for moment redistribution, so that the slab elements can reach their ultimate strength at sufficient number of sections, to convert the slab into a mechanism.
4. Membrane forces do not exist. It is acknowledged that the co-existance of such forces with flexural fields on the slab elements, will considerably effect the resisting moment of the slab element – depending on whether they are compressive or tensile and the restrained existing at the boundary of the slab.

For simplicity, the reinforcement in the element is assumed to lie parallel to the element sides as shown in Figure (3.2). The element may be reinforced on the top and bottom surfaces.

The basic idea is that, if at any point in the slab element (Figure 3.2), a line with a normal n and direction t is examined, then the normal moment M_n must not exceed the value M^*_n, where M^*_n is the moment of resistance that the reinforcement in the slab could develope in direction n. This is therefore a normal moment criterion.

Taking the normal to the yield line at an angle θ to the x-axis and considering the equilibrium of the element shown in Figure (3.3), we shall have

$$M_n = M_x \cos^2\theta + M_y \sin^2\theta - M_{xy} \sin 2\theta \qquad (3.1)$$

$$M_t = M_x \sin^2\theta + M_y \cos^2\theta - M_{xy} \sin 2\theta \qquad (3.2)$$

$$M_{nt} = 1/2\ (M_x - M_y) \sin 2\theta + M_{xy} \cos 2\theta \qquad (3.3)$$

The normal moment M_n should be compared with the resisting moment M^*_n. This resisting moment at the yield line can be expressed assuming that both x and y steel is at yield, as follows :

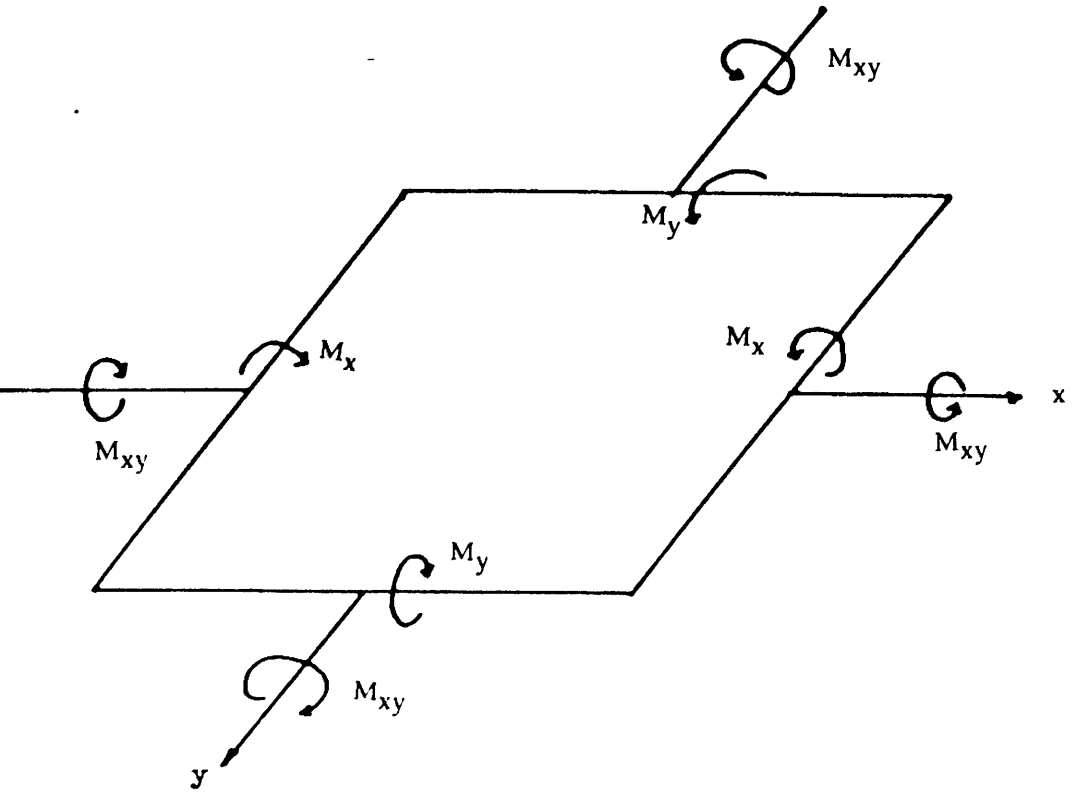

Figure (3.1) : A typical slab under moment field.

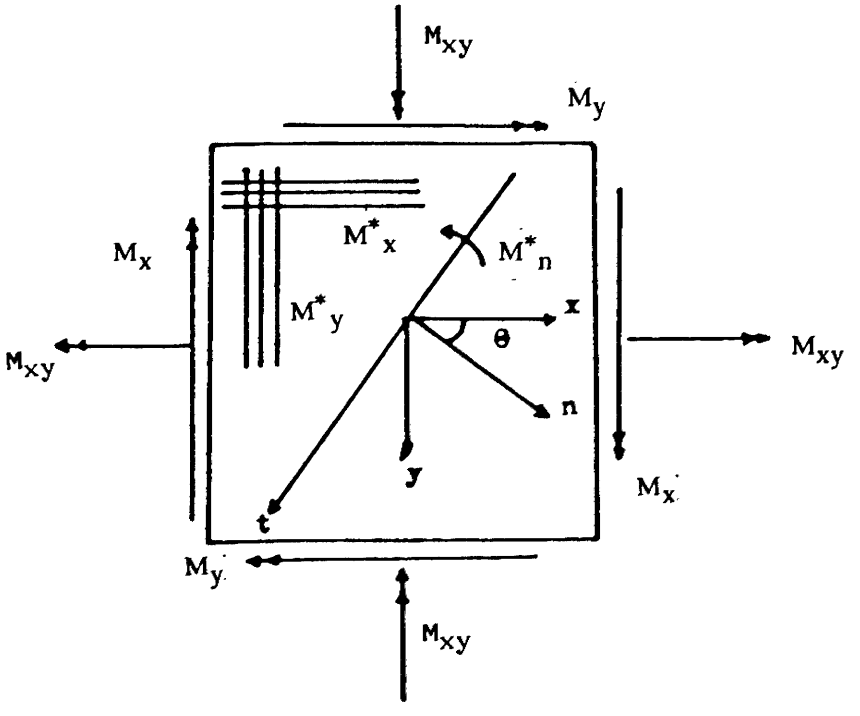

Figure (3.2) : A typical slab element with orthogonal reinforcement.

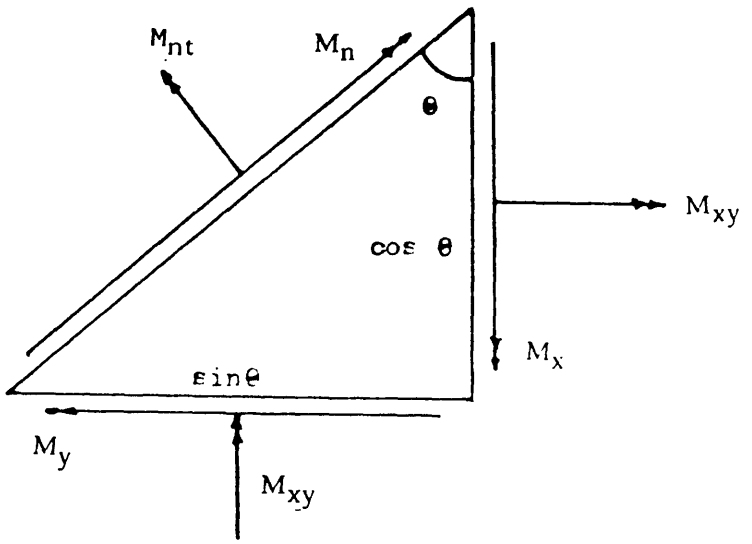

Figure (3.3) : Equilibrium of a slab element under applied moment field.

$$M^*_n = M^*x \cos^2\theta + M^*_y \sin^2\theta \quad (3.4)$$

where M^*_x = moment of resistance in x– direction.

M^*_y = moment of resistance in y– direction.

The value of M^*_n must always be greater than M_n, hence

$$(M^*_n - M_n) = 0 \quad (3.5)$$

Substituting (3.1) and (3.4) in (3.5) we have

$$(M^*_x - M_x)\cos^2\theta + (M^*_y - M_y)\sin^2\theta + M_{xy}\sin 2\theta = 0 \quad (3.6)$$

dividing by $\cos^2\theta$

$$(M^*_x - M_x) + (M^*_y - M_y)\tan^2\theta + 2 M_{xy}\tan\theta = 0 \quad (3.7)$$

At the yield line, the left hand side of equation (3.7) will be minimum. Differentiating with respect to $\tan\theta$, we have

$$2(M^*_y - M_y)\tan\theta + 2 M_{xy} = 0 \quad (3.8)$$

then

$$\tan\theta = - M_{xy}/(M^*_y - M_y) \quad (3.9)$$

Substituting $\tan\theta$ in equation (3.7) and rearranging

$$(M^*_x - M_x)(M^*_y - M_y) = M^2_{xy} \quad (3.10)$$

This equation is the yield criterion for orthotropically reinforced concrete slabs. This is often called Wood– Armer[45,46] yield criterion.

3.5 Direct Design Method

Progress in Computer aided design (CAD) methods demand the development of design procedures well backed by experimental evidence and amenable to automatic design with the minimum intervention by the designer. The currently adopted code rule based design procedures are not sufficiently general. On the other hand procedures based on Yield– line analysis or Hillerborg's Strip method, which although general procedures for the design of slabs, are not sufficiently CAD oriented. With the widespread availability of finite element programmes, it is possible to design slabs at ultimate load using elastic stress fields in conjunction with the Wood– Armer yield criteria for slabs (equation 3.10). This method called

'direct design method' was suggested by Wood[45] and extended by Armer[46] and later applied and tested by Hago[47] and Laila[47-a]. The steps involved are as follows:

i) the elastic distribution of moments at ultimate load is determined by the finite element method.

ii) Using the moment triad (M_x,M_y,M_{xy}) thus obtained, the design moments are calculated so as to satisfy the yield criterion of equation (3.10).

iii) Flexural steel area is then calculated to resist the corresponding ultimate design moments M^*_x and M^*_y.

The method satisfies the fundamental requirements of equilibrium, yield and mechanism conditions at ultimate collapse as dictated by classical plasticity theory as follows :

3.5.1 The Equilibrium Condition

To satisfy this condition, the elastic stresses must be in equilibrium with external loads. Since the distribution of stresses in this method is found using finite element method which is derived from equilibrium equations, this condition is automatically satisfied. Owing to its simplicity and versatility, the method can be applied to any type of slab problem with any edge condition.

3.5.2 The Yield Condition

Having got M_x , M_y , M_{xy} we have to derive M^*_x and M^*_y so as not to violate the yield condition as given by equation (3.10). This can be done as follows

i) if $M^*_y = 0$ then $M^*_x = M_x - M^2_{xy}/M_y$

ii) if $M^*_x = 0$ then $M^*_y = M_y - M^2_{xy}/M_x$

iii) if M^*_x and M^*_y not equal to zero;

we need to find minimum of $(M^*_x + M^*_y) = f$

From equation (3.10) : $M^*_y = M^2_{xy}/(M^*_x - M_x) + M_y$

$$\therefore \quad f = [M^*_x + (M^2_{xy}/(M^*_x - M_x)) + M_y] \qquad (3.11\text{-a})$$

For minimum or maximum of 'f'; $\partial(f)/\partial M^*_x = 0$

$$\text{i.e., } 1 - M^2_{xy}/((M^*_x - M_x)^2 = 0$$

$$\text{or} \quad (M^*_x - M_x) = \pm \mid M_{xy} \mid \qquad (3.11\text{-b})$$

For minimum of 'f' ; $\partial^2 f/\partial^2 M^*_x = +\text{ve}$

or $M^2_{xy}/(M^*_x - M_x)^3 > 0$; or $(M^*_x - M_x) > 0$

Taking positive sign from equation (3.11-b), we have

$$M^*_x - M_x = \mid M_{xy} \mid$$

$$M^*_x = M_x + \mid M_{xy} \mid \qquad (3.11\text{-c})$$

From equation (3.10),

$$M^*_y = M_y + \mid M_{xy} \mid \qquad (3.12)$$

For positive moment fields;

$M^*_x = 0$ when $M_x = - \mid M_{xy} \mid$

$M^*_y = 0$ when $M_y = - \mid M_{xy} \mid$

both M^*_x and $M^*_y = 0$ when $M_x . M_y = M^2_{xy}$

3.5.3 Rules for Placing Orthogonal Reinforcement

3.5.3.1 Bottom Steel

(a) Compute the normal design moments

$$M^*_x = M_x + \mid M_{xy} \mid \qquad (3.13)$$

$$M^*_y = M_y + \mid M_{xy} \mid \qquad (3.14)$$

if $M^*_x < 0$ then

$$M^*_y = M_y - (M^2_{xy}/M_x) \text{ with } M^*_x = 0 \qquad (3.15)$$

if $M^*_y < 0$ then

$$M^*_x = M_x - (M^2_{xy}/M_y) \text{ with } M^*_y = 0 \qquad (3.16)$$

(b) If still in (3.15) and (3.16) one gets a negative sign, then put such normal moment equal to zero, i.e., no reinforcement is required.

(c) If both M^*_x and M^*_y are negative, then no bottom steel is required.

3.5.3.2 Top Steel

(a) Compute the normal moments

$$M^*_x = M_x - | M_{xy} | \quad (3.17)$$

$$M^*_y = M_y - | M_{xy} | \quad (3.18)$$

if $M^*_x > 0$ then

$$M^*_y = M_y - (M^2_{xy}/M_x) \quad \text{with} \quad M^*_x = 0 \quad (3.19)$$

if $M^*_y > 0$ then

$$M^*_x = M_x - (M^2_{xy}/M_y) \quad \text{with} \quad M^*_y = 0 \quad (3.20)$$

(b) If still in (3.19) and (3.20) one gets a positive sign, then put such normal moment equal to zero, i.e., no reinforcement is required.

(c) If both M^*_x and M^*_y are positive, then no top steel is required.

Figures (3.4) to (3.6) give a detailed picture of these rules. For general use, the diagrams are sketched in a nondimensional form. The designer, after establishing the point ($M_x/| M_{xy} |$, $M_y/| M_{xy} |$) on the diagram, can easily know which equation to use to get the required design normal moments. Bottom steel equations are given in Figure (3.4), while those for top steel in Figure (3.5). Figure (3.6) shows the two branches of the yield hyperbola and indicates the directions of the steel to be provided at any point. (Primed moments refer to top steel).

A two dimensional finite element computer programme based on this direct design approach was used to calculate the flexural reinforcement needed in the slab. The flow chart is shown in Figure (3.7).

3.5.4 The Mechanism Condition

Because the necessary resistance is made equal to the calculated stress at every point in the slab, it is anticipated that all slab parts will attain their ultimate strength under the design load. Accordingly with minimum amount of redistribution, every point will yield at the design load, thus converting the slab into a

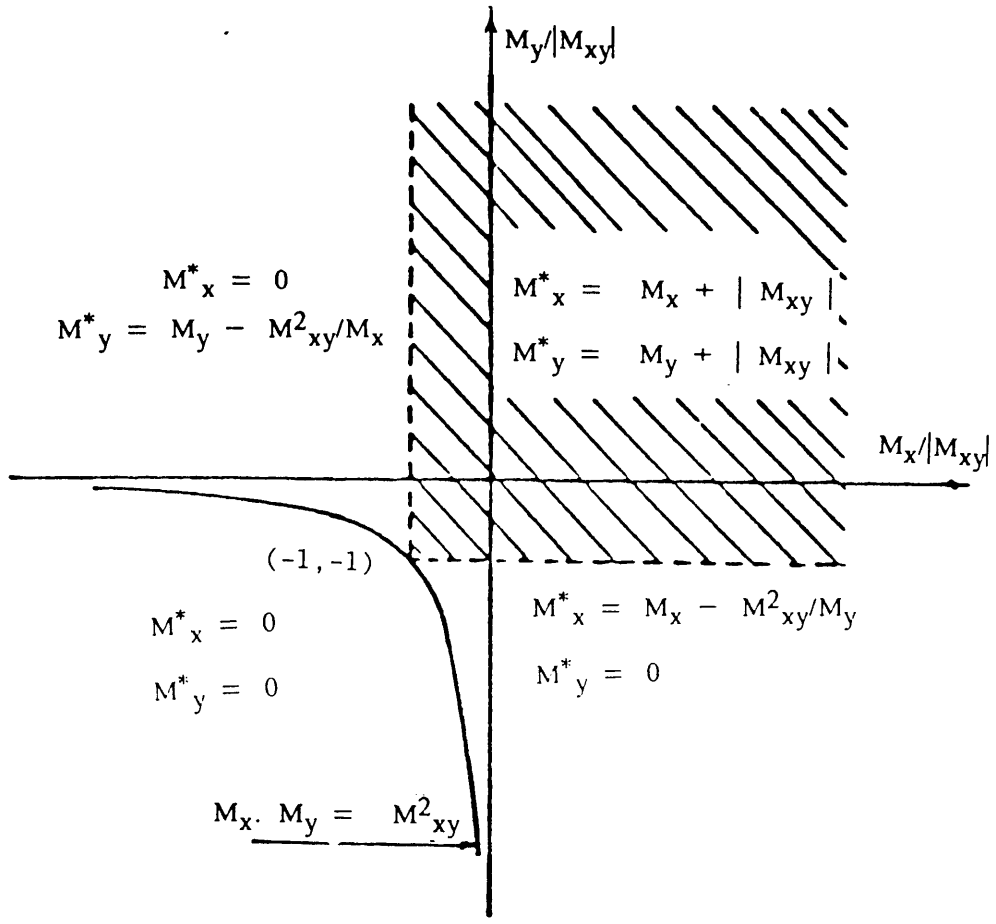

Figure (3.4) : Design equations for bottom steel.

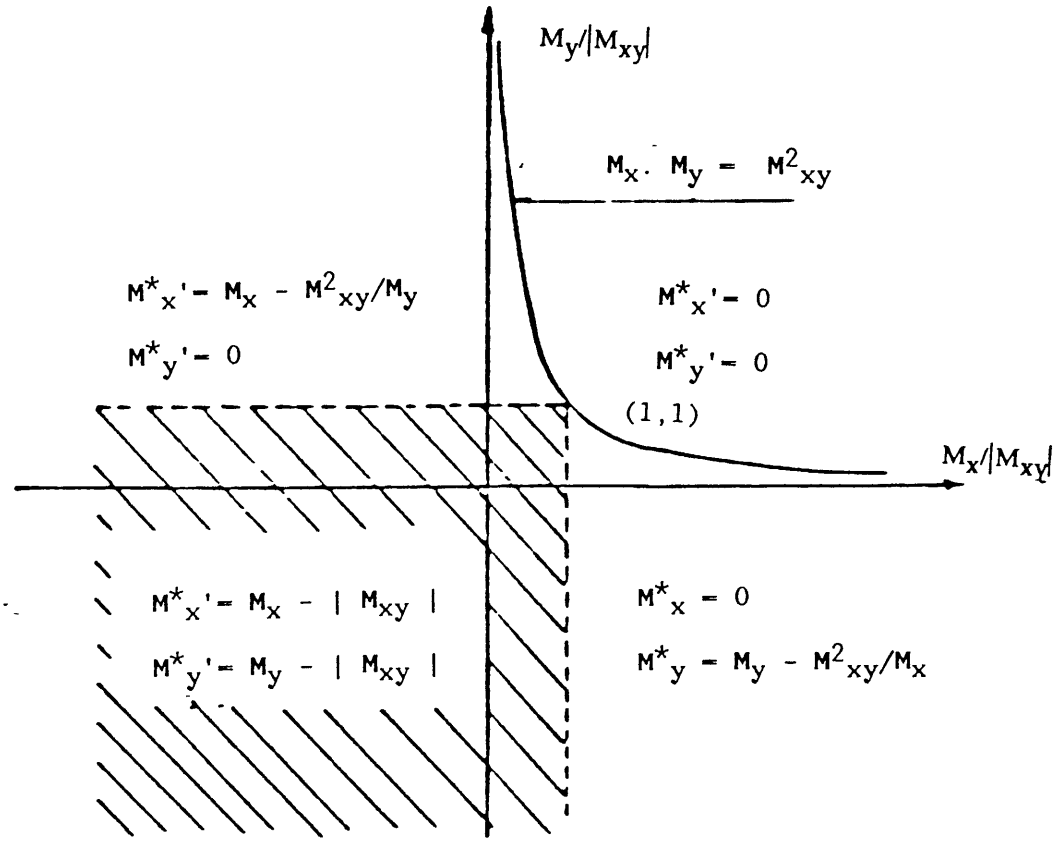

Figure (3.5) : Design equations for top steel.

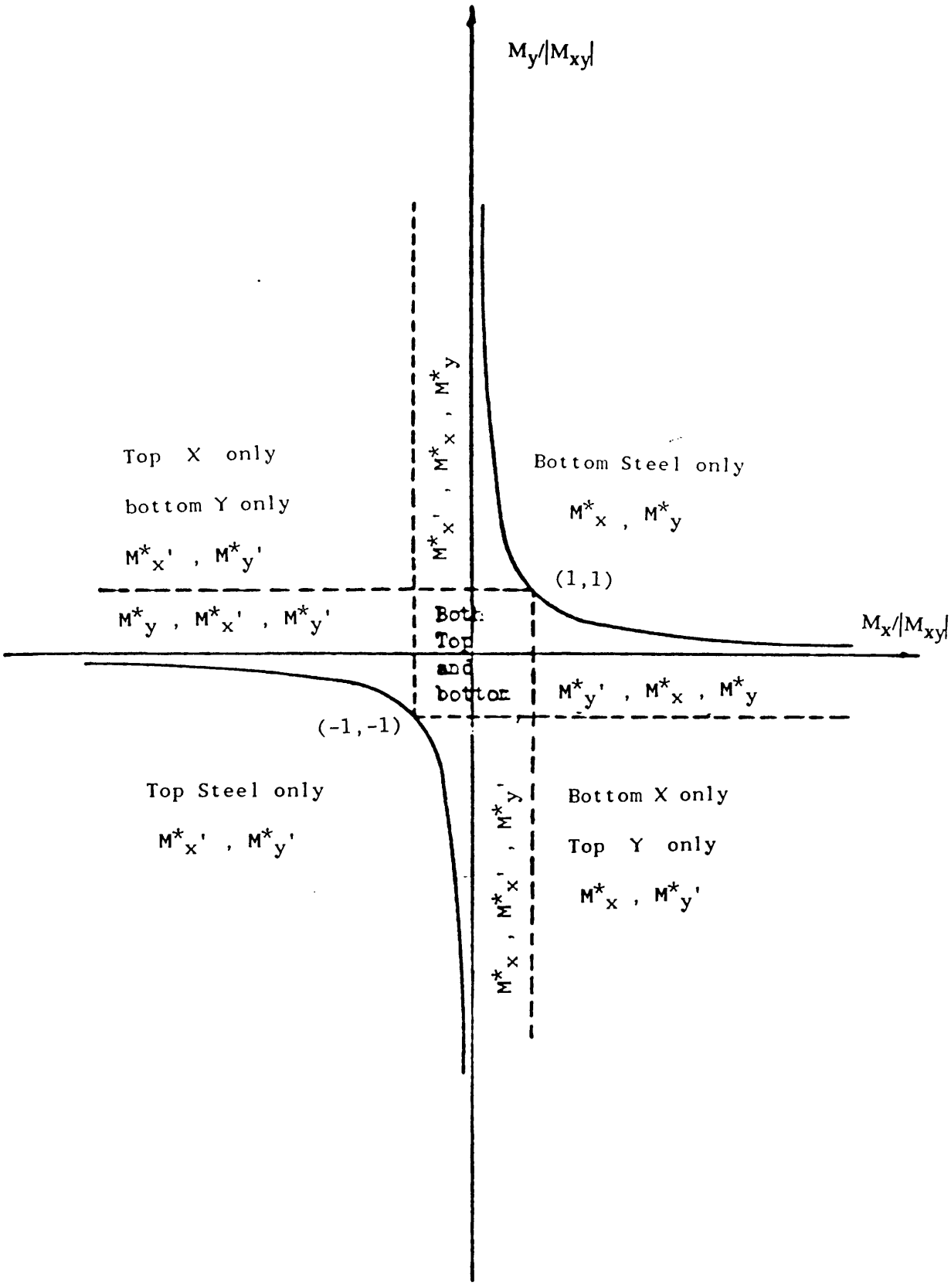

Figure (3.6) : Reinforcement required for a given moment triad.

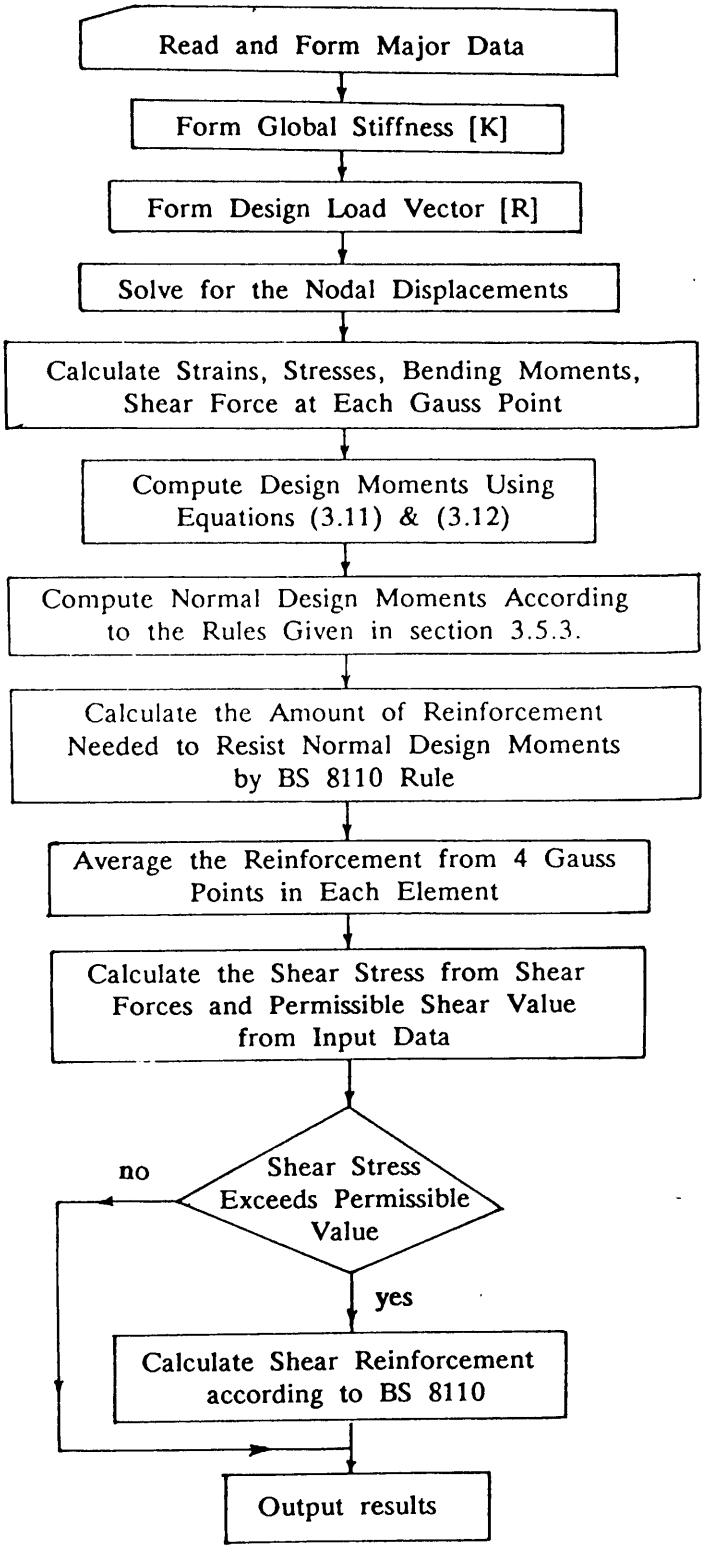

Figure (3.7) : Flow Chart of the Program

mechanism. Because of the fact that minimum redistribution is needed to achieve collapse by this method, the demand for ductility which depends on the difference between the first and last yield in the structure as normally emphasized by the theory of plasticity will obviously drop.

3.6 Design of Slabs in Experimental Models

3.6.1 General

It has been mentioned earlier that one of the aims of the present work is to study the strength of wall–slab connection using shear reinforcement in the slab. The slab flexural and shear reinforcement are believed to be a major parameter affecting the strength of the connection. Therefore, a rational method for the design of slab reinforcement of experimental models is presented here.

3.6.2 Analysis of tall buildings

Before going into the detailed design aspects , it may be useful to analyse some tall buildings to study the effect of different geometrical dimensions on the maximum value of vertical shear force applied on the coupling slabs due to lateral loads (termed here as Maximum "wind" shear). A typical plan of such building is shown in Figure (3.8).

It was assumed that the building were to be erected in Glasgow area with maximum basic wind speed of 51 meter per second (according to the recommendations of CP3[48]). From this speed, the equivalent static wind loading is calculated. Assuming the wind pressure to be constant with height, the maximum wind shear V_w, induced in most highly stressed slab was calculated by the continuous connection method making use of the recommendations of Coull and Wong[3] for the effective slab width (see Figures (2.3– a) and (2.3– b)). A slab thickness of 230 mm, and a floor to floor height of 3m were adopted to analyse all the structures as 25 storeys high buildings with rectangular shear wall. The

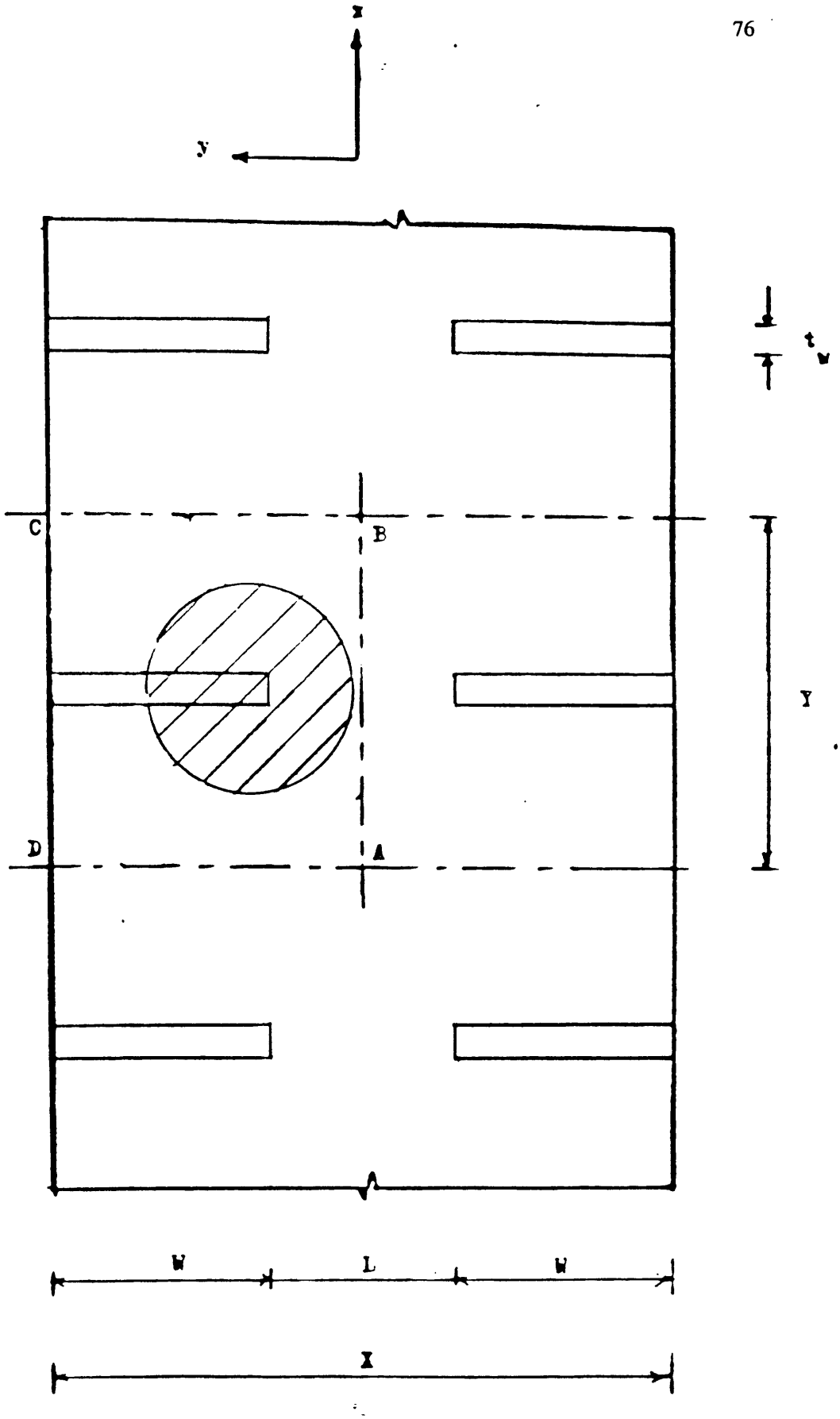

Figure (3.8) : Floor-plan of a typical shear wall structure.

other dimensions of the structures e.g. wall–web length, bay width, corridor width etc. were varied, one at a time and keeping others constant to study the effect of each parameter on the maximum "wind" shear value. Figure (3.9) shows that the corresponding maximum "wind" shear per unit bay width increases with the increase of bay width (Y); while the effect of wall–web length (W) is inversely proportional to the maximum wind shear as shown in Figure (3.10). Figures (3.11) and (3.12) show the effect of corridor opening width (L) and flange width (Z) on the maximum wind shear per unit bay width. From Figures (3.9) to (3.11), it is found that the values of the maximum "wind" shear per unit bay width ranges from about 16 to 32 KN depending on the geometry. Commonly encountered archietectural layouts of apartment buildings lead to bay sizes of 5–10 meters and widths of buildings between 10 to 20 meters. Therefore an average value of about 200 KN was taken into consideration in designing most of the models.

3.6.3 Procedure Adopted for the design of a Typical Model

Since the present study is a problem of local failure around the slab–wall junction, no great care is exercised to make the models conform to the laws of geometrical similitude. With reference to the plan shown in Figure (3.8), the model was chosen by isolating a wall and a portion of the slab (the shaded part). Therefore, a typical model was as shown in Figure (3.13) in which the lateral load will be simulated by a uniform displacement of the edge AB.

A two dimensional finite element computer programme for linear plate bending analysis has been used for the design of model slabs. For this purpose, use was made of symmetry so that only one half of the slab needs to be discretized using the finite element mesh shown in Figure (3.14). The boundary conditions used are as follows :

if w = translation in z–direction (normal to the paper)

$\partial w/\partial x$ = rotation about y–axis ;

$\partial w/\partial y$ = rotation about x–axis ;

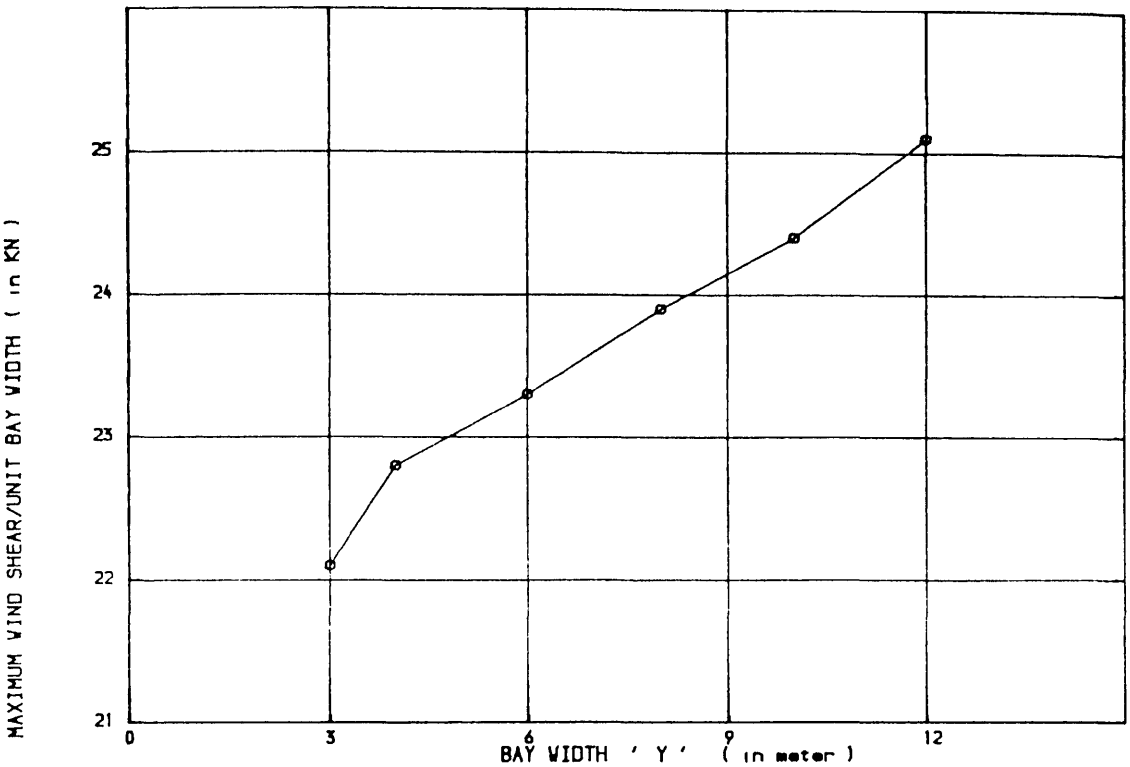

FIGURE (3.9) , EFFECT OF BAY WIDTH ON THE MAXIMUM WIND SHEAR VALUE INDUCED IN MOST HIGHLY STRESSED SLAB

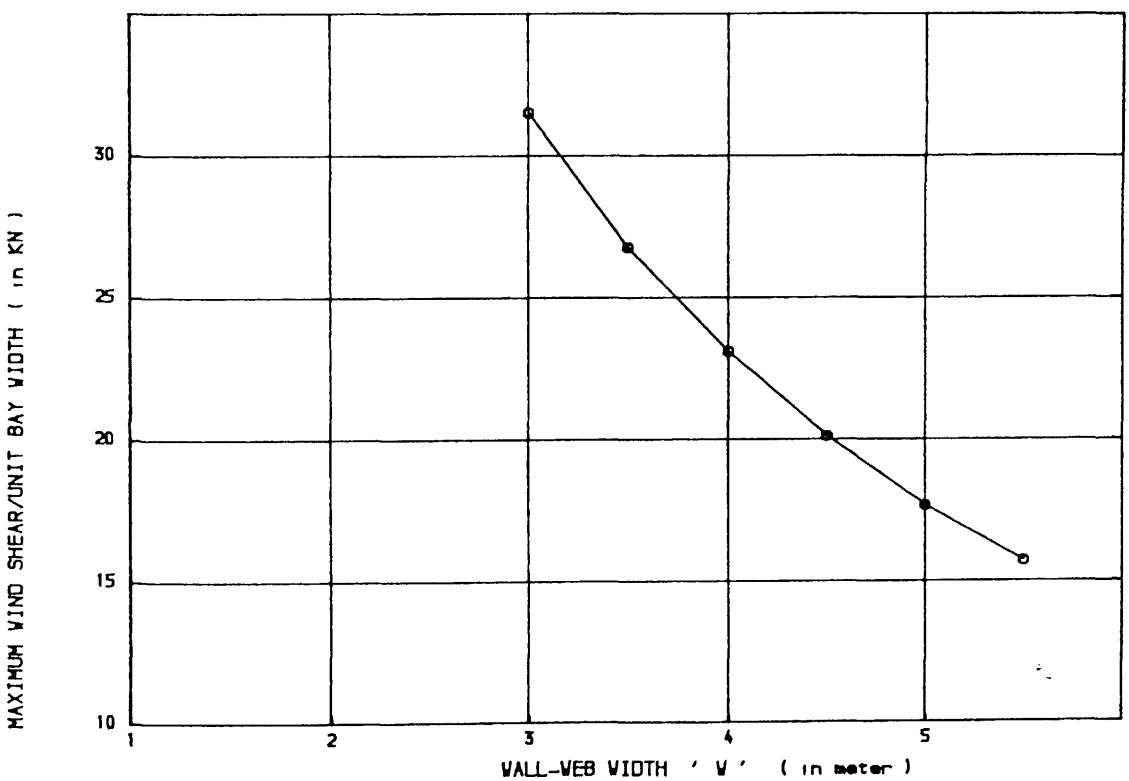

FIGURE (3.10) , EFFECT OF WALL-WEB WIDTH ON THE MAXIMUM WIND SHEAR VALUE INDUCED IN THE MOST HIGHLY STRESSED SLAB

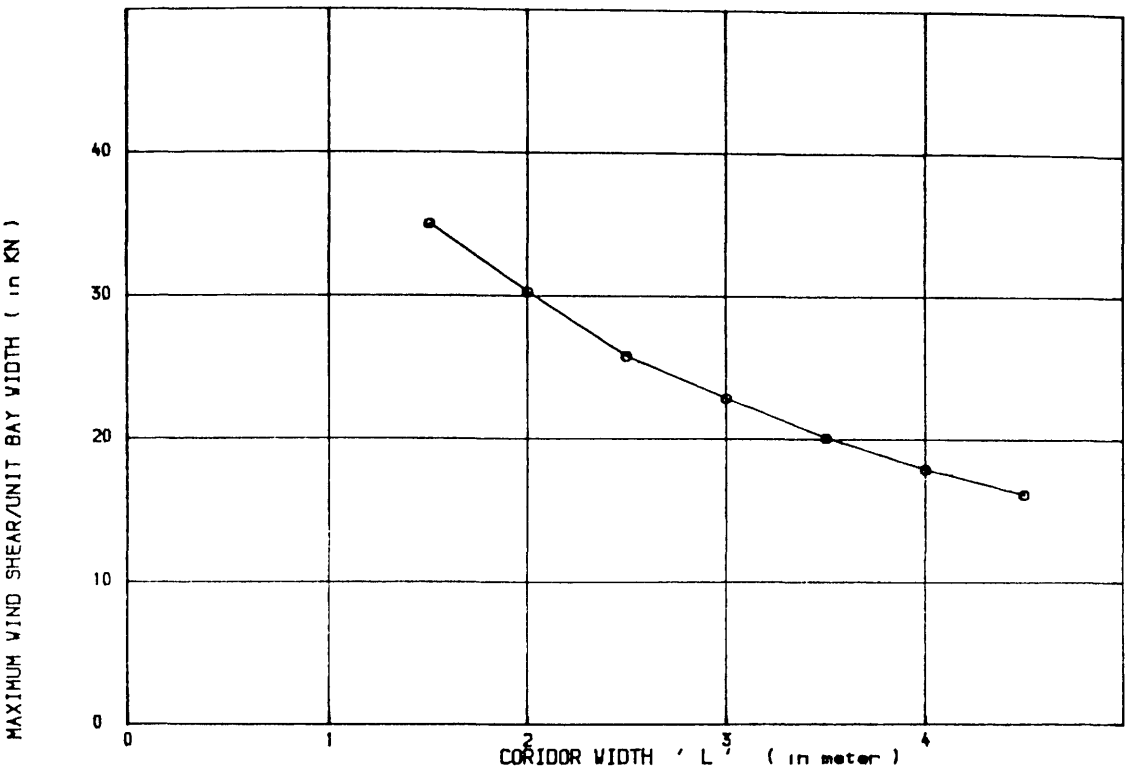

FIGURE (3.11) , EFFECT OF CORIDOR WIDTH ON THE MAXIMUM WIND SHEAR VALUE INDUCED IN THE MOST HIGHLY STRESSED SLAB

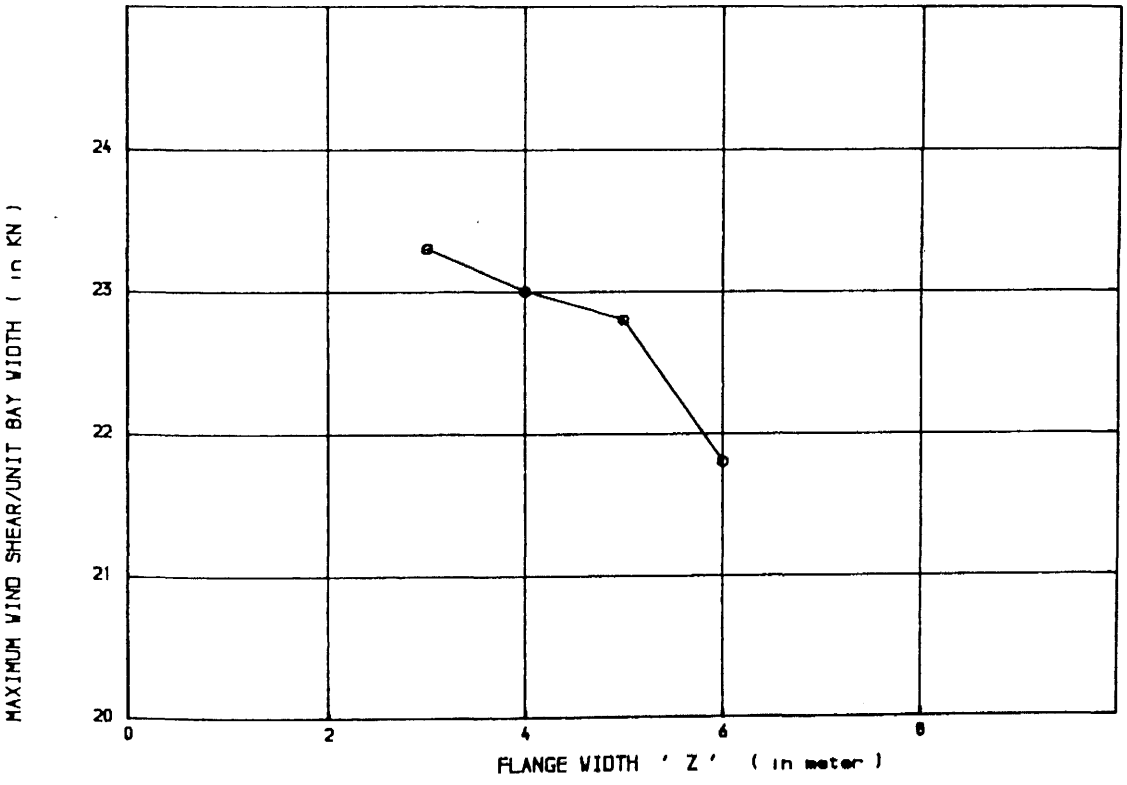

FIGURE (3.12) , EFFECT OF FLANGE WIDTH ON THE MAXIMUM WIND SHEAR VALUE INDUCED IN THE MOST HIGHLY STRESSED SLAB

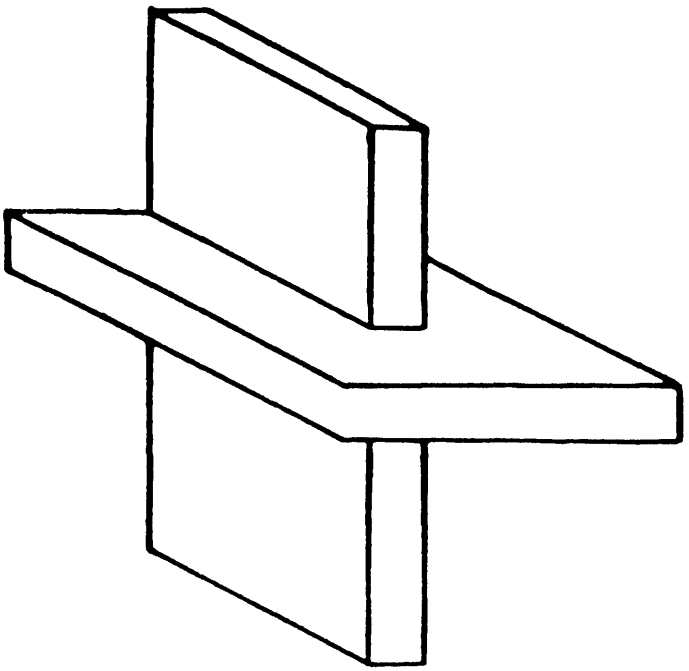

(a) Rectangular shear wall structure.

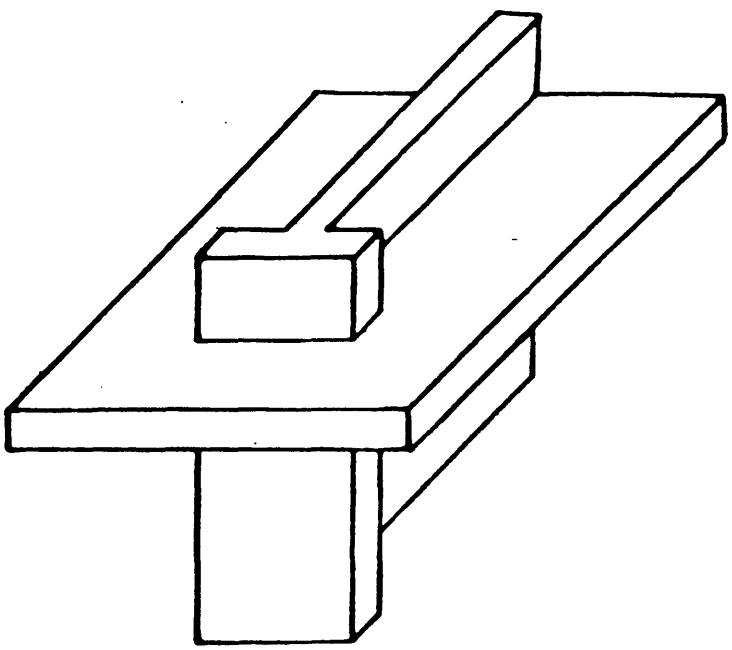

(b) Flanged shear wall structure.

Figure (3.13) : Typical model perspective.

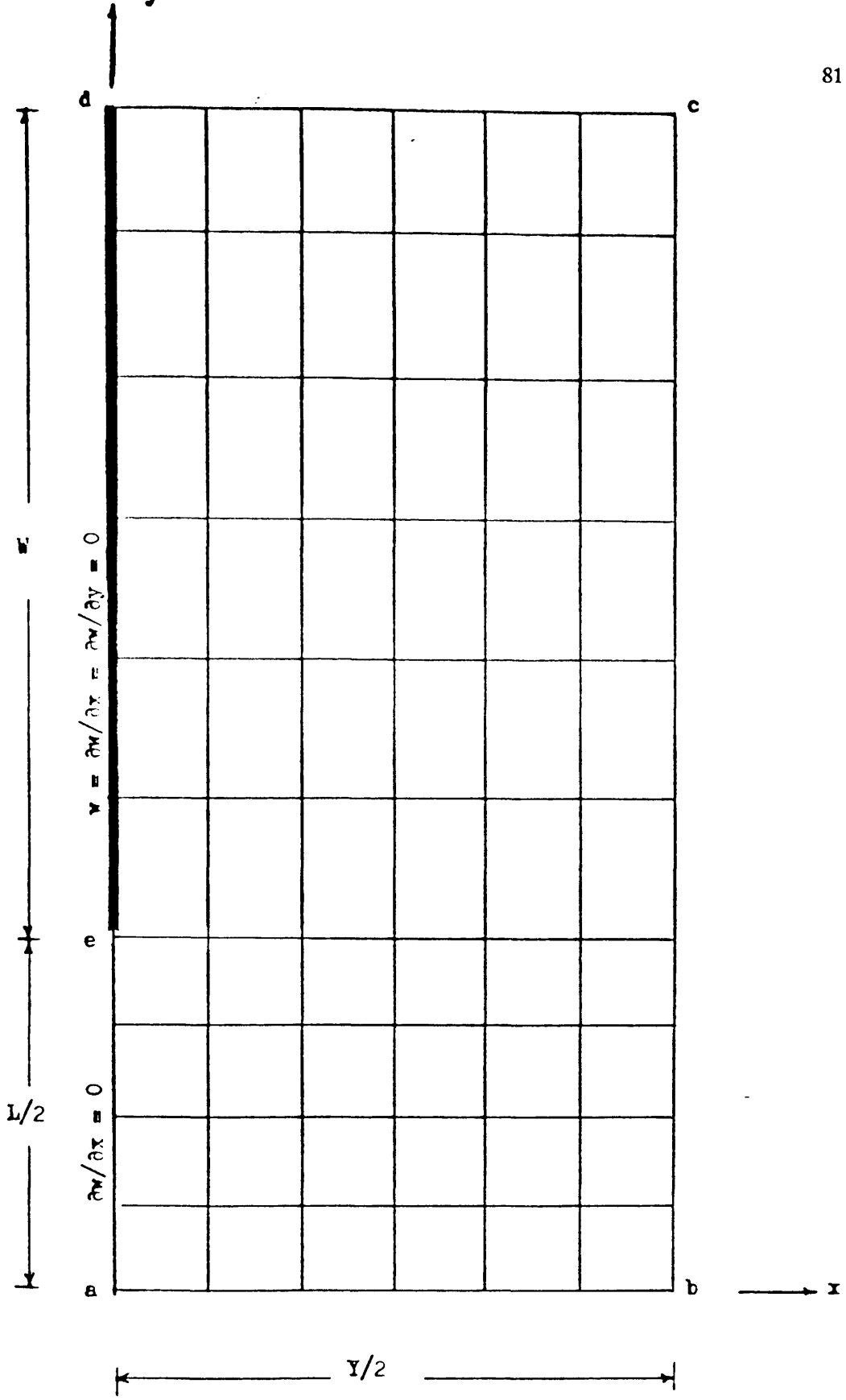

Figure (3.14) : Typical mesh with boundary conditions.

then all nodes along line 'de' will have $w = \partial w/\partial x = \partial w/\partial y = 0$; and all nodes along line 'ae' will have $\partial w/\partial x = 0$. Since we are interested in the local behaviour of the slab–wall junction, the violation of the boundary conditions of the real structure (which is discussed later in section 6.1.3) has minor importance.

A prescribed displacement, w, of all nodes along line 'ab' simulates lateral loading. Gravity loads were distributed on all nodes along line 'bc'. For the design lateral loads, the maximum "wind" shear was known but its distribution along line 'ab' which produced uniform displacement was needed. The distribution was obtained by imposing a unit prescribed displacement along line 'ab'. The corresponding reactions represented the required distribution which was then adjusted to match the value of the maximum "wind" shear. Figures (3.15) and (3.16) show the lateral load distribution pattern for a typical rectangular and flanged shear wall structure.

At the centre of each element, the computer programme provided the moment triad (M_x, M_y, M_{xy}) and shear forces (Q_x, Q_y) due to combined "wind" and gravity loadings. Using the moment triad, the values of the design moments M^*_x , M^*_y were evaluated according to the rules given in section (3.5.3) . Flexural steel required to resist these design moments at ultimate conditions was calculated using the recommendations of BS8110 with materials safety factors assumed to be unity.

The finite element programme results in a variable reinforcement pattern like the one given in Figure (3.17). The amounts of steel given at any point are per unit length. Two methods can be used to replace the distributed steel areas by discrete bars:

(a) If the variation of the distributed steel areas is not severe from one sampling point to another within the element, those areas can be averaged over a certain width. The total steel area is then obtained by multiplying the average value by the corresponding width and hence can be replaced by one bar of

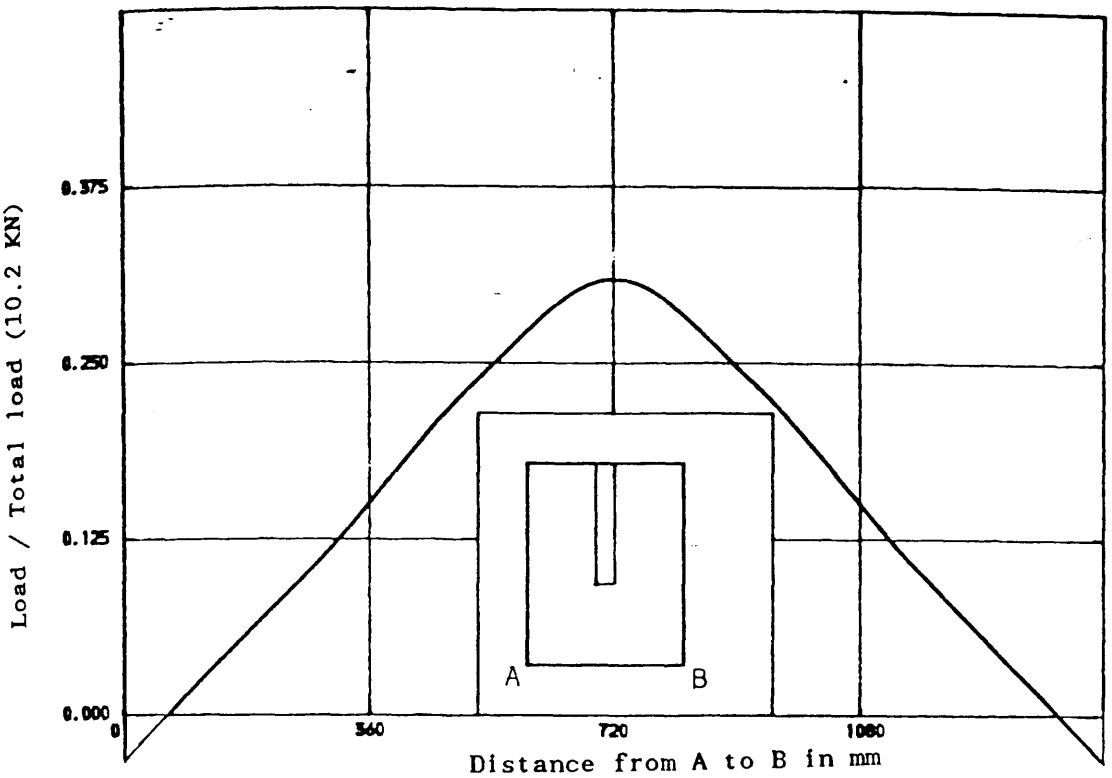

Figure (3.15) : Elastic distribution of wind shear required to displace the line of contraflexure, AB, uniformly by 0.05 mm for a rectangular shear wall structure

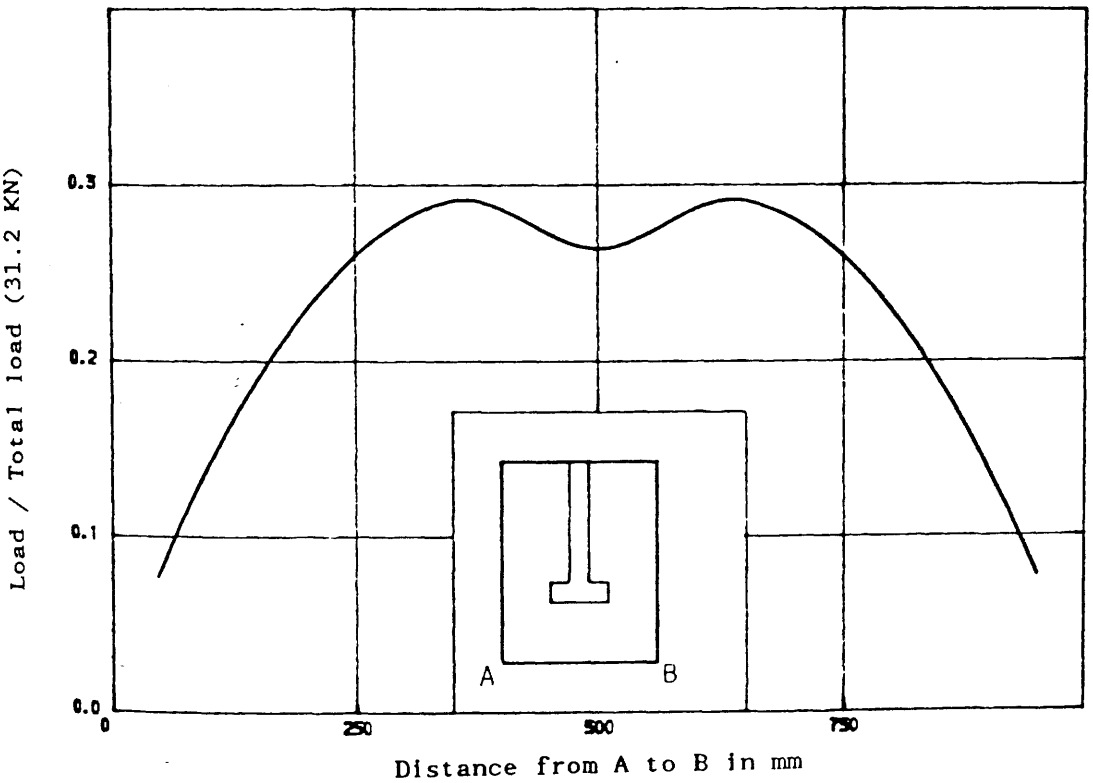

Figure (3.16) : Elastic distribution of wind shear required to displace the line of contraflexure, AB, uniformly by 0.05 mm for a flanged shear wall structure.

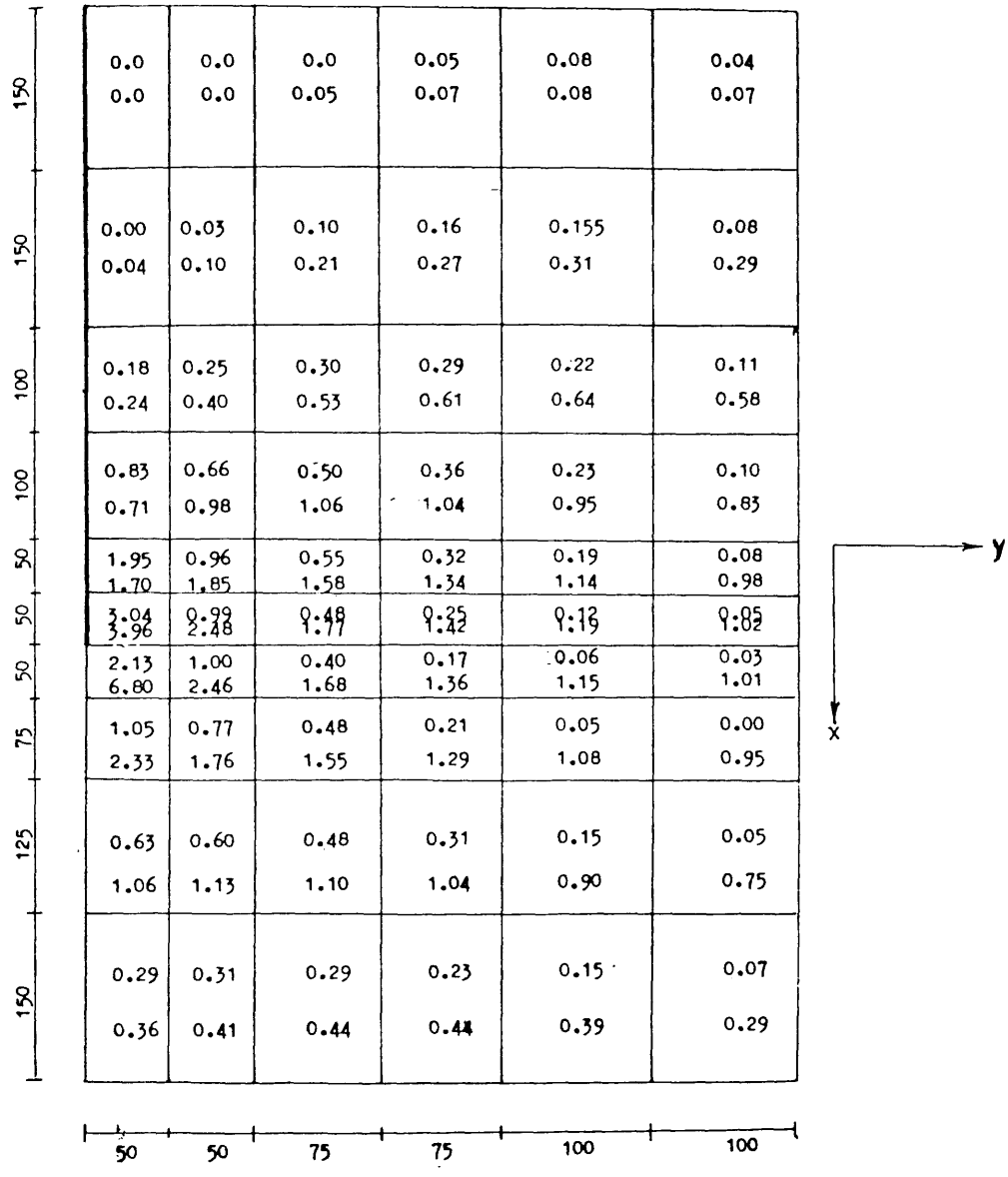

Figure (3.17) : Distributed steel in model MS7

(N.B. Quoted are elemental values averaged from 4 Gauss points in each element)

LEGEND

Top figures represent x steel while bottom figures represent y steel, e.g. :

0.29 - x steel

0.36 - y steel

an equivalent sectional area.

(b) Over a certain width, the design can be based on the maximum value of the distributed steel areas. Total steel area needed over such a width can thus be obtained by multiplying by the corresponding width.

For the type of meshes (see Figure 3.14) used in the programme, the reinforcement in the sampling points was approximately constant within the element. Accordingly, the design was based on averaging the distributed steel areas of the sampling points for each element. This reduced the problem to one of providing discrete bars in parallel strips, each covering the width of one element. Along the strips, the elements adjacent to the wall required in general more steel than others. The required steel quantities along transverse direction at the edge of the wall were maintained at a constant value throughout the slab, because the small dimensions of model slabs make it impractical to vary the bar diameter. The main longitudinal bars required at the edge of the wall were also provided at the constant value along corridor area but they were curtailed at the back of the slab after a certain length beyond the nose of the wall. In trying to achieve a reinforcement distribution close to that required by the elastic analysis, and at the same time to comply with the code regulations, the total steel (flexural) volume provided is in general much more than what is required. Figure (3.18) gives a comparison between the theoretical steel needed and that provided in each element of a typical model tested in this investigation. The allowable concrete shear stress ,v_c, for every element was calculated taking into consideration the required flexural steel area and concrete strength, f_{cu}. If the shear stress v obtained from Q_x or Q_y, exceeds v_c, shear reinforcement was calculated using following equation of BS8110 :

$$\frac{A_w}{S} = \frac{(v - v_c)\, b}{f_{yw}} \qquad (3.21)$$

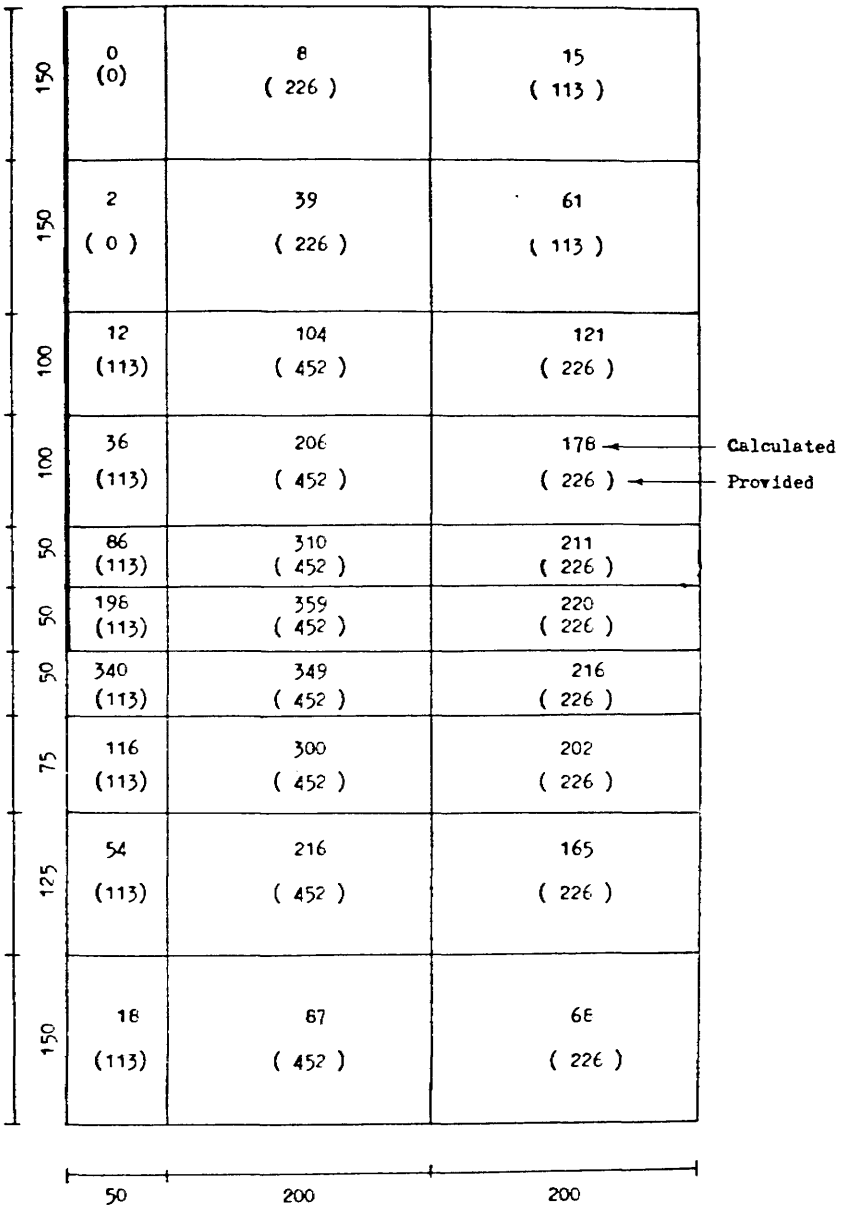

Figure (3.18) : Comparison between the theoretical steel needed and that provided in the elements of model MS7

where

f_{yw} = characteristic strength of shear steel ≥ 425 N/mm^2

A_w = cross sectional area of two legs of closed stirrup.

b = width of the element

s = spacing of the stirrup

CHAPTER FOUR

THE FINITE ELEMENT METHOD

4.1 Introduction

In recent years, the finite element method is firmly established as the most powerful general method for structural analysis and has provided engineers with a design tool of very wide applicability. In the case of reinforced concrete cracking, tension stiffening, nonlinear multiaxial material properties, complex interface behaviour, creep, shrinkage and other effects were previously ignored or treated in a very approximate manner. All those parameters can now be considered rationally by the finite element method.

The application of the finite element method to nonlinear problems is associated with a considerable increase in numerical work as compared with linear problems. However, development in the last two decades have ensured that high speed digital computers which meet this need are now available.

In this chapter, an approach for three dimensional nonlinear finite element analysis of reinforced concrete is presented. The theoretical results and their comparisons with the models which were tested in the present study will be shown in chapter seven.

4.2. Finite Element Formulation

As the main procedure of the finite element method is now well documented[49,50] no attempt will be made to describe it in detail. But in order to define terms for the sake of completeness a brief review of the method will be presented instead.

4.2.1 Discretisation by Finite Element

The finite element method started as an extension of the stiffness method of

analysis of skeletal structures and was applied to two – and three – dimensional problems in structural mechanics. However, unlike skeletal structures, there are no well–defined joints where equilibrium of forces can be established. So the continuum is divided into a series of elements of arbitrary shapes which are connected at a finite number of points known as nodal points. This process is known as discretisation.

For structural applications, one convenient method of obtaining the governing equilibrium equations is by minimizing the total potential energy of the system. The total potential energy, π, can be expressed as :

$$\pi = \frac{1}{2} \int_V [\sigma]^T [\epsilon] dv - \int_V [\delta]^T [p] dv - \int_S [\delta]^T [q] ds \qquad (4.1)$$

where $[\sigma]$ and $[\epsilon]$ are the stress and strain vectors respectively, $[\delta]$ the displacements at any point, [p] the body force per unit volume and [q] the applied surface tractions. Integrations are carried over the volume 'V' of the structure and loaded surface area 'S'.

The first term on the right hand side of equation (4.1) represents the internal strain energy and the second and third terms are respectively the work contributions of the body forces and distributed surface loads.

In the finite element displacement method, the displacement is assumed to have unknown values only at the nodal points so that the variation within any element is described in terms of the nodal values by means of interpolation functions. Thus

$$[\delta] = [N] [\delta^e] \qquad (4.2)$$

where [N] is the set of interpolation functions termed as shape functions and $[\delta^e]$ is the vector of nodal displacements of the element. The strains within the element can be expressed in terms of the element nodal displacements as

$$[\epsilon] = [B] [\delta^e] \qquad (4.3)$$

where [B] is the strain matrix generally composed of derivatives of shape functions. Finally, the stress may be related to the strains by use of an elasticity matrix [D] as follows

$$[\sigma] = [D]\,[\epsilon] \tag{4.4}$$

Provided that no singularities exist in the integrands of the functional, the total potential energy of the continuum will be the sum of the energy contributions of the individual elements. Thus

$$\pi = \Sigma\, \pi_e \tag{4.5}$$

where π_e represents the total potential of element 'e' which, using equation (4.1), can be written as

$$\pi_e = \frac{1}{2} \int_{V_e} [\delta^e]^T\, [B]^T\, [D]\, [B]\, [\delta^e]\, dV - \int_{V_e} [\delta^e]^T\, [N]^T\, [p]\, dV - \int_{S_e} [\delta^e]^T\, [N]^T\, [q]\, ds \tag{4.6}$$

where V_e is the element volume and S_e the loaded element surface area. Performance of minimisation for element 'e' with respect to the nodal displacement $[\delta^e]$ for the element results in

$$\frac{\partial\, \pi_e}{\partial\, \delta^e} = \int_{V_e} ([B]^T[D][B])\, [\delta^e] dV - \int_{V_e} [N]^T[p] dV - \int_{S_e} [N]^T[q] ds$$

$$= [K^e]\, [\delta^e] - [F^e] \tag{4.7}$$

where

$$[F^e] = \int_{V_e} [N]^T\, [P] dv + \int_{S_e} [N]^T\, [q] ds \tag{4.8}$$

are the equivalent nodal forces, and

$$[K^e] = \int_{V_e} [B]^T\, [D]\, [B] \tag{4.9}$$

is termed the 'element stiffness matrix'. The summation of the terms in equation (4.7) over all the elements, when equated to zero, results in a system of equilibrium equations for the complete continuum. These equations are then solved by any standard technique to yield the nodal displacements. The strains and therefore the stresses within each element can be calculated from the displacements

using equations (4.3) and (4.4).

4.2.2 Element Type

The selection of the element type is always related to the type of problems to be solved. As three dimensional nonlinear analysis is the prime concern of the analytical portion of this study, the 20-noded isoparametric brick element[49], as illustrated in Figure (4.1), is used throughout this work to represent concrete. Reinforcing steel is simulated by bars embeded inside the concrete element at their actual locations in the structure without imposing any restrictions on the mesh choice. The mathematical derivations of these bars can be found in Reference (24,56).

This element was chosen to consider the effect of the six stress components σ_x, σ_y, σ_z, τ_{xy}, τ_{yz}, τ_{zx} (Figure 4.2) and in particular the vertical shear stress components τ_{yz} and τ_{zx} which are vital for predicting shear failure of slab-wall junction. Each nodal point has three degrees of freedom, viz.,

translation in x-direction = u,

translation in y-direction = v, and

translation in z-direction = w.

Each element has its own local spatial coordinate system (ξ, η, ζ) (Figure 4.1), with the origin at the centre of element such that each local coordinate ranges from -1 to $+1$ only.

4.2.3 Shape Functions

Shape functions are interpolation functions which describe the variation within the element of the displacement in terms of the nodal displacement

$$[\delta] = \sum_{i=1}^{n} [N_i] [\delta_i] \tag{4.10}$$

where N_i is the shape function at the i-th node at which the nodal displacement

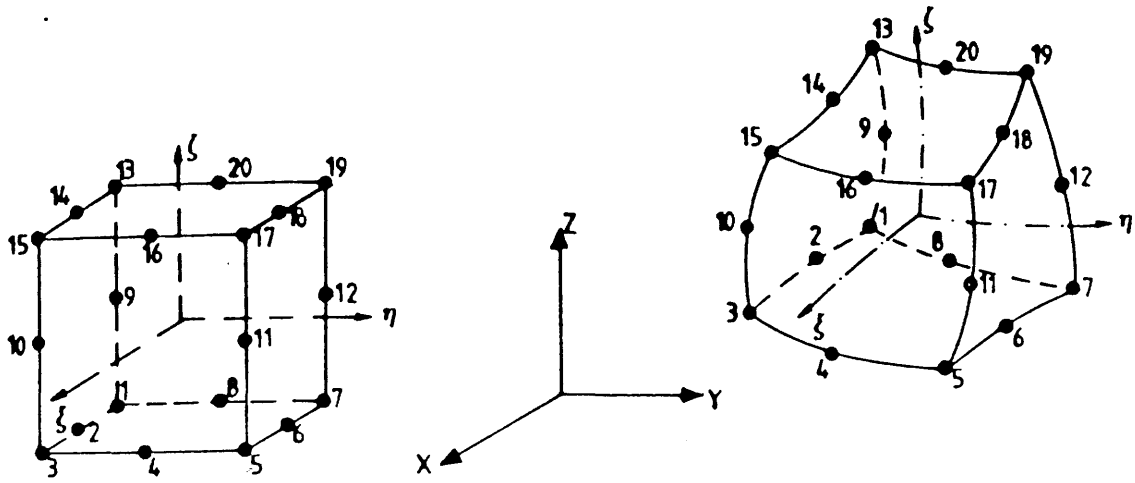

(a) Local coordinates

(b) Cartesian coordinates

Figure (4.1) : 20-Noded isoparametric brick element

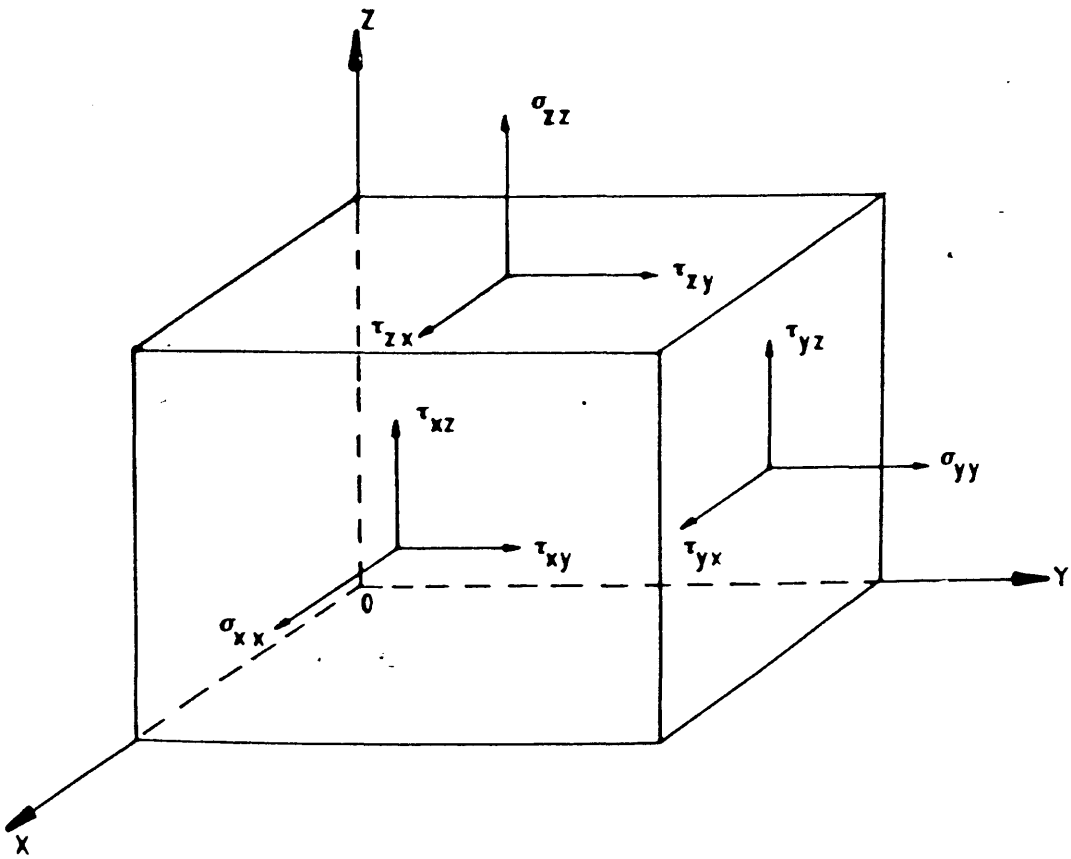

Figure (4.2) : Cartesian stress components

is δ_i.

The efficiency of any particular element type will depend on how well the shape functions are capable of representing the true displacement field. The isoparametric family are a group of elements in which the shape functions are used to define the geometry as well as the displacement field. This leads to reduced computational effort and efficiency. The isoparametric elements are better known for their accuracy and versatility over simpler type of elements. Moreover a considerable saving of computer effort is obtained, even though a complex element requires more time to formulate. This is because it requires fewer elements compared with more simple elements.

For three dimensional applications, the displacements field at a particular local coordinate (ξ,η,ζ) are $u(\xi,\eta,\zeta)$, $v(\xi,\eta,\zeta)$, $w(\xi,\eta,\zeta)$ and are defined using three displacements degrees of freedom u_i, v_i, w_i at each of the twenty nodes and a quadratic interpolation scheme.

The coordinate values $x(\xi,\eta,\zeta)$, $y(\xi,\eta,\zeta)$ and $z(\xi,\eta,\zeta)$ at any point (ξ,η,ζ) within the element may be defined by the expressions :

$$\begin{aligned} x(\xi,\eta,\zeta) &= \sum_{i=1}^{20} N_i\,(\xi,\eta,\zeta)\,.\,x_i \\ y(\xi,\eta,\zeta) &= \sum_{i=1}^{20} N_i\,(\xi,\eta,\zeta)\,.\,y_i \\ z(\xi,\eta,\zeta) &= \sum_{i=1}^{20} N_i\,(\xi,\eta,\zeta)\,.\,z_i \end{aligned} \qquad (4.11)$$

and where (x_i,y_i,z_i) are the coordinates of node 'i' and $N_i(\xi,\eta,\zeta)$ are three dimensional quadratic shape functions. In the present work, such shape functions of each of the twenty nodes were obtained from reference[49] as follows :

For corner nodes $\xi_i = \pm 1 \quad \eta_i = \pm 1 \quad \zeta_i = \pm 1$

$$N_i(\xi,\eta,\zeta) = \frac{1}{8}\,(1+\xi\xi_i)(1+\eta\eta_i)(1+\zeta\zeta_i)(\xi\xi_i + \eta\eta_i + \zeta\zeta_i - 2) \qquad (4.12)$$

For mid-side node $\xi_i = \pm 0 \quad \eta_i = \pm 1 \quad \zeta_i = \pm 1$

$$N_i(\xi,\eta,\zeta) = \frac{1}{4}(1-\xi^2)(1+\eta\eta_i)(1+\zeta\zeta_i) \tag{4.13}$$

For mid-side node $\xi_i = \pm 1 \quad \eta_i = \pm 0 \quad \zeta_i = \pm 1$

$$N_i(\xi,\eta,\zeta) = \frac{1}{4}(1+\xi\xi_i)(1-\eta^2)(1+\zeta\zeta_i) \tag{4.14}$$

For mid-side node $\xi_i = \pm 1 \quad \eta_i = \pm 1 \quad \zeta_i = \pm 0$

$$N_i(\xi,\eta,\zeta) = \frac{1}{4}(1+\xi\xi_i)(1+\eta\eta_i)(1-\zeta^2) \tag{4.15}$$

Each of the twenty shape function has a value of unity at the node to which it is related and zero at other nodes.

To calculate the displacements $u(\xi,\eta,\zeta)$, $v(\xi,\eta,\zeta)$ and $w(\xi,\eta,\zeta)$ at any point within the element, expressions similar to (4.10) may be written as follows :

$$\begin{aligned} u(\xi,\eta,\zeta) &= \sum_{i=1}^{20} N_i(\xi,\eta,\zeta) \cdot u_i \\ v(\xi,\eta,\zeta) &= \sum_{i=1}^{20} N_i(\xi,\eta,\zeta) \cdot v_i \\ w(\xi,\eta,\zeta) &= \sum_{i=1}^{20} N_i(\xi,\eta,\zeta) \cdot w_i \end{aligned} \tag{4.16}$$

4.2.4 Strain Matrix

In three dimensional linear analysis, the strain – displacement relationship from theory of elasticity may be written as :

$$\begin{aligned} \epsilon_x &= \partial u/\partial x \\ \epsilon_y &= \partial v/\partial y \\ \epsilon_z &= \partial w/\partial z \\ \gamma_{xy} &= \partial u/\partial y + \partial v/\partial x \\ \gamma_{yz} &= \partial v/\partial z + \partial w/\partial y \\ \gamma_{zx} &= \partial w/\partial x + \partial u/\partial z \end{aligned} \tag{4.17}$$

in which ϵ_x, ϵ_y, ϵ_z are the normal strain components and γ_{xy}, γ_{yz}, γ_{zx} are the shear strain components. Equations (4.17) may be written in matrix form as follows:

$$[\ \epsilon\ ] = \begin{bmatrix} \epsilon_x \\ \epsilon_y \\ \epsilon_z \\ \gamma_{xy} \\ \gamma_{yz} \\ \gamma_{zx} \end{bmatrix} = \begin{bmatrix} \partial/\partial x & 0 & 0 \\ 0 & \partial/\partial y & 0 \\ 0 & 0 & \partial/\partial z \\ \partial/\partial y & \partial/\partial x & 0 \\ 0 & \partial/\partial z & \partial/\partial y \\ \partial/\partial z & 0 & \partial/\partial x \end{bmatrix} \begin{bmatrix} u \\ v \\ w \end{bmatrix} \tag{4.18}$$

using the finite element idealisation we can write

$$[\ \epsilon\ ] = \sum_{i=1}^{20} \begin{bmatrix} \partial N_i/\partial x & 0 & 0 \\ 0 & \partial N_i/\partial y & 0 \\ 0 & 0 & \partial N_i/\partial z \\ \partial N_i/\partial y & \partial N_i/\partial x & 0 \\ 0 & \partial N_i/\partial z & \partial N_i/\partial y \\ \partial N_i/\partial z & 0 & \partial N_i/\partial x \end{bmatrix} \begin{bmatrix} u_i \\ v_i \\ w_i \end{bmatrix} \tag{4.19}$$

or simply

$$[\ \epsilon\ ] = \sum_{i=1}^{20} [B_i]\ [\delta_i] \tag{4.20}$$

where $[B_i]$ is the 6x3 strain matrix in equation (4.19) which contains the cartesian derivatives of the shape functions. Since the shape functions N_i are defined in terms of the local coordinates of the element (ξ, η, ζ) a transformation from local to global coordinates is required to obtain the [B] matrix in equation (4.19). This is done through the well known Jacobian matrix which is written as

$$[\ J\ ] = \begin{bmatrix} \partial x/\partial \xi & \partial y/\partial \xi & \partial z/\partial \xi \\ \partial x/\partial \eta & \partial y/\partial \eta & \partial z/\partial \eta \\ \partial x/\partial \zeta & \partial y/\partial \zeta & \partial z/\partial \zeta \end{bmatrix} \tag{4.21}$$

thus

$$[\ J\ ] = \sum_{i=1}^{20} \begin{bmatrix} \frac{\partial N_i}{\partial \xi}.x_i & \frac{\partial N_i}{\partial \xi}.y_i & \frac{\partial N_i}{\partial \xi}.z_i \\ \frac{\partial N_i}{\partial \eta}.x_i & \frac{\partial N_i}{\partial \eta}.y_i & \frac{\partial N_i}{\partial \eta}.z_i \\ \frac{\partial N_i}{\partial \zeta}.x_i & \frac{\partial N_i}{\partial \zeta}.y_i & \frac{\partial N_i}{\partial \zeta}.z_i \end{bmatrix} \qquad (4.22)$$

the inverse of the jacobian matrix will be

$$[\ J\ ]^{-1} = \begin{bmatrix} \frac{\partial \xi}{\partial x} & \frac{\partial \eta}{\partial x} & \frac{\partial \zeta}{\partial x} \\ \frac{\partial N_i}{\partial y} & \frac{\partial N_i}{\partial y} & \frac{\partial \zeta}{\partial y} \\ \frac{\partial N_i}{\partial z} & \frac{\partial N_i}{\partial z} & \frac{\partial \zeta}{\partial z} \end{bmatrix} \qquad (4.23)$$

Therefore the cartesian derivatives are given by

$$\begin{bmatrix} \frac{\partial N_i}{\partial x} \\ \frac{\partial N_i}{\partial y} \\ \frac{\partial N_i}{\partial z} \end{bmatrix} = [\ J\ ]^{-1} \begin{bmatrix} \frac{\partial N_i}{\partial \xi} \\ \frac{\partial N_i}{\partial \eta} \\ \frac{\partial N_i}{\partial \zeta} \end{bmatrix} \qquad (4.24)$$

4.2.5 Stress – Strain Relationship

For linear analysis of uncracked concrete, and in the abscence of initial stresses and strains, the stress–strain relationship may be written in the form

$$[\sigma] = [D]\ [\epsilon] \qquad (4.25)$$

where [D] is the elasticity matrix which takes the form

$$[D] = \frac{E(1-\nu)}{(1+\nu)(1-2\nu)} \begin{bmatrix} 1 & \frac{\nu}{(1-\nu)} & \frac{\nu}{(1-\nu)} & 0 & 0 & 0 \\ & 1 & \frac{\nu}{(1-\nu)} & 0 & 0 & 0 \\ & & 1 & 0 & 0 & 0 \\ & & & \frac{(1-2\nu)}{2(1-\nu)} & 0 & 0 \\ & \text{Symmetry} & & & \frac{(1-2\nu)}{2(1-\nu)} & 0 \\ & & & & & \frac{(1-2\nu)}{2(1-\nu)} \end{bmatrix} \quad (4.26)$$

where 'E' is the Young's modulus of elasticity and ν is Poission's ratio. The concrete nonlinearity as considered in this work is only the material nonlinearity and all changes in material properties enter through the changes in elasticity matrix [D]. This will be discussed later in section 4.4.4.3.

4.2.6 Numerical Integration

Analytical integration of equation (4.9) is impossible. Therefore some form of numerical integration must be resorted to. In this study Gauss–Legendre quadrature rules have been used exclusively because of their higher efficiency over other forms of quadrature. For n sampling points they can integrate exactly a polynomial $f(\xi)$ of degree $(2n-1)$. Also they are suitable for isoparametric elements because the range of these integration rules are ±1 on element boundaries. A 3x3x3 Gauss rule was used for monitoring nonlinear behaviour especially cracking, as shown in Figure (4.3), although 2x2x2 and 4x4x4 are also available.

4.2.7 Principal Stresses, Magnitudes and Directions

The evaluation of principal stresses and their respective directions in the global cartesian system of axes is important for the determination of the occurance and orientation of cracking in concrete. The solution of the resulting set of linear equations yields the nodal displacements and hence the strains. The strains are used

to obtain the stresses at each sampling point in the structure. From equation (4.25), there are six cartesian stress components at each Gauss point that can be evaluated, namely:

$$[\sigma] = [\ \sigma_x \quad \sigma_y \quad \sigma_z \quad \tau_{xy} \quad \tau_{yz} \quad \tau_{zx}\ ] \tag{4.27}$$

The values of the principal stresses, σ_i, can be obtained by solving the following cubic equation(51)

$$\sigma_i^3 - I_1\sigma_i^2 + I_2\sigma_i - I_3 = 0 \tag{4.28}$$

in which I_1, I_2, I_3 are the stress invariants, which may be expressed as follows:

$$I_1 = \sigma_x + \sigma_y + \sigma_z \tag{4.29}$$

$$I_2 = [\sigma_x\sigma_y + \sigma_y\sigma_z + \sigma_z\sigma_x - \tau^2_{xy} - \tau^2_{yz} - \tau^2_{zx}] \tag{4.30}$$

I_3 = determinant of the stress tensor

$$\begin{vmatrix} \sigma_x & \tau_{xy} & \tau_{zx} \\ \tau_{yx} & \sigma_y & \tau_{yz} \\ \tau_{zx} & \tau_{zy} & \sigma_z \end{vmatrix} \tag{4.31}$$

The principal directions which determine the principal planes can be expressed by their respective direction cosines such that:

$$\ell_i = \cos\ \theta x_i;\quad m_i = \cos\ \theta y_i;\quad n_i = \cos\ \theta z_i \tag{4.32}$$

Thus the direction cosines of σ_1 are ℓ_1, m_1, n_1; those for σ_2 are ℓ_2, m_2, n_2 and those for σ_3 are ℓ_3, m_3, n_3.

The method to evaluate these direction cosines is explained in details elsewhere(51) and is briefly presented here. Denoting

$$A = \begin{vmatrix} \sigma_y-\sigma_i & \tau_{zy} \\ \tau_{yz} & \sigma_z-\sigma_i \end{vmatrix} \quad B = -\begin{vmatrix} \tau_{xy} & \tau_{zy} \\ \tau_{xz} & \sigma_z-\sigma_i \end{vmatrix} \quad C = \begin{vmatrix} \tau_{xy} & \sigma_y-\sigma_i \\ \tau_{xz} & \tau_{yz} \end{vmatrix} \tag{4.33}$$

it can be shown that the three direction cosines can be expressed as :

$$\frac{\ell_i}{A} = \frac{m_i}{B} = \frac{n_i}{C} = K \tag{4.34}$$

where K is a non−zero constant to be determined. The subsidiary trigonometric condition:

$$\ell_i^2 + m_i^2 + n_i^2 = 1 \tag{4.35}$$

determines K as :

$$K = \frac{1}{\sqrt{A^2 + B^2 + C^2}} \tag{4.36}$$

then $\ell_i = A.\ K$; $m_i = B.\ K$ and $n_i = C.\ K$ (4.37)

4.3 Simulation of Steel Reinforcement

In modelling reinforced concrete by finite element methods, at least the following three alternative representations of the reinforcement have been used:

(a) distributed

(b) discrete

(c) embedded

For a distributed representation (Figure (4.4− a), the steel is assumed to be distributed over the concrete element, with a particular orientation angle. A composite concrete reinforcement constitutive relation need to be used in this case. To derive such a relation, perfect bond must be assumed between the concrete and steel[52,53].

A discrete representation of the reinforcement, using one− dimensional elements (Figure 4.4− b), has been widely used[53]. Axial force members are assumed to be pin connected with three degrees of freedom at the nodal points. The one− dimensional reinforcement element is superimposed on a three− dimensional finite element mesh representing concrete. The approach is simple and it is possible to account for possible displacement of the reinforcement with respect to the surrounding concrete. A serious disadvantage, however, is that the location of steel often dictates the concrete mesh. This may result in slender elements, where the reinforcing bars are too close together, violating the concept of aspect ratio of

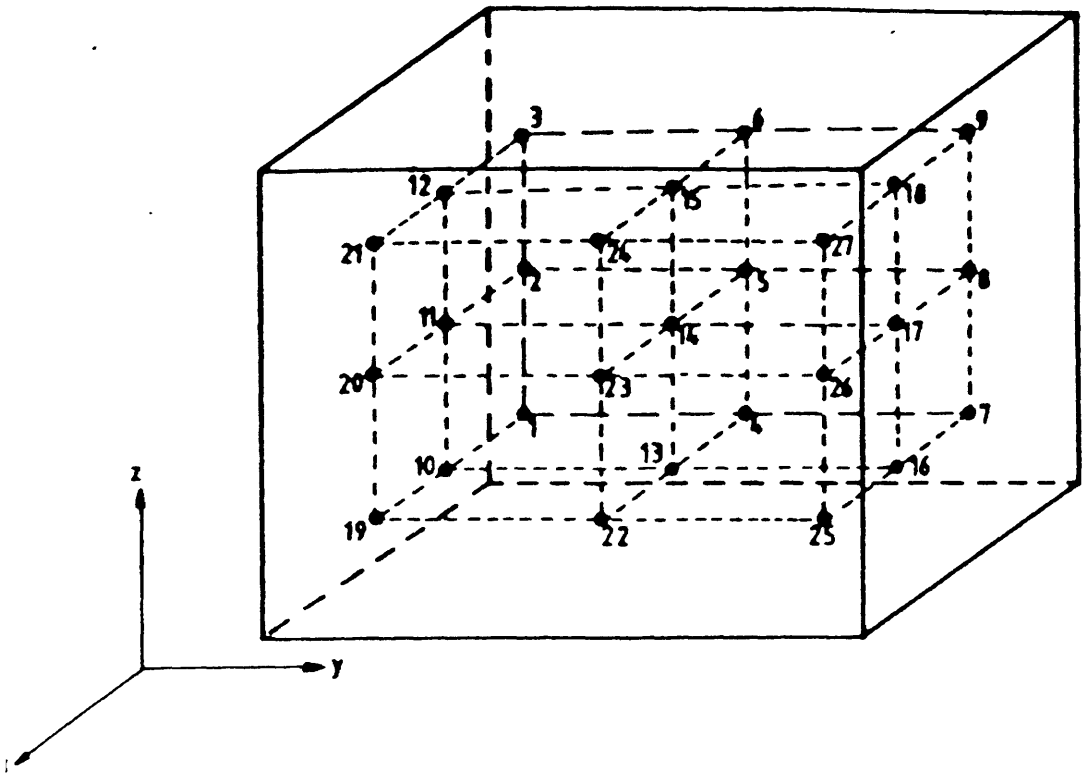

Figure (4.3) : Location of Gauss points for the 3x3x3 integration rule; those for the 2x2x2 and 4x4x4 rules follow the same order

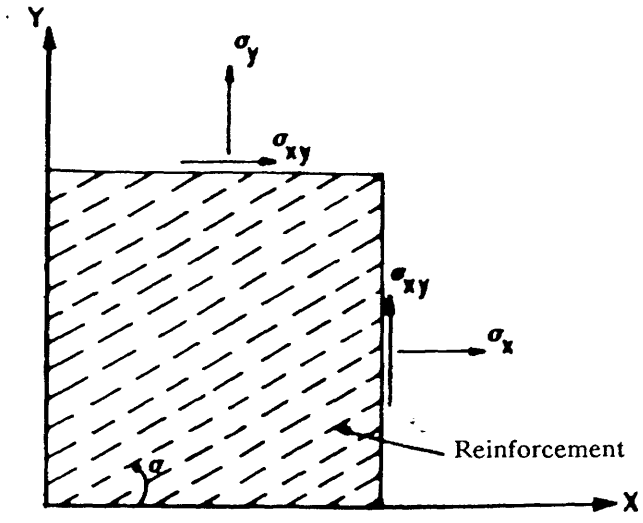

Figure (4.4-a) : Distributed representation of steel

the element being close to unity as far as possible.

An embedded representation (Figure 4.4– c) may be used in connection with higher order isoparametric concrete elements. The reinforcing bar is considered to be an axial member built into the isoparametric element such that its displacements are consistent with those of the element. Perfect bond is used in the original equations. The concept of embedding isoparametric elements with reinforcing bars was first suggested for plane stress, plane strain and axisymmetric analysis[54,55]. It allows an isoparametric element to cover a large volume whilst including the finer detail of reinforcement. Indeed the reinforcing steel can be in its exact position without imposing any restrictions on mesh choice.

In this study, reinforcing bars are embedded in the 20– noded isoparametric brick element used for concrete. The basic two– dimensional theoretical formulation[54,55] was extended[56] in a similar fashion for the three– dimensional case. The derivation requires that bars are restricted to lie along the local coordinate lines of the basic element as shown in figure (4.5). The details of the theoretical derivation of bar element stiffness can be found elsewhere[24,56].

4.4 Mathematical Modelling of Concrete

4.4.1 Introduction

A reliable prediction of the behaviour of reinforced concrete requires a knowledge of the behaviour of concrete in its elastic and inelastic coupled with a knowledge of the reinforcing steel behaviour. Although the steel behaviour is better defined and generally agreed upon, concrete behaviour shows considerable statistical scatter. Furthermore, the bond between concrete and the reinforcing steel is also not well defined.

Now– a– days more and more experimental knowledge is becoming available regarding the deformational behaviour and strength properties of concrete under

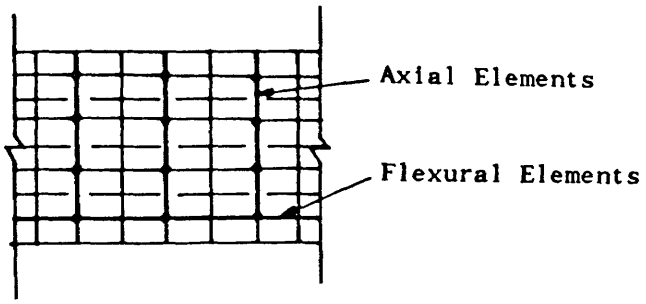

Figure (4.4-b) : Discrete representation of steel

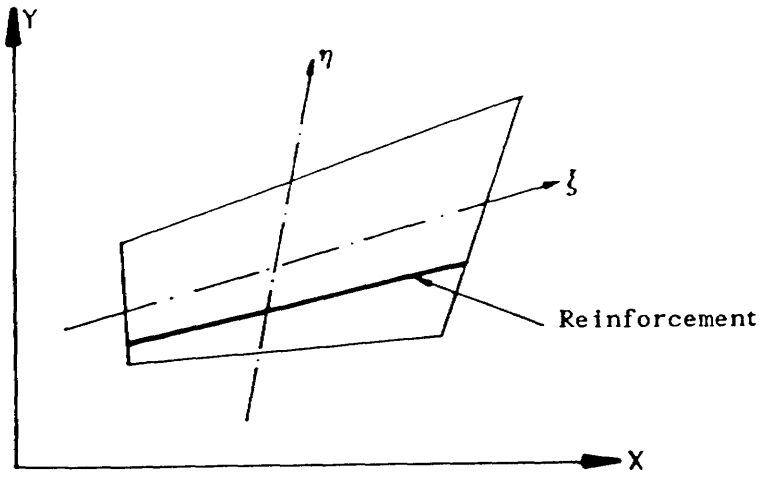

Figure (4.4-c) : Embedded representation of steel

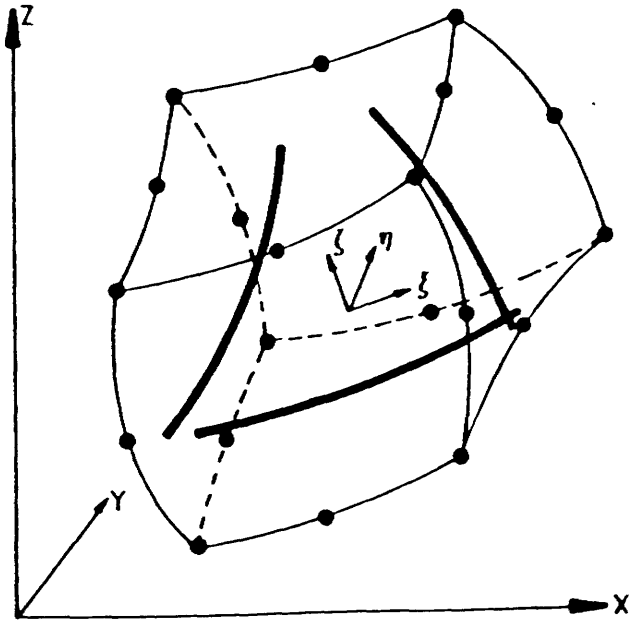

Figure (4.5) : Embedded bars within the 20-noded isoparametric brick element

various loading systems[57,58,59]. Having obtained such experimental data, it must be transformed into sets of mathematical formulae, adequately describing the basic characteristics to be of real use to reinforced concrete analysts. These mathematical formulae are normally called "constitutive equations" or sometimes, "constitutive models" for concrete. In recent years a lot of work have been carried out on this front, resulting in different models[60,61,62,63,64] being offered for the description of the behaviour of concrete under different stress states. These can be broadly grouped as: (1) uniaxial and equivalent uniaxial models; (2) linear elastic–fracture models; (3) nonlinear elastic and variable models; (4) elastic perfectly plastic–fracture models; (5) elastic strain hardening plastic and fracture models and (6) endochronic theory of plasticity for behaviour of concrete. Chen and Ting[65] have critically evaluated these models, within the context of their use in the numerical analysis of concrete structures. A good summary is also given by Chen[66].

No one mathematical model can completely describe the complex behaviour of real materials under all conditions. Each material model is aimed at a certain class of phenomena and captures their essential features and disregards what is considered to be of minor importance in that class of applications. The power of modern computers have ensured that more sophisticated and complex, but reasonably "accurate" constitutive laws can be incorporated into theoretical models without much difficulty. One such set of laws, used in this work to model concrete compressive triaxial behaviour, is due to Kotsovos et al[67,68]. The features of the model will be discussed later.

As cracking of concrete is probably the major cause of nonlinearity in most reinforced concrete structures, a separate three dimensional cracking model is developed and incorporated in the finite element programme. This will be dealt in section (4.4.4). Particular attention is paid to proper modelling of shear transfer across a cracked concrete surface. A biaxial stress–strain law is used for

reinforcing steel. Full bond is assumed between concrete and steel.

4.4.2 Kotsovos' Constitutive Laws for Concrete

Recently a comprehensive programme[67,68,69,70] of investigation into the behaviour of concrete under complex states of stress was carried out at the Imperial College, London. The testing techniques used to obtain these data have been validated by comparing them with those obtained in an international co-operative programme of research into the effect of testing techniques and apparatus upon the behaviour of concrete[58]. After analyzing the results, Kotsovos et el[67,68] provided mathematical expressions for deformational as well as strength properties of concrete suitable for use in nonlinear computer based methods to analyze concrete structures. These expressions were successfully implemented in the computer program by Elnounu[24] and subsequently used in the present work. A brief description of the model will be given in the following sections. References (24,67,68,69,70) give detailed description with verification of the model against experimental results.

4.4.2.1 State of Stress at a point

For the construction of the constitutive equations for concrete, the geometrical representation of the stress state at a point is very useful. Since the stress tensor σ_{ij} has six independent components, it is of course possible to consider these components as positioinal co-ordinates in a six-dimensional space. However it is too difficult to deal with. The simplest alternative is to take the three principal stresses σ_1, σ_2, σ_3 such that $\sigma_1 \geq \sigma_2 \geq \sigma_3$ as co-ordinates and represent the stress state at a point in the three-dimensional stress space. This orthogonal co-ordinate system σ_1, σ_2, σ_3 can be transformed into a cylindrical co-ordinate system q, r, θ and the two systems are related by the following equations:

$$q = (\sigma_1 + \sigma_2 + \sigma_3)/\sqrt{3}$$

$$r = [(\sigma_1 - \sigma_2)^2 + (\sigma_2 - \sigma_3)^2 + (\sigma_3 - \sigma_1)^2]^{0.5} / \sqrt{3} \qquad (4.38)$$

$$\cos\theta = 1/\sqrt{6}\ ((\sigma_1 + \sigma_2 - 2\sigma_3)/r)$$

The variables 'q' and 'r' define the hydrostatic and deviatoric components respectively, of a stress state, whereas the variable 'θ' defines the direction of the deviatoric component on the octahedral plane as shown in Figure (4.6) and varies from

$$\theta = 0^o \quad \text{for } \sigma_1 = \sigma_2 > \sigma_3$$

$$\theta = 60^0 \quad \text{for } \sigma_1 > \sigma_2 = \sigma_3$$

The hydrostatic and deviatoric components can also be expressed in terms of the normal (σ_{oct}) and shear (τ_{oct}) octahedral stresses which are defined as follows

$$\sigma_{oct} = \frac{\sigma_1 + \sigma_2 + \sigma_3}{3} = q/\sqrt{3} \qquad (4.39)$$

$$\tau_{oct} = 1/3\ \sqrt{(\sigma_1 - \sigma_2)^2 + (\sigma_2 - \sigma_3)^2 + (\sigma_3 - \sigma_1)^2} = r/\sqrt{3}$$

Similarly, the normal (ϵ_{oct}) and shear (γ_{oct}) octahedral strains are defined as follows:

$$\tau_{oct} = \frac{\tau_1 + \tau_2 + \tau_3}{3}$$

$$\gamma_{oct} = [(\tau_1-\tau_2)^2 + (\tau_2-\tau_3)^2 + (\tau_3-\tau_1)^2]^{0.5} / 3 \qquad (4.40)$$

where ϵ_1, ϵ_2, ϵ_3 are the principal strains.

The mathematical formulae reported here for the deformational and strength properties are applicable to a range of concretes with uniaxial cylinder compressive strength (f'_c) varying from about 15 to 65 N/mm^2.

For the deformational properties, use has been made of the secant bulk (K_s) and secant shear (G_s) moduli which are expressed as follows

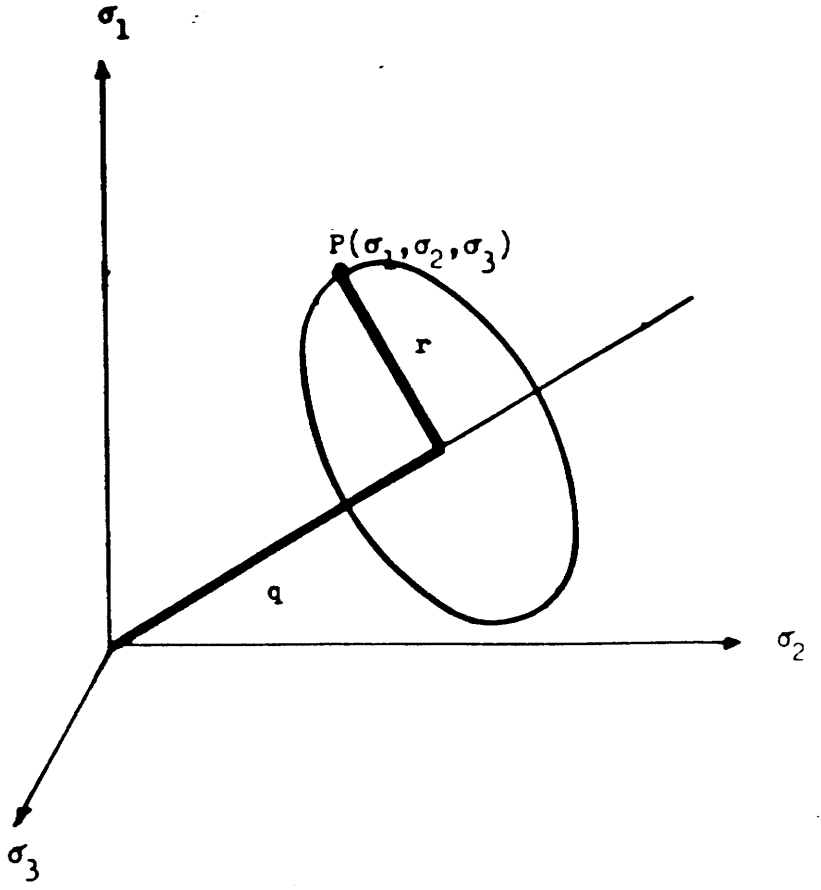

(a)

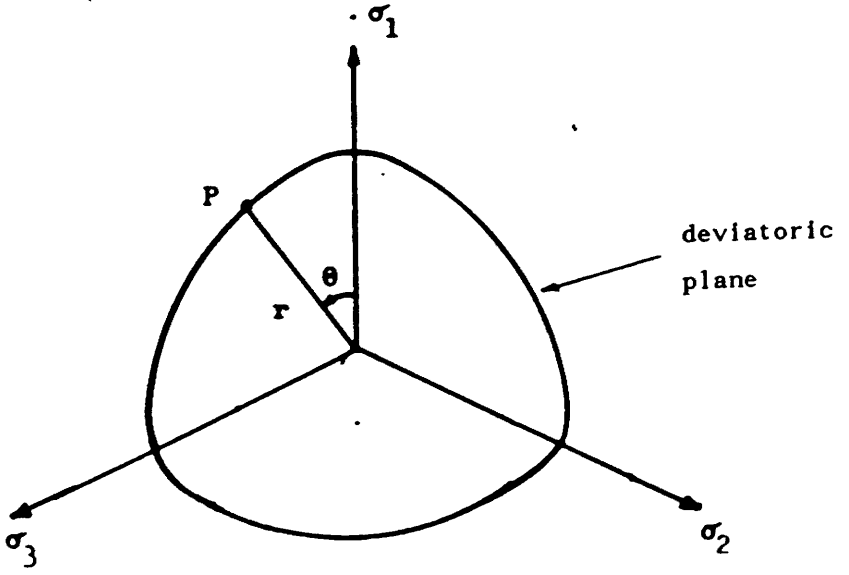

(b)

Figure (4.6) : Cylindrical coordinate system

$$K_s = \frac{\sigma_{oct}}{3\epsilon_{oct}}$$

$$G_s = \frac{\tau_{oct}}{2\gamma_{oct}} \qquad (4.41)$$

4.4.2.2 Deformational Properties

The deformational behaviour of concrete under increasing stress can be completely described [67] by the relationships between:

(a) hydrostatic stress, σ_{oct} and volumetric strain, ϵ_{oh};

(b) deviatoric stress, τ_{oct}, and deviatoric strain, γ_{oct}; and

(c) deviatoric stress, τ_{oct} and volumetric strain, ϵ_{od}.

(Note that for metals, ϵ_{od} is not effected by τ_{oct} but this may not be so for other materials.)

The $\sigma_{oct} - \epsilon_{oh}$ and $\tau_{oct} - \gamma_{oct}$ relationships can be described by the mechanical properties of the model[67] as follows:

$$\frac{K_s}{K_o} = \frac{1}{1 + A\left(\frac{\sigma_{oct}}{f'_c}\right)^{b-1}} \qquad \text{for } \frac{\sigma_{oct}}{f'_c} < 2.0$$

$$\frac{K_s}{K_o} = \frac{1}{1 + 2^{(b-1)} b\, A - 2^b\, (b-1) A \left(\frac{\sigma_{oct}}{f'_c}\right)^{-1}} \qquad \text{for } \frac{\sigma_{oct}}{f'_c} \geq 2.0 \qquad (4.42)$$

$$\frac{G_s}{G_o} = \frac{1}{1 + C\left(\frac{\tau_{oct}}{f'_c}\right)^{d-1}} \qquad (4.43)$$

where K_o and G_o (in KN/mm^2) are the initial values of the moduli K_s and G_s; and A, b, C, d are parameters which depend on the material properties such that

$$K_o = 11.0 + 0.0032\, f'^2_c$$

$$G_o = 9.224 + 0.136\, f'_c + 3.296 \times 10^{-15}\, f'_c \qquad (8.273)$$

$$A = 0.516 \quad \text{for } f'_c \leq 31.7 \text{ N/mm}^2 \text{ , or}$$

$$= \frac{0.516}{1.0 + 0.0027(f'_c - 31.7)^{2.397}} \quad \text{for } f'_c > 31.7 \text{ N/mm}^2$$

$$b = 2.0 + 1.81 \times 10^{-8} f'^4_c \quad (4.461)$$

$$C = 3.573 \quad \text{for } f'_c \leq 31.7 \text{ N/mm}^2 \text{ , or} \quad (4.44)$$

$$= \frac{3.573}{1.0 + 0.0134 (f'_c - 31.7)^{1.414}} \quad \text{for } f'_c > 31.7 \text{ N/mm}^2$$

$$d = 2.12 + 0.0183 f'_c \quad \text{for } f'_c > 31.7 \text{ N/mm}^2$$

$$= 2.7 \quad \text{for } f'_c \leq 31.7 \text{ N/mm}^2$$

In order to evaluate[67] the effect of internal stresses on deformation, use is made of the artificial concept that the volume strain (i.e. ϵ_{od}) under deviatoric stress is due to the hydrostatic component of such stresses, σ_{int}. Since

$$\sigma_{int} = 3 K_s \epsilon_{od} \quad (4.45)$$

the $\tau_{oct} - \epsilon_{od}$ relationship was expressed[67] in a nondimensionalised form as follows:

$$\sigma_{int}/f'_c = M (\tau_{oct} / f'_c)^{d1} \quad (4.46)$$

where $$M = \frac{k}{1 + d_2 (\sigma_{oct} / f'_c)^{d3}} \quad (4.47)$$

and $$k = \frac{4.0}{1.0 + 1.087 (f'_c - 15.0)^{0.23}} \quad (4.47)$$

$$d_1 = 1.0 \quad \text{for } f'_c \leq 31.7 \text{ N/mm}^2 \text{ , or}$$

$$= 0.3124 + 0.0217 f'_c \quad \text{for } f'_c > 31.7 \text{ N/mm}^2$$

$$d_2 = 0.222 + 0.01086\, f'_c - 0.000122 f'^2_c$$

$$d_3 = -2.415 \quad \text{for } f'_c \leq 31.7 \text{ N/mm}^2 \text{, or} \tag{4.48}$$

$$= -3.5308 + 0.0352\, f'_c \quad \text{for } f'_c > 31.7 \text{ N/mm}^2$$

The hydrostatic component σ_{int} is equivalent to three principal stresses, $\sigma_1 = \sigma_2 = \sigma_3 = \sigma_{int}$; and its effect on deformation, ϵ_{od}, will be the deformational response of the model under these principal stresses.

Equations (4.42) and (4.43) when used with equation (4.41), the resulting value of ϵ_{oct} (in 4.41) will be ϵ_{oh}, thus the total octahedral normal strain will be

$$\epsilon_{oct} = \epsilon_{oh} + \epsilon_{od} \tag{4.49}$$

4.4.2.3 Strength Properties of Concrete

The strength of concrete under multiaxial stresses is a function of the state of stress consisting of six components. Based on an analysis of strength data, Kotsovos[68] derived mathematical expressions to describe the strength properties of concrete under biaxial or triaxial stress states which can be presented as follows:

τ_{oe} is the value of τ_{oct} at the ultimate strength level for $\theta = 0$ degree;

τ_{oc} is the value of τ_{oct} at the ultimate strength level for $\theta = 60$ degrees;

the value of τ_{oct} at the ultimate strength level for any values of θ such that $0 \leq \theta \leq 60$ degrees may be given by the following expression:

$$\tau_{of} = \frac{2\tau_{oc}(\tau_{oc}^2 - \tau_{oe})\cos\theta + \tau_{oc}(2\tau_{oe} - \tau_{oc})[4(\tau_{oc}^2 - \tau_{oe}^2)\cos^2\theta + 5\tau_{oe}^2 - 4\tau_{oc}\tau_{oe}]^{0.5}}{4(\tau_{oc}^2 - \tau_{oe}^2)\cos^2\theta + (\tau_{oc} - 2\tau_{oe})^2} \tag{4.50}$$

This expression describes on the deviatoric plane a smooth convex curve with tangents perpendicular to the directions of τ_{oe} and τ_{oc} at $\theta = 0$ and $\theta = 60$ degrees respectively (see Figure 4.7).

If isotropic material behaviour is assumed, equation (4.50) may be used to define a six–fold symmetric (about the space diagonal) ultimate strength surface, provided the variations of τ_{oe} and τ_{oc} with σ_{oct} are established (Figure 4.7).

Figure (4.8) shows the normalized (with respect to the uniaxial cylinder compressive strength, f'c) combinations of octahedral stresses at the ultimate strength level obtained from triaxial tests[68]. The envelopes in this figure are considered[68] to describe adequately the strength of most concretes likely to be encountered in practice. A mathematical description of the above strength envelopes was obtained[68] as follows

$$\begin{aligned} \tau_{oc}/f'c &= 0.944\ [(\sigma_{oct}/f'c) + 0.05]^{0.724} \\ \tau_{oe}/f'c &= 0.633\ [(\sigma_{oct}/f'c) + 0.05]^{0.857} \end{aligned} \qquad (4.51)$$

Equation (4.51) represents two open ended convex envelopes whose slope tends to become equal to that of the space diagonal as σ_{oct} tends to infinity. These expressions together with equation (4.50) are used in this work to define an ultimate strength surface which conforms with generally accepted[67] shape requirements such as six–fold symmetry, convexity with respect to the space diagonal, and open ended shape which tends to become cylindrical as σ_{oct} tends to infinity.

4.4.3 Failure Criteria of Concrete

4.4.3.1 Introduction

Criteria such as yielding, initiation of cracking, load–carrying capacity, and extent of deformation are generally used to define failure. But failure is defined in this study as the ultimate load–carrying capacity of a test specimen or a concrete material element. In general, concrete failures can be divided into two types: tensile type and compressive type. Tensile type and compressive type of failures are generally characterised by brittleness and ductility, respectively. With respect to the

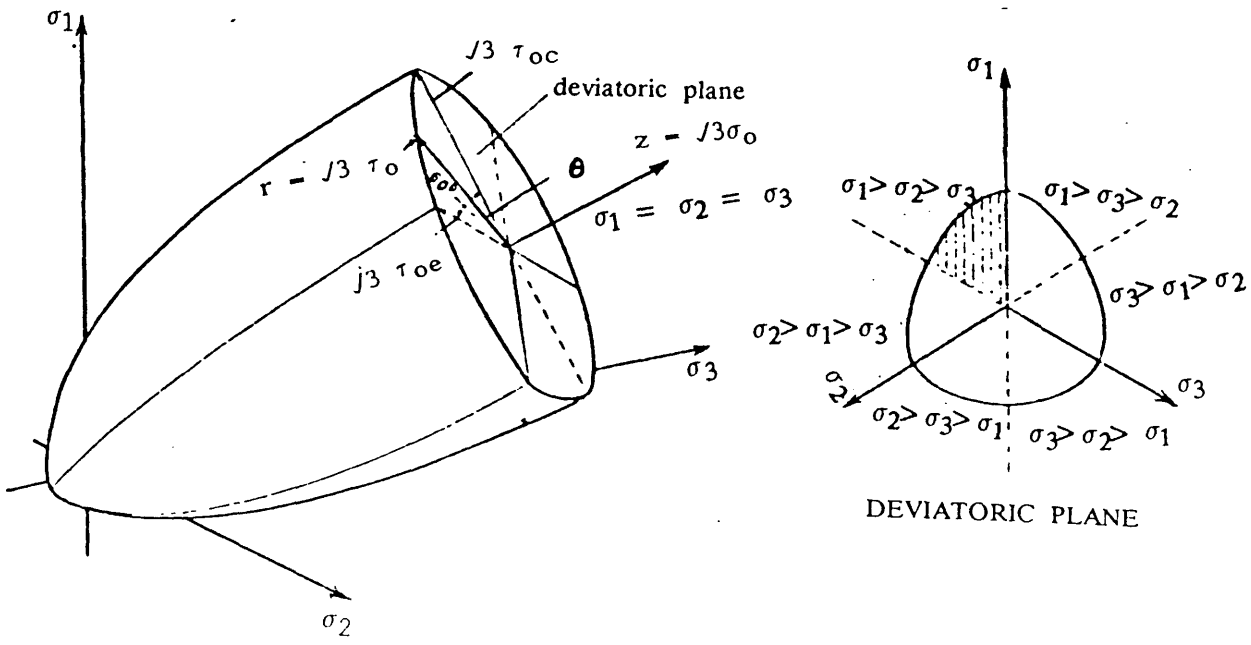

Figure (4.7) : Schematic representation of the ultimate strength surface

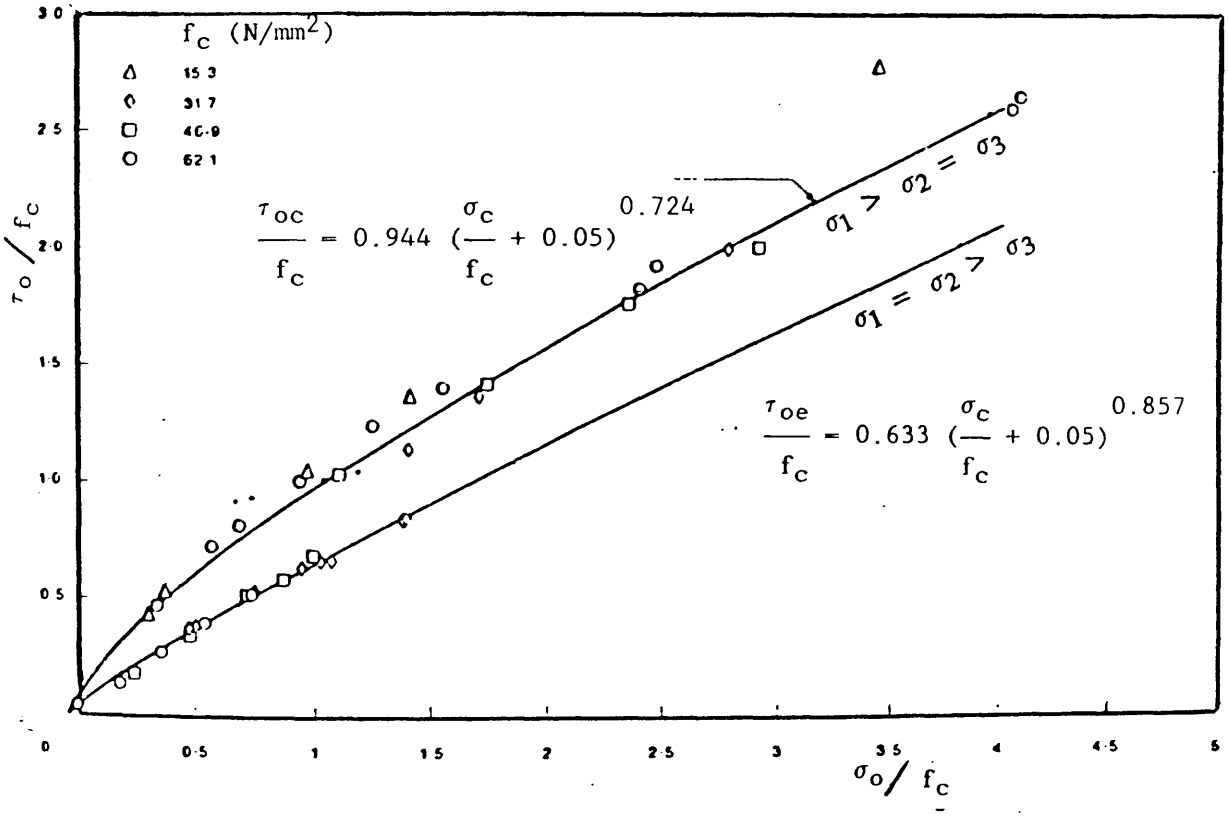

Figure (4.8) : Combinations of octahedral stresses at ultimate strength for concrete under the axisymmetric stress states $\sigma_1 > \sigma_2 = \sigma_3$ and $\sigma_1 = \sigma_2 > \sigma_3$

present definition of failure, tensile type of failure is defined by the formation of major cracks and the loss of the tensile strength normal to the crack direction. In the case of compressive type of failure, many small cracks develop and the concrete element loses its strength completely.

4.4.3.2 Concrete Compressive Failure Criteria

In this work, it is assumed that concrete suffers a crushing type of failure if:

(a) the failure surface presented in section (4.4.2.3) is violated, or

(b) the maximum principal compressive strain is greater than a specified value (which is taken as 0.0035 according to BS 8110)

Condition (a) holds for isotropic (uncracked) concrete material, and it is found that condition (b) will never be satisfied prior to condition (a) as long as the material is isotropic. But when a crack exists, condition (a) is not applicable; thus only condition (b) holds.

After crushing, the current stresses drop abruptly to zero and the concrete is assumed to lose its resistance completely against further deformation. Therefore the rigidity matrix [D] will be zero.

4.4.3.3 Concrete Tensile Failure Criteria

In this study it is assumed that concrete will suffer a cracking type of failure if:

(a) the failure surface presented in section (4.4.2.3) is violated, or

(b) the maximum tensile principal stress exceeds a specified value. A value equals $f_t/2$, is approximately the value on the failure surface[68] for uniaxial tensile stress state.

Condition (a) holds for isotropic (uncracked) concrete material. Under multiaxial stress state, condition (b) will never be satisfied prior to condition (a) as long as the material is uncracked. When at least one crack exists at any point due

to condition (a), only condition (b) is applicable to check against a second or a third crack.

Once a crack has formed, the tensile stress across the crack drops abruptly to zero and the resistance of the material against further deformation normal to the crack direction is reduced to zero. However, material parallel to the crack is assumed to carry stress according to the uniaxial or biaxial conditions prevailing parallel to the crack. Further details of cracks handling will be discussed later in this chapter.

4.4.4 Modelling of Concrete Cracking

4.4.4.1 Introduction

The tensile weakness of concrete results in cracking which is regarded as a major factor contributing to the nonlinear behaviour of reinforced concrete structures. Early studies on modelling of reinforced concrete nonlinear behaviour resulted in two methods of representing the cracking of concrete. The first approach, termed discrete crack representation[71], uses a predefined discrete crack system. The major drawbacks of this procedure, however, are that the topology of the structure has to be continuously altered as cracking progresses and that a previous knowledge of the crack pattern might be necessary. There is also a lack of generality in the possible crack directions as these are dictated by element boundaries rather than the resulting principal stresses or strains.

The second approach, known as the smeared crack model[55,72,73], assumes the cracked concrete remains a continuum. This implies that an infinite number of parallel cracks occur at a specific point if a certain cracking criterion is satisfied. By using the smeared cracking approach the problem of changing the topology of the structure with crack propagation is overcome. Moreover the initiation, orientation and propagation of cracks at the sampling points are automatically generated resulting in complete generality. Figure (4.9) illustrates both cracking models as applied to two dimensional analysis.

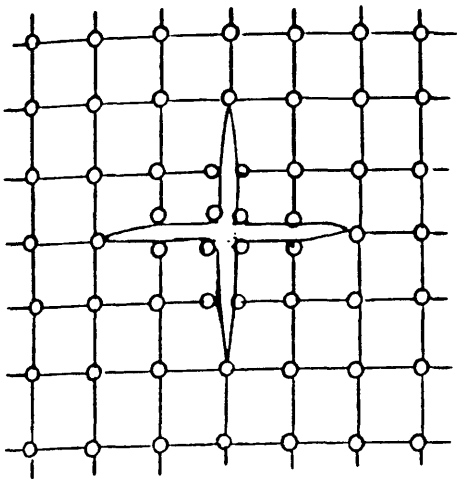

(a) Two - directional cracking

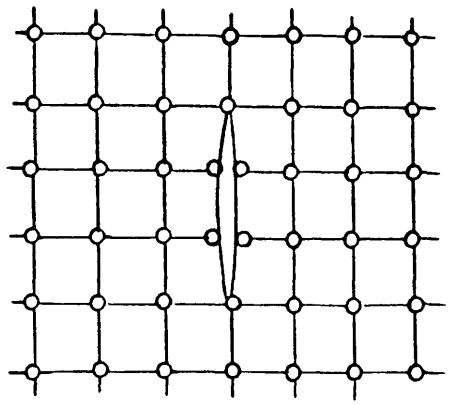

(b) One - directional cracking

(i) Discrete cracking model

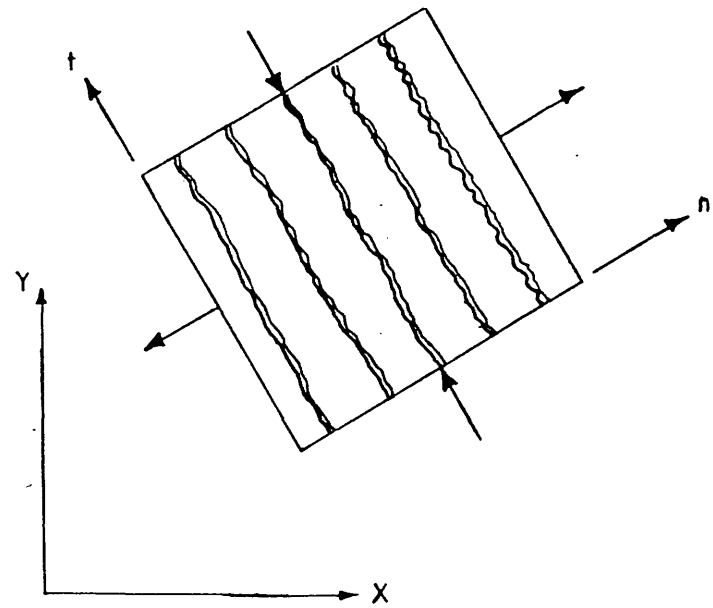

(ii) Smeared cracking model

Figure (4.9) : Discrete and smeared cracking models

The selection of which cracking model to use depends largely upon the purpose of the finite element study undertaken and the nature of the output desired[72]. Generally, if overall load–displacement behaviour, without regard to local stresses and 'realistic' crack patterns is desired, the smeared crack representation is probably the best choice. If, on the other hand, detailed local behaviour is of prime importance, adaptations of the discrete cracking model is useful. The element type, size and grid pattern have significant effects on both models. The smeared crack approach is the most commonly used because it is easy to implement. Further details on this aspect can be found elsewhere[55,65].

In this study the overall structural behaviour is of particular importance. Furthermore, the efficient 20–noded isoparametric brick element is used to represent concrete with embedded bars to simulate the reinforcing steel at its exact locations in the structure. Therefore, the smeared crack simulation is adopted.

4.4.4.2 Smeared Cracking Model

The main feature of the present cracking model may be summarized as follows:

i) cracking in one, two or three directions is allowed

ii) cracks are allowed to open or close during the load increment

iii) no tension stiffening but shear retention is allowed.

iv) variable crack direction is allowed.

(a) Fixed Crack Direction Analysis:

In this analysis, in the three dimensional stress spaces; $\sigma 1$, $\sigma 2$, $\sigma 3$; cracks might occur normal to any of the principal stresses (Figure 4.10). It is quite possible for any point to be cracked in more than one direction. Up to three cracks at a point are allowed in this analysis provided that they are orthogonal to one another. Once a crack occurs, its direction in the cartesian xyz space is fixed and retained as such in all subsequent loading. In this method, matrix [D] is

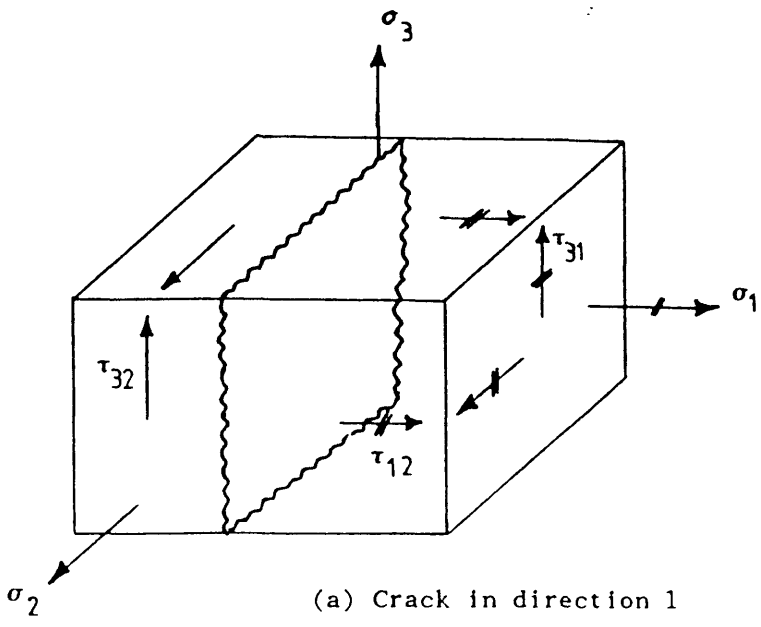

(a) Crack in direction 1

stress affected by cracking. ——//——→ (only normal stress is set to zero).

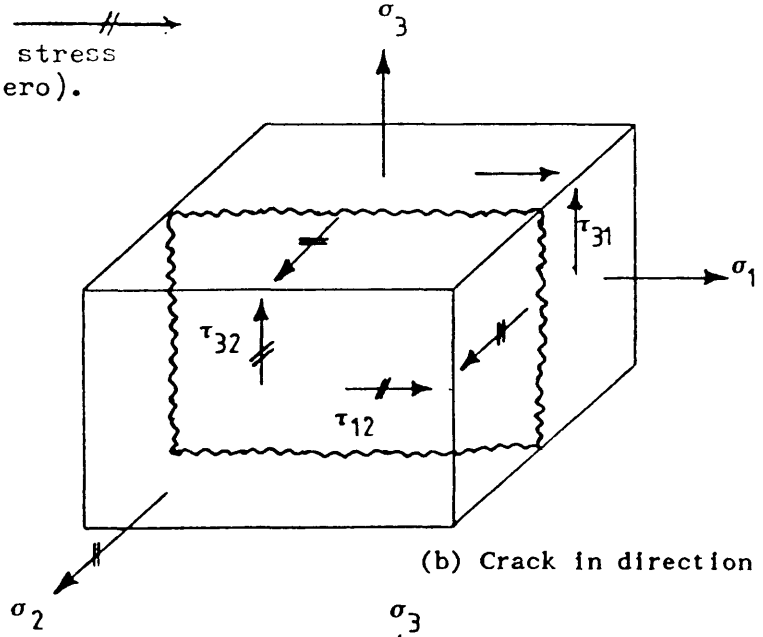

(b) Crack in direction 2

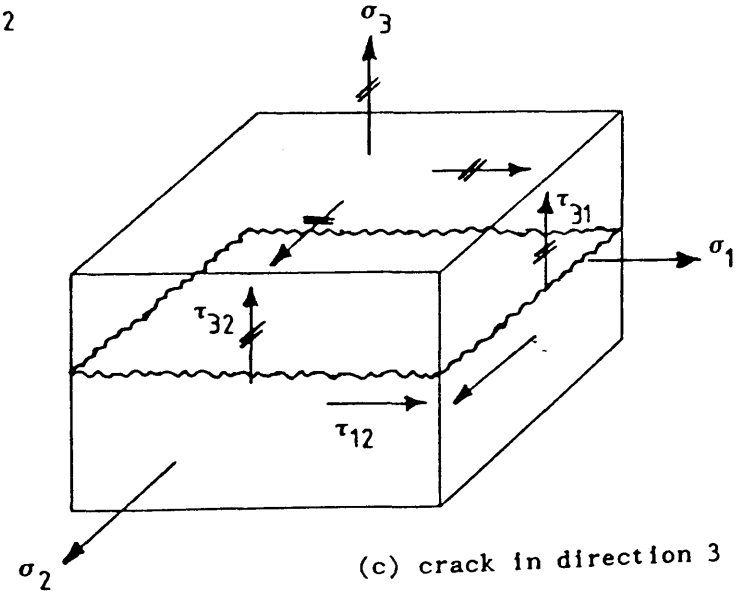

(c) crack in direction 3

Figure (4.10) : Types of cracks in concrete

modified such that the modulus of elasticity 'E' of the concrete is reduced to zero in the direction normal to the crack. Further, a reduced shear modulus 'G' is assumed on the cracked plane to account for the aggregate interlocking. Because of the fact that shear stress is allowed to act at the cracked surfaces, this procedure allows tensile stress to built up on surface other than the crack direction.

(b) No Tension Analysis

In this analysis, the principal stresses are evaluated from the current state of stress, σ_{ij}, in every iteration and if they are found tensile, are brought back to zero. No modification in the material stiffness matrix is involved in this type of analysis. In addition, the method accords with the assumption normally made in design of not relying on the tensile strength of concrete.

(c) Closing and Opening of Cracks

In order to improve the realism of the present cracking model, the possibility of crack closing is considered. This behaviour may take place due to the redistribution of stresses during an iteration or upon further loading. In the present work, the possibility of cracking of any sampling point is re-examined within each iteration until the numerical solution converges within the permissible convergence. After convergence, the direction of any cracking is fixed and orthotopic behaviour is assumed as explained before.

The fictitious principal strain normal to the crack direction is monitored to assess the state of the cracks in the cracked concrete. If this strain has a negative value, then the crack is assumed to be closed and the modulus of elasticity normal to the crack is restored back to initial value 'E'. However, the poisson effect is ignored.

(d) Variable Crack Direction

Because of the fact that shear stress is allowed on the cracked planes, for later stages of loading, the principal stress direction changes from the previous one. Gupta and Akbar (74) reported in the analysis of reinforced concrete that, the

direction of the initial and final cracks do not coincide. In this analysis, instead of fixing the direction of the first crack once it develops, the crack direction is monitored for every iteration in every increment. If the crack rotates by more than ± 10% from its previous direction, that direction is changed and the new correct direction is fixed, until the direction again changes by ± 10% in further iterations.

In chapter seven, a full incremental nonlinear analysis will be performed to study critically different methods of analysis.

4.4.4.3 Rigidity Matrix for Fixed Crack Analysis

It has been reported earlier in this work that the triaxial rigidity matrix for uncracked isotropic concrete is

$$[D] = \frac{E(1-\nu)}{(1+\nu)(1-2\nu)} \begin{bmatrix} 1 & \frac{\nu}{(1-\nu)} & \frac{\nu}{(1-\nu)} & 0 & 0 & 0 \\ & 1 & \frac{\nu}{(1-\nu)} & 0 & 0 & 0 \\ & & 1 & 0 & 0 & 0 \\ & & & \frac{(1-2\nu)}{2(1-\nu)} & 0 & 0 \\ & \text{Symmetry} & & & \frac{(1-2\nu)}{2(1-\nu)} & 0 \\ & & & & & \frac{(1-2\nu)}{2(1-\nu)} \end{bmatrix} \quad (4.52)$$

In principal stress space, and with reference to the adopted cracking criterion, if the concrete is cracked in direction 1 (Figure 4.10– a) the rigidity matrix will be

$$[D_c]_1 = \begin{bmatrix} 0 & 0 & 0 & 0 & 0 & 0 \\ & D_{22} & D_{23} & 0 & 0 & 0 \\ & & D_{33} & 0 & 0 & 0 \\ & & & \beta G & 0 & 0 \\ & \text{Symmetry} & & & D_{55} & 0 \\ & & & & & \beta G \end{bmatrix} \quad (4.53)$$

where D_{ij} are the corresponding values in the [D] matrix and β is the shear retention factor, $0 \leq \beta \leq 1$. Shear retention factor will be dealt with in section 4.4.5. 'G' is the shear modulus of the material; its value will be the value obtained from the constitutive laws prior to cracking.

If the concrete is said to be cracked in direction 2 (Figure 4.10– b), the rigidity matrix will be

$$[D_c]_2 = \begin{bmatrix} D_{11} & 0 & D_{13} & 0 & 0 & 0 \\ & 0 & 0 & 0 & 0 & 0 \\ & & D_{33} & 0 & 0 & 0 \\ & \text{Symmetry} & & \beta G & 0 & 0 \\ & & & & \beta G & 0 \\ & & & & & D_{66} \end{bmatrix} \qquad (4.54)$$

and if it is said to be cracked in direction 3 (Figure 4.10– c) the rigidity matrix will be

$$[D_c]_3 = \begin{bmatrix} D_{11} & D_{12} & 0 & 0 & 0 & 0 \\ & D_{22} & 0 & 0 & 0 & 0 \\ & & 0 & 0 & 0 & 0 \\ & \text{Symmetry} & & D_{44} & 0 & 0 \\ & & & & \beta G & 0 \\ & & & & & \beta G \end{bmatrix} \qquad (4.55)$$

Depending on the stress situation, cracks may occur in more than one direction at a single Gauss point. In this case combinations between $[Dc]_1$, $[Dc]_2$, and $[Dc]_3$ may be necessary as follows:

If craced in direction 1 and direction 2, then D matrix is given by

$$[D_c]_{1,2} = \begin{bmatrix} 0 & 0 & 0 & 0 & 0 & 0 \\ & 0 & 0 & 0 & 0 & 0 \\ & & D_{33} & 0 & 0 & 0 \\ & \text{Symmetry} & & \beta G & 0 & 0 \\ & & & & \beta G & 0 \\ & & & & & \beta G \end{bmatrix} \quad (4.56)$$

If craced in direction 2 and direction 3, then D matrix is given by

$$[D_c]_{2,3} = \begin{bmatrix} D_{11} & 0 & 0 & 0 & 0 & 0 \\ & 0 & 0 & 0 & 0 & 0 \\ & & 0 & 0 & 0 & 0 \\ & \text{Symmetry} & & \beta G & 0 & 0 \\ & & & & \beta G & 0 \\ & & & & & \beta G \end{bmatrix} \quad (4.57)$$

If craced in direction 3 and direction 1, then D matrix is given by

$$[D_c]_{3,1} = \begin{bmatrix} 0 & 0 & 0 & 0 & 0 & 0 \\ & D_{22} & 0 & 0 & 0 & 0 \\ & & 0 & 0 & 0 & 0 \\ & \text{Symmetry} & & \beta G & 0 & 0 \\ & & & & \beta G & 0 \\ & & & & & \beta G \end{bmatrix} \quad (4.58)$$

and finally if cracked in all three principal directions it is assumed that this cracked point is incapable of resisting any stress. Therefore

$$[D_c]_{1,2,3} = [0] \quad (4.59)$$

Depending on the number of cracks which occur at a Gauss point at a particular

level of loading, the appropriate rigidity matrix will be evaluated at that Gauss point and for simplifying the discussion it will be merely termed hereafter as $[D_c]$ and used in the evaluation of the stiffness matrix.

The rigidity matrix $[D_c]$ is defined with respect to the directions of principal stresses at the Gauss point under consideration. To enable its use in the global x, y, z space, a process of transformation must follow using the procedure described in reference(50) as follows:

$$[\ D_c\ ]_{x,y,z} = [\ T_\epsilon\ ]^T\ [\ D_c\ ]\ [\ T_\epsilon\ ] \tag{4.60}$$

where $[T_\epsilon]$ is the transformation matrix for strain tensor which takes the following form:

$$[T_\epsilon] = \begin{bmatrix} \ell_1^2 & m_1^2 & n_1^2 & \ell_1 m_1 & m_1 n_1 & n_1 \ell_1 \\ \ell_2^2 & m_2^2 & n_2^2 & \ell_2 m_2 & m_2 n_2 & n_2 \ell_2 \\ \ell_3^2 & m_3^2 & n_3^2 & \ell_3 m_3 & m_3 n_3 & n_3 \ell_3 \\ 2\ell_1\ell_2 & 2m_1m_2 & 2n_1n_2 & (\ell_1 m_2 + \ell_2 m_1) & (m_1 n_2 + m_2 n_1) & (n_1 \ell_2 + n_2 \ell_1) \\ 2\ell_1\ell_3 & 2m_2m_3 & 2n_2n_3 & (\ell_2 m_3 + \ell_3 m_2) & (m_2 n_3 + m_3 n_2) & (n_2 \ell_3 + n_3 \ell_2) \\ 2\ell_3\ell_1 & 2m_3m_1 & 2n_3n_1 & (\ell_3 m_1 + \ell_1 m_3) & (m_3 n_1 + m_1 n_3) & (n_3 \ell_1 + n_1 \ell_3) \end{bmatrix}$$

where ℓ_1, m_1, n_1 are the direction cosines of the first principal stress; ℓ_2, m_2, n_2 are those for the second principal stress; and ℓ_3, m_3, n_3 are for the third principal stress.

The three principal directions are orthogonal to each other. This may be assured by satisfying the following set of equations(51)

$$\begin{aligned} \ell_1\ell_2 + m_1m_2 + n_1n_2 &= 0 \\ \ell_2\ell_3 + m_2m_3 + n_2n_3 &= 0 \\ \ell_3\ell_1 + m_3m_1 + n_3n_1 &= 0 \end{aligned} \tag{4.62}$$

The three principal directions at a point can vary during loading before

cracking is initiated, but they are fixed if at least two cracks exist at that point. One crack fixes only one principal direction but constraints the other two to be perpendicular to the crack.

The process described earlier in section (4.2.7) for the calculation of the principal stresses in three dimensional analysis applies to the case when the direction of one or more principal stress is not constrained. Once a crack occurs due to any principal stress, say σ_1, this stress will be set to zero and the crack plane must be perpendicular to the direction of this principal stress. In subsequent load cycles, the direction of crack will be fixed and a two dimensional analysis on the crack plane will be followed to evaluate the values and directions of the other two principal stresses (in fact they will not be principal stresses due to the fact that shear stresses will exist also as in Figure 4.10). Section (4.5.6) explains the procedure followed for this purpose.

If the material cracks in two directions, all the principal directions will be fixed, and the values of the 'offending' principal stresses will be set to zero.

4.4.5 Modelling of Shear Transfer Across Cracks

4.4.5.1 Introduction

After cracking of concrete two main mechanisms develop through which shear is transferred from the weak cracked section to the surrounding sound concrete; namely (1) aggregate interlocking on the two adjacent surfaces and (2) dowel action of any reinforcing bars crossing these cracks. The two mechanisms are interrelated and several factors govern their relative contribution towards the total shear transferred. The main known factors are: (1) crack spacing, (2) presence or otherwise of reinforcement crossing the cracks, (3) bar size, (4) total number of bars crossing, (5) bar orientation relative to the crack direction, (6) aggregate size and roughness, (7) concrete strength, (8) crack width and (9) mode of failure.

The mechanisms of shear transfer have been investigated experimentally and consequently several analytical expressions have been suggested. In the finite element modelling, however, these expressions cannot be directly used. In the smeared cracking approach the shear transfer is modelled through the so-called "shear retention factor", β, which varies between 0 and 1 and is defined as:

$$\beta = G'/G \tag{4.63}$$

where G' is the reduced shear modulus for cracked concrete and G is the shear modulus for the uncracked concrete. Many investigators have used a constant value for β[52,55,75,76], the value of which was normally determined by trying several reduction factors and finally choosing the value that gave predictions closest to the experimental results of the problem in question. Others used a gradually decreasing value for β [77,78], following either linear or nonlinear curves. In both cases it seems that the shear retention factor has been used more as a numerical device to obtain good results to match experimental data than as a real physical phenomenon. This seems inevitable because of the following reasons: (1) the actual contribution of the shear transfer mechanisms, i.e., aggregate interlocking and dowel action is not precisely known yet, (2) more experimental data and also a unification of existing data is needed, (3) even if all that is done, the treatment of shear transfer with all its components is still uncertain to produce a single finite element model to suit all stress states at one stroke. Because of the variation of the reinforced concrete behaviour under different loading conditions, (4) the shear transfer is interrelated with the other aspects of nonlinear behaviour of reinforced concrete such as tension stiffening and bond-slip behaviour and (5) in nonlinear finite element analysis numerical factors, e.g., convergence tolerance, maximum number of iterations, increment size etc., also affect results obtained using whatever shear retention model is used[76].

4.4.5.2 Shear Retention Factor Used in This Work

To achieve the aim of incorporating a realistic shear retention factor to model

shear transfer across cracked concrete, the following nonlinear relationship based on the average of the three principal strains at any cracked point is used.

$$\beta = 1 \qquad \text{for } \epsilon_m < \epsilon_{to} \text{ (for uncracked concrete)}$$
$$\beta = 0.25\,\epsilon_{to}/\epsilon_m \qquad \text{for } \epsilon_m \geq \epsilon_{to} \tag{4.64}$$

where β is the shear retention factor; ϵ_m is the average of the three principal strains at a cracked point; and ϵ_{to} is the cracking tensile strain which was taken as 0.0001. The above relationship seems more realistic than a constant factor because the physical contact between the two faces of the cracked planes weakens at larger crack widths, thus decreasing the aggregate interlocking forces. The above equation (4.64) is a modified version of equation (4.65) proposed originally by Al– Mahadi[77] for two dimensional analysis.

$$\beta = 1 \qquad \text{for } \epsilon_1 < \epsilon_{to} \text{ (for uncracked concrete)}$$
$$\beta = 0.4\ \epsilon_{to}/\epsilon_1 \qquad \text{for } \epsilon_1 \geq \epsilon_{to} \tag{4.65}$$

where ϵ_1 is the maximum principal tensile strain and ϵ_{to} is the cracking tensile strain which was taken as 0.0002.

In the present work, irrespective of the number of cracks at a single Gauss point one shear retention factor is used for all the cracks at that point. The equation (4.65) which contains maximum principal tensile strain only was modified to reflect the effect of all the three principal strains.

4.5 Nonlinear Method of Solution

4.5.1 Introduction

A nonlinear structural problem must obey the basic laws of continuum mechanics, i.e., equilibrium, compatibility, and the constitutive relations of the material. Displacement compatibility is automatically satisfied in the displacement finite element technique. Common nodes between elements ensure continuity and

compatibility of displacements along element boundaries, and polynominal shape functions ensure continuity and single valued displacements internally. Therefore it becomes necessary only to enforce that the nonlinear constitutive relations are correctly satisfied whilst at the same time preserving the equilibrium of the structure.

There can be several causes of nonlinear behaviour in a structure, which can be divided into three categories:

1) Material nonlinearity
2) Geometric nonlinearity
3) Mixed material and geometric nonlinearity

Stress–strain relations are a major source of nonlinearity. These can vary from short–term nonlinear relationships between stress and strain such as plasticity, cracking, nonlinear elasticity, etc. to time–dependent effects such as creep and shrinkage.

Only nonlinearity caused by short–term nonlinear behaviour of concrete and steel is considered in this study. These include the tensile cracking of concrete, the nonlinear stress–strain relations of concrete, and the yielding and work–hardening of steel. Details of the laws representing these behaviour have been discussed earlier in this chapter.

A nonlinear solution is obtained by solving a series of linear problems such that the appropriate nonlinear conditions are satisfied at any stage to a specified degree of accuracy. This technique is required because contrary to linear equations, there is no general method which uniquely solves nonlinear equations. In fact it is usually impossible to obtain the explicit form of these equations in the first place. One way of achieving this goal is to ensure that at any loading stage, the solution results in stresses consistent with the displacement field and satisfying the given constitutive equations. These stresses will be statically equivalent to a set of internal nodal forces which should be in equilibrium with the externally applied loads. In

general, these equivalent nodal forces are not equal and the differences between the external and internal forces are termed "residual forces". These residuals must be removed by repeatedly applying them on the structure until an acceptable tolerance is achieved.

4.5.2 Numerical Techniques for Nonlinear Analysis

The solution of nonlinear problems by the finite element method are usually attempted by one of the following three basic techniques:

a) Incremental (step– wise procedure)

b) Iterative (Newton methods)

c) Incremental– Iterative (mixed procedure)

where the nonlinearity occurs in the stiffness matrix [K] which, in the case of short– term behaviour of reinforced concrete, is a function of nonlinear material properties.

The general method of each method is similar. For problems where only the material behaviour is nonlinear, as in our case, the relationship between stress and strain is assumed to be of the form:

$$f (\sigma, \epsilon) = 0 \tag{4.66}$$

The element stiffness matrix is a function of the material properties and can be written as:

$$[K] = K (\sigma, \epsilon) \tag{4.67}$$

The external nodal forces [R] are related to the nodal displacements [δ] through the element stiffness and can be expressed by:

$$[R] = [K] [\delta] \tag{4.68}$$

which on inversion becomes:

$$[\delta] = [K]^{-1} [R] \tag{4.69}$$

or

$$[\delta] = [K (\sigma, \epsilon)]^{-1} [R] \tag{4.70}$$

This derivation illustrates the basic nonlinear relationship between [δ] and [R], due to the influence of the material laws on [K].

Equation (4.70) is sloved by successive linear approximations. The three methods mentioned above are now briefly discussed. Further details are given in References[49,77,79].

4.5.2.1 Incremental Method

The basis of the incremental method is the subdivision of the total applied load vector into smaller increments, which do not necessarily need to be equal. During each load increment, Equation (4.69) is assumed to be linear, i.e., a fixed value of [K] is assumed using material data existing at the end of the previous increment. Nodal displacements can be obtained for each increment and these are added to the previously accumulated displacements. The process is repeated until the total load is reached. No account is taken of the force redistribution during the application of the incremental load (i.e., no iteration process exists to restore equilibrium).

The accuracy of the incremental method can be improved by using small increment size, but this results in increased computational effort. The mid–point Runge–Kutta scheme is a modification of the incremental method which utilizes the additional computational effort, where two cycles of analysis are performed for each load increment. The first step is to apply half the load increment and to calculate new stiffness corresponding to the total stresses at this value. These stiffnesses are then utilized to compute an approximation for the full load increment.

4.5.2.2 Iterative Method

In this method, the full load is applied in one increment. Stresses are evaluated at that load according to the material law. Then the equivalent nodal

forces are computed using these stresses. These may not be in equilibrium with the externally applied loads. The unbalanced nodal forces $[F_u]$, i.e., the difference between the external and internal forces, is calculated. These unbalanced forces are then used to compute an additional increment of displacement, and hence new stresses, which give a new set of equivalent nodal forces. This process is repeated until equilibrium is approximated to some acceptable degree. When this stage is reached the total displacement is taken as the sum of the accumulated displacements from each iteration.

4.5.2.3 Mixed Method (Incremental– Iterative)

The mixed method utilizes a combination of the incremental and iterative schemes. In this case the load is applied in increments, but after each increment successive iterations are performed until equilibrium is achieved to the acceptable level of accuracy. Because the mixed method combines the advantages of both the incremental and iterative procedures and tends to minimize the disadvantages of each[80], the method is widely used. The additional computational effort is justified by the fact that the iterative part of the procedure permits one to assess the 'quality' of the approximate equilibrium at each stage. Further discussions on the merits and demerits of each technique can be found in references[49,50,80].

4.5.2.4 Methods Used in This Work

A modified version of the mixed procedure is used in the present work. The modified "Newton– Raphson" approach is used to evaluate the stiffnesses. The stiffnesses are evaluated using a secant rigidity matrix; and it was found that varying the stiffness at the second iteration in each increment results in the "cheapest" solution. For the calculation of the unbalanced nodal forces, a modification of the initial stress method is used, termed the method of "Residual Forces" [73,76,81]. The basic technique is that, at any stage, a load system equivalent to the total stress level is evaluated and checked against the applied

loading system. The difference between the two will result in a set of residuals that are a measure of lack of equilibrium. These residuals are then applied to the structure to restore equilibrium. The process is then repeatedly continued to dissipate the out–of–balance forces (or the residuals) to a sufficiently small value. Thus for equilibrium it is required that:

$$[\ F_u] = \int_V [\ B\ ]^T [\ \sigma\ ]\ dv - [\ R\ ] = 0 \qquad (4.71)$$

where $[\sigma]$ are the actual stresses depending on the constitutive law being used, [R] is external load vector, $[F_u]$ the residual forces.

4.5.3 Convergence Criteria

4.5.3.1 General

Since the main purpose of the iteration process is the redistribution of the out–of–balance residual forces, a reliable convergence criterion must be used to monitor the convergence to equilibrium state and terminate the iterative process when the desired accuracy has been achieved. The accuracy is specified by the user through what is called "convergence tolerances" (Ref.49,73,76,81). These convergence tolerances are quantitative values that determine the accuracy of equilibrium acceptable to the user. The convergence tolerances must be realistic. If they are too 'loose', inaccuracy may result, if they are too 'tight', much expensive effort is spent to obtain needless accuracy.

One possible method of checking convergence is to compare each individual nodal value (displacement) with the corresponding value obtained on the previous iteration(81). Then, provided that this change is negligibly small for all nodal points, convergence can be deemed to have occured. This local checking is expensive. Therefore a check based on some global norm is preferable. The convergence criteria can be based on various quantities; either directly on the unbalanced forces, indirectly on displacements, on energy changes or on changes in stress values.

Three types of convergence criteria have been in common use for structural analysis, namely:

(a) Force convergence criterion

(b) Displacement convergence criterion

(c) Energy convergence criterion

Each of the three alternatives has its merits, and the selection of a suitable one depends on many factors. In the displacement criterion inconsistencies in units (e.g., displacements and rotations) may occur and must be avoided. The same holds true for force criterion (i.e., inconsistencies of force and moment units). Although the use of a combination of displacement and force criterion may seem ideal and has been recommended by some investigators [82,83], the equilibrium of forces is sometimes difficult to achieve even when iterative displacements are converging within 'tight' tolerances. This is particularly true for reinforced concrete structures when cracking of concrete usually makes it very difficult to achieve equilibrium because large residual forces are released.

This observation is supplemented by the findings of Cope and Rao[84], in their study on the monitoring indices for nonlinear analysis of reinforced concrete. However, the rate of convergence depends on the method used in the solution (e.g., constant or variable stiffness). It is also required to specify a maximum number of iterations, irrespective of the state of convergence. The maximum number of iterations may influence the predicted shape of the load–deflection curve, but it is an important safeguard against unlimited and often unnecessary cycles of full solution.

An energy convergence criterion has been used by Cope and Rao[84], where they found that a convergence tolerance of 1–2.5% was appropriate to yield acceptable results in an analysis of reinforced concrete skew slabs. However, whatever criterion is chosen, care must be taken to avoid spending much effort

trying to obtain the unattainable and perhaps needless accuracy. Special attention must be given to the cracking stage when large forces are suddenly released into the system.

4.5.3.2 Convergence Criterion Used in This Work

In this study, the convergence process is based on a force convergence criterion. Because it is a direct measure of equilibrium between the internal and external forces. A global approach is adopted, where convergence is monitored using norms as follows:

$$\frac{\left| \sum_{i=1}^{N} (F_{u.i}^{r})^2 \right|^{0.5}}{\left| \sum_{i=1}^{N} (R_i)^2 \right|^{0.5}} \times 100 \leq Toler \qquad (4.72)$$

where N is the total number of nodal points in the system, r denotes the iteration number, F_{ui} is the residual force at node i and R_i is the total external applied load at node i.

This criterion states that the convergence occurs if the norm of the residual forces becomes less than a specified tolerance times the norm of the total applied forces.

4.5.4 Analysis Termination Criterion

The program must have some means of detecting the collapse of the structure. The failure of the structure takes place when no further loading can be sustained. A maximum deflection can be used as a criterion to stop the analysis at failure[85]. An empirical expression can be used to detect maximum deflection, but obviously this needs great care and no one expression can fit all situations.

The maximum iterations can also be used. When a specified number of

iterations has been performed without achieving convergence, the structure is deemed to have failed and the failure load can then be estimated. It must be mentioned here that this criterion is not always sufficient to indicate the failure of the structure. Since it can be satisfied while the solution is slowly converging when severe discontinuity occurs due to extensive cracking or in the event of large displacements. It may also occur when large load increments are used or very tight convergence tolerances are specified. However, if realistic maximum number of iterations (which may be expensive) is used and the solution continues not to converge, for a number of load increments, then this can be a realistic indication of failure.

In this study, however, the growth of iterative displacements is used to detect failure. This is coupled with a search through the diagonal terms of the stiffness matrix to detect zero or negative values, in which case the analysis is terminated. It was found that negative or zero pivots were always associated with very large displacements at or immediately beyond the failure loads and always occured after 2–3 unconverged (sometimes diverged) increments. This was also associated with severe cracking, yielding and eventually crushing situations.

4.5.5 The Frontal Solution Technique

In the nonlinear stress analysis using finite elements, researchers are now more interested in using elements with higher degrees of freedom. This inevitably results in a large set of simultaneous equations to be solved repeatedly, thus creating high demand for computer storage.

The three main solution strategies for large equation systems are bandsolvers, partitioning methods, and frontal solutions. In this work a version of the frontal solution, originally introduced by Irons[86] and later modified by Hinton and Owen[87], is used. The main feature of the frontal solution technique is that, it assembles the equations and eliminates the variables at the same time. This means

that the total stiffness matrix of the structure is never formed as such, since the reduced equations corresponding to the eliminated variables are stored in core in a temporary array called a buffer area[81]. As soon as this array is full, the information is then transferred to disc. This process results in a considerable efficiency in the way core storage is handled. Thus much valuable computer time is saved through proper housekeeping. The saving due to the use of buffer area may amount to about 50% compared with the use of ordinary backing disc store[76]. Another important feature of the frontal technique is that, in contrast to a band solver, node numbering is irrelevant and it is the element numbering that matters[87]. Because in a band solver the storage allocation is determined by the order in which the nodes are presented for assembly, while in the front solver the storage is determined by the order in which the elements are presented. Further details about the frontal method can be found in references[76,81,87].

4.5.6 Computations Procedure for Fixed Crack Analysis

Consider the analysis at a particular iteration i. The displacements are calculated according to equation (4.70) using the appropriate rigidity matrix $[D]_{x,y,z}$.

(1) For every stress sampling point, evaluate the incremental values of strains $[\Delta\epsilon_i]$ and stresses $[\Delta\sigma_i]$ using the appropriate rigidity matrix $[D]_{x,y,z}$.

(2) Check whether the sampling point under consideration has suffered from a compressive crushing situation in any of the previous load cycles, if so step (8) will be executed.

(3) Check whether this stress sampling point has suffered from a tensile cracking situation in any of the previous load cycles, if so step (7) will be executed.

(4) Using the stress–strain relationships described in the concrete material law, evaluate the total actual stresses in concrete $[\sigma_i]$ which correspond to the

linearly calculated total strains.

$$[\ \epsilon_i\ ] = [\ \epsilon_{i-1}\ ] + [\ \Delta\epsilon_i\ ]$$

$$[\ \sigma_i\ ] = [\ \sigma_{i-1}\ ] + [\ D_{x,y,z}\ ]\ [\ \Delta\epsilon_i\ ]$$

(5) Check for concrete compressive failure criteria violation. If violated, all the stress components at this Gauss point will be set to zero in this iteration and in all the subsequent load cycles: $[\sigma_i] = 0.0$; also the components of the rigidity matrix will be set to zero for stiffness calculations in all the subsequent load cycles.

$$[D]_{x,y,z} = 0.0$$

(6) Check for concrete tensile failure criteria. If violated a crack will occur, thus a new rigidity matrix $[D_c]_{x,y,z}$ will be formulated according to the number and directions of the cracks.

(7) If previously cracked in one direction, it is required to check for further cracking as follows:

(a) for the previous load cycle, the principal stresses σ_1; σ_2; σ_3 had the direction cosines (ℓ_1, m_1, n_1); (ℓ_2, m_2, n_2) and (ℓ_3, m_3, n_3). These directions are termed here as x', y', z' as shown in Figure (4.11).

(b) In the present load cycle, these direction cosines which were obtained from the previous load cycle were used in stiffness calculation to evaluate the new stress vector $[\sigma]$ with regard to the appropriate rigidity matrix $[D_c]$.

(c) Now for principal stress calculation in cracked material, the new stress vector $[\sigma]$ will be transformed from x, y, z space to $[\sigma']$ in x', y', z' space by

$$[\sigma'] = [T_\sigma].\ [\sigma] \qquad (4.73)$$

where $[T_\sigma]$ is the transformation matrix for stress vector[50] which takes the following form:

$$[T_\sigma] = \begin{bmatrix} \ell_1^2 & m_1^2 & n_1^2 & \ell_1 m_1 & m_1 n_1 & n_1 \ell_1 \\ \ell_2^2 & m_2^2 & n_2^2 & \ell_2 m_2 & m_2 n_2 & n_2 \ell_2 \\ \ell_3^2 & m_3^2 & n_3^2 & \ell_3 m_3 & m_3 n_3 & n_3 \ell_3 \\ \ell_1\ell_2 & m_1 m_2 & n_1 n_2 & (\ell_1 m_2 + \ell_2 m_1) & (m_1 n_2 + m_2 n_1) & (n_1 \ell_2 + n_2 \ell_1) \\ \ell_1\ell_3 & m_2 m_3 & n_2 n_3 & (\ell_2 m_3 + \ell_3 m_2) & (m_2 n_3 + m_3 n_2) & (n_2 \ell_3 + n_3 \ell_2) \\ \ell_3\ell_1 & m_3 m_1 & n_3 n_1 & (\ell_3 m_1 + \ell_1 m_3) & (m_3 n_1 + m_1 n_3) & (n_3 \ell_1 + n_1 \ell_3) \end{bmatrix}$$

The new transformed stress tensor, $[\sigma']$ will be (see Figure 4.11)

$$[\sigma'] = [\ \sigma'_x \quad \sigma'_y \quad \sigma'_z \quad \tau'_{xy} \quad \tau'_{yz} \quad \tau'_{zx}\ ]^T \tag{4.75}$$

and for the instance of a crack caused by σ_1, the value of σ'_x will be set to zero ($\sigma_1 = \sigma'_x$), and to evaluate the new values of σ'_2 and σ'_3 we are dealing with a two dimensional problem of which the active stress components are σ'_y, σ'_z, τ'_{yz}, thus

$$\sigma'_2\ ,\ \sigma'_3 = \frac{\sigma'_y + \sigma'_z}{2} \pm \sqrt{\left[\frac{\sigma'_y - \sigma'_z}{2}\right]^2 + (\tau'_{yz})^2} \tag{4.76}$$

$$\tan 2\alpha = \frac{2\tau'_{yz}}{\sigma'_y - \sigma'_z} \tag{4.77}$$

where α is the angle by which the directions of σ'_2, σ'_3 deviated from y', z' axes in the event of a crack caused by σ_1 (Figure 4.12)

(d) Having got the angle α, and knowing the direction cosines of x', y', z' axes with respect to the global x, y, z space, we need to calculate the direction cosines of σ'_2; σ'_3 which are (ℓ'_2, m'_2, n'_2), (ℓ'_3, m'_3, n'_3), such

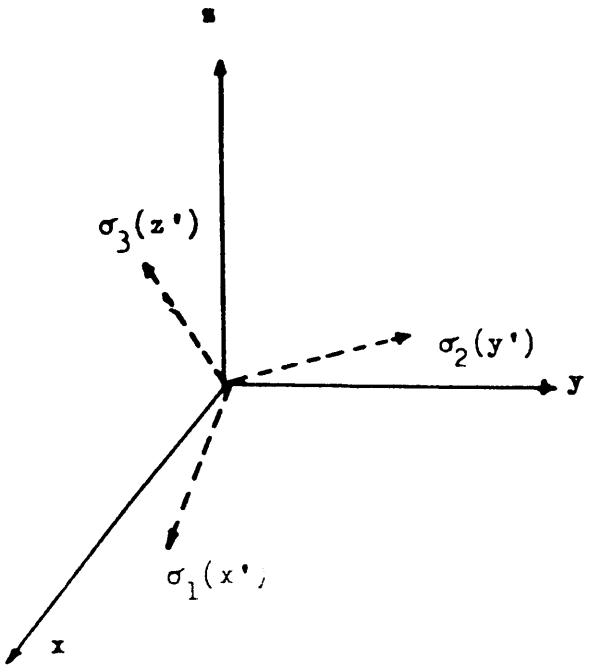

Figure (4.11) : Principal stresses in global axes.

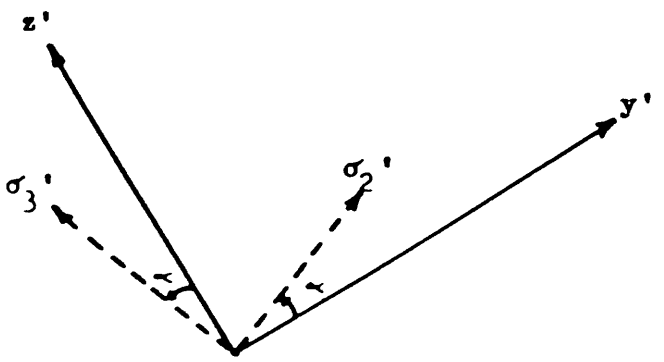

Figure (4.12) : The angle of the new principal stress direction

that their plane remains perpendicular to the already fixed direction of σ_1 which caused the crack in our example. This can be done as follows:

$$\begin{aligned} &\text{if } [\sigma'] = [A]\,[\sigma] \\ &\text{and } [\sigma''] = [C]\,[\sigma'] \\ &\text{then } [\sigma''] = [C]\,[A]\,[\sigma] \end{aligned} \tag{4.78}$$

where [A] and [C] are the appropriate transformation matrices. The product [C] [A] will contain all the required direction cosines of the new principal stresses contained in $[\sigma'']$.

(e) These nine values of direction cosines will be the ones to be used in the next load cycle for stiffness and new stress vector calculations; and the values of the principal stresses σ'_2, σ'_3 will be used to check against the cracking criterion because σ_1 was set to zero (in this example). If the cracking criterion is violated further cracks will occur and the appropriate rigidity matrix $[D_c]$ must be used.

(8) Evaluate the equivalent nodal forces contributed by concrete element

$$[\,P_i\,]_{conc} = \int_V [\,B\,]^T\,[\,\sigma_i\,]\,dv$$

(9) Add the equivalent nodal forces contributed by concrete element to those contributed by steel reinforcement to get the total equivalent nodal forces of the element, $[P_i]$

$$[P_i] = [P_i]_{conc} + [P_i]_{steel}$$

(10) Check for convergence.

CHAPTER FIVE

TEST SETUP, MATERIALS AND INSTRUMENTATION

5.1 Introduction

This chapter describes in detail the experimental set-up which was designed and constructed to study the strength and behaviour of a series of reinforced concrete shearwall-floor slab connections under monotonic and reverse cyclic loading. The experimental work is divided into three test series, viz. (a) preliminary test series, which consisted of three models (PS1 to PS3), (b) main test series which consisted of nine models (MS4 to MS12), and (c) reverse cyclic loading test series comprising three models (MRS13 to MRS15). The detailed description of these models and their behaviour during loading will be described in chapters six and eight. In this chapter the materials used for the construction of the models and their properties are described. The instruments employed for measurements of the various quantities during the tests, as well as the test procedure, are also explained.

5.2 Experimental Setup

The test specimens consisted of either rectangular or flanged shear wall supporting a horizontal slab. The overall shape of a typical model from both the groups is shown in Figure (5.1). A three dimensional steel test-rig was designed and constructed to hold the model in position for a maximum wind load of about 400 KN applied in both vertically up and downward direction. The supporting system and the loading rig used for testing the models under both gravity and lateral "wind" load will be discussed in the following sections.

5.2.1 Supporting Arrangement

When "wind" load was applied in downward direction along the line 'AB' of the slab (See Figure 5.1), a steel stand assisted in resisting the rotation of the model

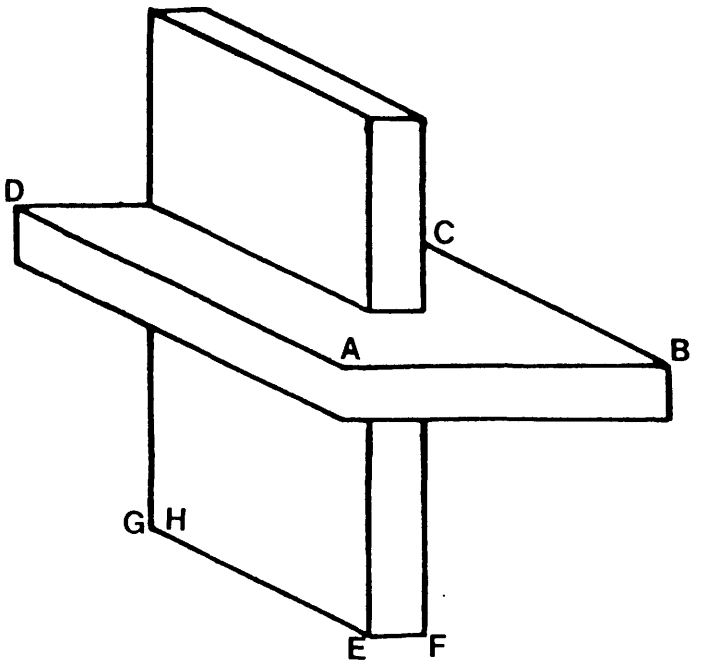

a) Rectangular shear wall.

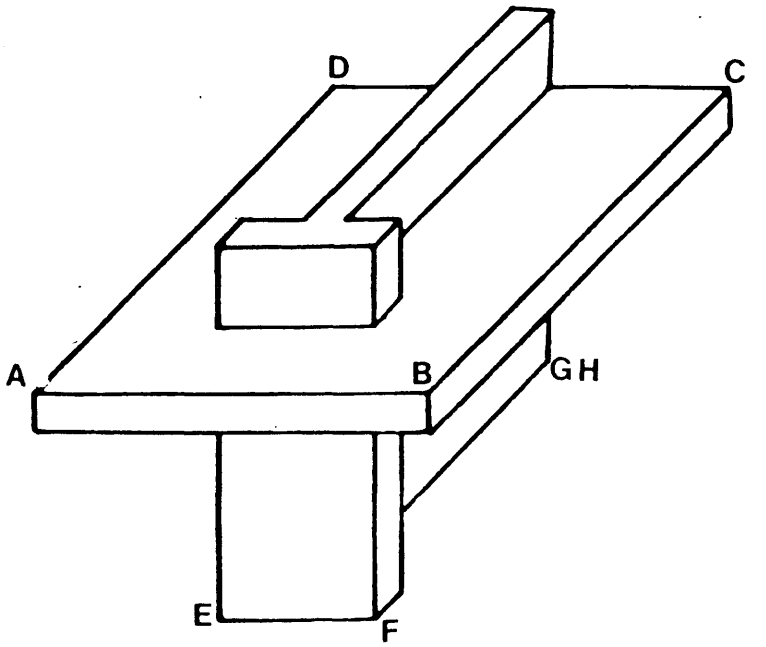

b) Flanged shear wall.

Figure (5.1) : Isometric view of typical models.

as shown in Figure 5.2. The model had a vertical hole in the wall. Through this hole the model was clamped to the "strong floor" using a 12 mm prestressing strand with a force of 2 KN.

During the testing of the fifth model, when applied lateral load was higher than the design load, the model started to rotate at front edge of the wall 'EF' (see Figure 5.1). It was found very difficult to resist the rigid body movement of the model using one prestressing strand. To avoid rotation and the large rigid body movement, two vertical holes were provided in the wall of the rest of the models and they were clamped to the floor of the laboratory using two prestressing strand as shown in Figure (5.3).

For reverse cyclic loading series, when lateral load was applied in upward direction, the model started to rotate at the back edge of the wall 'GH' (Figure 5.1) and the previous supporting system was found ineffective in resisting the upward rigid body movement of the model. The wall at the back started crushing due to the concentration of the stresses along line GH. Another hollow beam section was designed and the model was held down by that transverse beam using three 15 mm high strength prestressing strand. Figure (5.4) shows the supporting arrangement used for the models of cyclic loading series.

5.2.2 Loading Arrangement

5.2.2.1 Gravity Load

Gravity load was applied through two beams placed on the edge of the slab parallel to the web of the wall as shown in Figures (5.5) and (5.6– a). The load was applied to each side of the model by tightening the nuts on two rods. One end of the rod was anchored to the floor of the laboratory and the other end to the top beam (resting on the slab). 50 KN load cells, one for each bar were used to monitor the applied gravity load.

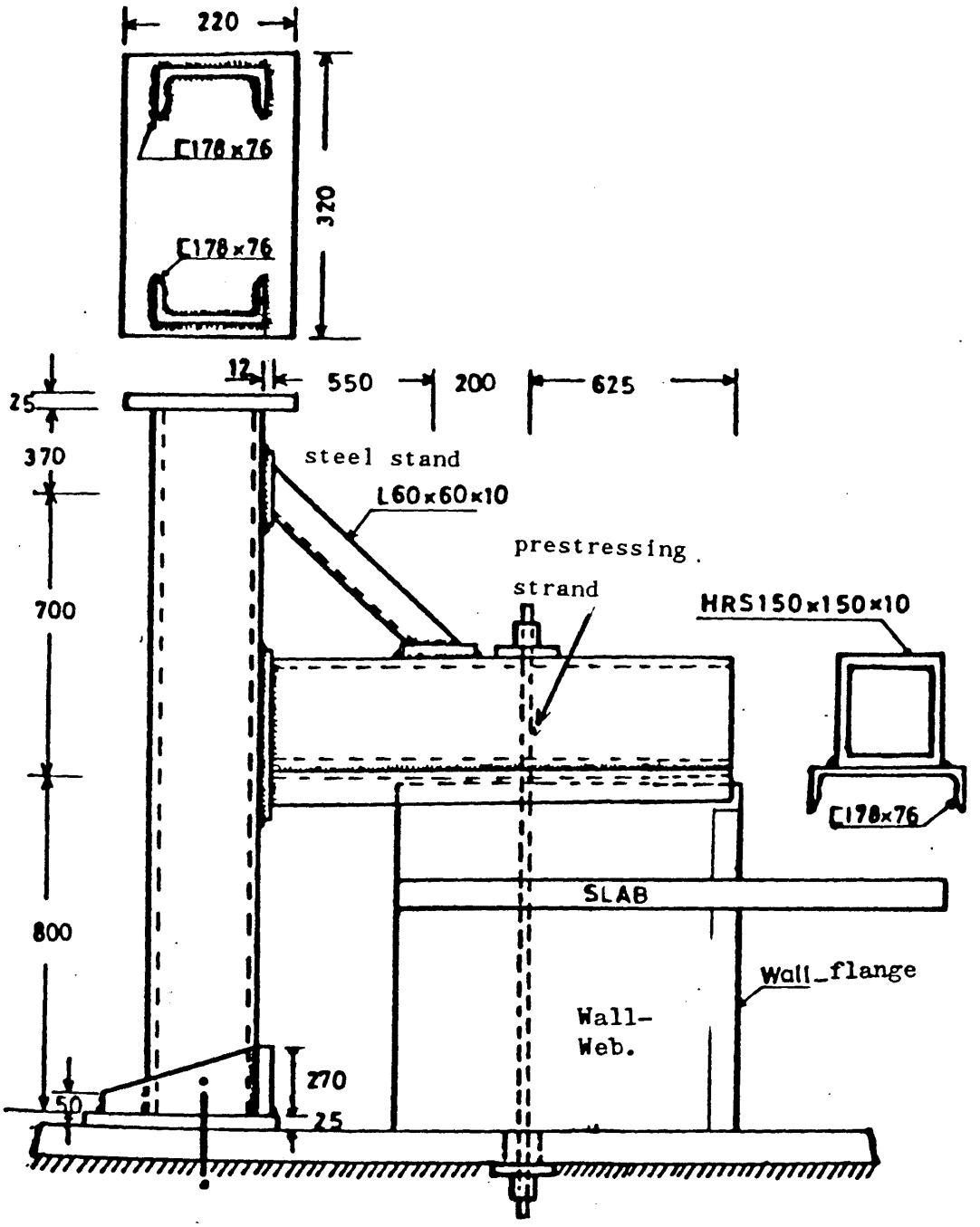

Figure (5.2) : Supporting arrangement for models PS1 to MS5.

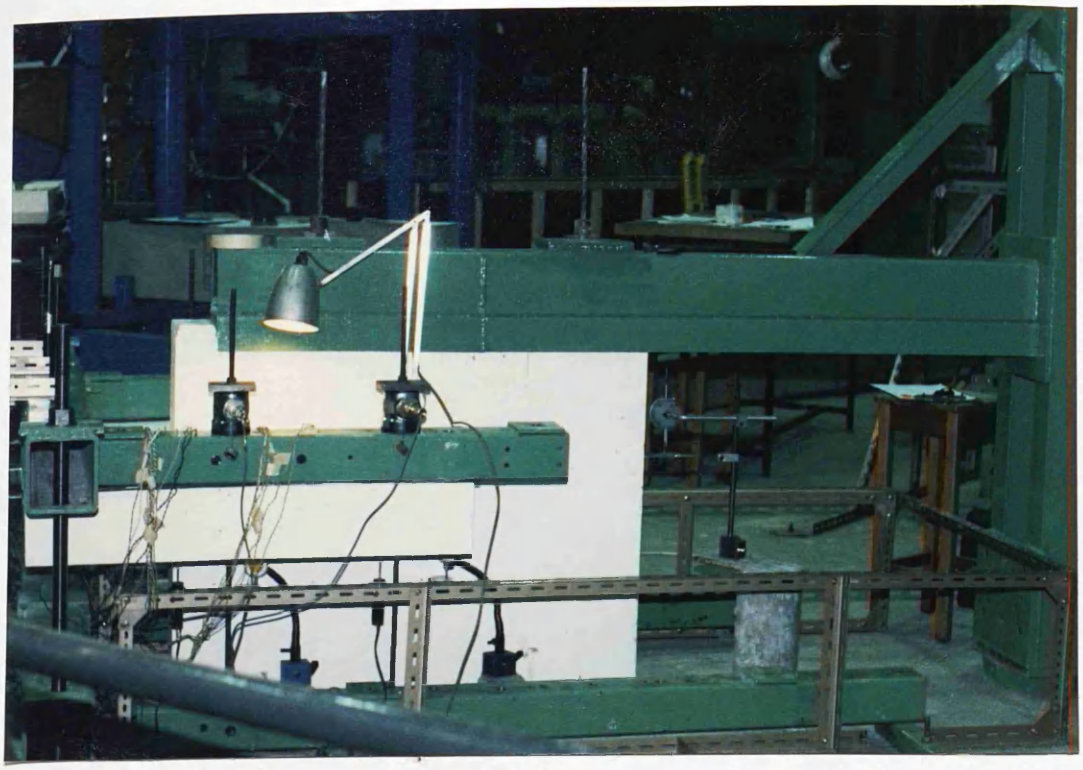

Figure (5.3) : Photograph showing supporting arrangement for models MS6 to MS12.

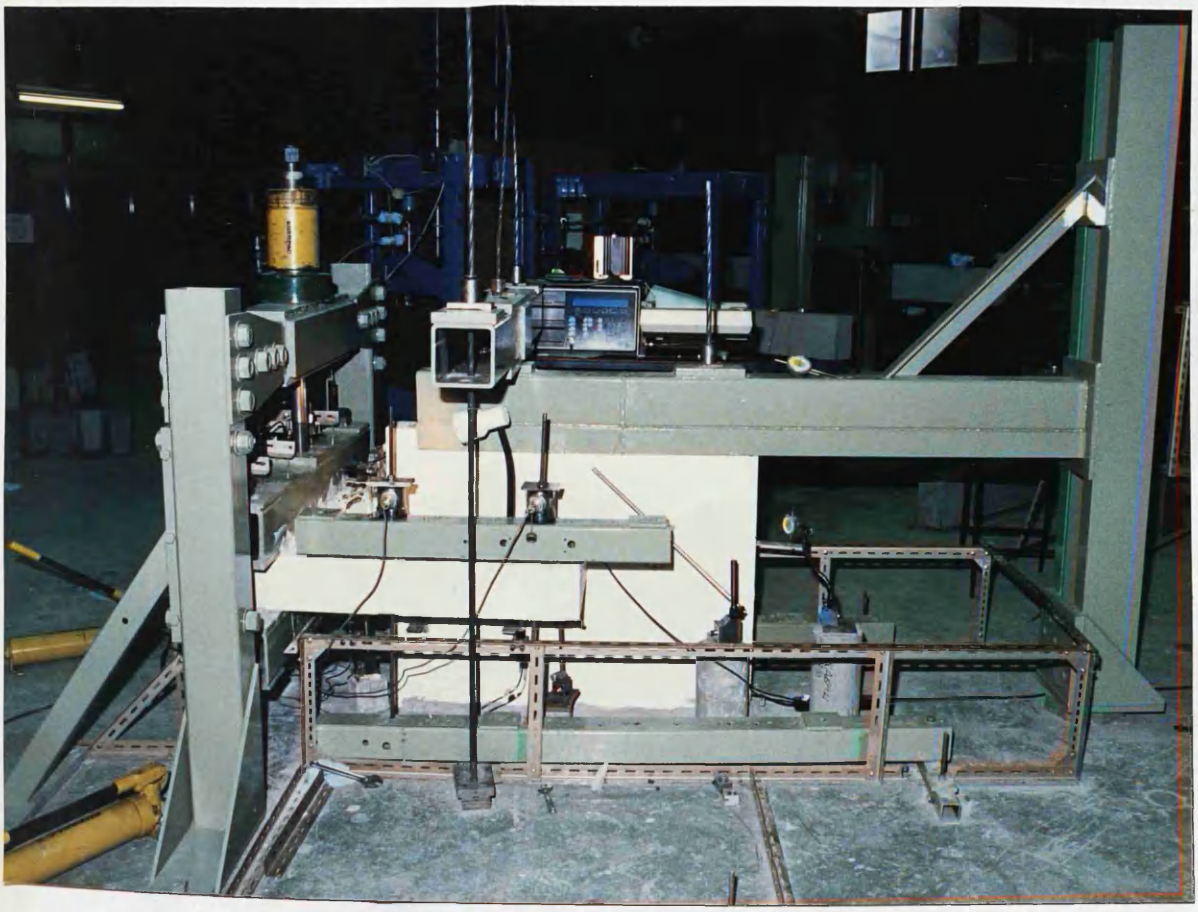

Figure (5.4) : Photograph showing supporting arrangement for reverse cycling models.

5.2.2.2 Lateral Load

In this investigation, the lateral load is simulated by a uniform displacement of the edge of the slab ('AB' in Figure 5.1). This was achieved for the models, loaded monotonically to failure, by means of a loading frame which consisted of two 150 x 150 x 10 mm square hollow sections, strengthened by welding 12 mm thick plates. The upper beam rested on the edge of the slab while the lower beam was supported from upper beam by means of two threaded steel rods of 35 mm diameter mild steel, one on each side of the beams, as shown in Figures (5.5) and (5.6– b). The frame was pulled down by a manually operated hydraulic jack of 500 KN capacity using a steel rod of 50 mm diameter. The upper end of which was fixed to the lower beam at its centre. Photograph (5.7– a) shows this arrangement.

For the models which were tested for reverse cyclic loading, the downward and upward load was applied by a slightly modified loading frame as shown in Figure (5.7– b). An additional steel tubular portal frame was designed and constructed to carry the downward (pushing) reaction of the hydraulic jack when the frame was pulled up by another additional steel rod of 50 mm diameter. The lower end of this rod was fixed to the top beam at its centre. Both the top and bottom beams were placed on the slab edge by means of plaster and connected to each other by the same two rods of 35 mm diameter. For lateral stability, the portal frame was supported by two inclined steel sections at the two edges of the vertical post. Two 500 KN load cells, one at the bottom of the 'strong' floor and the other at top of portal frame, were used to measure the amount of wind load applied to the model.

5.2.3 Installation of Specimen

This involved the following steps:

(a) For reverse cyclic loading, placing the steel tubular portal frame in position and anchoring to the laboratory floor.

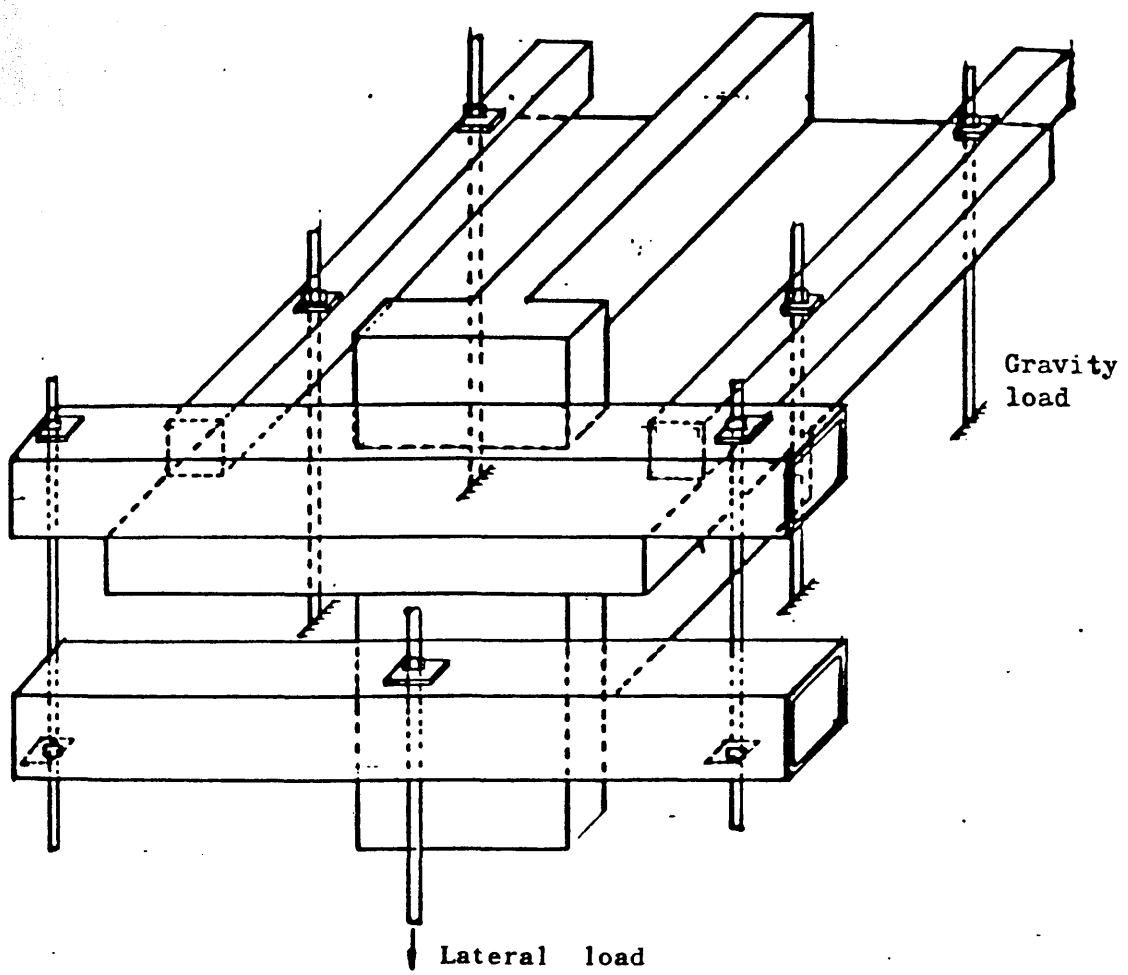

Figure (5.5) : Typical model with loading beams.

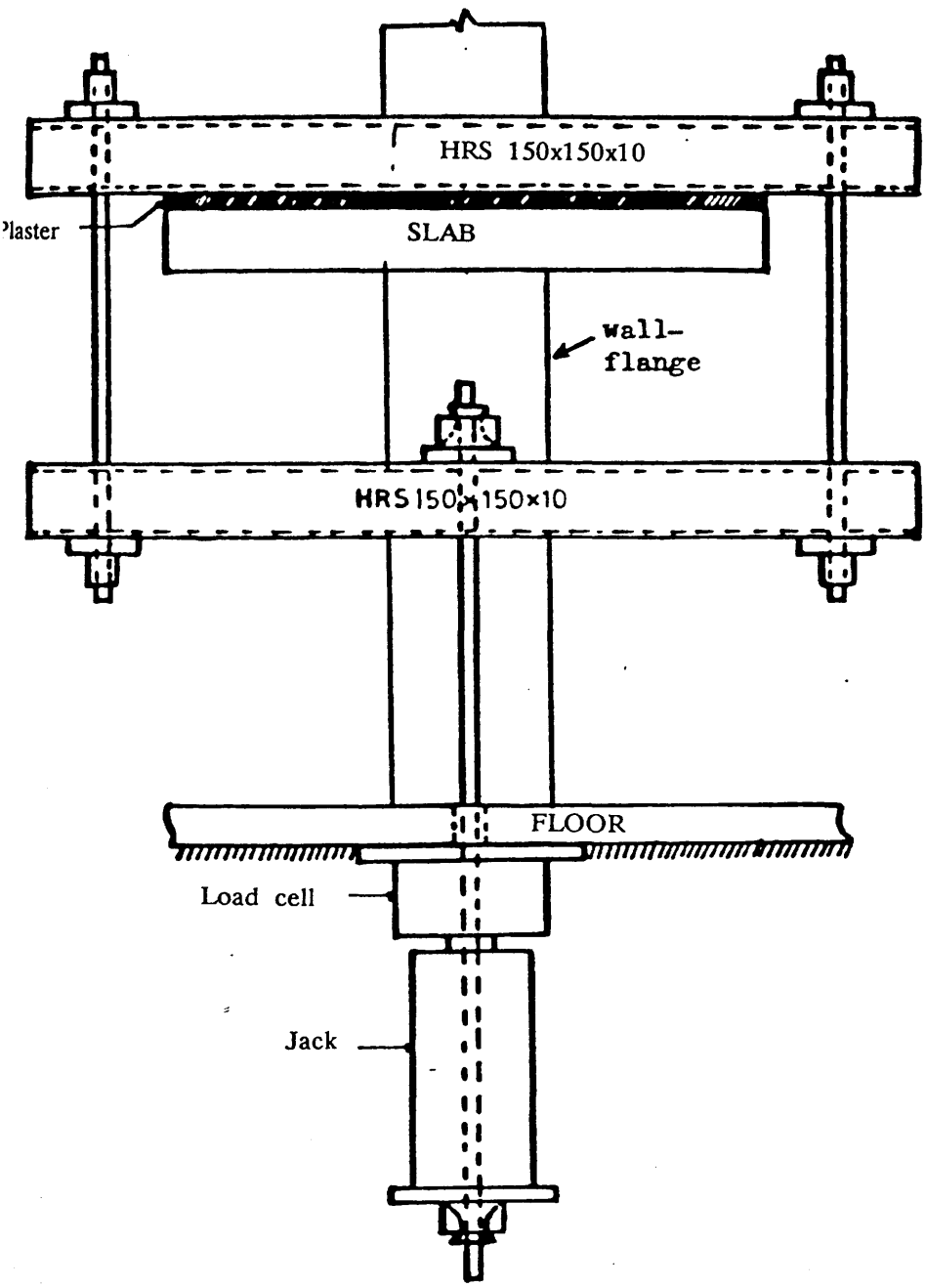

Figure (5.6-a) : Loading arrangement for models.
(gravity load omitted)

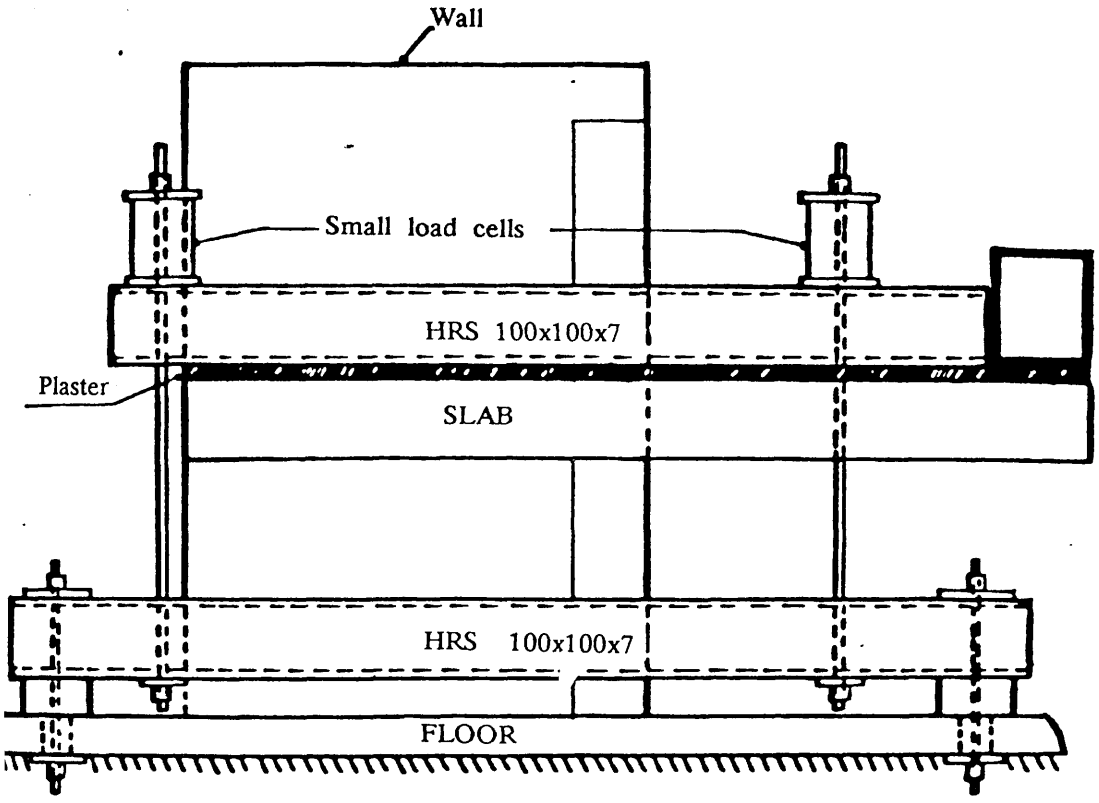

Figure (5.6-b) : Loading arrangement for models.
(gravity load alone)

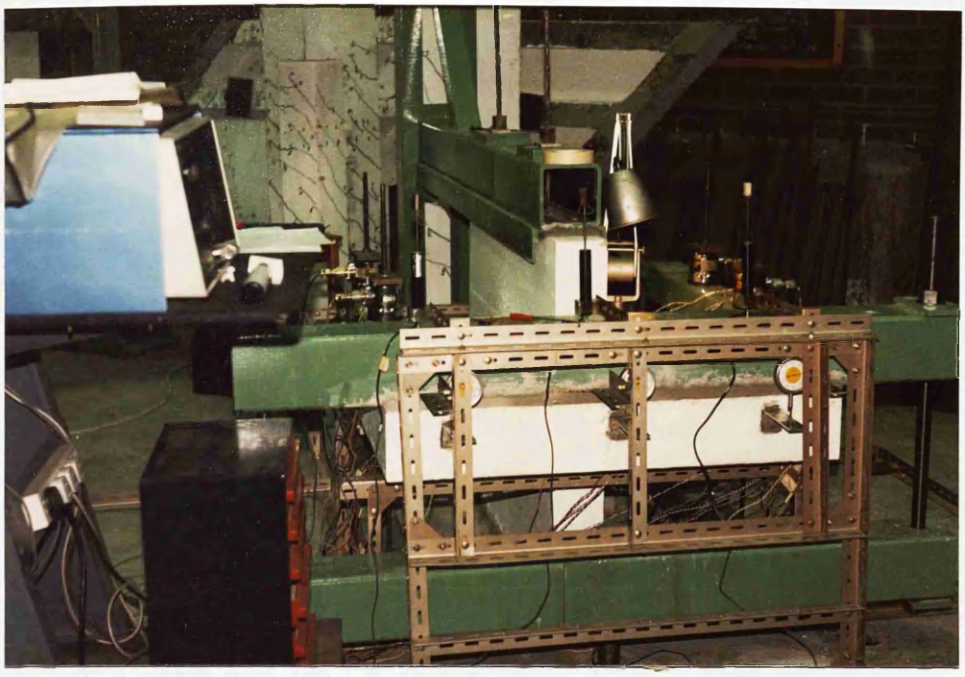

Figure (5.7-a) : Photograph showing loading arrangement for models PS1 to MS12

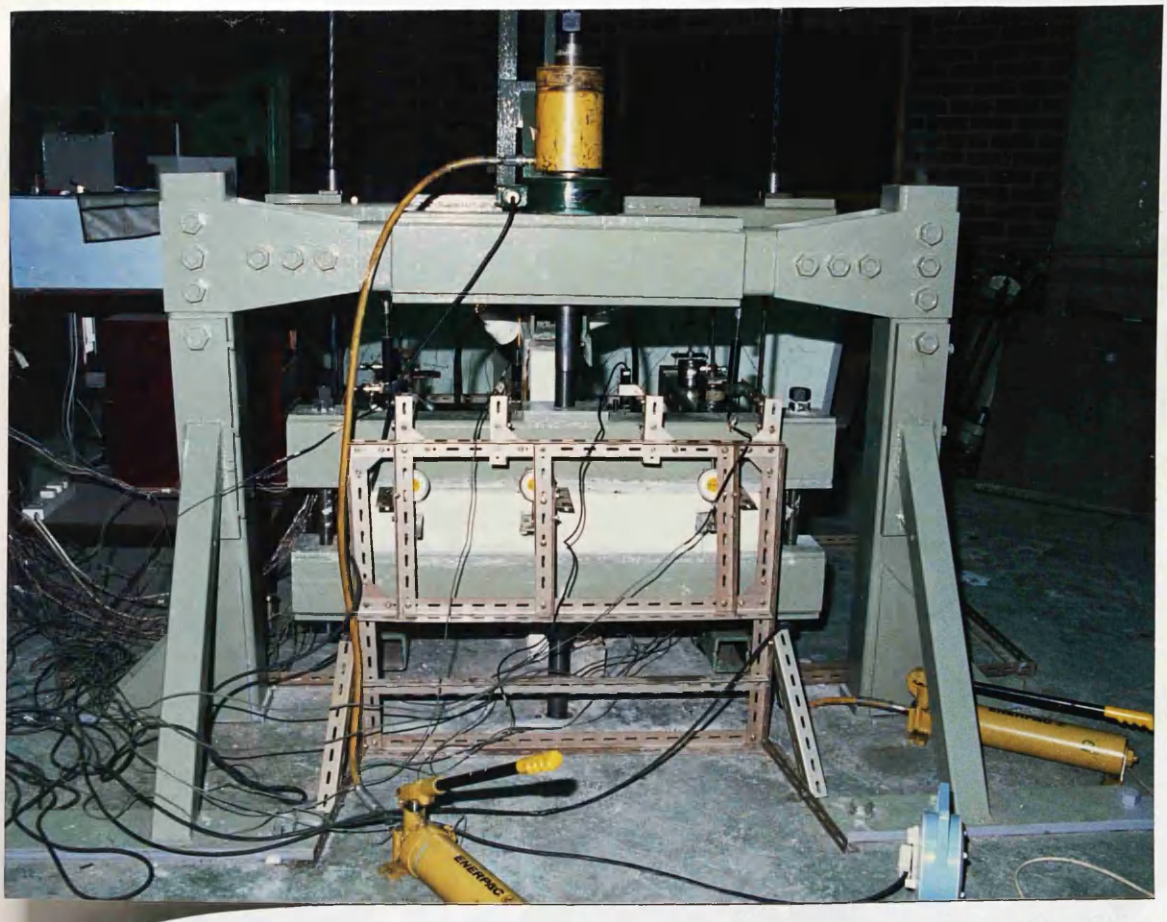

Figure (5.7-b) : Photograph showing loading arrangement for reverse cyclic models.

(b) Placing the model with the help of plaster in marked position of the 'strong floor' and checking the leveling by spirit level.

(c) Anchoring the wall using the steel stand.

(d) For reverse cyclic loading series, placing the transverse beam perpendicular to the steel stand and tightening the additional prestressing strands.

(e) Placing the top and bottom lateral loading beams on the slab edge of corridor opening with the help of plaster and two 35 mm threaded steel rods.

(f) Placing the 50 mm diameter steel rod vertically up through the strong floor in position and connecting with the bottom loading beam.

(g) For reverse cyclic loading, connecting similar vertical steel rod passing through the portal frame with the top loading beam.

(h) Placing the load cells and the hydraulic jacks through each vertical rod and then nuts are tightened.

(i) Placing the gravity load beams on both sides and the four 12 mm diameter steel rods with nuts and load cells for gravity loading.

(k) Placing the steel angle frame with dial gauges in appropriate position.

(l) Connecting the load cells, transducers and strain gauges to the data logger for continuous measurements of the various quantities.

5.3 Materials Used

5.3.1 Concrete

The concrete mix consisted of rapid hardening portland cement, 10 mm uncrushed gravels and zone 2 Hyndford sand. The coarse and fine aggregate used in the concrete mix were obtained from Lanarkshire. A mix proportion of 1:1.48:2.6 was used for an average cube strength of 40 N/mm^2 at 7 days. After having mixed these materials for about two minutes in a dry state, water was added such that the water cement ratio was 0.48. Six 100 mm cubes and at least four 150 mm x 300 mm cylinders were cast with each specimen. The cubes were used to determine the cube strength, two cylinders for the split tensile strength and

remaining cylinders to determine the concrete Young's modulus (and the stress–strain curve) and the cylinder compressive strength. A typical stress–strain curve of concrete is shown in Figure (5.8).

5.3.2 Reinforcing Steel

High yield deformed, hot rolled and cold twisted, bars of diameter 6, 8, 10 and 12 mm were used as reinforcement. Random samples were cut from the batches of steel bars for all the different diameters and were tested in Tinus Olsen Universal Class A testing machine, fitted with a S–type electronic extensometer. Tests were carried out in accordance with the manufacturer's instruction manual. Typical stress–strain curves for each diameter as obtained from the testing machine are presented in Figures (5.10) to (5.13). Since the yield point for all the bars was not well defined (see Figures (5.10) to (5.13)), the yield stress of the bar was taken as the stress at which a line parallel to the initial slope of the curve from 0.2% proof strain intersects the curve. The yield strain was taken as the strain at which the straight line portion, when extended, intersects with the yield stress as illustrated in Figure (5.9). The mean value of three specimens from each diameter are presented in table (5.1).

Table (5.1) Properties of Steel Reinforcement

Bar size	Yield Stress N/mm^2	Yield Strain	Young's modulus N/mm^2
6	570	0.002817	204.8
8	477	0.002425	202.8
10	523	0.002536	211.0
12	531	0.002499	212.9

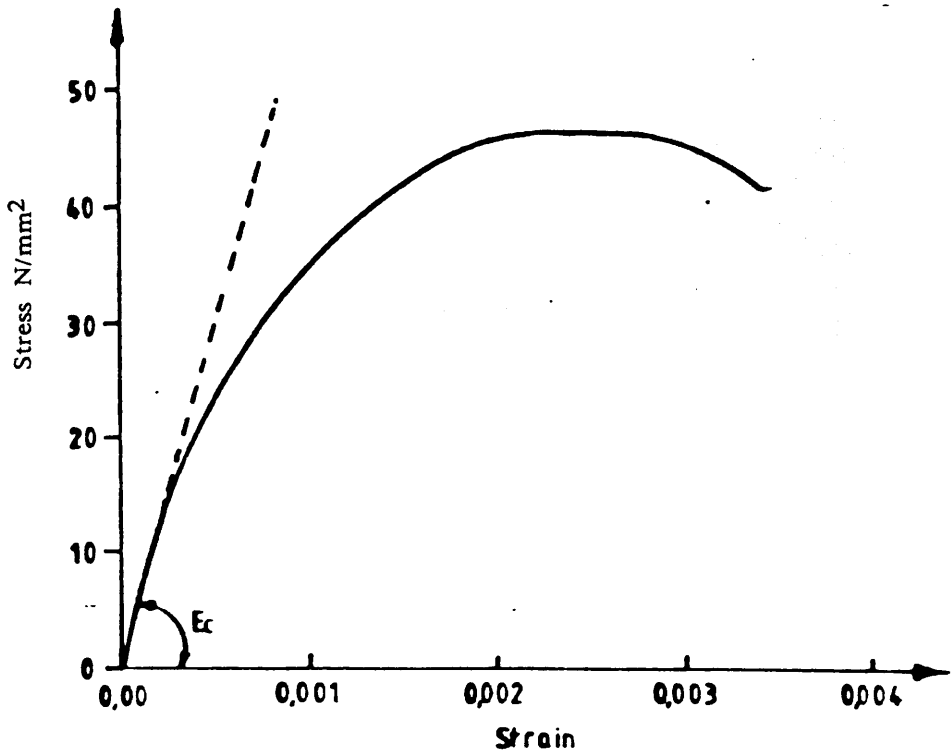

Figure (5.8) : Typical stress-strain curve for concrete.

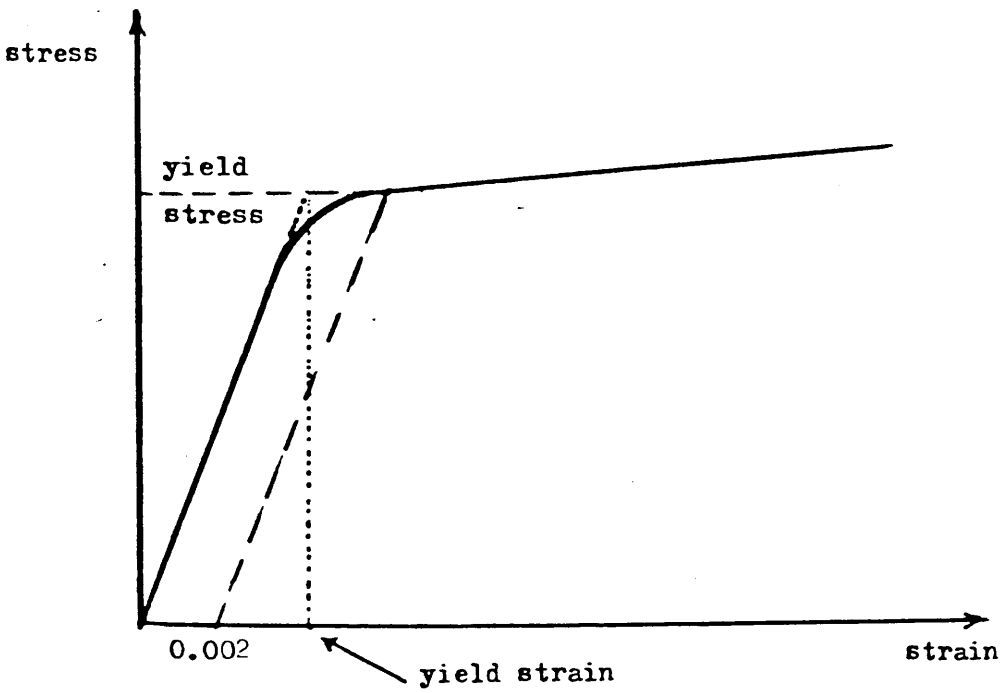

Figure (5.9) : Definitions of yield stress and strain of steel reinforcement.

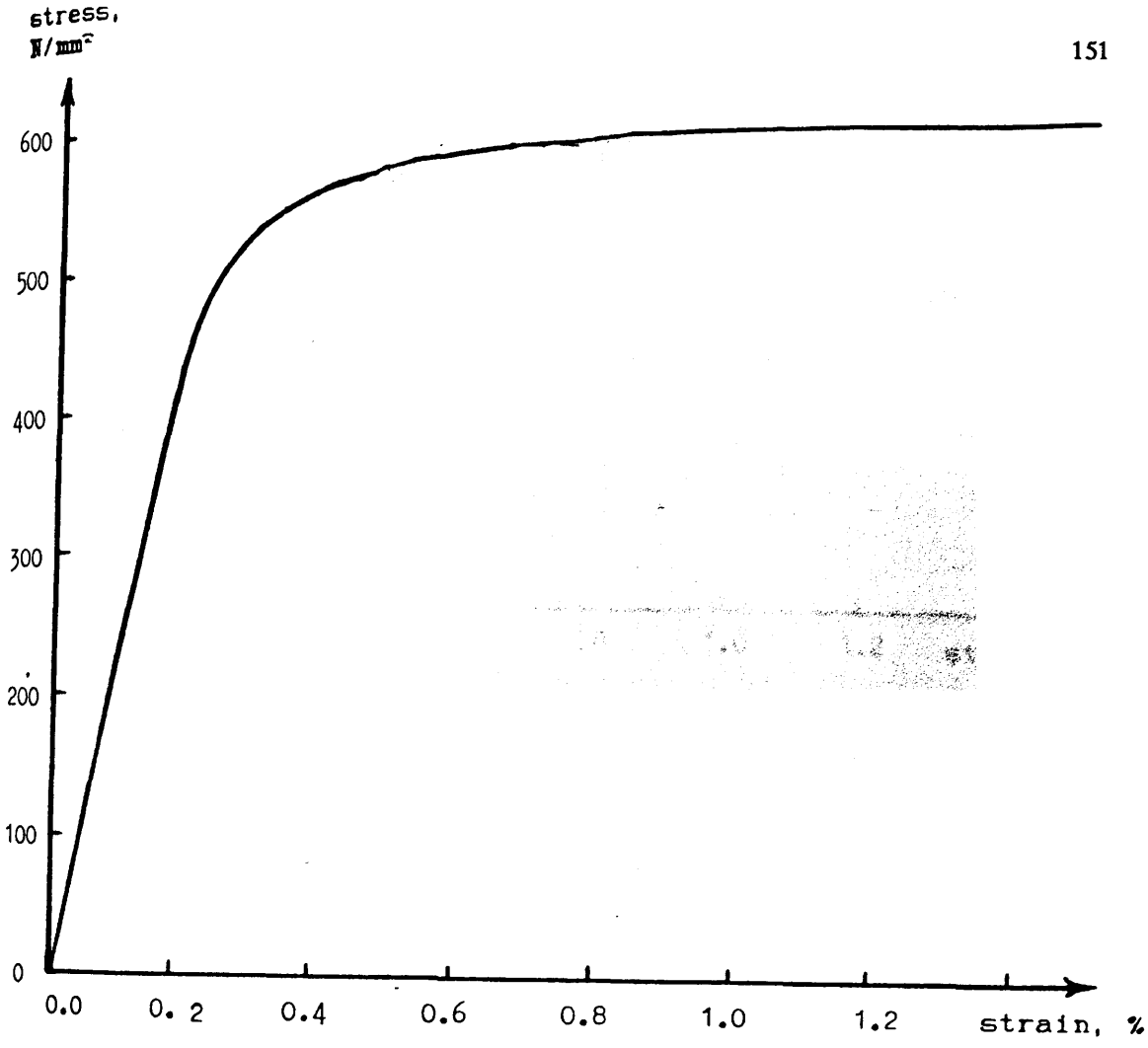

Figure (5.10) : Typical stress-strain curve for a bar of 6 mm diameter.

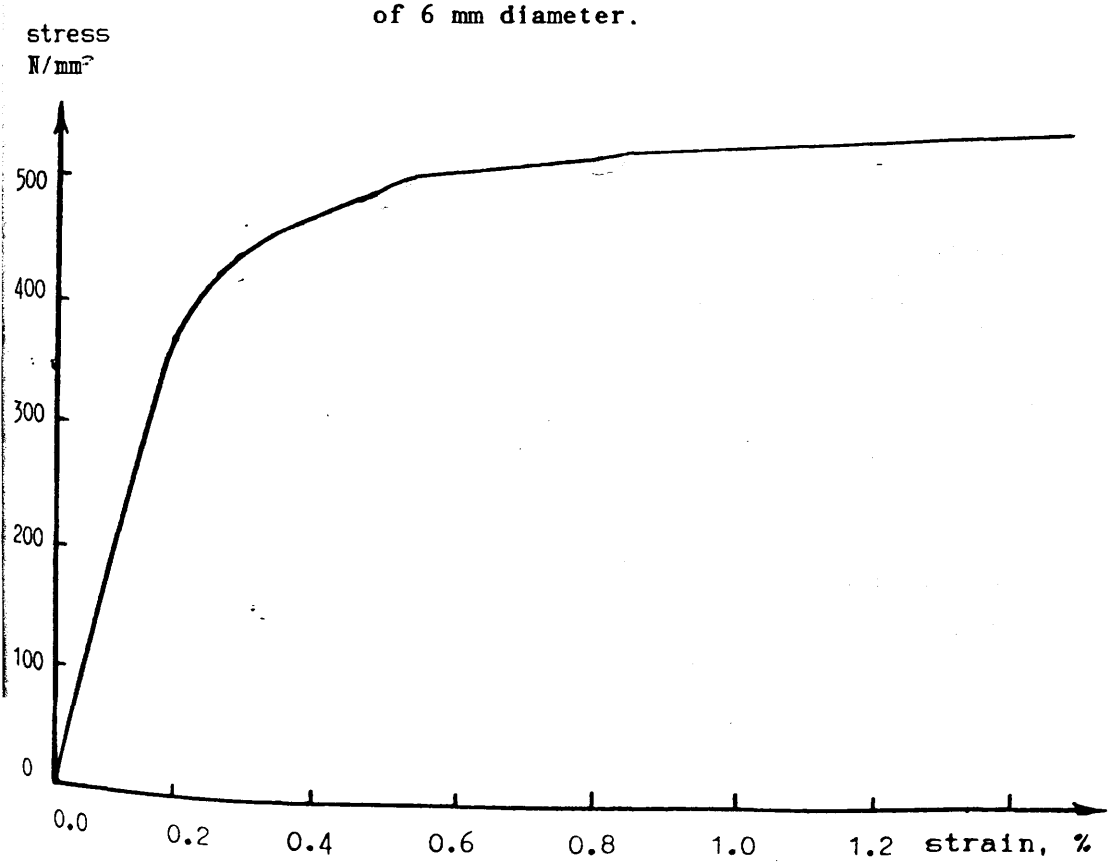

Figure (5.11) : Typical stress-strain curve for a bar of 8 mm diameter.

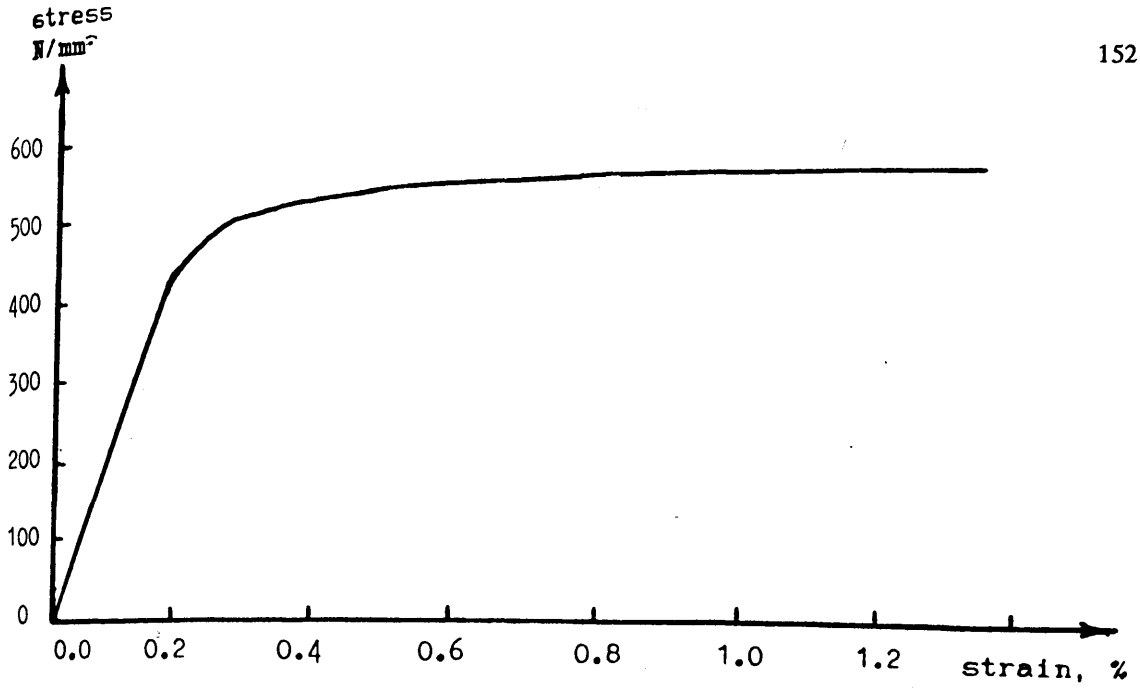

Figure (5.12) : Typical stress-strain curve for a bar of 10 mm diameter.

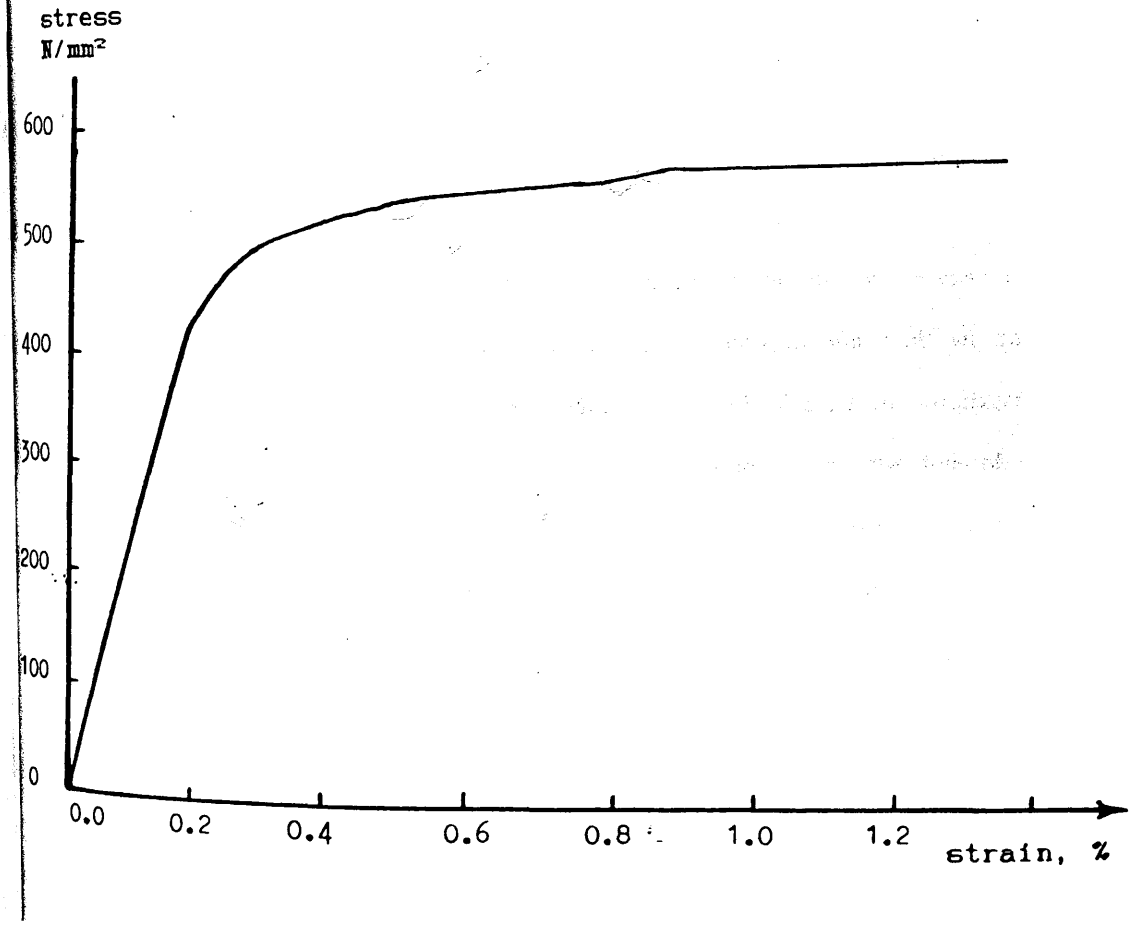

Figure (5.13) : Typical stress-strain curve for a bar of 12 mm diameter.

5.4 Instrumentation.

All the models were instrumented to measure the loads, deflections and strains. Models of reverse cyclic loading test series were additionally instrumented to measure the rotation of the slab with respect to the wall.

5.4.1 Measurement of the Applied Loads

The total applied lateral load was monitored by means of a compression load cell of 500 KN capacity for models PS1 to MS12. An additional load cell of same capacity was used for reverse cyclic models MRS13 to MRS15. Gravity loads were monitored by four 50 KN capacity load cells attached to each of the four bars used for gravity loading (Figure 5.5).

5.4.2 Measurement of Vertical Displacements

Deflections were measured at various points of the slab as shown in Figure (5.14) by means of electrical displacement transducers. A supporting frame of 'Handy Angles' was made and the transducers were fixed to it at the required points by using clamp brackets. To facilitate recording of results, linear voltage displacement transducers (LVDT) were used in conjunction with an automatic data storing and processing data logger, which recorded directly the displacement in mm to an accuracy of 0.01 mm. The average deflection along the line of contraflexure (line AB in Figure 5.14– a) was considered for lateral load– deflection relationships; while other readings of deflection were taken mainly to monitor the variation of deflection along the line of contraflexure.

In addition three dial gauges reading to 0.01 mm were also installed in the front of the slab to cross check the accuracy of the transducer measurements. Upward / downward deflections at the back and along the wall were also measured by dial gauges to allow for necessary corrections of slab deflections due to rigid body rotation.

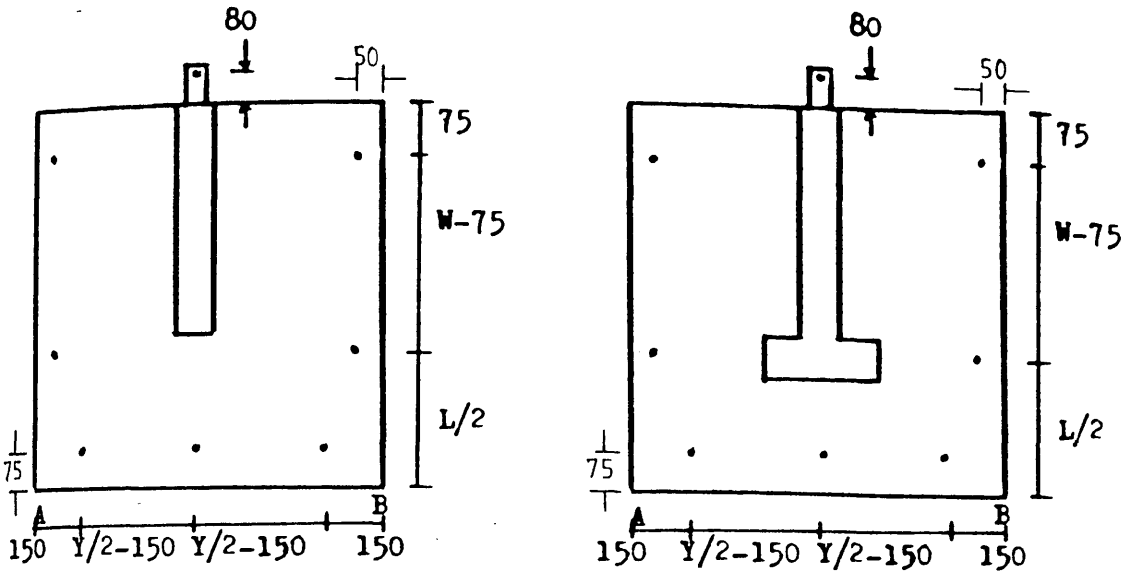

(a) Models under monotonic loading

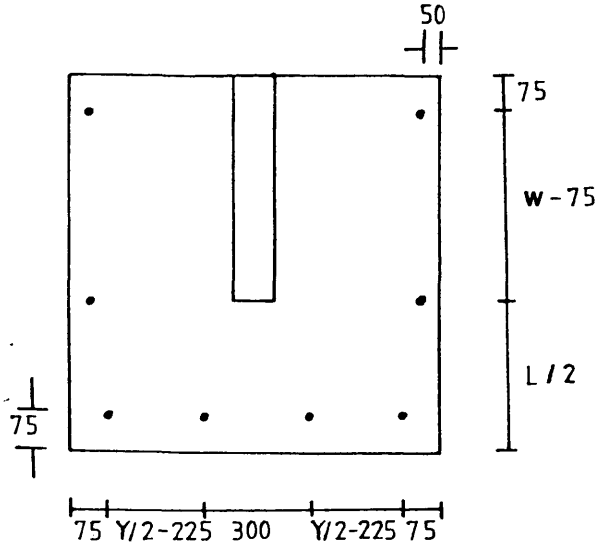

(b) Models under reversed cyclic loading

Figure (5.14) : Location of displacement transducers

5.4.3 Rotation of the Slab Relative to the Wall

For reverse cyclic loading models, the rotation of the slab relative to the wall was measured at one slab thickness from the slab by two transducers, (one above and one below the slab– wall connection) mounted on two steel plates attached to the slab as shown in Figure (5.15). From an external supply, both transducers were supplied 1 volt across resistor 'ab'. Terminal c of the transducers were then connected across the voltage input terminal of the Orion Data Logger. As the resistors are linear, the initial voltage across the terminal reads zero. During loading, when the wall rotates, the point c on each terminal moves on resistor 'ab'. This causes a voltage change (in milivolt) at Data Logger input. The voltage was converted to read displacement in milimeter by multiplying by calibration factor of 59.9434.

5.4.4 Measurement of Strains

Electrical resistance strain gauges were used to measure the tensile strain in steel and surface compressive strain on the concrete. The compressive strains were measured on the bottom of the slab along a section passing through the slab near the inner edge of wall. Strains in wall at certain sections were also measured. The location of these points in the slab and wall of a typical model is shown in Figure (5.16). The strain gauges used for concrete were 10 mm long with the elongation capacity of ± 6% and a gauge factor of 2.04 at a temperature of 75^0 F. Their internal resistance was 120 ± 0.3 % ohms. Depending on the availability, two different types of strain gauges, namely student EA.0.6.2401Z–120 and Jurvis Cu45Ni, were used on the steel bars. All strain gauges were connected to a linear voltage processing data logger (Type Orion A), which directly recorded the strains at each point for each load increment.

5.4.5 Crack Width

Crack width was measured by means of a hand held crack width microscope

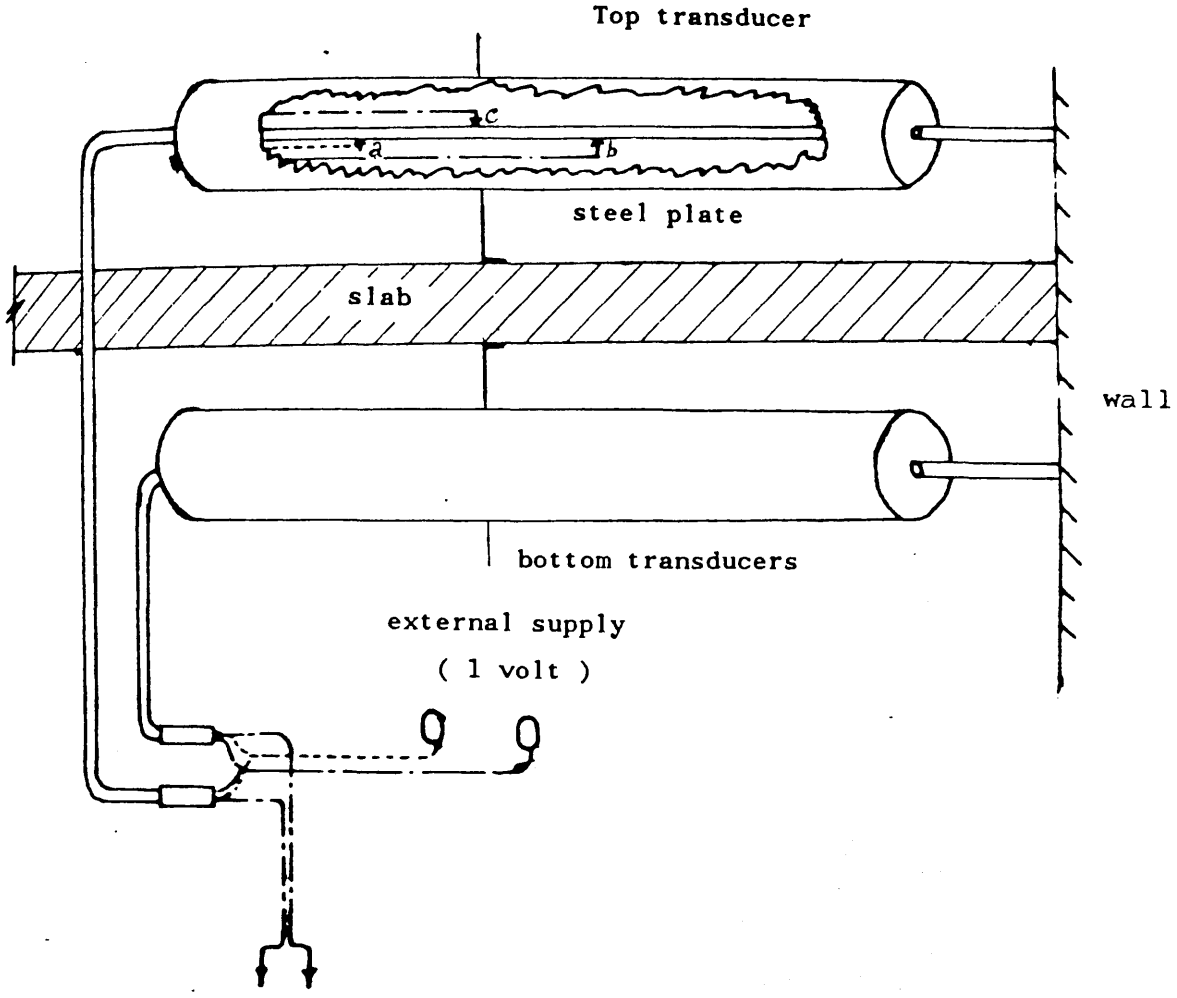

Figure (5.15) : Arrangement to measure the rotation of the slab relative to the wall

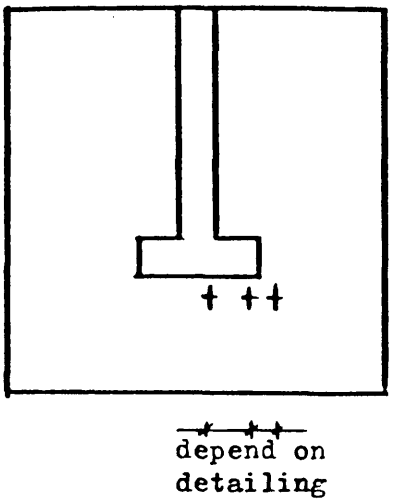

(a) On longitudinal steel bars

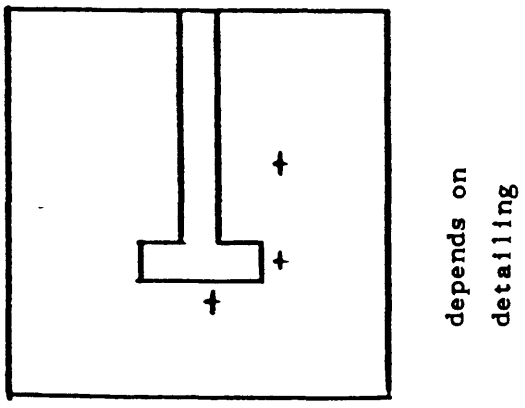

(b) On transverse steel bars

Figure (5.16) : Location of strain gauges on steel bars

measuring to 0.05 mm. The selection of the crack for measurement was based on the most dominant cracks at the nose of the rectangular wall models and at the inner flange– tip of the T– section wall in the case of flanged models.

5.5 Preparation of Specimens and Test Procedure

5.5.1 Strain Gauging

The first step towards specimen preparation was the fabrication of reinforcement and mounting of the steel strain gauges at the selected positions on the reinforcing bar. For fixing strain gauges on steel, the bar surface at the required location was filed and smoothened with sand paper. Care was taken not to remove considerable area of steel during the operation. The surface was then treated with M– prep neutralizer to remove dirt and grease(88). To cement the strain gauge and terminal strip to the bar, M– bond 200 adhesive was employed. For gauge protection against moisture and mechanical damage during casting etc., protective coating white M– coat D and epoxy resin were applied on the gauge and terminal. A final resistance check was carried out by voltmeter for each strain gauge.

5.5.2 Formwork and Reinforcement Cage

The formwork needed for fabrication was made from 18 mm thick coated plywood sheet and 50 x 50 mm timber battens were used to reinforce the corners. To achieve flexibility and reuse of the formwork for more than one specimen, slab dimensions were adjusted on a 1500 x 1500 mm plywood sheet. All formwork was oiled for easy removal. Wall reinforcement cage was properly positioned first in the formwork and then the slab reinforcing cage was placed inside the wall reinforcement and formwork ready for casting. 15 mm concrete cover was maintained on top and bottom surface of the slab, using plastic cover spacers.

5.5.3 Casting and Curing

Casting was normally done in six to eight batches of concrete, depending on the size of the model. In order to prevent the downward drift of fresh concrete in the upper portion of the wall towards the slab, the slab and the lower portion of wall were cast first and after a break of about three hours, the upper portion of wall was cast. Care was taken to ensure bonding of the two mixes and collection of control specimens (cubes and cylinders) from both batches. The specimen was compacted using 12 mm internal poker vibrator. The cubes and cylinders were compacted by means of a vibrating table. The steel rods used for providing holes in the wall and slab were removed at the end of the day.

After casting, the model and the control cubes and cylinders were cured under damp hessian for the first three days. The specimen was then removed from the formwork for final curing under laborartory conditions until the time of testing.

5.5.4 Demec Gauges and Electrical Resistance Strain Gauges on Concrete Surface

The specimen was painted white in order to enable clear tracing of cracks. Demec gauges were glued to the top concrete surface using Araldite. On the bottom compressive side (except for models MRS13 to MRS15) concrete strain gauges were fixed at marked position as shown in Figure (5.17). For fixing the strain gauges, the concrete surface was firstly cleaned and made smooth by grinding, using a grinding stone and then smoothened by a fine emery paper. Carbon tetrachloride was used to remove the grease and dirt. A thin coating of Adhesive and Hardener mixture was applied to the cleaned surface and the strain gauge was stuck on it by firmly pressing with the thumb for about two minutes. After a few hours, the wires were soldered to the gauges and terminals. Protective coating (white M–Coat D) was then applied to the strain gauges. The specimen was then installed in position ready for testing (section 5.2).

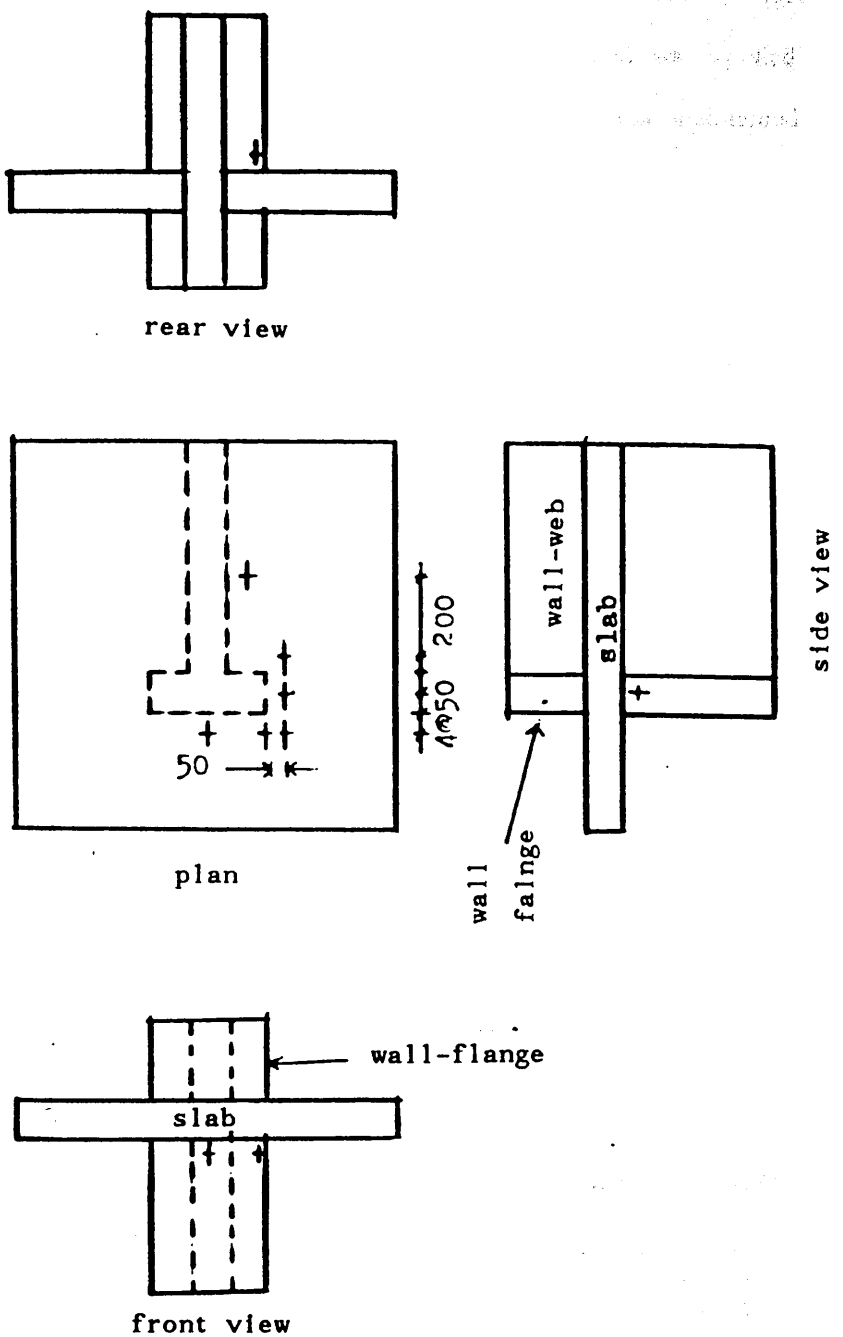

Figure (5.17) : Location of strain gauges on the surface of concrete

5.5.5 Test Procedure

Initial zero load readings were taken of all load cells, transducers, and strain gauges for each model before starting the test. In all models gravity loads were applied in the first five equal increments and then lateral load was applied in 10 KN increments. The gravity load was constantly monitored and maintained at its ultimate value as far as practicable while lateral load was applied. The reason for the adjustment is that the deflection of the slab due to lateral load alters gravity load. Therefore gravity loads were readjusted to the desired values after each lateral load application. Care was taken to see that the applied load was not causing any eccentricity and consequent twisting of the model. Loading was continued until failure was noted by either a continuous drop of applied load value or a sudden fall of that value combined by a physically noticeable failure.

For models of reverse cyclic loadings, gravity load was applied first and then a downward load was applied in increments to the cantilever slab and the relative rotation between the wall and cantilever slab was measured by transducers. From a plot of the load versus the rotation and load versus the steel strain, the yield rotation, θ_y, was calculated. After this initial loading, the downward load was released and the cantilever slab was reloaded in the upward direction. The cycles of loading as discussed in chapter eight, was maintained until the model failed in the same way as for monotonic loading.

During loading, crack propagation was closely monitored and traced on the slab. The corresponding load increment was recorded on the top surface at the tip of each crack. The total duration of a test for monotonic loading averaged between 6 to 8 hours depending on the total number of load increments applied. For reverse cyclic loading, the test was continued over several days.

CHAPTER SIX

EXPERIMENTAL STUDY

6.1 Introduction

In this chapter, details of twelve 'large scale' reinforced concrete models tested under monotonic loading condition are reported. Nine models had a slab connected to a rectangular shearwall, while the remaining three had a T–section shearwall, as shown in Figures (6.1) and (6.2) respectively. Detailed description of another three models tested under reversed cyclic loading condition will be reported in chapter eight.

It was stated in chapter two, that when load is transferred between slab and column, either as a result of lateral loadings or unbalanced gravity loadings, conditions at the slab to column connection are critical for determining the strength and stiffness of flat–slab structure. A typical wall–slab junction acted upon by shear and moment due to wind and gravity loads is shown in Figure (6.3). The shear force due to "wind" load acts along the line of contraflexure (which is approximately the centre line of the corridor opening), while the critical section for moment passes through the slab at the inner edge of the wall (see Figure (6.3)). This region around the shear wall – floor slab connection is the area of interest in this study.

Since the distribution of shear due to "wind" loads, as discussed in chapter two, is not uniform, this shear will hereafter be referred to as uneven shear and the moments due to "wind" load will be called unbalanced moments. Unbalanced moment results from unequal consecutive slab spans, uneven loading of adjacent bays, edge column and in the case of slab–column structures due to lateral load.

6.1.1 Object of Tests

The object of the experimental study is to improve the shear strength and

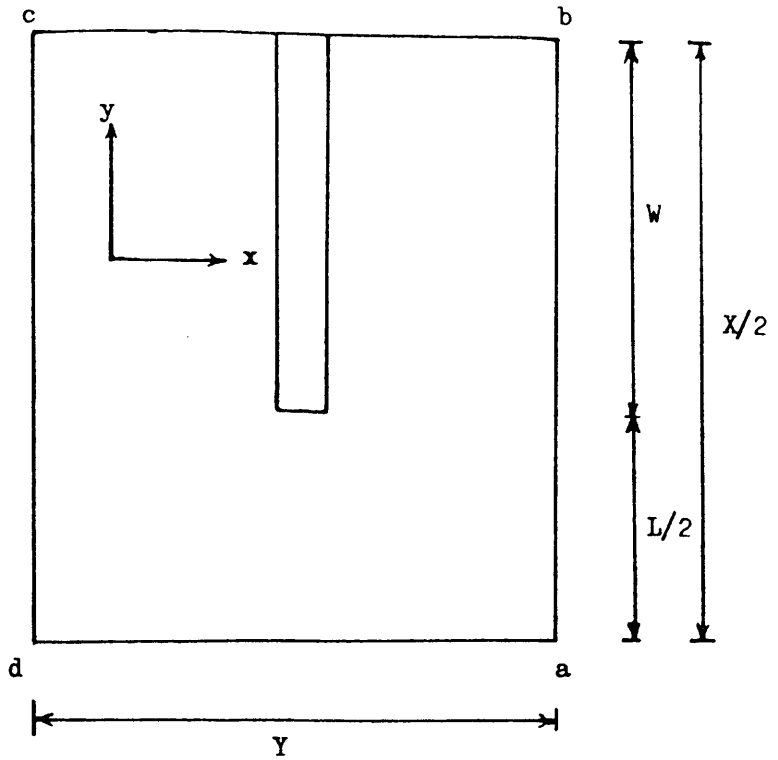

Figure (6.1) : Plan of a typical model with rectangular shear wall

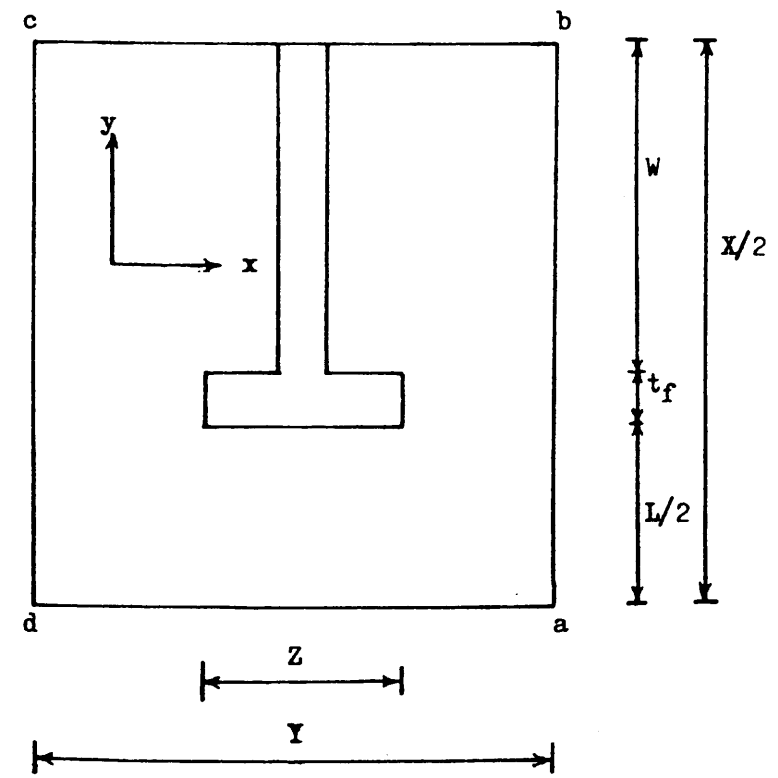

Figure (6.2) : Plan of a typical model with T-section shear wall

ductility of the slab – wall junctions, using various type of shear reinforcement, when they are subjected to different combinations of lateral (wind) and vertical (gravity) loads. There is a lack of information on the behaviour and performance of shear wall–slab connections under seismic loading conditions. Some cyclic load tests were conducted to get informations on the deformations that may safely occur and the deterioration of load–carrying capacity of shear wall–floor slab connections. It was intended to study the behaviour of every models in terms of :

a) Load–deflection relationship.

b) Strain distribution in steel and concrete around the wall

c) Strain distribution in stirrup.

d) Crack pattern and crack propagation.

e) Ultimate load.

f) Modes of failure and failure characteristics.

6.1.2 Parameters of Study

To investigate the effectiveness of various type of shear reinforcement in preventing the brittle failure due to shear before failure by yielding of the most of the flexural reinforcement, preliminary tests were conducted on three models. The test results showed that vertical stirrups enclosing the top and bottom longitudinal reinforcement are effective in increasing the ductility and strength of the wall–slab junction.

The rest of the experimental models (which contained closed vertical stirrups as shear reinforcements) were devoted to investigate the effect of the following geometrical parameters (see Figure 6.2):

1) Wall–web length, (W)

2) Wall–flange width, (Z)

3) Corridor opening width, (L)

4) Bay width of connecting slab, (Y)

5) Ratio of total gravity load to "wind" load, (V_g/V_ℓ) and

6) Ratio of moment due to gravity load to shear due to gravity load (M_g/V_g)

The range of parameters were so chosen that the nondimensional structural parametric ratios would cover the practical range of tall buildings. In addition to the above, three models were tested under reverse cyclic loading conditions.

6.1.3 Boundary Conditions and Overall dimensions of models

The area of interest is the local stresses around the junction and therefore it is not important to duplicate all the boundary conditions of the structure. In the real structure of Figure (6.4), the boundary conditions for gravity load require zero rotations around Y– axis at edges 'ab' and 'cd' i,e., no slope, torsion and shear force along edges 'ab' and 'cd' and zero rotations around X– axis at edge 'ad' i.e., no slope, torsion and shear force – only moment will exist at edge 'ad' (see Figure 6.5). At the same time the boundary conditions for lateral load require zero rotations around Y– axis at edges 'ab', 'cd', and 'da' i.e., the "wind" loading causes slope, torsion and shear force but no moment along the line of contraflexure 'ad' as shown in Figure (6.6). These requirements are not satisfied during testing of the models of Figures (6.1) and (6.2). Only a portion of the floor plan which is shown shaded in Figure (6.4), with all the edges free as shown in Figure (6.3), was chosen for this study.

No great care was taken to make the models conform to the laws of geometrical similitude. The slab and wall thickness were maintained nearly equal to the prototype dimensions, to avoid size effect on the shear capacity and failure criteria of the slab. The overall slab width, corridor width, flange width etc. were fixed to study the parameters of section 6.1.2. Other dimensions were dictated by the location of the anchoring holes in the strong floor of the laboratory. Since our investigation was concerned with the local effect (punching) around the wall–slab junction – the violation of uniform scaling down of the dimensions is unlikely to

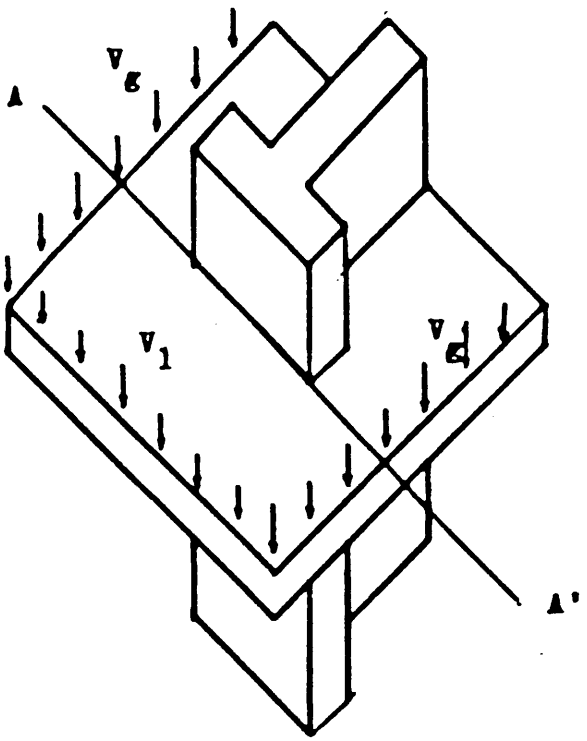

V_1-uneven shear due to lateral loads.

V_g-gravity loads

Figure (6.3) : An isometric view of a typical model with shears due to lateral and gravity loads

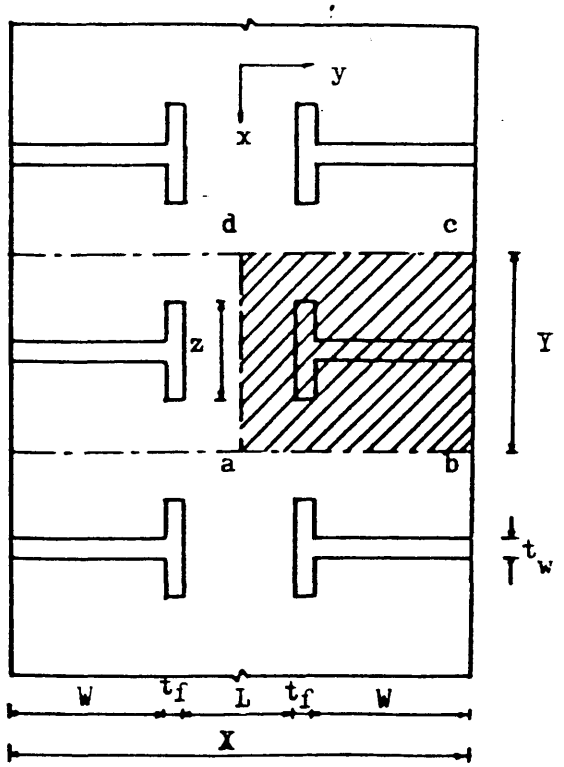

Figure (6.4) : Plan of a typical structure

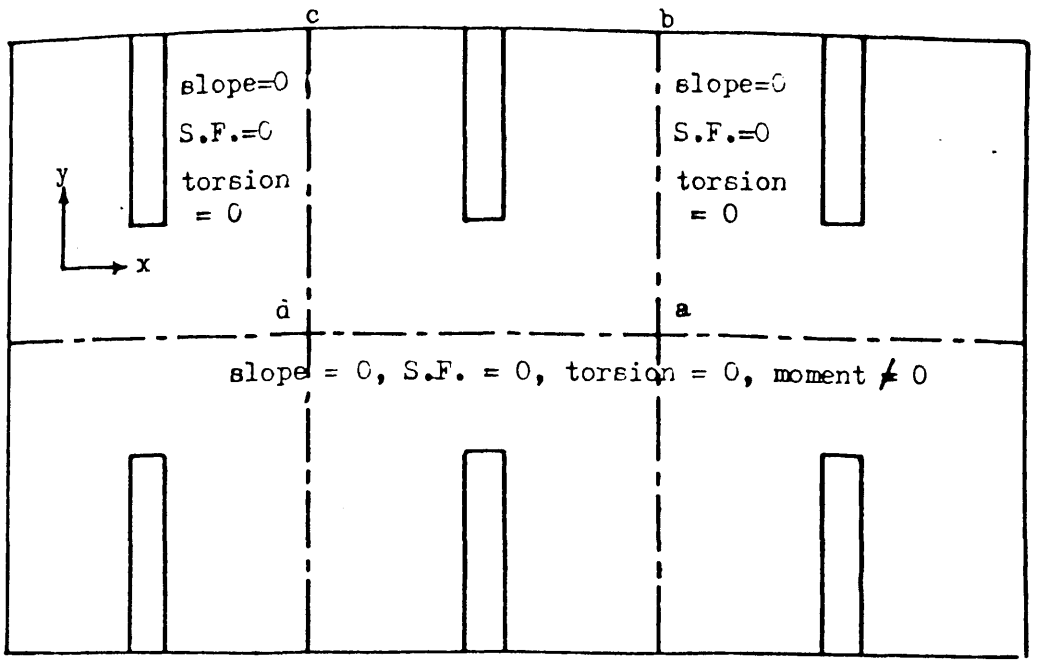

Figure (6.5) : Boundary condition of the slab due to gravity load

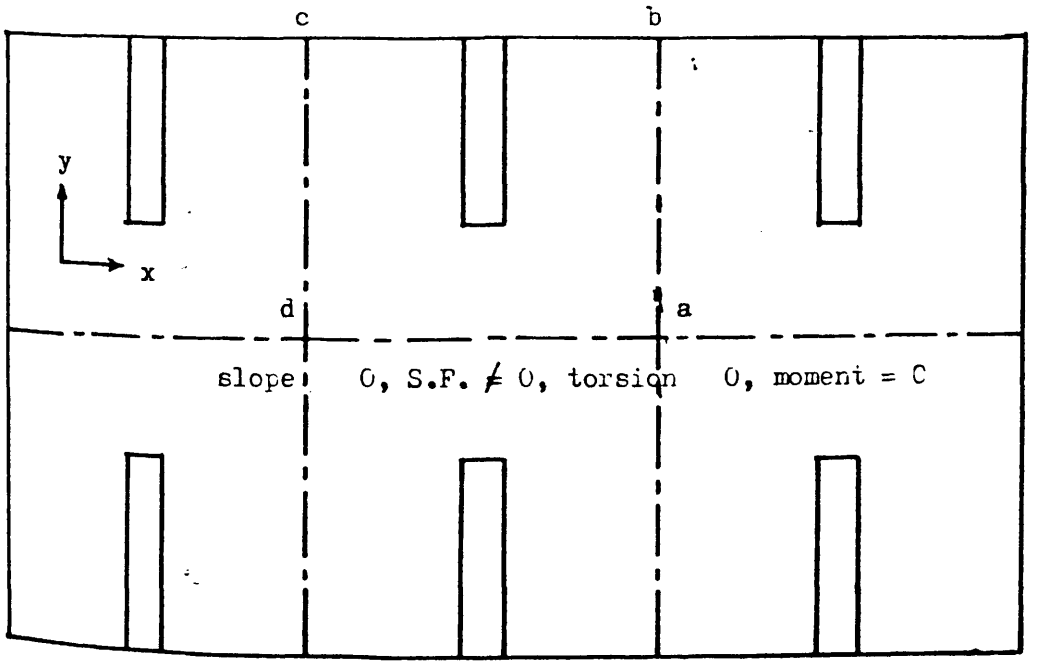

Figure (6.6) : Boundary condition of the slab due to wind load

affect the structural behaviour of the model.

6.2 Test Programme

The experimental program may be divided into three parts :

i) *Preliminary Test Series* (or PS Series):

This series contains three models. The object was to find suitable form of shear reinforcement that can be used in the slab and to explore the design procedure for the shear steel in such a way that the final failure of the model will be flexural.

ii) *Main Test Series* (or MS Series):

This series contains nine models. The object of this series was to verify the validity of the design procedure as described in details in section 3.6. No systematic exploration of the parameters governing the problem was carried out in this series. On the otherhand, representative models from the previous test series[23,24] were chosen and tested after redesigning them with shear reinforcement.

iii) *Reverse Cyclic Loading Series* (or MRS Series):

This series contains three models. They were designed to study the effect of repeated and reversed lateral loading due to wind forces, earthquake etc. on the behaviour and strength of wall–slab connection. The detailed description of the models of this series will be described in chapter eight.

Table (6.1) shows the geometrical dimensions of the models and Table (6.2) shows the grouping of the models to study various parameters. All the models were tested for combined wind and gravity loading. Gravity loads were applied in the first five equal increments. After this the lateral load was applied in 10 KN increments. The deflection due to lateral load affects gravity load values. Therefore gravity loads were adjusted to the desired values after each lateral load application.

TABLE (6.1) : Dimension of models (in milimeter)

model no	wall web	wall flange	wall thickness	slab cantilever	slab width	slab thickness
PS1	900	125	125	450	1000	150
PS2	900	125	125	450	1000	150
PS3	900	125	125	450	1000	150
MS4	400	125	125	475	1000	150
MS5	400	125	125	595	1000	150
MS6	600	125	125	355	1000	150
MS7	600	125	125	475	1000	150
MS8	600	125	125	475	1000	150
MS9	600	125	125	475	1440	150
MS10	700	300	100	300	1000	100
MS11	700	200	100	300	1000	100
MS12	700	400	100	300	1000	100
MRS13	700	300	100	300	1000	100
MRS14	600	125	125	475	1000	150
MRS15	600	125	125	355	1000	150

TABLE (6.2) : Grouping of models

Parameters involved	Models in the group
Wall length	MS4 and MS7
Wind moment / "Wind" shear ratio	MS5, MS6 and MS7
Gravity / "Wind" load ratio	MS7 and MS8
Gravity moment / Gravity shear ratio	MS7 and MS9
Flange width	MS10, MS11 and MS12
Reverse cyclic loading	MRS13, MRS14 and MRS15

All the measured displacements along the centre of the corridor opening were corrected for rigid body rotations of the models and the wall deformation from the dial gauge readings taken at 3 to 4 positions along the wall as shown in Figures (6.7) and (6.8). The deflection at front edge due to rigid body rotation was calculated and deducted from the measured transducer displacements. The correction against wall deformation was calculated using the following procedure.

It is assumed that along a vertical line, the strains are constant in the wall. However variation of strain at a horizontal section is linear. Therefore referring to Figure (6.9) :

$$\theta = \frac{(\epsilon_1 - \epsilon_2)H}{B}$$

where ϵ_1 and ϵ_2 are the measured strains in the walls at points (1) and (2). and H and B are as shown in Figure (6.9).

Then correction = $\theta \cdot L_c$ (6.1)

where L_c is as shown in Figure (6.9).

The various experimental data on the behaviour of the models and the results are presented for each model in the following order:

i) Sketches showing shape and dimensions of the model,

ii) Reinforcement details,

iii) Load– deflection curve,

iv) Distribution of strains, and

v) Crack pattern.

All fifteen models reported in this thesis were designed using direct design approach explained in chapter three assuming cube crushing strength of concrete equals to 40 N/mm^2. But the actual cube strength of concrete, fcu, on the day each model was tested was different as shown in Table (6.3). So the design load is normalised by multiplying it by a multiplication factor $(fcu/40)^{1/3}$. Therefore, the design lateral load, referred anywhere in this thesis, means normalized design

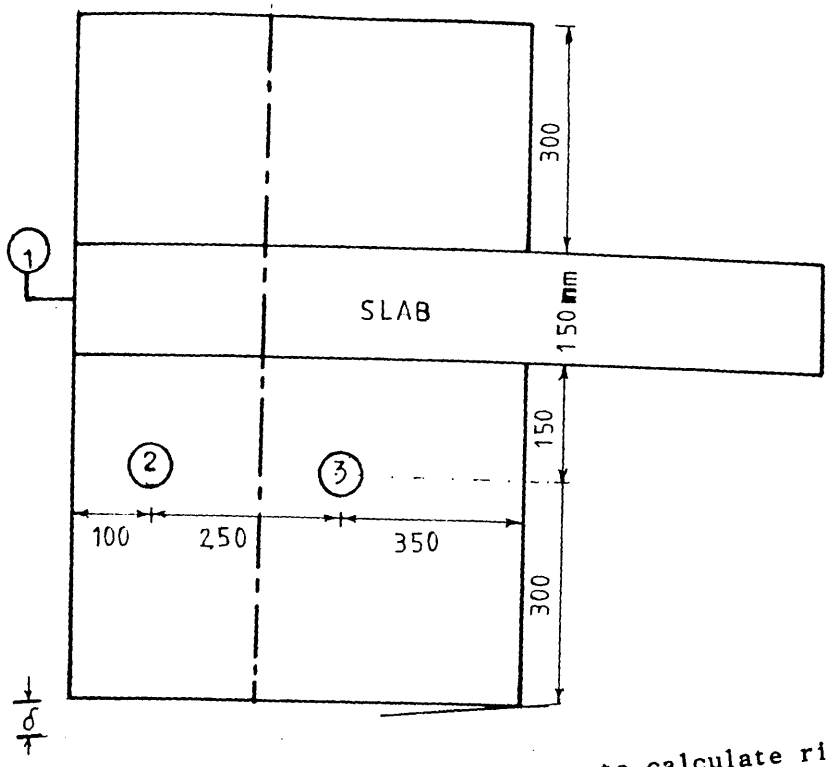

Figure (6.7) : Position of dial gauges to calculate rigid body rotation of models PS1 to MS5

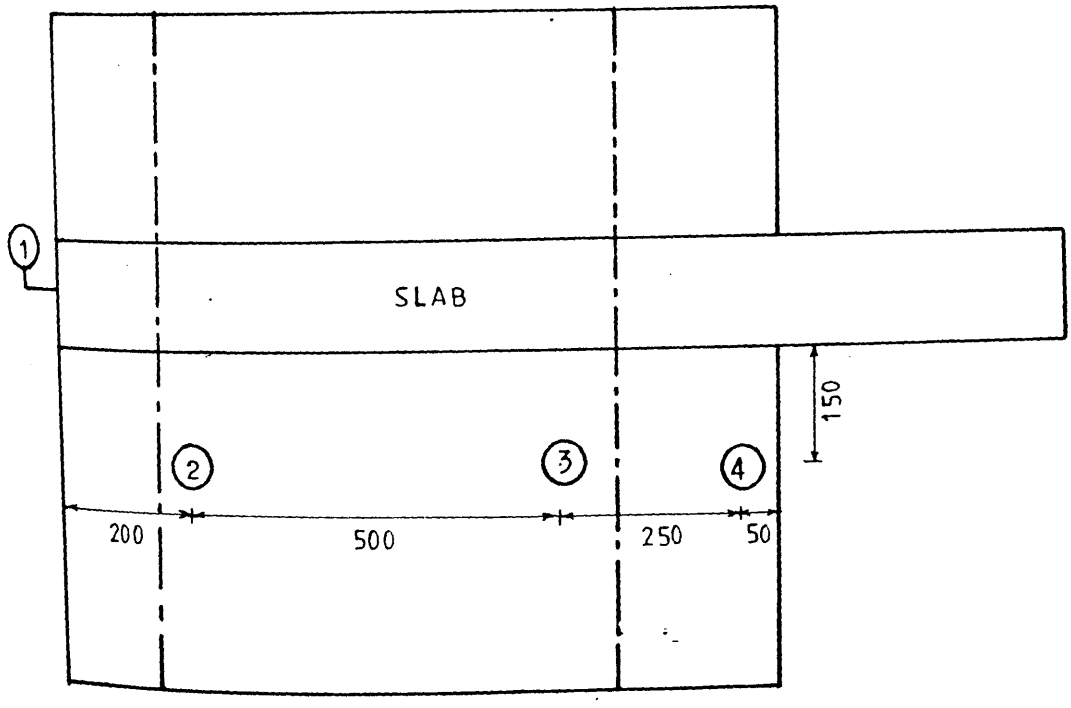

Figure (6.8) : Position of dial gauges to calculate rigid body rotation of models MS6to MRS15

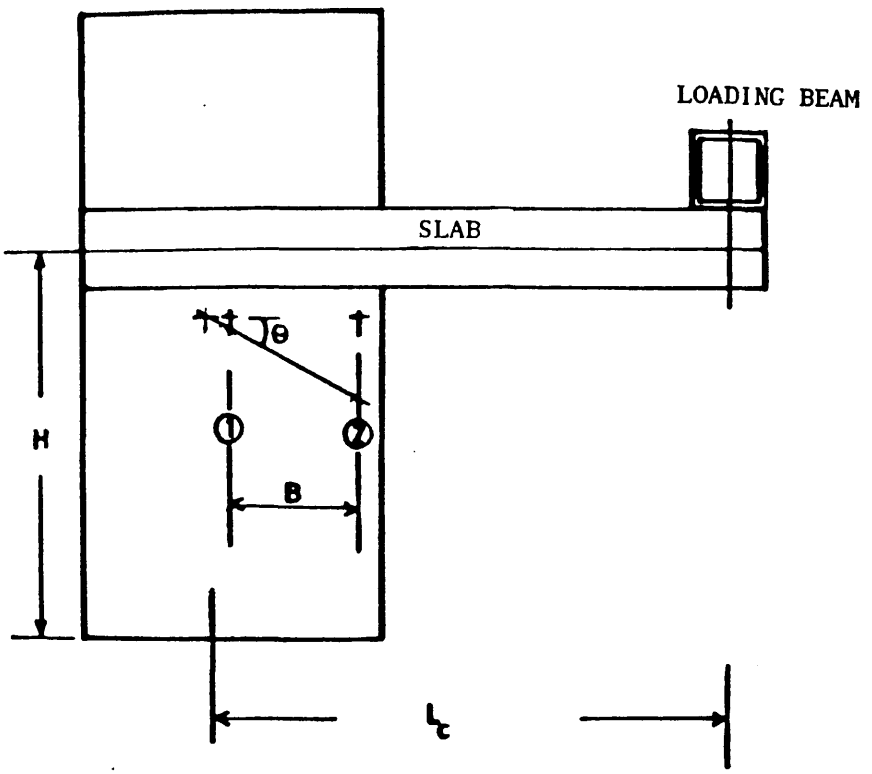

Figure (6.9) : Correction of displacement due to wind loading against wall deformation

TABLE (6.3) : Properties of Concrete for Each Model

Model no	No. of days	f_{cu} N/mm^2	f_t N/mm^2	E KN/mm^2
PS1	21	42.9	3.54	-
PS2	11	40.5	2.91	-
PS3	12	42.2	3.08	-
MS4	14	43.9	2.87	22.4
MS5	10	33.1	3.01	20.5
MS6	23	51.6	3.14	-
MS7	35	56.5	3.29	22.2
MS8	33	68.0	3.18	22.4
MS9	21	64.5	2.90	19.7
MS10	20	57.5	3.48	19.7
MS11	25	47.7	-	-
MS12	15	50.3	3.36	22.0
MRS13	27	47.2	2.79	-
MRS14	16	45.8	3.12	19.0
MRS15	19	51.0	2.97	19.3

lateral load (i.e., design load corrected for actual cube strength of concrete).

6.3 Preliminary Test Series – PS Series

6.3.1 Model PS1

Having decided to use shear reinforcement in the slab, Memon's[23] model 'MT1' was chosen as the basis of experimental work. The plan of the model is shown in Figure (6.10). The reinforcement used in the wall and in the slab was exactly same as 'MT1' as shown in Figures (6.11) and (6.12) respectively, except for shear reinforcement used in the slab, shown in Figure (6.13). The slab was designed for an ultimate unbalanced moment due to wind of 85 KN·m along the critical section for flexure and the moment induced along the sides of the walls due to gravity load of 34.84 KN. Using Memon's[23] recommendation for critical section, as discussed in section 2.4.7, the ultimate shear strength of the wall–slab connection was calculated. The shear strength, V_u, was found to be less than design lateral load, V_d, indicating the necessity of using shear steel around the critical section. Using the recommendations of Britsh code of practice BS 8110, the shear steel was obtained from equation (6.2) with material safety factor taken as unity.

$$A_{sv} = \frac{V_d - V_u}{f_{yw}} \qquad (6.2)$$

where A_{sv} = area of shear steel needed around critical section

f_{yw} = yield strength of shear steel

The form of shear steel, shown in Figure (6.13) was chosen. This type of shear steel facilitates easier placement of the shear steel in the slab by insertion from top, after all flexural reinforcements are in place. Figure (6.14) shows the location of shear steel in this model.

Behaviour of the Model

No hairline cracks were detected after the application of the total gravity load.

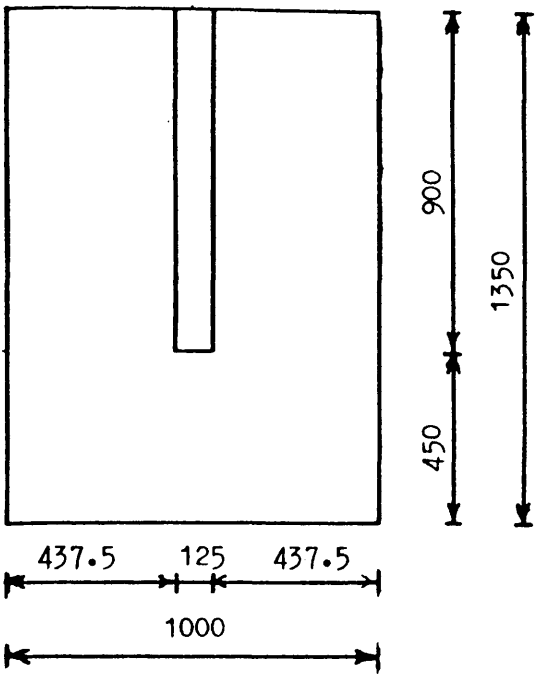

Figure (6.10) : Plan and dimensions of model PS1

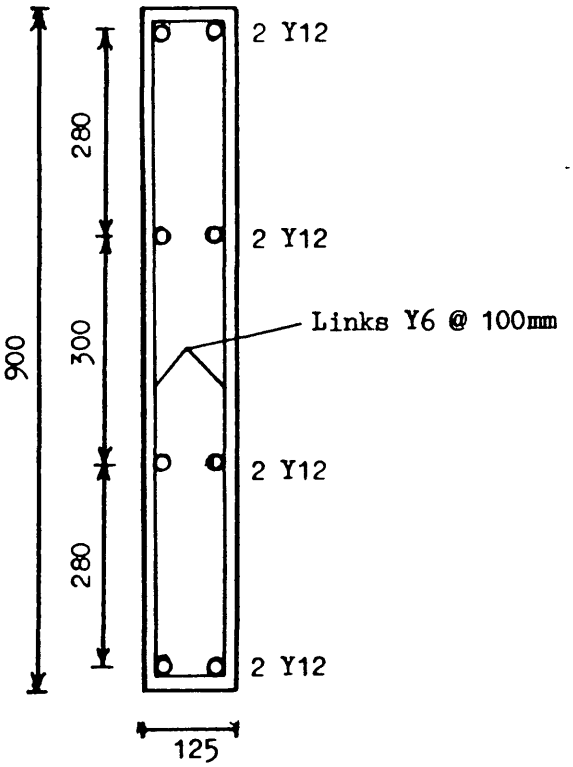

Figure (6.11) : A horizontal section in the wall of model PS1 showing the reinforcing details

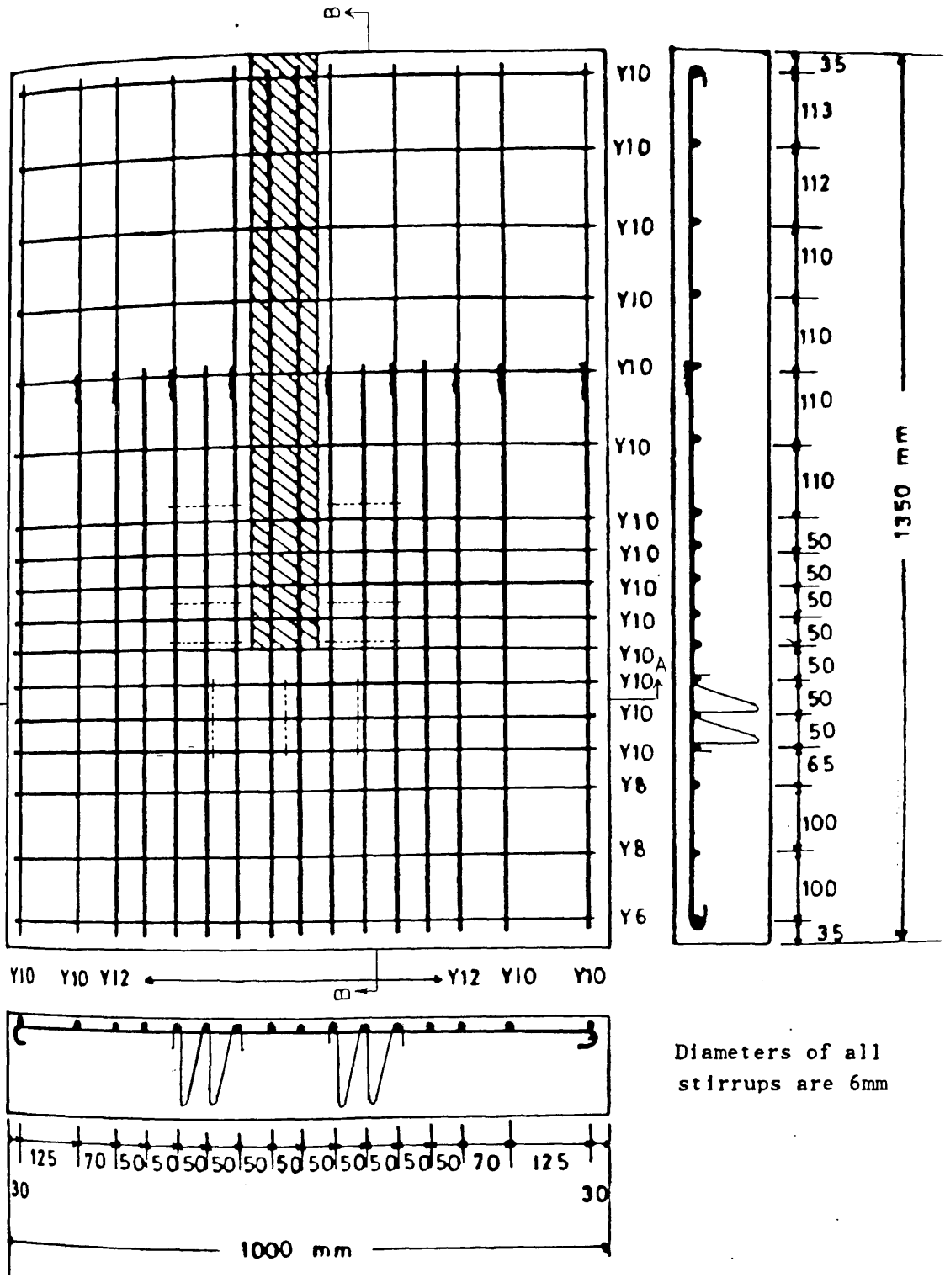

Section A–A

Figure (6.12) : Arrangement of reinforcing bars including shear steel in the slab of model PS1

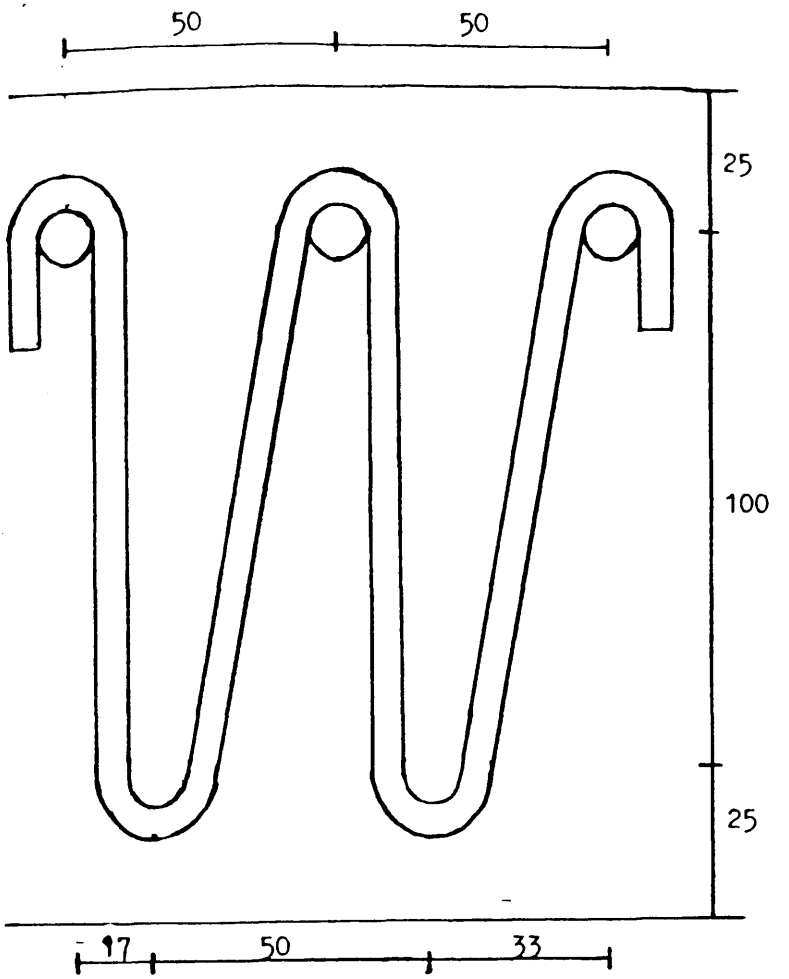

Figure (6.13) : Type of shear steel used in the slab of models PS1 and PS2

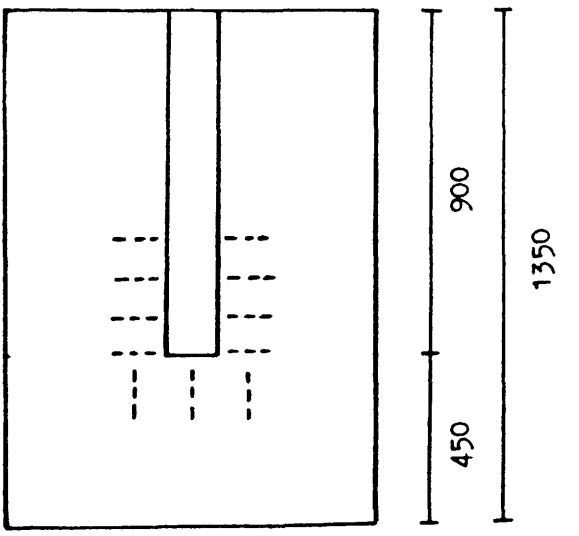

Figure (6.14) : Location of shear steel in the slab of model PS1

At about 23.5% of design lateral load, two cracks parallel to the wall were observed as shown in Figure (6.15– a). As the loading progressed, a new crack perpendicular to the wall was observed at a load of 37.5% of design lateral load as shown in Figure (6.15– b). Further loading caused cracks to spread around the wall–slab junction at various angles with the wall. These cracks starting from the wall–slab junction were limited to within 300 mm length of the wall from its nose, beyond that length no cracks were found originating from the junction. The cracks did not widen to any measurable extent. Failure took place suddenly along the inner edge of the loading beam at a lateral load of 219.3 KN (i.e., 102.0% of the design load) implying that it was a local failure of the slab. The crack pattern on the tension side of the slab after failure is shown in Figure (6.16). Due to the difficulty in observing cracks on the compressive side of the slab during testing, only the final crack pattern was obtained as shown in Figure (6.17). The diagonal cracks starting from the loading beam on the sides of the slab are clearly visible in photograph of Figure (6.18). Figure (6.19) shows the experimental load–deflection curve. Note that on the vertical axis, the ratio of the applied loads to the normalised design lateral load of the slab is plotted. Figures (6.20) shows the curves for tensile strains in steel bars in windward direction. The steel bar at the centre of the slab passing through the wall yielded first at 84.6% of design load. All other bars also yielded just before the failure. Figure (6.22) and (6.23) show the curves for tensile strains in transverse and shear steel. The curves for compressive strains on the bottom surface of the slab (the dotted line of the wall in the model plan indicates that the compressive side is shown) are shown in Figures (6.24) and (6.26). The variation of the concrete strain in windward direction along transverse section at different stages of loading is shown in Figure (6.25). The compressive strain on the wall at two points just underneath the slab is plotted and shown in Figure (6.26– a). This strain in wall was used to calculate the correction against the wall deformation for edge deflection of the slab, as mentioned in section 6.2. The exact locations of all the strain gauges used in the

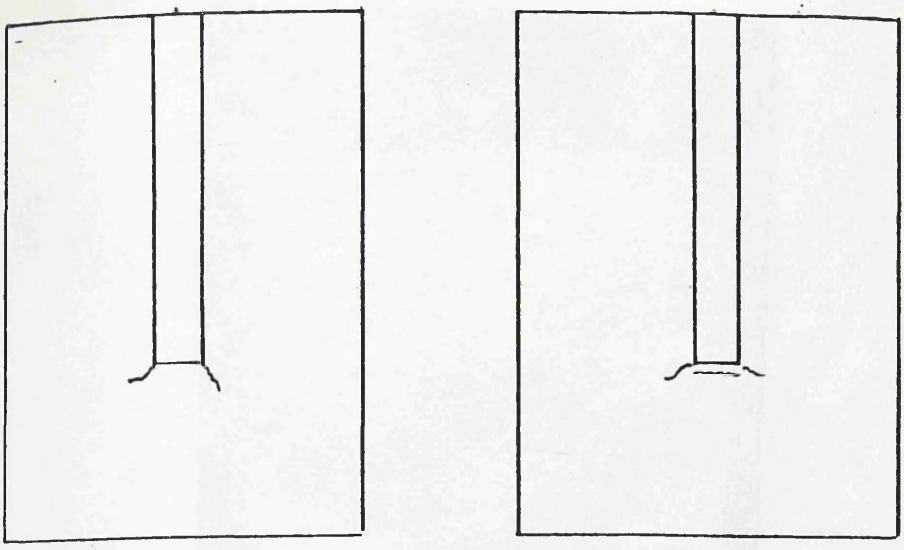

(a) at 23.5 %

(b) at 37.5 %

Figure (6.15) : Cracks initiation during testing of model PS1 at different percentages of design lateral load

Figure (6.16) : Crack pattern on the tensile side of the slab of model PS1

Figure (6.17) : Bottom failure surface of model PS1

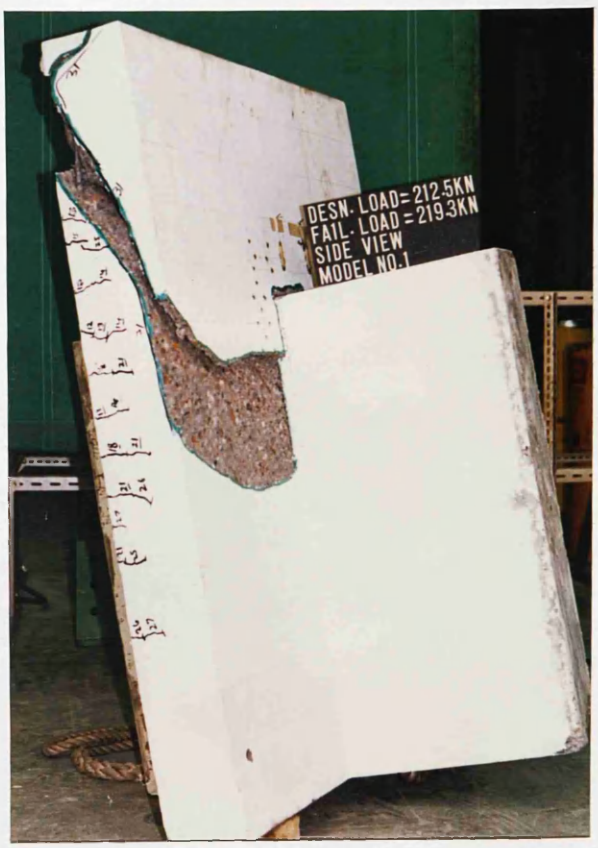

Figure (6.18) : Side view of model PS1 after failure

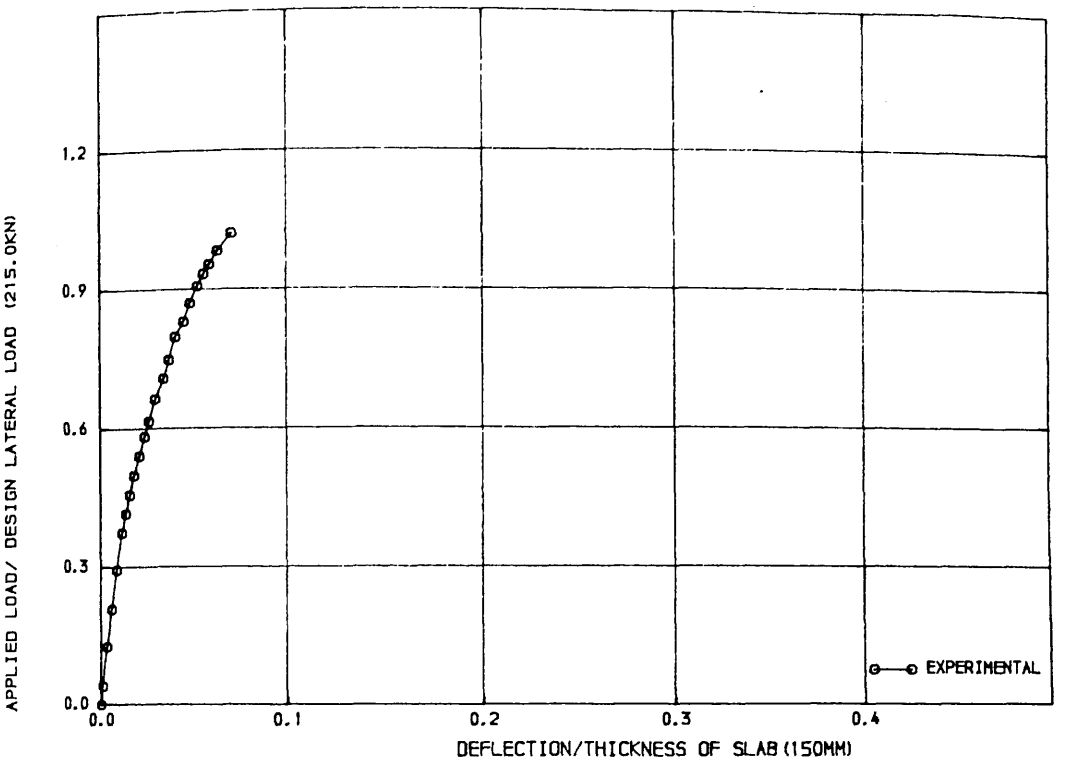

FIGURE (6.19) LOAD-DEFLECTION CURVE FOR MODEL PS1

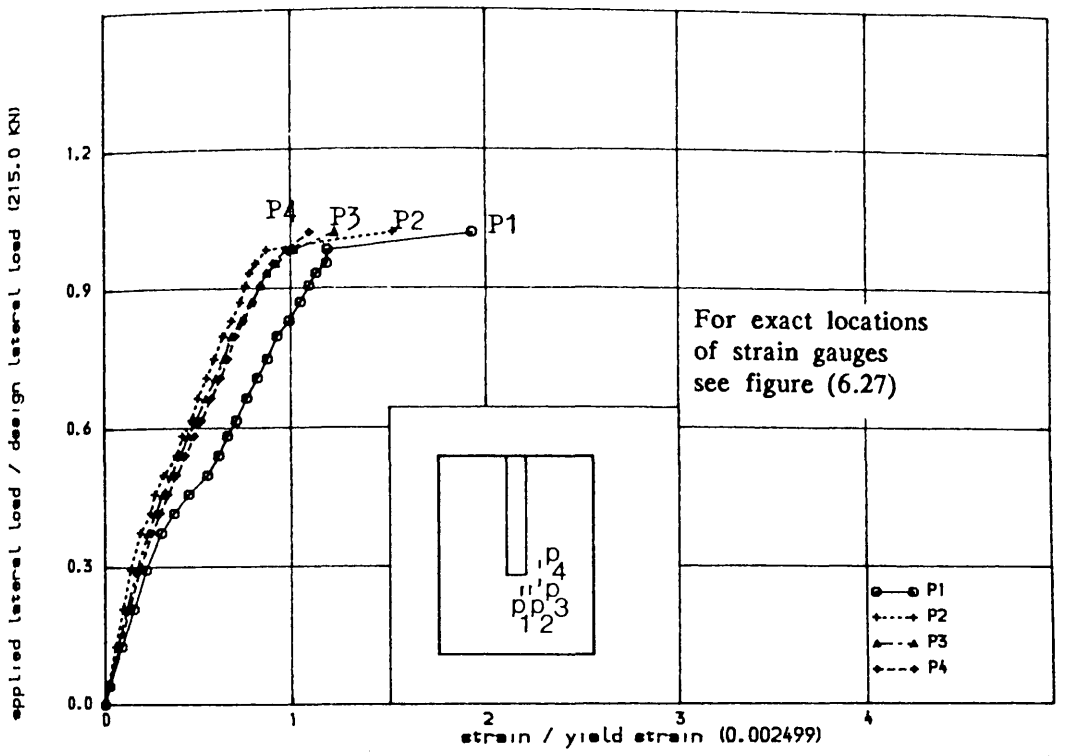

FIGURE (6.20) , TENSILE STRAIN IN STEEL IN VINDVARD DIRECTION ALONG TRANSVERSE SECTION IN THE SLAB OF MODEL PS1

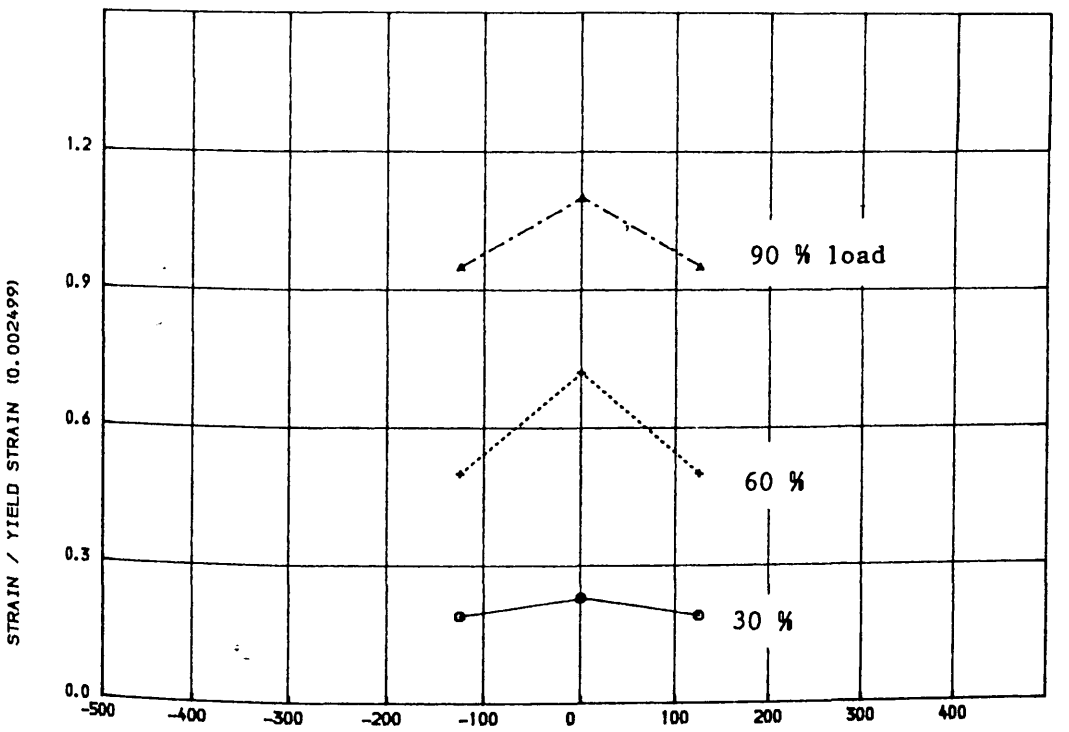

FIGURE (6.21) , VARIATION OF STRAIN IN STEEL IN VINDVARD DIRECTION ALONG TRANSVERSE SECTION AT DIFFERENT STAGES OF LOADING IN THE SLAB OF MODEL PS1

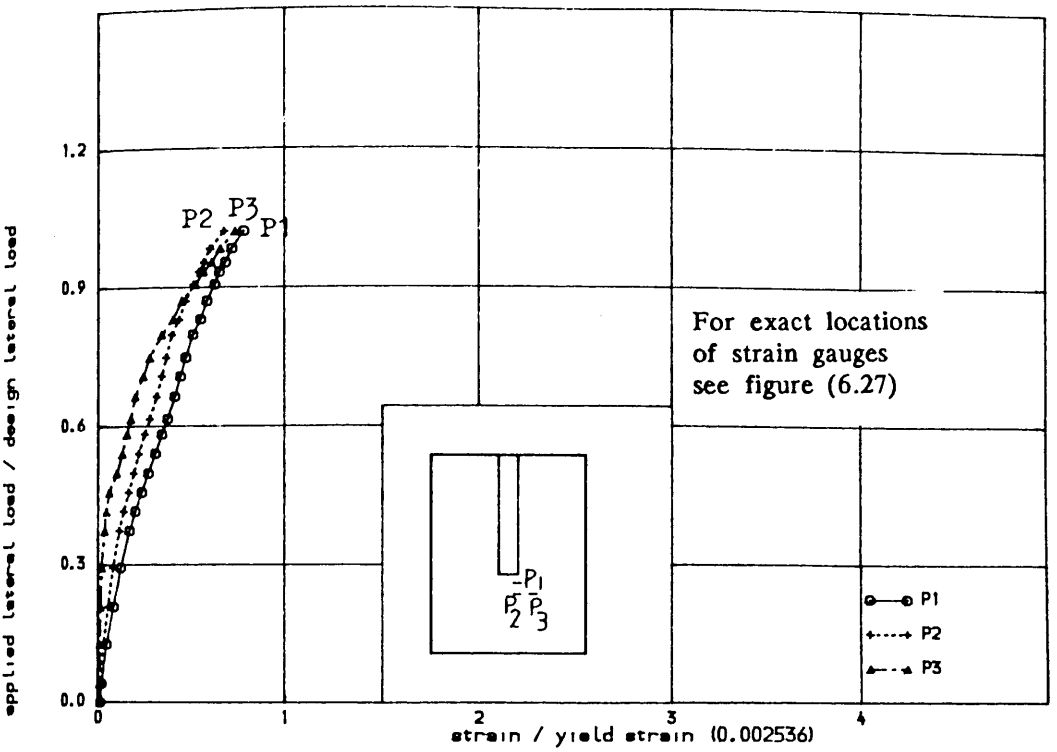

FIGURE (6.22) TENSILE STRAIN IN STEEL IN TRANSVERSE DIRECTION IN THE SLAB OF MODEL PS1

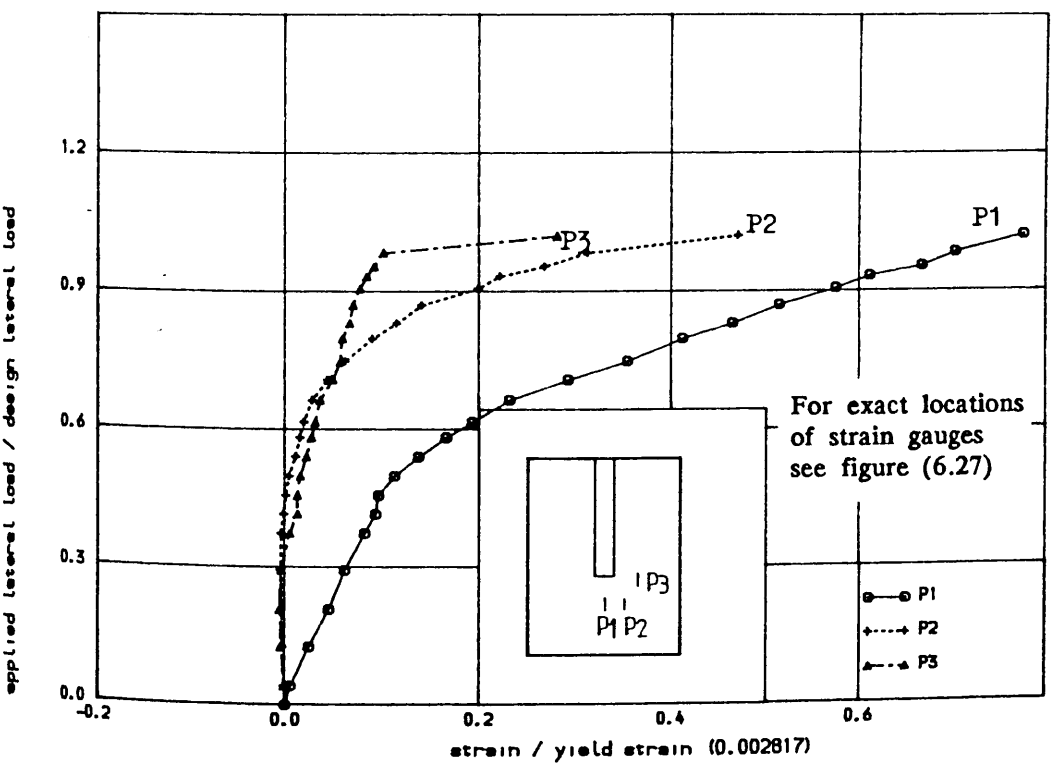

FIGURE (6.23) STRAIN IN SHEAR STEEL AT DIFFERENT LOCATIONS IN THE SLAB OF MODEL PS1

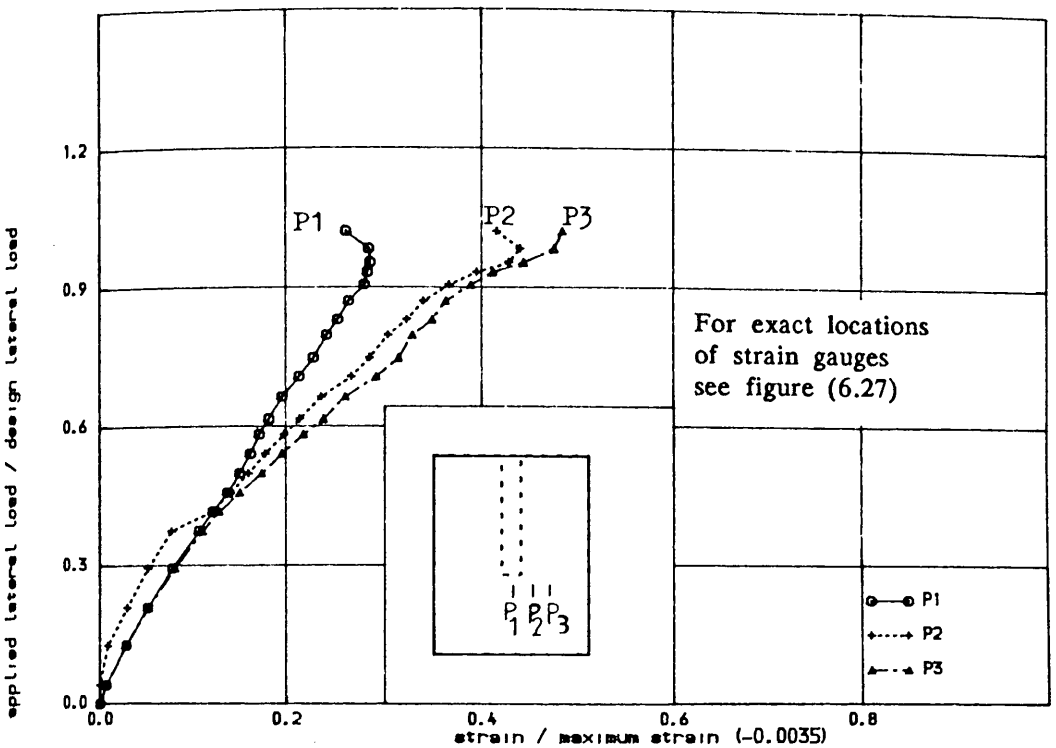

FIGURE (6.24) COMPRESSIVE STRAIN IN CONCRETE IN WINDWARD DIRECTION IN THE SLAB OF MODEL PS1

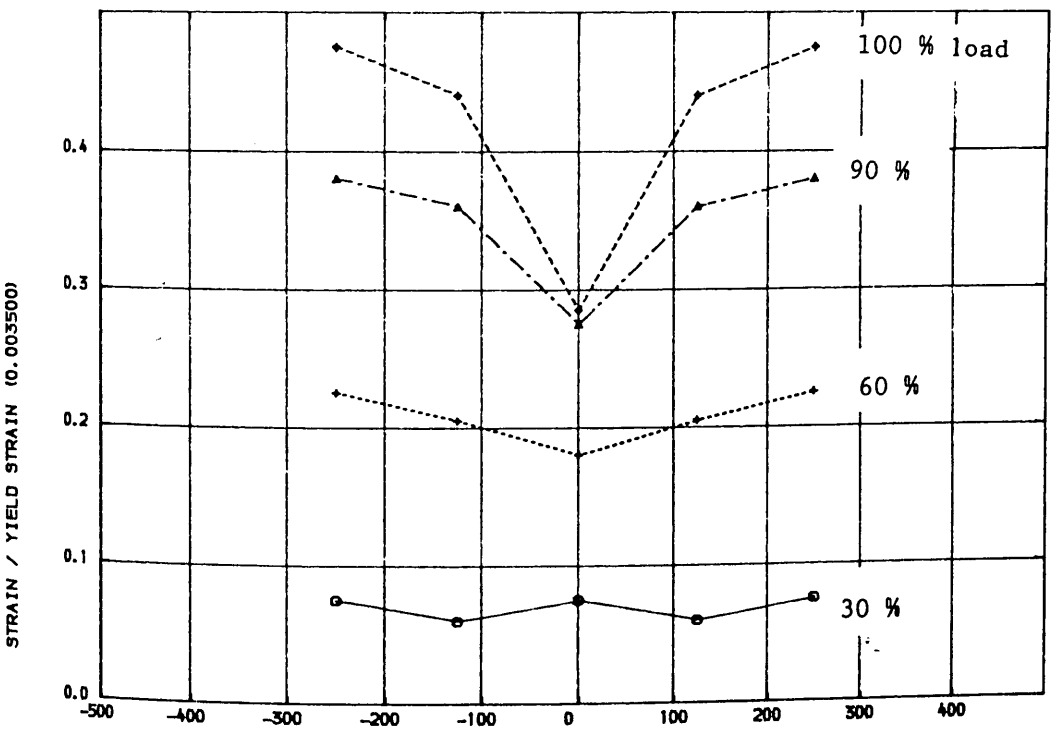

FIGURE (6.25) : VARIATION OF COMPRESSIVE STRAIN IN CONCRETE ALONG TRANSVERSE CRITICAL SECTION AT DIFFERENT STAGES OF LOADING IN THE SLAB OF MODEL PS1

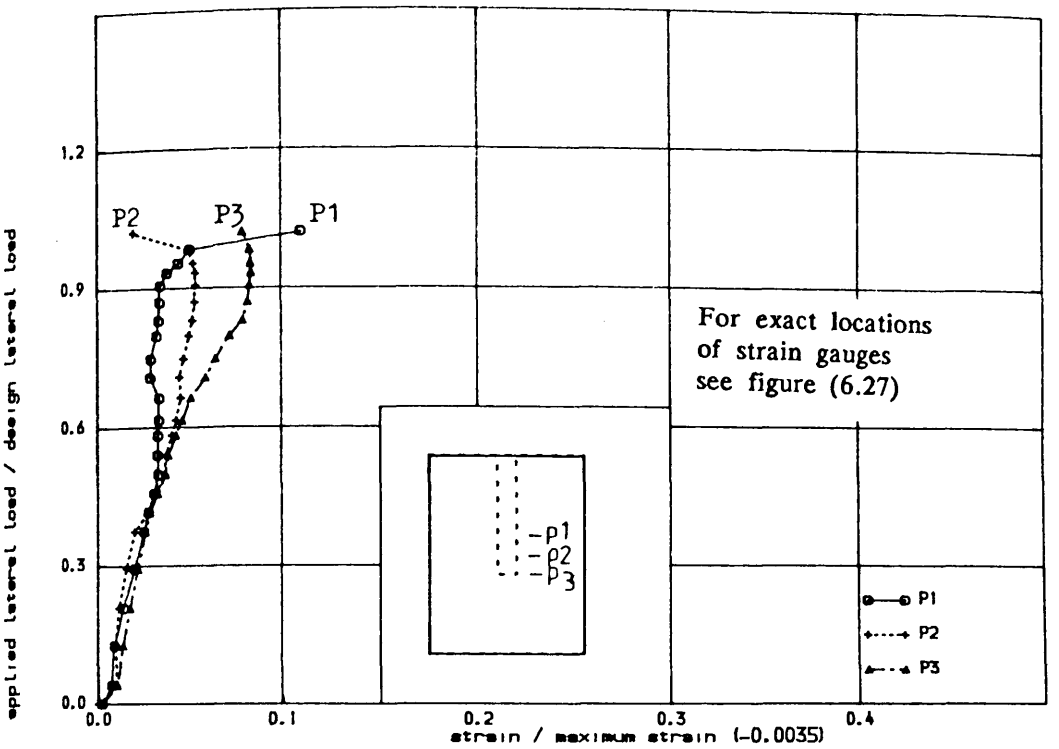

FIGURE (6.26) COMPRESSIVE STRAIN IN CONCRETE IN TRANSVERSE DIRECTION IN THE SLAB OF MODEL PS1

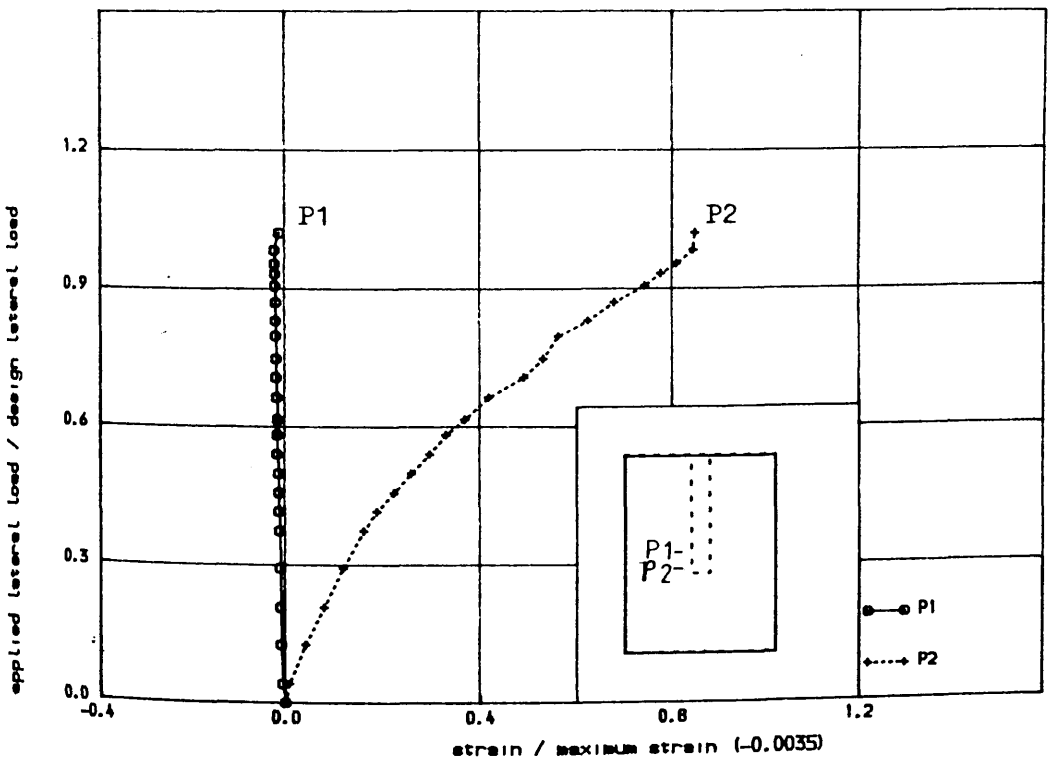

FIGURE (6.26-a) COMPRESSIVE AND TENSILE STRAIN IN WALL JUST UNDERNEATH THE SLAB OF MODEL PS1

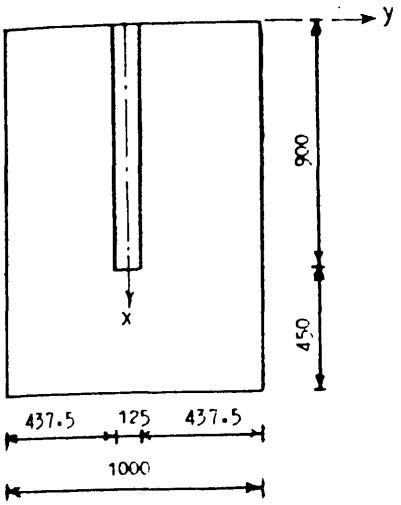

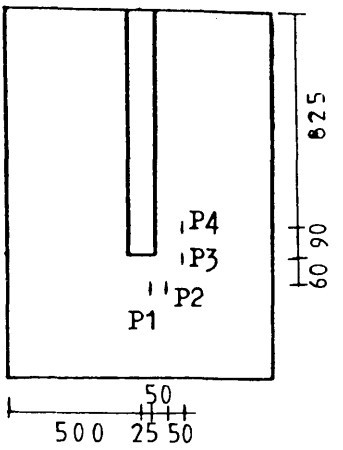

(a) Strain gauges in Figure (6.20)

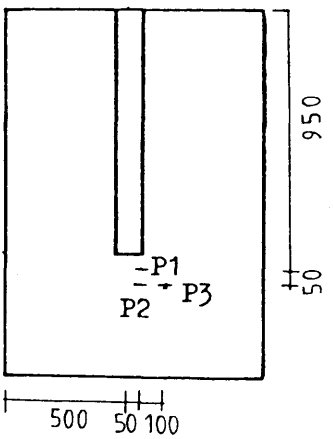

(b) Strain gauges in Figure (6.22)

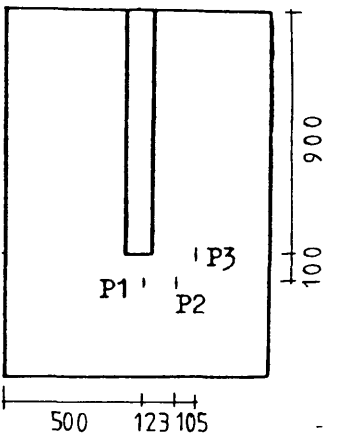

(c) Strain gauges in Figure (6.23)

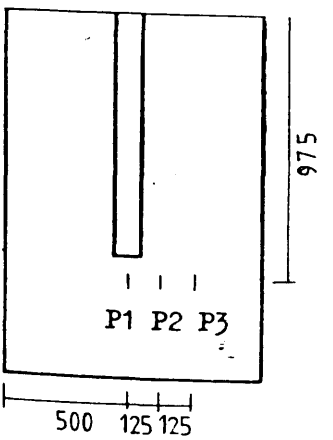

(d) Strain gauges in Figure (6.24)

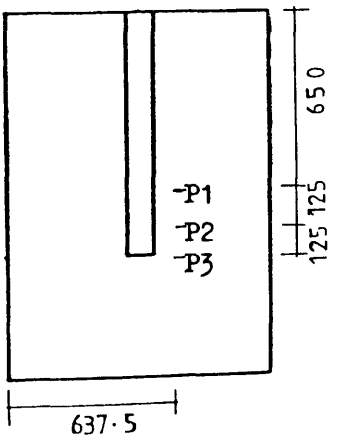

(e) Strain gauges in Figure (6.26)

FIGURE (6.27) : Exact locations of strain gauges in the slab of model PS1 as shown in Figures (6.20), (6.22), (6.23), (6.24) and (6.26)

slab of this model are shown in Figure (6.27).

6.3.2 Model PS2

Local failure occured in the slab of the previous model PS1. The average shear stress in concrete slab along the loading beam was very high ($219300/1000*125 \simeq 1.75$ N/mm^2) and no shear steel was provided in any area of the slab except the critical section to take care of the excess shear stress. That may be the reason for local failure of the slab. It was decided to test another model similar to PS1 but for a lower design (both lateral and gravity) load. To ensure proper anchorage of the flexural rinforcement – the slab was also extended 150 mm beyond the outer edge of the loading beam. The shear reinforcement around the critical section was calculated using the same procedure as described in section 6.3.1 and the same type (Figure 6.13) of shear steel was provided. To avoid local failure along the inner edge of the loading beam, additional shear steel was provided in the corridor area of the slab to take care of stress in excess of allowable concrete shear stress. The plan of this model is shown in Figure (6.28) and Figure (6.29) shows the location of shear steel in the slab. The same wall reinforcement as shown in Figure (6.11) was used. The arrangement of flexural reinforcement used in the slab is shown in Figure (6.30).

Behaviour of the Model

Like model PS1, no hairline crack appeared after the application of total gravity load (18 KN). At a lateral load of 13.0% of the design load, two cracks perpendicular to the inner edge of the wall were first observed as shown in Figure (6.31–a). On further loading, more cracks appeared in the same fashion and at 40% of the design load, new cracks parallel to the wind loaded edge appeared as shown in Figure (6.31–b). Cracks radiated from the side of the wall at various angles at different loading stages until the slab failed suddenly. The ultimate failure occured along the inner edge of the loading beam at a load of 159.0 KN (106%

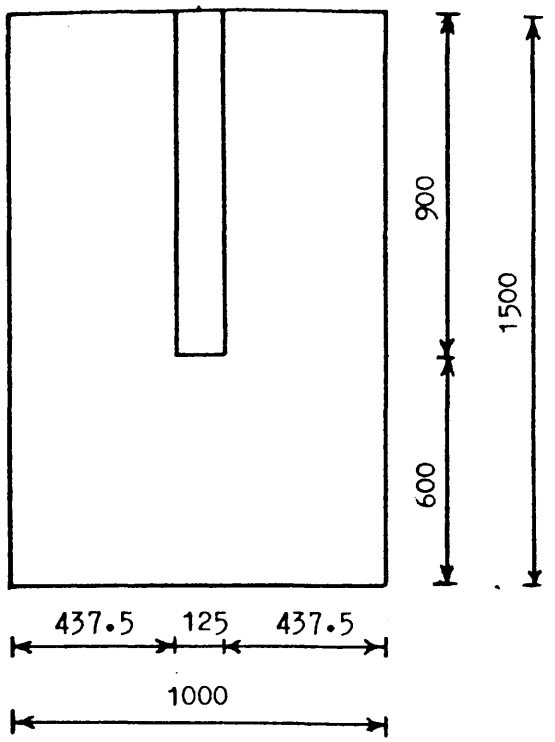

Figure (6.28) : Plan and dimensions of models PS2 and PS3

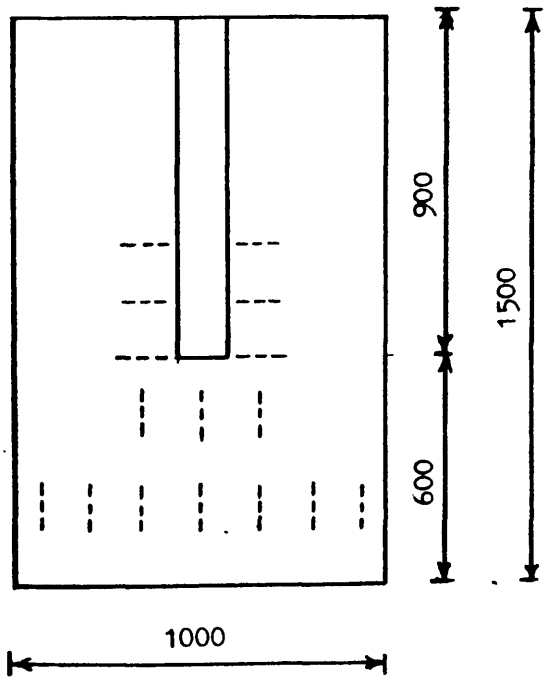

Figure (6.29) : Location of shear steel in the slab of model PS2

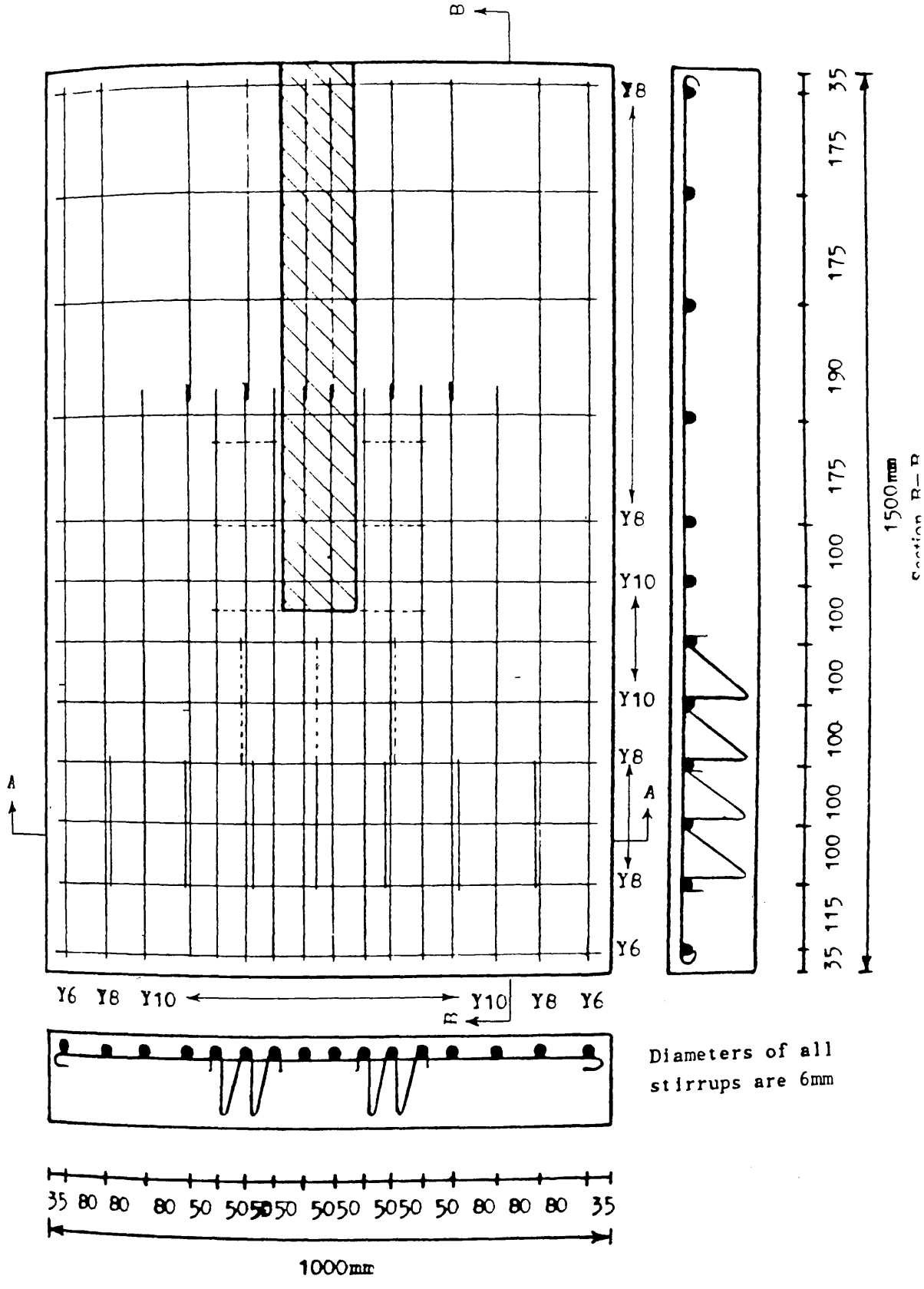

Section A–A

Figure (6.30) : Arrangement of reinforcing bars including shear steel in the slab of model PS2

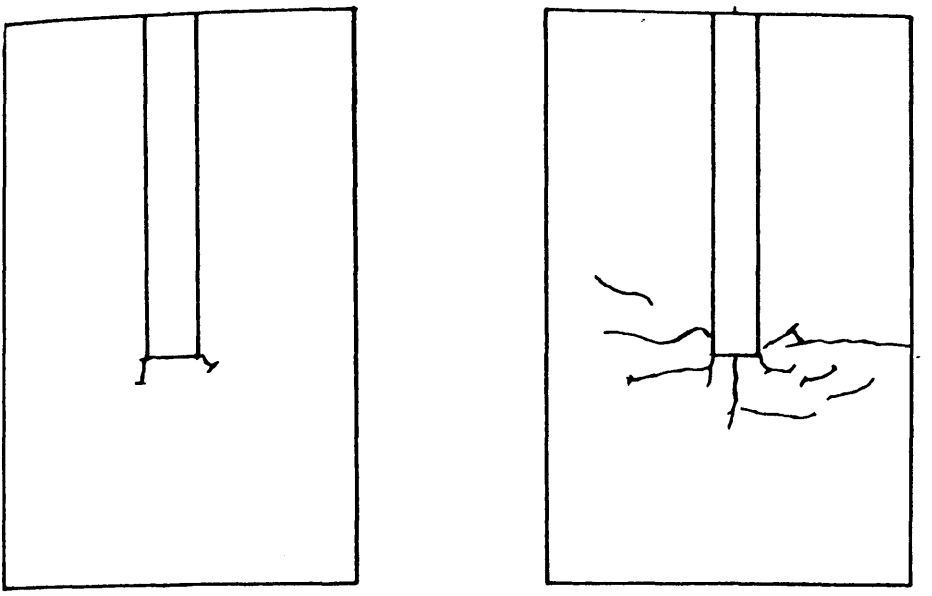

(a) at 13 %

(b) at 40 %

Figure (6.31) : Cracks initiation during testing of model PS2 at different percentages of design lateral load

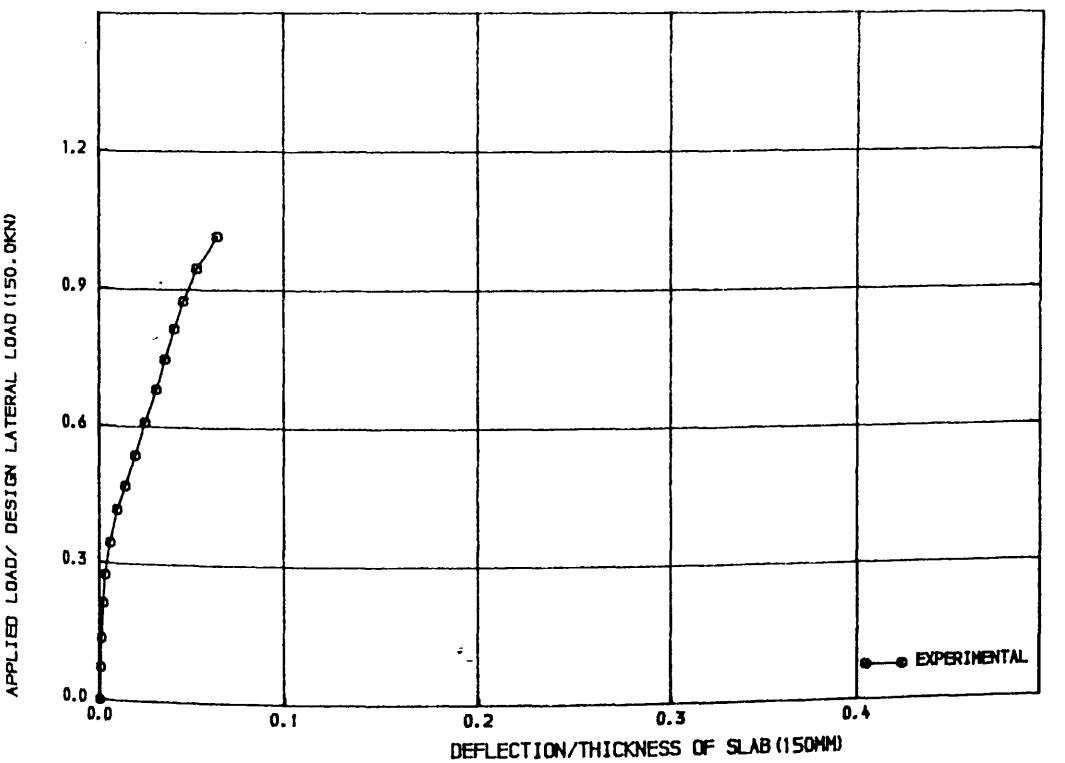

FIGURE (6.32) LOAD-DEFLECTION CURVE FOR MODEL PS2

of the design load). Photographs showing crack pattern of this model after failure are shown in Figures (6.33– a) and (6.33– b). The non– dimensional lateral load versus slab deflection is shown in Figure (6.32). Curves for strain distribution are shown in Figures (6.34) to (6.39). The exact locations of all the strain gauges used in the slab of this model are shown in Figure (6.40).

Along the critical section parallel to the wall, up to approximately 48% of the design load, the measured strain at point P1 in Figure (6.38) was equal to that of the other points P2 (mid point) and P3 (edge point). Afterwards, the rate of increase of strain at point P1 decreased with the increase of load upto 60% of design load. After that the strain at central point P1 started decreasing and reached below the strain at 48% of design load. When the applied wind load was nearly equal to the ultimate load, the strain at point P1 was 32% of that at point P2 and 40% of that at point P3. This effect was noticed to a certain extent in model PS1 as well but it was not so pronounced. This behaviour of the measured strain in concrete at the bottom of the slab at point P1 was also reported by Memon[23]. The theoretical analysis did not show any decrease in concrete strain at point P_1 in the slab of model PS2 as the loading progressed (see figure (7.69)).

6.3.3 Model PS3

Though punching type of shear failure was avoided around the junction, both models PS1 and PS2 failed locally along the edge of the lateral loading beam. Use of shear reinforcement in the corridor area in model PS2 did not help to change the type of failure. It was felt, however, to understand the actual shear stress distribution at different sections of the slab (windward and transverse) due to lateral loading and then design the shear steel in a systematic fashion as dictated by the state of stress. For that purpose, the standard computer programme 'FLASH'[89] was used for the grillage analysis of the slab. The slab was discretized into 126 finite, straight prismatic beam elements as shown in Figure (6.41). The width of individual beam was chosen as half the distance between the centre– line of each

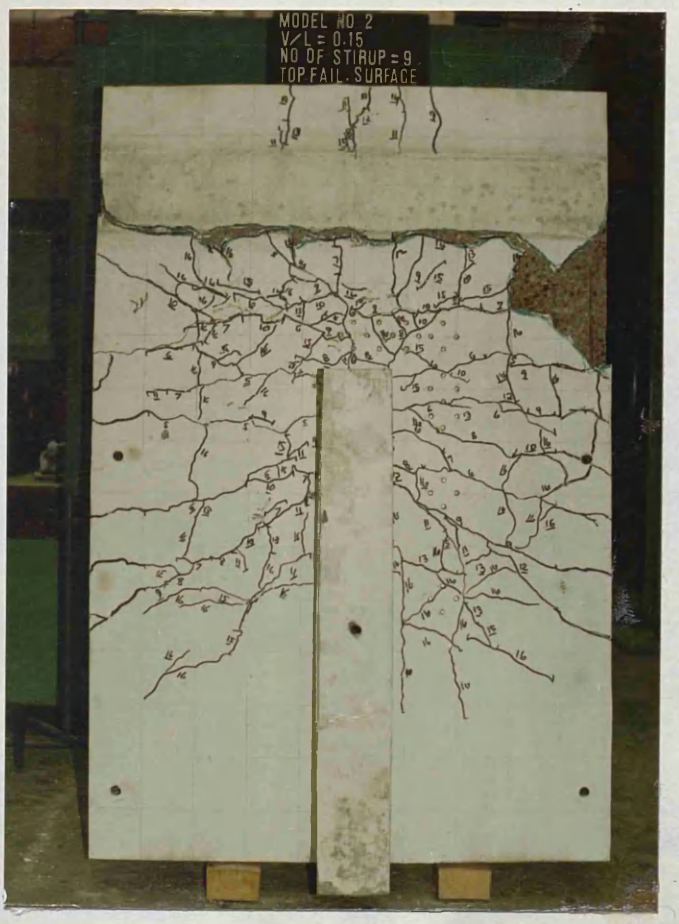

(a) On the tensile side

(b) On the compressive side

Figure (6.33) : Photographs showing the crack pattern on the slab of model PS2

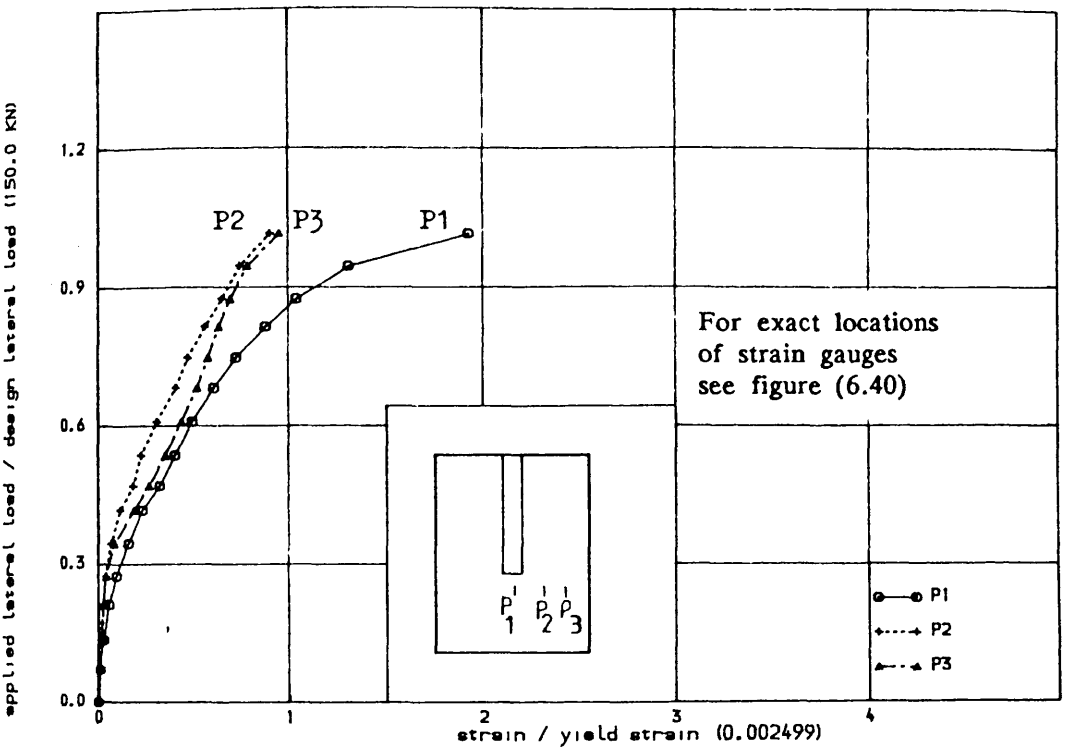

FIGURE (6.34) , TENSILE STRAIN IN STEEL IN WINDWARD DIRECTION ALONG TRANSVERSE SECTION IN THE SLAB OF MODEL PS2

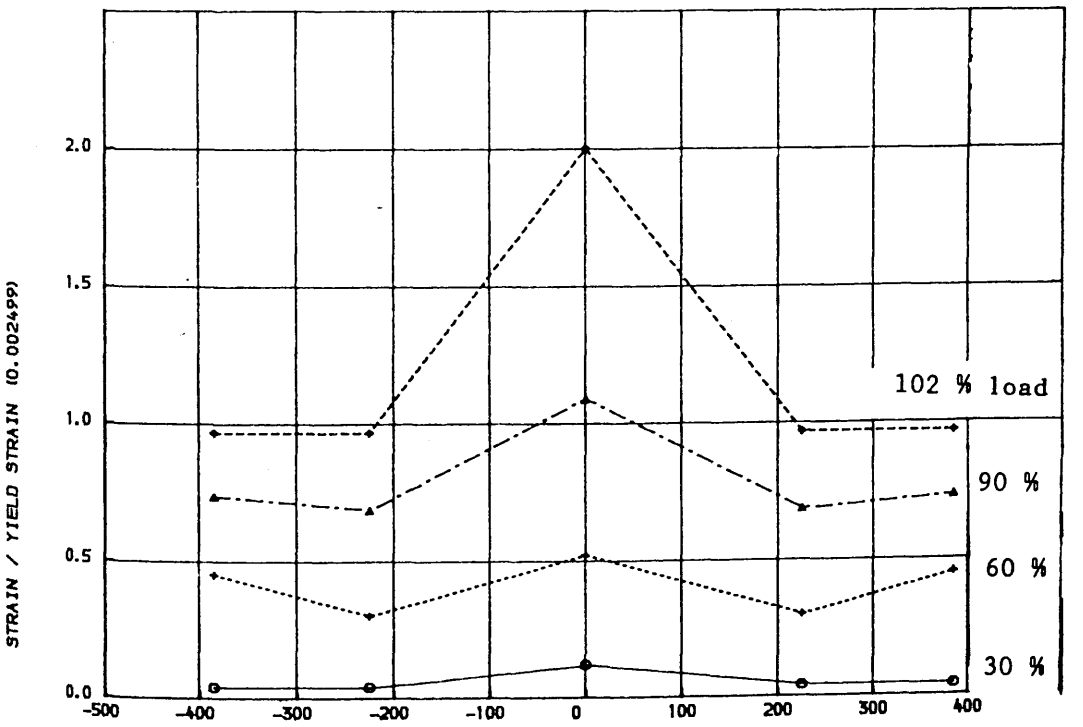

FIGURE (6.35) , VARIATION OF STRAIN IN STEEL IN WINDWARD DIRECTION ALONG TRANSVERSE SECTION AT DIFFERENT STAGES OF LOADING IN THE SLAB OF MODEL PS2

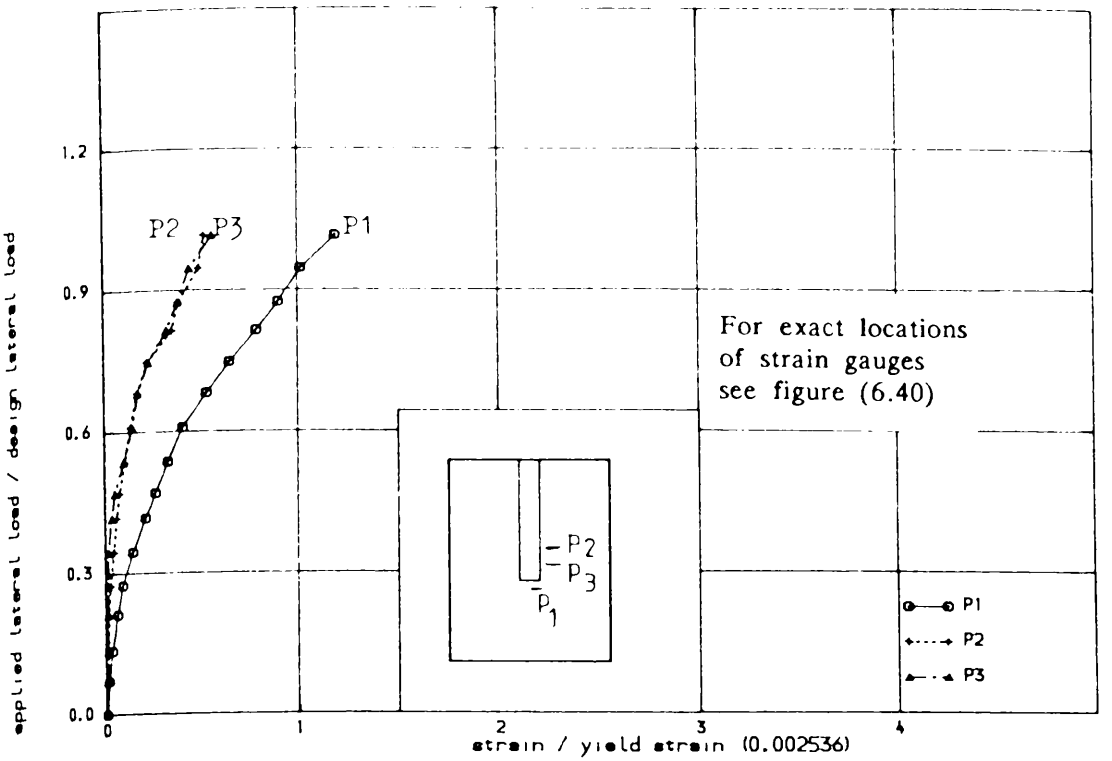

FIGURE (6.36) , TENSILE STRAIN IN STEEL IN TRANSVERSE DIRECTION IN THE SLAB OF MODEL PS2

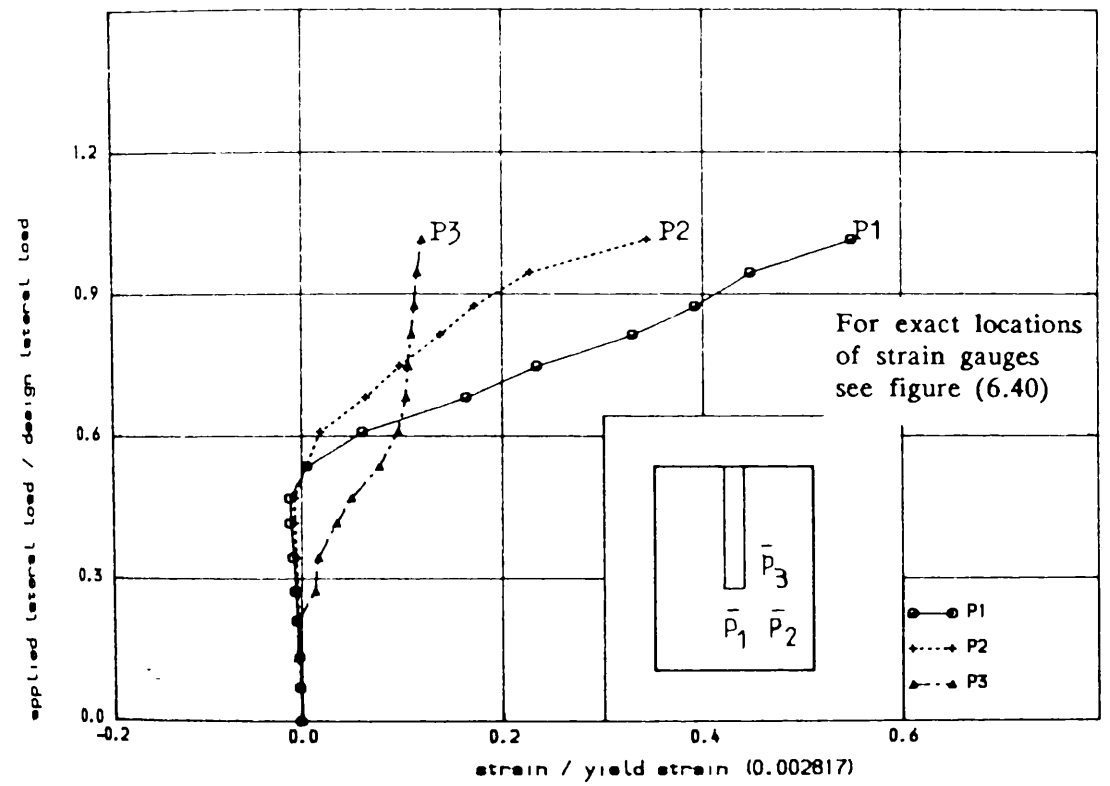

FIGURE (6.37) , STRAIN IN SHEAR STEEL AT DIFFERENT LOCATIONS IN THE SLAB OF MODEL PS2

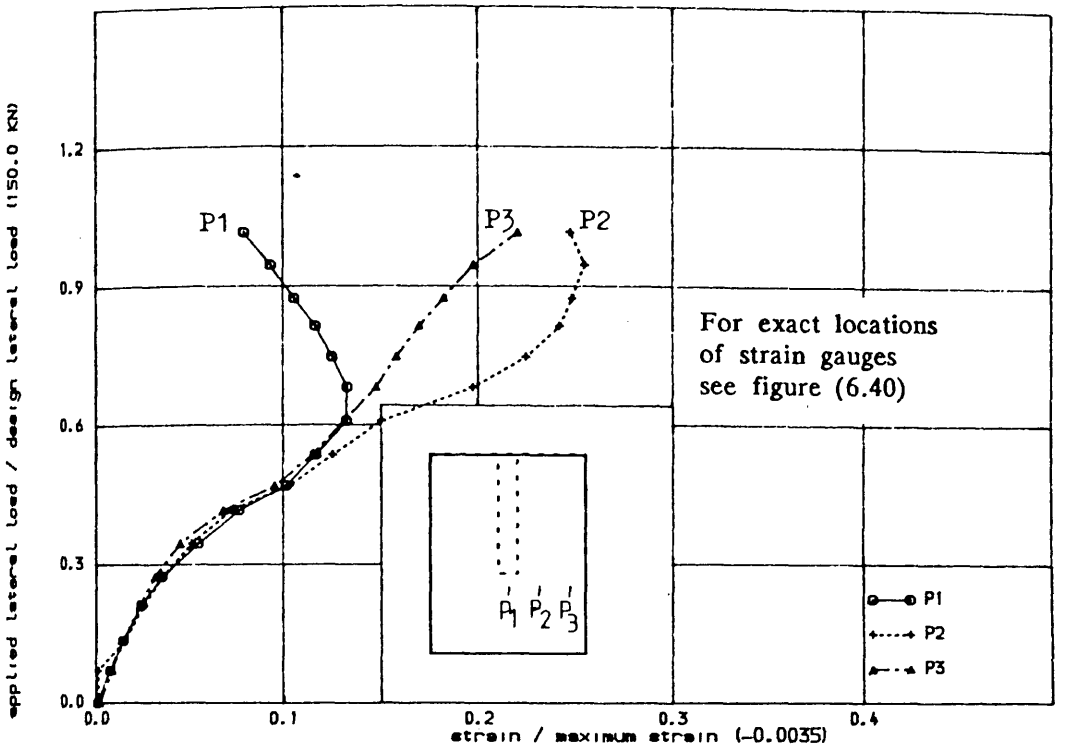

FIGURE (6.38) , COMPRESSIVE STRAIN IN CONCRETE IN WINDWARD DIRECTION IN THE SLAB OF MODEL PS2

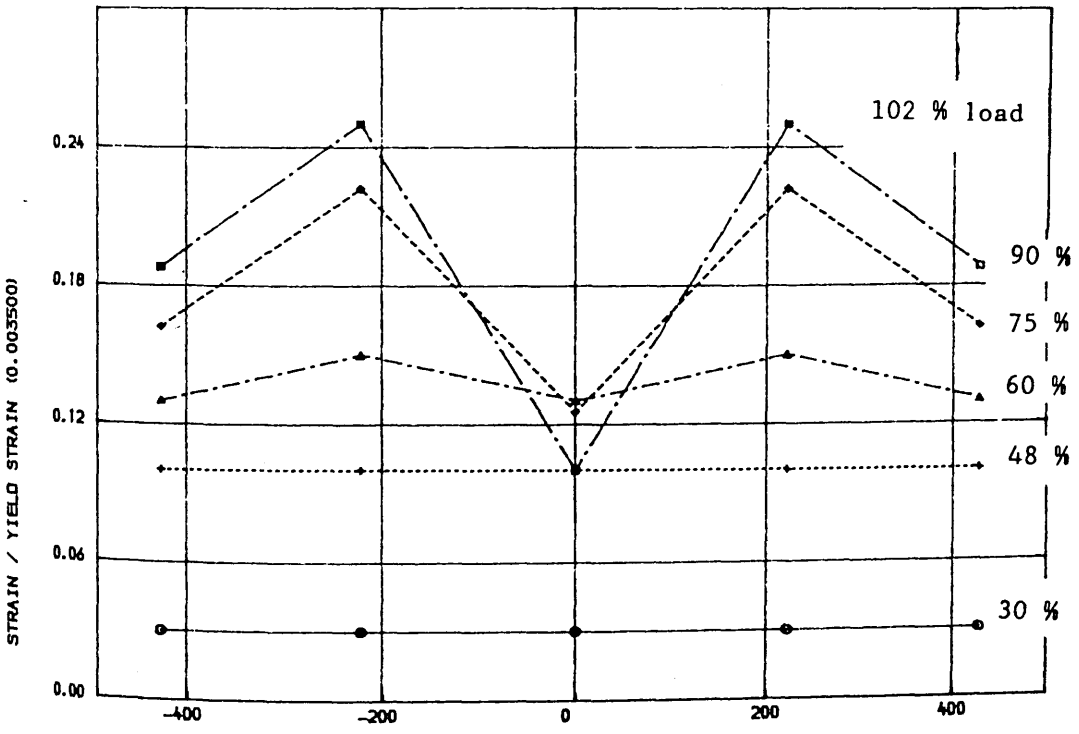

FIGURE (6.39) , VARIATION OF COMPRESSIVE STRAIN IN CONCRETE ALONG TRANSVERSE CRITICAL SECTION AT DIFFERENT STAGES OF LOADING IN THE SLAB OF MODEL PS2

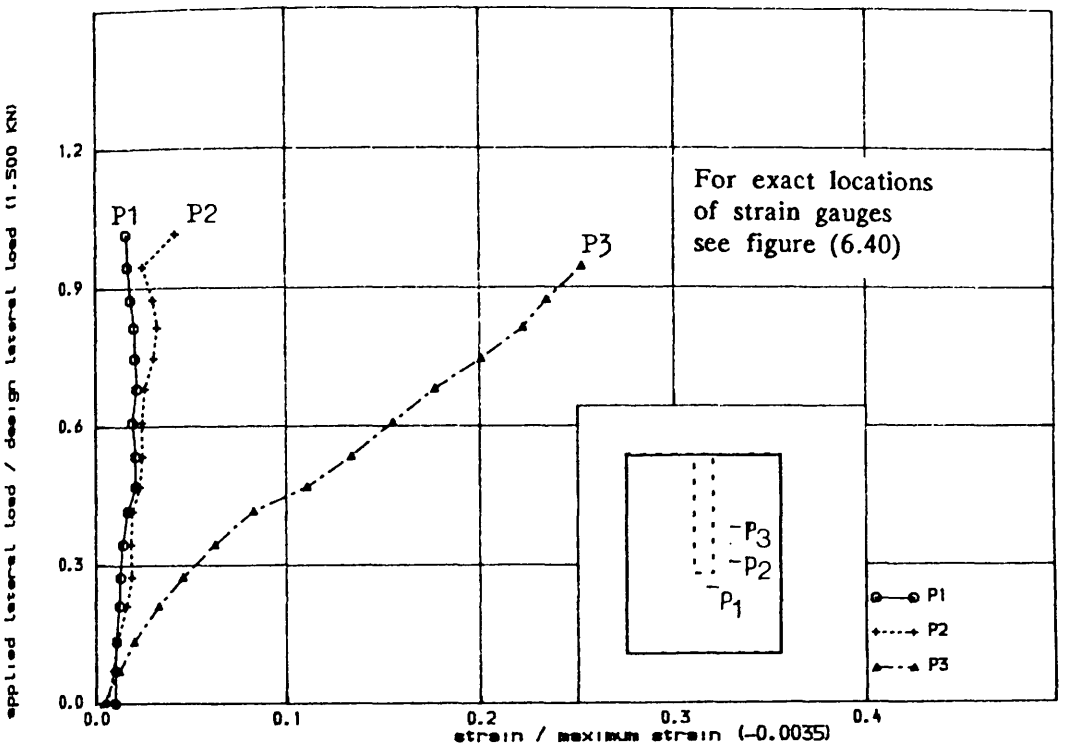

FIGURE (6.39-a) , COMPRESSIVE STRAIN IN CONCRETE IN TRANSVERSE DIRECTION IN THE SLAB OF MODEL PS2

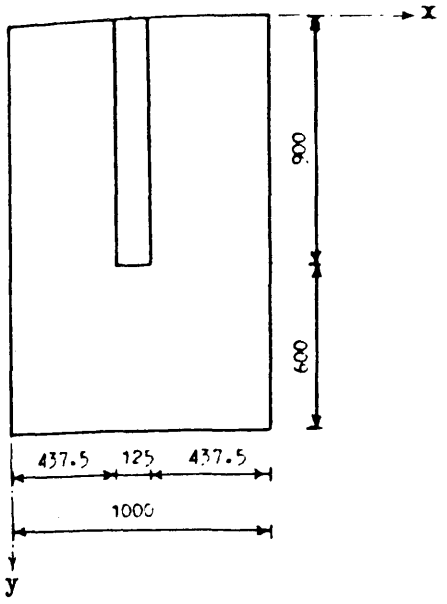

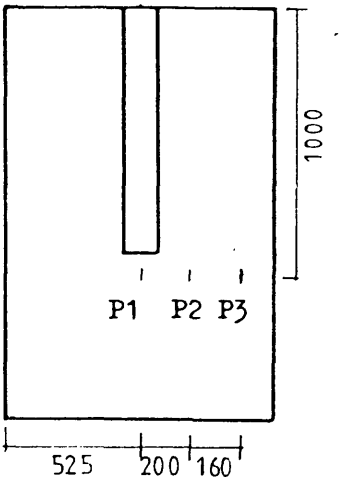

(a) Strain gauges in Figure (6.34)

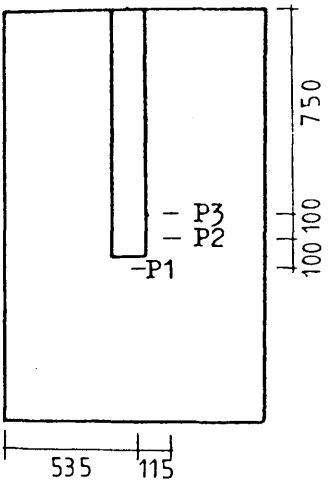

(b) Strain gauges in Figure (6.36)

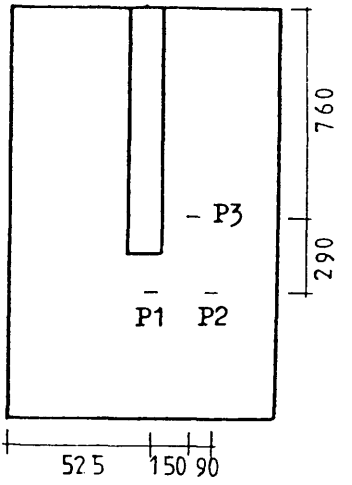

(c) Strain gauges in Figure (6.37)

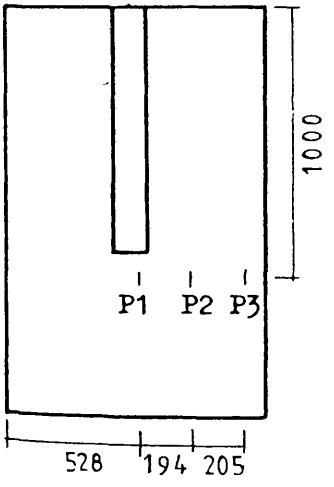

(d) Strain gauges in Figure (6.38)

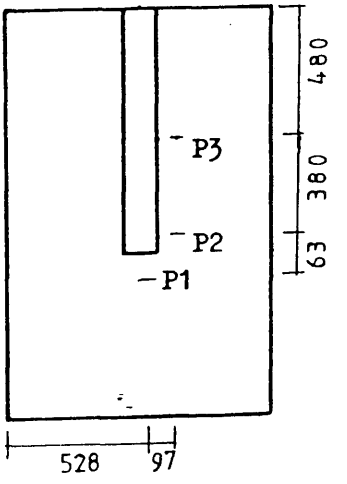

(e) Strain gauges in Figure (6.39)

FIGURE (6.40) : Exact locations of strain gauges in the slab of model PS2 as shown in Figures (6.34), (6.36), (6.37), (6.38) and (6.39)

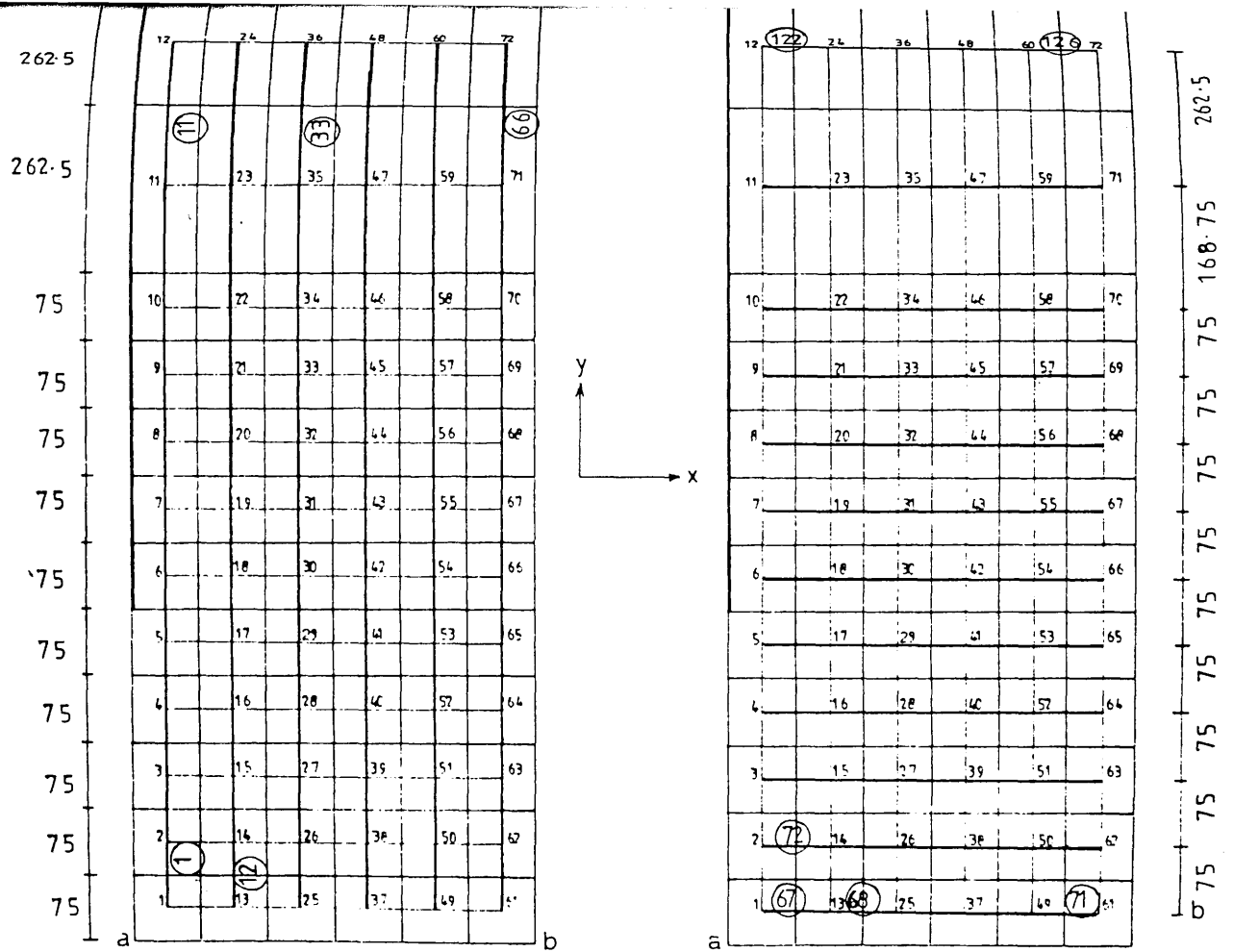

(a) : Discretization of slab as a beam element along y-axis

(b) : Discretization of slab as a beam element along x-axis

Figure (6.41)

member. The gross inertia of the concrete slab (ignoring reinforcement) and gross cross-sectional area were used in the analysis. Elastic distribution of design lateral load along the line of contraflexure was obtained using finite element method and it was applied at the nodes of line 'ab' as shown in Figure (6.41). The gravity load was uniformly distributed along line 'bc' of Figure (6.41). The shear force, torsion and moments were obtained at each end of the beam due to combined wind and gravity load. The shear stress, v, at any cross-section in a beam was calculated from

$$v = \frac{V}{b\ d} \tag{6.3}$$

where V is shear force due to ultimate load

b is the breadth of the beam section

d is the effective depth of slab.

The shear stress at the tip of the wall, due to stress concentration, was found very high – sometimes more than twice the maximum allowable shear stress value. The torsional stress was also higher than the allowable stress value. To resist both shear and torsional stresses it was decided to use two-leg vertical closed stirrup as shear reinforcement and the amount of shear reinforcement was calculated from the equation:

$$\frac{A_w}{s} = \frac{b\ (v - v_c)}{f_{yw}} \tag{6.4}$$

where A_w = cross-sectional area of two legs of vertical stirrup

b = width of the beam in consideration

s = spacing of stirrup along beam

v_c = allowable shear stress in concrete

f_{yw} = characteristic strength of the shear steel $\leq$ 425 N/mm^2

To ensure the anchorage of the stirrup, nominal bottom reinforcement of diameter 8mm was provided. The plan and dimension of this model was identical to that of model PS2. The top and bottom reinforcement pattern in the slab are shown in Figures (6.42– a) and (6.42– b). This reinforcement was designed to resist flexural stresses exerted by 155 KN lateral load and 18 KN gravity load.

Behaviour of the Model

At about 27% of the design lateral load, a number of cracks were observed around the wall as shown in Figure (6.43– a). In the next increment of load, at about 33% of design lateral load, the crack perpendicular to the wall at an average distance of 75mm from the inner edge of the wall became prominent and it was extended towards the free edge of the slab as shown in Figure (6.43– b). On further loading, the previous cracks widened further and more new cracks appeared. Large deflection of the slab was observed at about 90% of design load, implying the flexural nature of the behaviour as clear from photograph (6.45– b) and from the load– deflection curve as shown in Figure (6.44). Failure took place gradually at ultimate load of 175.0 KN (i.e., 113% of design load) at which deflection increased considerably, and it was clear that it was a ductile failure. Figure (6.46) shows the photograph of bottom failure surface. The strain distribution in steel and concrete is shown in Figures (6.47) to (6.51). Yielding of steel in windward direction started at about 70% of design lateral load. The exact locations of all the strain gauges used in the slab of this model are shown in Figure (6.52).

At failure load, all the steel (both transverse and longitudinal) around junction reached their yield strength and some of them were strained more than twice the yield strain.

6.3.4 Comparisons and Discussions

From Figure (6.53) which compares the load– deflection curves for all the

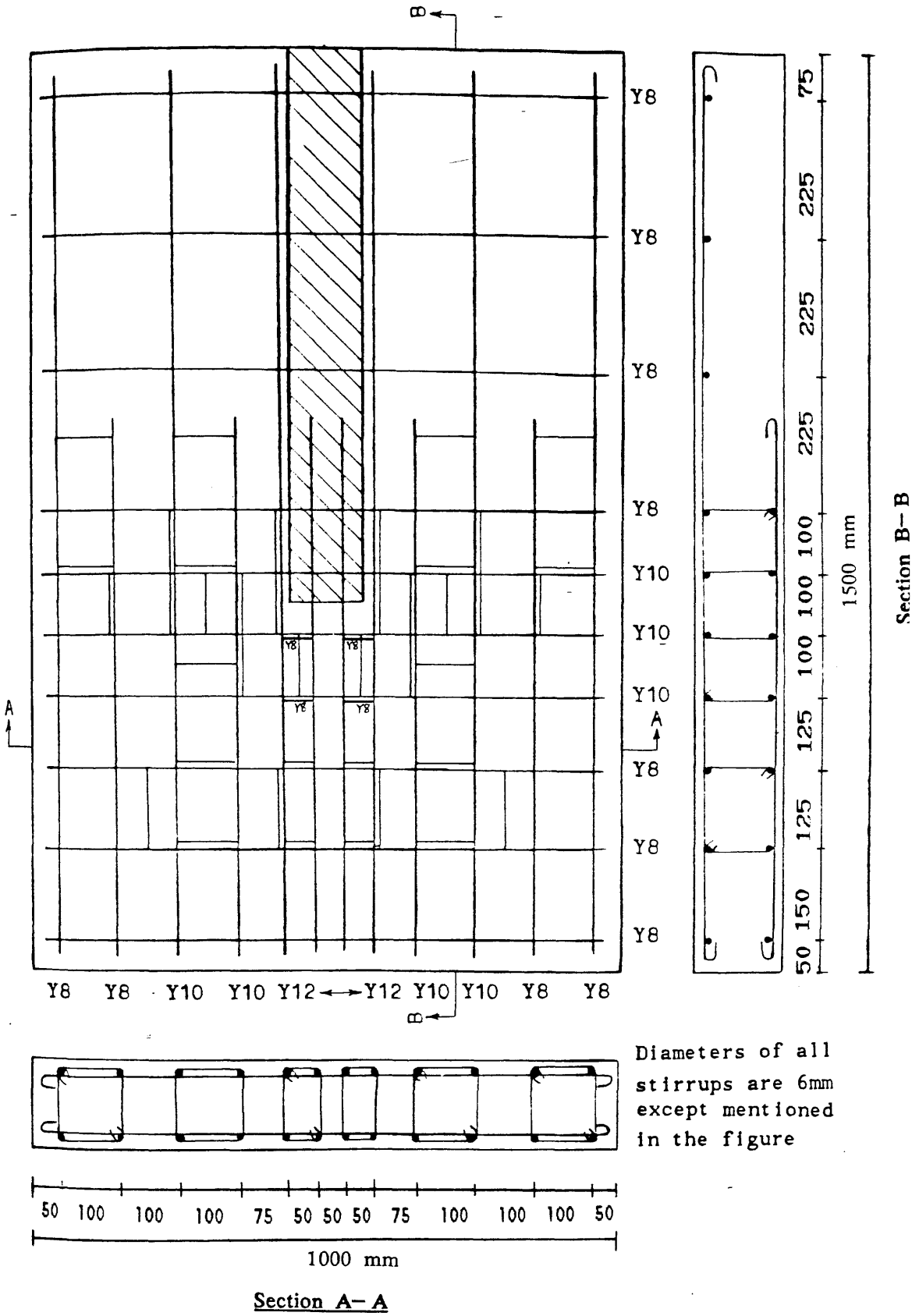

Figure (6.42-a) : Arrangement of top reinforcing bars including closed vertical stirrup in the slab of model PS3

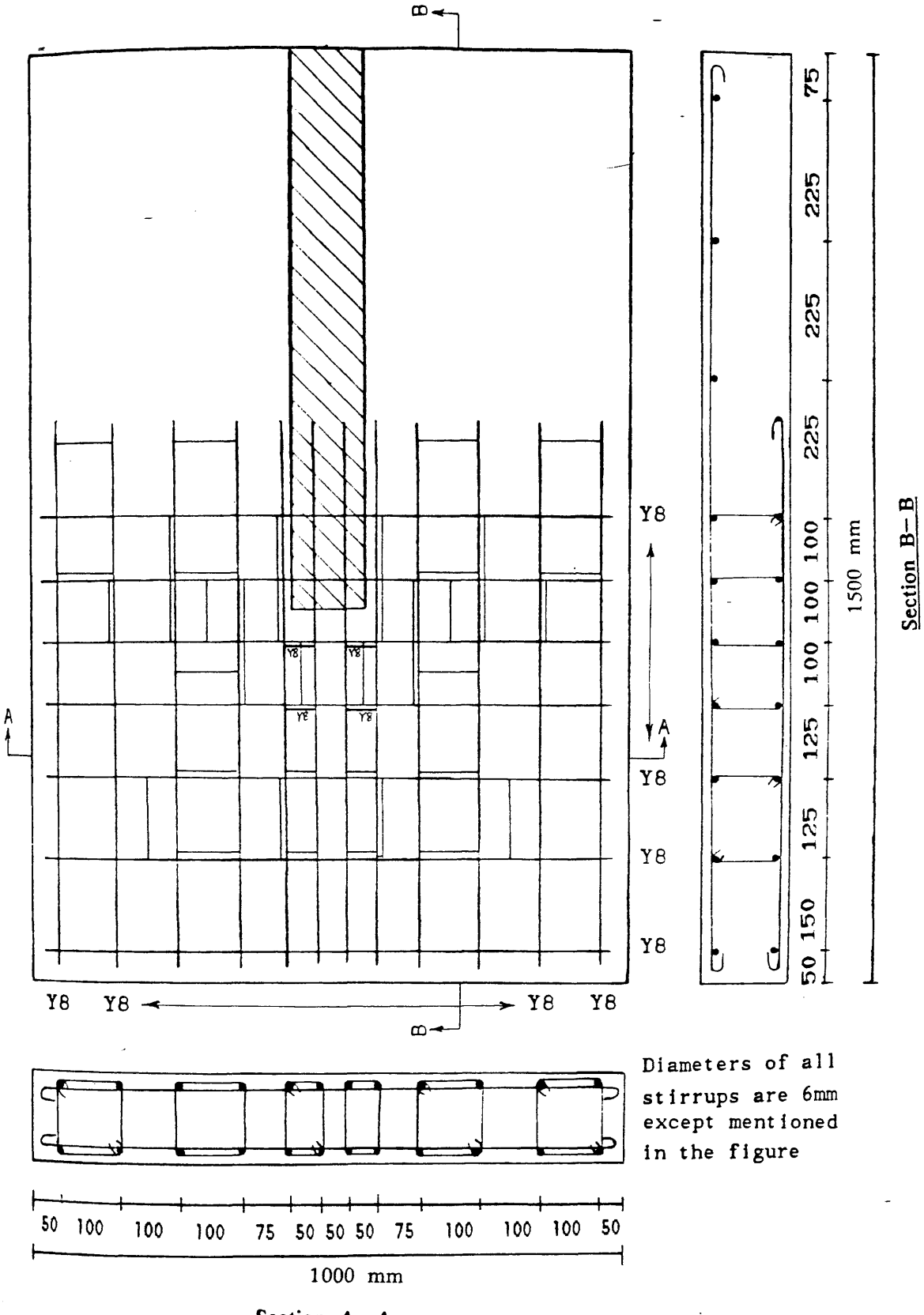

Figure (6.42-b) : Arrangement of bottom reinforcing bars including closed vertical stirrup in the slab of model PS3

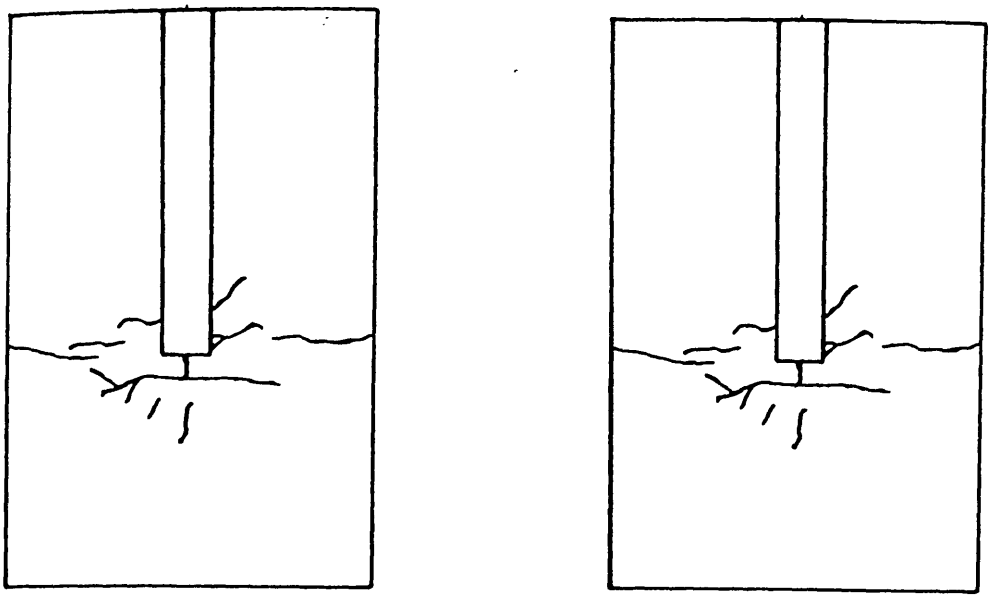

(a) at 27 %

(b) at 33 %

Figure (6.43) : Cracks initiation during testing of model PS3 at different percentages of design lateral load

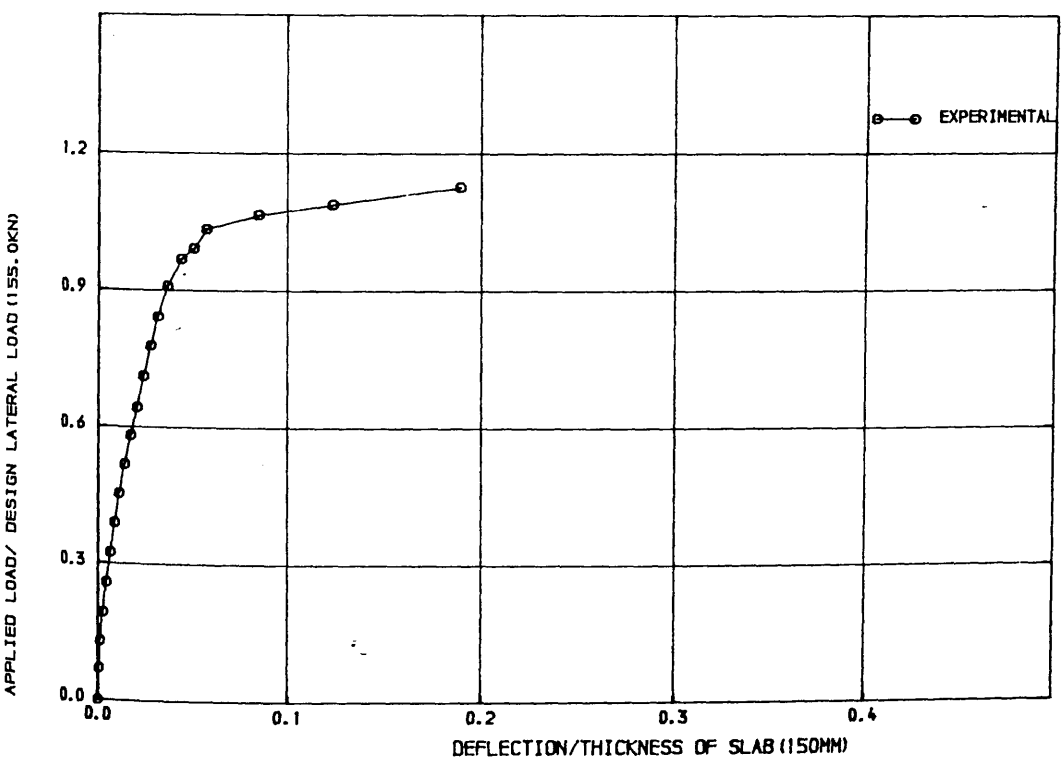

FIGURE (6.44) LOAD-DEFLECTION CURVE FOR MODEL PS3

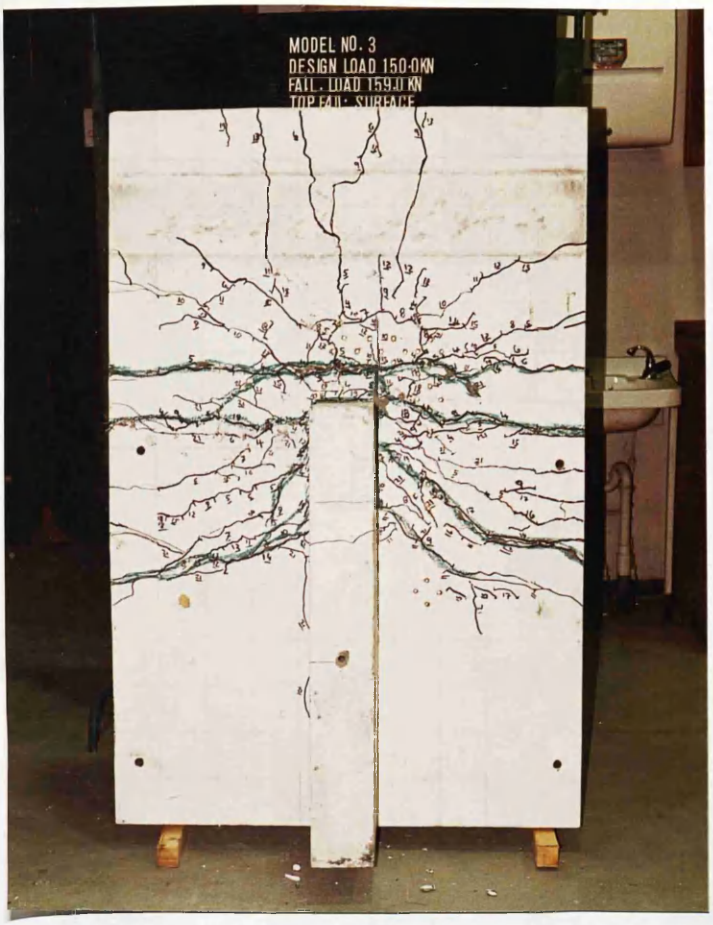

(a) On the tensile side

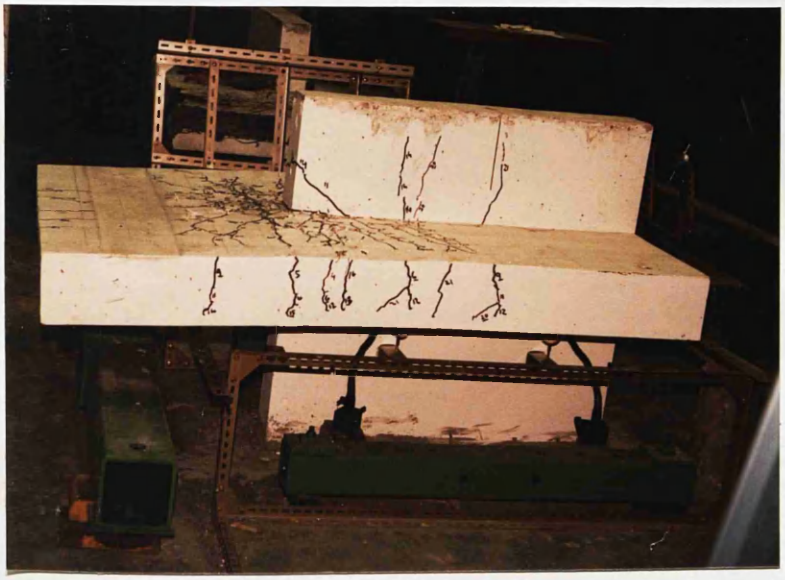

(b) Side view showing the excessive deflection

Figure (6.45) : Photographs showing the crack pattern on the slab of model PS3

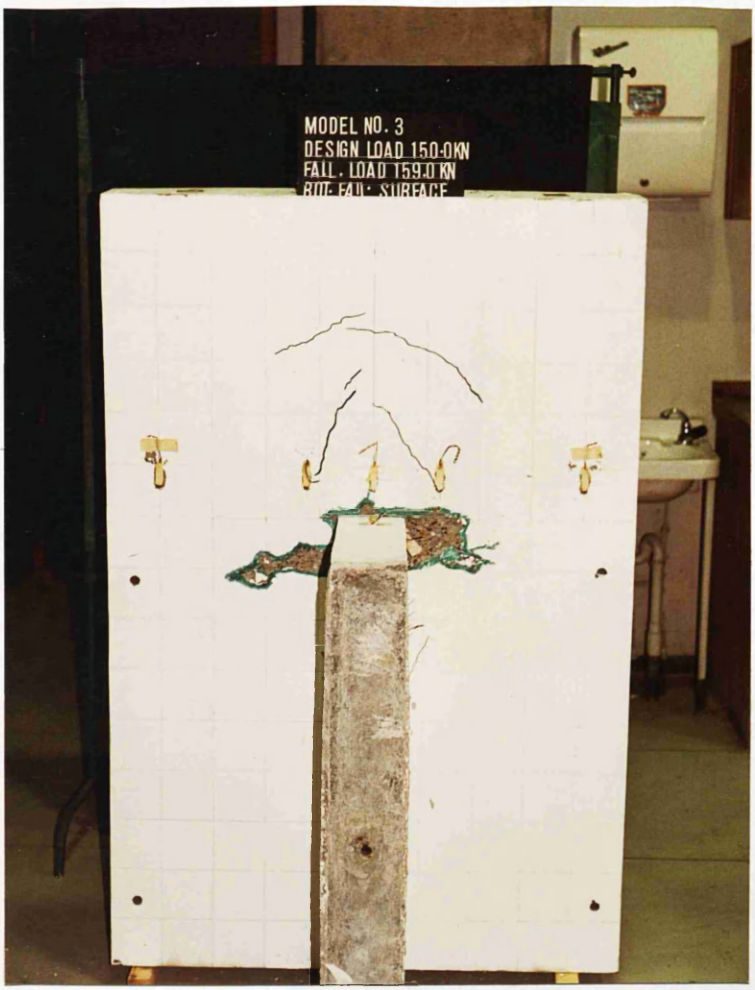

Figure (6.46) : Photograph showing the bottom failure surface of model PS3

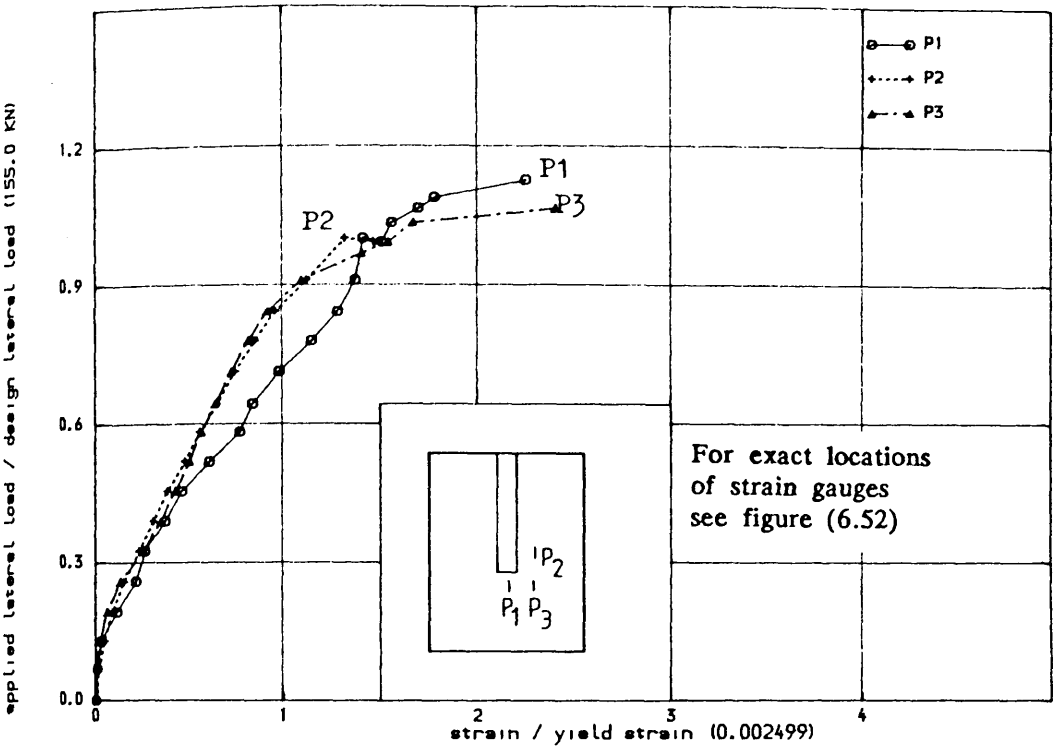

FIGURE (6.47) : TENSILE STRAIN IN STEEL IN VINDVARD DIRECTION ALONG TRANSVERSE SECTION IN THE SLAB OF MODEL PS3

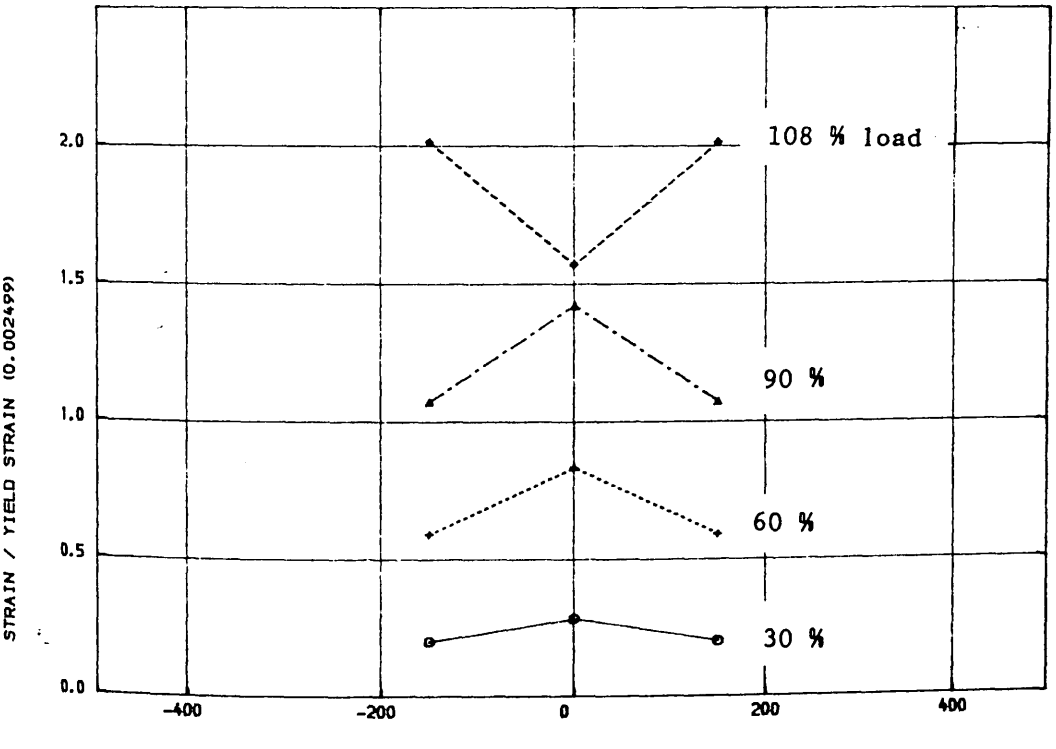

FIGURE (6.48) : VARIATION OF STRAIN IN STEEL IN VINDVARD DIRECTION ALONG TRANSVERSE SECTION AT DIFFERENT STAGES OF LOADING IN THE SLAB OF MODEL PS3

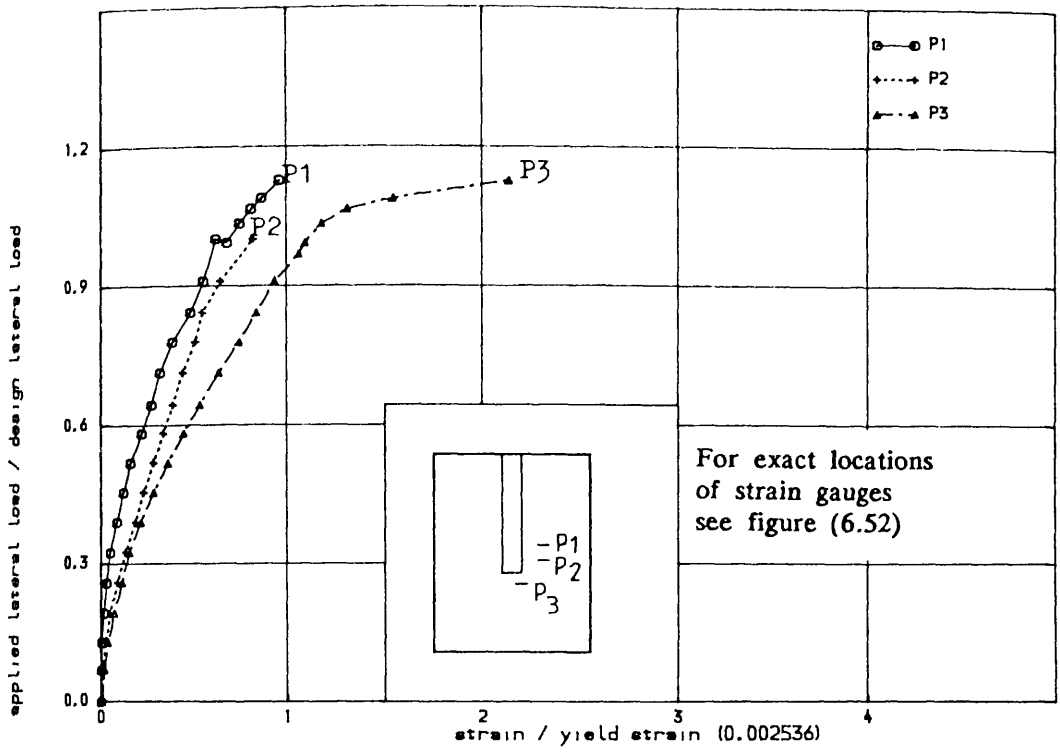

FIGURE (6.49) , TENSILE STRAIN IN STEEL IN TRANSVERSE DIRECTION IN THE SLAB OF MODEL PS3

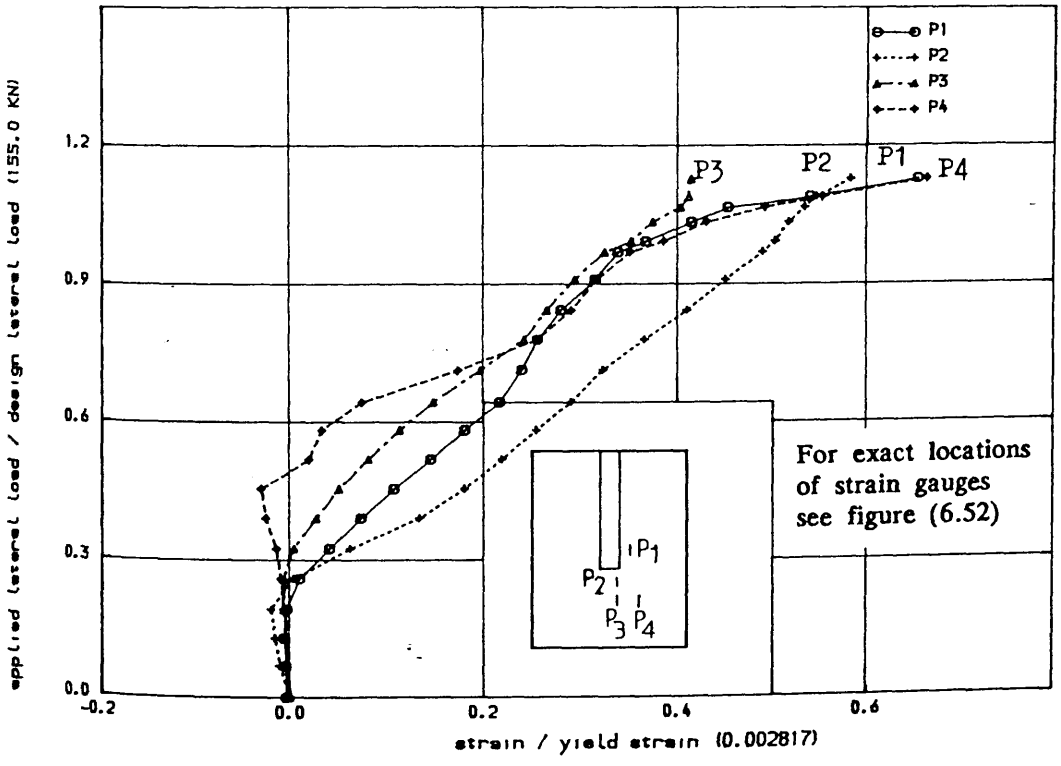

FIGURE (6.50) , STRAIN IN CLOSED VERTICAL STIRUP AT DIFFERENT LOCATIONS IN THE SLAB OF MODEL PS3

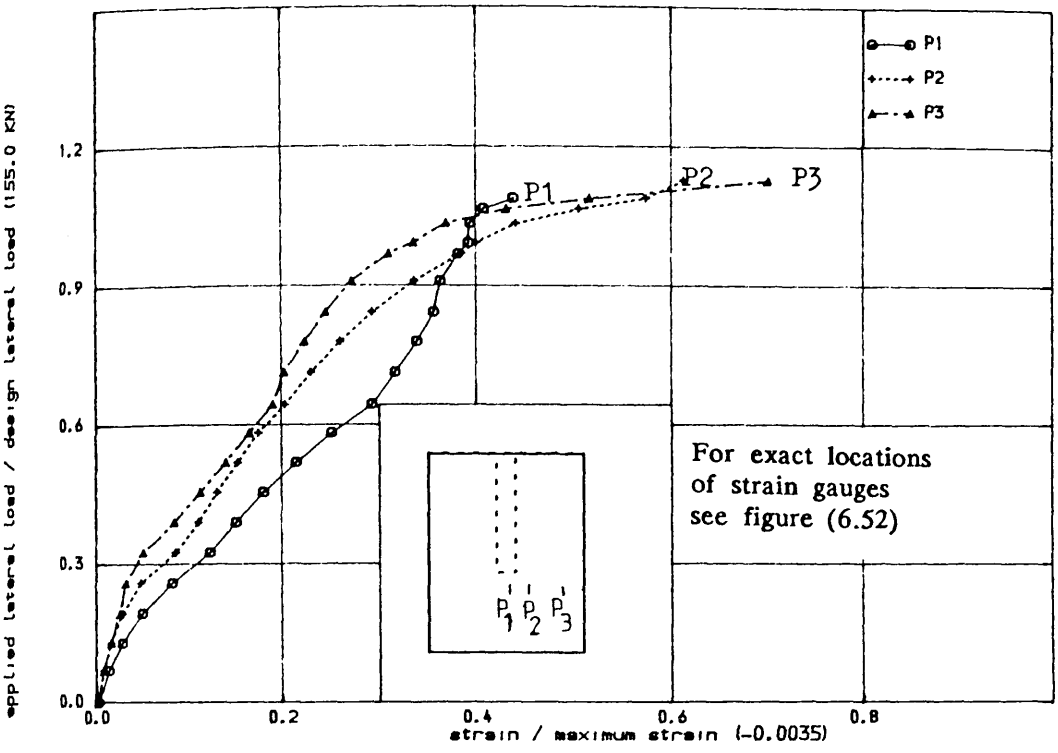

FIGURE (6.51) , COMPRESSIVE STRAIN IN CONCRETE IN VINDVARD DIRECTION IN THE SLAB OF MODEL PS3

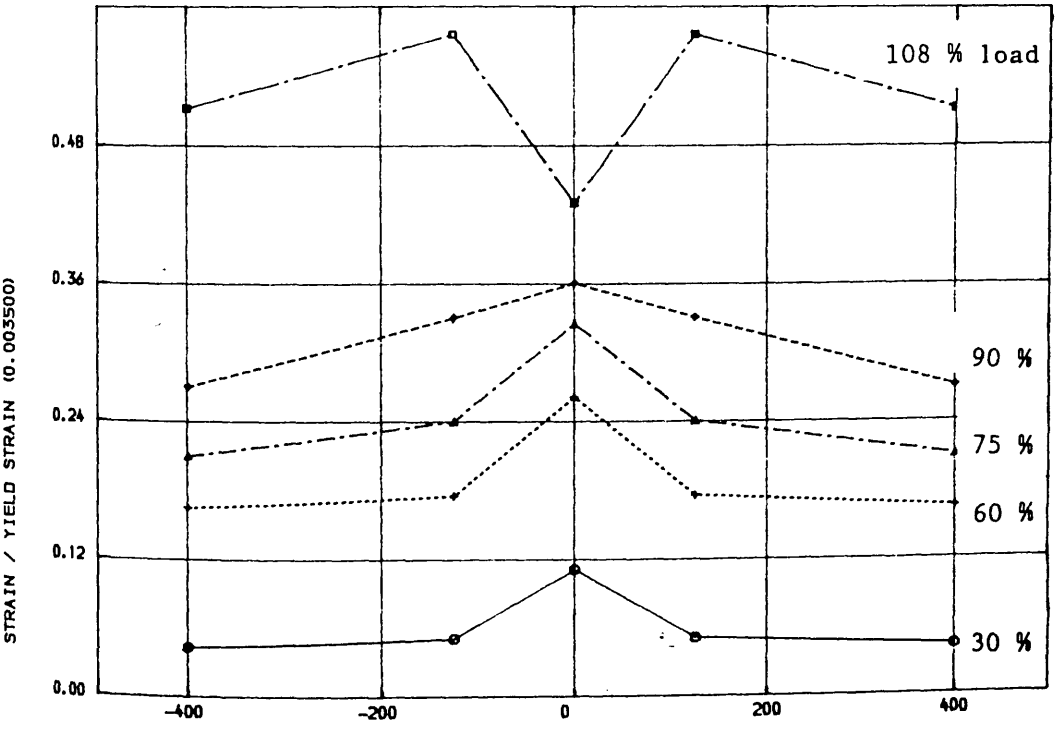

FIGURE (6.51-a) , VARIATION OF COMPRESSIVE STRAIN IN CONCRETE ALONG TRANSVERSE CRITICAL SECTION AT DIFFERENT STAGES OF LOADING IN THE SLAB OF MODEL PS3

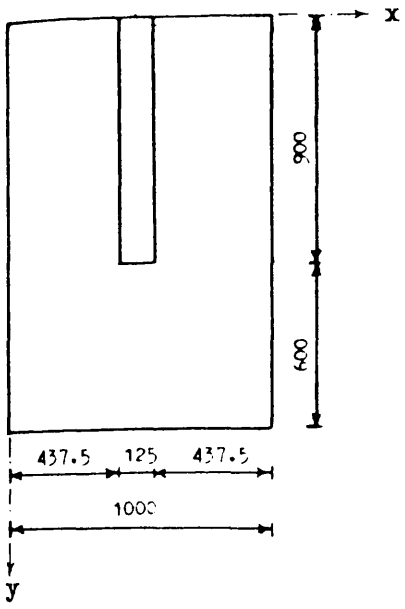

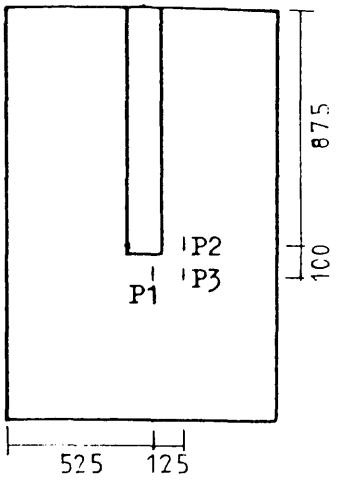

(a) Strain gauges in Figure (6.47)

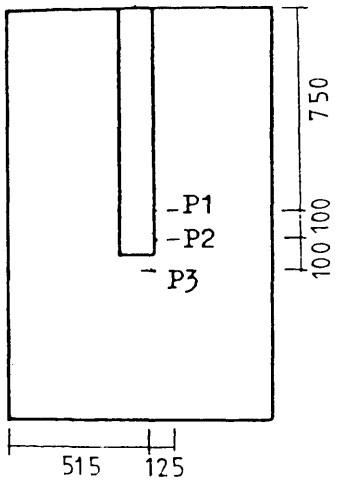

(b) Strain gauges in Figure (6.49)

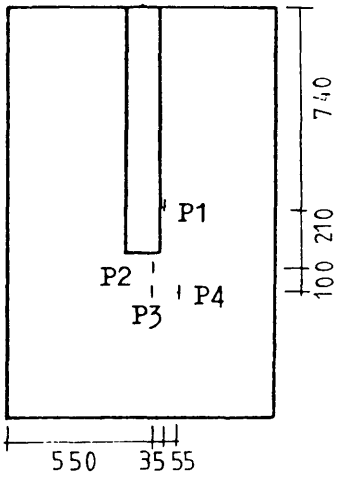

(c) Strain gauges in Figure (6.50)

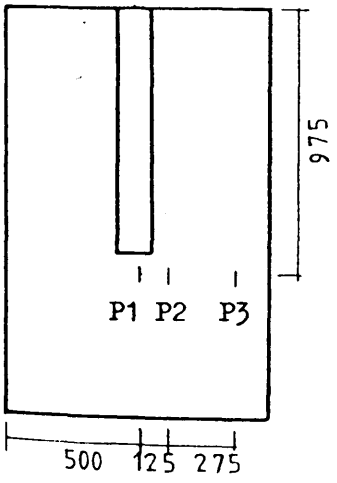

(d) Strain gauges in Figure (6.51)

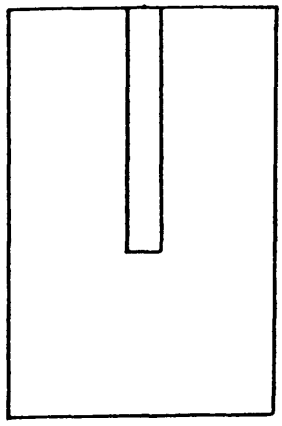

FIGURE (6.52) : Exact locations of strain gauges in the slab of model PS3 as shown in Figures (6.47), (6.49), (6.50) and (6.51)

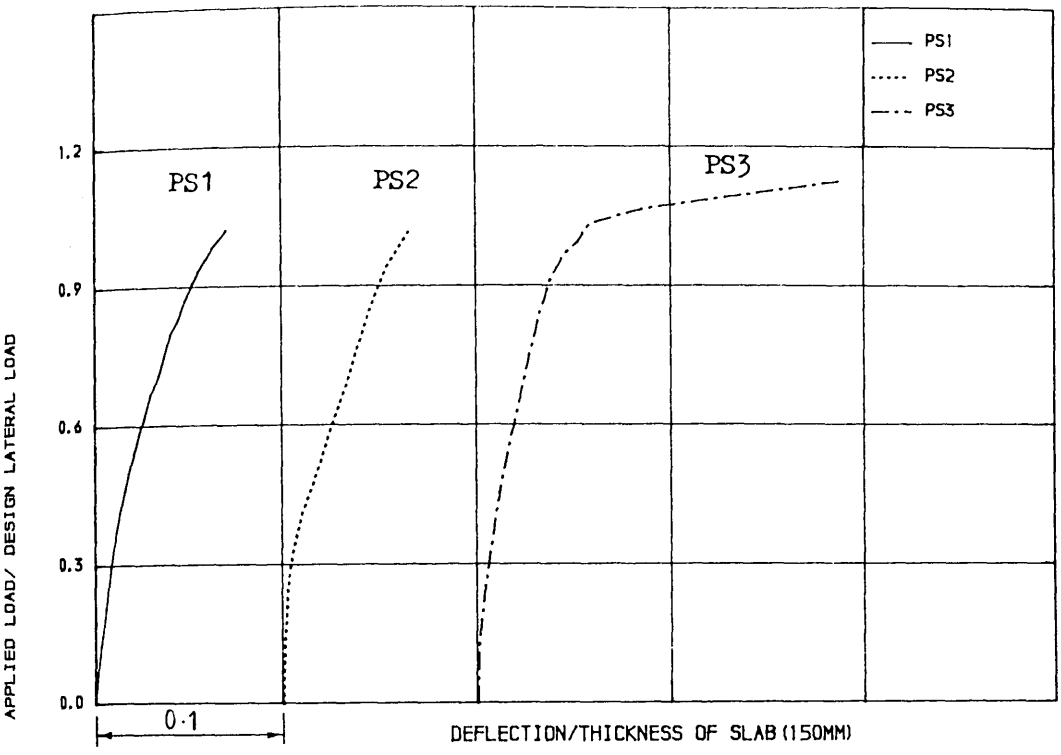

FIGURE (6.53) , COMPARATIVE STUDY OF THE LOAD-DEFLECTION CURVES FOR THE MODELS OF PRELIMINARY TEST SERIES

three models of preliminary test series, it can be observed that these curves closely follow each other, though model PS3 shows slightly higher stiffness. The ductile behaviour is clear in the curve for PS3, in contrast to the brittle type of failure as apparent from curves for models PS1 and PS2. This is due to the fact that, the vertical closed stirrup was provided throughout the slab of model PS3 in order to take care of shear stress in excess of allowable concrete shear stress, v_c.

Failure took place at 102%, 106% and 113% of design load for models PS1, PS2 and PS3 respectively. At failure, the ultimate load dropped suddenly for models PS1 and PS2, accompanied by the crushing of large area of concrete on the compressive side (see Figures (6.17) and (6.18) for PS1 and (6.33– b) for PS2). However the ultimate load was found to decrease slowly for model PS3, accompanied by large deflection of the slab without crushing of concrete on the compressive side (see Figure (6.46)).

As can be seen from Figure (6.21) of model PS1, the curves showing the variation of tensile strain in steel from free edge to centre of the slab, became steeper with the increase of load till the load reached 60% of its design load. The rate of increase of strain at every point remained fairly constant afterwards. As is apparent from Figure (6.35), the measured strain at point P1 of model PS2 was maximum and it increased with load more than others as the load increased until failure. A different behaviour was noticed for model PS3 (Figure 6.48), where the strain at point P1 was higher than the point P3 until 90% of design load but near failure the strain at point P1 was smaller than the neighbouring point P3.

From figures (6.25), (6.39) and (6.52), where the variation of compressive strain along transverse critical section is shown at different stages of loading, it can be seen that the models PS1 and PS2 were behaved similarly but model PS3 was very different. At ultimate failure load, the maximum strain in the compressive side of the slab was 48% of yield strain (0.0035) at point P3 for model PS1; 25% of yield strain at point P2 for model PS2 and 57% of yield strain at point P2 for

model PS3.

The closed vertical stirrup used in the slab of model PS3 started to carry load at about 30% of design load, when the cracks appeared on the tensile surface of the model. This behaviour was not noticed in the type of shear steel (Figure 6.13) used in the slab of models PS1 and PS2. One stirrup in model PS1 started to carry load from the very begining of lateral load and other two were strained at about 23% of design load. One stirrup in model PS2 was found strained at about 25% of design load and the other two at about 55% of design load, whereas first crack appeared at about 13% of design load. The steel strains measured on closed vertical stirrups indicated their effectiveness in carrying load at the onset of concrete cracking.

The concept of providing shear reinforcement only around the critical section was found unsatisfactory in models PS1 and PS2 to make the wall– slab connection ductile. However, the shear steel in the form of closed vertical stirrup provided in the slab of model PS3 in a fashion as dictated by the state of stress resulted the connection very ductile. That is why, it was decided to use shear reinforcement in the form of closed verical stirrup in rest of the models.

6.4 MAIN TEST SERIES – MS Series:

As stated before, the object of this series was to verify the validity of the design procedure adopted and described in details in section 3.6. For that reason, no systematic exploration of the parameters governing the problem was carried out in this series. On the otherhand, nine representative models, MS4 to MS12, from the previous test series[23,24] were chosen and tested after redesigning them with shear reinforcement. Model PS3 indicated the need for using closed form of vertical stirrups and this was adopted in all the models of this test series. As determined by the position of the stirrups, longitudinal steel was provided in the compression face to ensure proper anchoring of the stirrup. In practice, since steel will have to be provided on both faces of the slab to cater for the reversibility of

wind forces, there is no need to provide a separate layer of bars for anchoring purposes. In the following subsections, the details of the models tested in this series will be discussed.

6.4.1 Model MS4 to study the effect of wall– web length

This model was chosen to study the effect of wall web length. This is similar to model MT3[23] except the use of closed vertical stirrups in the slab. The plan of the model is shown in Figure (6.54). The length of the slab in connection with the wall was 400mm, whereas total length of wall was kept 600mm because of the requirement of the supporting and testing arrangement of the model. The flexural steel reinforcement in the slab was redesigned, using the procedure explained in chapter three, to resist a lateral load equals 220.0 KN as well as an ultimate gravity load of 18.0 KN. Figures (6.56– a) and (6.56– b) show the reinforcement details. Total flexural steel area (excluding shear steel) provided in this slab is about 86% of that of the model MT3. Besides, some longitudinal bars were curtailed at the back of the slab to match with the calculated steel area. The reinforcement provided in the wall as shown in Figure (6.55), was exactly similar to that of the model MT3[23].

Behaviour of the Model

A number of cracks were observed at a lateral load equal to 18% of the design load. Most of them were parallel to the inner edge of the wall as shown in Figure (6.57– a). This was particularly true at the corridor area of the slab. On further loading, these cracks extended towards the free edge of the slab and some new 'torsional' cracks (those cracks which occurred behind the nose of the wall) radiated from the wall– slab junction at various angles. The shear cracks in the slab at the back of the model appeared at a load of 37% of design lateral load as shown in Figure (6.57– b). The wall started cracking at 42% of design load and a number of cracks appeared at the nose of the wall. On further loading, shear

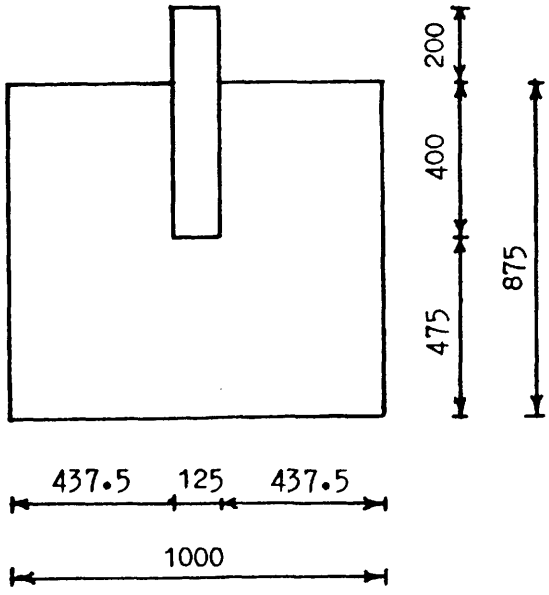

Figure (6.54) : Plan and dimensions of model MS4

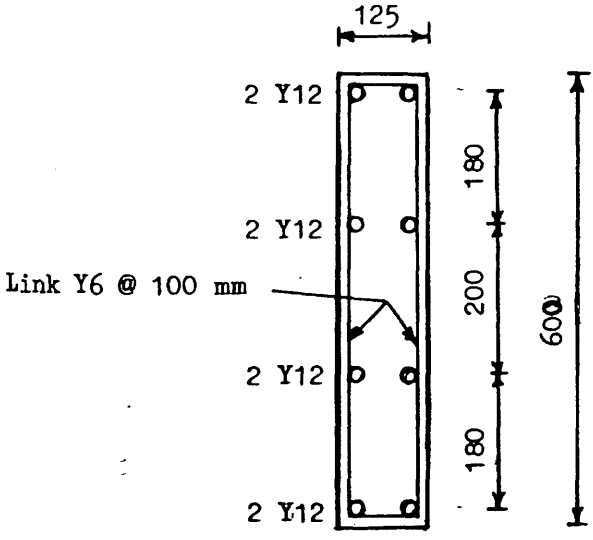

Figure (6.55) : A horizontal section in the wall of model MS4 showing the reinforcing details

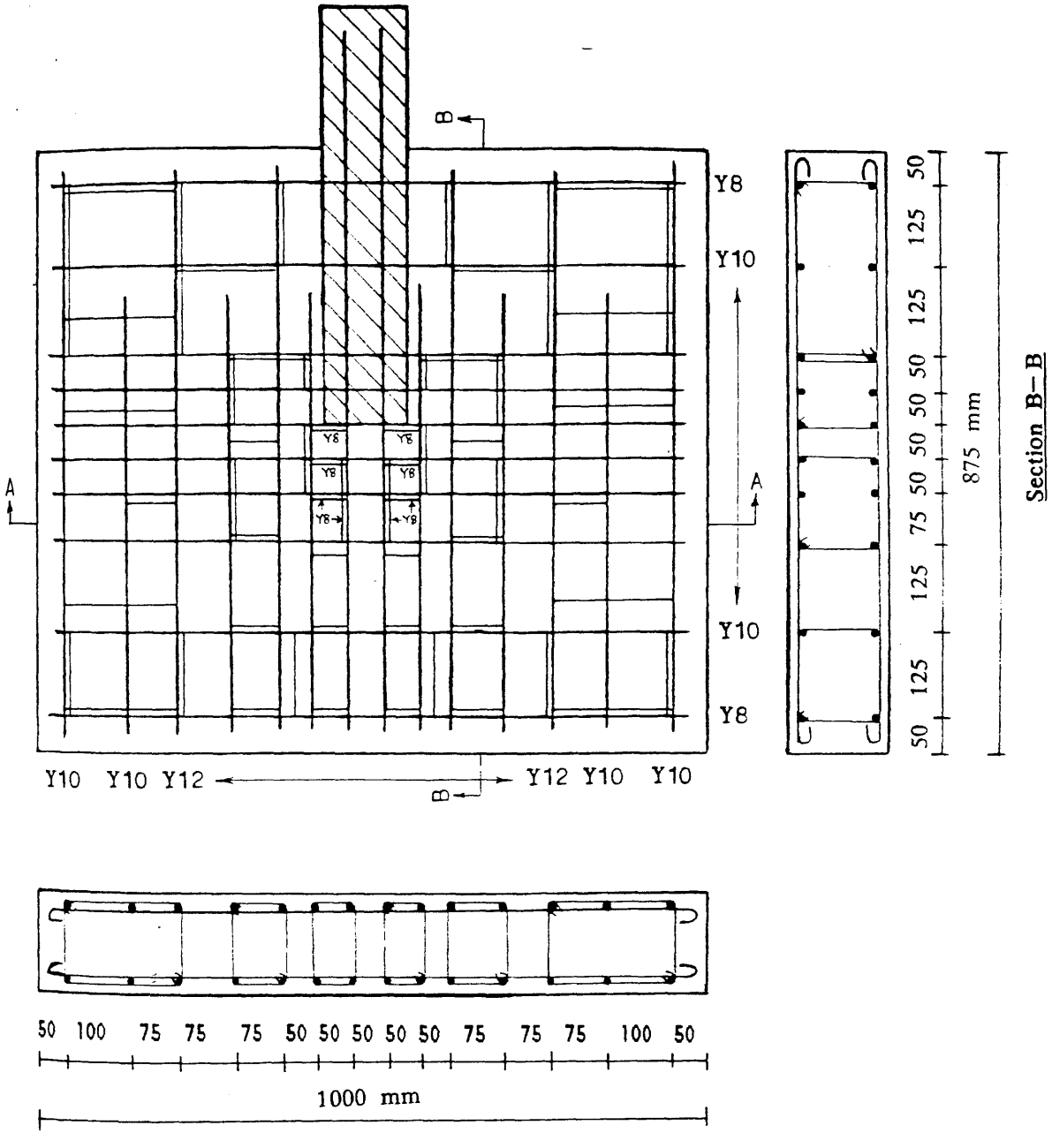

Diameters of all stirrups are 6mm except mentioned in the figure

Figure (6.56-a) : Arrangement of top reinforcing bars including closed vertical stirrup in the slab of model MS4

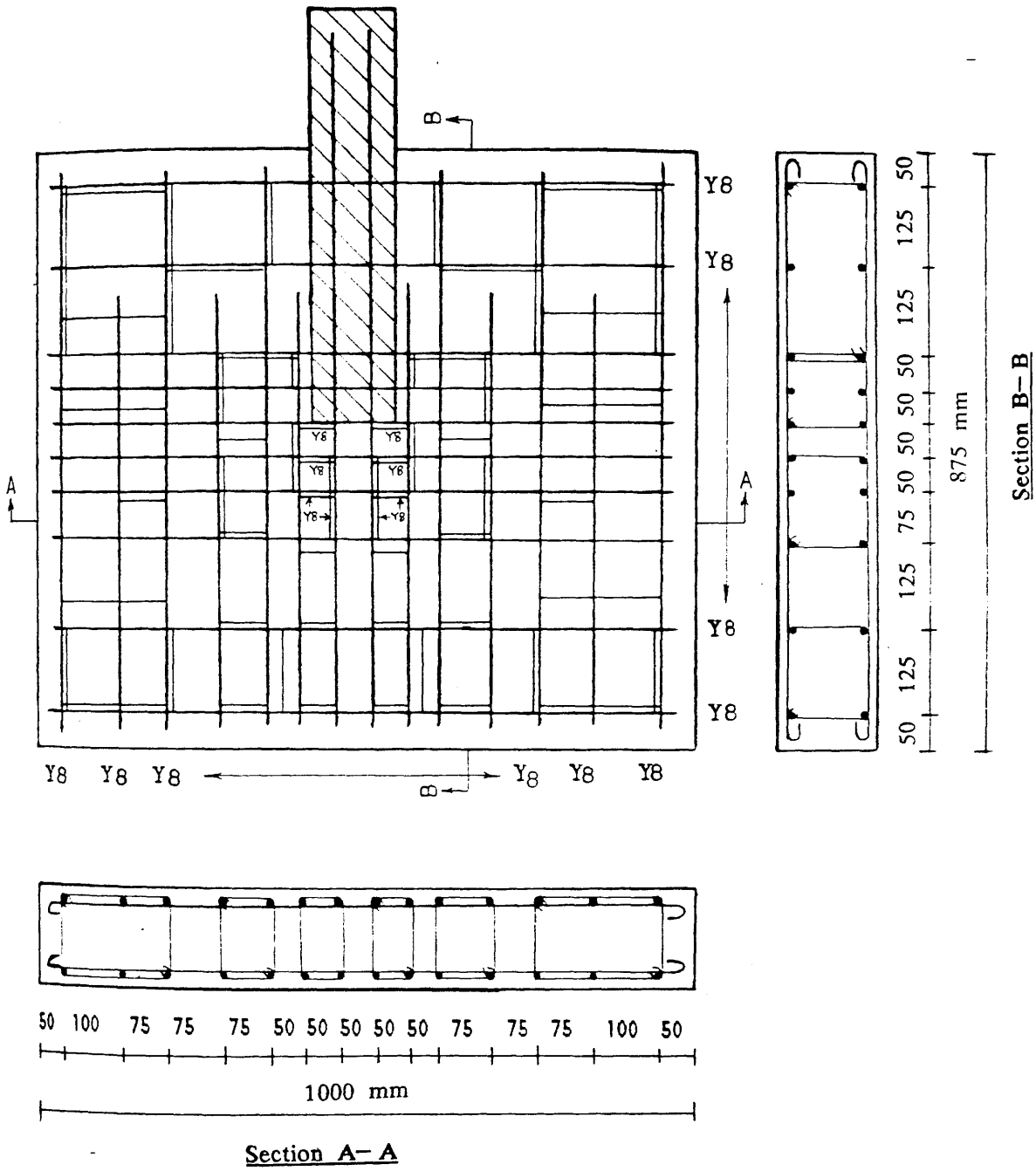

Diameters of all stirrups are 6mm except mentioned in the figure

Figure (6.56-b) : Arrangement of bottom reinforcing bars including closed vertical stirrup in the slab of model MS4

crack at the back widened and failure took place suddenly at a lateral load equals 190.4 KN (86.5% of the design load). The photographs showing the crack pattern of the model after failure are presented in Figures (6.60) to (6.61). Figure (6.58) shows the non− dimensional load− deflection curve. The other experimental data are shown in Figures (6.62) to (6.66). The exact locations of all the strain gauges used in the slab of this model are shown in Figure (6.67).

A number of cracks were noticed in the wall. The rear end of the top surface of the shear wall was found crushing against the supporting beam and the front edge of the bottom surface of the shear wall was found crushing against the 'strong − floor' of the laboratory (see Figure (6.59)). This may be one of the reasons for the early failure of the whole structure, although the shear crack at the back of the slab was the main cause of failure. The reinforcement distribution (equally spaced) in the wall was insufficient. In real structure, reinforcements in the shear wall are usually concentrated at two ends, to get longer lever arm and hence more resisting forces. So it was decided to increase the amount of wall reinforcement in the next model and concentrate them towards the edge with additional stirrups to hold them together.

6.4.2 Models to study the effect of corridor opening width

The magnitude of the unbalanced moments has a very pronounced effect on the overall strength of connection. Models MS5, MS6 and MS7 were chosen from previous test series[23] to investigate the effect of the variation in the ratio of unbalanced moment due to wind load, M_{ℓ} to uneven shear due to wind load V_{ℓ}. This ratio is varied by changing the width of corridor opening. For each model of this group half corridor opening width (L/2) is shown in Table (6.4). The reinforcement ratio which appears in Table (6.4) is for those bars in windward direction within 1.5d on either side of the wall (where d is the effective depth of the slab)

Table (6.4) : Models to study the effect of corridor opening width

Model	Half of corridor opening width L (mm)	Bay width Y (mm)	Normalised design wind shear Vl (KN)	Design wind moment Ml (KN)	Gravity load Vg (KN)	Moment due to gravity Mg (KN.M)	Reiforcement ratio (%)
MS5	520	1000	155	80.6	18	7.9	1.67
MS6	280	1000	330	92.4	18	7.9	1.67
MS7	400	1000	240	96.0	18	7.9	1.67

Table (6.5) : Models to study the effect of flange width

Model	Flange width Z mm	Bay width Y mm	Normalised design wind shear V_ℓ KN	Design wind moment M_ℓ KN.M	Gravity load V_g KN	Moment due to gravity M_g KN.M	Reiforcement ratio (%)
MS10	300	1000	220	60.5	20	4.5	2.23
MS11	200	1000	215	59.0	20	4.5	2.51
MS12	400	1000	215	59.0	20	4.5	2.14

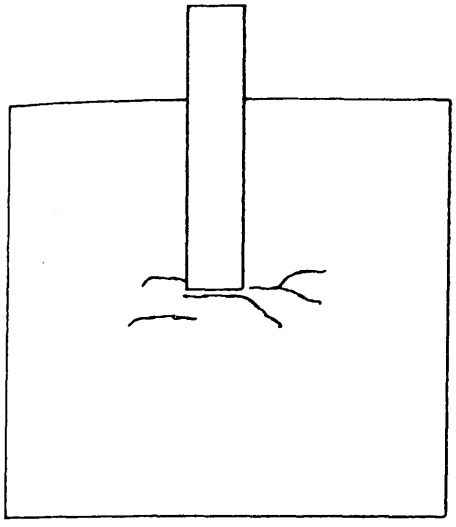

(a) Initiation of cracks in the slab of model MS4

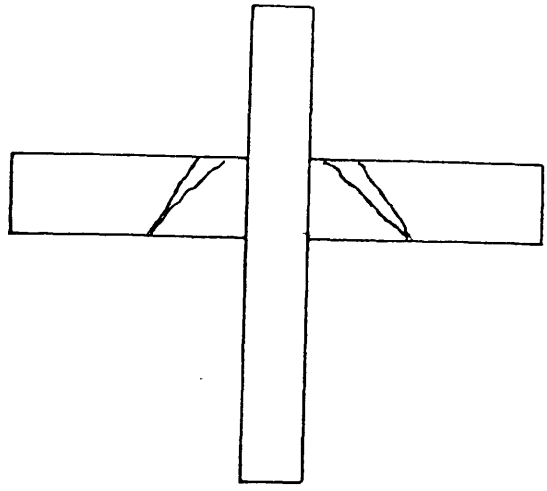

(b) Shear cracks in the slab at the back of model MS4

Figure (6.57)

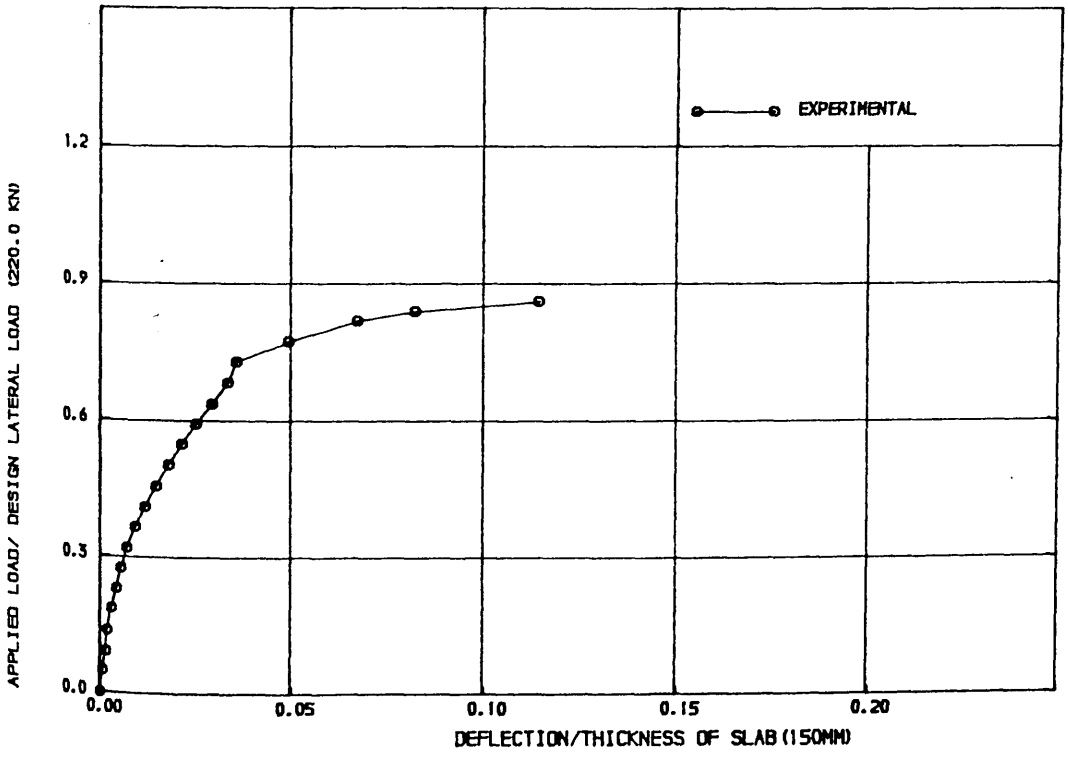

FIGURE (6.58) , LOAD-DEFLECTION CURVE FOR MODEL MS4

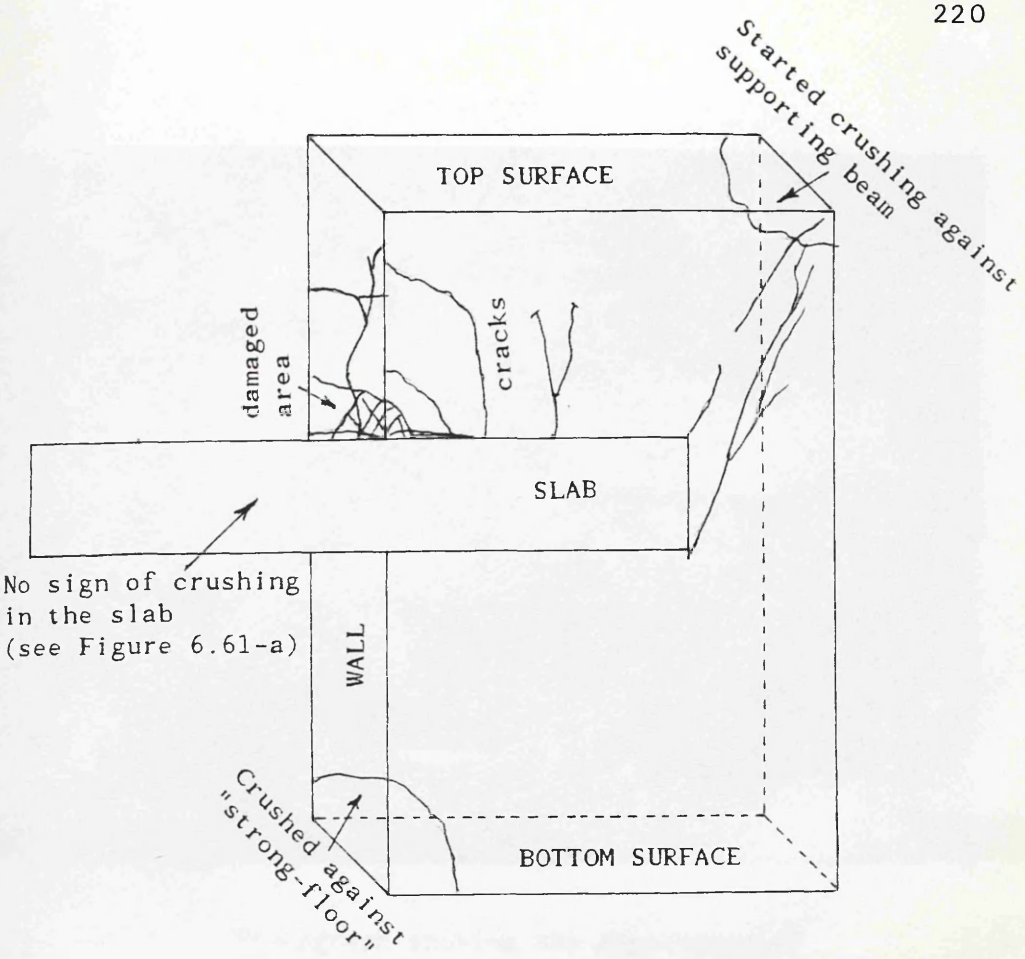

Figure (6.59-a) : Sketch showing the crack pattern and crushing zones in the wall of model MS4

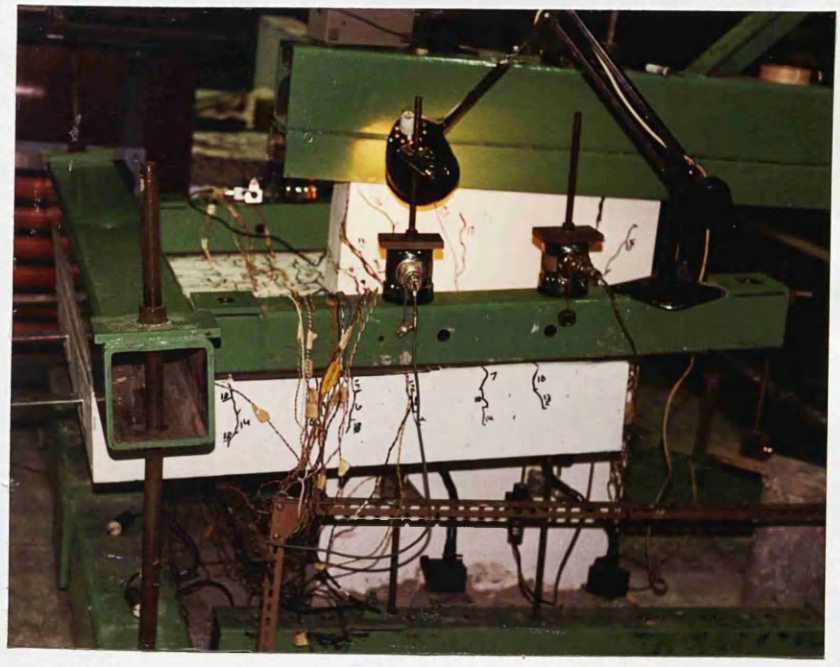

Figure (6.59-b) : Photograph showing the cracks in the wall of model MS4 at 50% of design load

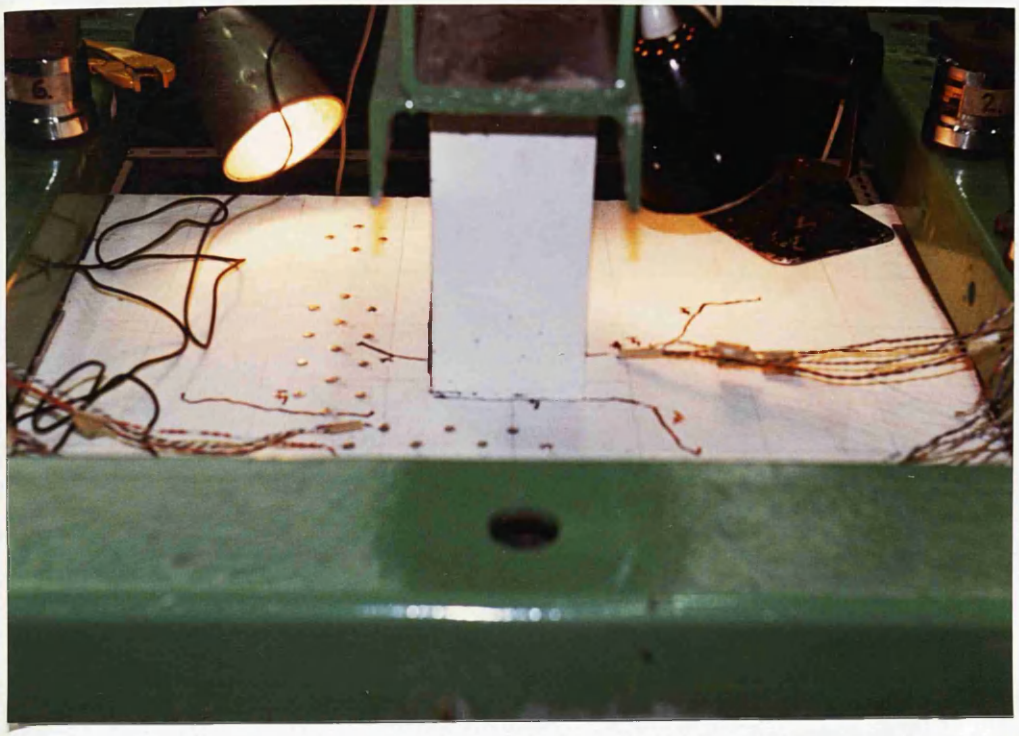

Figure (6.60– a) : Photograph showing the appearance of first crack in the slab of model MS4

Figure (6.60– b) : Photograph showing the back failure surface of model MS4

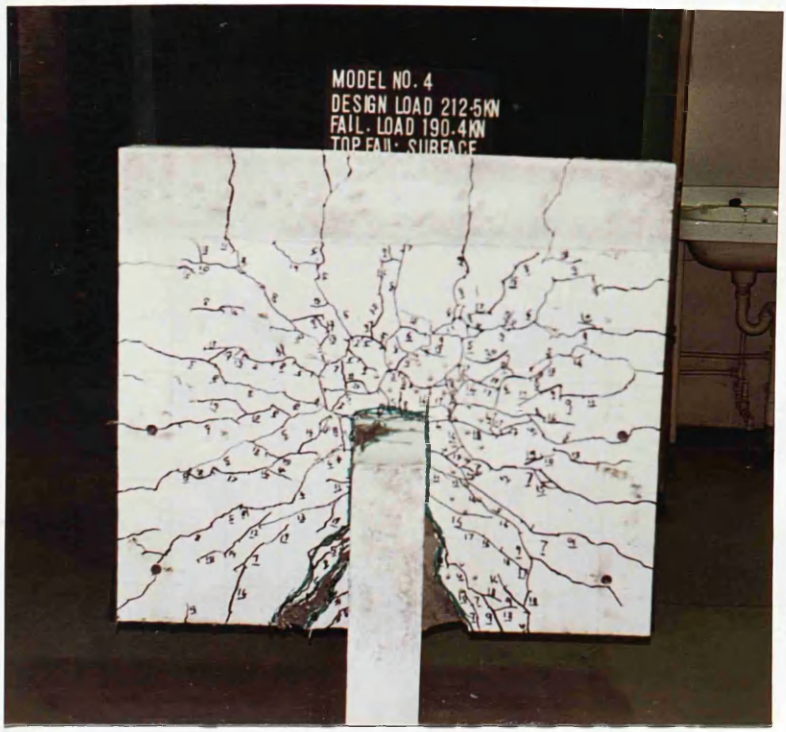

(a) On the tensile side

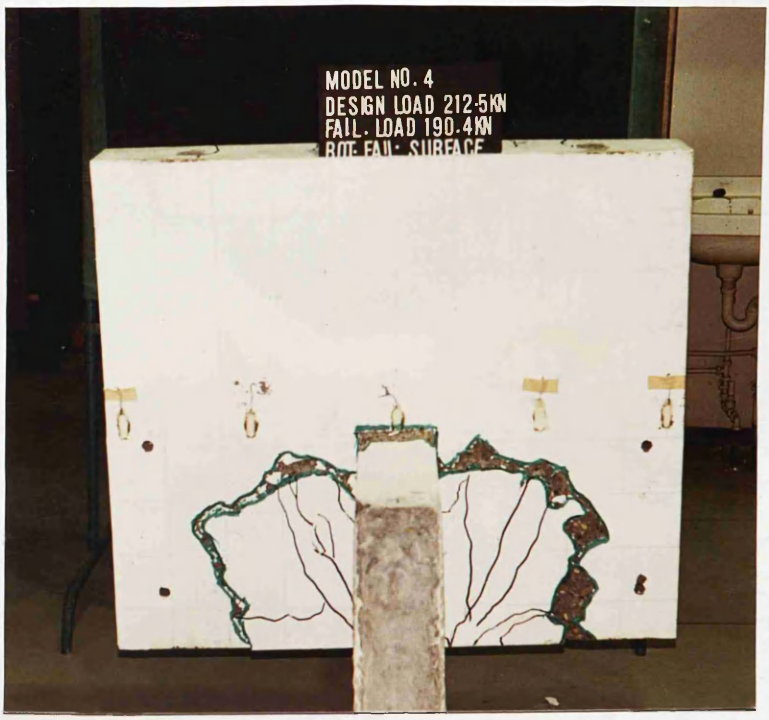

(b) On the compressive side

Figure (6.61) : **Photographs showing the crack pattern on the slab of model MS4**

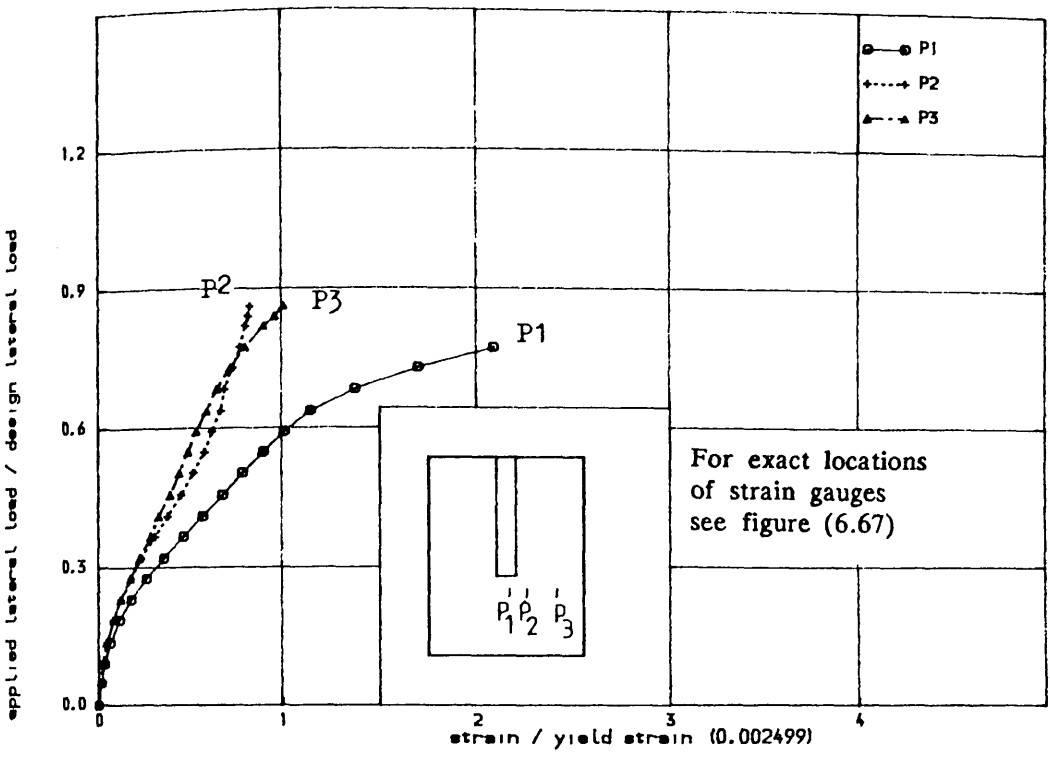

FIGURE (6.62) : TENSILE STRAIN IN STEEL IN VINDVARD DIRECTION ALONG TRANSVERSE SECTION IN THE SLAB OF MODEL MS4

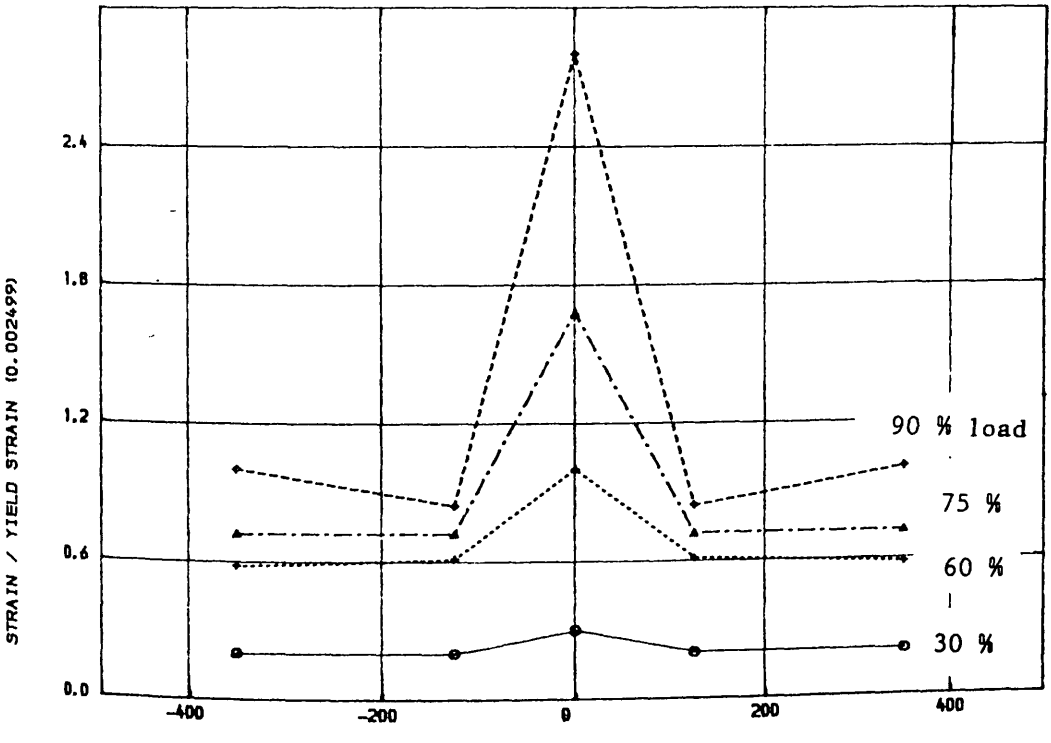

FIGURE (6.63) : VARIATION OF STRAIN IN STEEL IN VINDVARD DIRECTION ALONG TRANSVERSE SECTION AT DIFFERENT STAGES OF LOADING IN THE SLAB OF MODEL MS4

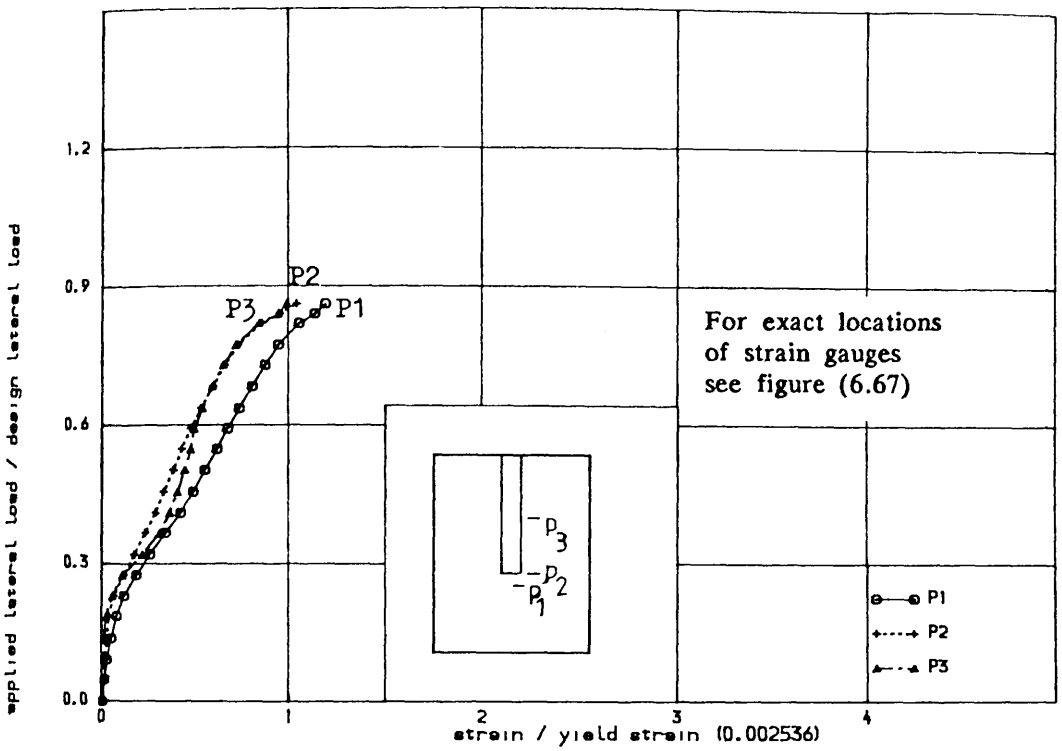

FIGURE (6.64) , TENSILE STRAIN IN STEEL IN TRANSVERSE DIRECTION IN THE SLAB OF MODEL MS4

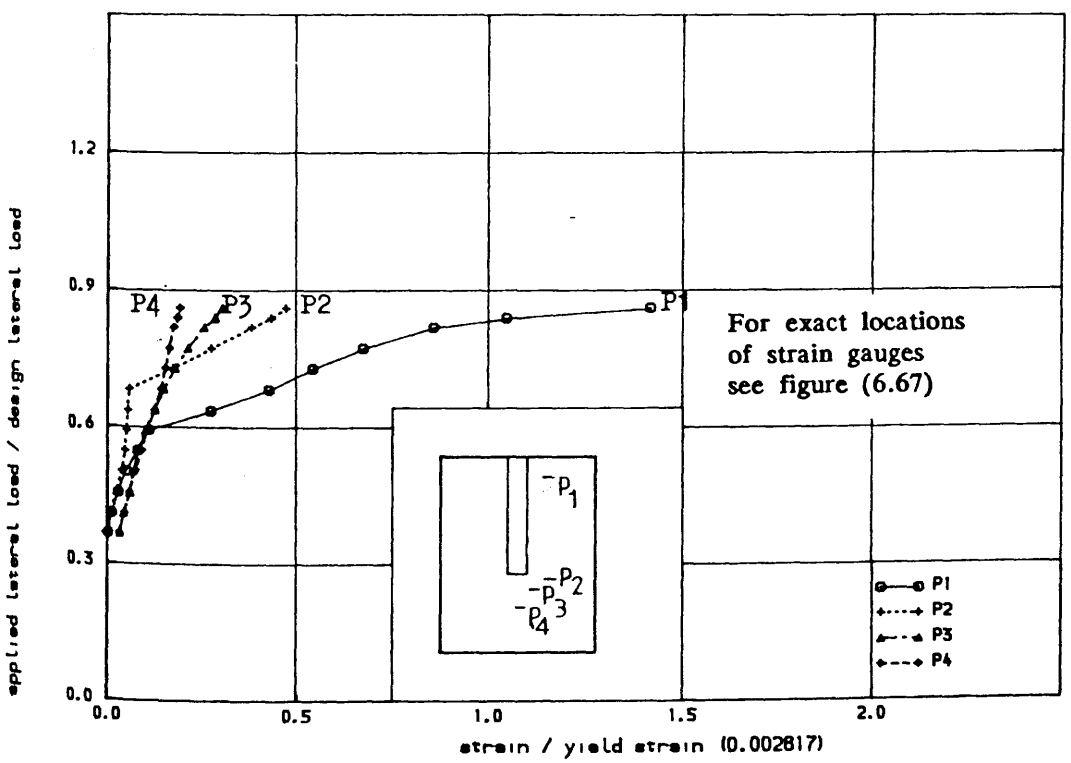

FIGURE (6.65) , STRAIN IN CLOSED VERTICAL STIRUP AT DIFFERENT LOCATIONS IN THE SLAB OF MODEL MS4

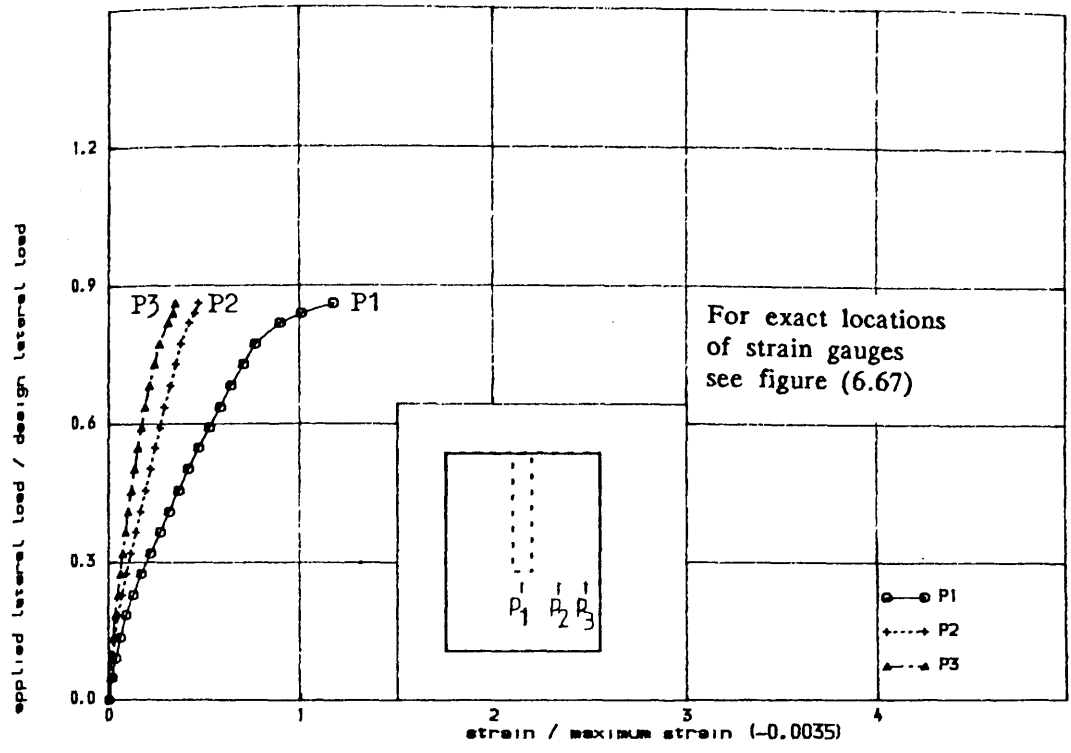

FIGURE (6.66) , COMPRESSIVE STRAIN IN CONCRETE IN WINDWARD DIRECTION IN THE SLAB OF MODEL MS4

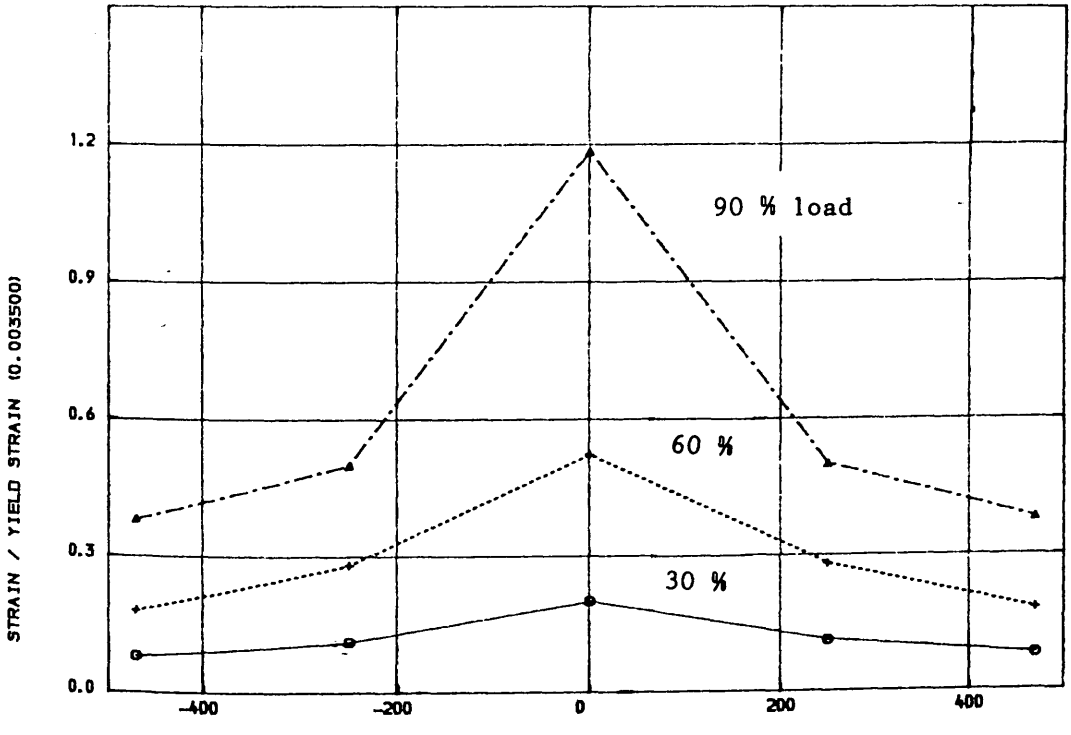

FIGURE (6.66-a) , VARIATION OF COMPRESSIVE STRAIN IN CONCRETE ALONG TRANSVERSE CRITICAL SECTION AT DIFFERENT STAGES OF LOADING IN THE SLAB OF MODEL FS2

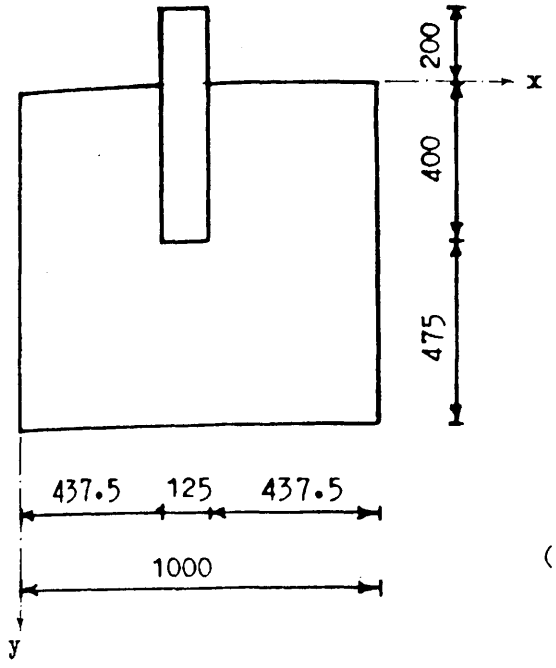

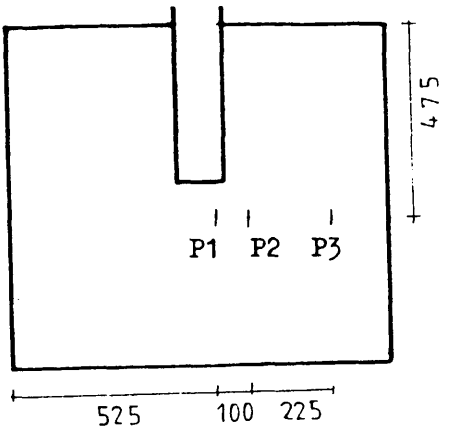

(a) Strain gauges in Figure (6.62)

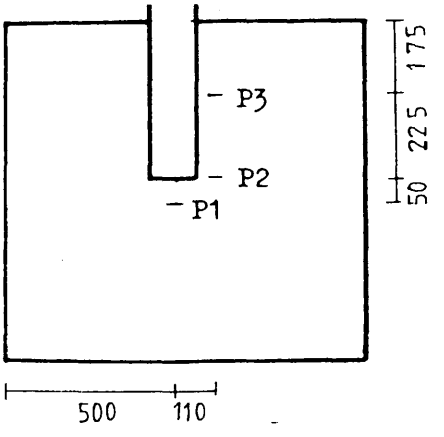

(b) Strain gauges in Figure (6.64)

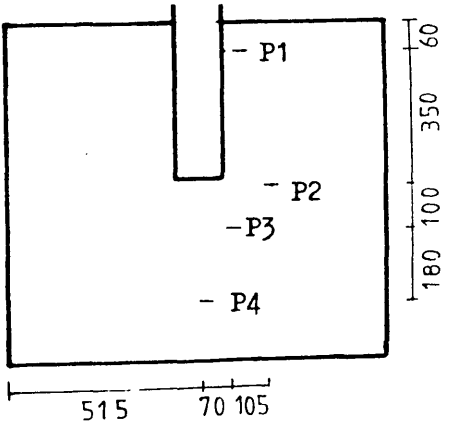

(c) Strain gauges in Figure (6.65)

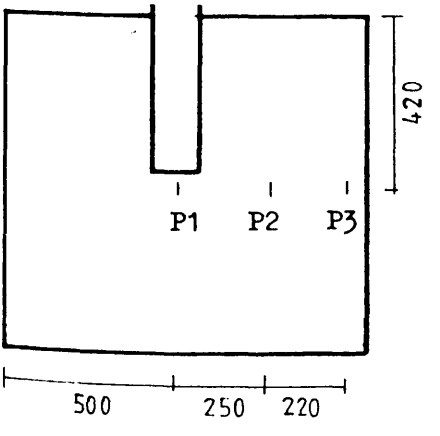

(d) Strain gauges in Figure (6.66)

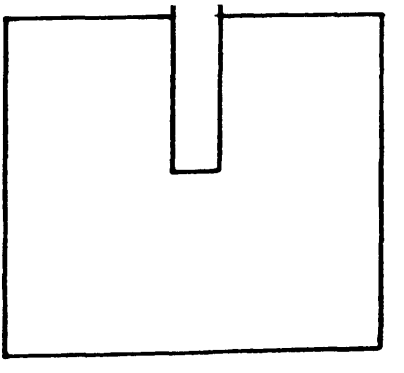

FIGURE (6.67) : Exact locations of strain gauges in the slab of model MS4 as shown in Figures (6.62), (6.64), (6.65) and (6.66)

6.4.2.1 Model MS5

The plan of this model is shown in Figure (6.68). The amount of total wall reinforcement was 34% more than that of model MS4 and the bars were concentrated at the two edges of the wall as shown in Figure (6.69). The flexural steel reinforcement in the slab was designed to resist a lateral load equals 155.0 KN as well as an ultimate gravity load of 18.0 KN. The amount of steel required in the area just around the wall–slab connection was used throughout the slab in this model. No curtailment of the longitudinal bars was done at the back of the slab. The amount of reinforcement was more than that required in other parts of the slab. The shear reinforcement in the form of closed vertical stirrup was provided in the slab where the shear stress exceeded allowable concrete shear stress. Figures (6.70– a) and (6.70– b) show the top and bottom reinforcement layout along with the arrangement of shear reinforcement in the slab. To ensure the proper anchorage of the stirrup, nominal bottom reinforcement was provided at the bottom of the slab. This model is similar to model MT6[23] which was designed and tested for the same load but without using any shear reinforcement in the slab.

Behaviour of the Model

A number of cracks parallel to loaded edge appeared on the top surface of the slab at a lateral load of 21% of design load as shown in Figure (6.71– a). In the next load increment i.e., at 28% of design load, more new cracks were observed as shown in Figure (6.71– b). The cracks were generally normal to the inner edge of the wall and also to the side of the wall with some cracks inclined to the wall. The shear crack in the slab at the back of the model was observed at about 89% of design load. The crack parallel to the loaded beam and at a distance about 60mm from the nose of the wall widened more than 1.0 mm and excessive deflections occurred at loads equal to the design load, implying the ductile nature of behaviour. On further loading, the rigid body movement of the

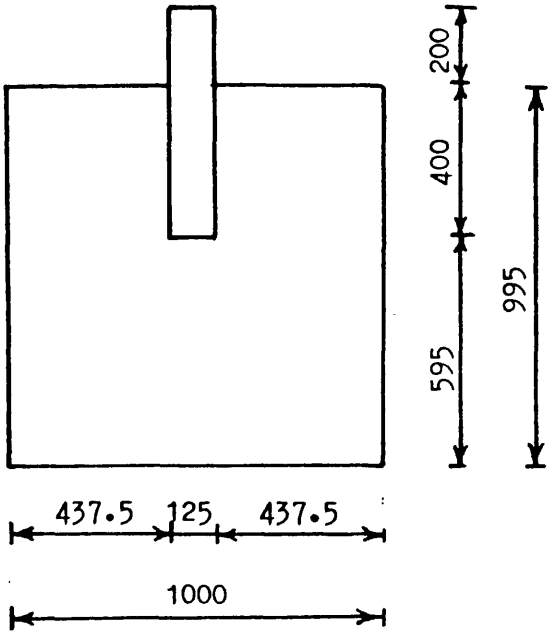

Figure (6.68) : Plan and dimensions of model MS5

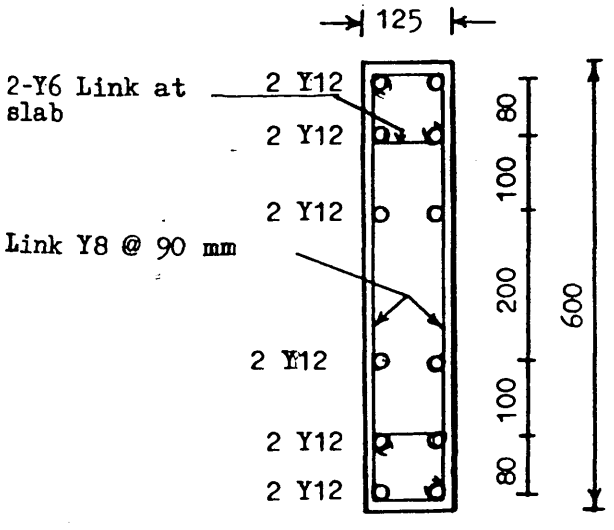

Figure (6.69) : A horizontal section in the wall of model MS5 showing the reinforcing details

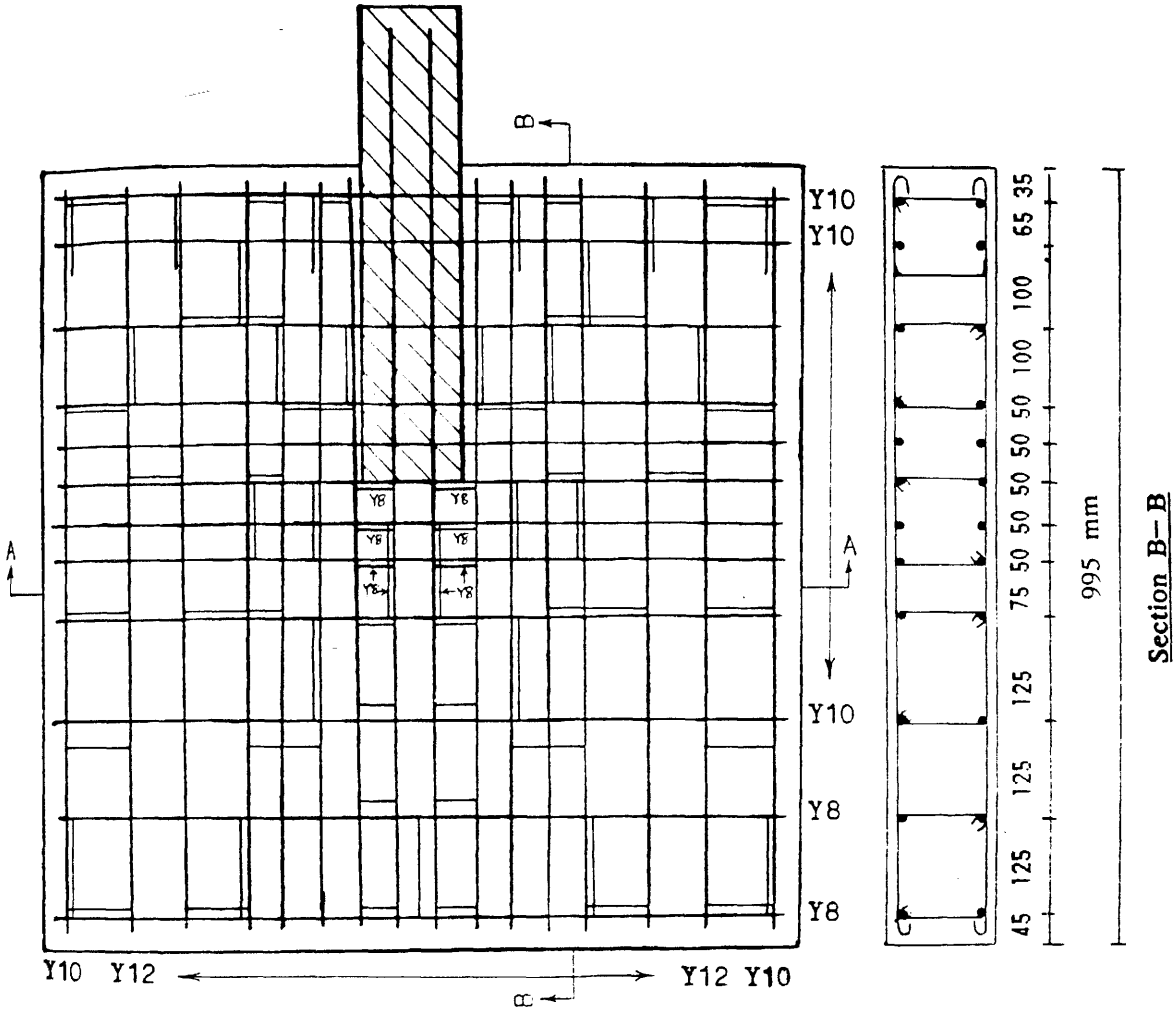

Diameters of all stirrups are 6mm except mentioned in the figure

Figure (6.70-a) : Arrangement of top reinforcing bars including closed vertical stirrup in the slab of model MS5

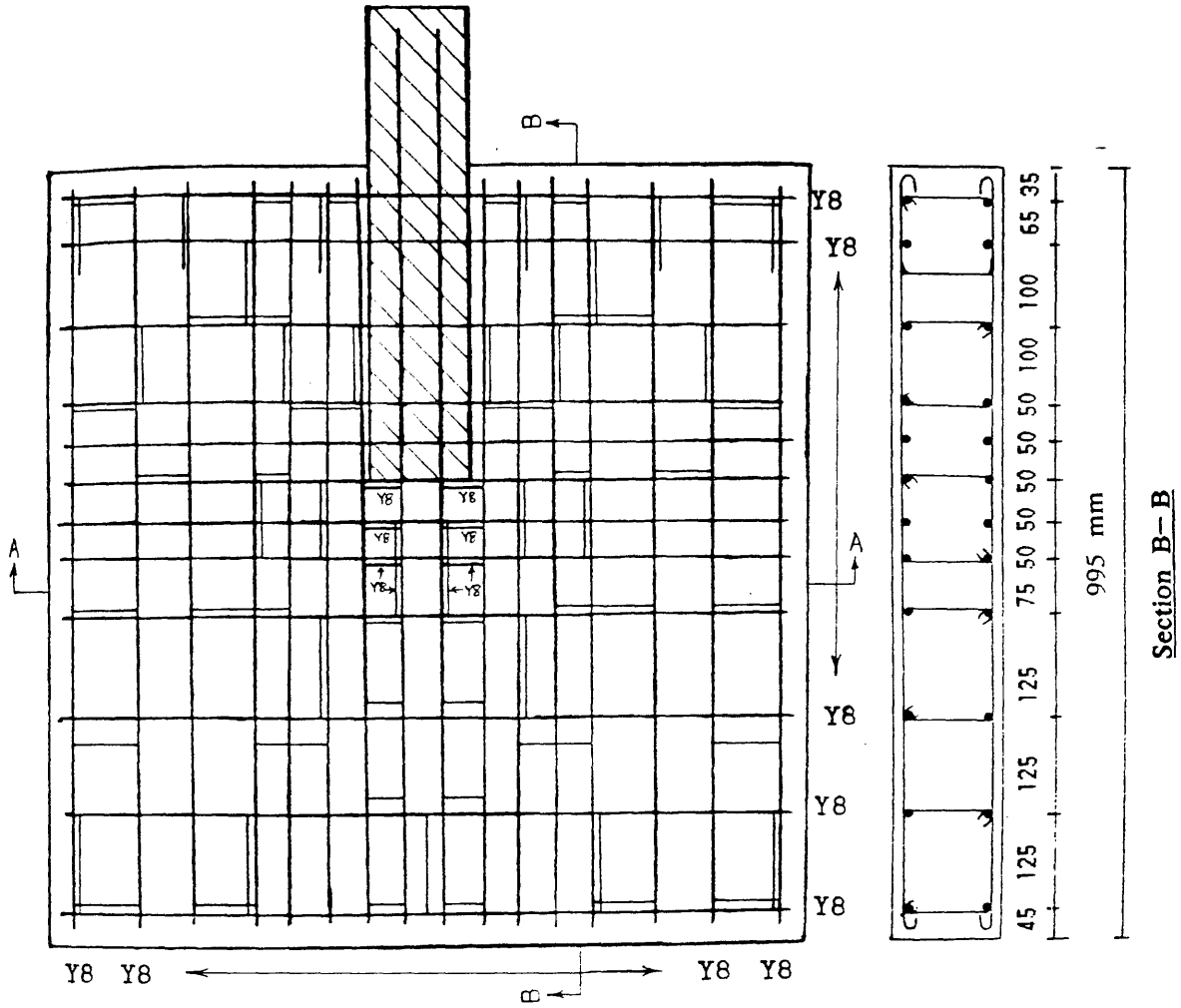

Figure (6.70-b) : Arrangement of bottom reinforcing bars including closed vertical stirrup in the slab of model MS5

model started increasing out of control and total movement was very large. The prestressed wire was tightened as much as possible to bring the wall in contact with the floor of the laboratory. The torsional (inclined) cracks which were extended towards the back of the model became very wide and prominent and the width of shear crack at the back was more than 3.0 mm at about 120% of design load. Finallly the structure failed at a lateral load of 203.0 KN (i.e., 130% of design load). The photographs showing the crack pattern of the model after failure are presented in Figure (6.73). The nondimensional load–deflection curve is shown in Figure (6.72). The results of other experimental data are shown in Figures (6.74) to (6.79). Figure (6.80) shows the exact locations of all the strain gauges used in the slab of this model.

The amount of steel required in the area just around the wall–slab connection was used throughout the slab in this model. No curtailment of the longitudinal bars was done at the back of the slab. The amount of reinforcement was more than that required in other parts of the slab. Therefore, once the reinforcement at the connection yielded, a great deal of stress redistribution took place towards the sides of the wall. That is why, some reinforcement at wall–slab connection of this model though yielded at 73% of design load, the model was capable of carrying upto 130% of design load. Slightly more shear steel was also provided in the model. The main reason behind using same steel throughout the slab in this model was the early failure of model MS4 at 86.5% of design lateral load.

6.4.2.2 Model MS6

Due to problems encountered in model MS5 due to rigid body rotation, two prestressing strands were used to anchor the wall to the floor. To allow the modification of the clamping arrangement, the wall length in this model was increased from 600 mm to 1100 mm but the length of the slab attached to the wall was kept the same at 600 mm. The plan of this model is shown in Figure (6.81). Wall reinforcement is shown in Figure (6.82).

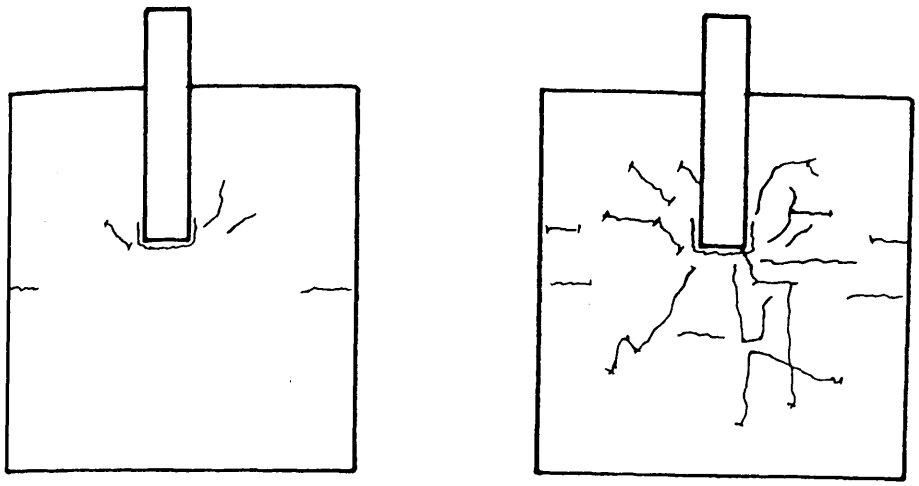

(a) at 21 %

(b) at 28 %

Figure (6.71) : Cracks initiation during testing of model MS5 at different percentages of design lateral load

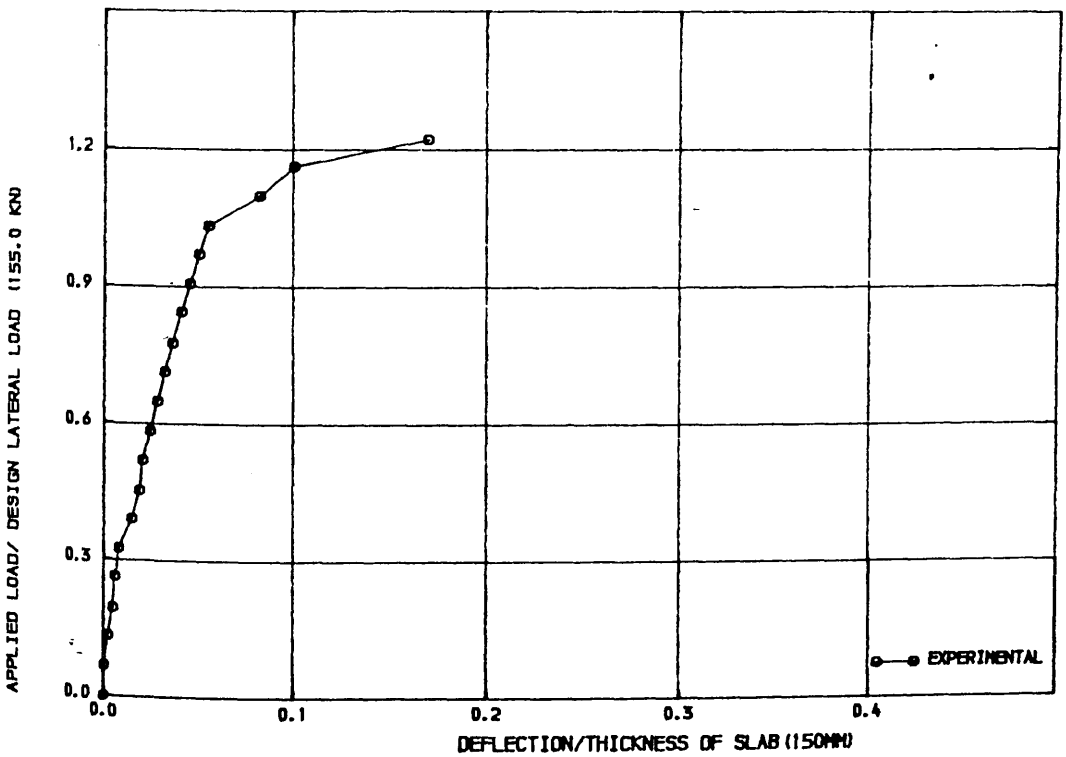

FIGURE (6.72) , LOAD-DEFLECTION CURVE FOR MODEL MS5

(a) On the tensile side

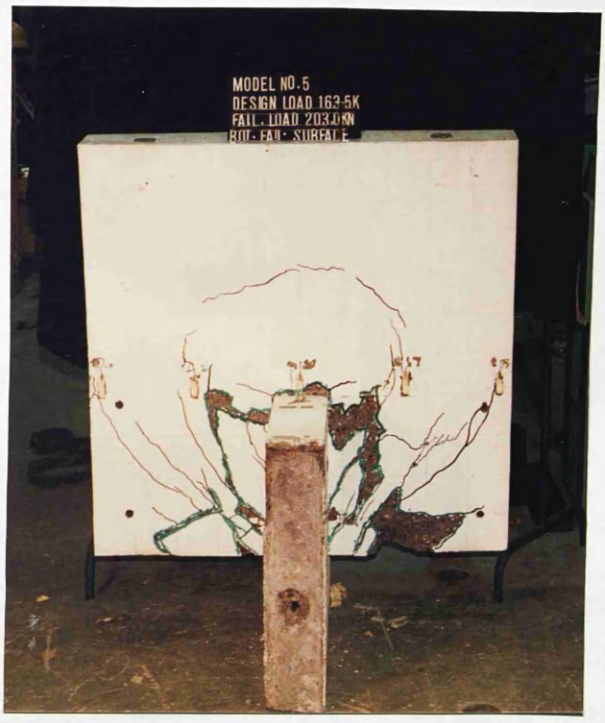

(b) On the compressive side

Figure (6.73) : Photographs showing the crack pattern on the slab of model MS5

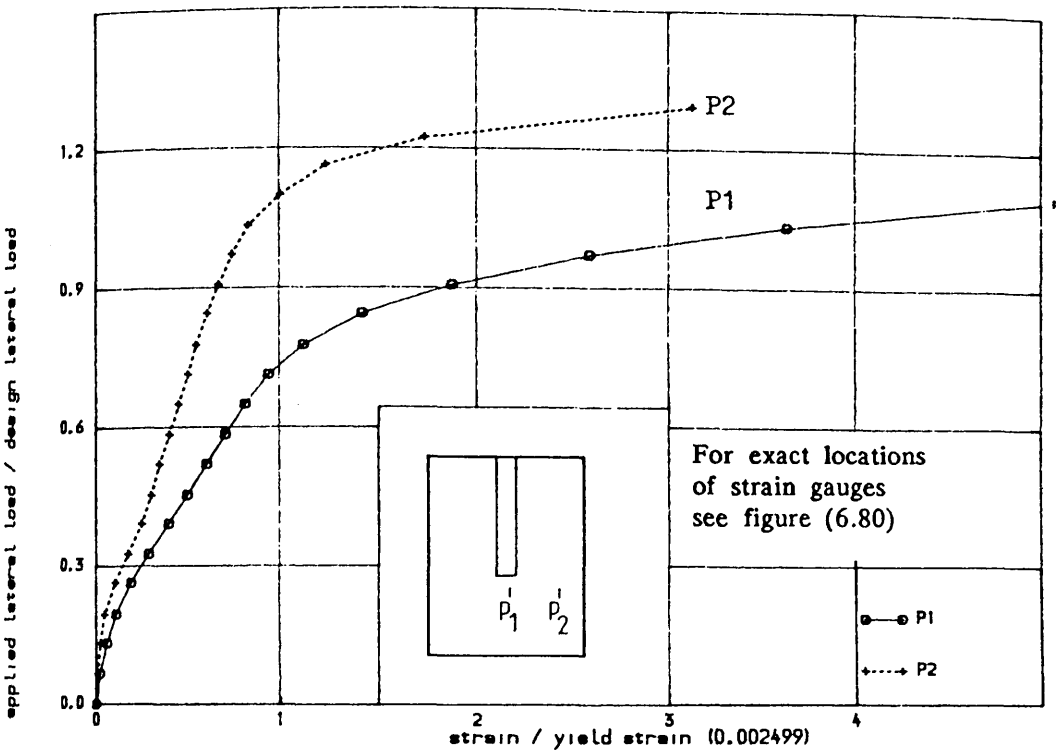

FIGURE (6.74) : TENSILE STRAIN IN STEEL IN WINDWARD DIRECTION ALONG TRANSVERSE SECTION IN THE SLAB OF MODEL MS5

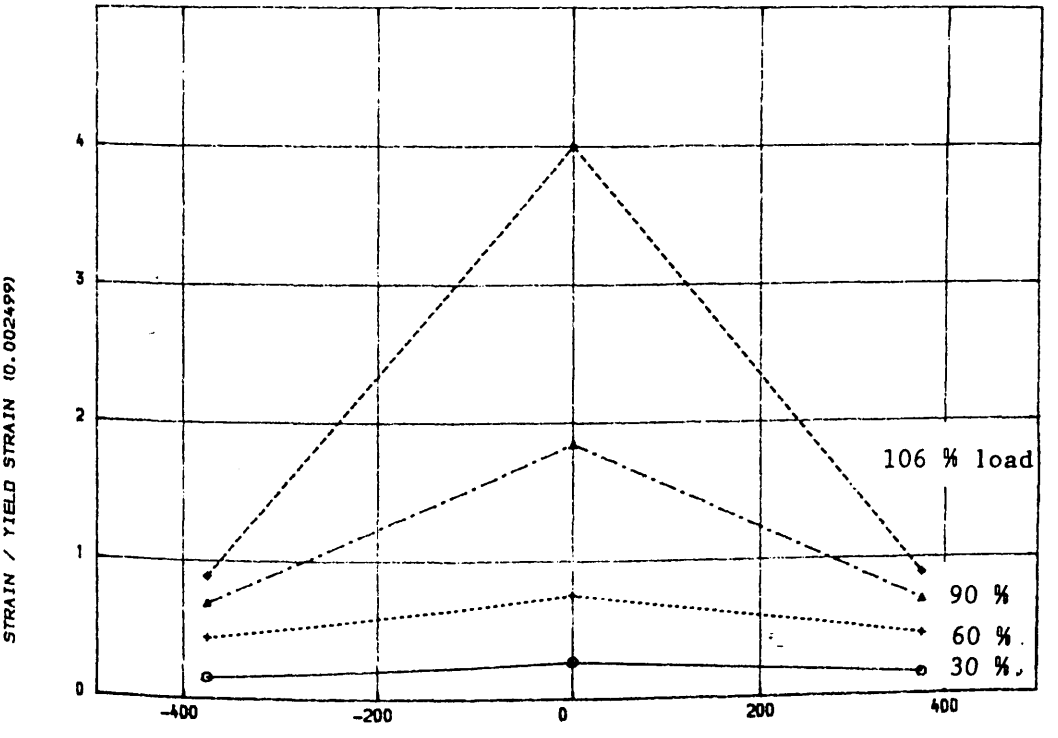

FIGURE (6.75) : VARIATION OF STRAIN IN STEEL IN WINDWARD DIRECTION ALONG TRANSVERSE SECTION AT DIFFERENT STAGES OF LOADING IN THE SLAB OF MODEL MS5

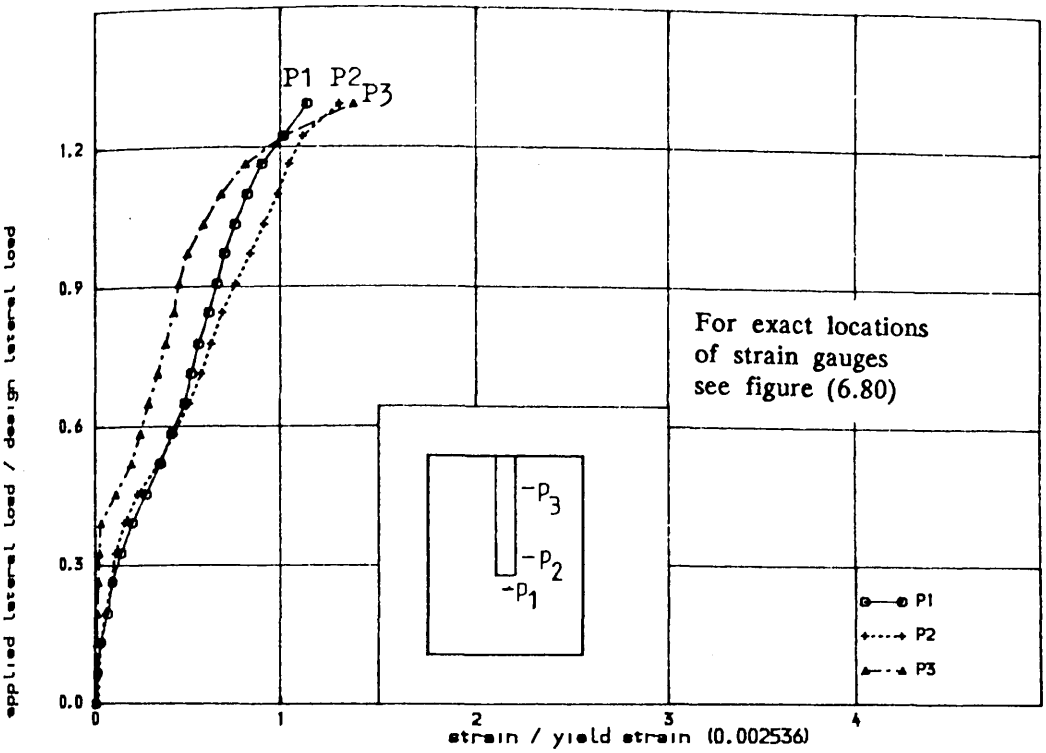

FIGURE (6.76) : TENSILE STRAIN IN STEEL IN TRANSVERSE DIRECTION IN THE SLAB OF MODEL MS5

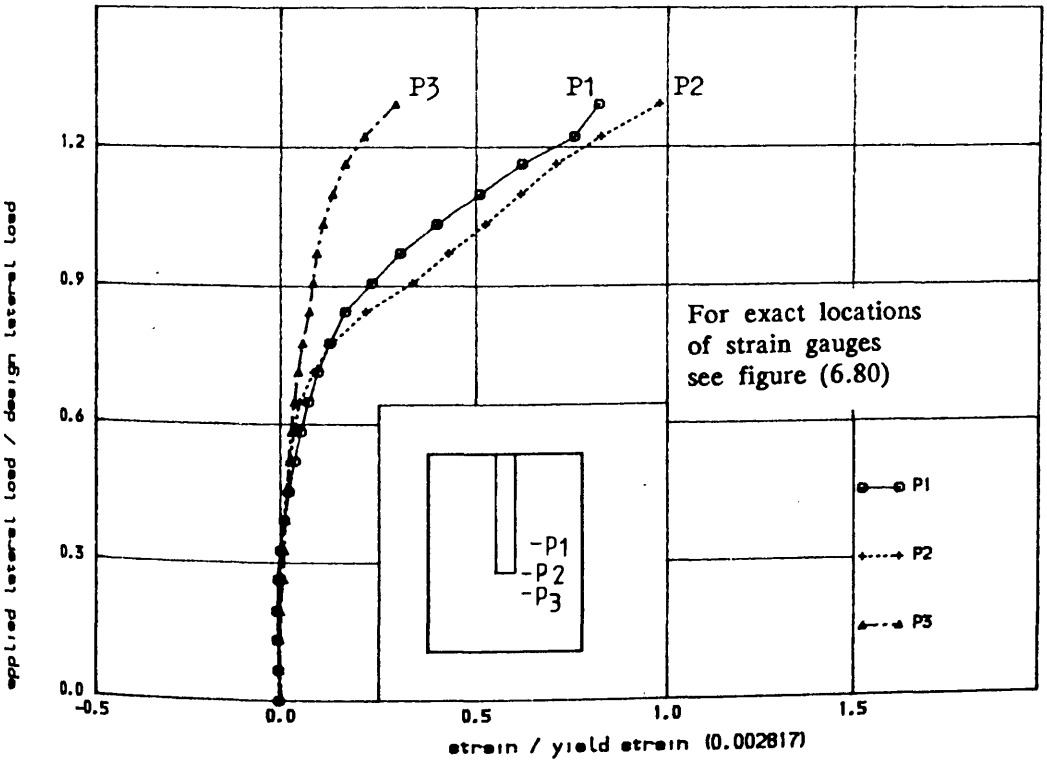

FIGURE (6.77) : TENSILE STRAIN IN CLOSED VERTICAL STIRUP AT DIFFERENT LOCATIONS IN THE SLAB OF MODEL MS5

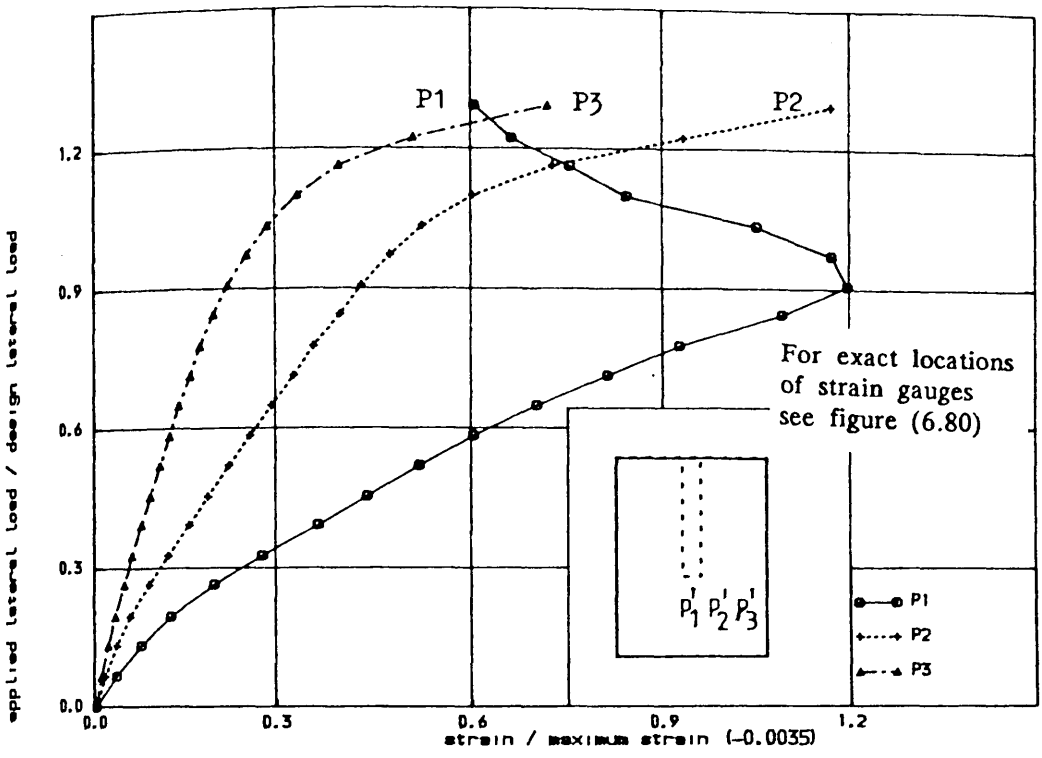

FIGURE (6.78) , COMPRESSIVE STRAIN IN CONCRETE IN WINDWARD DIRECTION IN THE SLAB OF MODEL MS5

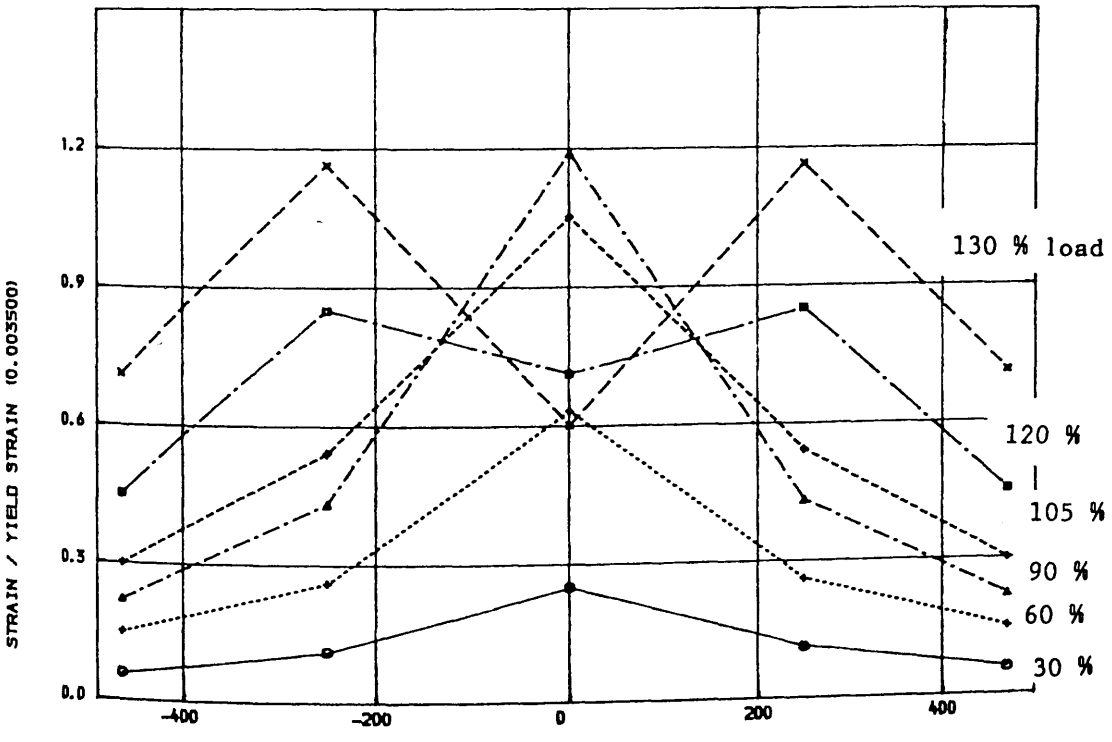

FIGURE (6.79) , VARIATION OF COMPRESSIVE STRAIN IN CONCRETE ALONG TRANSVERSE CRITICAL SECTION AT DIFFERENT STAGES OF LOADING IN THE SLAB OF MODEL MS5

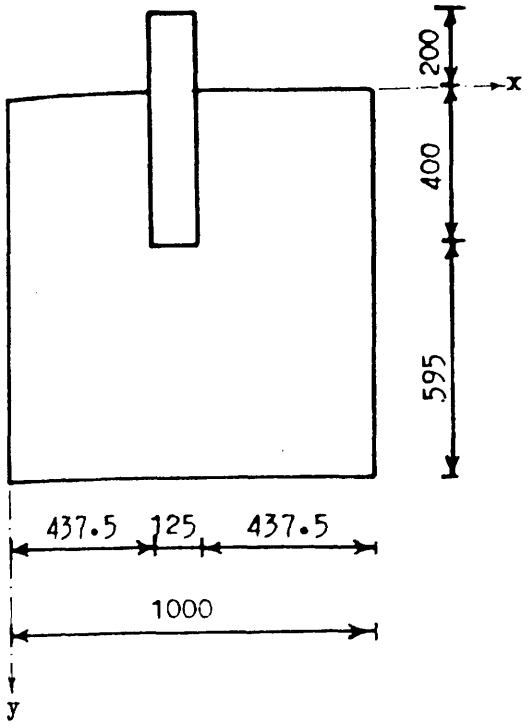

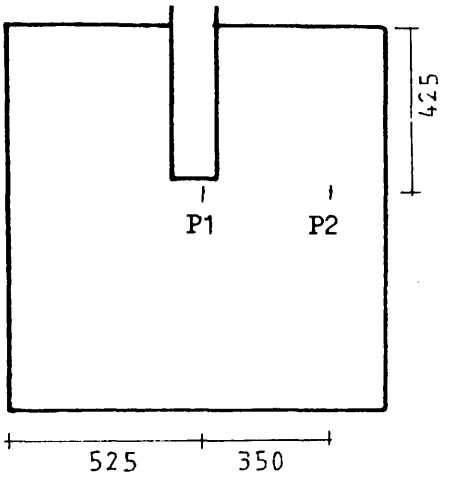

(a) Strain gauges in Figure (6.74)

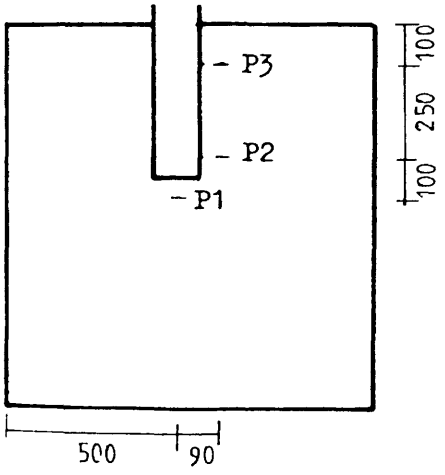

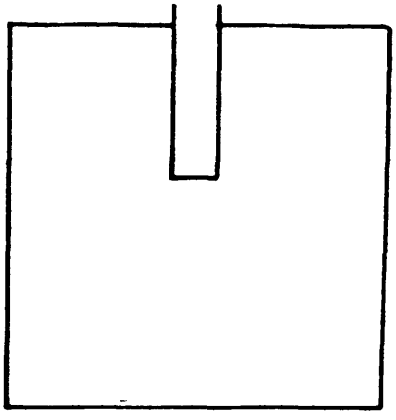

(b) Strain gauges in Figure (6.76)

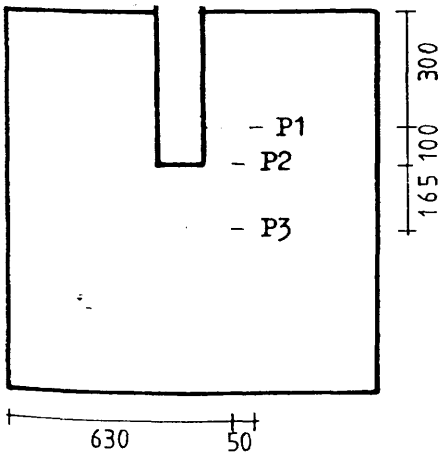

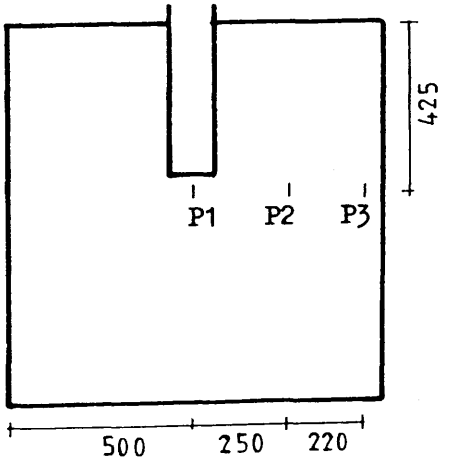

(c) Strain gauges in Figure (6.77)

(d) Strain gauges in Figure (6.78)

FIGURE (6.80) : Exact locations of strain gauges in the slab of model MS5 as shown in Figures (6.74), (6.76), (6.77) and (6.78)

A two dimensional, finite element, computer programme for linear plate bending analysis was used for the design of flexural reinforcement while for the design of shear reinforcement in slabs, computer programme "FLASH" was used for the models PS3 to MS5. The model MS6 and the rest of the models were analysed and designed using a finite element program as an elastic plate fixed along the junction with the wall and subjected to the appropriate loads and boundary conditions prevailing in the experiment. 8– noded isoparametric element and 2 x 2 Gauss rule was used for both shear and bending terms. At the centre of each element, the computer program provided the moment triad (M_x, M_y, M_{xy}) and shear forces (Q_x and Q_y) due to combined wind and gravity loadings. The moment triad was used to calculate the appropriate design moments in two orthogonal directions using the Wood– Armer[45,46] equations. The shear stress for the element was obtained by dividing the force by the element length and its effective depth. The necessary amount of steel (both flexural and shear) was calculated using the procedure as laid down in the British Code of Practice for reinforced concrete BS 8110 with materials safety factors assumed to be unity.

The flexural and shear reinforcement in the slab was designed to resist a lateral load equals 330 KN and an ultimate gravity load of 18.0 KN. Figures (6.83– a) and (6.83– b) show the required reinforcement pattern.

Behaviour of the Model

Cracks were observed for the first time on the top surface of the slab at a lateral load 20% of design load as shown in Figure (6.84– a). All the cracks started from the tip of the wall. Two of them, originating from the wall, were inclined towards the sides. On further loading, earlier cracks widened and extended a little and were joined by new crack. The applied lateral load at failure was 343 KN (104% of design lateral load). The photographs showing the crack pattern of this model after failure are presented in Figure (6.86). The wind load– displacement curve of the model is shown in Figure (6.85). Figure (6.87)

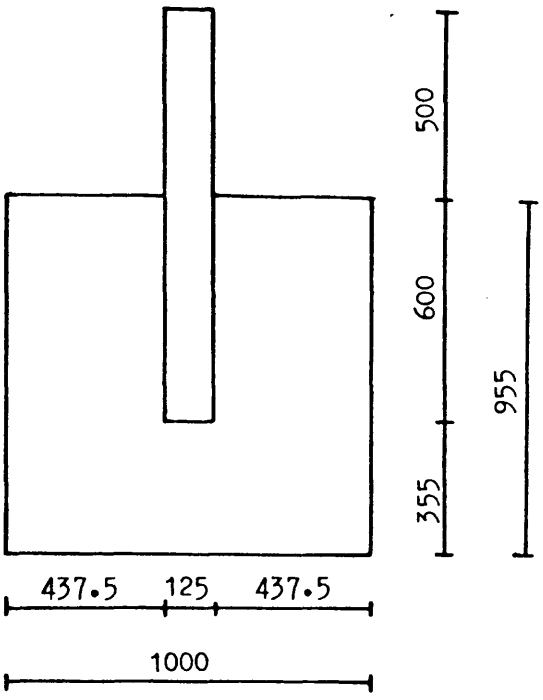

Figure (6.81) : Plan and dimensions of model MS6

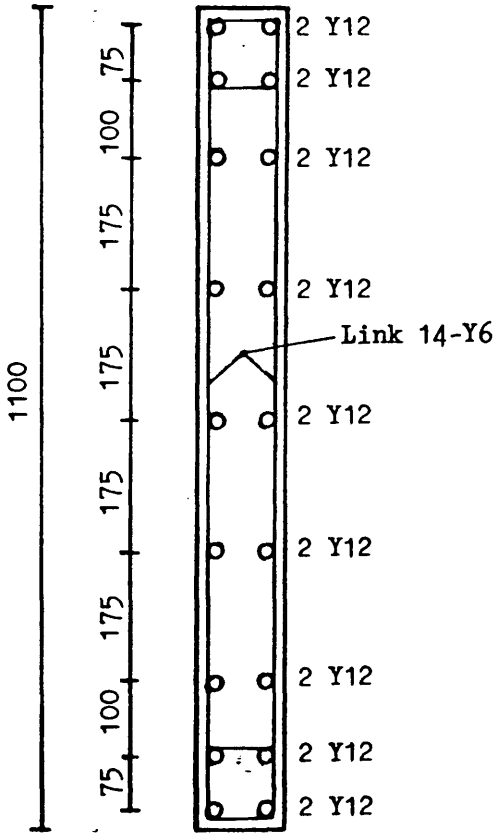

Figure (6.82) : A horizontal section in the wall of model MS6 showing the reinforcing details

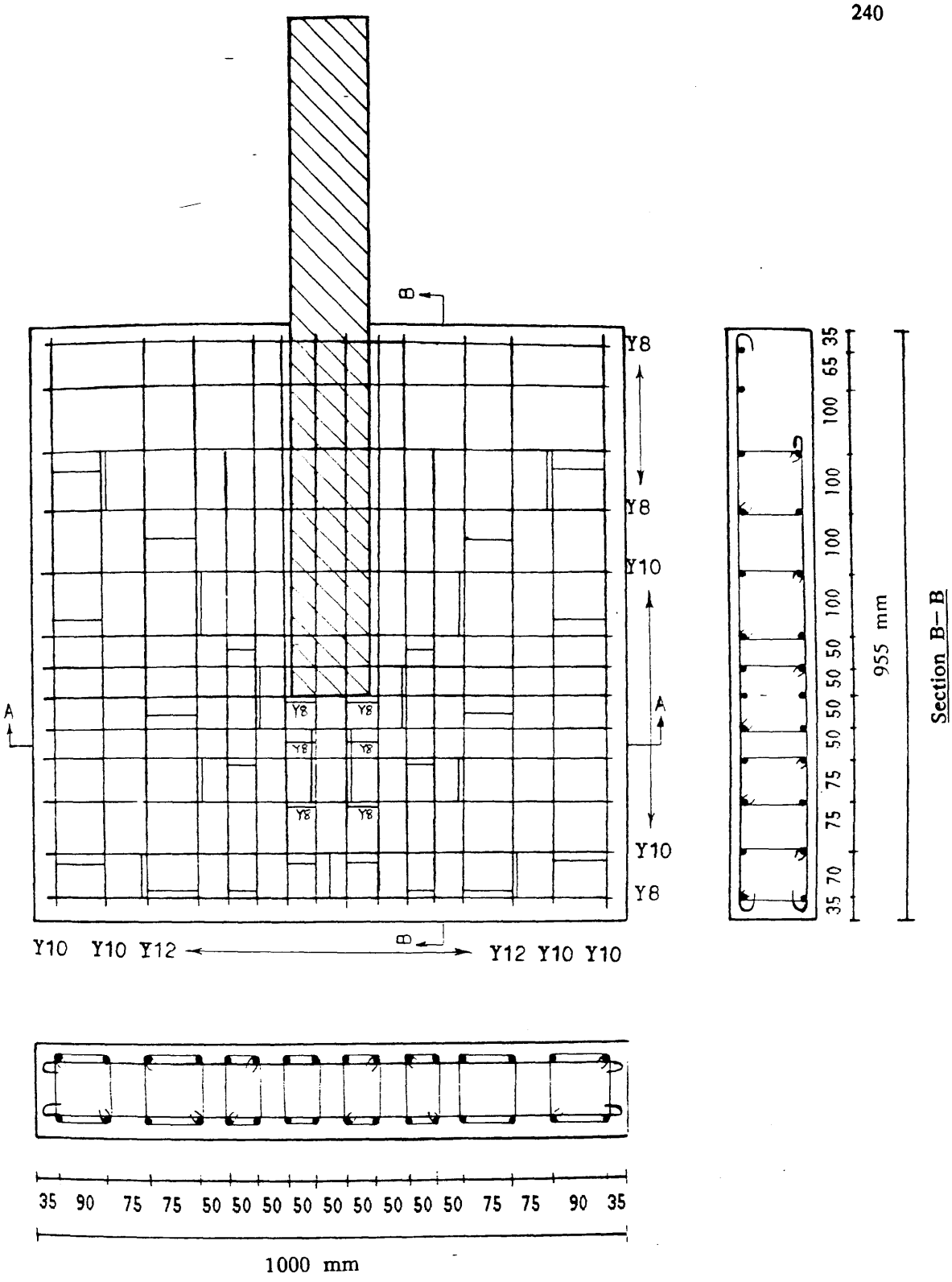

Section A–A

Diameters of all stirrups are 6mm except mentioned in the figure

Figure (6.83-a) : Arrangement of top reinforcing bars including closed vertical stirrup in the slab of model MS6

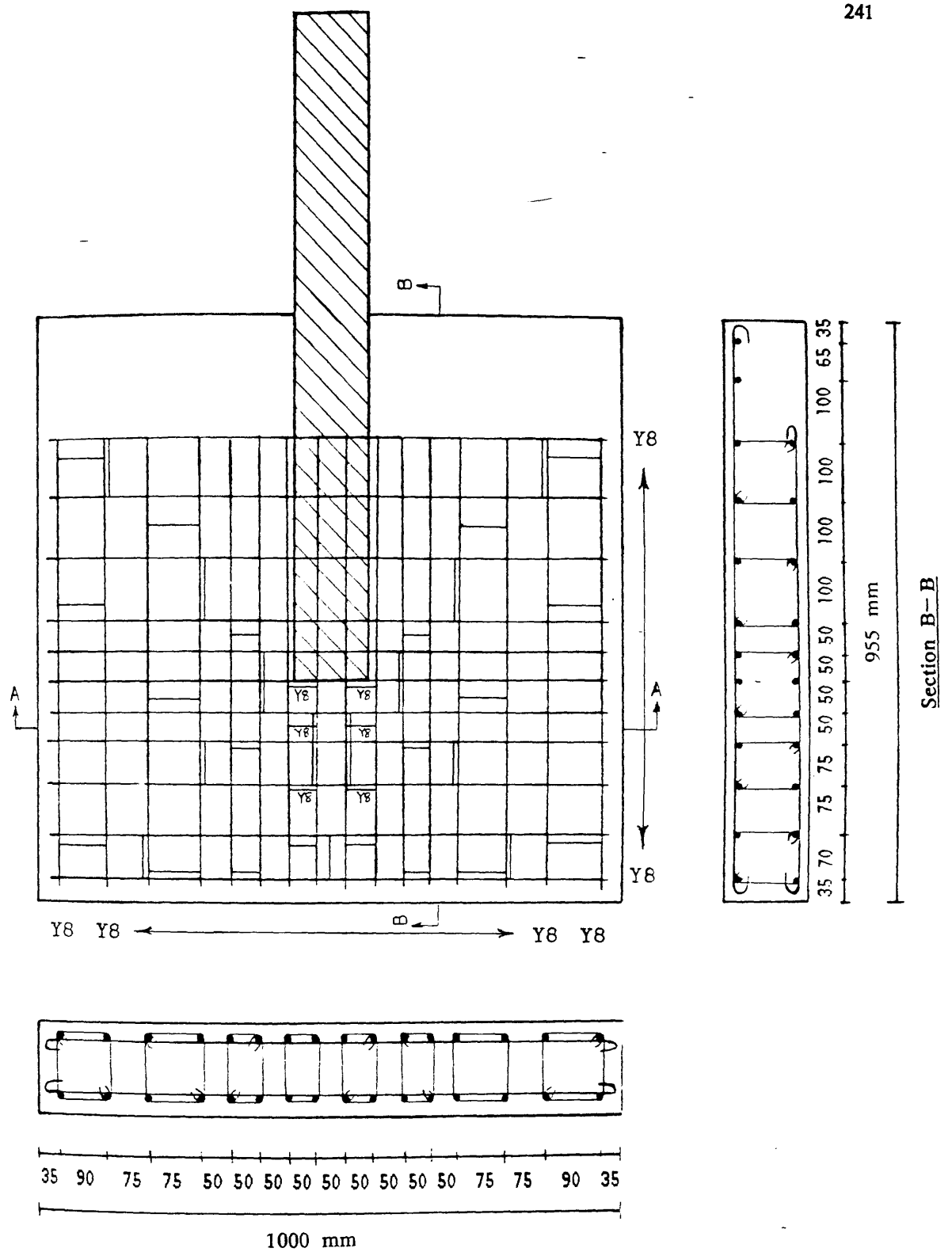

Section A–A

Diameters of all stirrups are 6mm except mentioned in the figure

Figure (6.83-b) : Arrangement of bottom reinforcing bars including closed vertical stirrup in the slab of model MS6

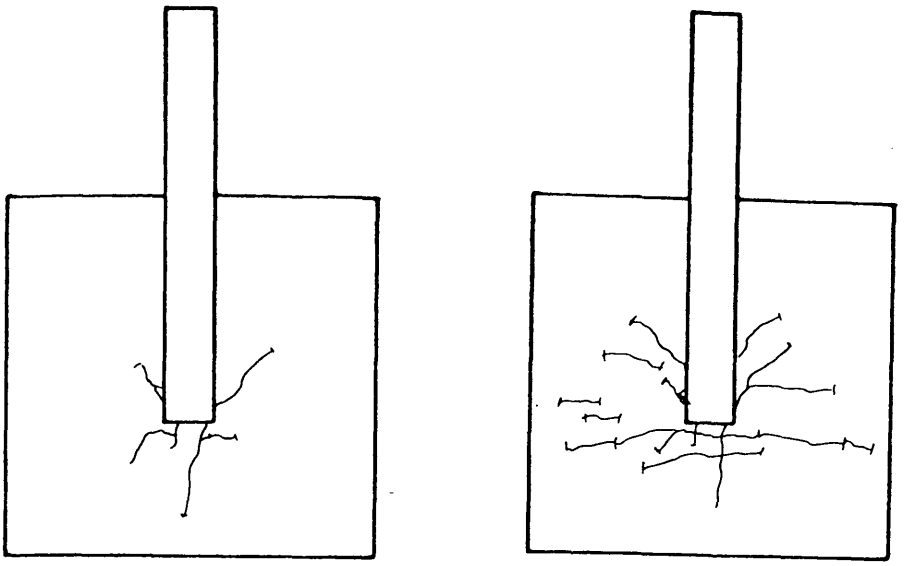

(a) at 20 %

(b) at 27 %

Figure (6.84) : Cracks initiation during testing of model MS6 at different percentages of design lateral load

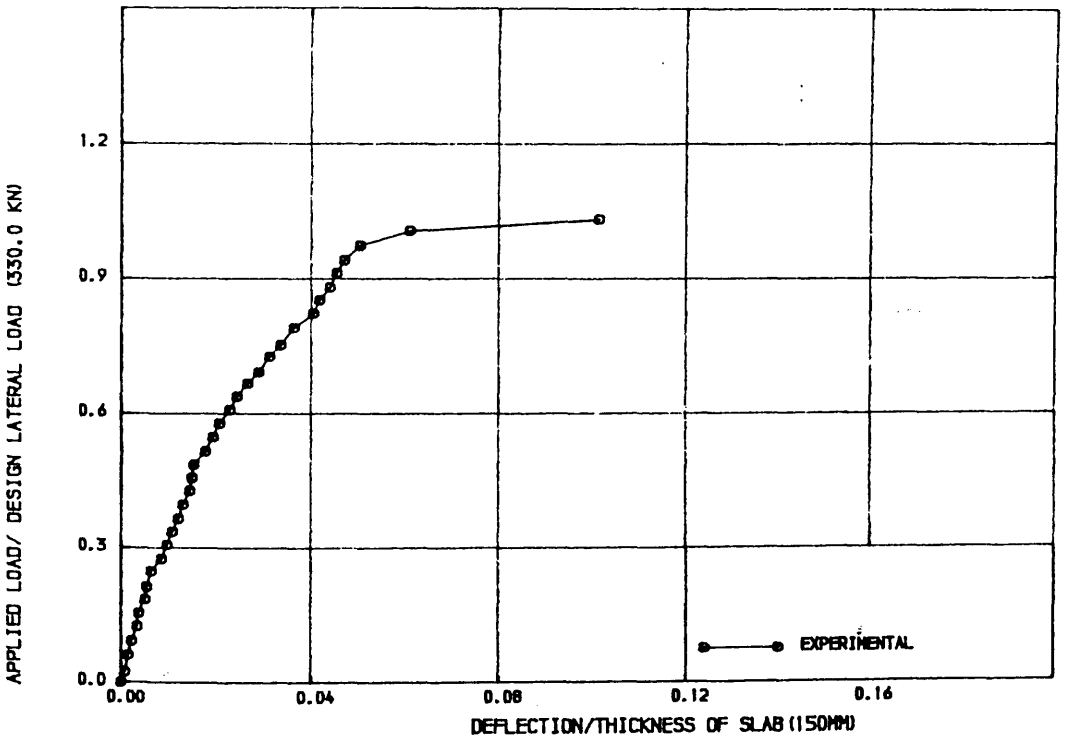

FIGURE (6.85) , LOAD-DEFLECTION CURVE FOR MODEL MS6

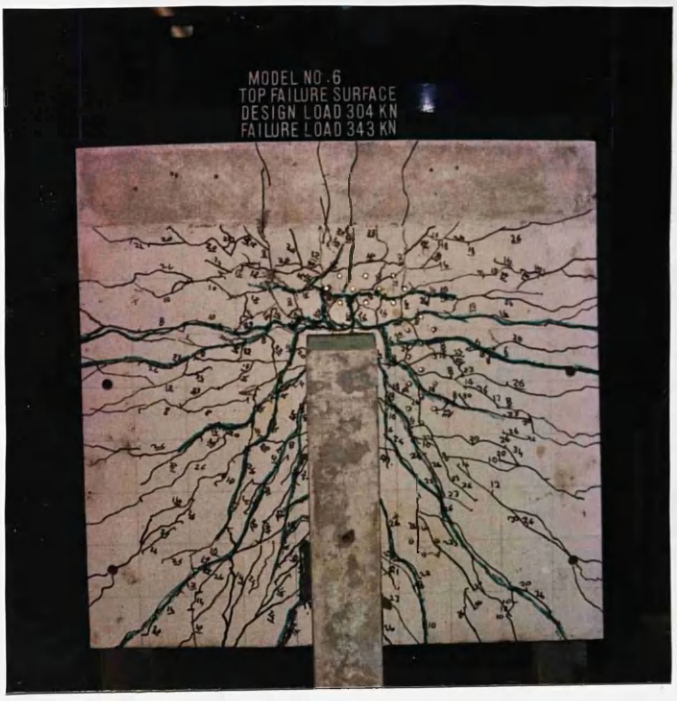

(a) On the tensile side

(b) On the compressive side

Figure (6.86) : Photographs showing the crack pattern on the slab of model MS6

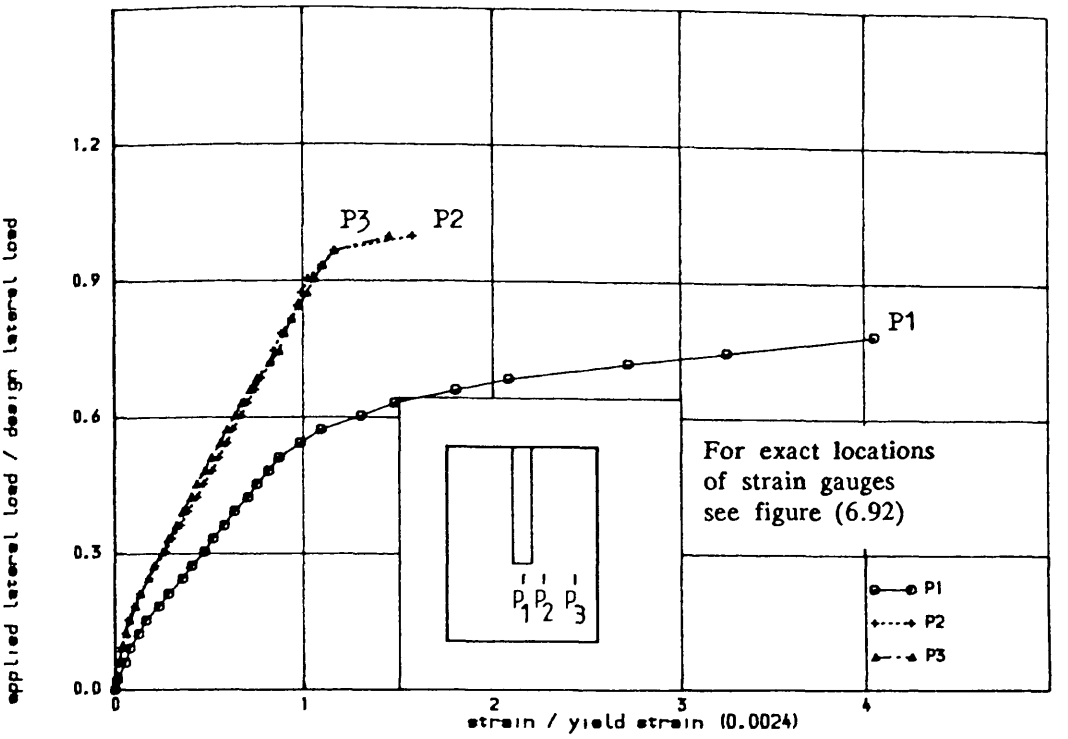

FIGURE (6.87) , TENSILE STRAIN IN STEEL IN VINDVARD DIRECTION ALONG TRANSVERSE SECTION IN THE SLAB OF MODEL MS6

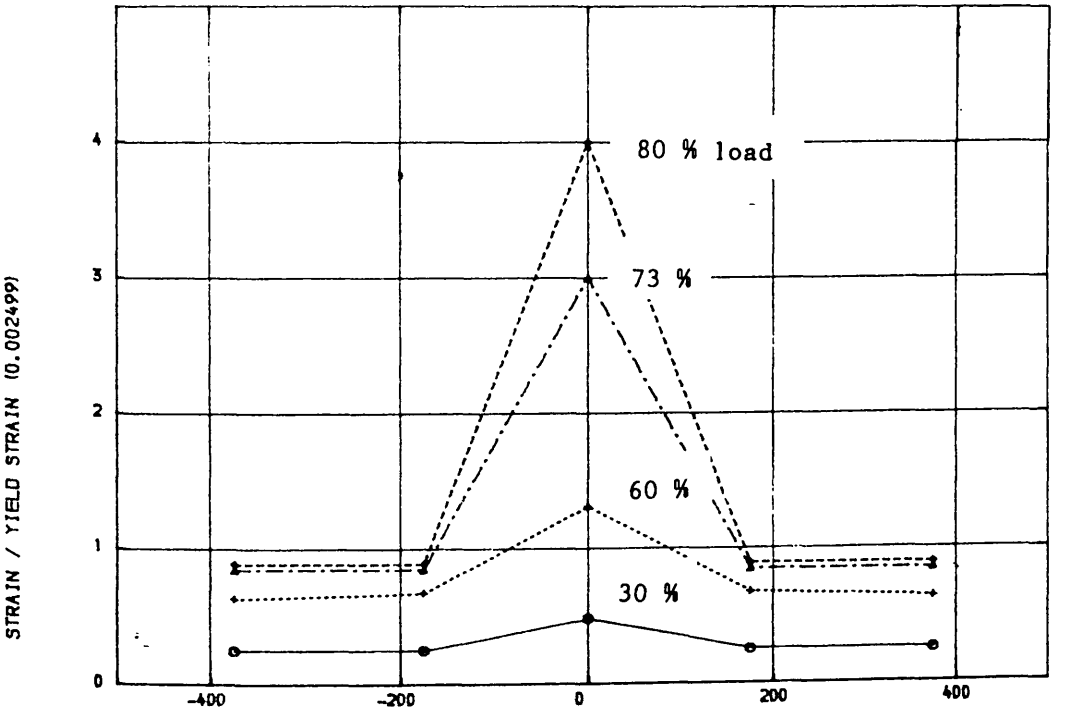

FIGURE (6.88) , VARIATION OF STRAIN IN STEEL IN VINDVARD DIRECTION ALONG TRANSVERSE SECTION AT DIFFERENT STAGES OF LOADING IN THE SLAB OF MODEL MS6

shows the tensile strain in steel in windward direction where yielding started at a lateral load 56% of the design load. The strains in steel in transverse direction at different locations in the slab is shown in Figure (6.89) from where it is clear that all the steel yielded before failure of the structure. The tensile strain in closed vertical stirrups as shown in Figure (6.90) shows that they were stressed to the full. The compressive strain on the bottom surface of slab in Figure (6.91) is generally very small near the tip of the wall (at point P1) and free edge (at point P3). The strain is reasonably high at point P2 midway between the wall and the free edge.

6.4.2.3 Model MS7

The plan of the model and the reinforcement used in the wall are shown in Figures (6.93) and (6.94). This model was similar to model MS4 except the length of the slab attached to the wall which was increased from 400 mm to 600 mm and the length of the wall itself which was increased from 600 mm to 1000 mm for modified supporting arrangement. The model MS7 was designed and tested to avoid punching shear failure and early crushing of wall which occurred during the testing of model MS4. The slab of the model was designed to resist 240.0 KN of lateral load and 18.0 KN of gravity load. The reinforcement pattern (both flexural and shear) in the slab is shown in Figure (6.95).

Behaviour of the Model

No cracks were found after the ultimate gravity load was fully applied. At 20% of design load, two cracks around the nose of the wall were observed. One of them, as shown in Figure (6.96– a), was perpendicular to the wall and the other originating from wall– tip extended in to the corridor area. On further loading, at about 30% of design load, the cracks spreaded in the slab as shown in Figure (6.96– b). The overall crack pattern is similar to model MS6. Failure took place at a lateral load of 262.0 KN (109% of design load). The crack pattern on

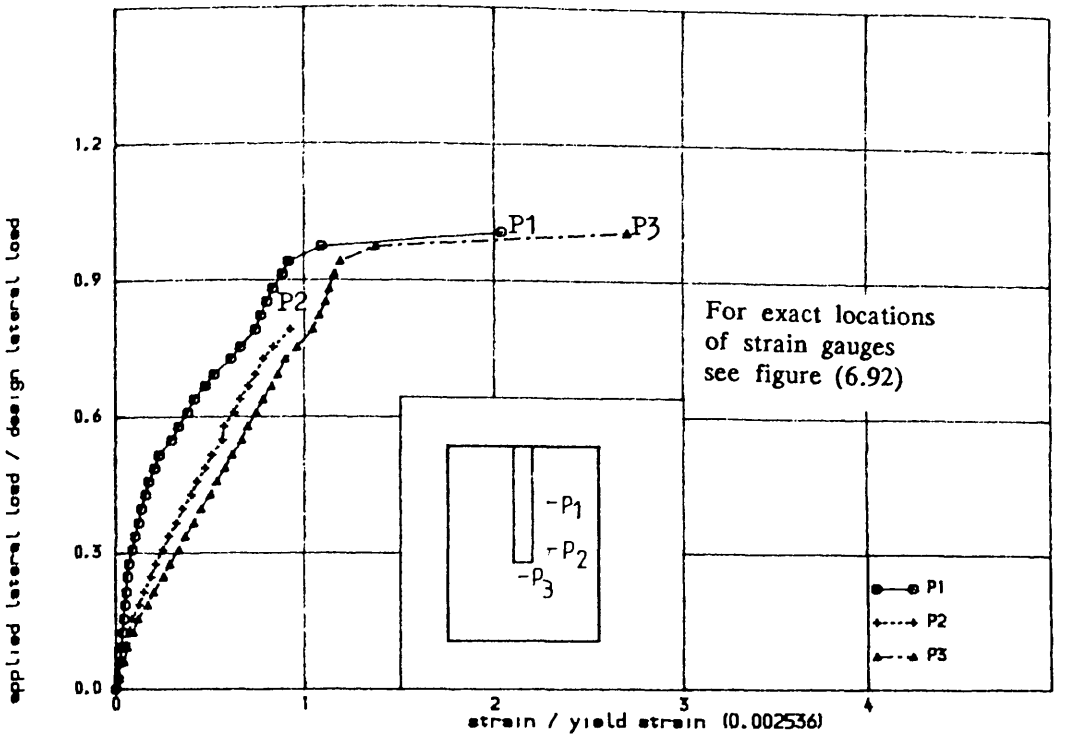

FIGURE (6.89) , TENSILE STRAIN IN STEEL IN TRANSVERSE DIRECTION IN THE SLAB OF MODEL MS6

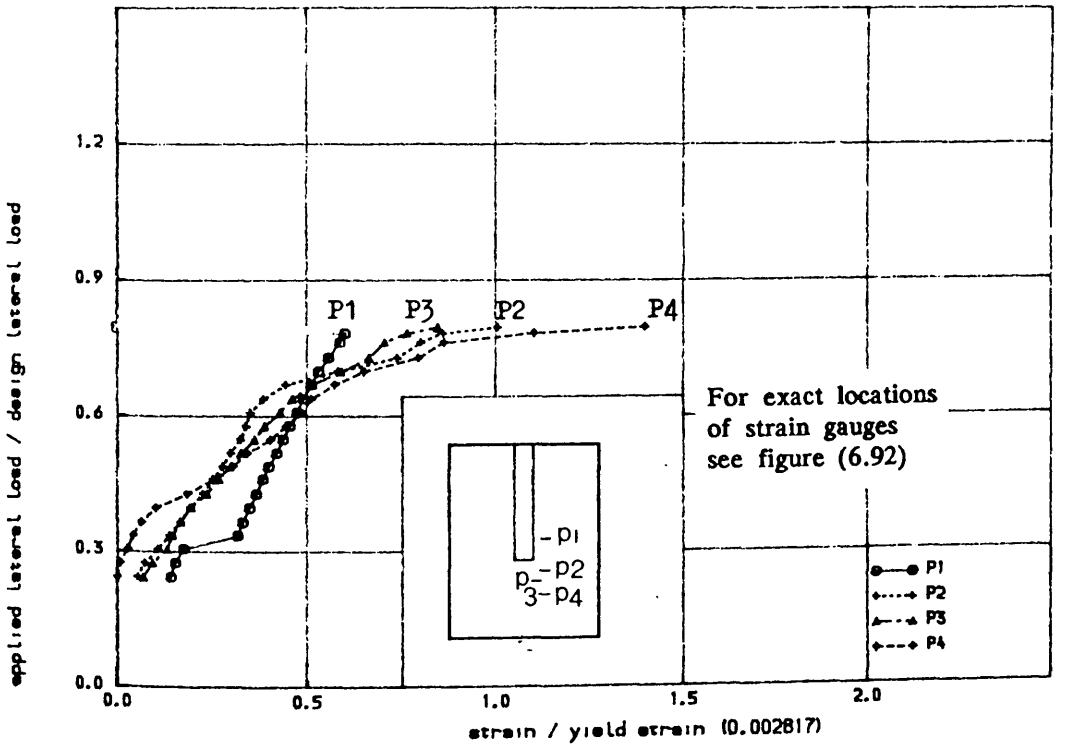

FIGURE (6.90) , STRAIN IN CLOSED VERTICAL STIRUP AT DIFFERENT LOCATIONS IN THE SLAB OF MODEL MS6

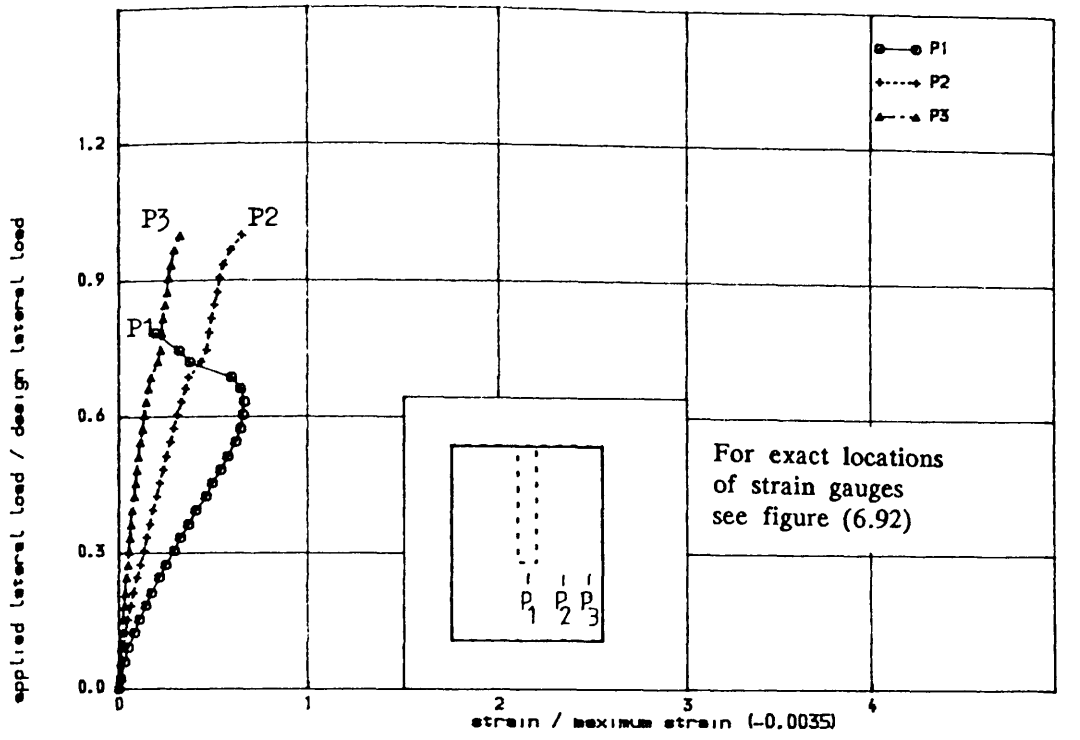

FIGURE (6.91) : COMPRESSIVE STRAIN IN CONCRETE IN WINDWARD DIRECTION IN THE SLAB OF MODEL MS6

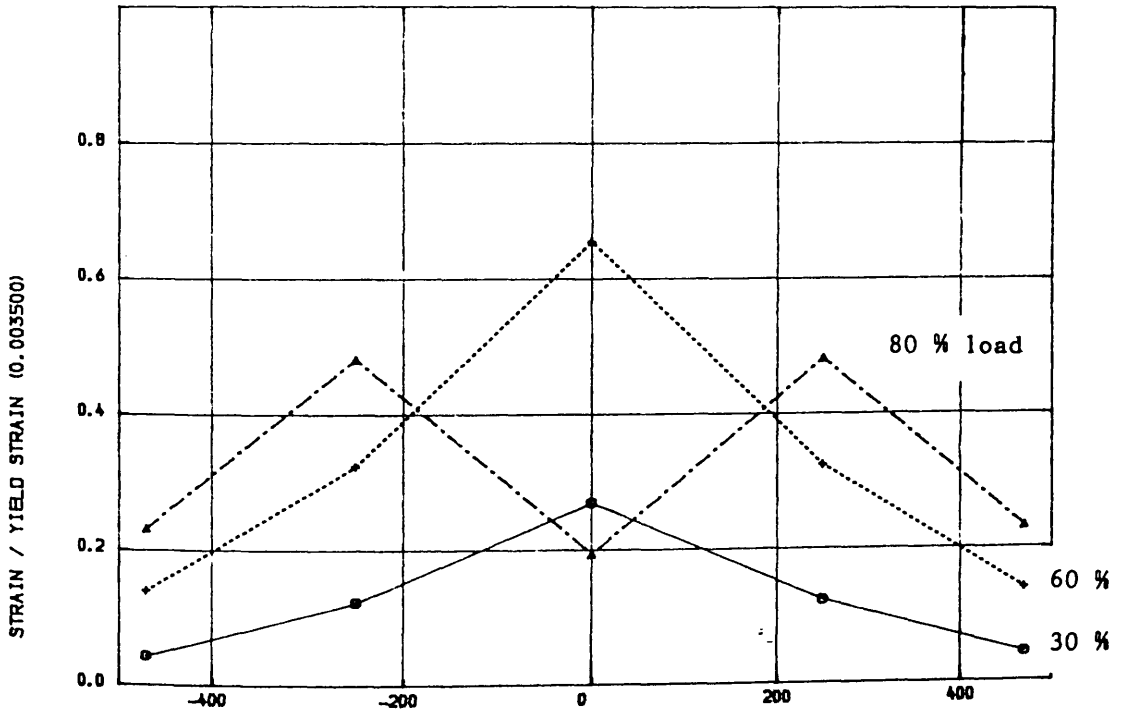

FIGURE (6.91-a) : VARIATION OF COMPRESSIVE STRAIN IN CONCRETE ALONG TRANSVERSE CRITICAL SECTION AT DIFFERENT STAGES OF LOADING IN THE SLAB OF MODEL MS6

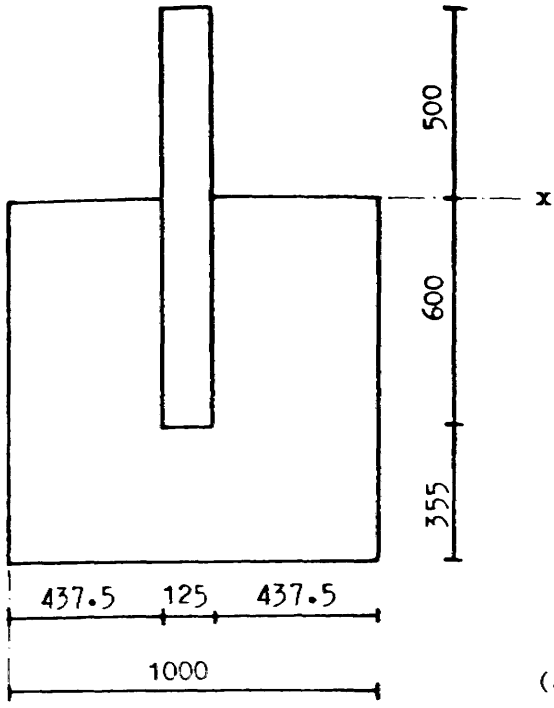

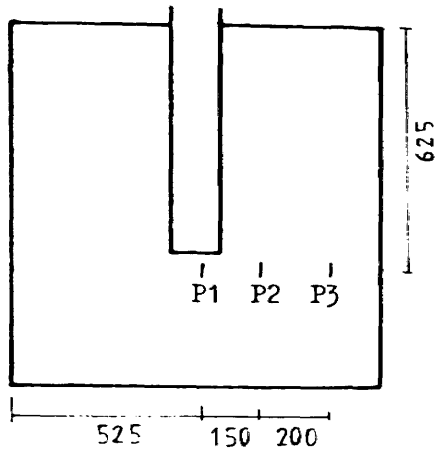

(a) Strain gauges in Figure (6.87)

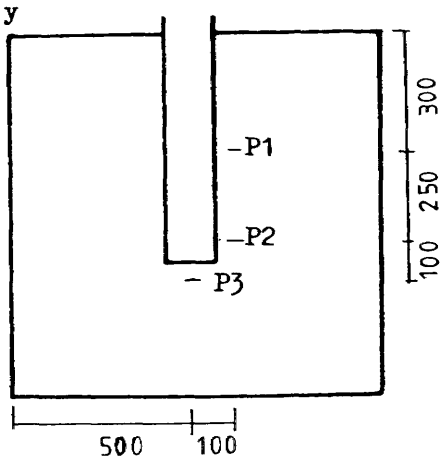

(b) Strain gauges in Figure (6.89)

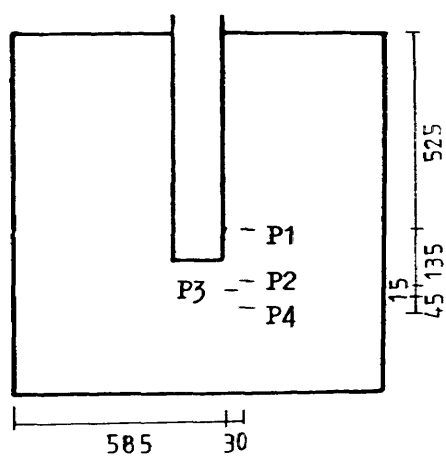

(c) Strain gauges in Figure (6.90)

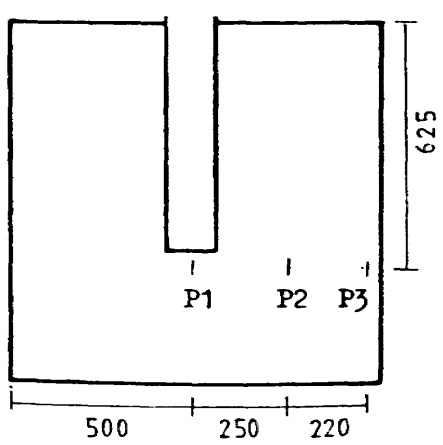

(d) Strain gauges in Figure (6.91)

FIGURE (6.92) : Exact locations of strain gauges in the slab of model MS6 as shown in Figures (6.87), (6.89), (6.90) and (6.91)

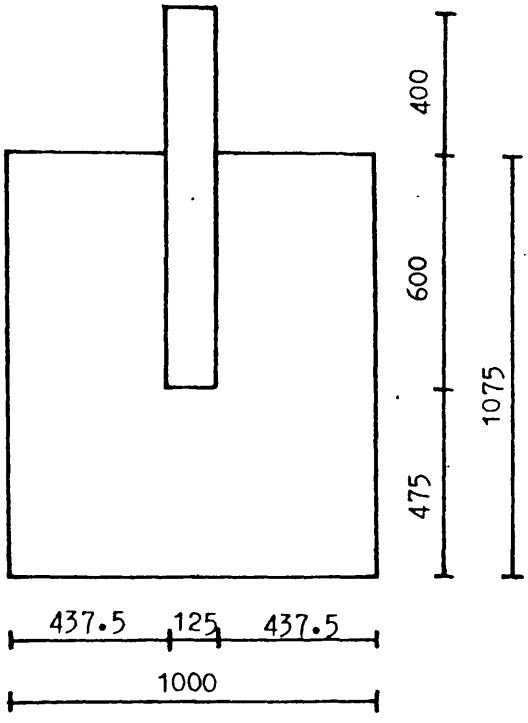

Figure (6.93) : Plan and dimensions of models MS7 and MS8

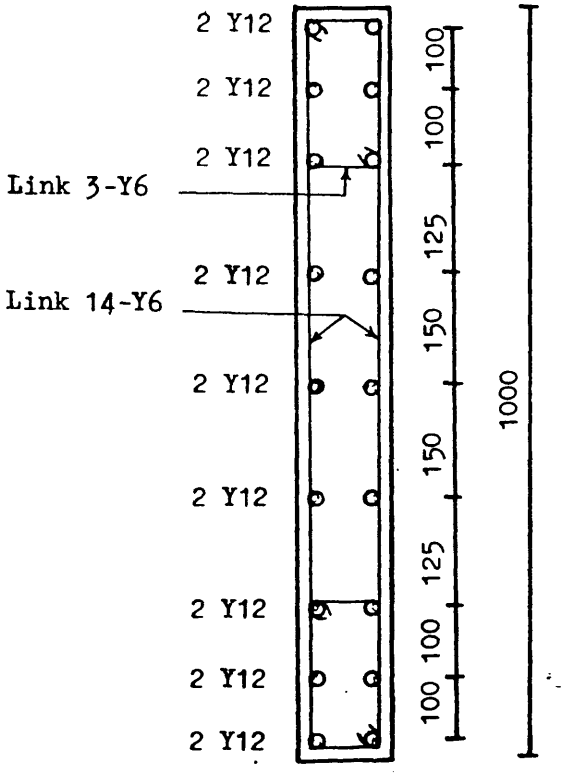

Figure (6.94) : A horizontal section in the wall of Models MS7, MS8 and MS9 showing the reinforcing details

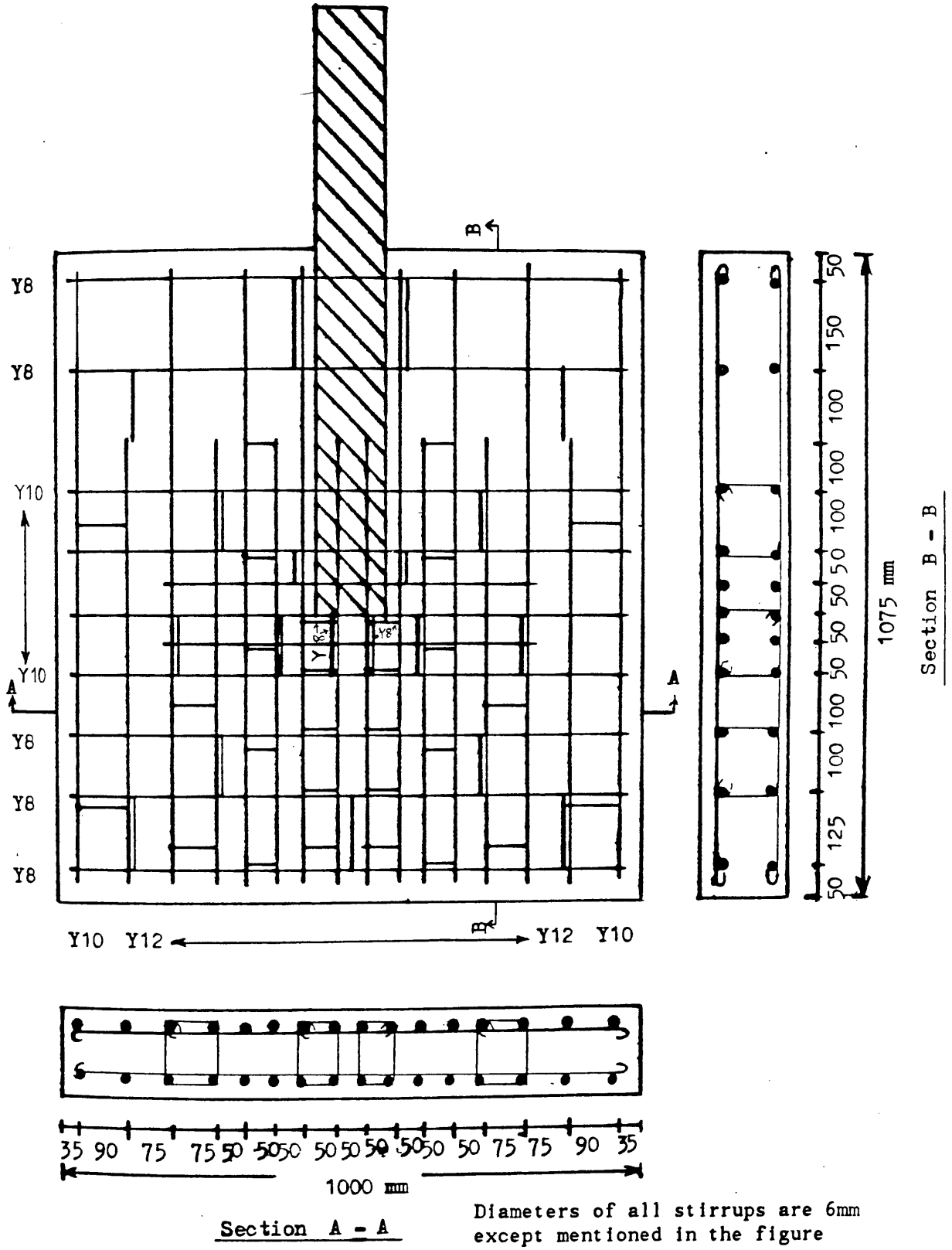

Figure (6.95-a) : Arrangement of top reinforcing bars including closed vertical stirrup in the slab of model MS7

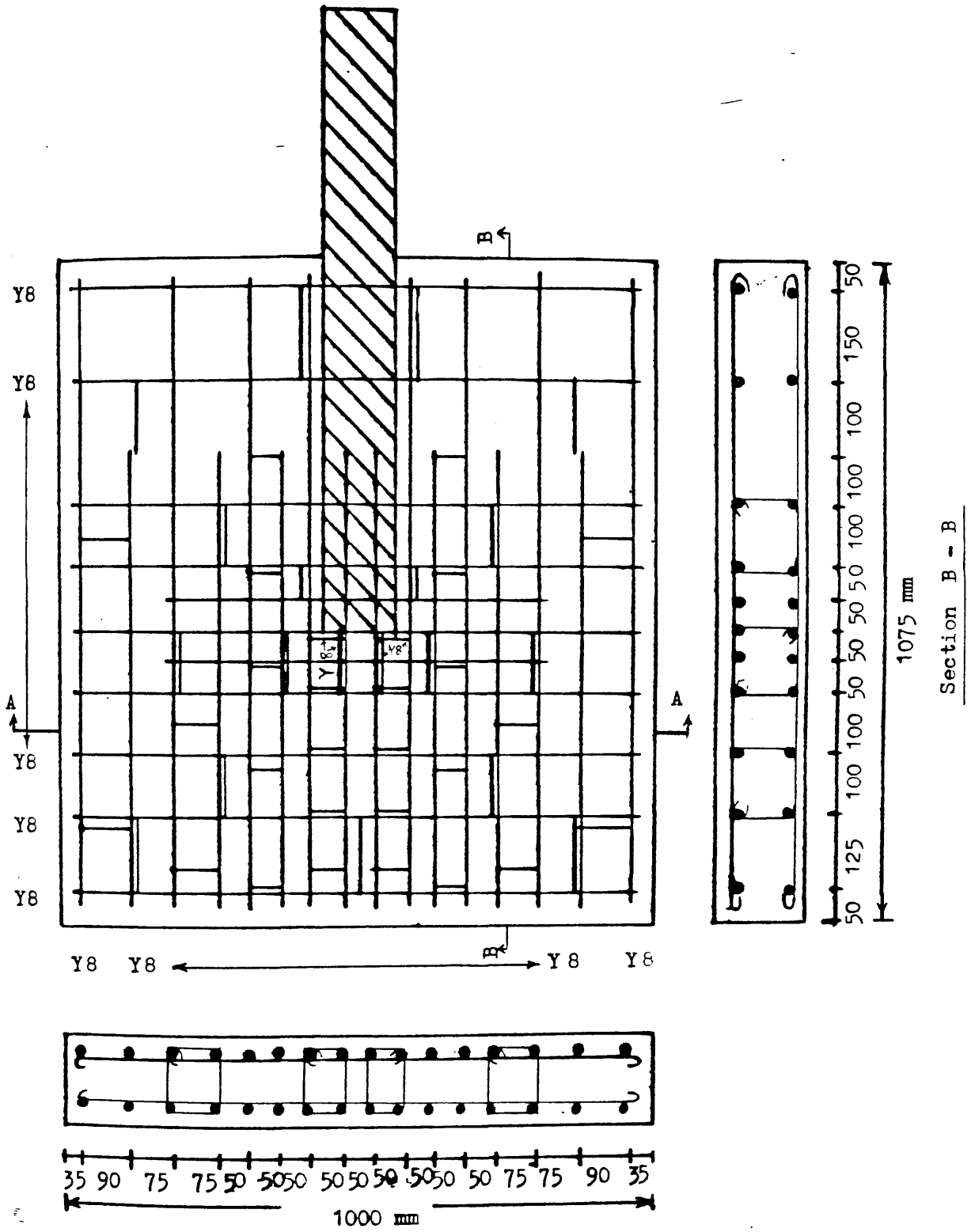

Figure (6.95-b) : Arrangement of bottom reinforcing bars including closed vertical stirrup in the slab of model MS7

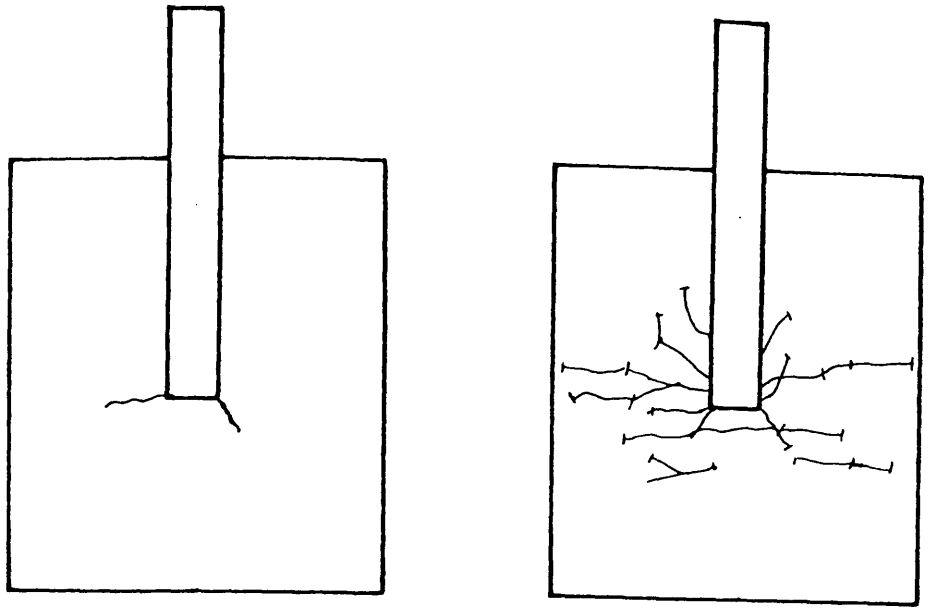

(a) at 20.5 %

(b) at 29.6 %

Figure (6.96) : Cracks initiation during testing of model MS7 at different percentages of design lateral load

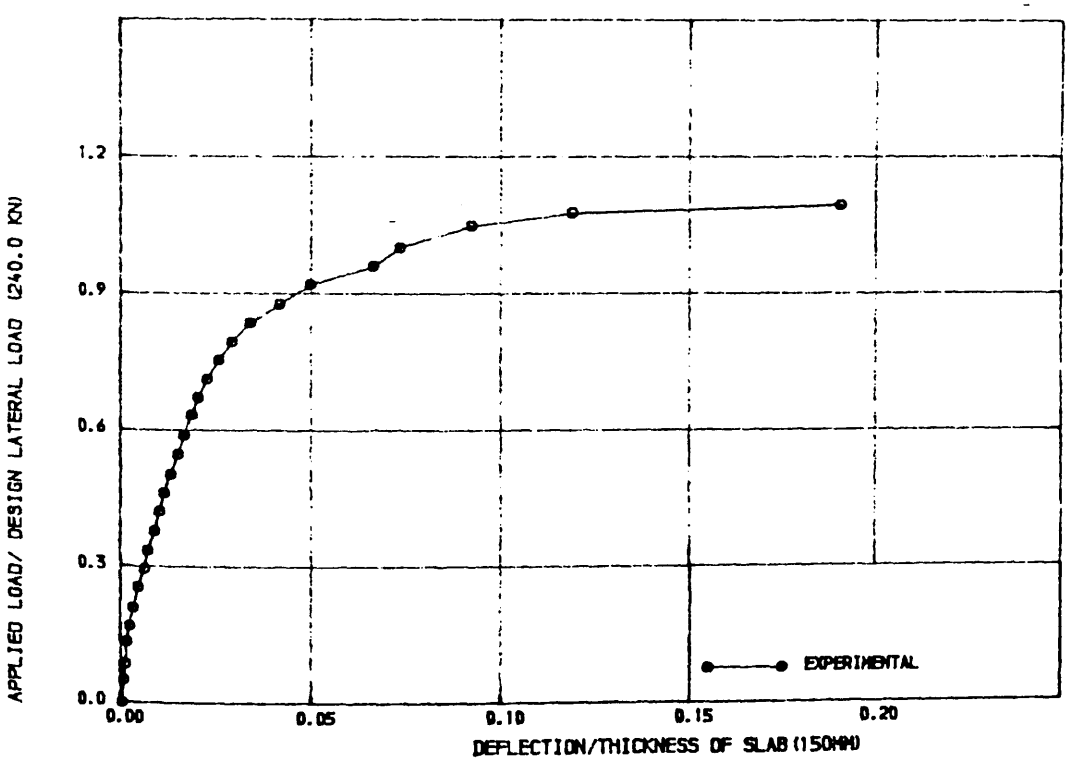

FIGURE (6.97) , LOAD-DEFLECTION CURVE FOR MODEL MS7

the tensile surface of the slab with the apparent failure line (heavily marked) is shown in Figure (6.98). The crushing pattern on the bottom compressive side of the slab after removing the broken pieces is shown in Figure (6.99). The load–deflection relationship is shown in Figure (6.97). The tensile strains in steel in windward and transverse directions are shown in Figures (6.100) and (6.102) respectively. The deflection and strain readings indicate the ductile behaviour of the slab. The closed vertical stirrups started straining at about 30% of the design load and Figure (6.103) shows the tensile strain in shear steel where nearly 90% of them yielded before failure of the model. The compressive strain in concrete is shown in Figure (6.104), while Figure (6.106) shows the vertical strain in wall near the nose.

6.4.2.4 Comparisons and Discussions

Figure (6.107) shows the lateral load–displacement curves for all the models of this series. These curves show that model MS5 with maximum corridor width suffered more displacements than MS6 and MS7 at approximately similar percentages of design load. All the three models MS5, MS6 and MS7 failed in a ductile manner at 130%, 104% and 109% of design load respectively. In all cases, large deflection and yielding of all steels in windward and transverse direction around the junction was noticed. The reason for the higher failure load for model MS5 was due to the use of same amount of flexural reinforcement all over the slab. The 'exact' reinforcement areas which are required to resist the design loads were used to predict theoretically the ultimate failure load for model MS5 using the computer programme. It was found that for the 'exact' reinforcement the theoretical failure load equals the design load, and for the 'actual' reinforcement used in the slab it has been shown in chapter seven that the theoretical failure load is 1.3 times the design load. The steel in windward direction passing through the wall started yielding at 74%, 56% and 71% of design load for models MS5, MS6 and MS7 respectively. The steel bars passing through the wall in model MS6 were yielded earlier than the adjacent steel bars resulting a large difference in the strain with the neighbouring bars (see Figure (6.88)). In models MS5 and MS7 the load–strain curves of the adjacent steel bars closely followed that of

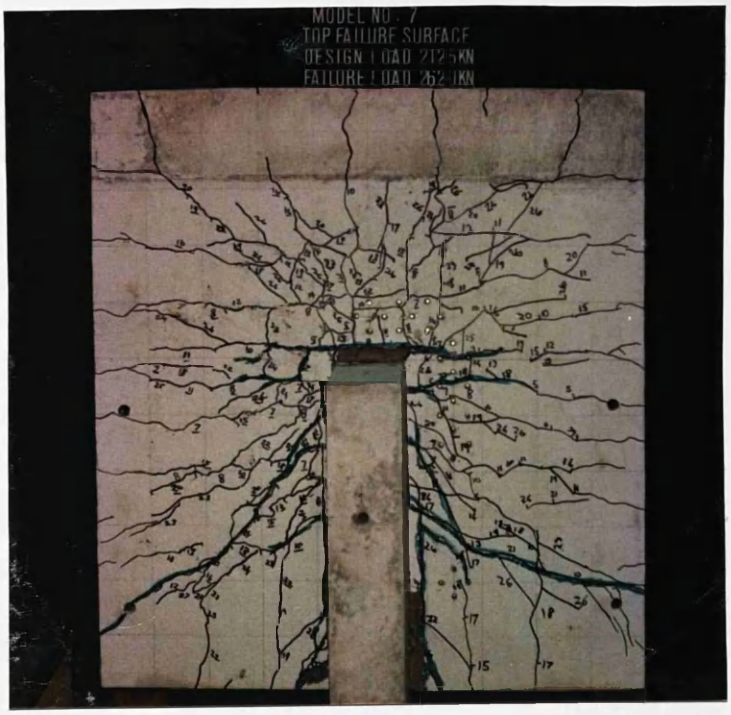

Figure (6.98) : Photograph showing the crack pattern and failure surface on the tensile side of the slab of model MS7

Figure (6.99) : Bottom failure surface of model MS7

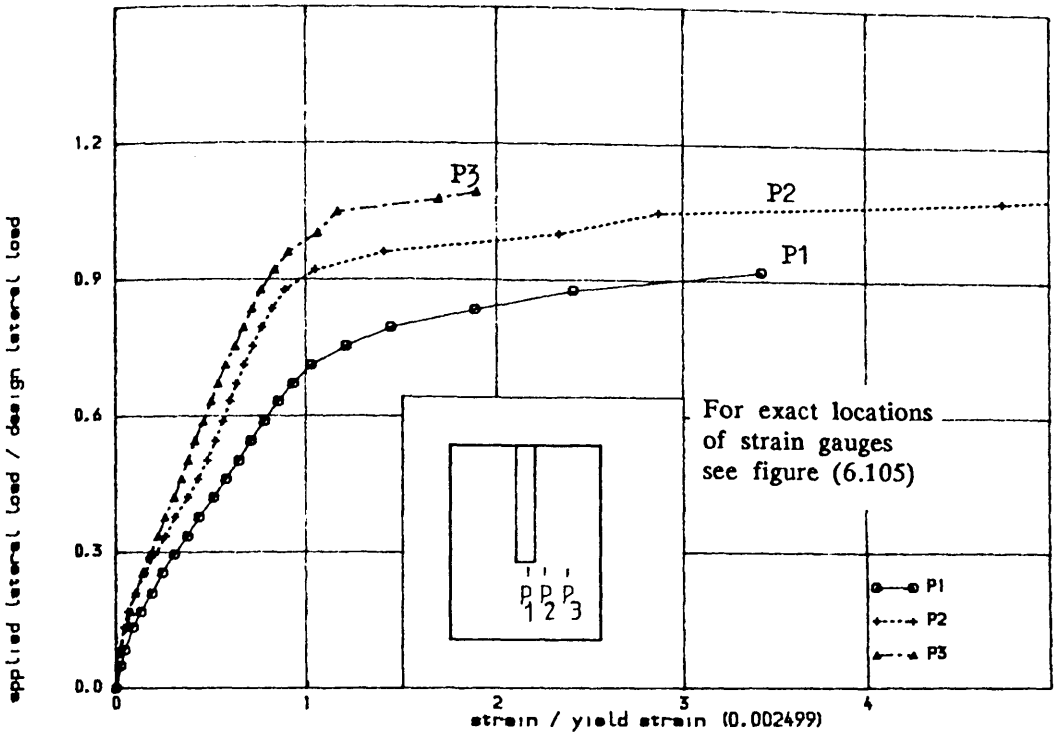

FIGURE (6.100) , TENSILE STRAIN IN STEEL IN VINDVARD DIRECTION ALONG TRANSVERSE SECTION IN THE SLAB OF MODEL MS7

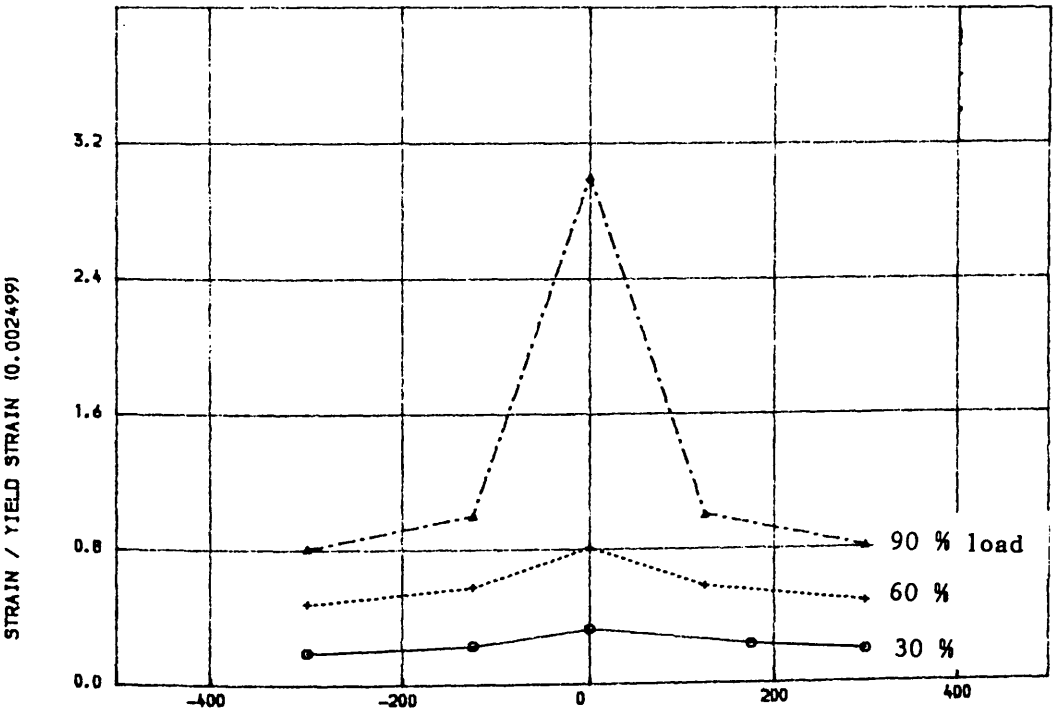

FIGURE (6.101) , VARIATION OF STRAIN IN STEEL IN VINDVARD DIRECTION ALONG TRANSVERSE SECTION AT DIFFERENT STAGES OF LOADING IN THE SLAB OF MODEL MS7

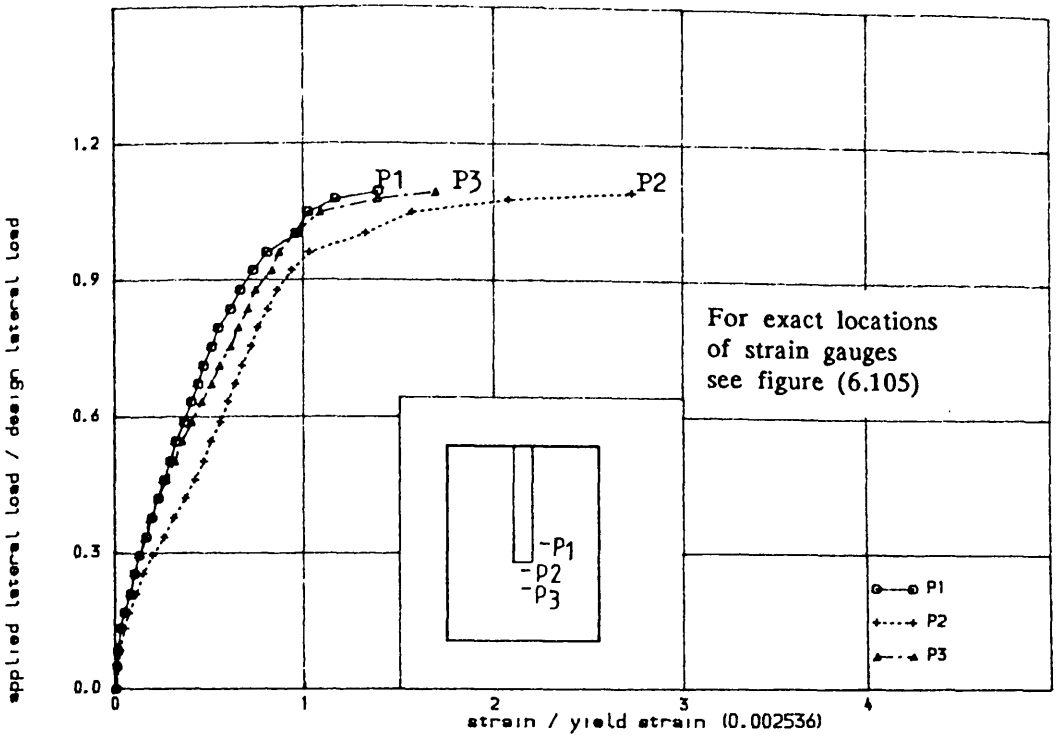

FIGURE (6.102) , TENSILE STRAIN IN STEEL IN TRANSVERSE DIRECTION IN THE SLAB OF MODEL MS7

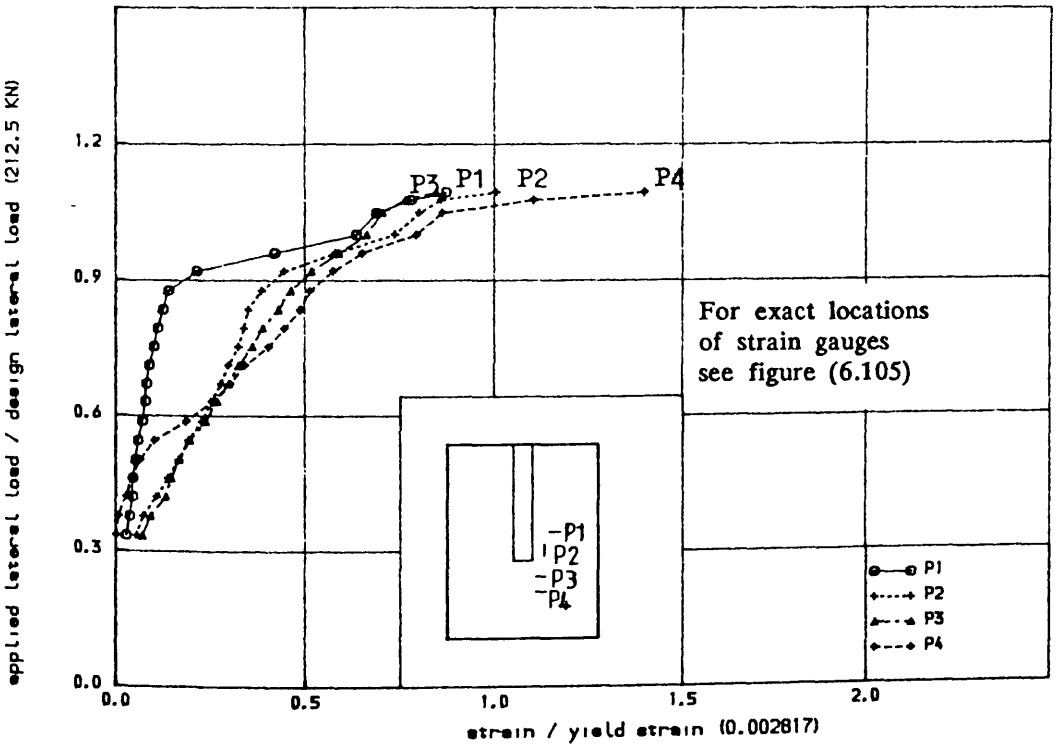

FIGURE (6.103) , STRAIN IN CLOSED VERTICAL STIRUP AT DIFFERENT LOCATIONS IN THE SLAB OF MODEL MS7

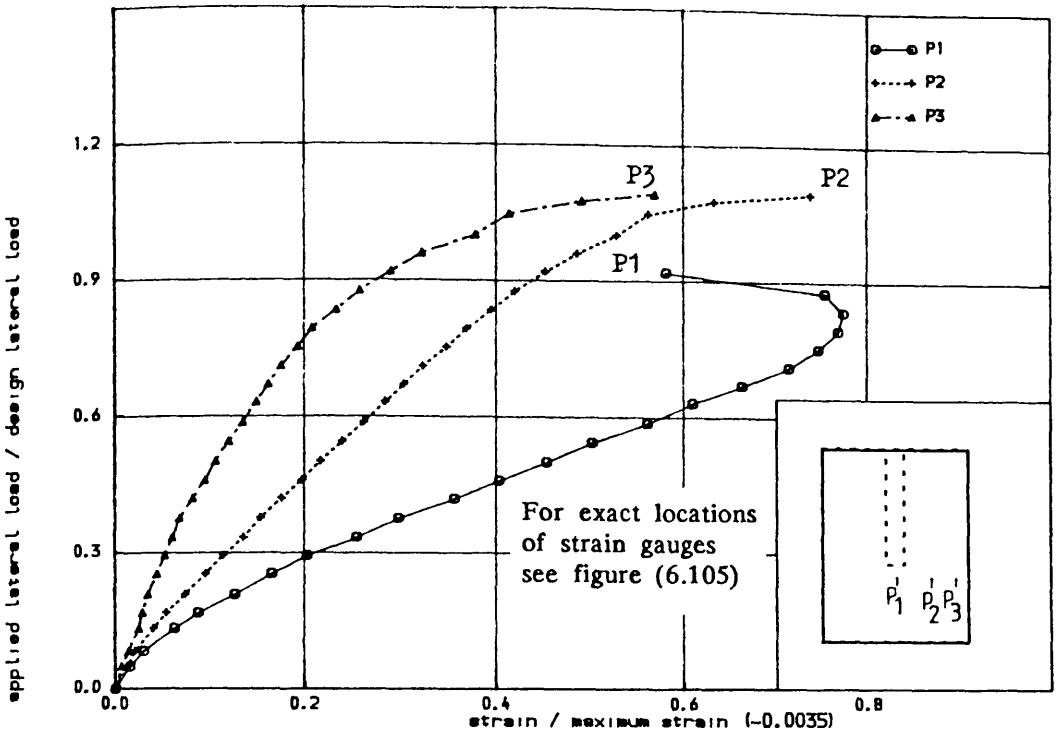

FIGURE (6.104) , COMPRESSIVE STRAIN IN CONCRETE IN VINDVARD DIRECTION IN THE SLAB OF MODEL MS7

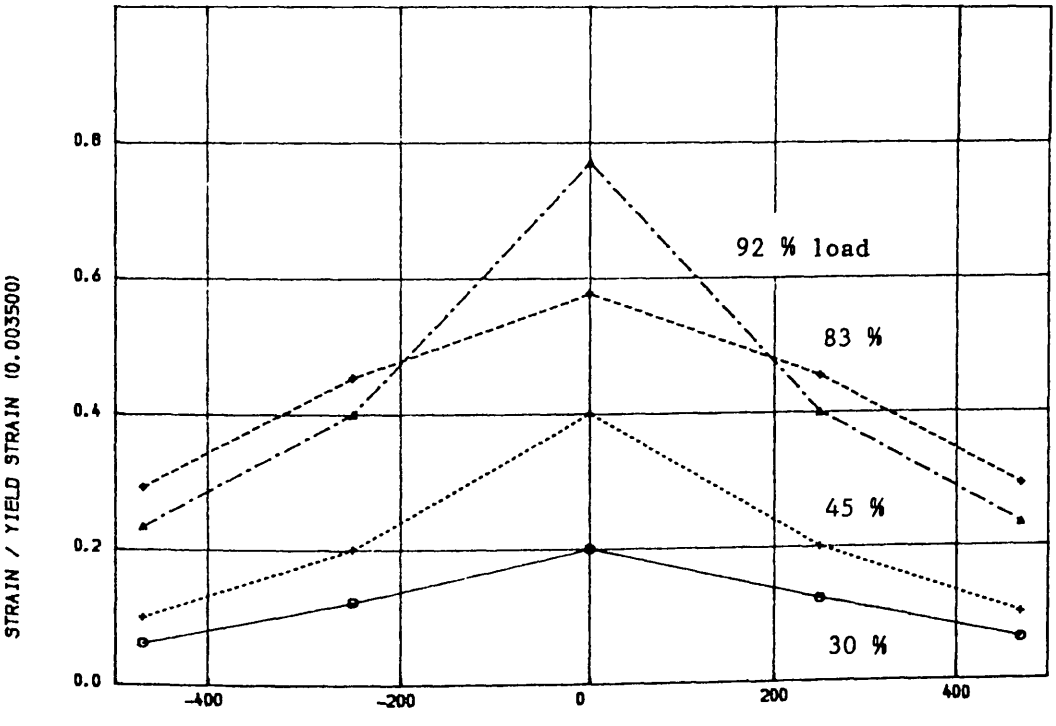

FIGURE (6.104-a) , VARIATION OF COMPRESSIVE STRAIN IN CONCRETE ALONG TRANSVERSE CRITICAL SECTION AT DIFFERENT STAGES OF LOADING IN THE SLAB OF MODEL MS7

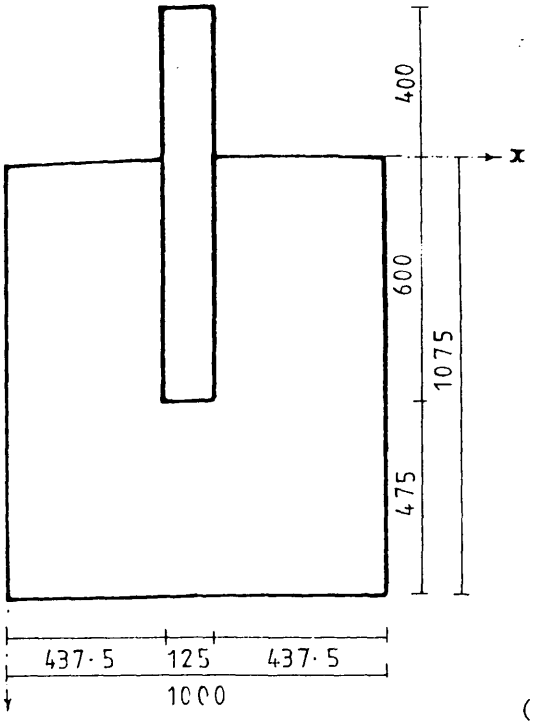

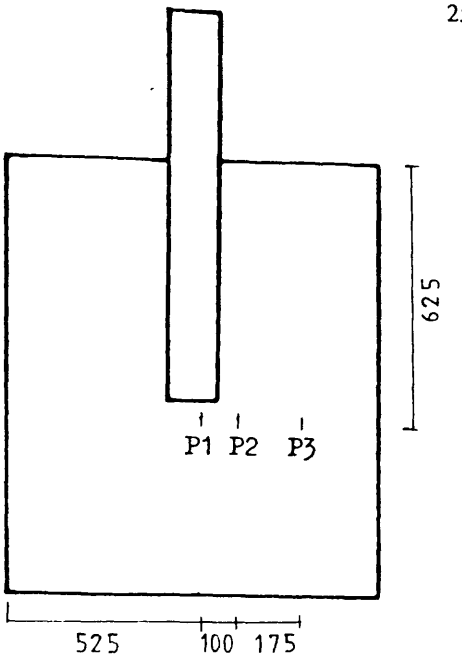

(a) Strain gauges in Figure (6.100)

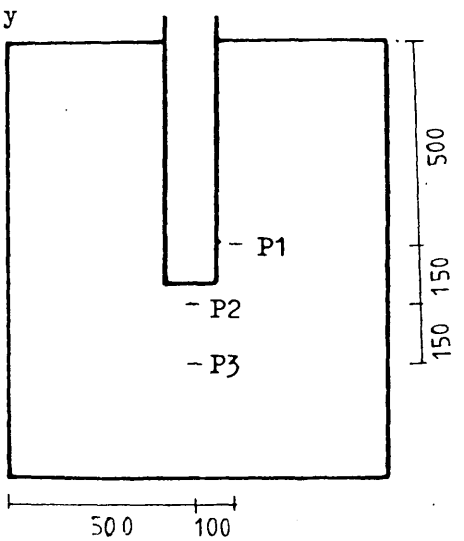

(b) Strain gauges in Figure (6.102)

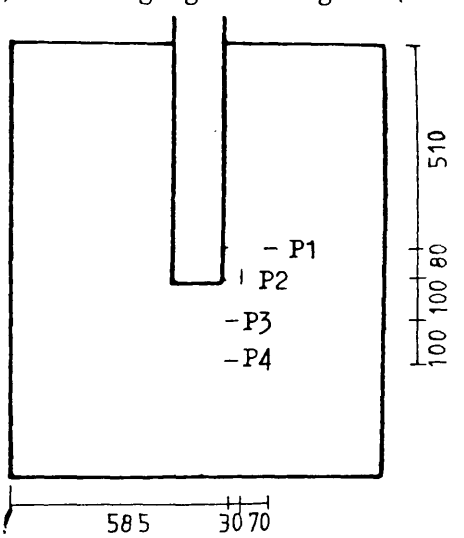

(c) Strain gauges in Figure (6.103)

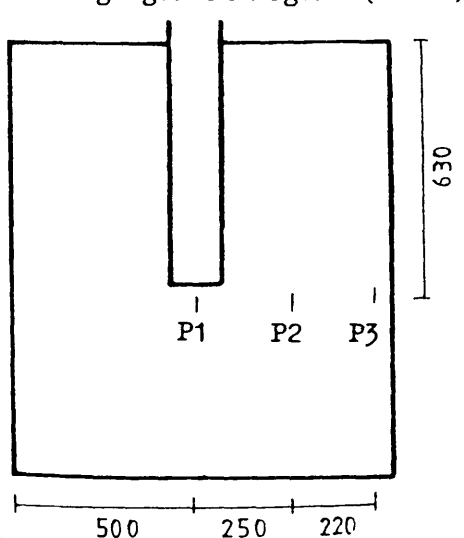

(d) Strain gauges in Figure (6.104)

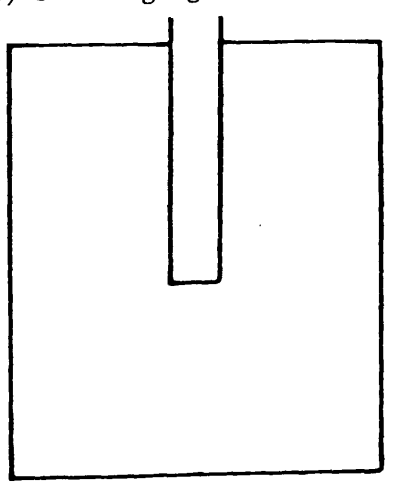

FIGURE (6.105) : Exact locations of strain gauges in the slab of model MS7 as shown in Figures (6.100), (6.102), (6.103) and (6.104))

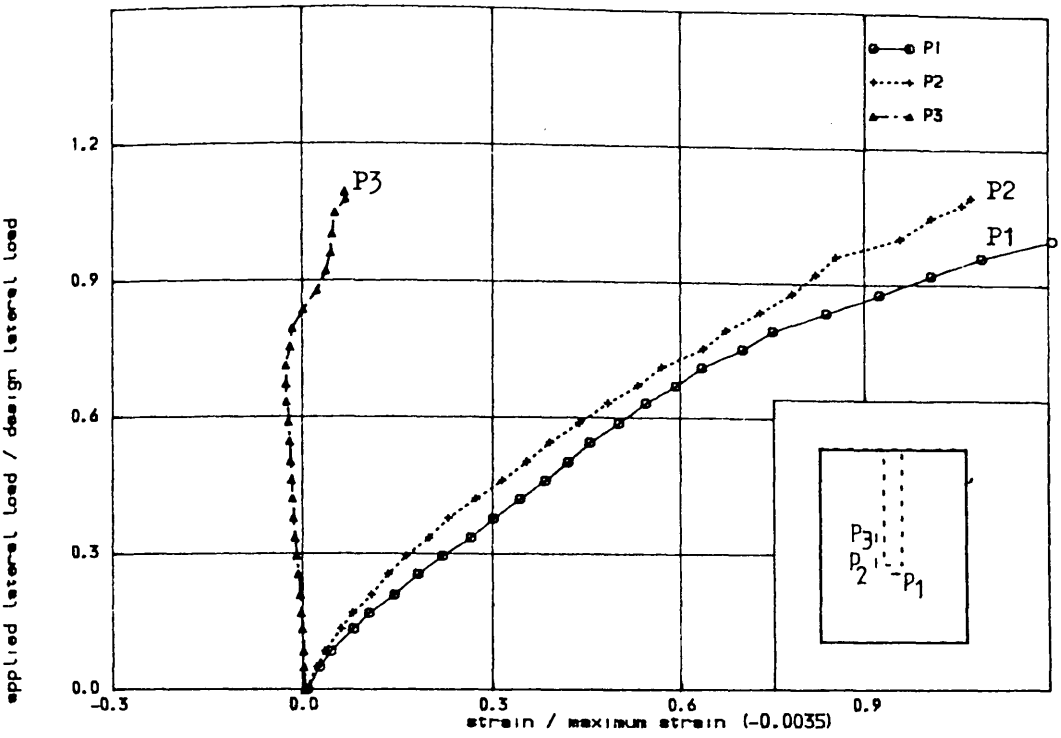

FIGURE (6.106) , COMPRESSIVE AND TENSILE STRAIN IN WALL JUST UNDERNEATH THE SLAB OF MODEL MS7

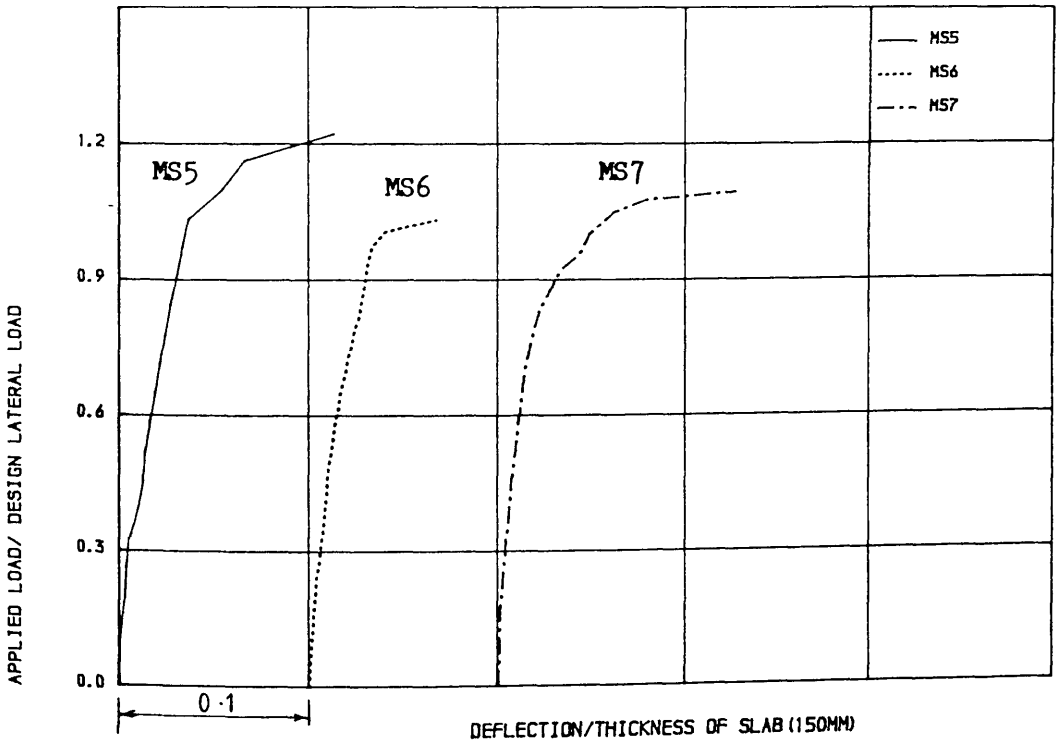

FIGURE (6.107) , COMPARATIVE STUDY OF THE LOAD-DEFLECTION CURVES FOR THE MODELS TO STUDY THE EFFECT OF CORRIDOR OPENING WIDTH

steel bar passing through the wall (see Figure (6.74) for MS5 and Figure (6.100) for MS7). On the compressive side of the slab, the failure line started from the nose of the wall and failure by crushing was similar for all the models (see Figures (6.73) for MS5, (6.86) for MS6 and (6.99) for MS7). The compressive strain on the bottom surface of the slab at central point P1 was found to decrease in all the models near the ultimate load. This unloading behaviour at point P1 was found in models MS5, MS6 and MS7 at 90%, 66% and 83% of design load respectively. At failure load, the maximum strain in the compressive side of the slab was more than yield strain of concrete (about 116%) at point P2 for model MS5, about 70% of yield strain (−0.0035) at point P2 for model MS6 and 75% of yield strain for model MS7 at the same point P2.

The stirrups started to carry load at about 40% of design load for model MS5, although it was expected to strain at earlier load. The stirrups in models MS6 and MS7 started to carry load at the load when cracks appeared on the slab of those models. The nondimensional load versus strain curves for closed vertical stirrups of models MS6 and MS7 show nonlinear behaviour after cracking of concrete. Most of the stirrups reached their yield strain at failure of the models.

6.4.3 Model MS8 to study the effect of gravity load

This model was intended to study the effect of the ratio V_g/V_ℓ, where V_g is the ultimate gravity load on slab and V_ℓ is the design lateral load. This model is similar to the previous model MS7 except that the intensity of gravity load was three times of MS7. The model was designed to resist lateral and gravity load, equal to 255.0 KN and 54.0 KN respectively. Gravity load was applied in first five increments of 10.8 KN and the lateral load was applied in equal increments of 10 KN upto failure. The plan of the model and the reinforcement used in the wall was similar to those of model MS7 as shown in Figures (6.93) and (6.94). The reinforcement used in the slab is shown in Figure (6.108).

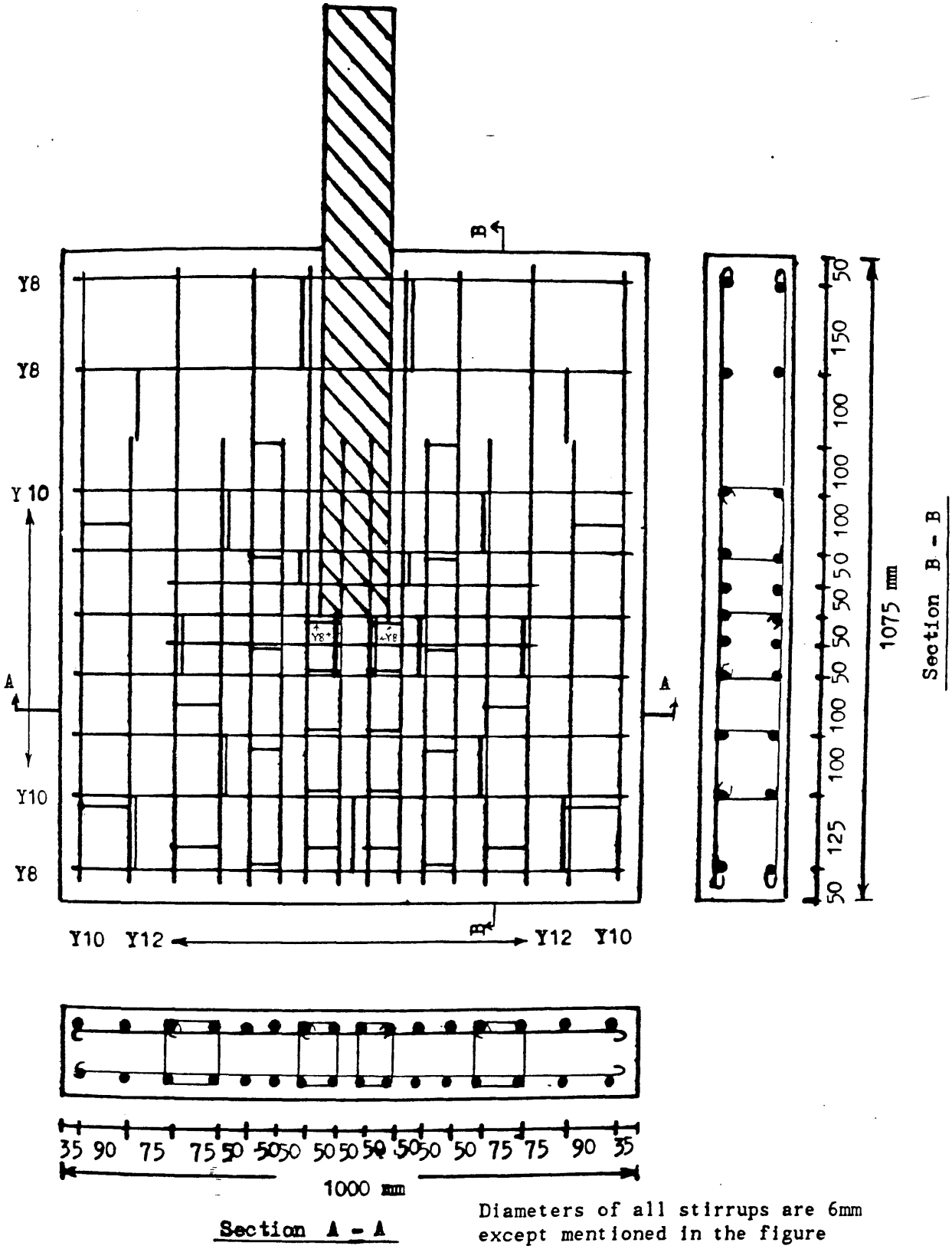

Figure (6.108-a) : Arrangement of top reinforcing bars including closed vertical stirrup in the slab of model MS8

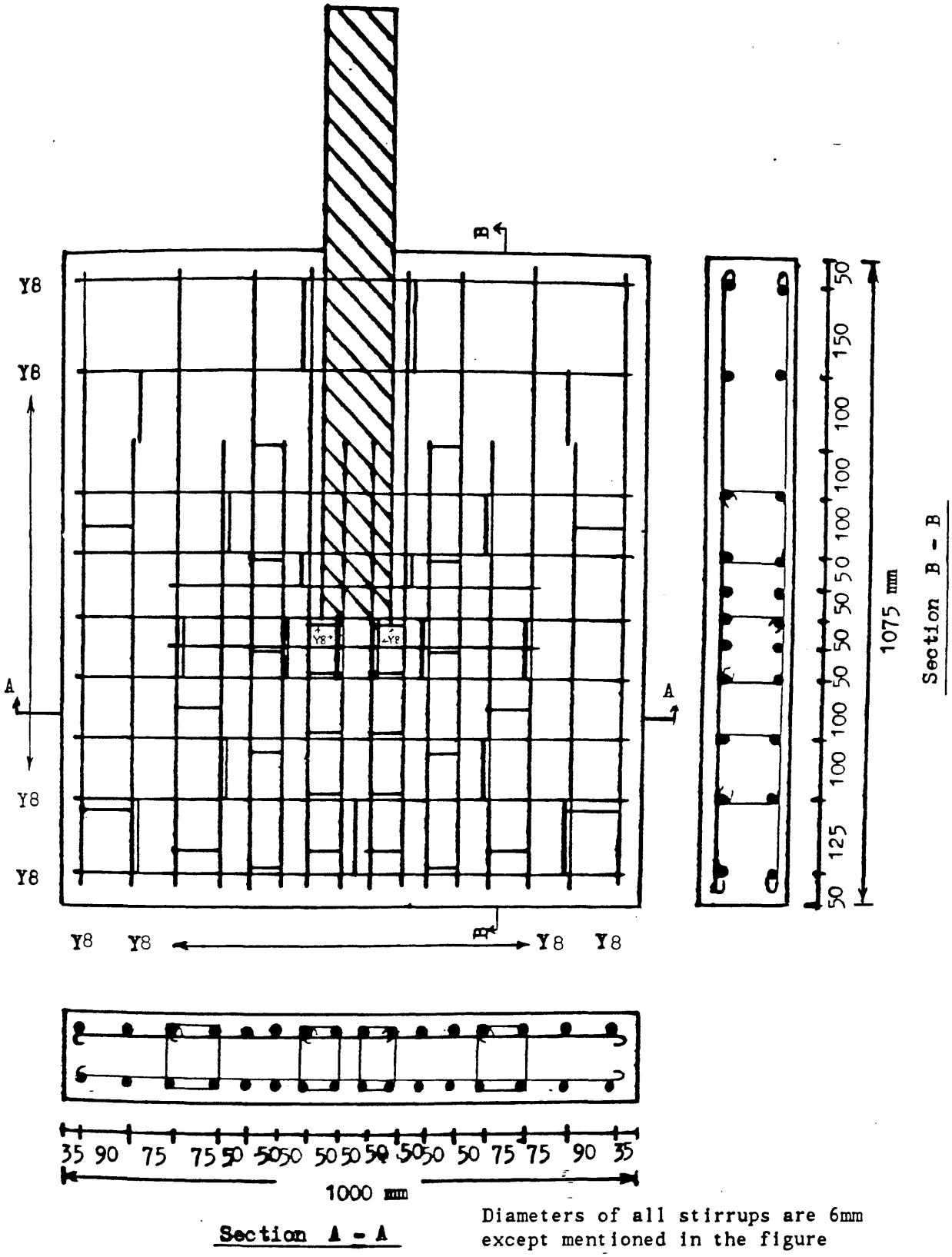

Figure (6.108-b) : Arrangement of bottom reinforcing bars including closed vertical stirrup in the slab of model MS8

Behaviour of the Model

No cracks were observed due to gravity load until the ultimate design gravity load of 54.0 KN was applied. At this stage two long cracks parallel to the wall appeared and extended upto the far end of slab as in Figure (6.109– a). Another small crack parallel to the wall also appeared on one side but no similar crack was visible at that stage on the other side. At a lateral load of 9% of the design load, two cracks were observed at the nose of the wall, extending towards the corridor area as shown in Figure (6.109– b). As loading progressed, cracks developed from the nose of the wall in such a way that they were, in general, parallel to the loading beam in the corridor area. Some of the cracks, originating from the wall, extended to the end of slab being parallel to the lateral loading edge. The other cracks originating from the back of the wall, terminated at the rear end of the slab being parallel to the wall. Failure took place gradually at a lateral load of 280 KN (110.0% of design load). Failure of this model was ductile as can be seen from the load– deflection curve shown in Figure (6.110).

Tensile strains in steel in windward direction at different locations along a section perpendicular to the wall are shown in Figure (6.111). Yielding of steel in this direction was first observed at a lateral load 64% of design load. All other experimental test data concerning strains are shown in Figures (6.113) to (6.115). In all these figures, strains at zero lateral load are due to gravity load alone. All the longitudinal, transverse and shear steels where strain gauges were fixed, yielded before the failure took place. The variation of compressive strain in concrete (See Figure (6.115– a)) shows a different behaviour from the previous models. The compressive strains in the previous models were maximum at the inner edge of the wall (point P1) than other points (P2 and P3) at early stages of loading and showed unloading behaviour at point P1 at later stage of loading. But the compressive strain in this model at point P1 (inner edge of the wall) was minimum than points P_2 and P_3 from the begining and showed the unloading behaviour at about 85% of design load and unlike previous models the strain was found incrasing at ultimate load. The crack

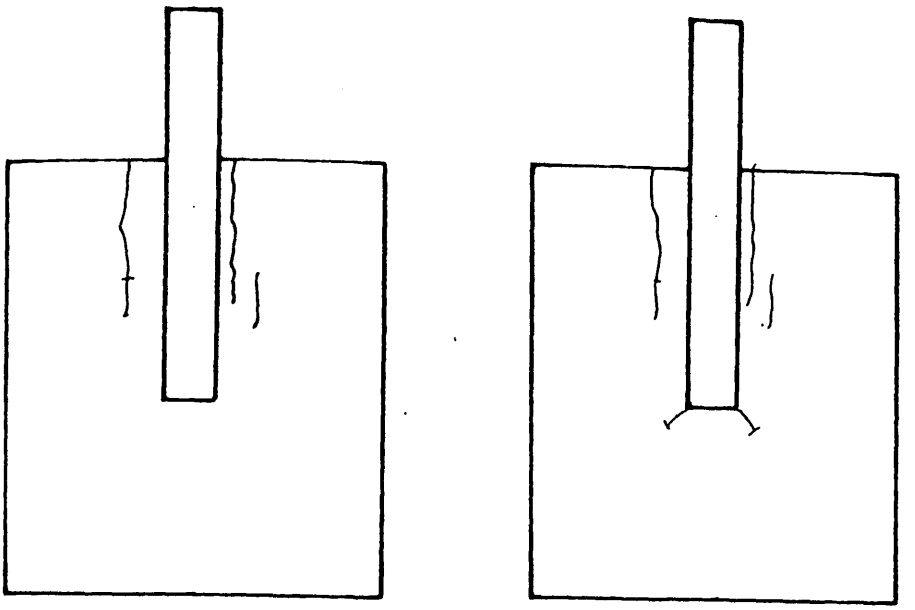

(a) Due to ultimate gravity load only

(b) at a lateral load 19 % of the design load

Figure (6.109) : Cracks initiation during testing of model MS8 at different percentages of design lateral load

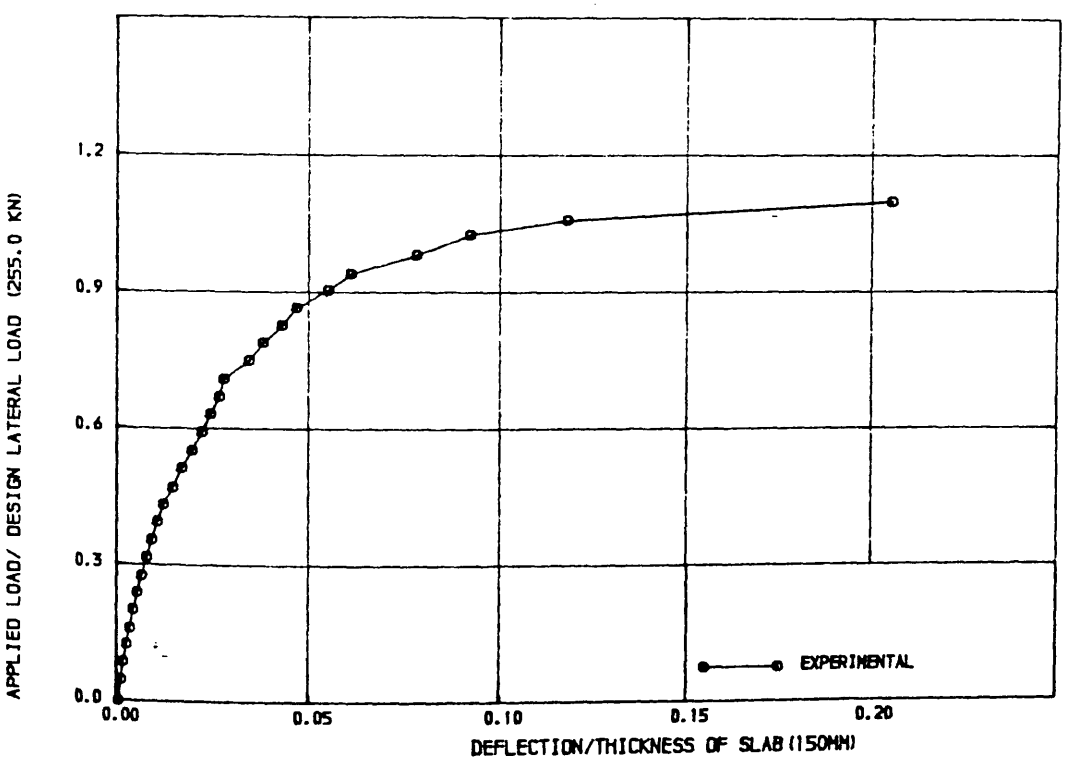

FIGURE (6.110) , LOAD-DEFLECTION CURVE FOR MODEL MS8

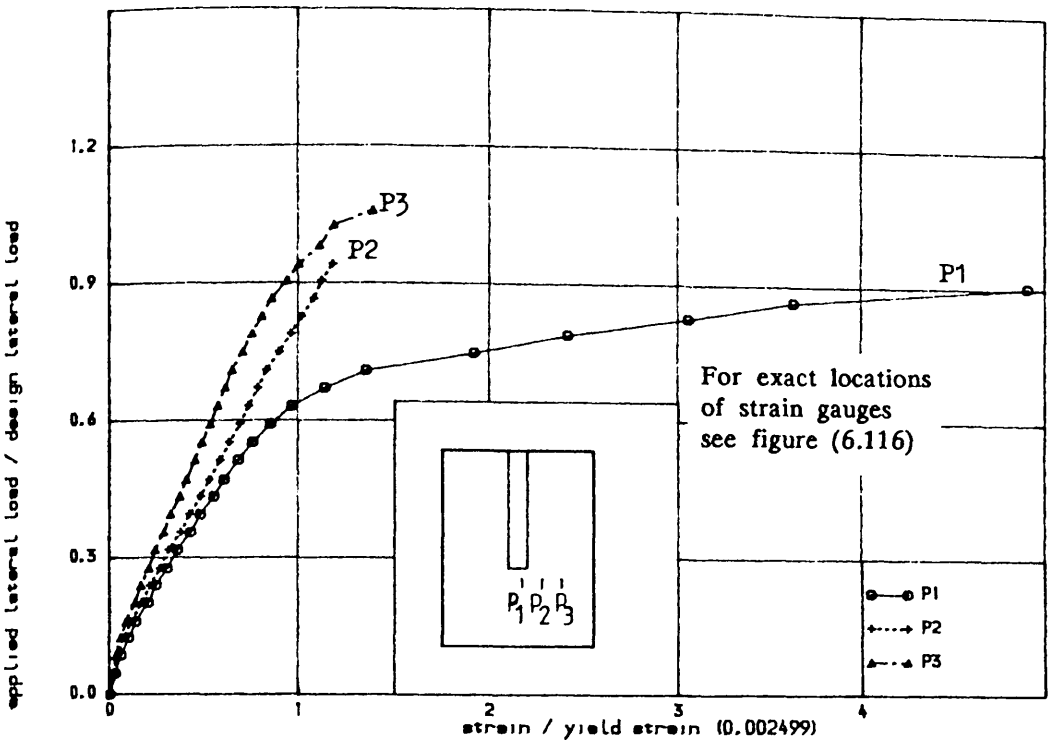

FIGURE (6.111) : TENSILE STRAIN IN STEEL IN VINDVARD DIRECTION ALONG TRANSVERSE SECTION IN THE SLAB OF MODEL MS8

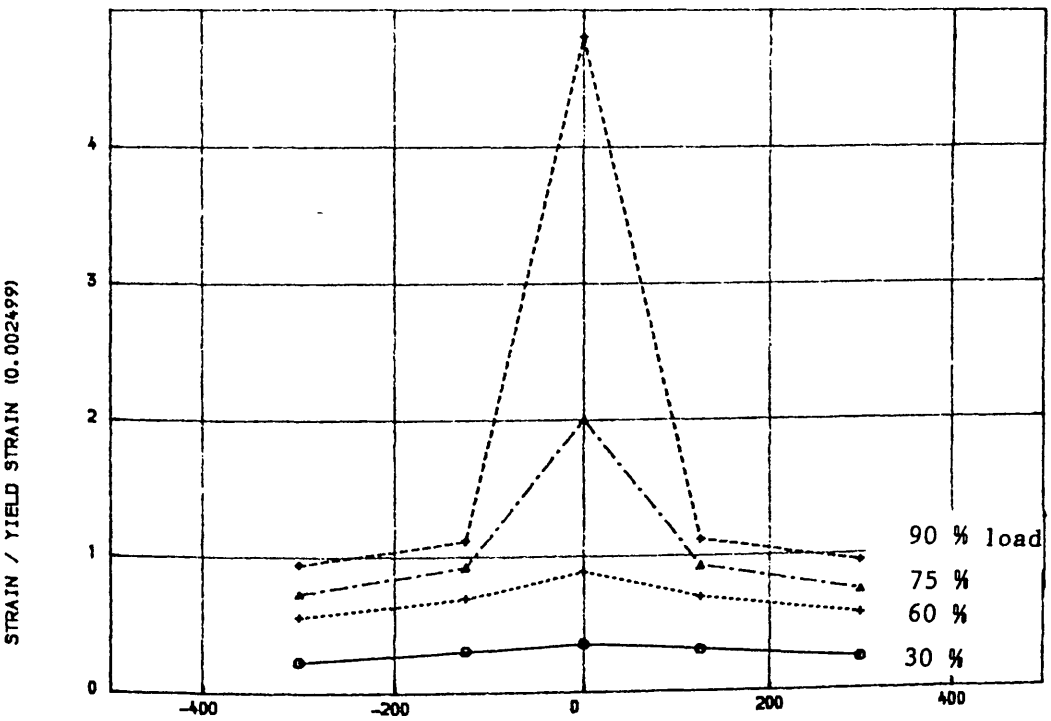

FIGURE (6.112) : VARIATION OF STRAIN IN STEEL IN VINDVARD DIRECTION ALONG TRANSVERSE SECTION AT DIFFERENT STAGES OF LOADING IN THE SLAB OF MODEL MS8

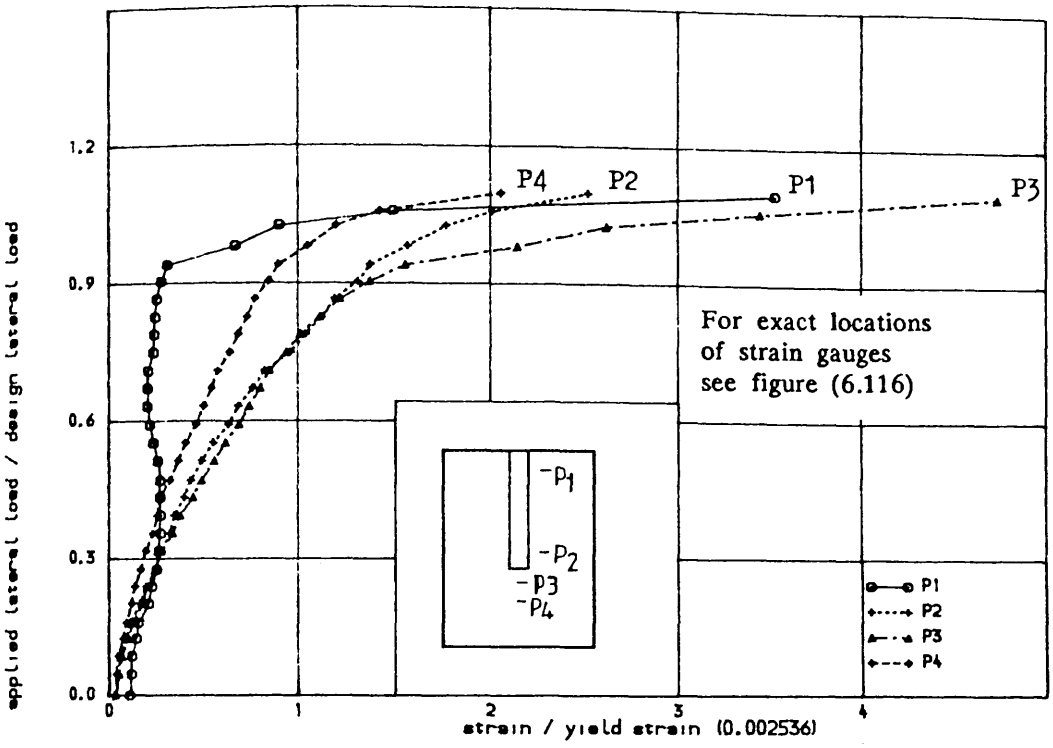

FIGURE (6.113) , TENSILE STRAIN IN STEEL IN TRANSVERSE DIRECTION IN THE SLAB OF MODEL MS8

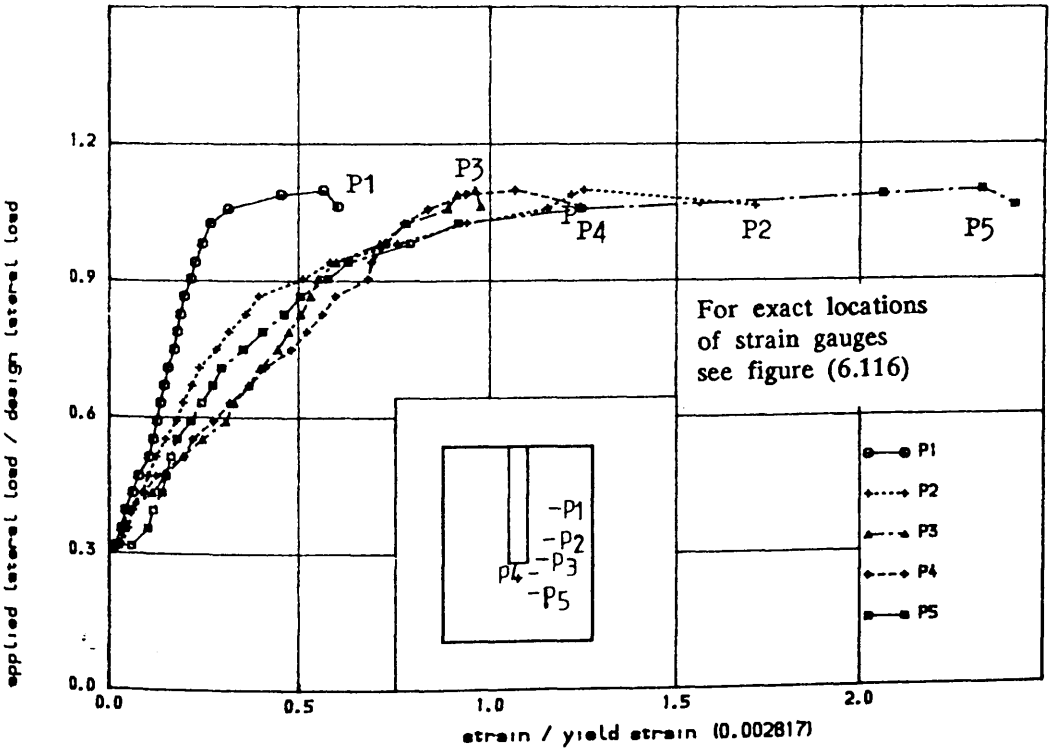

FIGURE (6.114) , TENSILE STRAIN IN CLOSED VERTICAL STIRUP AT DIFFERENT LOCATIONS IN THE SLAB OF MODEL MS8

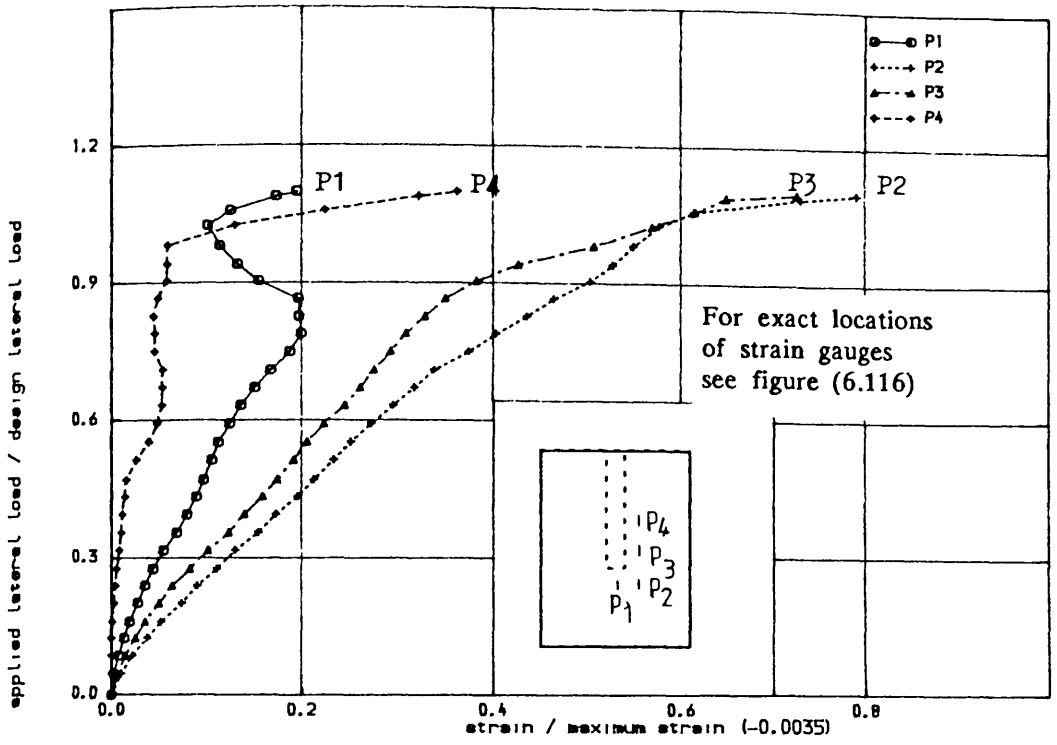

FIGURE (6.115) , COMPRESSIVE STRAIN IN CONCRETE IN WINDWARD DIRECTION IN THE SLAB OF MODEL MS8

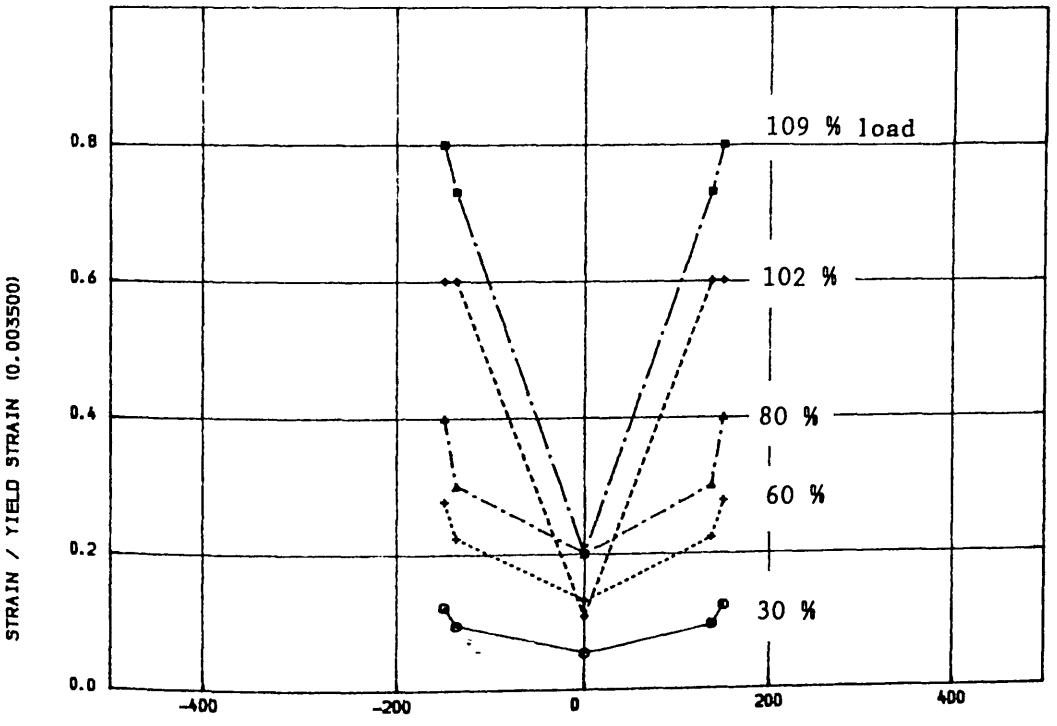

FIGURE (6.115-a) , VARIATION OF COMPRESSIVE STRAIN IN CONCRETE ALONG TRANSVERSE CRITICAL SECTION AT DIFFERENT STAGES OF LOADING IN THE SLAB OF MODEL MS8

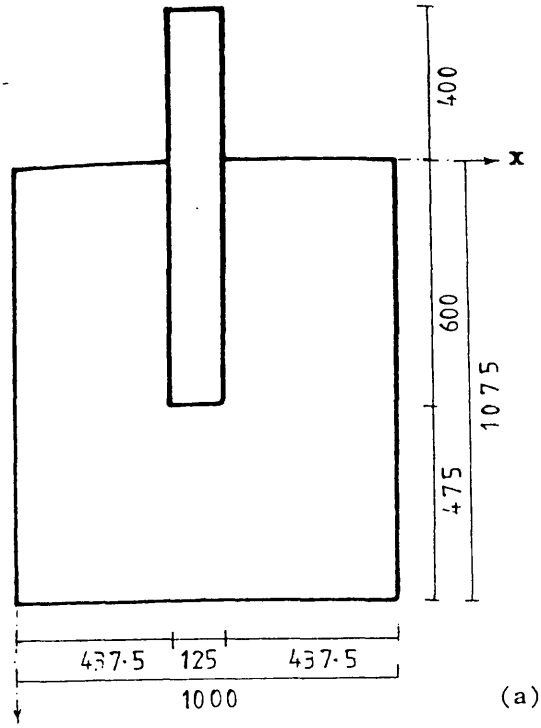

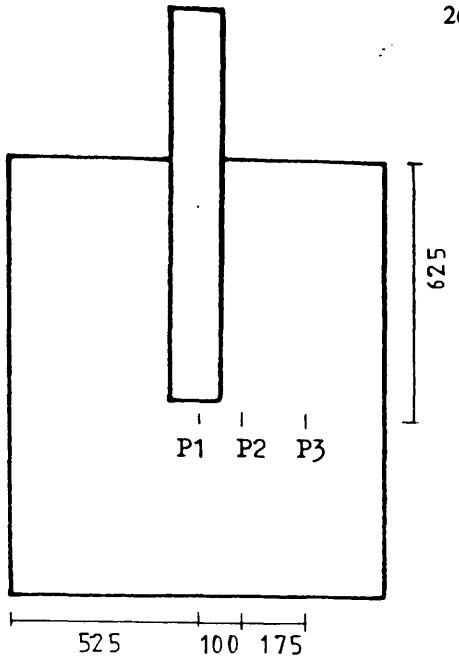

(a) Strain gauges in Figure (6.111)

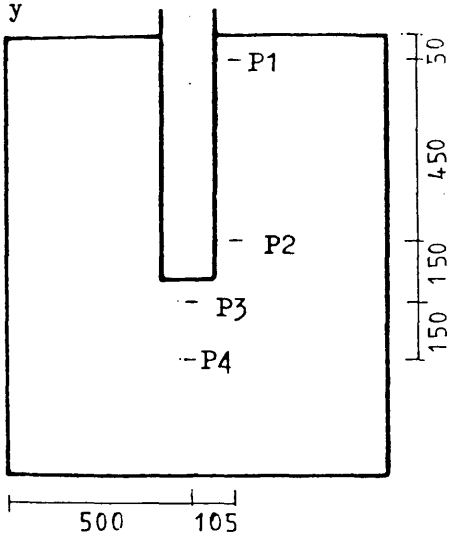

(b) Strain gauges in Figure (6.113)

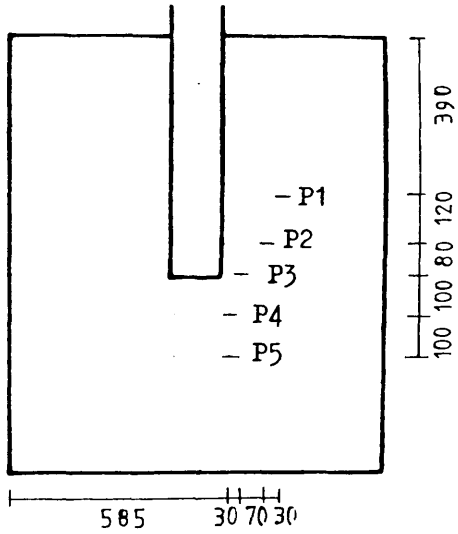

(c) Strain gauges in Figure (6.114)

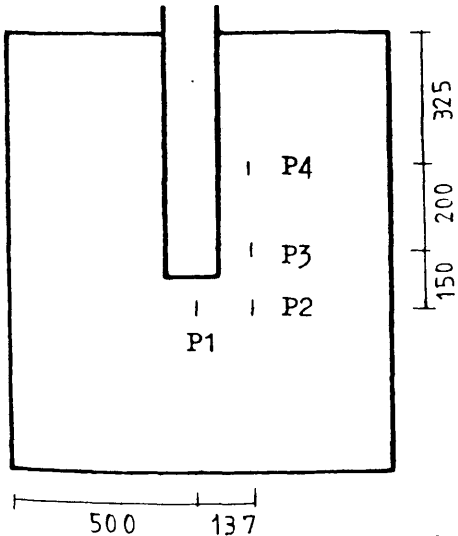

(d) Strain gauges in Figure (6.115)

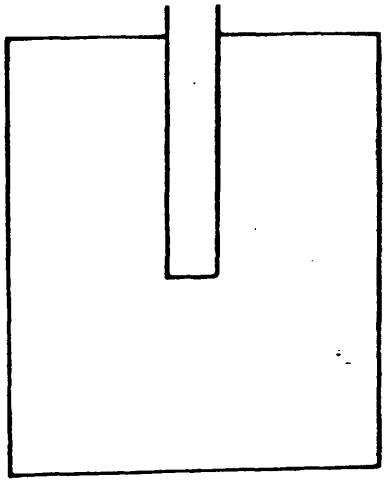

FIGURE (6.116) : Exact locations of strain gauges in the slab of model MS8 as shown in Figures (6.111), (6.113), (6.114)

(a) Before removing the broken pieces

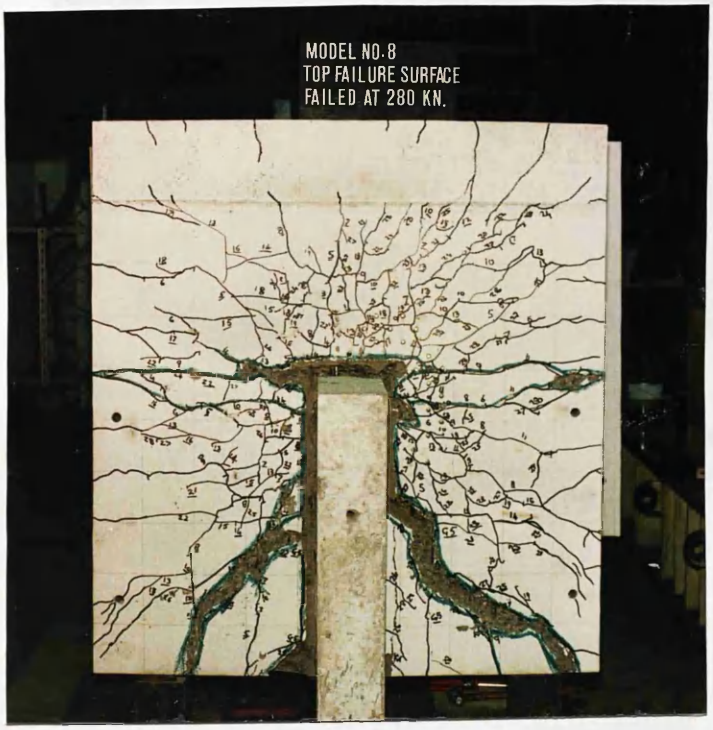

(b) After removing the broken pieces

Figure (6.117) : Crack pattern on the tensile surface of the slab of model MS8

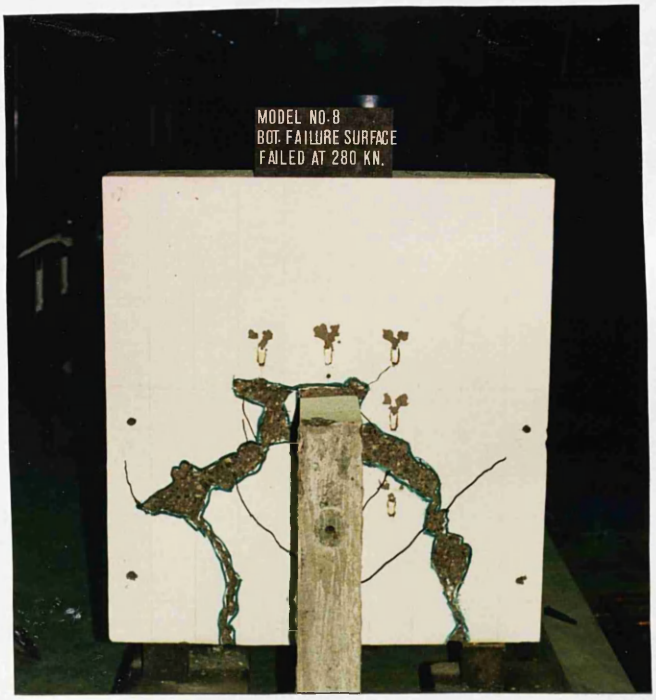

Figure (6.118) : Bottom failure surface of model MS8

pattern of this model after failure is shown in Figures (6.117) and (6.118).

6.4.4 Model MS9 to study the effect of Bay width

This model was tested to study the effect of change in bay width of slab on the strength of connection. The change in the bay width of a slab causes a change in the structural parametric ratio L/Y (where Y is the bay width and L is the corridor opening width) and change in the ratio M_g/V_g (where M_g is the moment due to gravity load and V_g is the shear due to gravity load). The plan of this model as shown in Figure (6.119) is similar to that of model MS7 except that the bay width is increased from 1000 mm to 1440 mm. The plan of the model is exactly similar to that of model MT8[23] and subjected to almost same combination of lateral and gravity load. The flexural and shear reinforcements are shown in Figures (6.121−a) and (6.121−b). The reinforcement used in the wall is shown in Figure (6.120). The lateral load− dispalacement curve for the model is shown in Figure (6.123). The other experimental data are shown in Figures (6.124) to (6.129). The total gravity load applied to this model was same as that of MS7 and MT8 (i.e, 18 KN).

Behaviour of the Model

The first crack appeared at a load of 16% of design lateral load in addition to full gravity load, as shown in Figure (6.122−a). In the next load increment, the crack increased in length and new cracks appeared on the surface. More cracks appeared on right side of the slab than on the left side. On further loading, more new cracks, originating from wall−slab connection, extended all over the slab equally on both sides. It is interesting to note that no cracks were visible under the lateral loading beam over a central strip of 400 mm. This type of crack pattern was found in the models with flanged shear walls. Photographs showing the crack pattern of this model are presented in Figures (6.130) to (6.132). The failure load for this model was 247 KN (99% of design load).

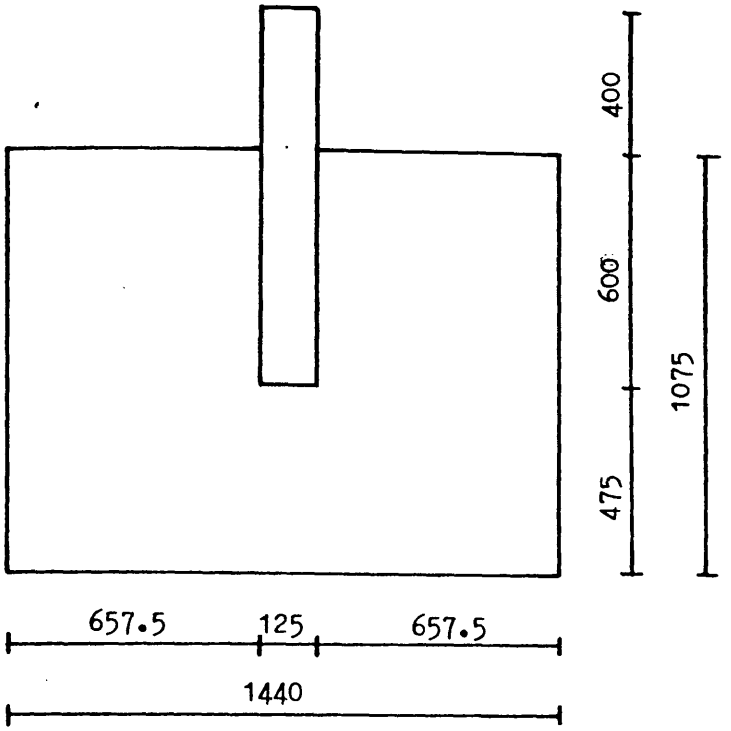

Figure (6.119) : Plan and dimensions of model MS9

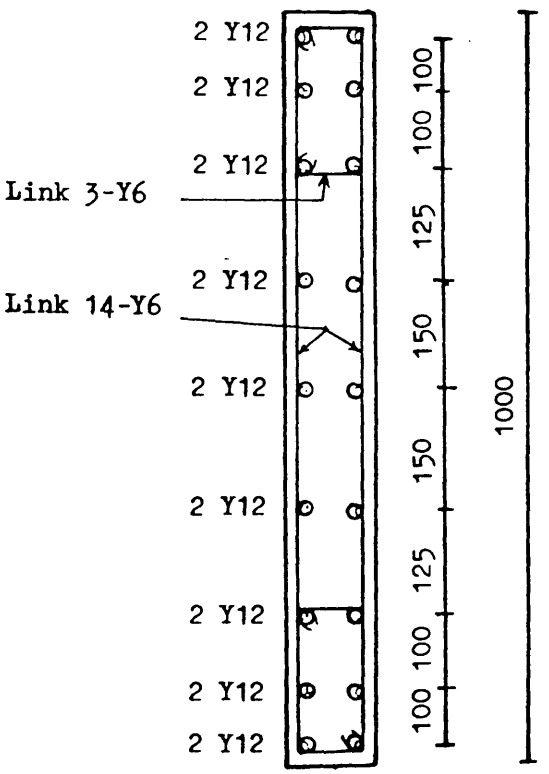

Figure (6.120) : A horizontal section in the wall of model MS9 showing the reinforcing details

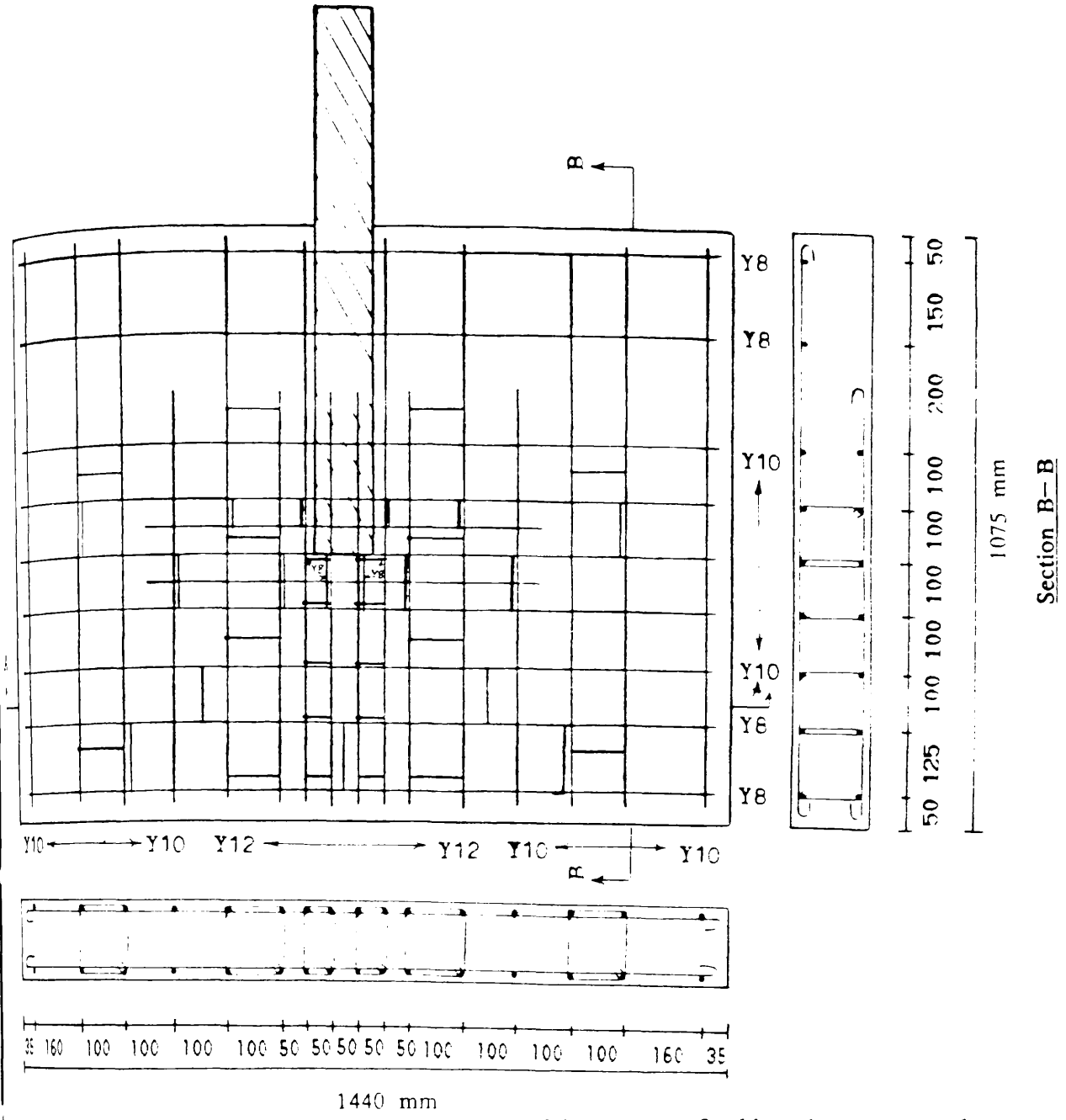

Diameters of all stirrups are 6mm except mentioned in the figure

Figure (6.121-a) : Arrangement of top reinforcing bars including closed vertical stirrup in the slab of model MS9

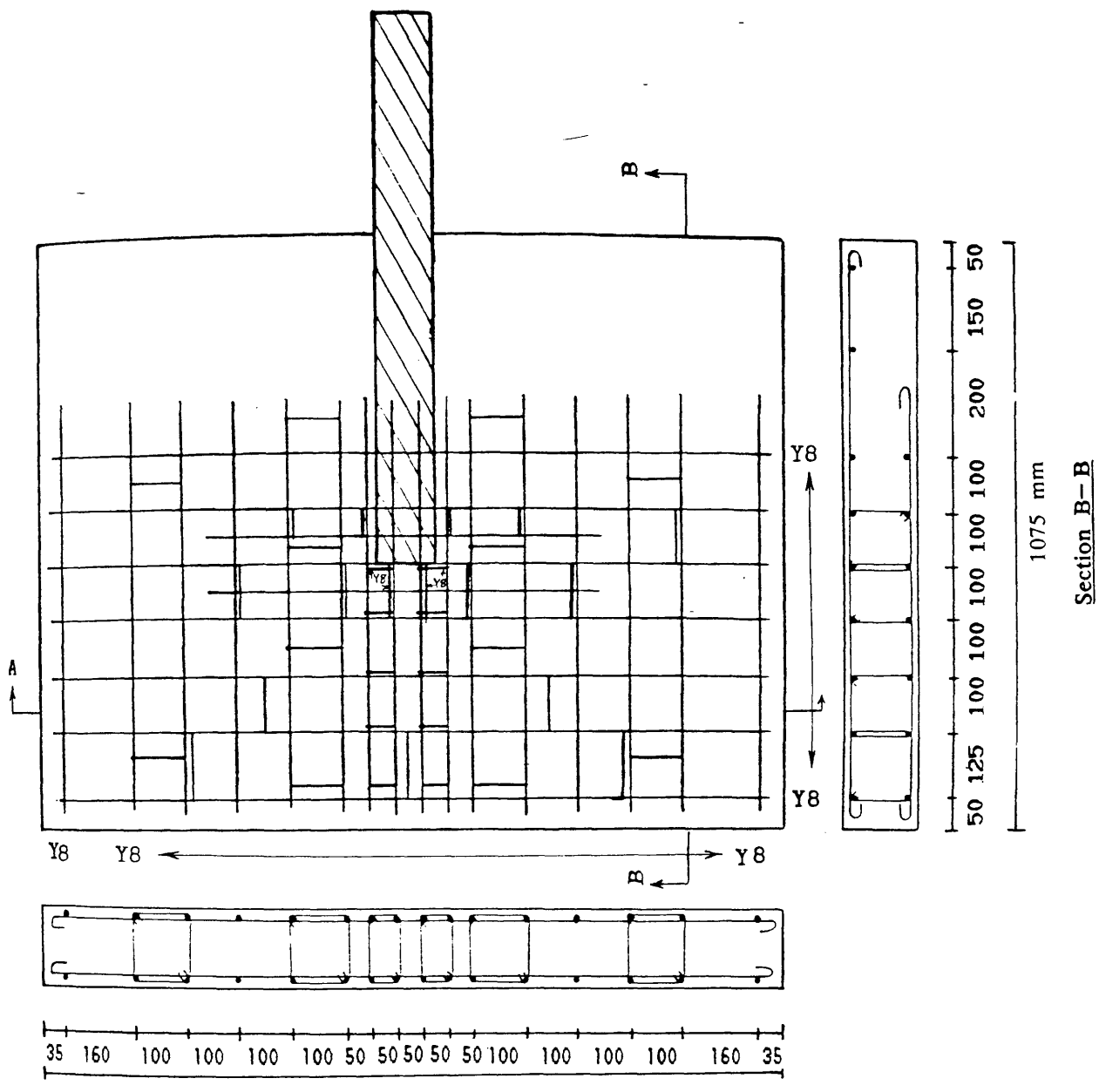

Figure (6.121-b) : Arrangement of bottom reinforcing bars including closed vertical stirrup in the slab of model MS9

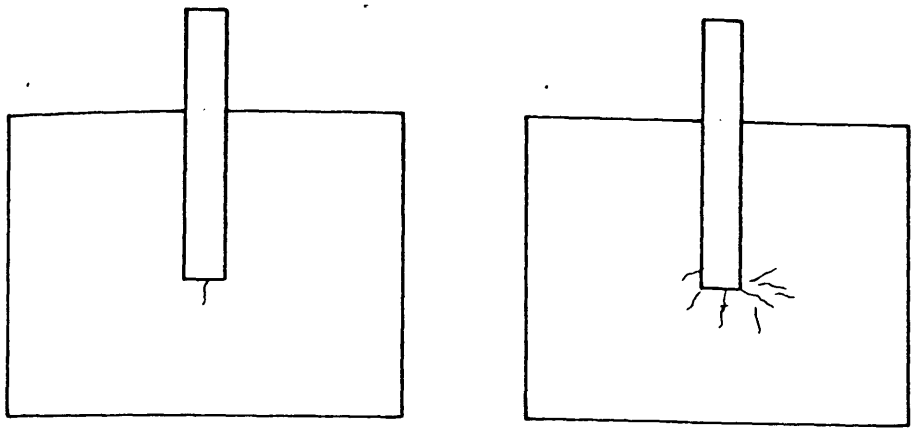

(a) at 16.2 %

(b) at 20.4 %

Figure (6.122) : Cracks initiation during testing of model MS9 at different percentages of design lateral load

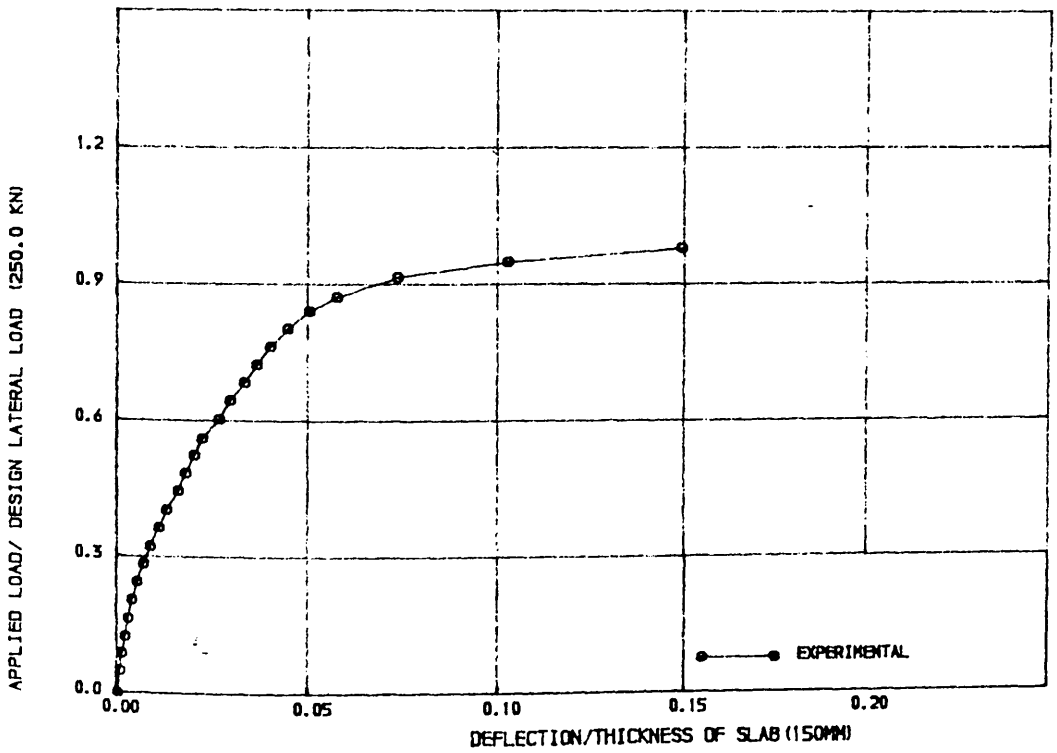

FIGURE (6.123) , LOAD-DEFLECTION CURVE FOR MODEL MS9

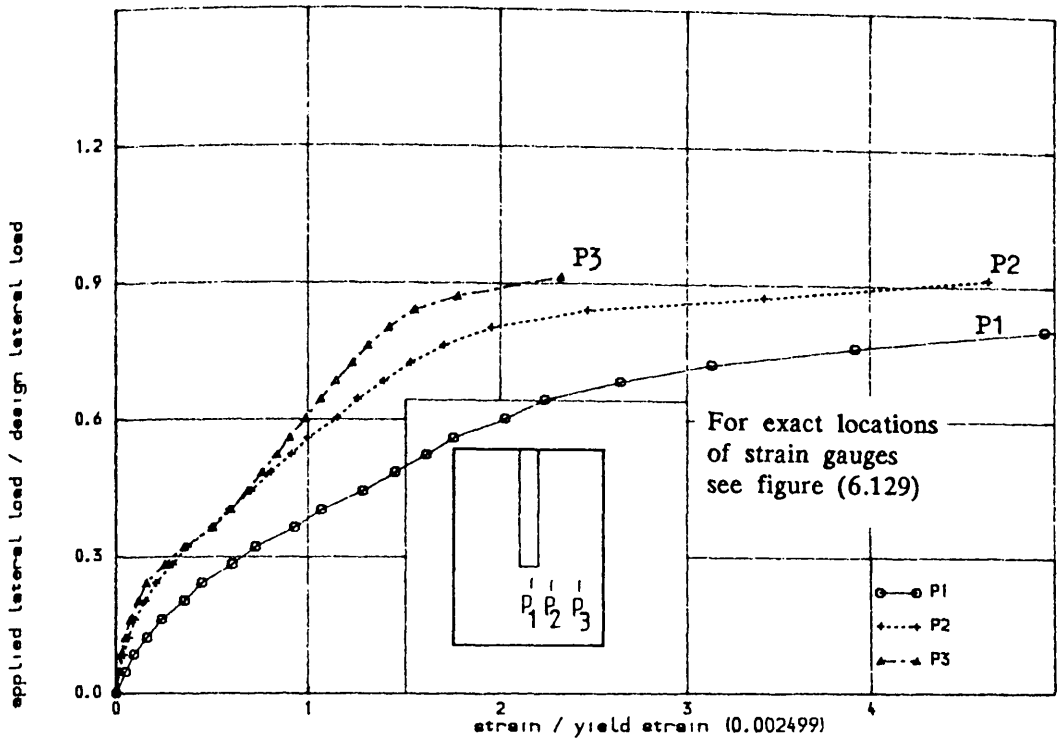

FIGURE (6.124) , TENSILE STRAIN IN STEEL IN WINDWARD DIRECTION ALONG TRANSVERSE SECTION IN THE SLAB OF MODEL MS9

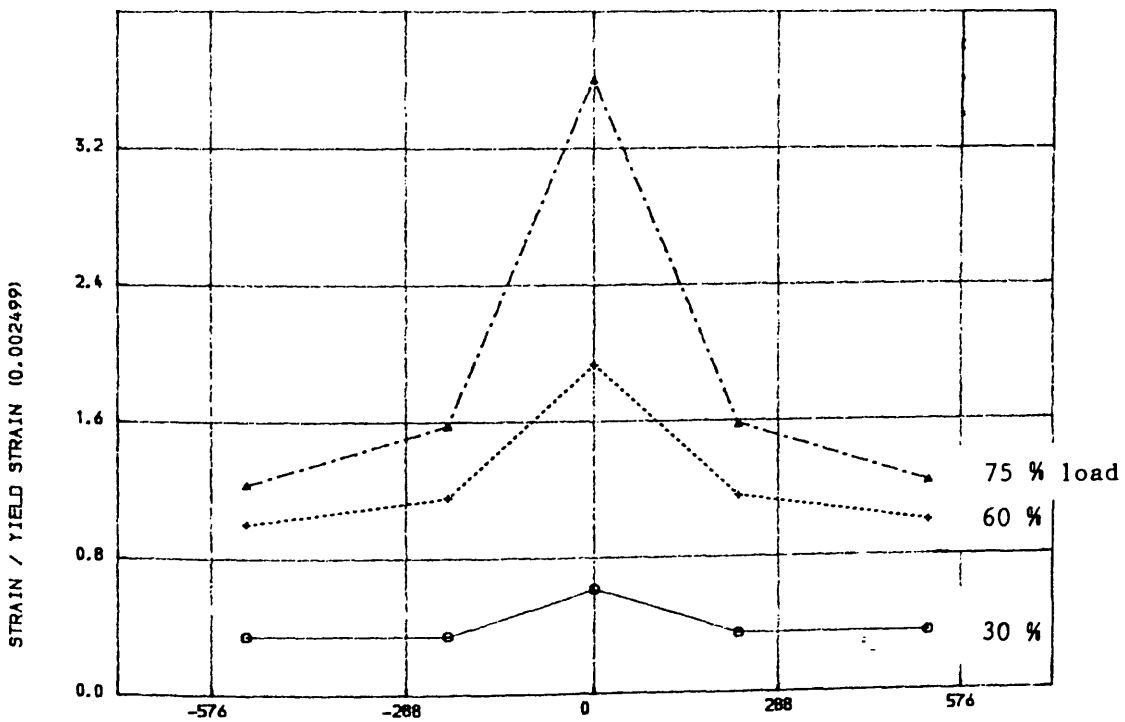

FIGURE (6.125) , VARIATION OF STRAIN IN STEEL IN WINDWARD DIRECTION ALONG TRANSVERSE SECTION AT DIFFERENT STAGES OF LOADING IN THE SLAB OF MODEL MS9

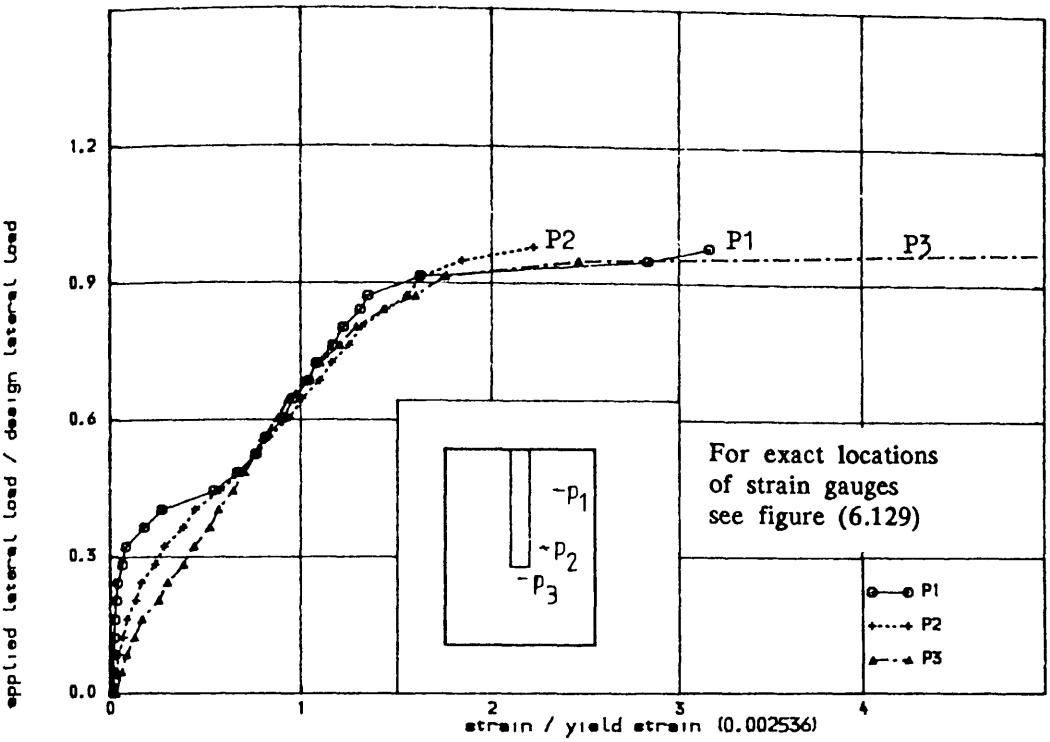

FIGURE (6.126) , TENSILE STRAIN IN STEEL IN TRANSVERSE DIRECTION IN THE SLAB OF MODEL MS9

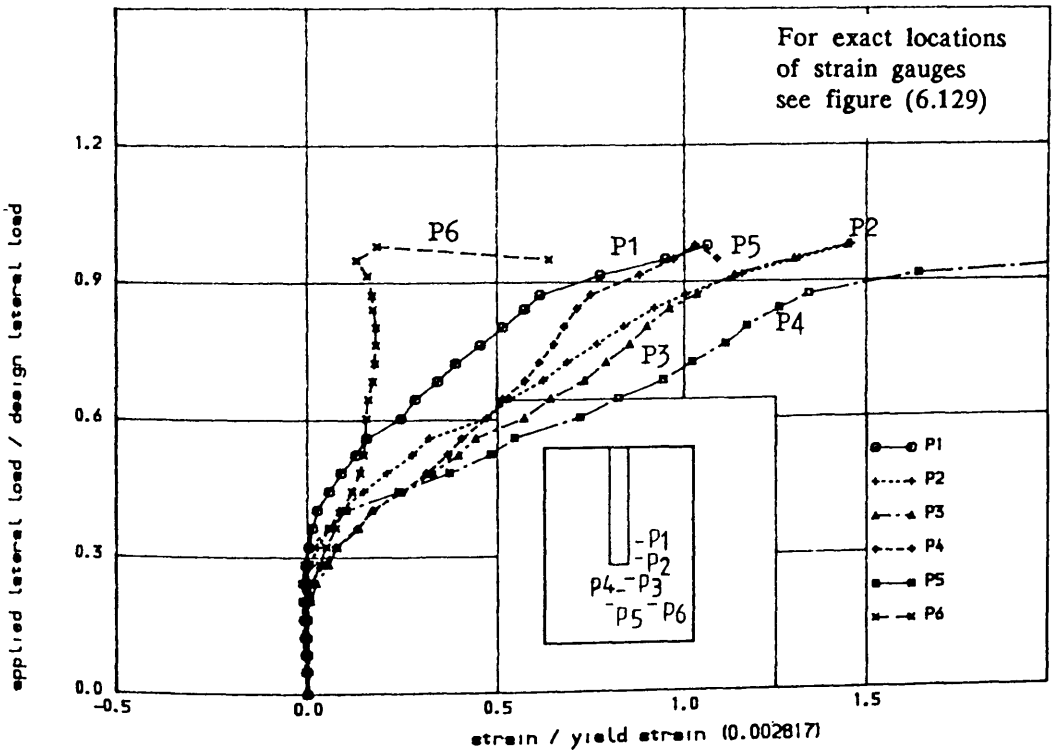

FIGURE (6.127) , TENSILE STRAIN IN CLOSED VERTICAL STIRUP AT DIFFERENT LOCATIONS IN THE SLAB OF MODEL MS9

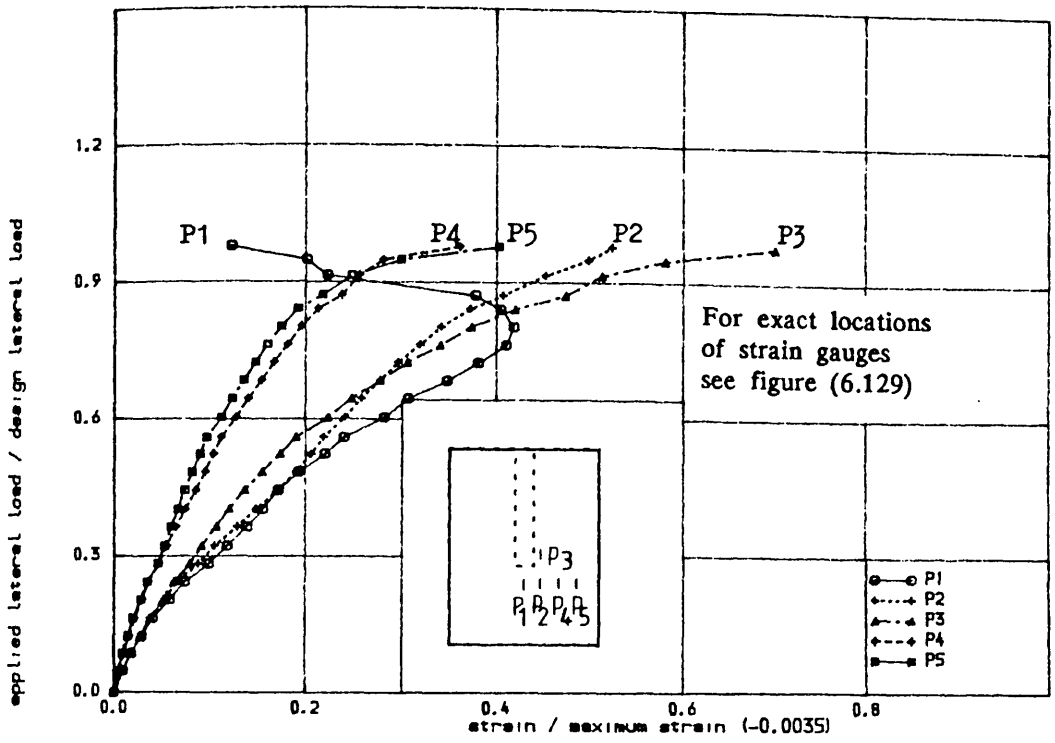

FIGURE (6.128) , COMPRESSIVE STRAIN IN CONCRETE IN VINDVARD DIRECTION IN THE SLAB OF MODEL MS9

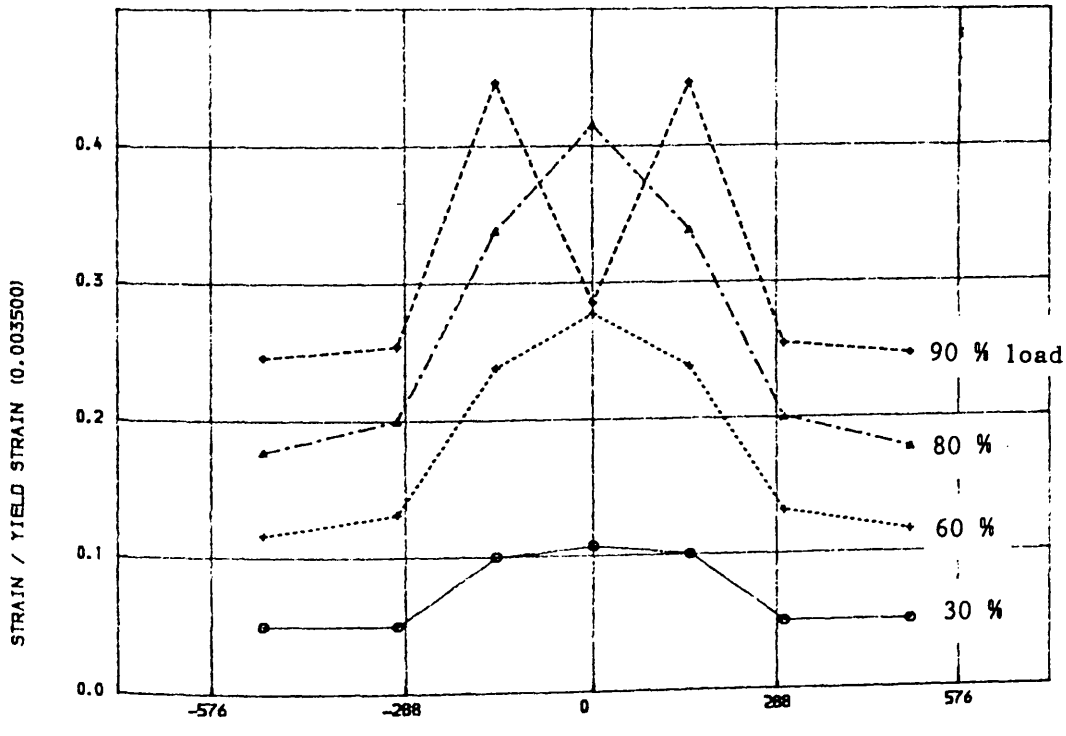

FIGURE (6.128-a) , VARIATION OF COMPRESSIVE STRAIN IN CONCRETE ALONG TRANSVERSE CRITICAL SECTION AT DIFFERENT STAGES OF LOADING IN THE SLAB OF MODEL MS9

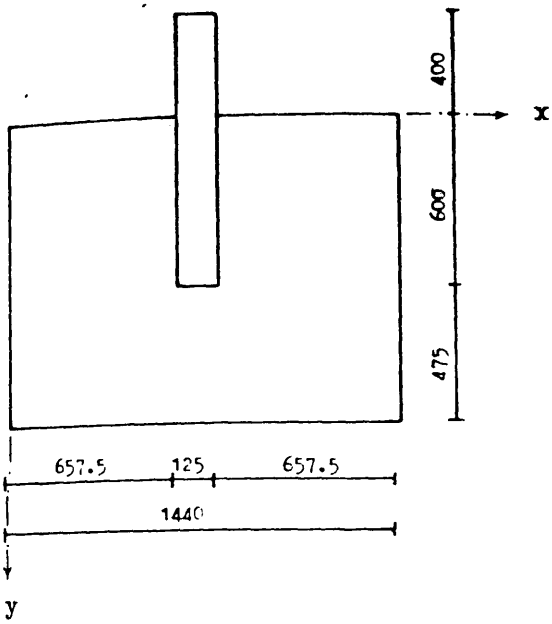

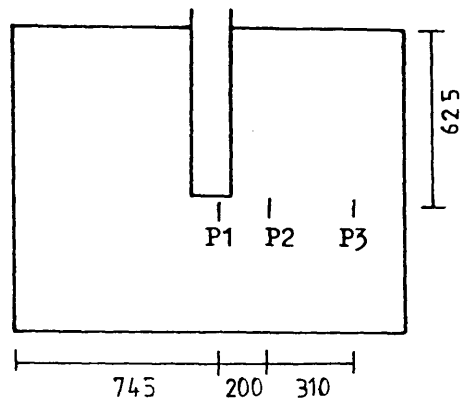

(a) Strain gauges in Figure (6.124)

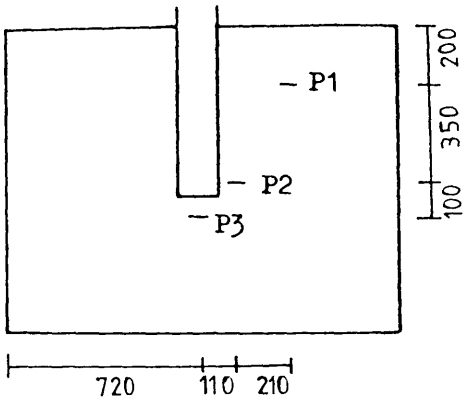

(b) Strain gauges in Figure (6.126)

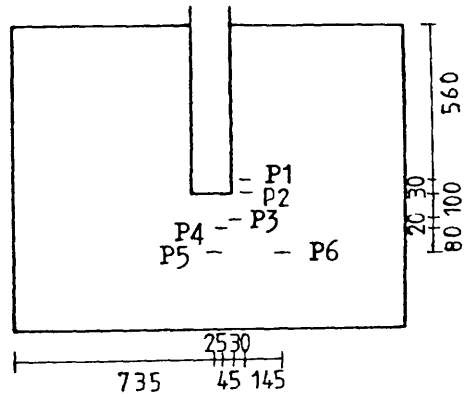

(c) Strain gauges in Figure (6.127)

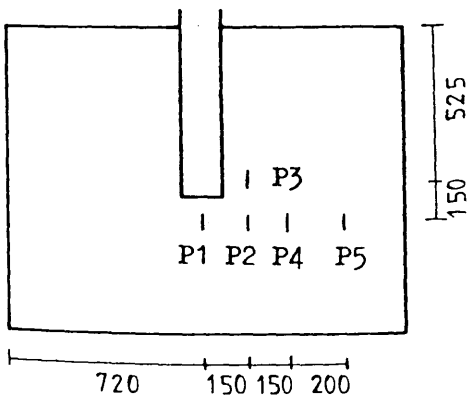

(d) Strain gauges in Figure (6.128)

FIGURE (6.129) : Exact locations of strain gauges in the slab of model MS9 as shown in Figures (6.124), (6.126), (6.127) and (6.128)

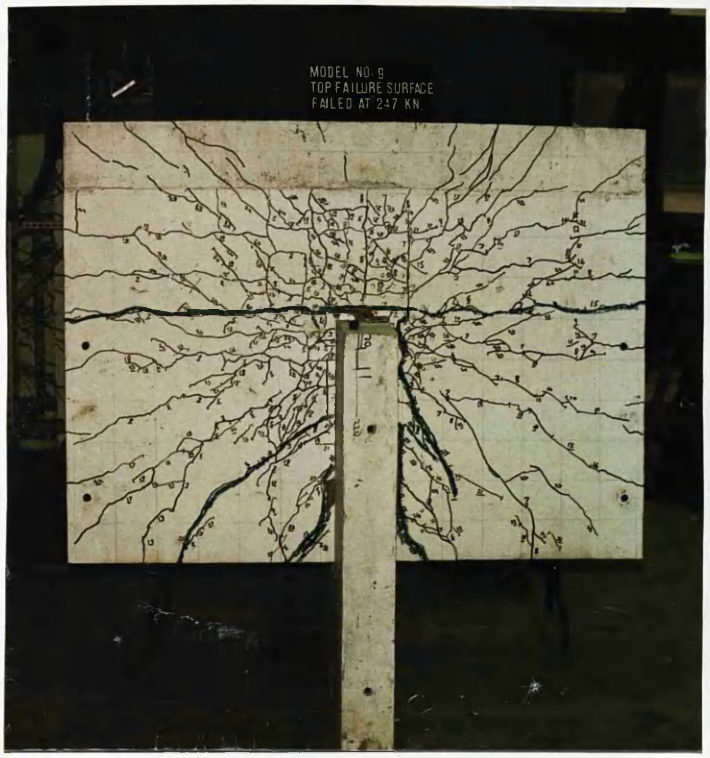

(a) Before removing the broken pieces

(b) After removing the broken pieces

Figure (6.130) : Crack pattern on the tensile surface of the slab of model MS9

Figure (6.131) : Bottom failure surface of model MS9

Figure (6.132) : Side view of model MS9 showing the excessive deflection at failure

6.4.5 Models to Study the Effect of Flange Width

It was shown by Elnounu[24] in his test series that the flange enhances the punching shear resistance of the wall–slab connection. Models MS10, MS11 and MS12 were chosen from previous test series[24] to investigate the effect of flange width ratio (Z/Y) adopting the values for flange width (Z) as shown in Table (6.5). In the previous test series[24], same amount of reinforcement was used in all slabs of the models. This time, each model was designed separately and the required amount of both flexural and shear reinforcement was provided in the slab. The reinforcement ratio which appears in Table (6.5) is for those bars in windward direction (i.e., parallel to the web) within 1.5d on either side of flange (where d is the effective depth of the slab).

6.4.5.1 Model MS10

The dimensions of the model is shown in Figure (6.133), wall reinforcement in Figure (6.134) and slab reinforcement pattern in Figures (6.135– a) and (6.135– b).

Behaviour of the Model

No crack was observed after the ultimate gravity load was applied. At a lateral load of 23% of the design load, a number of cracks around the flange appeared as shown in Figure (6.136– a). As the loading progressed, they were joined by others until at a lateral load 32% of the design load, two long cracks appeared parallel to web as in Figure (6.136– b). On further loading, the crack parallel to flange at a distance 60 mm from its tip, extended to the end of the slab and more new cracks appeared until failure took place at a lateral load of 209 KN (95% of design load). The crack pattern after failure is shown in Figures (6.138) and (6.139), and the lateral load–displacement relationship in Figure (6.137). The strains in steel bars in windward direction (Figure 6.140) indicate that the first yielding occurred at a lateral load 74% of design load. Figure (6.142) shows the tensile strains in windward direction at different points along a bar running parallel to web, while Figure (6.143)

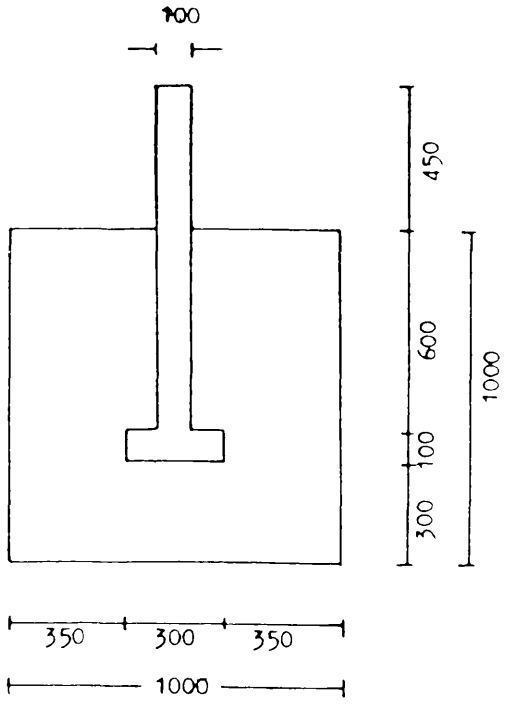

Figure (6.133) : Plan and dimensions of model MS10

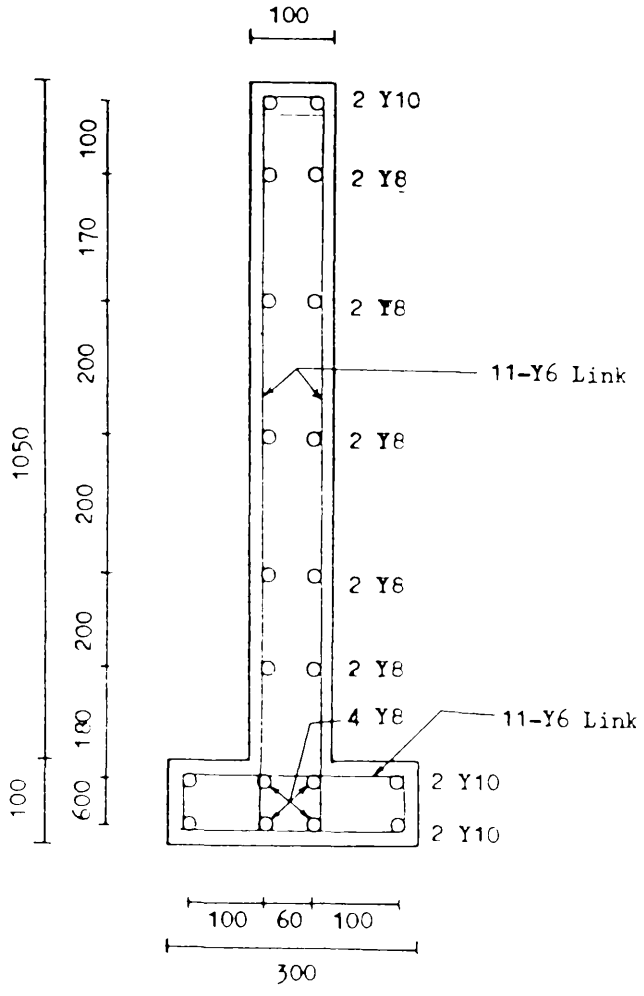

Figure (6.134) : A horizontal section in the wall of model MS10 showing the reinforcing details

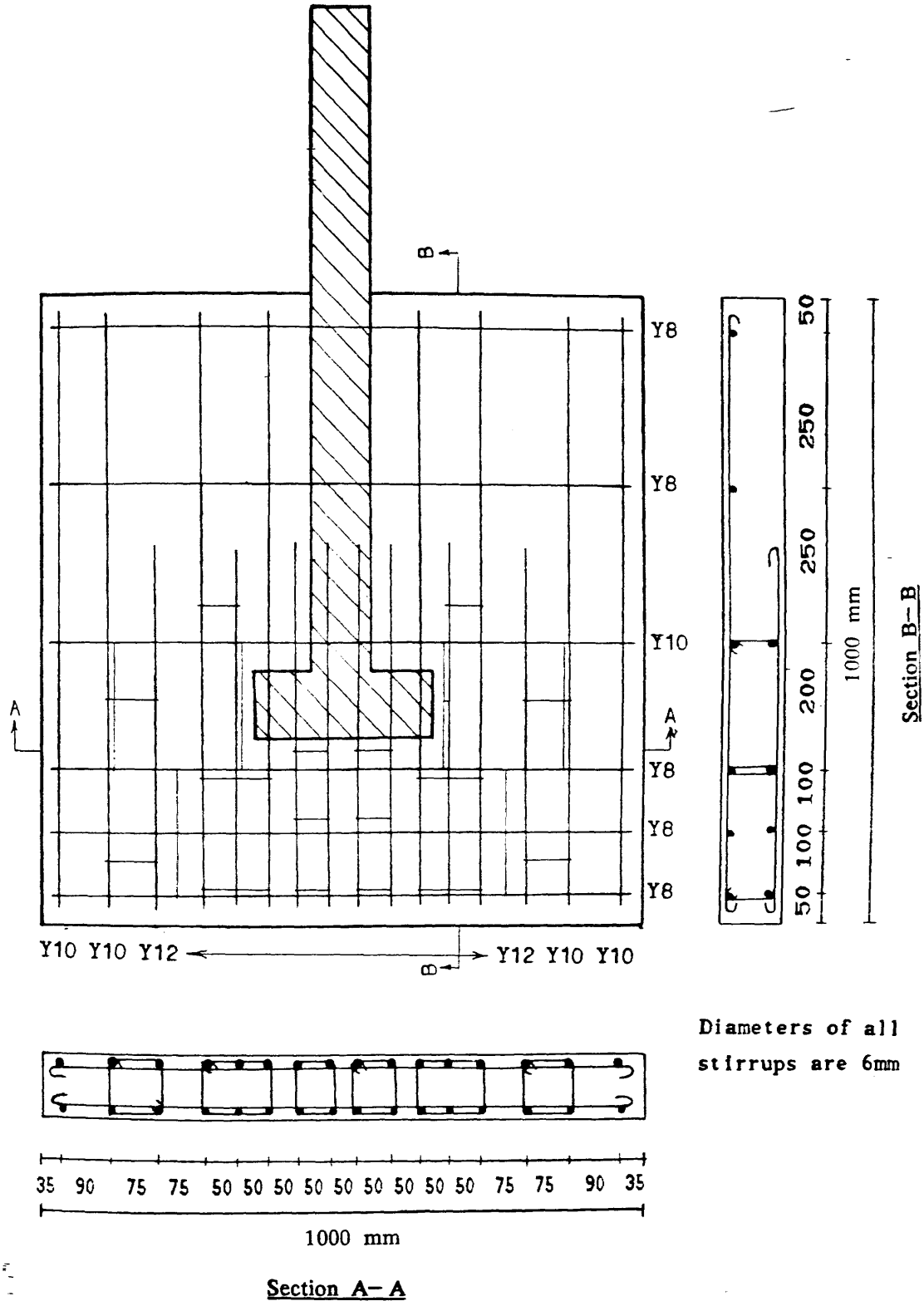

Figure (6.135-a) : Arrangement of top reinforcing bars including closed vertical stirrup in the slab of model MS10

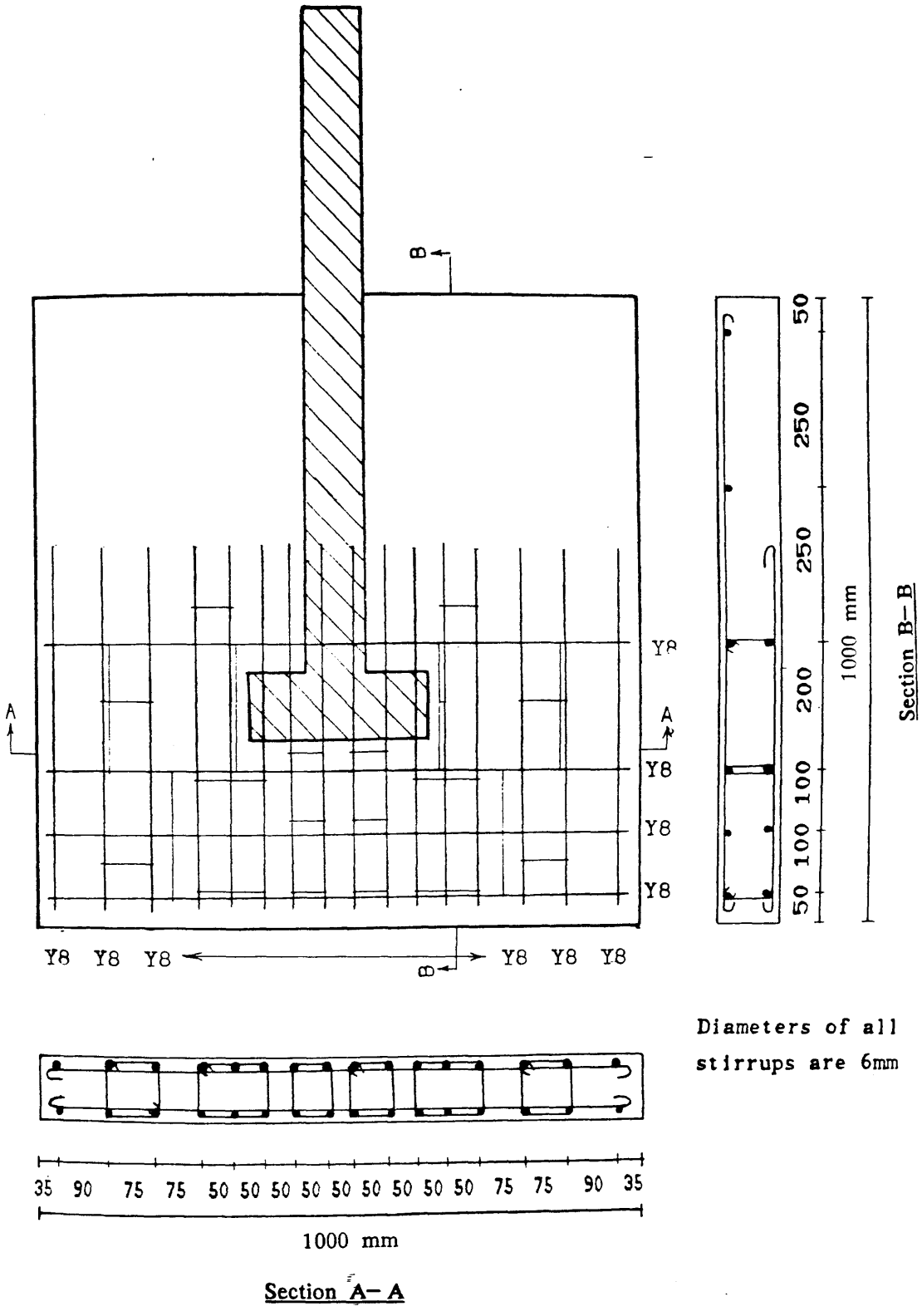

Figure (6.135-b) : Arrangement of bottom reinforcing bars including closed vertical stirrup in the slab of model MS10

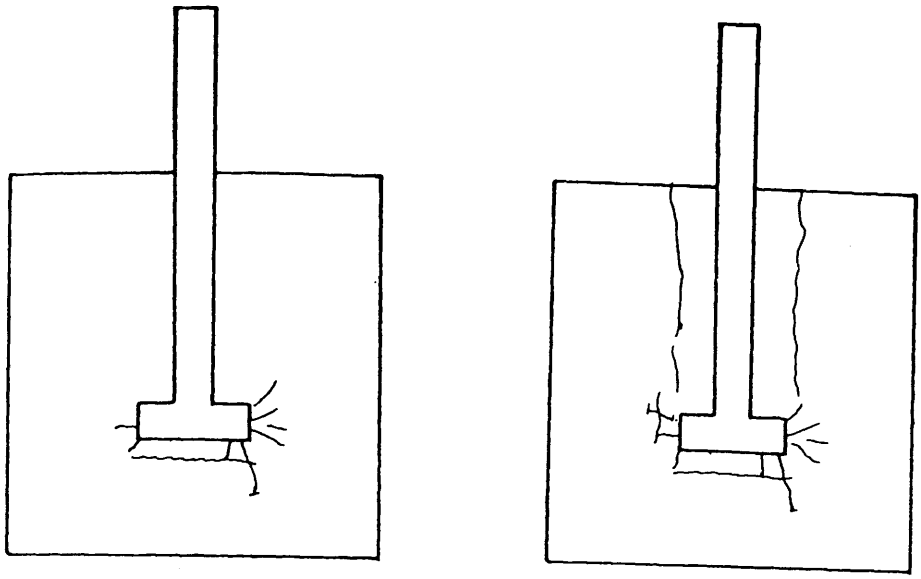

(a) at 23 %

(b) at 32 %

Figure (6.136) : Cracks initiation during testing of model MS10 at different percentages of design lateral load

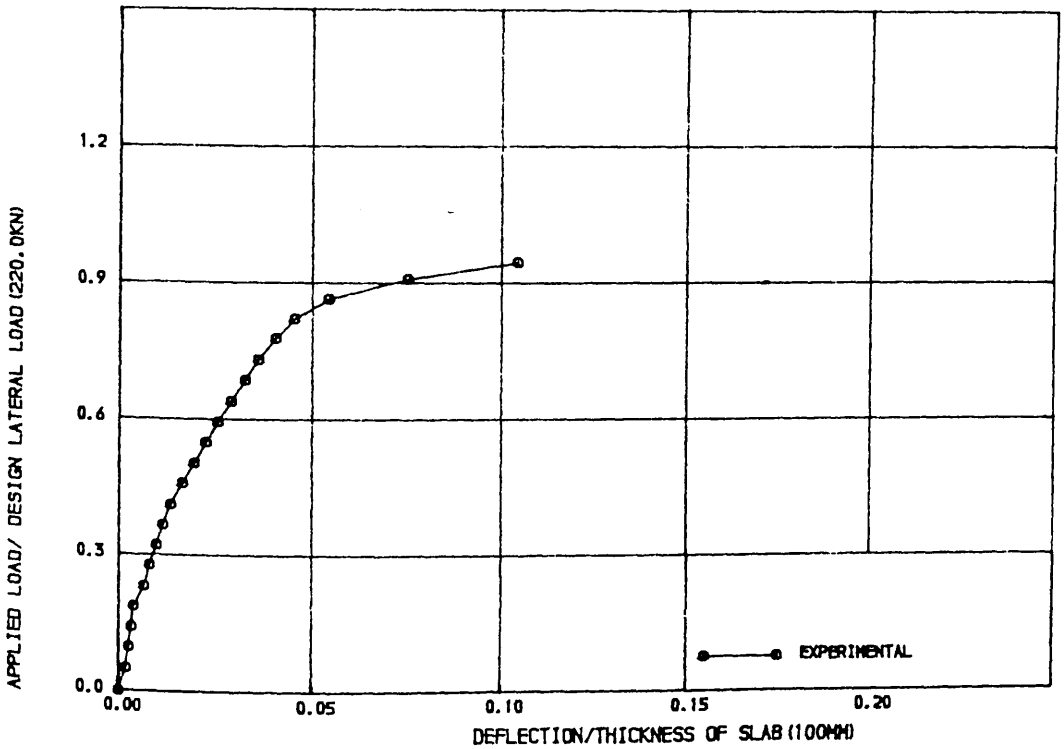

FIGURE (6.137) , LOAD-DEFLECTION CURVE FOR MODEL MS10

(a) Before removing the broken pieces

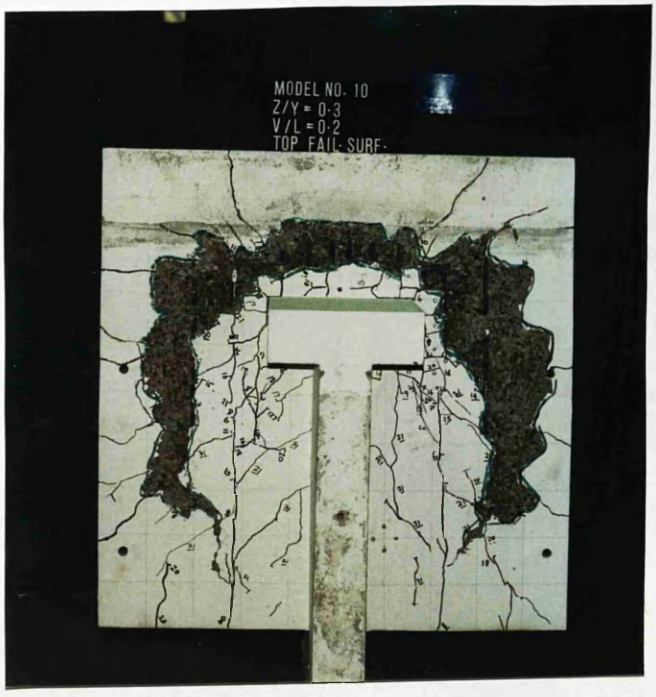

(b) After removing the broken pieces

Figure (6.138) : Crack pattern on the tensile surface of the slab of model MS10

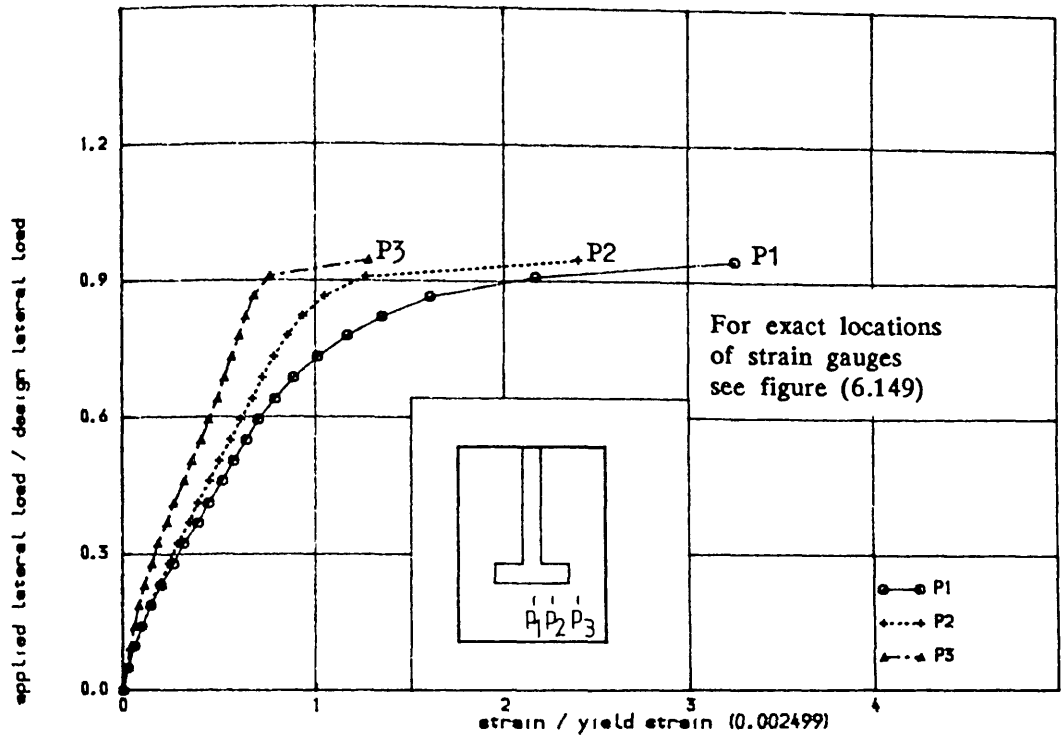

FIGURE (6.140) : TENSILE STRAIN IN STEEL IN WINDWARD DIRECTION ALONG TRANSVERSE SECTION IN THE SLAB OF MODEL MS10

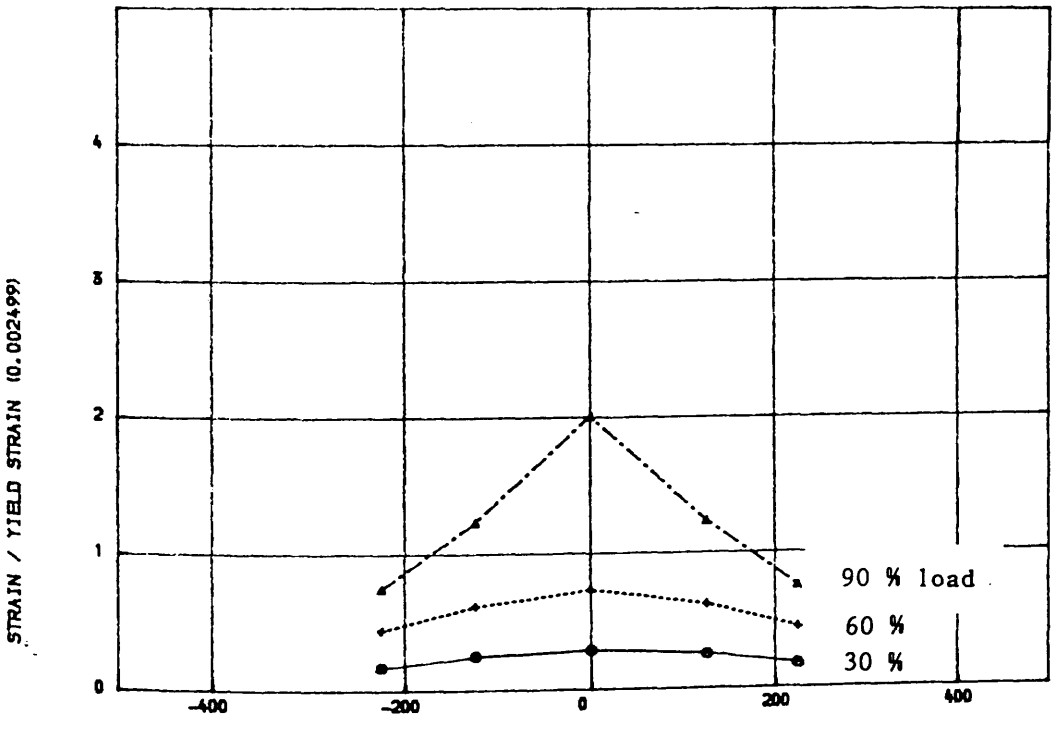

FIGURE (6.141) : VARIATION OF STRAIN IN STEEL IN WINDWARD DIRECTION ALONG TRANSVERSE SECTION AT DIFFERENT STAGES OF LOADING IN THE SLAB OF MODEL MS10

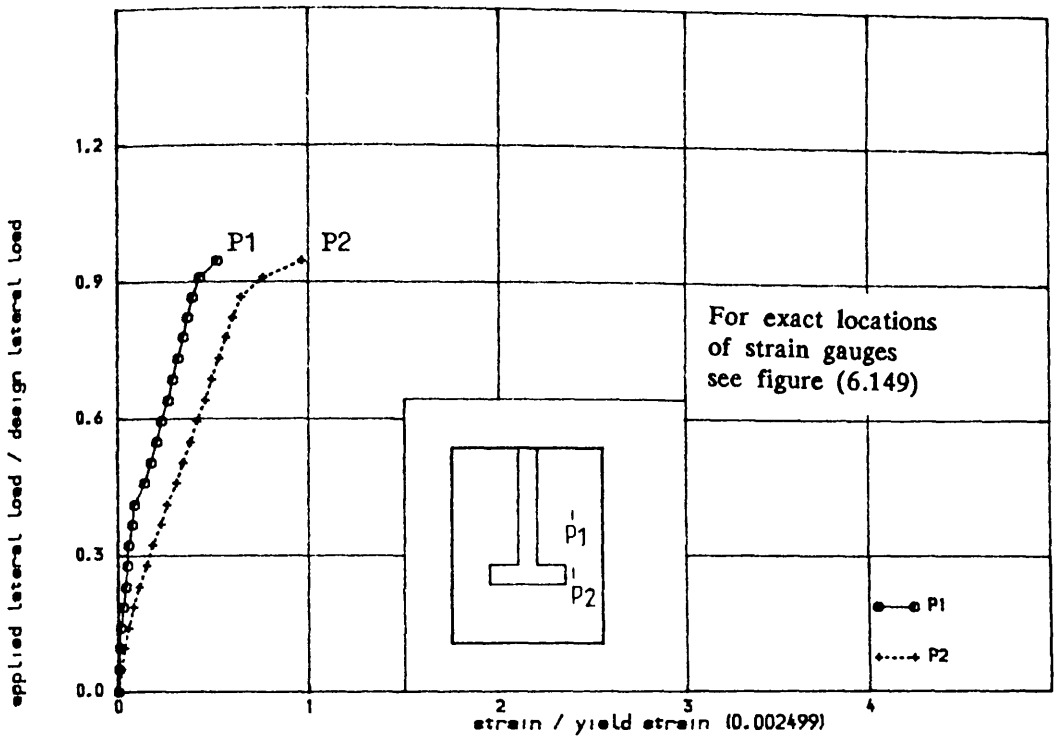

FIGURE (6.142) : TENSILE STRAIN IN STEEL IN WINDWARD DIRECTION ALONG A BAR RUNNING PARALLEL TO WEB IN THE SLAB OF MODEL MS10

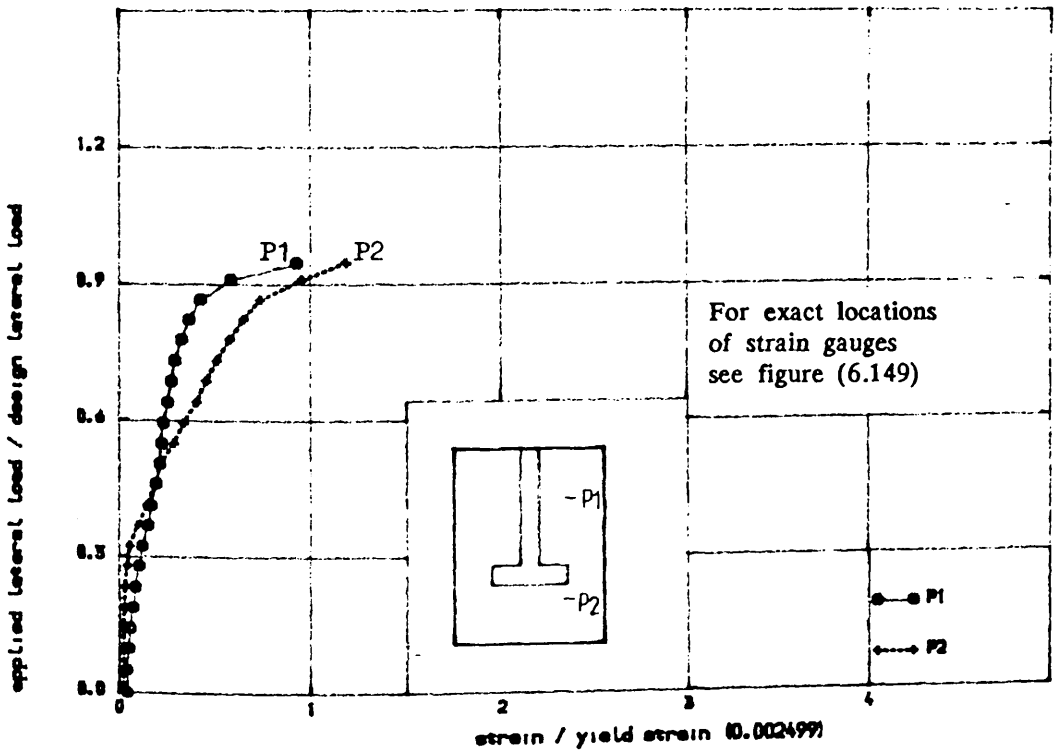

FIGURE (6.143) : TENSILE STRAIN IN STEEL IN TRANSVERSE DIRECTION ALONG WINDWARD SECTION IN THE SLAB OF MODEL MS10

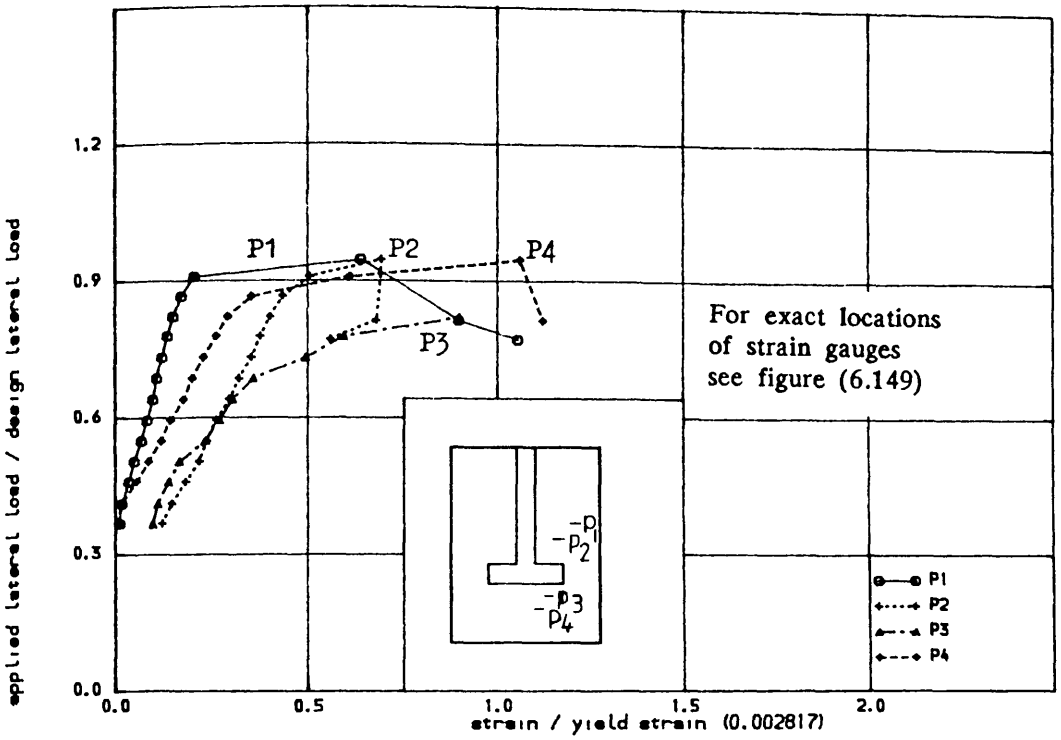

FIGURE (6.144) , STRAIN IN CLOSED VERTICAL STIRUP AT DIFFERENT LOCATIONS IN THE SLAB OF MODEL MS10

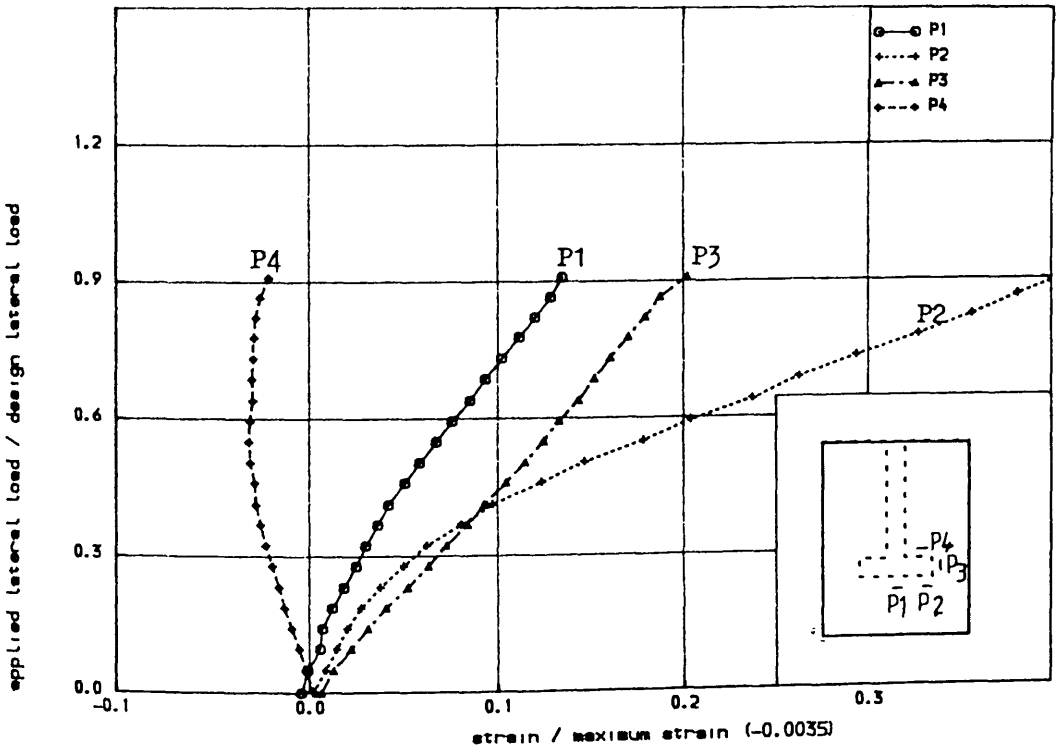

FIGURE (6.145) COMPRESSIVE AND TENSILE STRAIN IN FLANGE WALL JUST UNDERNEATH THE SLAB OF MODEL MS10

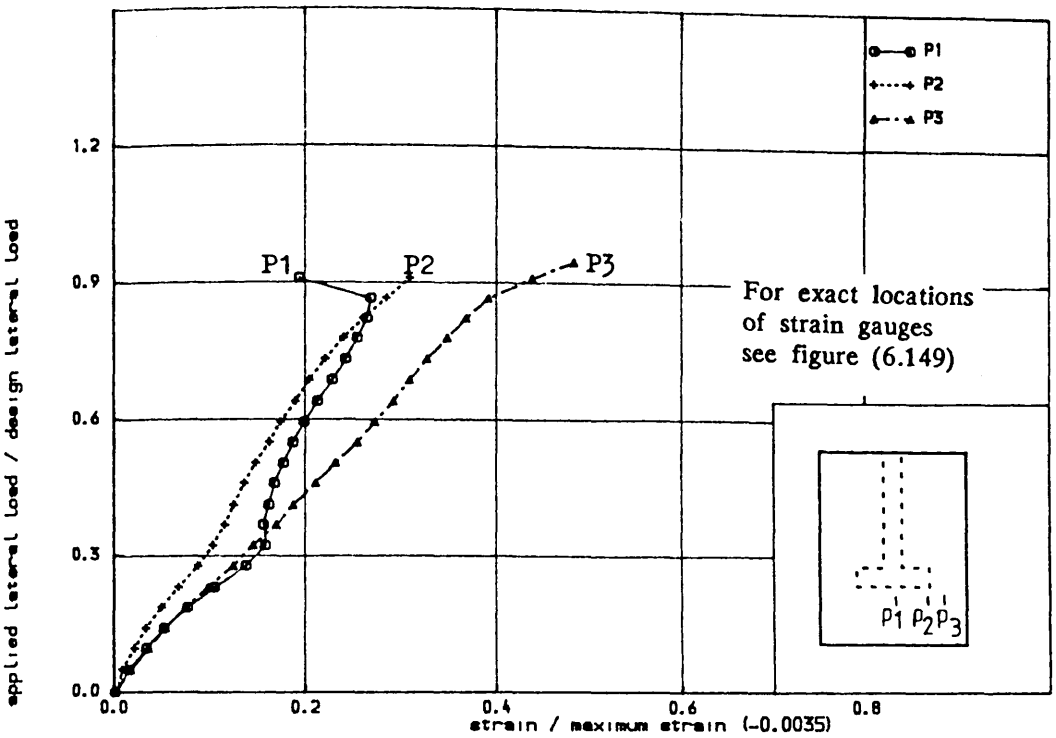

FIGURE (6.146) , COMPRESSIVE STRAIN IN CONCRETE IN WINDWARD DIRECTION IN THE SLAB OF MODEL MS10

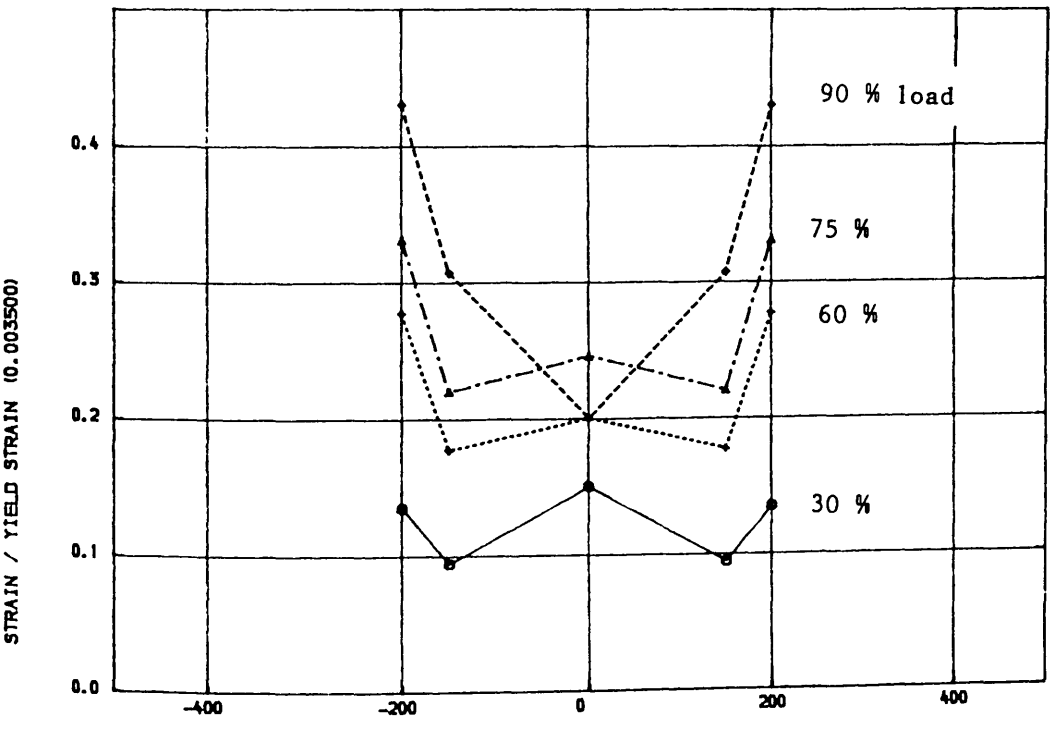

FIGURE (6.147) , VARIATION OF COMPRESSIVE STRAIN IN CONCRETE ALONG TRANSVERSE CRITICAL SECTION AT DIFFERENT STAGES OF LOADING IN THE SLAB OF MODEL MS10

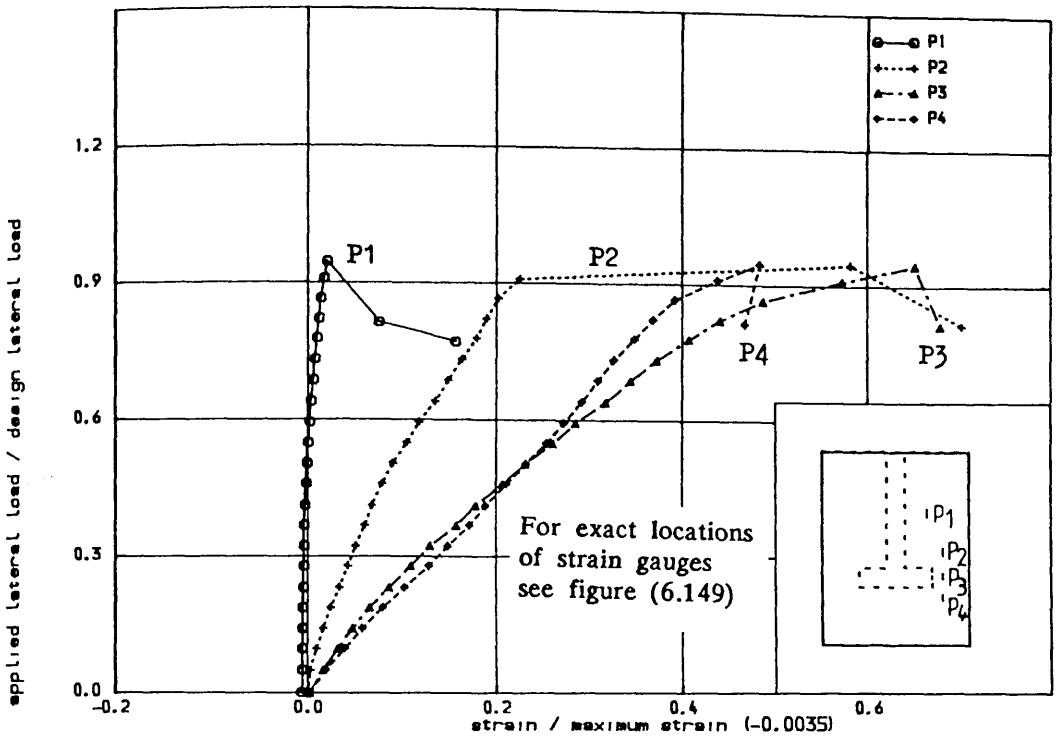

FIGURE (6.148) , COMPRESSIVE STRAIN IN CONCRETE IN WINDWARD DIRECTION ALONG A SECTION PARALLEL TO WEB IN THE SLAB OF MODEL MS10

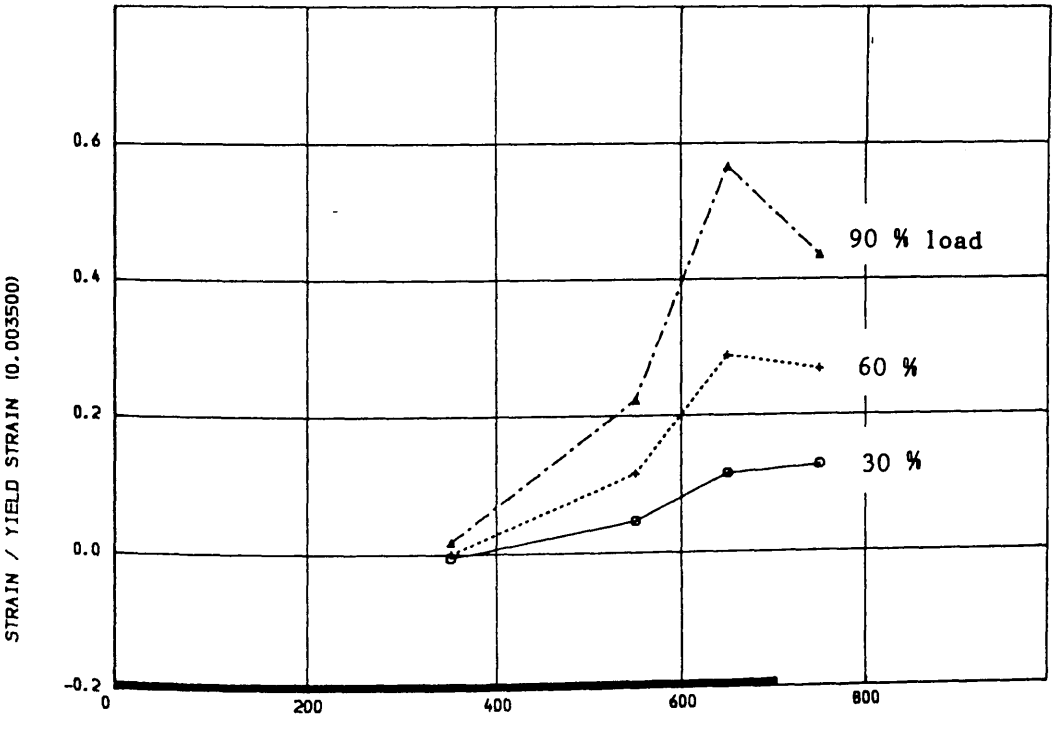

FIGURE (6.148-a) , VARIATION OF COMPRESSIVE STRAIN IN CONCRETE ALONG A SECTION PARALLEL TO WEB AT DIFFERENT STAGES OF LOADING IN THE SLAB OF MODEL MS10

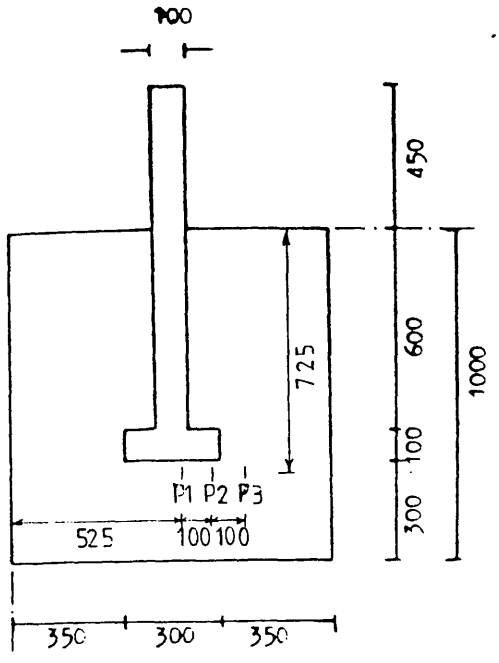

(a) Strain gauges in Figure (6.140)

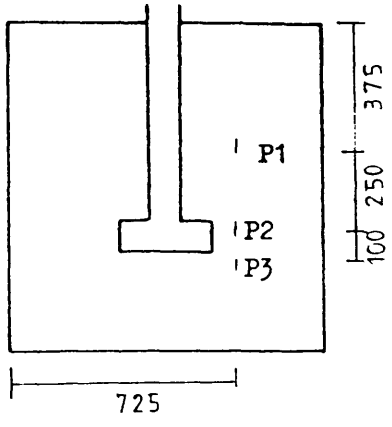

(b) Strain gauges in Figure (6.142)

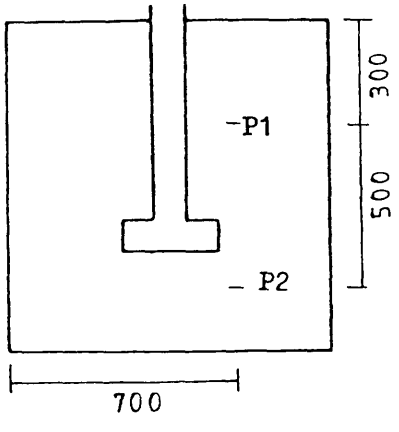

(c) Strain gauges in Figure (6.143)

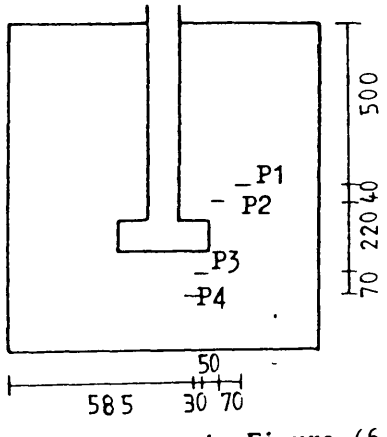

(d) Strain gauges in Figure (6.144)

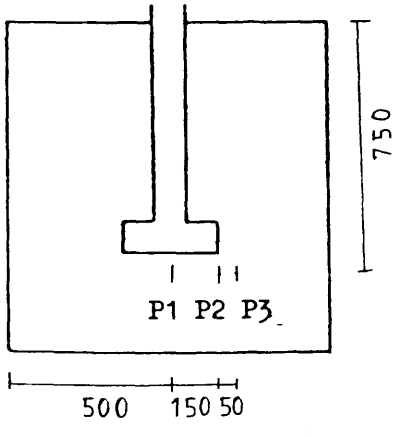

(e) Strain gauges in Figure (6.146)

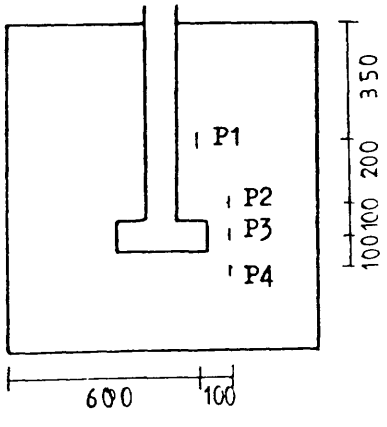

(f) Strain gauges in Figure (6.148)

FIGURE (6.149) : Exact locations of strain gauges in the slab of model MS10 as shown in Figures (6.140), (6.142), (6.143), (6.144), (6.146) and (6.148)

shows the tensile strain in transverse direction in steel bars. Figure (6.146) shows the compressive strains on slab and vertical strains on flange just at the front end are shown in Figure (6.145). In all these figures strains at zero lateral load are due to gravity load alone.

6.4.5.2 Model MS11

The plan of this model is shown in Figure (6.150), wall reinforcement in Figure (6.151) and reinforcement pattern in the slab in Figures (6.152– a) and (6.152– b).

Behaviour of the Model

During the application of gravity load, cracks around the flange were initiated at a load equals 16 KN (80% of the ultimate gravity load) as shown in Figure (6.153– a). After the ultimate gravity load was applied, no new cracks appeared. As the lateral loading progressed, a few new cracks were observed until 37% of design load at which stage long cracks parallel to web and some new cracks were observed as shown in Figure (6.153– b). When the load approached failure, many cracks were observed as shown in Figure (6.165). Some were in the corridor area parallel to flange and some were at the back of the slab, behind the flange and parallel to web. Failure took place at a lateral load equals 219 KN (102% of design load).

The load deflection curve in Figure (6.154) shows the ductile behaviour of the slab. Tensile and compressive strains in windward direction at locations along a section parallel to flange are shown in Figures (6.155) and (6.162) respectively. Yielding of steel in windward direction was first observed at a lateral load 71% of design load. Tensile and compressive strains in windward direction at locations along a section parallel to web are shown in Figures (6.157) and (6.163) respectively. Tensile strains of steel in transverse direction are shown in Figure (6.158) and strains on closed vertical stirrups are shown in Figure (6.159). Vertical strains on flange just underneath the slab are shown in Figure (6.160). The crack pattern after failure is shown in Figures (6.165) and (6.166).

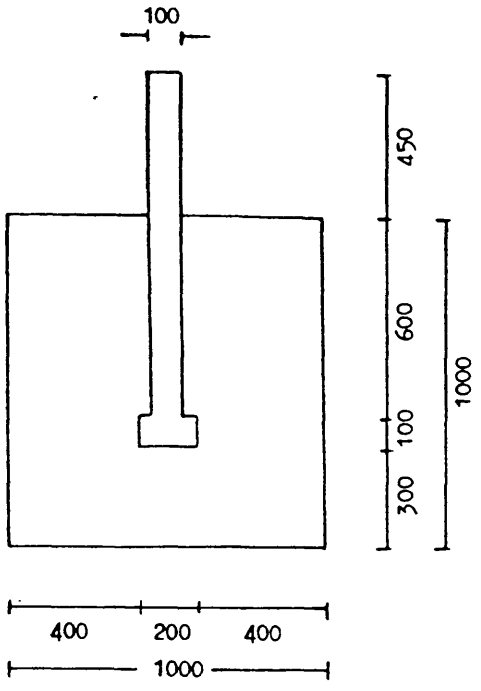

Figure (6.150) : Plan and dimensions of model MS11

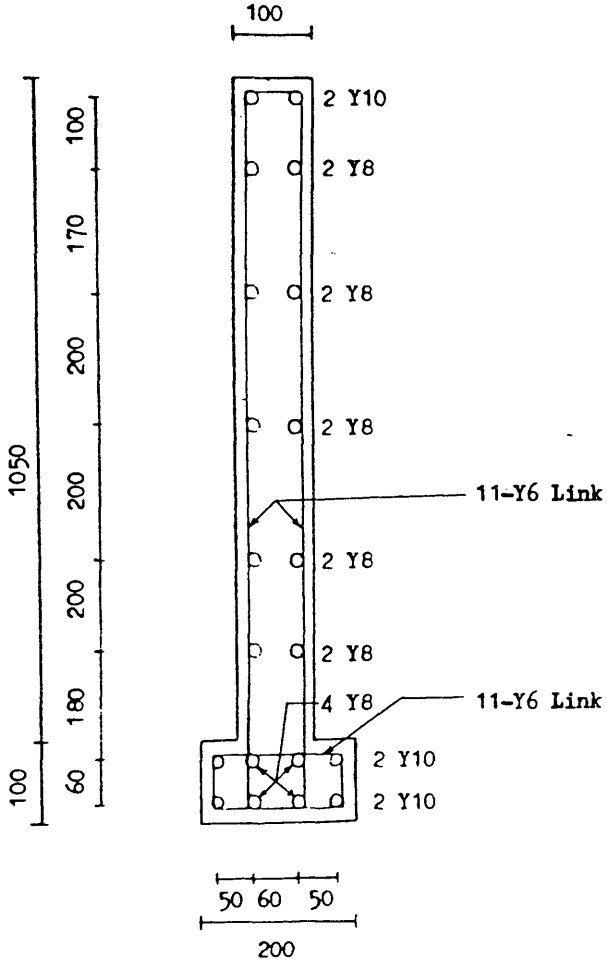

Figure (6.151) : A horizontal section in the wall of model MS11 showing the reinforcing details

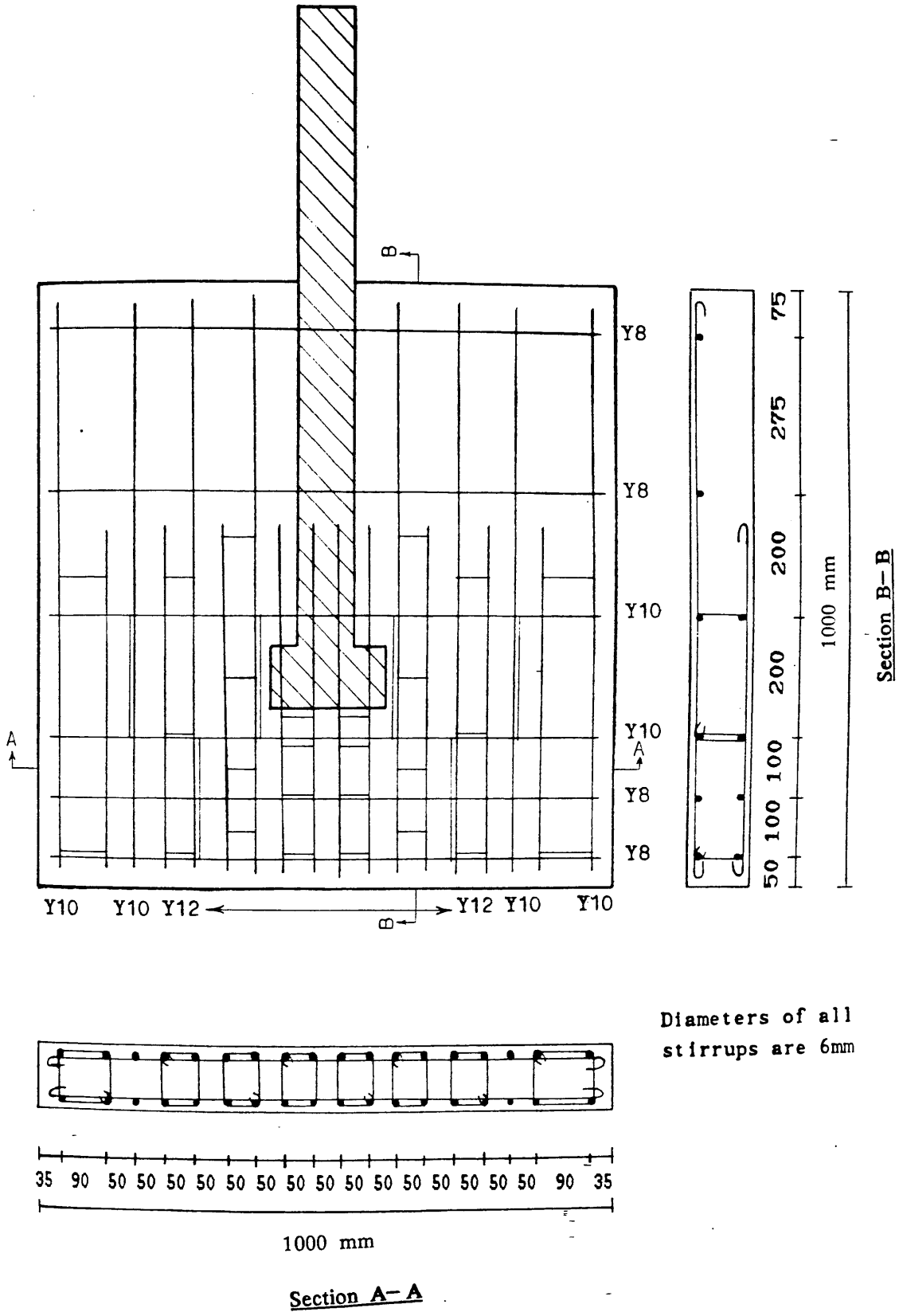

Figure (6.152-a) : Arrangement of top reinforcing bars including closed vertical stirrup in the slab of model MS11

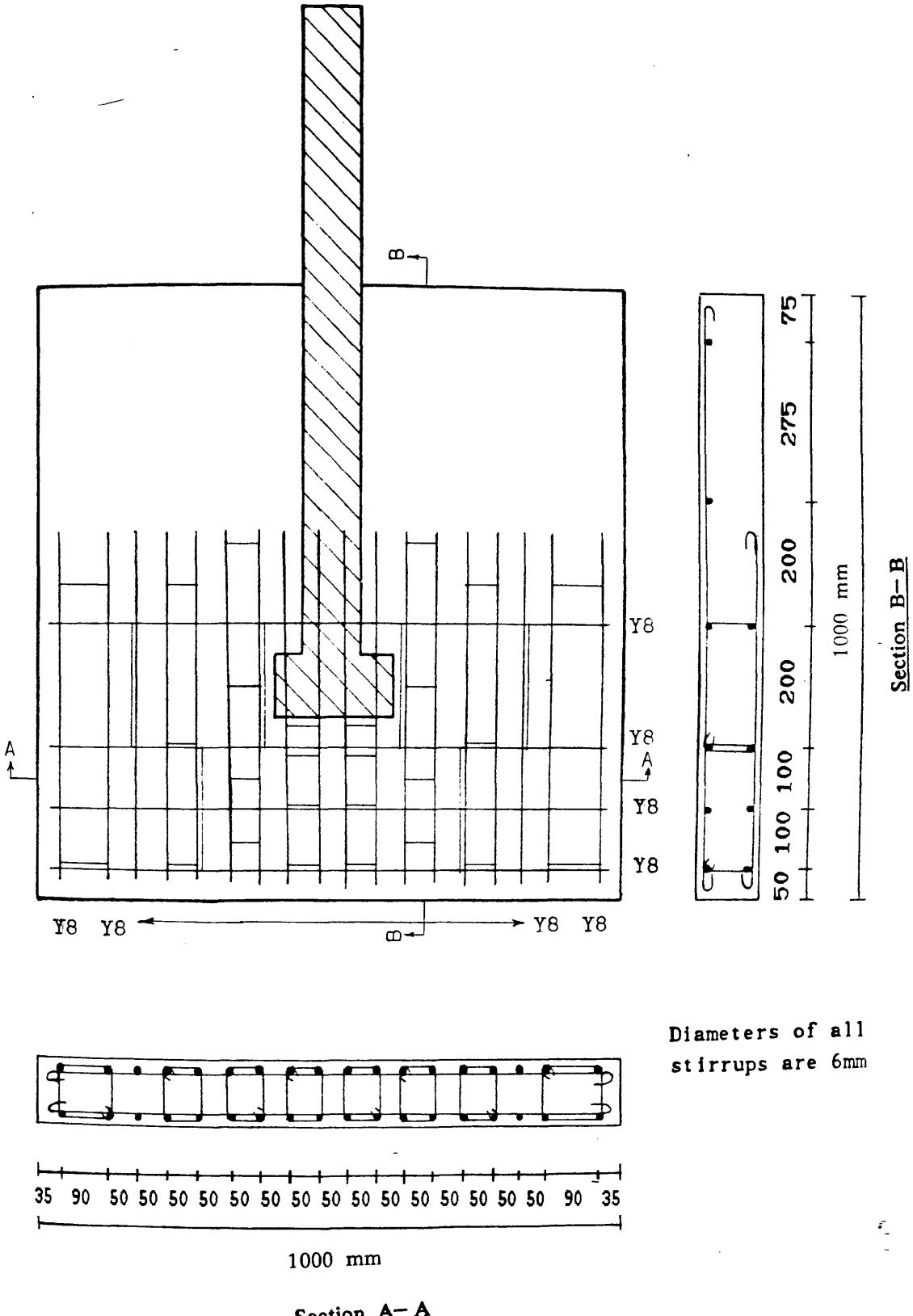

Figure (6.152-b) : Arrangement of bottom reinforcing bars including closed vertical stirrup in the slab of model MS11

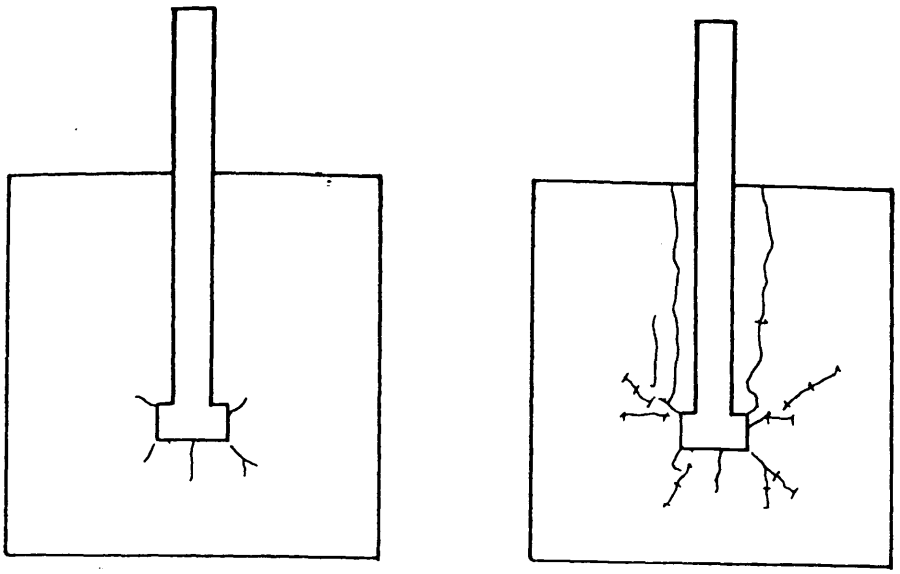

(a) at 80 % of ultimate gravity load (and zero lateral load)

(b) at a lateral load 37 % of design load

Figure (6.153) : Cracks initiation during testing of model MS11 at different percentages of design lateral load

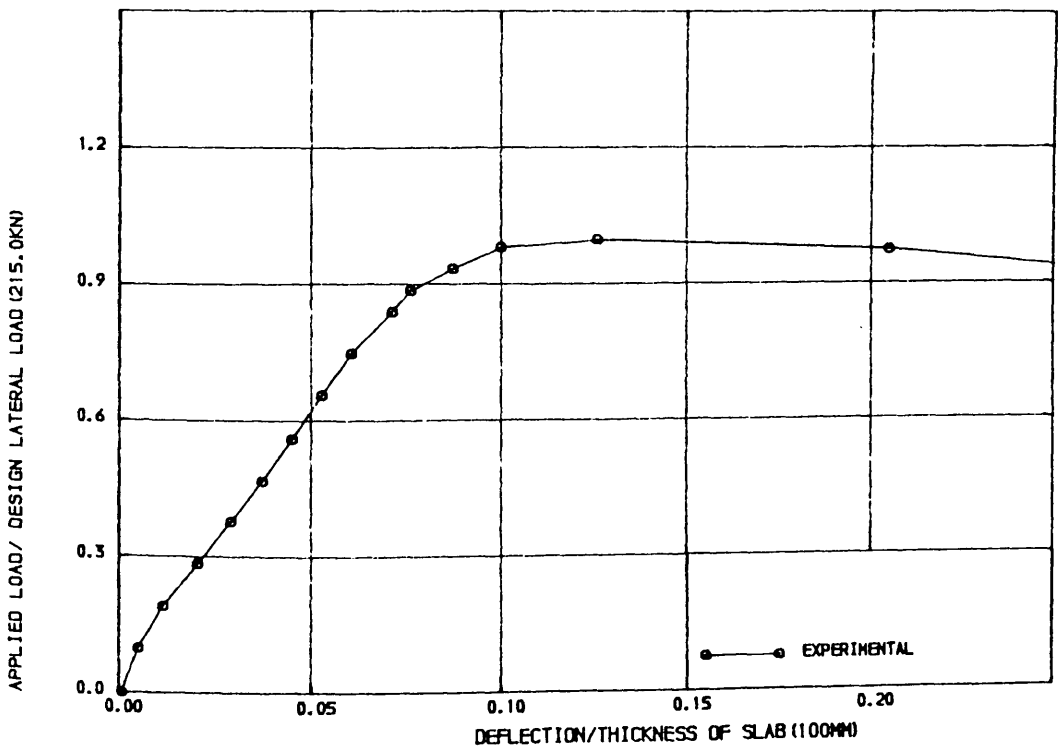

FIGURE (6.154) , LOAD-DEFLECTION CURVE FOR MODEL MS11

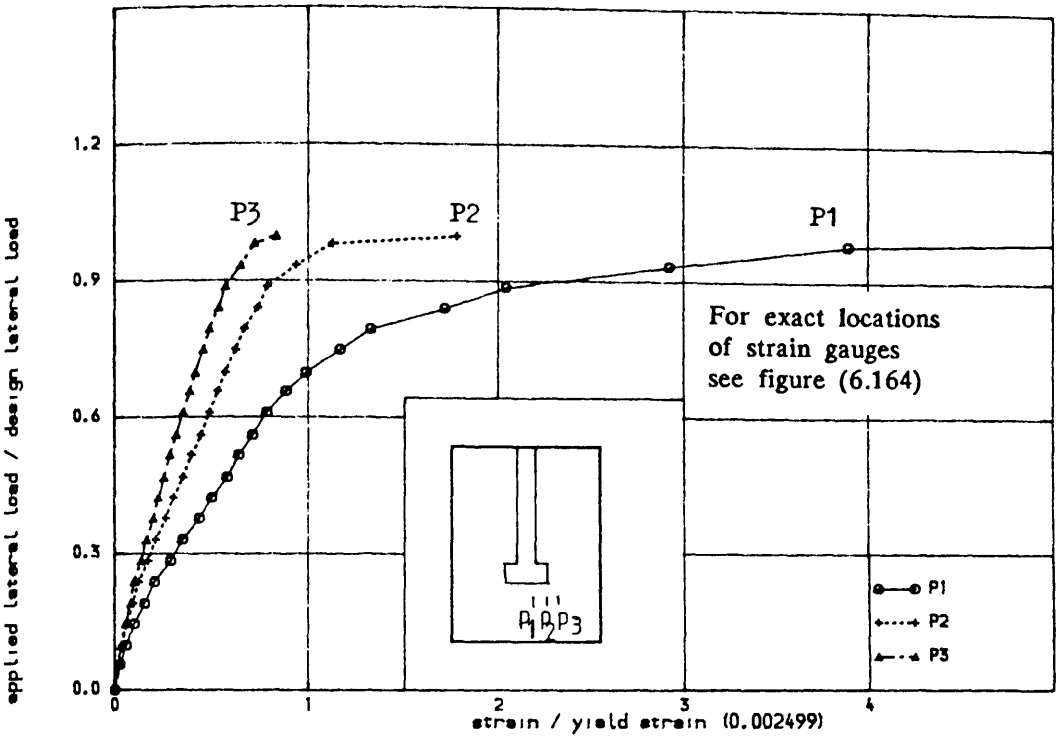

FIGURE (6.155) , TENSILE STRAIN IN STEEL IN WINDWARD DIRECTION ALONG TRANSVERSE SECTION IN THE SLAB OF MODEL MS11

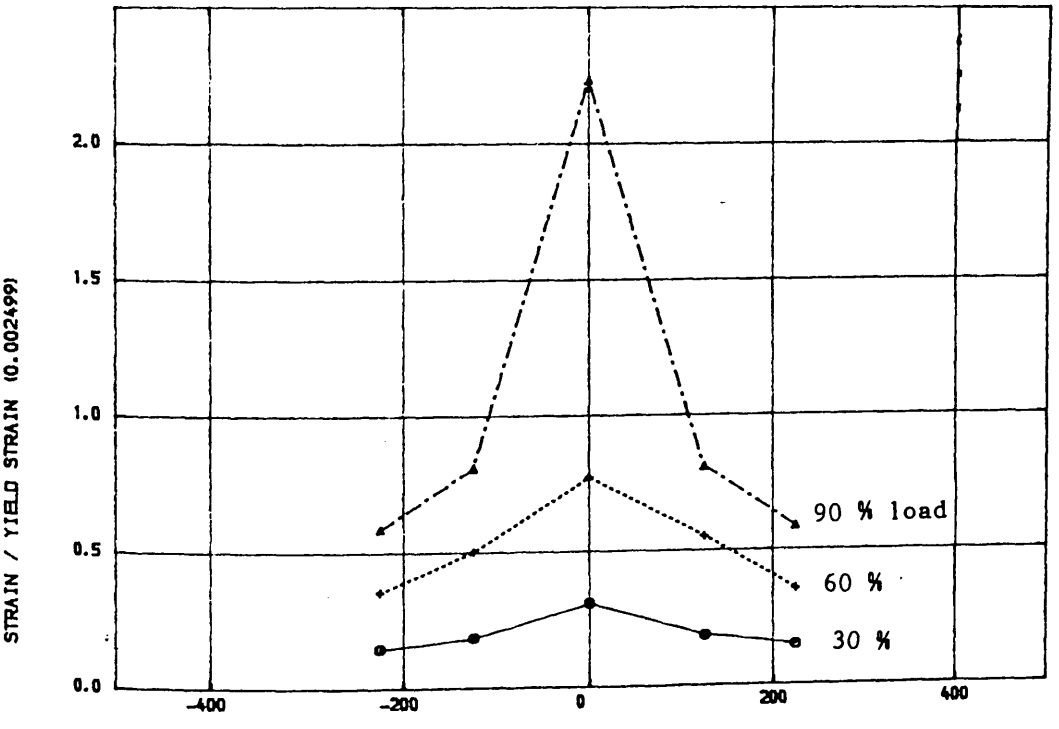

FIGURE (6.156) , VARIATION OF STRAIN IN STEEL IN WINDWARD DIRECTION ALONG TRANSVERSE SECTION AT DIFFERENT STAGES OF LOADING IN THE SLAB OF MODEL MS11

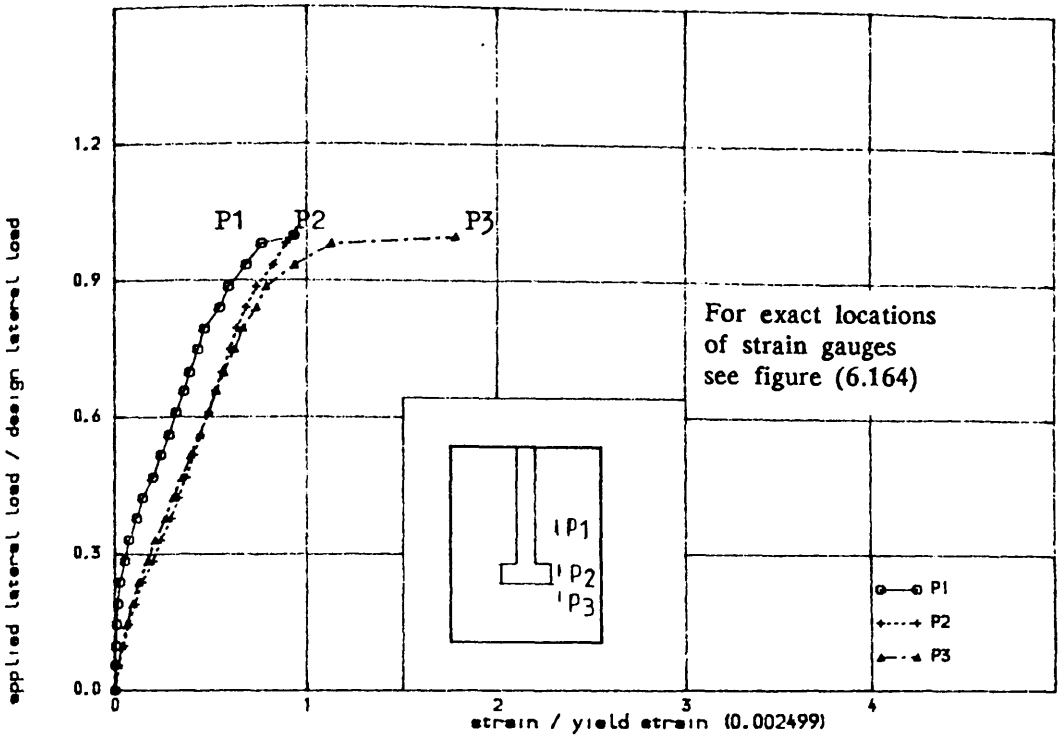

FIGURE (6.157) , TENSILE STRAIN IN STEEL IN VINDVARD DIRECTION ALONG A BAR RUNNING PARALLEL TO VEB IN THE SLAB OF MODEL MS11

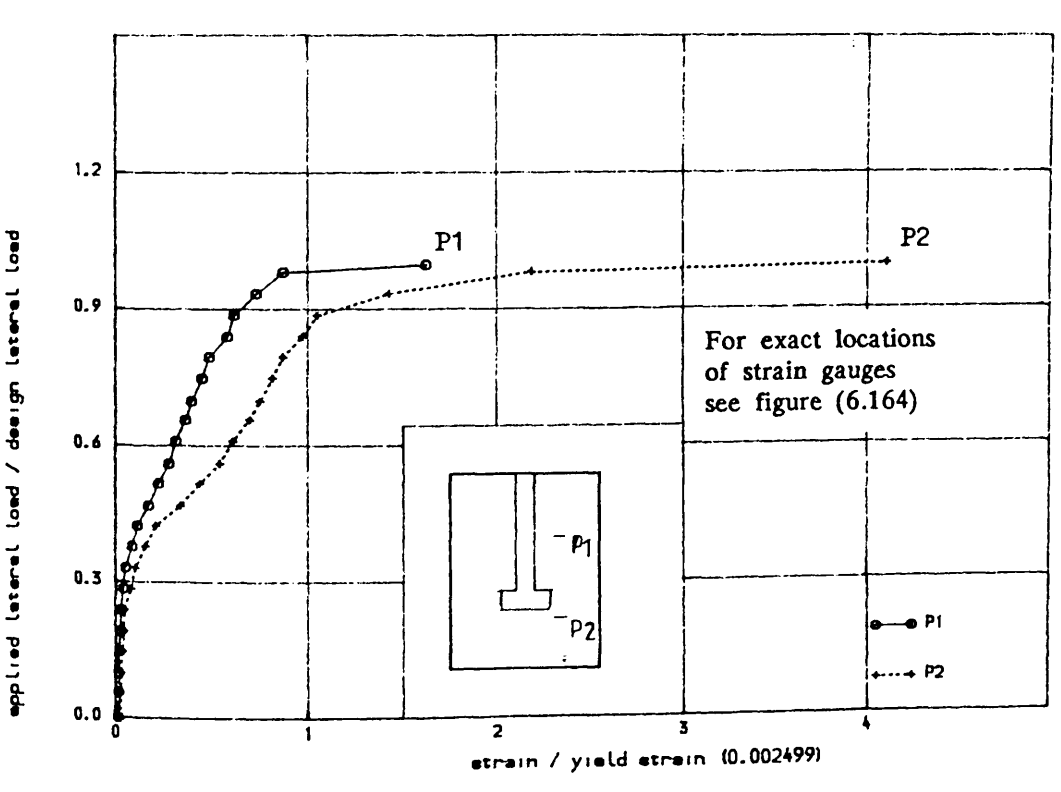

FIGURE (6.158) , TENSILE STRAIN IN STEEL IN TRANSVERSE DIRECTION ALONG VINDVARD SECTION IN THE SLAB OF MODEL MS11

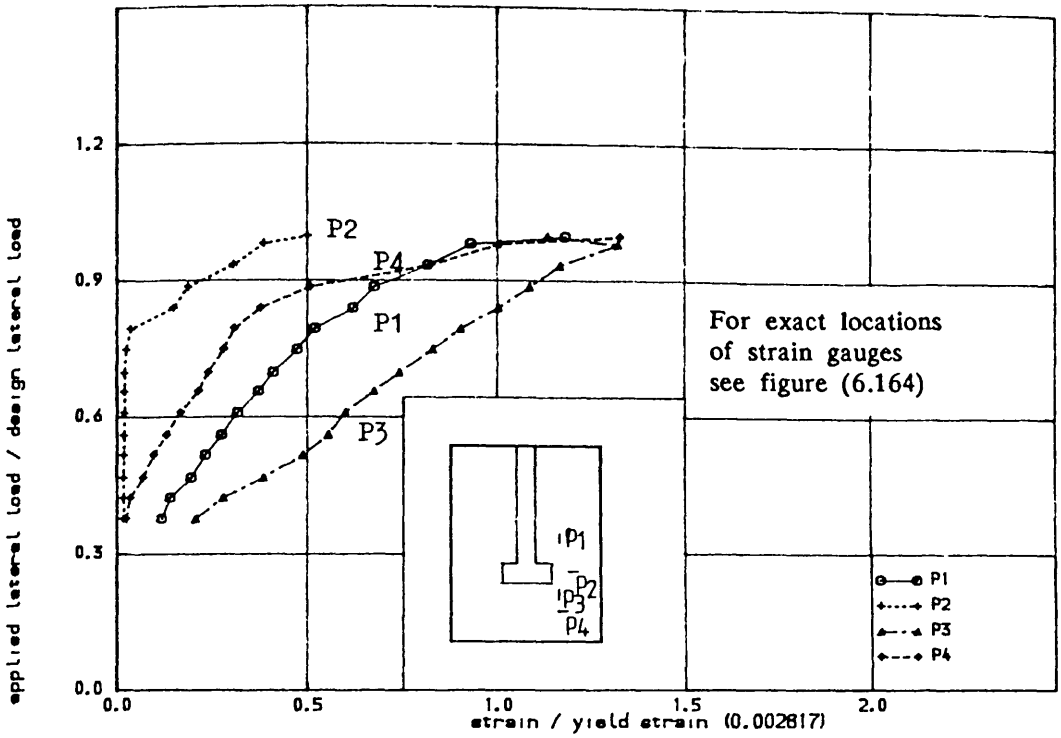

FIGURE (6.159) , STRAIN IN CLOSED VERTICAL STIRUP AT DIFFERENT LOCATIONS IN THE SLAB OF MODEL MS11

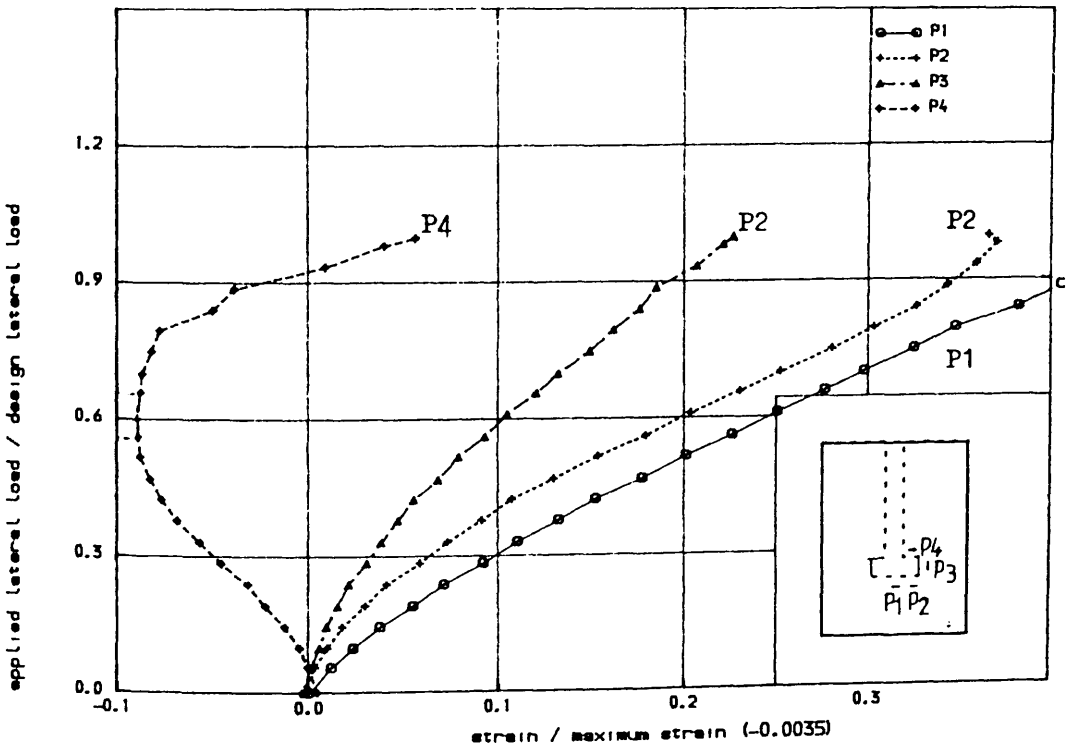

FIGURE (6.160) , COMPRESSIVE AND TENSILE STRAIN IN FLANGE WALL JUST UNDERNEATH THE SLAB OF MODEL MS11

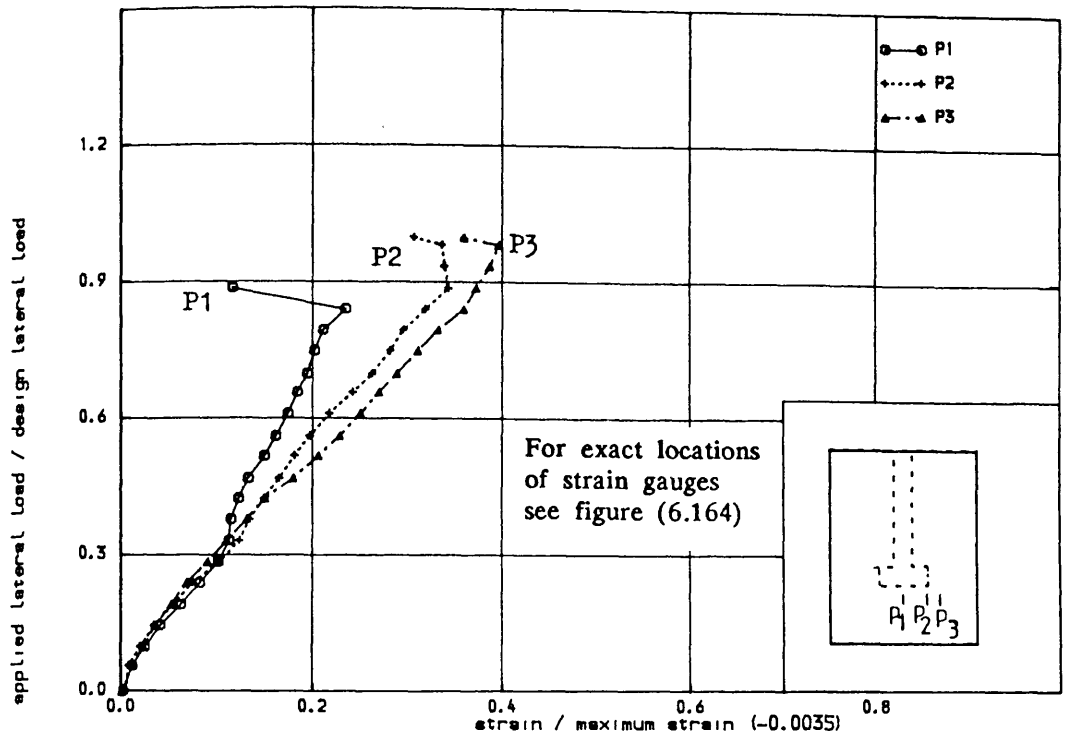

FIGURE (6.161) , COMPRESSIVE STRAIN IN CONCRETE IN VINDVARD DIRECTION IN THE SLAB OF MODEL MS11

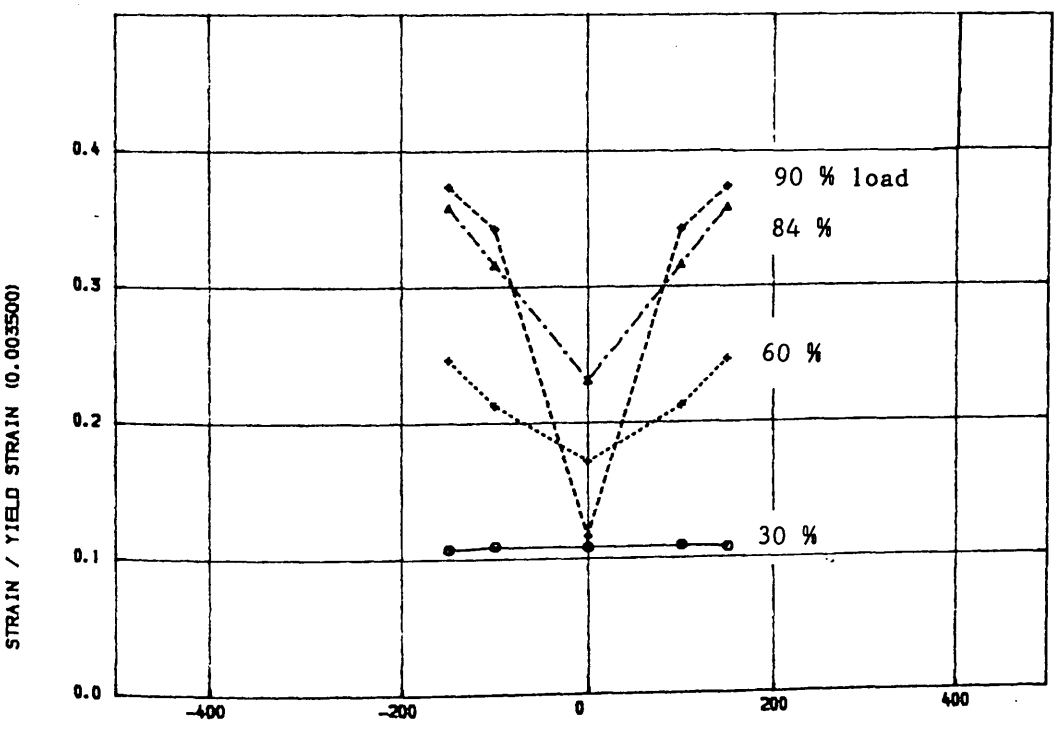

FIGURE (6.162) , VARIATION OF COMPRESSIVE STRAIN IN CONCRETE ALONG TRANSVERSE CRITICAL SECTION AT DIFFERENT STAGES OF LOADING IN THE SLAB OF MODEL MS11

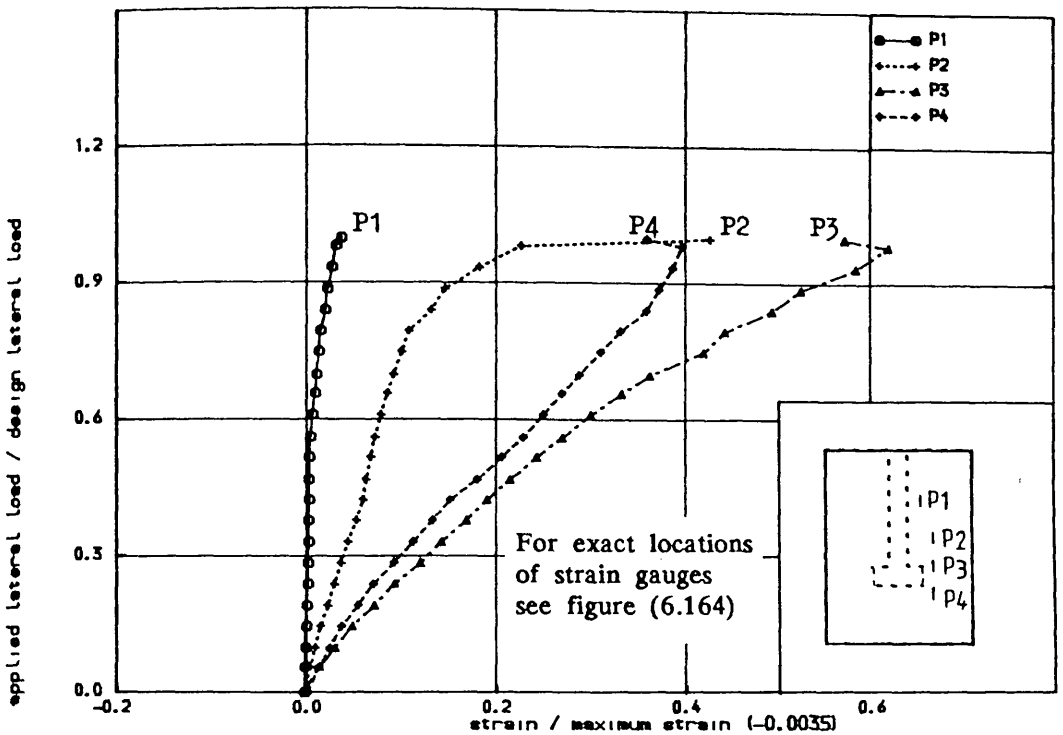

FIGURE (6.163) , COMPRESSIVE STRAIN IN CONCRETE IN WINDWARD DIRECTION ALONG A SECTION PARALLEL TO WEB IN THE SLAB OF MODEL MS11

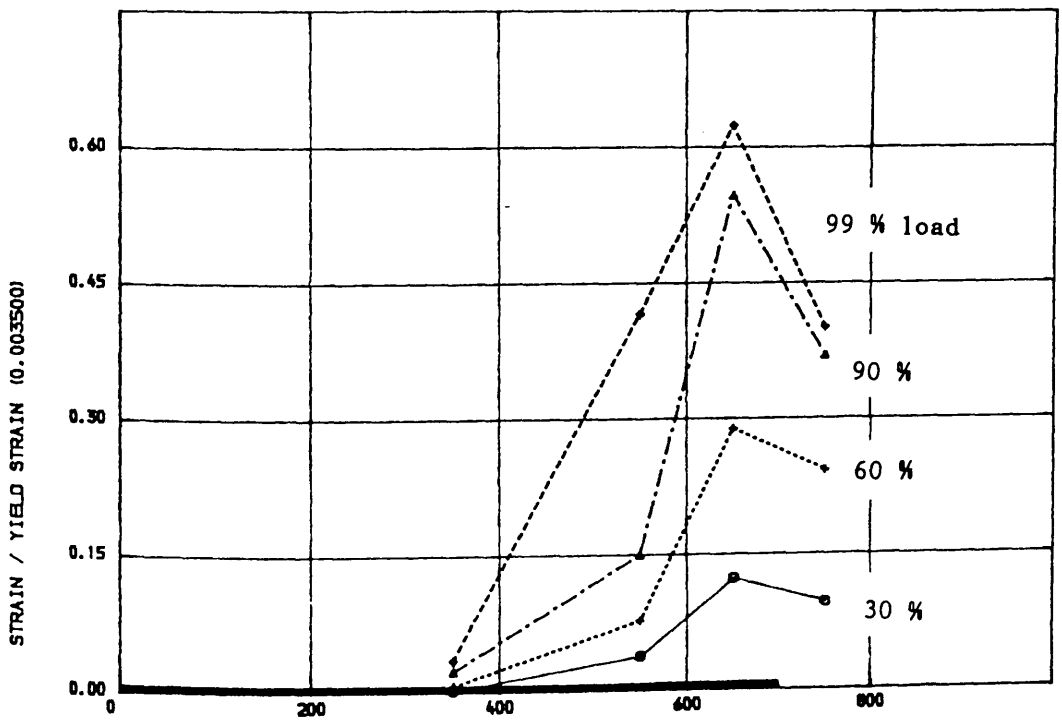

FIGURE (6.163-a) , VARIATION OF COMPRESSIVE STRAIN IN CONCRETE ALONG A SECTION PARALLEL TO WEB AT DIFFERENT STAGES OF LOADING IN THE SLAB OF MODEL MS11

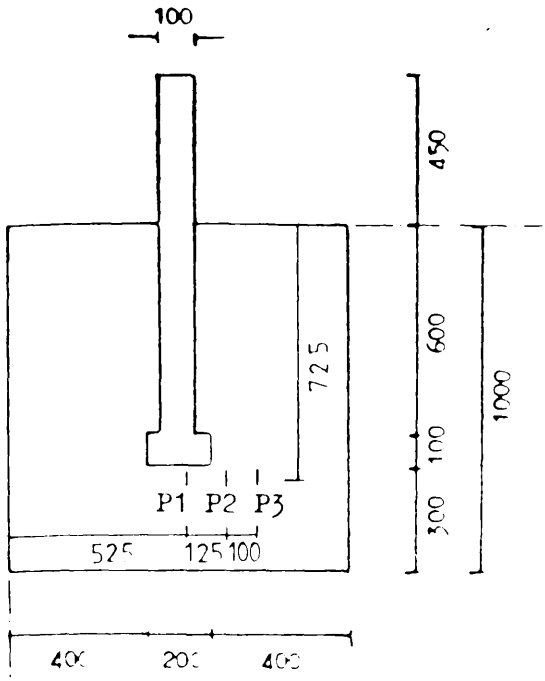

(a) Strain gauges in Figure (6.155)

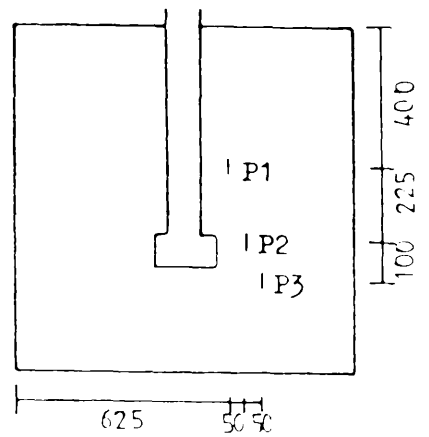

(b) Strain gauges in Figure (6.157)

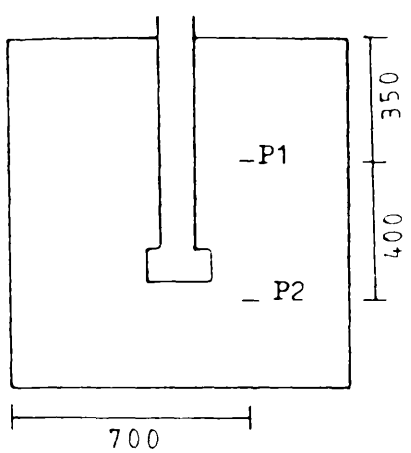

(c) Strain gauges in Figure (6.158)

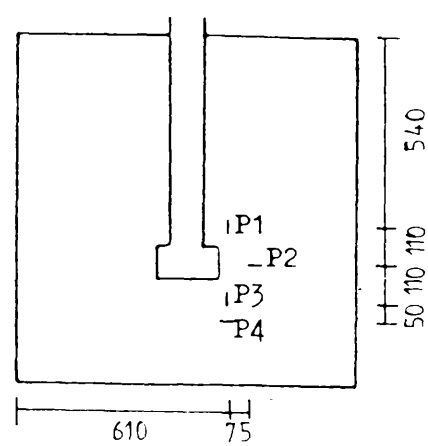

(d) Strain gauges in Figure (6.159)

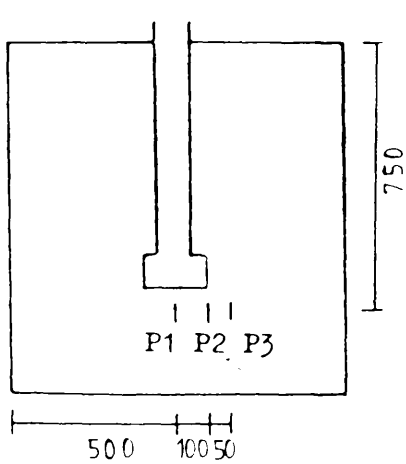

(e) Strain gauges in Figure (6.161)

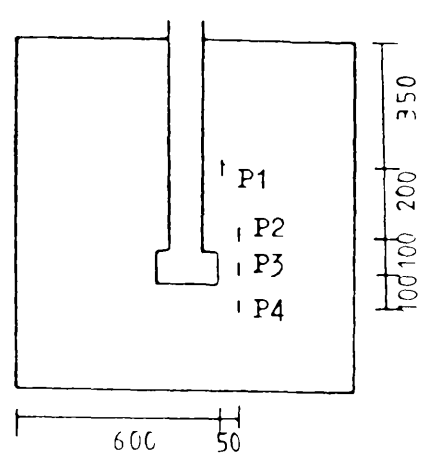

(f) Strain gauges in Figure (6.163)

FIGURE (6.164) : Exact locations of strain gauges in the slab of model MS11 as shown in Figures (6.155), (6.157), (6.158), (6.159), (6.161) and (6.163)

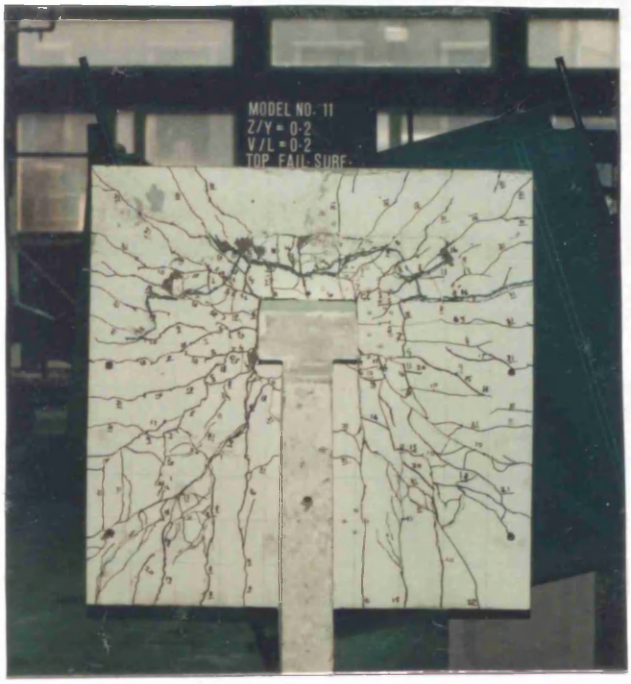

(a) Before removing the broken pieces

(b) After removing the broken pieces

Figure (6.165) : Crack pattern on the tensile surface of the slab of model MS11

(a) On the compressive side

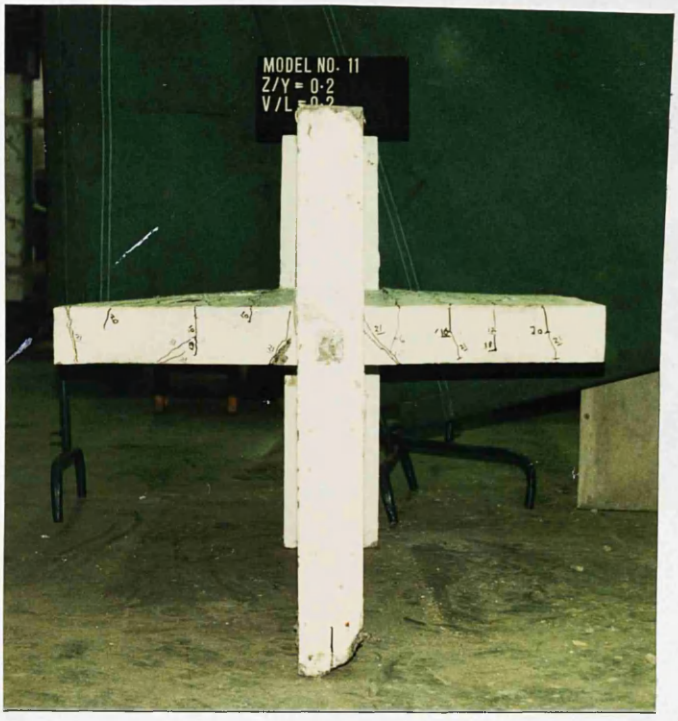

(b) On the back surface

Figure (6.166) : Crack pattern on the slab of model MS11

6.4.5.3 Model MS12

The plan of this model is shown in figure (6.167). Wall reinforcement is shown in Figure (6.168) and the reinforcement pattern in slab is shown in Figure (6.169).

Behaviour of the Model

No cracks were observed after the ultimate gravity load was fully applied. Two cracks as shown in Figure (6.170– a) were first observed at a lateral load 19% of the design load. On further loading, these cracks extended and more new cracks developed in the corridor area parallel and normal to the flange until the load was 37% of the design load. The crack pattern was as shown in Figure (6.170– b). On further loading, more cracks appeared until failure took place at a lateral load of 235 KN (109% of design load). The crack pattern after failure is shown in Figures (6.172) and (6.173) and the lateral load– displacement relationship in Figure (6.171). The strains in steel bars in windward direction (Figure 6.174) indicate that the first yielding occurred at a lateral load of about 80% of design load. The other experimental data are shown in Figures (6.175) to (6.183).

6.4.5.4 Comparisons and Discussions

Figure (6.184) shows the lateral load – deflection curves for the models of this series. These curves show that model MS11 with minimum flange width suffered more displacements than models MS10 and MS12 at approximately similar percentage of design load indicating, as is to be expected, an increase in stiffness with increase of flange width. All the three models MS10, MS11 and MS12 failed in a ductile manner at 95%, 102% and 109% of design lateral load. Steel in windward direction yielded at 74%, 71% and 80% of design load respectively.

Considering the crack patterns in Figures (6.138) for MS10, (6.165) for MS11 and (6.172) for MS12, it can be said in general that very few cracks existed on the tensile side of slab in the area within the flange boundaries which is a 'dead' area. In the corridor area, more cracks parallel to flange occured with the increase in

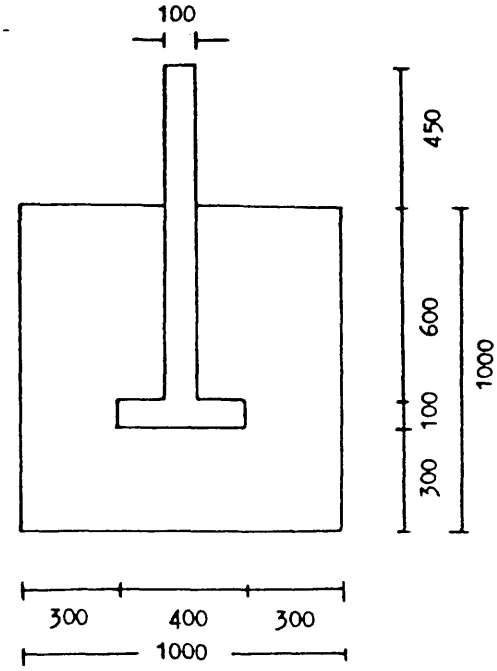

Figure (6.167) : Plan and dimensions of model MS12

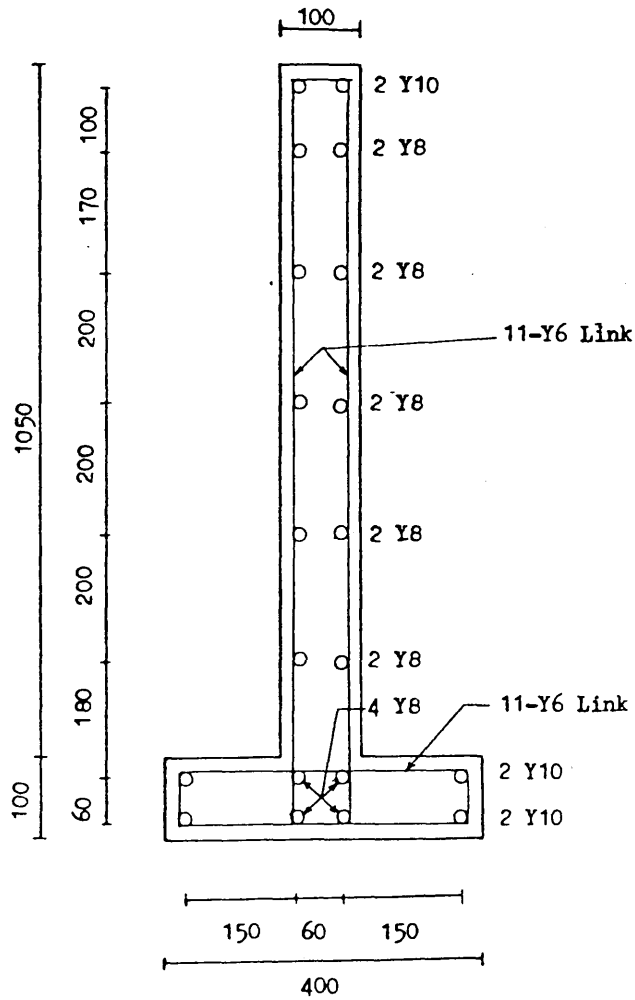

Figure (6.168) : A horizontal section in the wall of model MS12 showing the reinforcing details

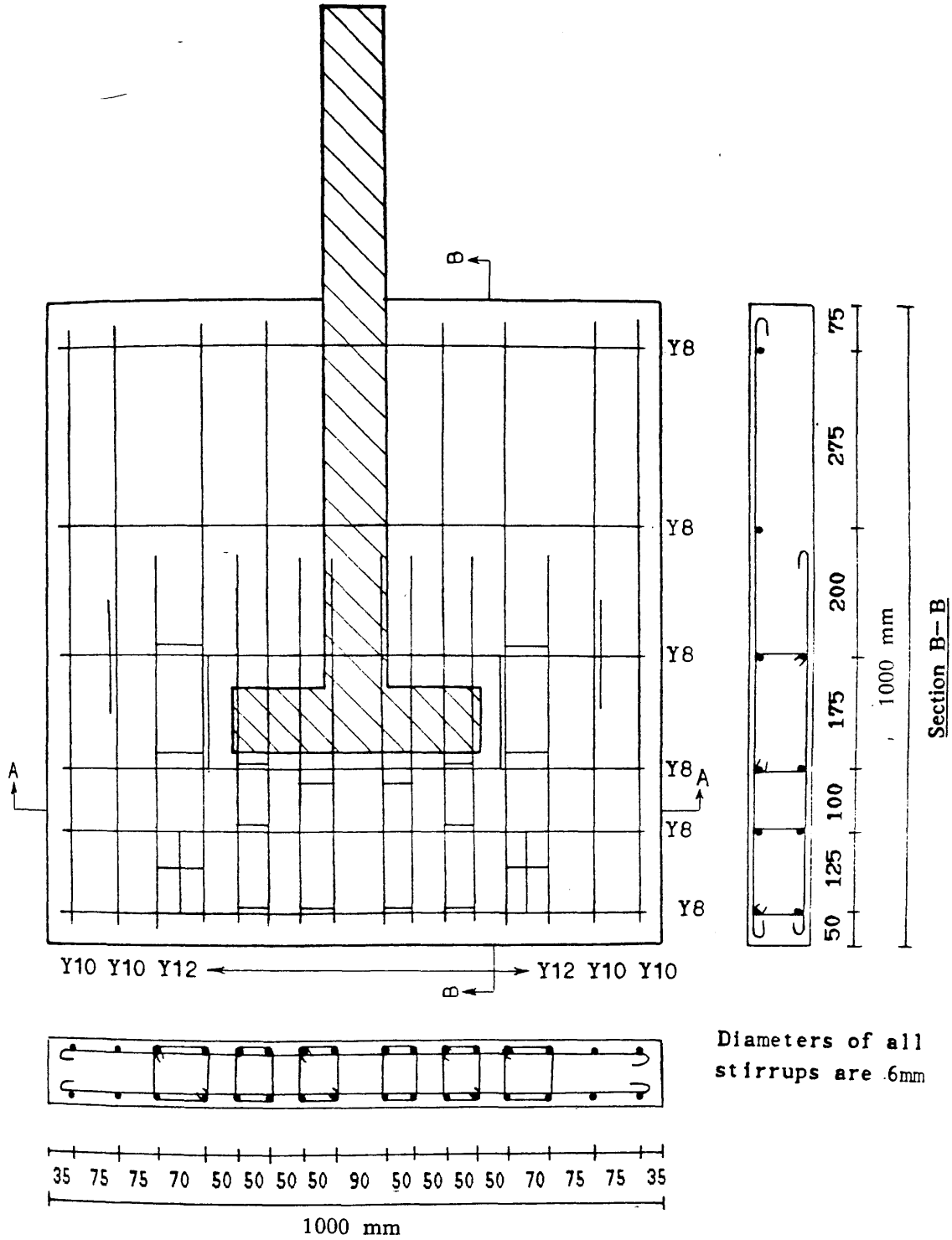

Figure (6.169-a) : Arrangement of top reinforcing bars including closed vertical stirrup in the slab of model MS12

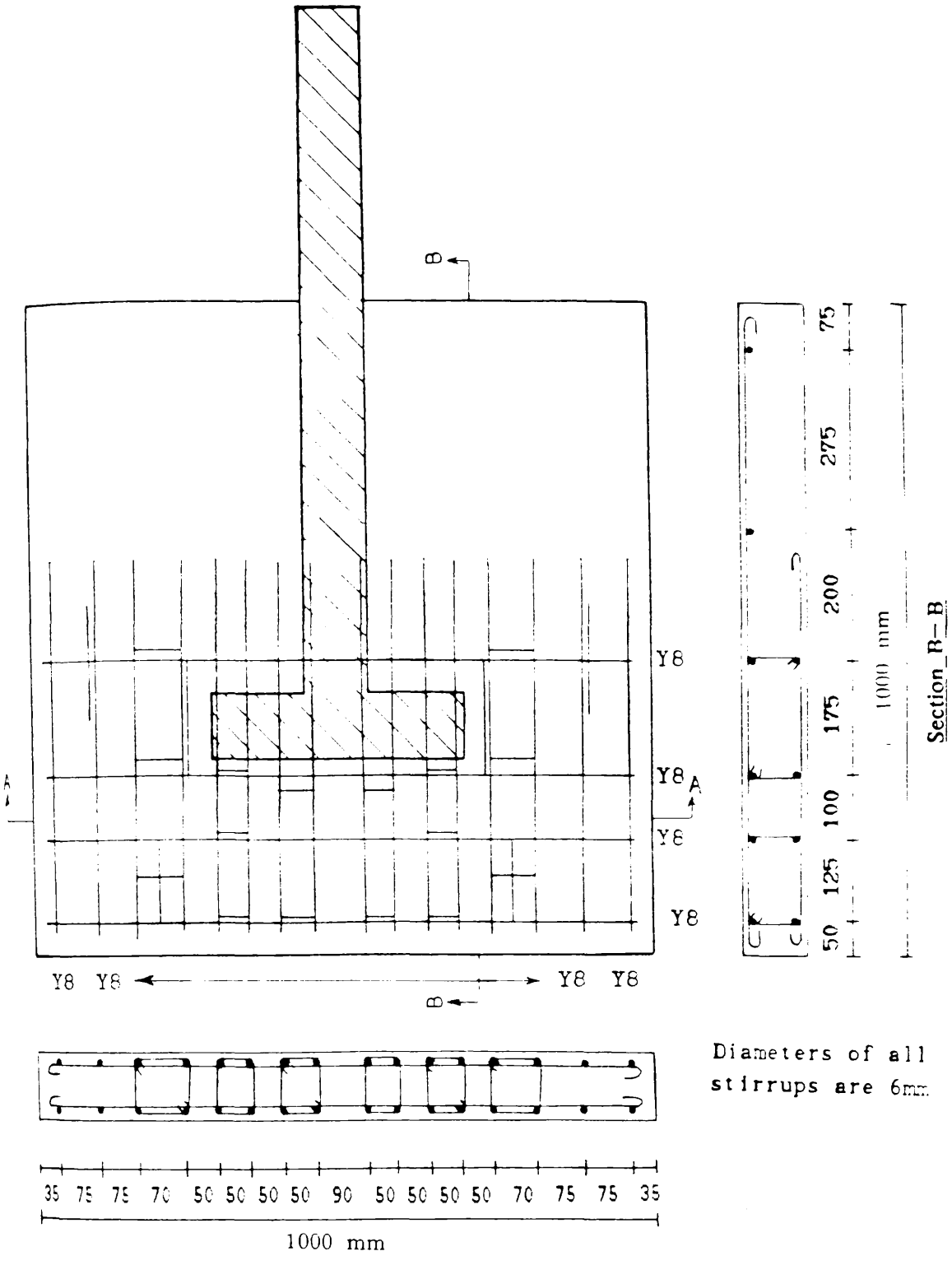

Figure (6.169-b) : Arrangement of bottom reinforcing bars including closed vertical stirrup in the slab of model MS12

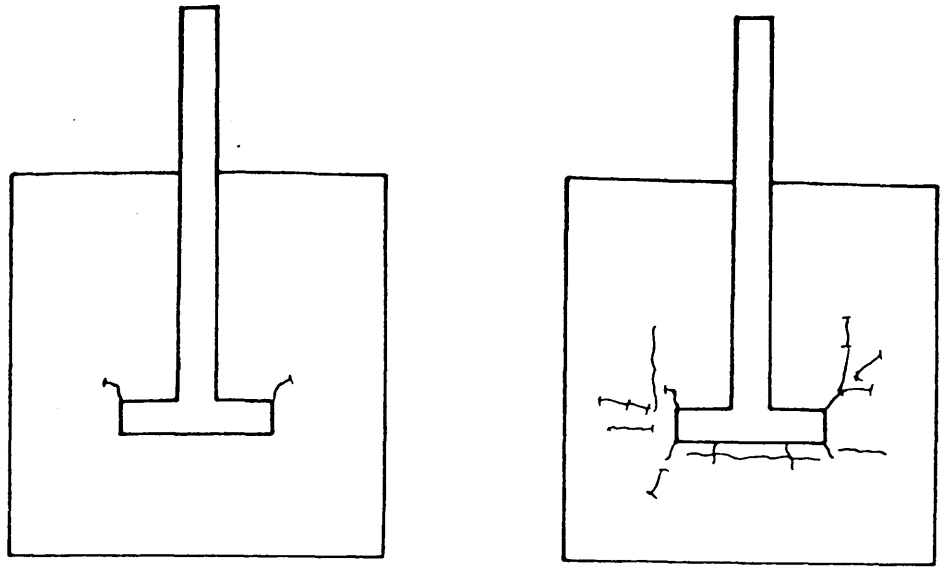

(a) at 19 %

(b) at 37 %

Figure (6.170) : Cracks initiation during testing of model MS12 at different percentages of design lateral load

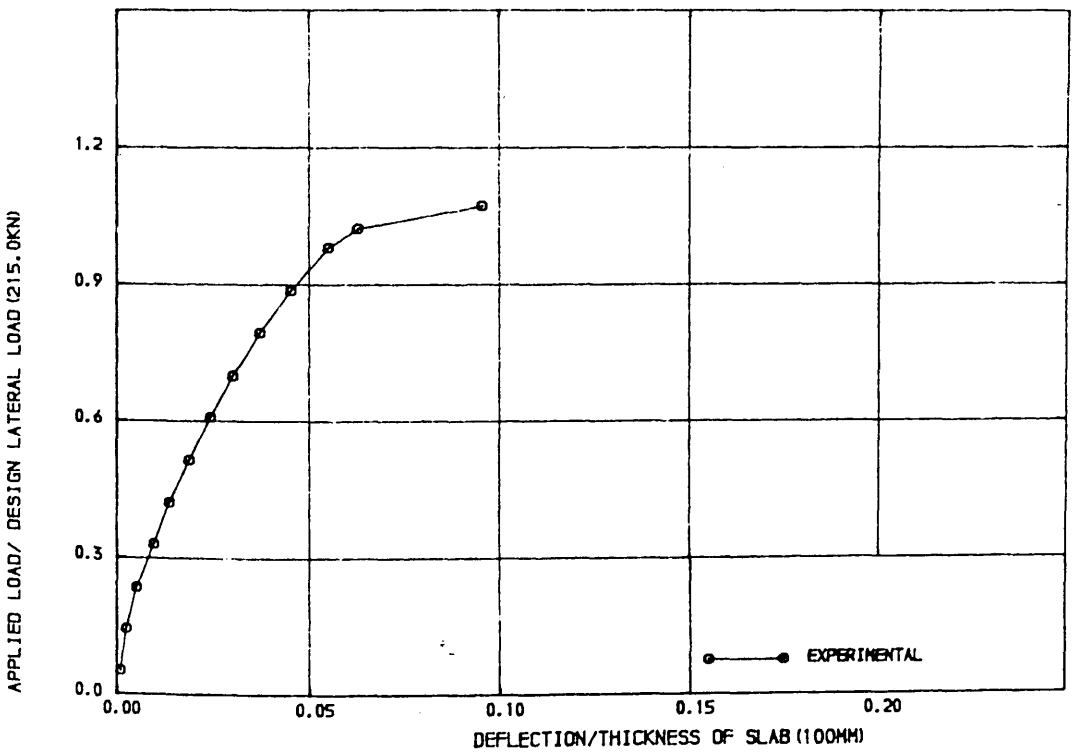

FIGURE (6.171) , LOAD-DEFLECTION CURVE FOR MODEL MS12

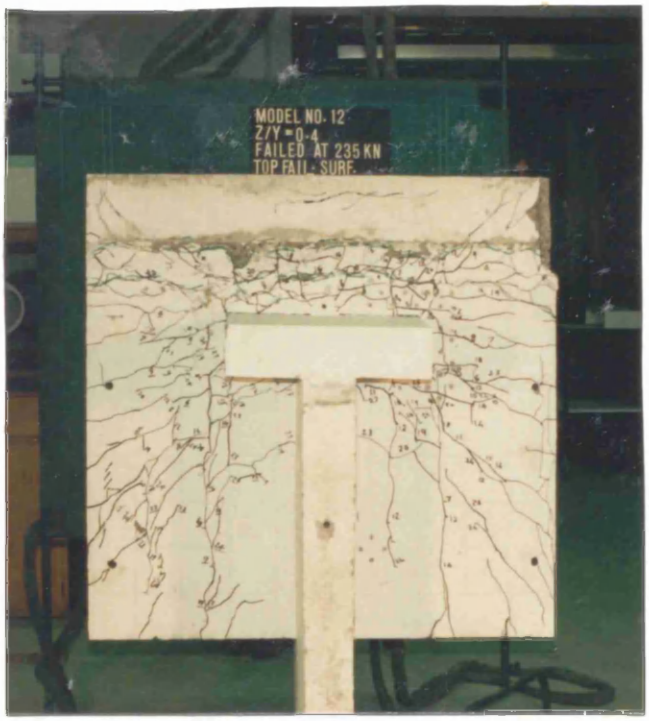

(a) Before removing the broken pieces

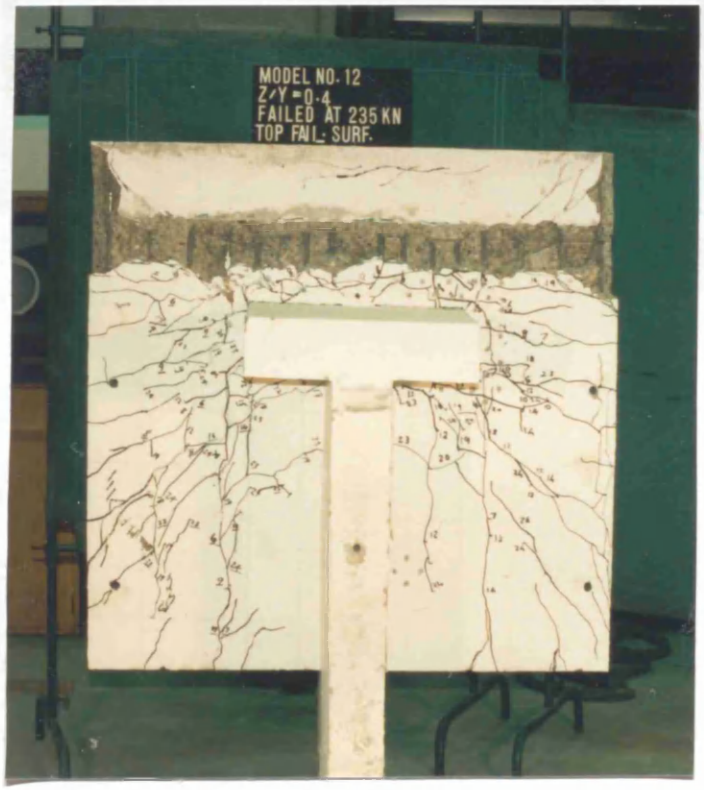

(b) After removing the broken pieces

Figure (6.172) : Crack pattern on the tensile surface of the slab of model MS12

(a) On the compressive side

(b) On the back surface

Figure (6.173) : Crack pattern on the slab of model MS12

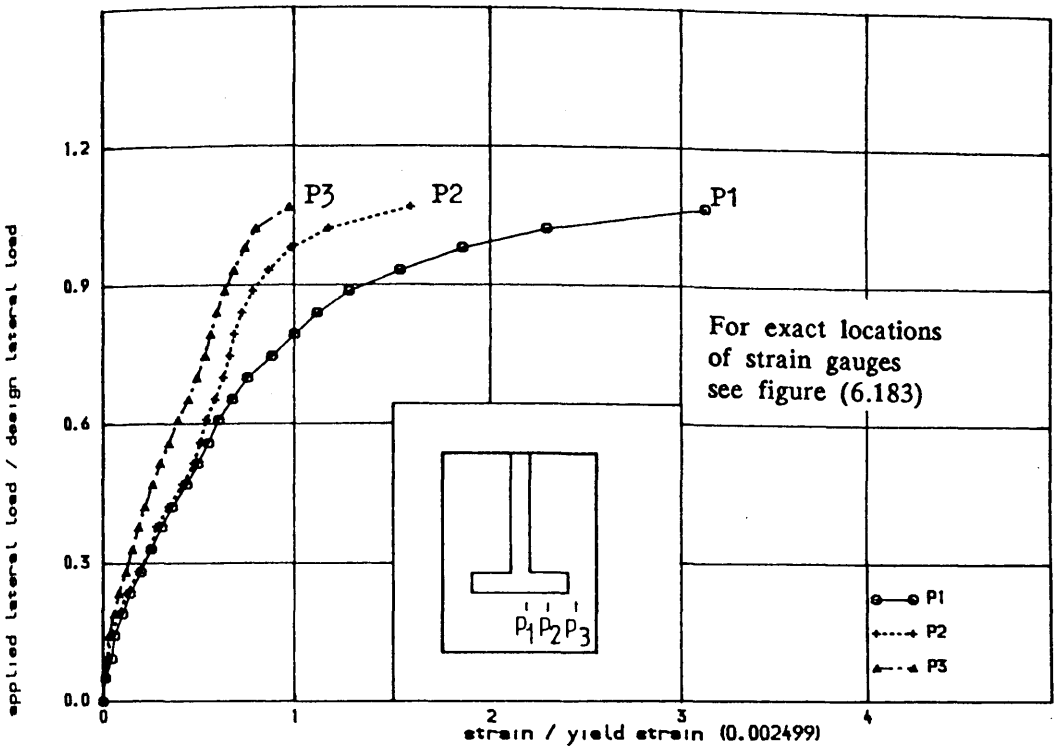

FIGURE (6.174) , TENSILE STRAIN IN STEEL IN VINDVARD DIRECTION ALONG TRANSVERSE SECTION IN THE SLAB OF MODEL MS12

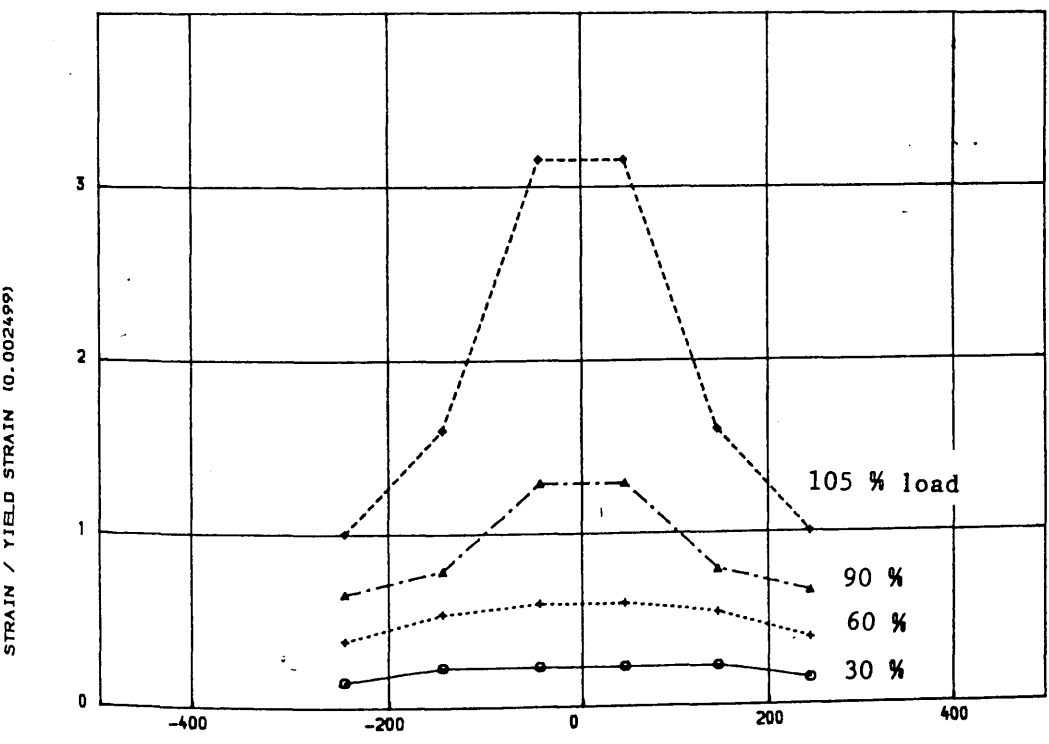

FIGURE (6.175) , VARIATION OF STRAIN IN STEEL IN VINDVARD DIRECTION ALONG TRANSVERSE SECTION AT DIFFERENT STAGES OF LOADING IN THE SLAB OF MODEL MS12

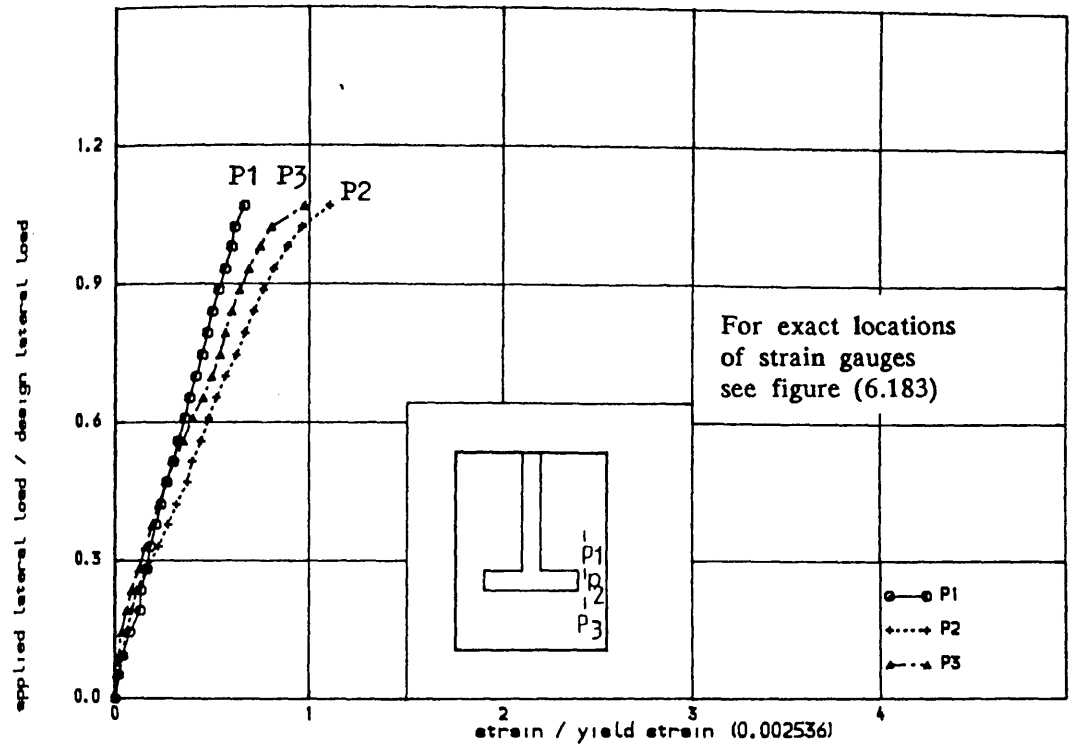

FIGURE (6.176) : TENSILE STRAIN IN STEEL IN WINDWARD DIRECTION IN THE SLAB OF MODEL MS12

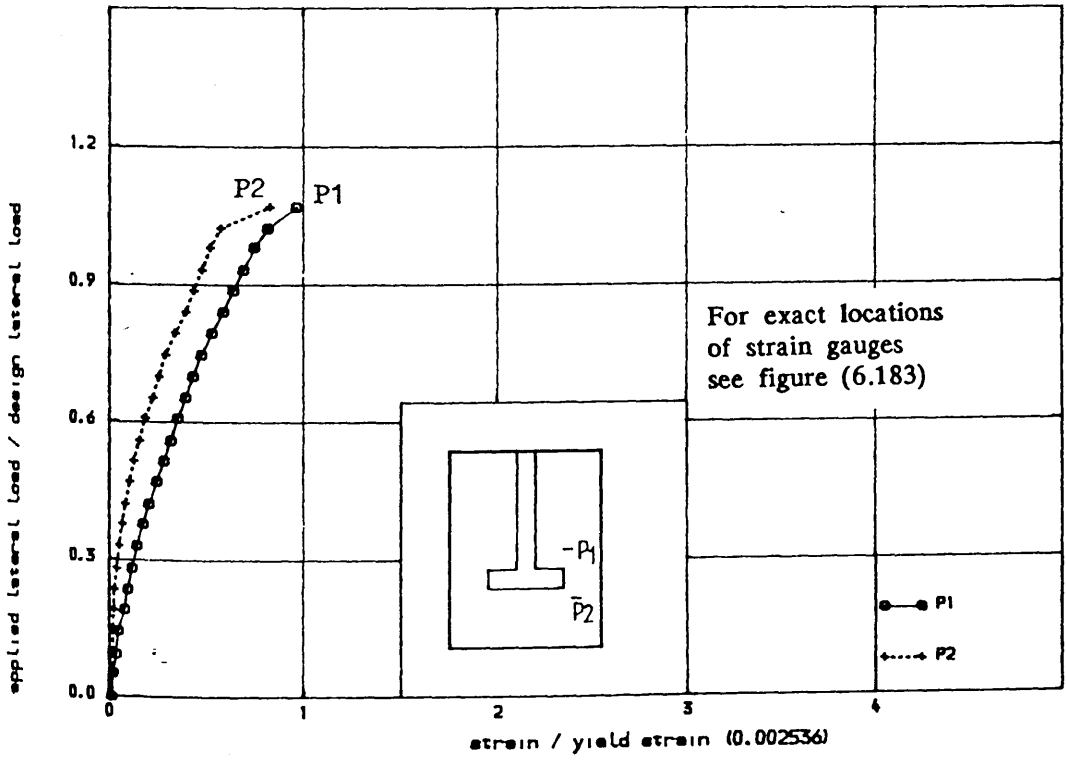

FIGURE (6.177) : TENSILE STRAIN IN STEEL IN TRANSVERSE DIRECTION IN THE SLAB OF MODEL MS12

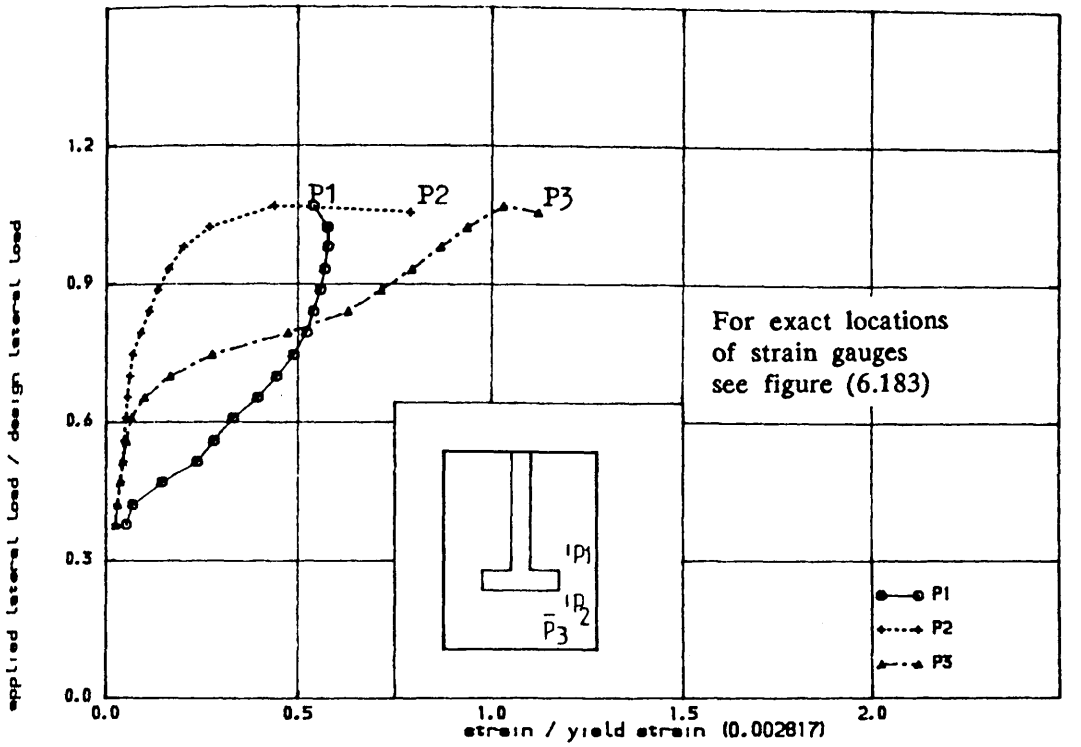

FIGURE (6.178) : STRAIN IN CLOSED VERTICAL STIRUP AT DIFFERENT LOCATIONS IN THE SLAB OF MODEL MS12

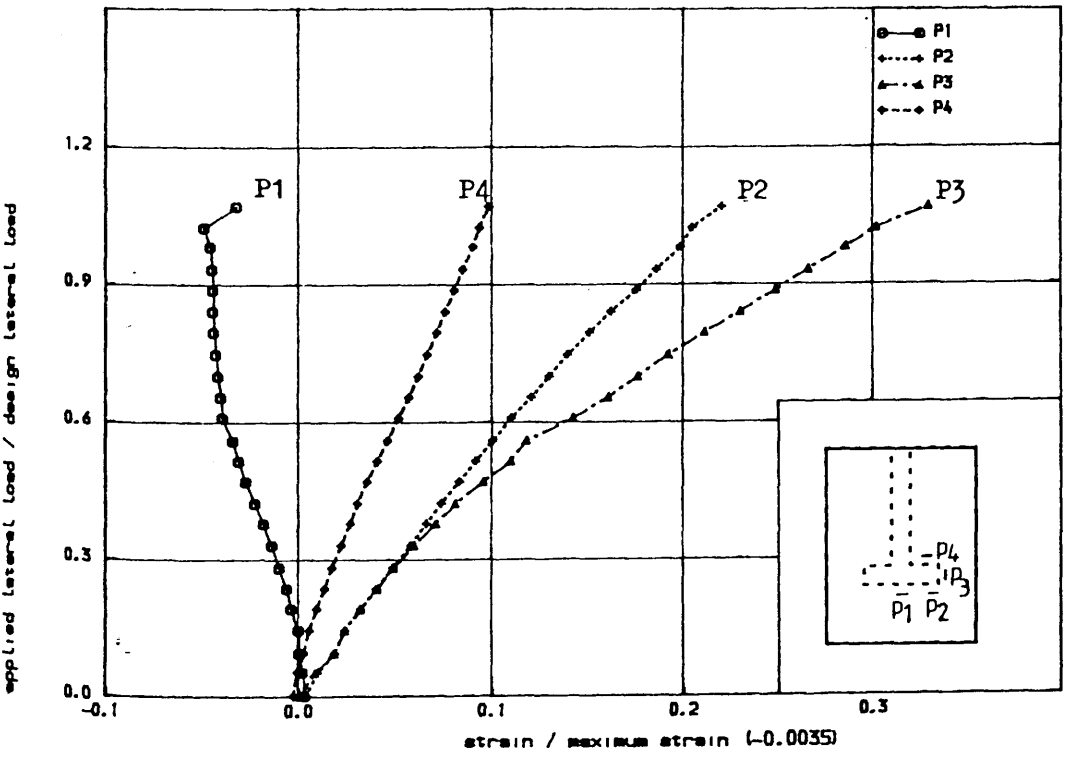

FIGURE (6.179) COMPRESSIVE AND TENSILE STRAIN IN FLANGE WALL JUST UNDERNEATH THE SLAB OF MODEL MS12

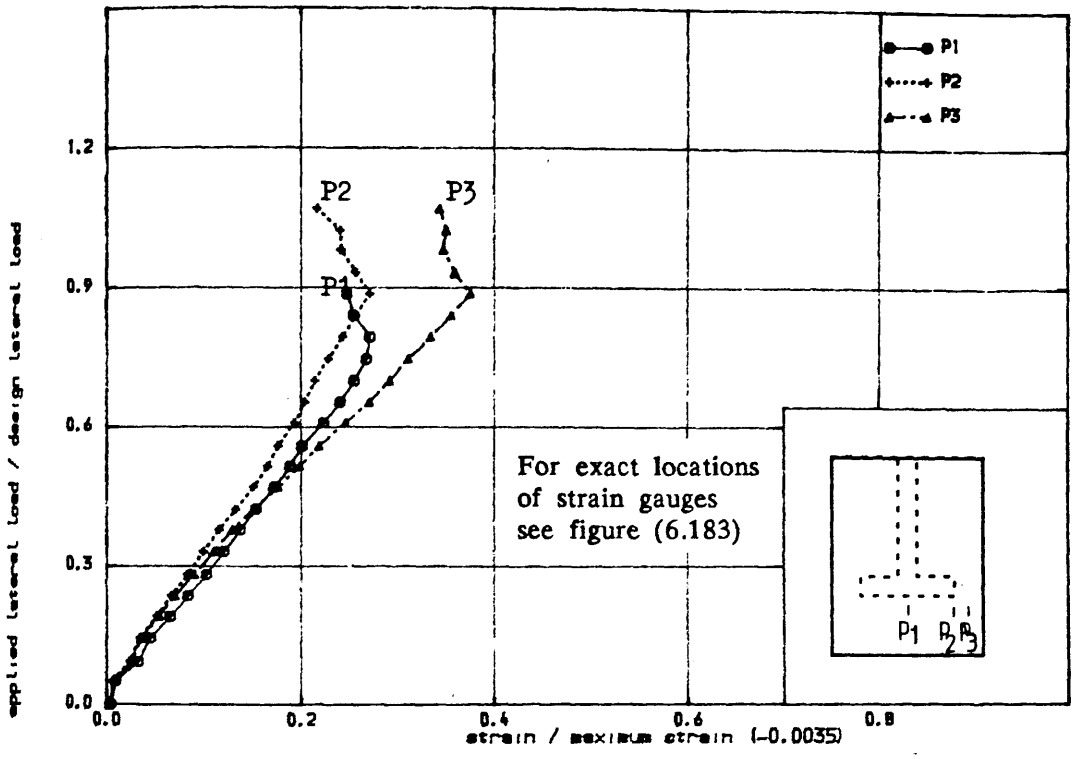

FIGURE (6.180) , COMPRESSIVE STRAIN IN CONCRETE IN WINDWARD DIRECTION IN THE SLAB OF MODEL MS12

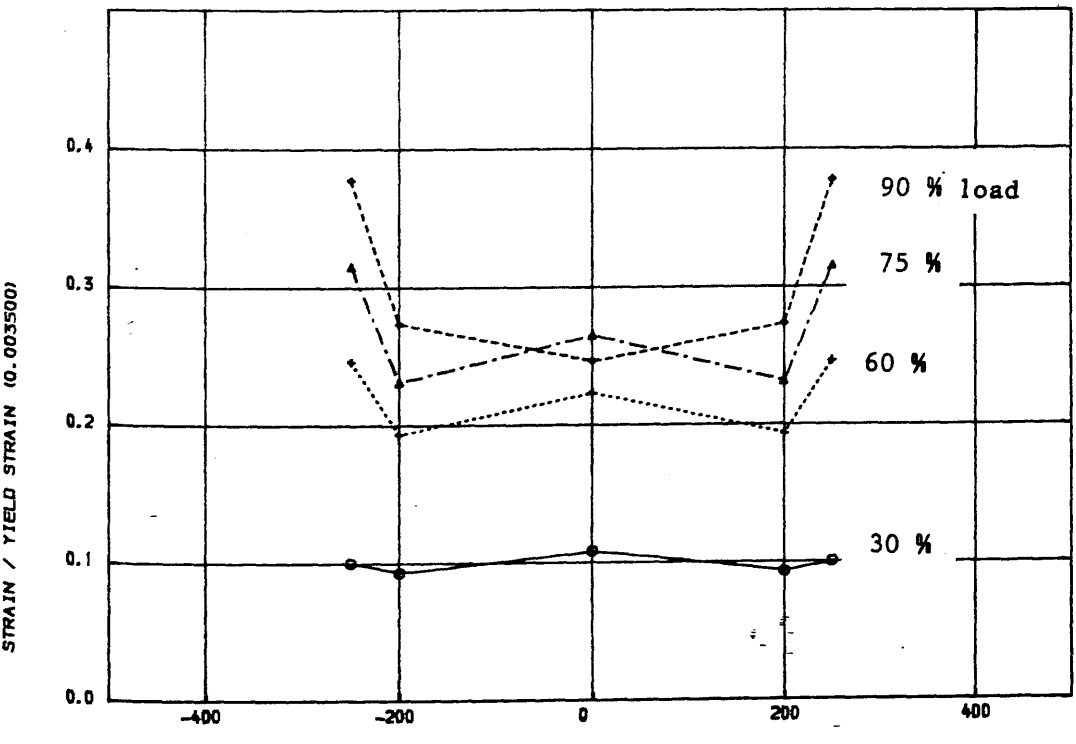

FIGURE (6.181) , VARIATION OF COMPRESSIVE STRAIN IN CONCRETE ALONG TRANSVERSE CRITICAL SECTION AT DIFFERENT STAGES OF LOADING IN THE SLAB OF MODEL MS12

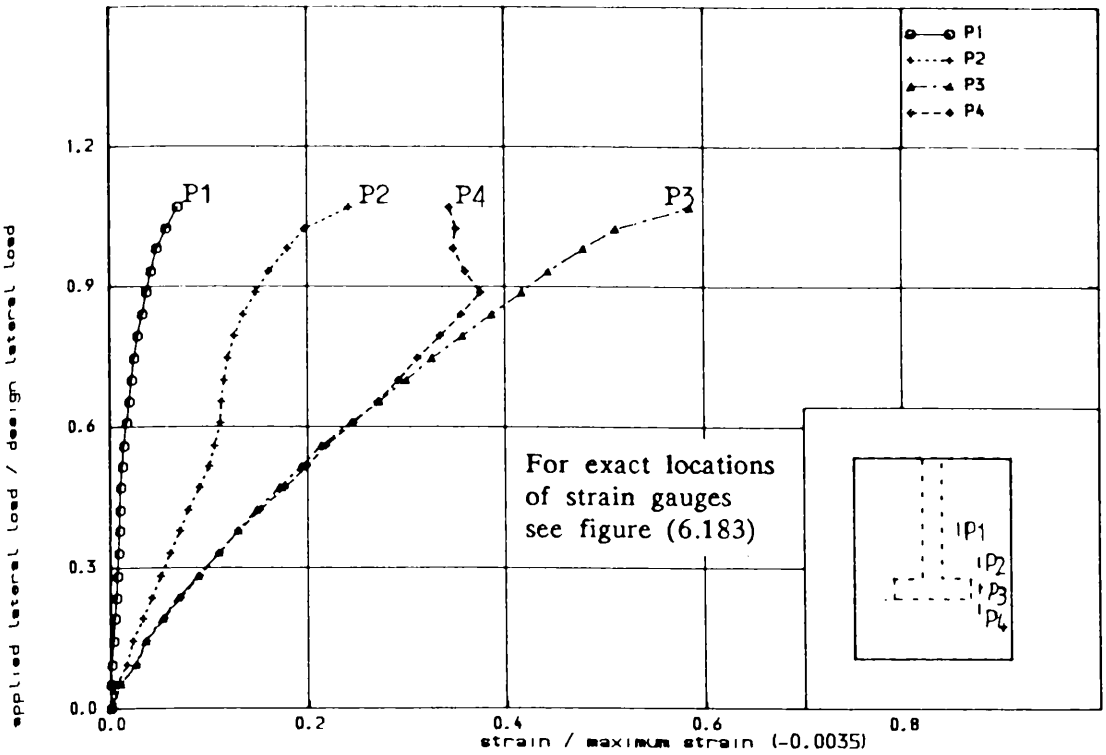

FIGURE (6.182) , COMPRESSIVE STRAIN IN CONCRETE IN WINDWARD DIRECTION ALONG A SECTION PARALLEL TO WEB IN THE SLAB OF MODEL MS12

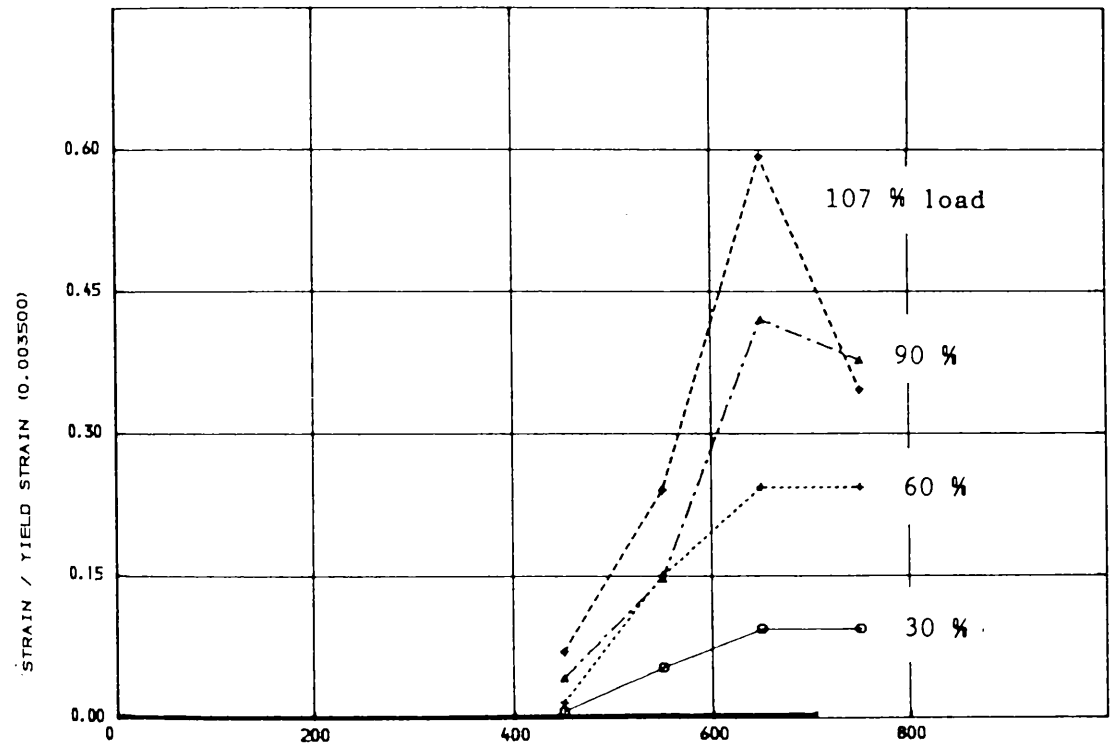

FIGURE (6.182-a) , VARIATION OF COMPRESSIVE STRAIN IN CONCRETE ALONG A SECTION PARALLEL TO WEB AT DIFFERENT STAGES OF LOADING IN THE SLAB OF MODEL MS12

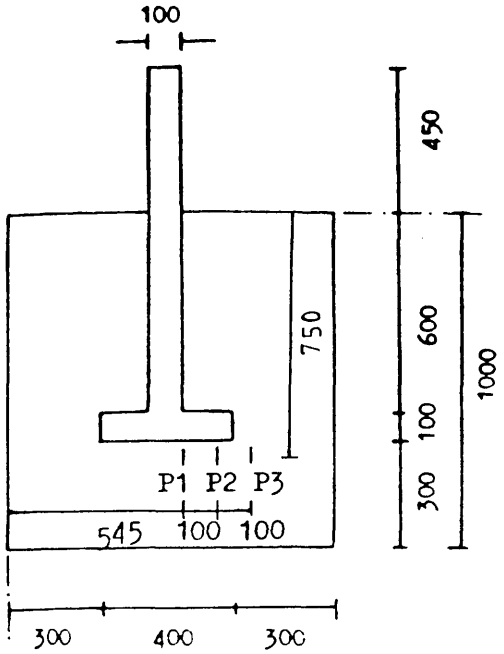

(a) Strain gauges in Figure (6.174)

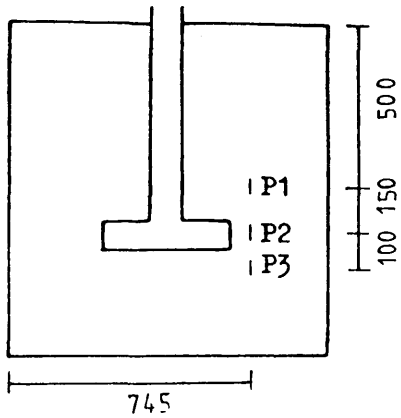

(b) Strain gauges in Figure (6.176)

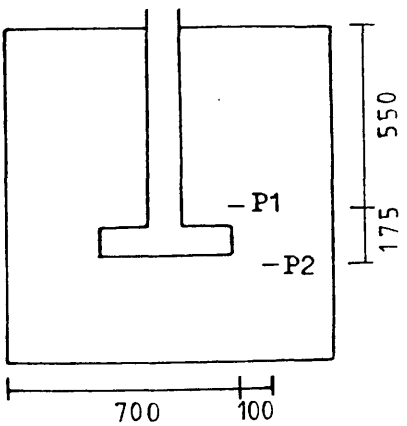

(c) Strain gauges in Figure (6.177)

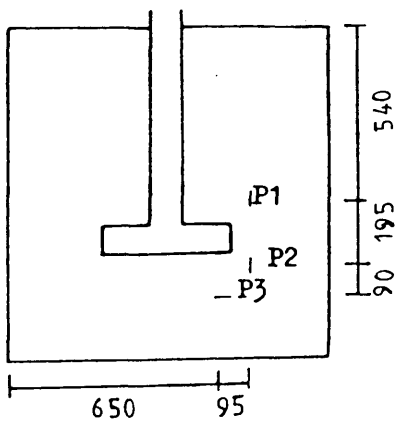

(d) Strain gauges in Figure (6.178)

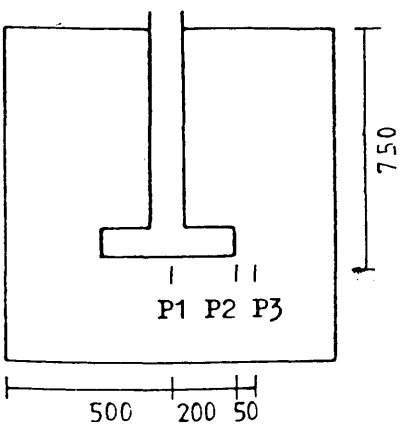

(e) Strain gauges in Figure (6.180)

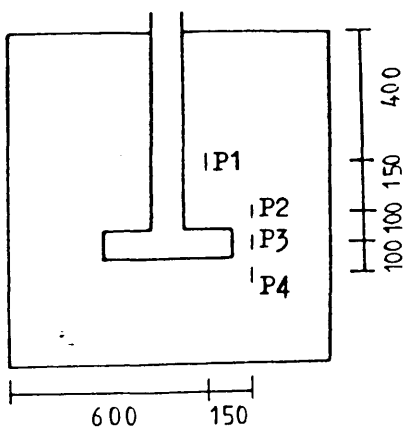

(f) Strain gauges in Figure (6.182)

FIGURE (6.183) : Exact locations of strain gauges in the slab of model MS12 as shown in Figures (6.174), (6.176), (6.177), (6.178), (6.180) and (6.182)

flange width. The final failure line on the top tensile surface changes considerably as the width of the flange increases. On the compressive side of slab it is noticed that in all models, the failure lines behind flange are inclined to the web. The compressive strain in concrete in windward direction at the centre of the slab (point P1) showed unloading in all the models of this series near the ultimate failure load like the models with rectangular shear walls. The variation in compressive strain in concrete along a section parallel to web is shown in Figures (6.149), (6.164) and (6.183). All these figures show maximum strain (about 60% of yield strain) at the tip of the flange and negligible strain at the back of the flange even at failure load. All the models will be more critically analysed in the following section.

6.5 Discussion and Analysis of Test Results

6.5.1 Ultimate Failure Load

As stated earlier in section 6.2, the actual cube strength of concrete on the day each model was tested was different from the cube strength assumed in the design of the model. In an effort to make a comparison of ultimate loads of various models with the corresponding design lateral loads, the design loads of the models are corrected for the actual cube strength of concrete. This is done as follows :

British Code BS 8110 relates the allowable shear stress in concrete slabs with the cylinder crushing strength of concrete by the relation :

$$v_c = 0.79(100As/bd)^{1/3}(f'c/25)^{1/3}(400/d)^{1/4} / \gamma_m \quad N/mm^2$$

where f'c is the cylinder crushing strength of concrete and γ_m is the partial safety factor.

Since shear strength of slab–wall junction is a function of v_c and provided all other parameters are same, then the design loads are related by

$$\frac{V_{d2}}{V_{d1}} = \frac{f(v_{c2})}{f(v_{c1})}$$

$$\text{or} \quad V_{d2} = \frac{f(v_{c2})}{f(v_{c1})} \cdot V_{d1}$$

This formula is used to find the normalised design lateral load, using the actual cube strength of concrete. In table (6.6) the corrected design loads are compared with the experimental failure load for all the models. The first two preliminary models PS1 and PS2 failed locally along the loaded edge beam. The model MS4 failed in shear which was initiated by the early crushing of wall itself. All other models failed in flexure accompanied by considerable amount of steel yielding around the connection. Model MS5 failed at much higher load than the design lateral load. The reason for this is discussed in section (6.4.2.1).

The mean ratio of experimental failur load, V_{exp} to design lateral load, V_{design} is 1.07 with standard deviation equals 0.09 for all 12 models tested monotonically. But if we neglect the results of models PS1, PS2 and MS4 and consider other models which failed in flexure, the ratio increases to 1.08 with the co−efficient of variation equals to 0.10. From the above, it can be said that the adopted design procedure is capable of resisting the ultimate design strength of wall − slab connections for all the range of parameters tested in this study.

6.5.2 Load − Deflection Relationship

Figures (6.53), (6.58), (6.107), (6.110), (6.123) and (6.184) show the non−dimensionalized curves of lateral load versus slab deflection for all twelve models tested under monotonic loading. For discussion purposes and to analyse them critically, each curve will be idealized in the manner as shown in Figure (6.185). The slope of the initial linear part of the load − displacement curve 'oc' is the pre−cracking stiffness (K_0) and the displacement at the end of this part is termed as 'displacement at cracking δ_{cr}'. The point 'c' on the curve is roughly an indication for the first apperance of torsional cracks (i.e. those cracks occured on slab area behind the flange for models with flanges and on the back side of the slab behind the nose of the wall for models with rectangular shear walls). After cracking of concrete, the first part of the nonlinear curve is approximated by a straight line 'cy' and the slope of this part will be called 'cracked section stiffness K_{cr}'. The point 'y' on the curve is roughly an

Table (6.6) : Comparisons of design lateral load with the experimental failure load

Model	Normalised design load V_{design} KN	Experimental failure load V_{exp} KN	$\frac{V_{exp}}{V_{design}}$	Failure mode	Main variables
PS1	215.0	219.0	1.02	Local	
PS2	150.0	159.0	1.06	Local	Shear steel
PS3	155.0	175.0	1.13	Flexural	
MS4	220.0	190.4	0.87	Shear	Wall web length 67% of MS7
MS5	155.0	203.0	1.31	Flexural	Corridor opening width 280mm for MS5 400mm for MS6 520mm for MS7
MS6	330.0	343.0	1.04	"	
MS7	240.0	262.0	1.09	"	
MS8	255.0	280.0	1.10	"	Gravity load 3 times of MS7
MS9	250.0	247.0	0.99	"	Bay width 1.44 times of MS7
MS10	220.0	209.0	0.95	"	Flange width 300mm for MS10 200mm for MS11 400mm for MS12
MS11	215.0	219.0	1.02	"	
MS12	215.0	235.0	1.09	"	

mean = 1.07

S.D. = 0.09

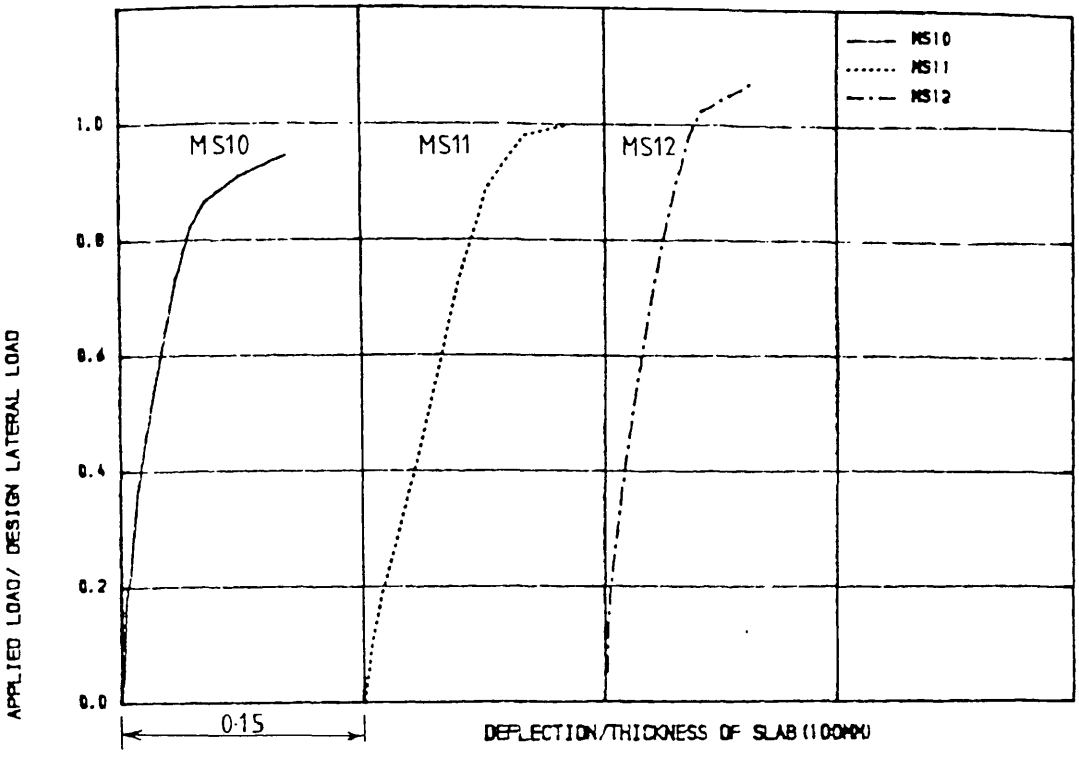

FIGURE (6.184) : COMPARATIVE STUDY OF THE LOAD-DEFLECTION CURVES FOR THE MODELS TO STUDY THE EFFECT OF FLANGE WIDTH

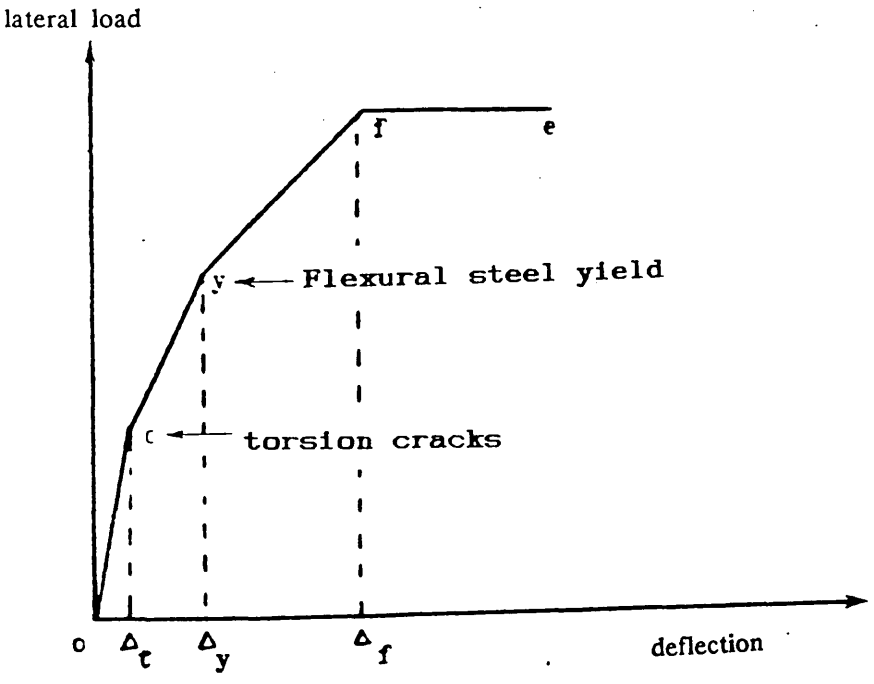

Figure (6.185) : Idealized load – deflection curve

indication for the first yielding in flexural reinforcement. The portion 'yf' terminates at punching or excessive deflections and portion 'fe' indicates the model failure.

Following this process, Figures (6.186) and (6.187) show the idealized curves from which table (6.7) was calculated. Because every model had a different cube strength, it was assumed for comparison purposes a inear relationship between f_{cu} and stiffness. Thus modified values of stiffness pertaining to f_{cu}= 40 N/mm^2 are shown in brackets. These values are plotted against the corridor opening width and flange width in Figures (6.188) and (6.189). Examination of the figures reveals

i) a decrase in stiffness of the structure with an increase of corridor opening width by the relation

$$K_0 = 40.348 + 9388.7 \; / \; L$$
$$K_{cr} = 14166.0 \; (L)^{-1.0571} \qquad (6.5)$$

where L is the corridor opening width.

ii) an incrase in stiffness with the increase of flange width (Z) by the relation

$$K_0 = 0.19432 \; (Z)^{1.0532}$$
$$K_{cr} = 1.0651 \; (Z)^{0.56328} \qquad (6.6)$$

As was expected, the stiffness decreased with the increase of gravity load and with the increase of bay width. The table (6.7) shows that the ratio of the post– to pre–cracking stiffness ranges betwen 27% to 50% for the models of main test series.

6.5.3 Ductility of Wall – Slab Connection

The ratio of edge displacement at ultimate load to the edge displacement at first yield in the main reinforcing bar can be used as a measure of ductility. This ratio is similar in concept to the ductility factor which is used in reinforced

Table (6.7) : Pre- and Post- Cracking Stiffness for all the models

Model	f_{cu} N/mm^2	Pre-cracking stiffness K_o KN/mm	Cracked section stiffness K_{cr} KN/mm	$\frac{K_{cr}}{K_o} \times 100$	Main variables
PS1	42.9	53.5 (50.0)	18.9 (17.6)	35.2	
PS2	40.5	65.3 (64.5)	11.92 (11.8)	18.3	Shear steel
PS3	42.2	67.4 (64.0)	18.0 (17.1)	26.7	
MS4	43.9	63.8 (58.0)	19.6 (17.9)	30.8	Wall web length 67% of MS7
MS5	33.1	49.0 (59.0)	16.0 (19.3)	32.7	Corridor opening width
MS6	51.6	95.7 (74.2)	47.8 (37.0)	49.9	280mm for MS5 400mm for MS6 520mm for MS7
MS7	56.5	88.9 (62.9)	34.8 (24.6)	39.1	
MS8	68.0	85.3 (50.2)	29.6 (17.4)	34.7	Gravity load 3 times of MS7
MS9	64.5	96.5 (60.0)	27.9 (17.3)	28.8	Bay width 1.44 times of MS7
MS10	57.5	114.8 (80.0)	38.3 (26.6)	33.2	Flange width 300mm for MS10 200mm for MS11 400mm for MS12
MS11	47.7	61.0 (51.2)	25.0 (21.0)	41.0	
MS12	50.3	133.6 (106.0)	39.0 (31.0)	29.2	

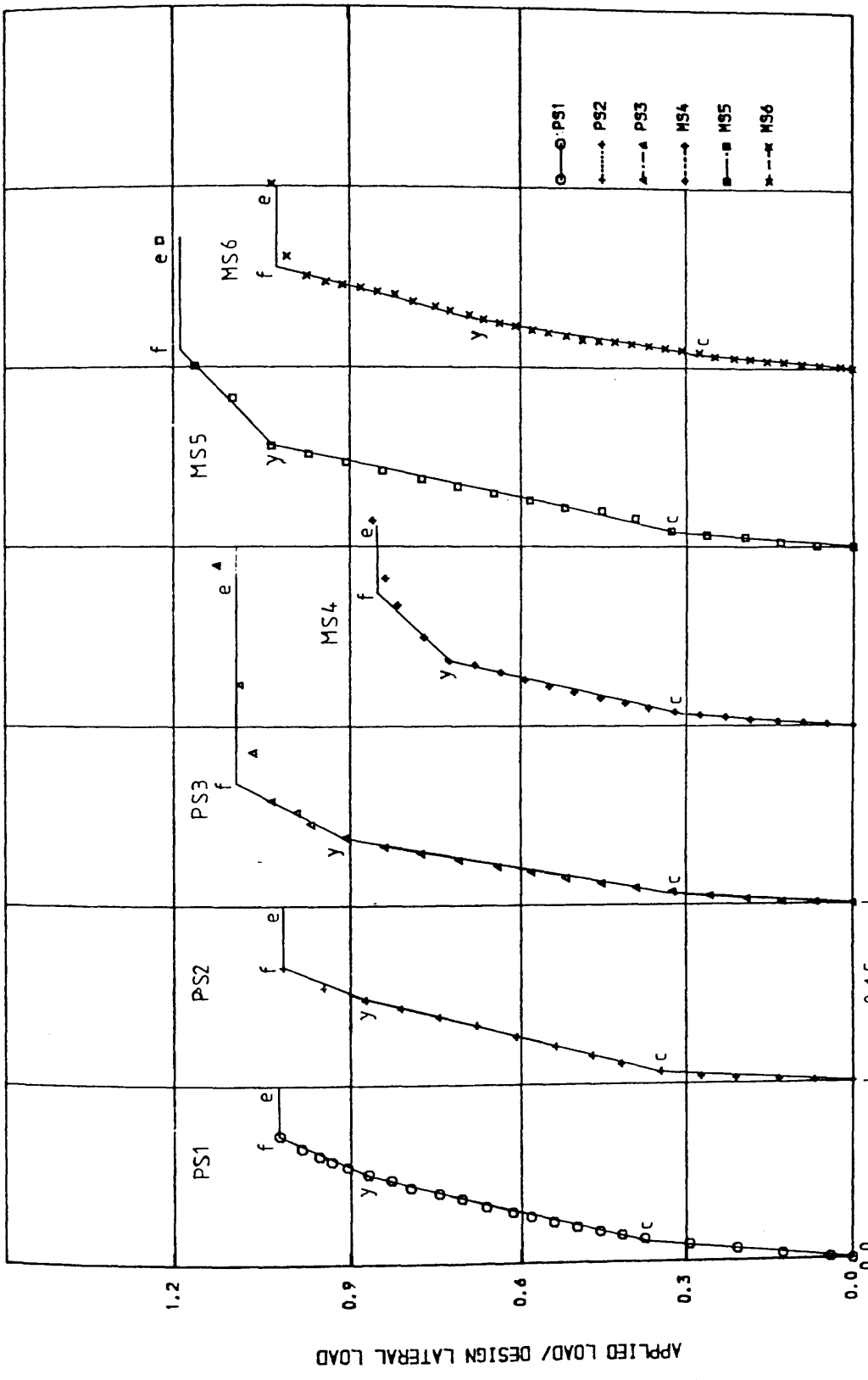

FIGURE (6.186) : IDEALIZED LOAD-DEFLECTION CURVES FOR MODELS PS1, PS2 PS3, MS4, MS5 AND MS6

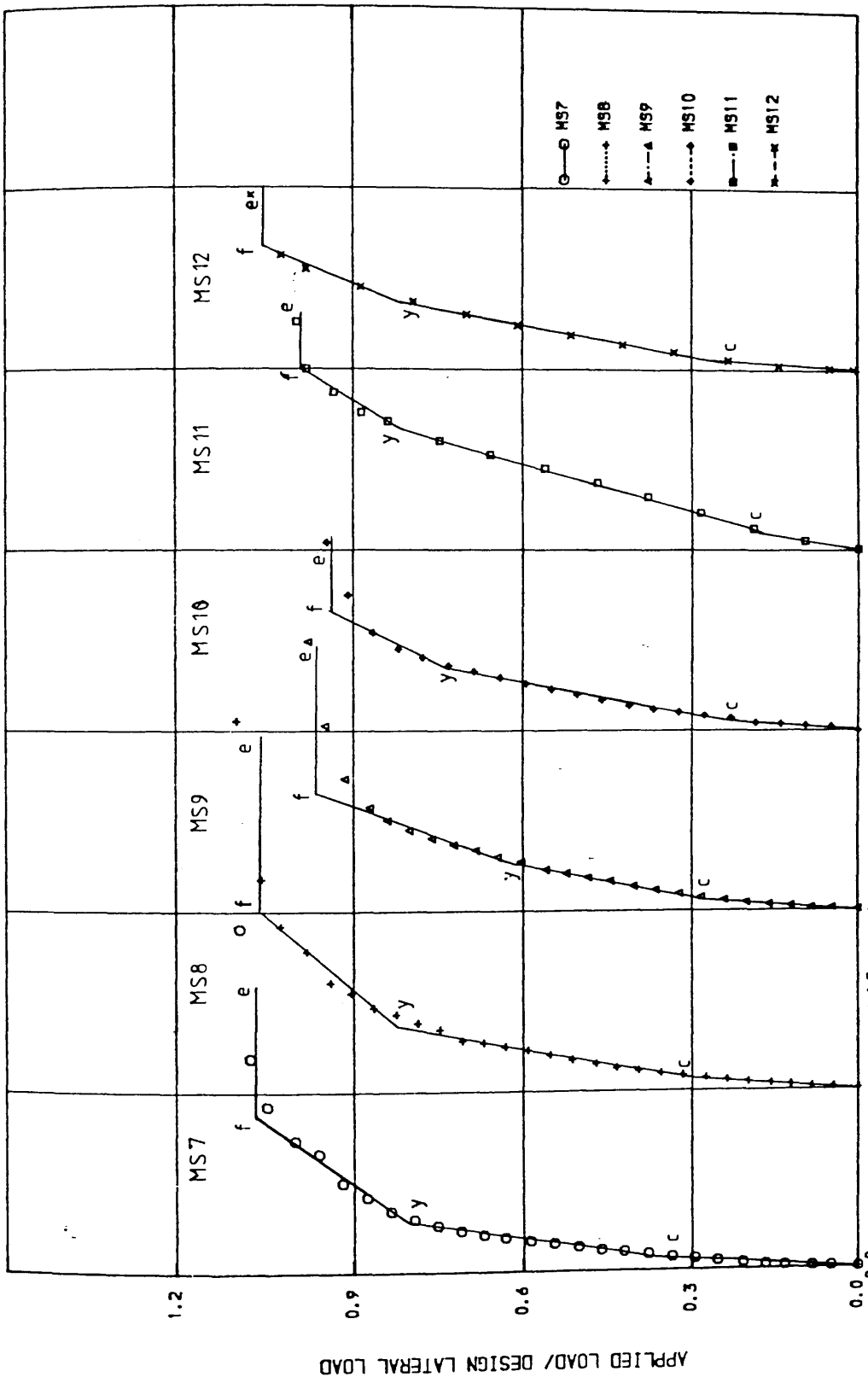

FIGURE (6.18) , IDEALIZED LOAD-DEFLECTION CURVES FOR MODELS MS7, MS8 MS9, MS10, MS11 AMD MS12.

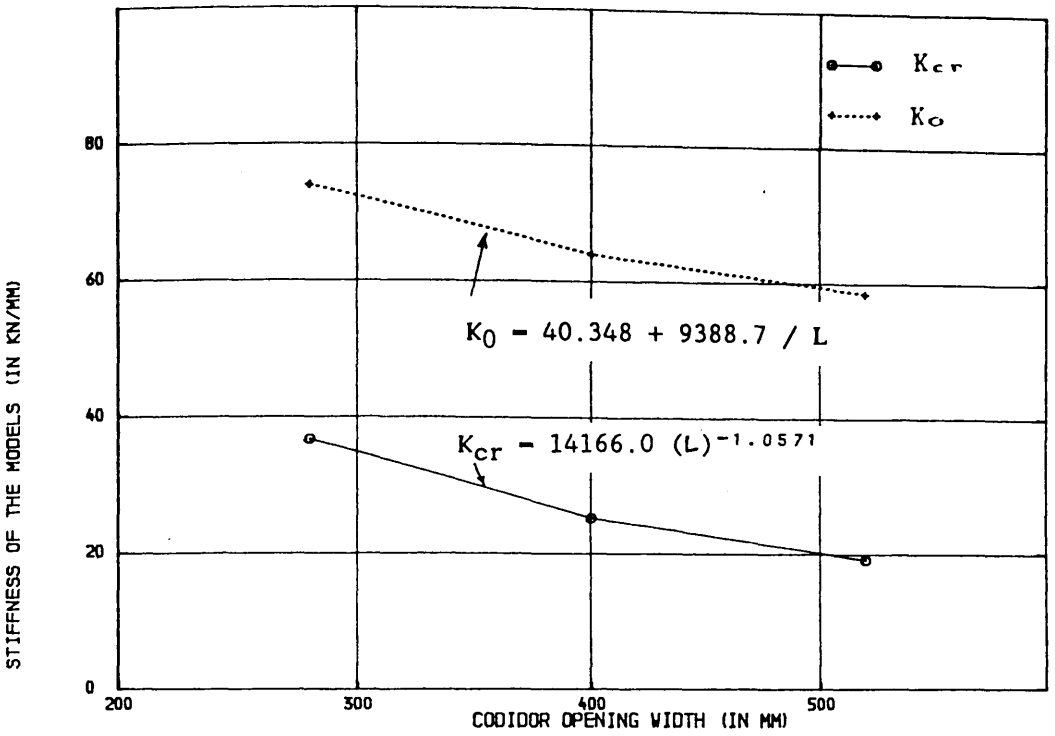

FIGURE (6.188) , RELATIONSHIP BETWEEN 'CRACKED SECTION STIFFNESS' WITH THE CORIDOR OPENING WIDTH

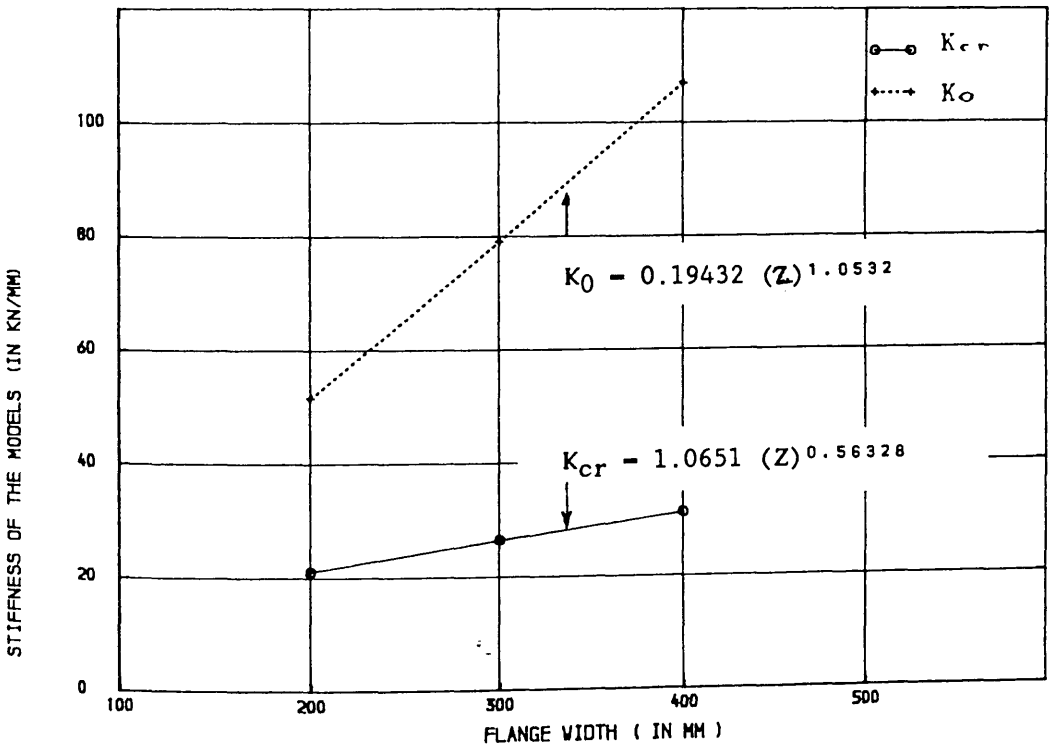

FIGURE (6.189) , RELATIONSHIP BETWEEN 'CRACKED SECTION STIFFNESS' WITH THE FLANGE WIDTH

concrete frames and defined as the ratio of lateral deflection at ultimate load to lateral deflection at first yield load. Table (6.8) lists the edge displacement corresponding to the first yielding of steel and the edge displacement at ultimate load. From the table it is apparent that the model PS3 with closed vertical stirrup as shear reinforcement shows the greatest amount of ductility compared to the models PS1 and PS2 with the type of shear steel in Figure (6.13). This is why, all the rest of the models were tested using closed vertical stirrup as shear reinforcement. The range of ductility measured by the ratio of edge displacements is 2.23 – 2.79 for models with T–section shear walls and 4 – 11 for models with rectangular shear walls. The lower ratio for the models with T–section shear walls is due to the fact that the concentration of stress near the nose is not as serious as in the case of rectangular walls.

6.5.4 Strains in Flexural Steel

The load versus steel strain curves for all the models tested in this study are given in sections 6.3 and 6.4. The general behaviour can be described as trilinear consisting of

(a) Behaviour before cracking,

(b) Behaviour after cracking,

(c) Behaviour after yielding of steel,

Before the development of the first crack, very little strain was normally observed in the reinforcing steel and the load–strain relationship is linear. At this load level, applied loading on the model is resisted mainly by concrete, hence the steel is inactive.

After cracking, a gradual increase in strain was observed in the steel bars both in windward and transverse direction and the load–strain curve remains linear until yield.

After yielding, a rapid increase was recorded in strain with little increase of

Table (6.8) : Ductility calculation for the models

Model	δ_{yield} mm	δ_u mm	Ductility $\frac{\delta_u}{\delta_{yield}}$	Main variables
PS1	6.6	12.1	1.84	
PS2	6.1	10.4	1.71	Shear steel
PS3	3.5	28.8	8.23	
MS4	4.0	17.3	4.32	Wall web length 67% of MS7
MS5	5.8	26.9	4.64	Corridor opening width
MS6	2.8	11.3	4.04	280mm for MS5 400mm for MS6 520mm for MS7
MS7	3.5	28.8	8.23	
MS8	3.75	31.2	8.32	Gravity load 3times of MS7
MS9	1.97	22.4	11.37	Bay width 1.44 times of MS7
MS10	3.8	10.6	2.79	Flange width
MS11	5.7	12.7	2.23	300mm for MS10 200mm for MS11 400mm for MS12
MS12	3.8	9.7	2.53	

load before failure. At this load stage, the load – strain curve is nonlinear and is almost flat. This represents the development of plastic strains. At ultimate load, most of the tension steel around the junction had yielded.

Table (6.9) shows the lateral load as a percentage of the design load at which steel in windward direction yielded. The load at first yield of steel took place outside the serviceability limit load (0.625 X design load) in all the models except models MS6 (with small corridor opening width) and MS9 (with large bay width) which is 55% and 40% of design load respectively. The average load at first yield of steel of the models of main test series is equal to 66% of design load with the co– efficient of variation of 0.11. This value is slightly higher than the service load of 0.625 X design load. The average load for the models of MS series at first yield of steel in transverse direction is equal to 0.88 X design load

An increase in bay width of about 44% shows experimentally a decrease in yield load of about 43%. An increase in corridor width results an increased yield load and an increase in gravity load causes a decrease in yield load, but they are not so significant.

Lateral load at which steel bars in windward direction yielded in the corridor area can be used to evaluate the amount of unbalanced moment which is directly transferred by flexure. This can be done following the provision of BS 8110 for singly reinforced rectangular section under flexure (neglecting the contribution of bottom bar which was used to ensure anchorage of the stirrup only). According to figure (6.190) : let

b = width of the section

d = effective depth of tension reinforcement

f_{cu} = cube crushing strength of concrete

f_y = yield strength of steel

A_s = total area of tension reinforcement

Table (6.9) : Lateral load at which steel yielding was first observed, $V_{L.Y}$ as a ratio of the design lateral load, V_{design}

Model	V_{design} Kn	$(V_{L.Y.} / V_{design} \times 100)$		Main Variables
		Longitudinal Steel	Transverse Steel	
PS1	215.0	84.6	-	
PS2	150.0	86.0	94.8	Shear steel
PS3	155.0	71.4	93.7	
MS4	220.0	63.2	79.5	Wall web length 67% of MS7
MS5	155.0	73.8	111.9	Corridor opening width
MS6	330.0	55.2	77.9	280mm for MS5 400mm for MS6 520mm for MS7
MS7	240.0	71.0	94.9	
MS8	255.0	64.1	78.7	Gravity load 3 times of MS7
MS9	250.0	40.3	64.9	Bay width 1.44 times of MS7
MS10	220.0	74.3	93.2	Flange width 300mm for MS10 200mm for MS11 400mm for MS12
MS11	215.0	70.6	85.6	
MS12	215.0	79.4	107.9	

x = depth of concrete rectangular stress block

M_f = ultimate flexural capacity of a slab section of width 'b'

After removing the partial safety factors, we can write

$$f_y A_s = 0.67\ f_{cu}\ b\ (0.9x) \tag{6.7}$$

and

$$M_f = f_y\ A_s\ (\ d - 0.45x\ ) \tag{6.8}$$

$$= 0.67\ f_{cu}\ b\ (0.9x)\ (d - 0.45x) \tag{6.9}$$

For discussion purposes, it may not be unreasonable to consider a width 'b' equal to

$b = t_w + d$ for models with rectangular walls, and

$b = Z + d$ for models with T-section walls

where tw is the thickness of the wall and Z is the width of the flange.

Within this width, all the steel did not yield at one time. Using the recorded stress of steel within this width, at the onset of first yielding of any steel bar, the above equations will take the form

$$\sum_{i=1}^{N} A_{si}\ f_{si} = 0.67\ f_{cu}\ b\ (0.9x)$$

$$M_f = \sum_{i=1}^{N} A_{si}\ f_{si}\ (d - 0.45x)$$

$$= 0.67\ f_{cu}\ b\ (0.9x)\ (d-0.45x)$$

where N is the number of steel bar within the width equal to 'b'

A_{si} is the area of individual steel bar

f_{si} is the recorded stress in that bar

The total applied (exparimental) unbalanced moment M_o, at the onset of steel yielding may be calculated from

$$M_o = V_{L.y}\ .\ L/2 \tag{6.10}$$

where $V_{L.y}$ is the lateral load at which steel yielding was first observed and L/2 is the half of the corridor opening width. The ratio of the calculated flexural moment

to the total applied unbalanced moment (M_f/M_o) is shown in table (6.10).

The American Code provides a formula for the fraction of the unbalanced moment to be transferred directly by flexure, γ_f, in case of slab–column connection as given in equation (6.11):

$$\gamma_f = \frac{1}{1 + 2/3 \sqrt{(C_1+d)(C_2+d)}} \qquad (6.11)$$

where C_1 = column dimension in the direction of unbalanced moment

C_2 = column dimension measured transverse to the direction of unbalanced moment

To apply this for the models without flanges, the factor γ_f, may be calculated using wall thicknes, t_w as C_2 and wall–web length, W as C_1. To apply the above formula for the models with flanges, it may not be unreasonable to use flange dimensions as C_1 and C_2 (see Figure (6.191)). In table (6.10), the ratios of calculated flexral moment to the total unbalanced moment (M_f/M_o) are compared with the factor γ_f.

It appears from the table that the factor, γ_f results in slight underestimation of the moment transferred for models of small corridor opening width, when the full length of shear wall is used as C_1 in the calculation of γ_f. For larger bay width, equation (6.11) proposed in ACI Code, calculates approximately 36% less moment actually transferred in flexure. In other words, the full wall–web length is not effective in resisting the unbalanced moment when corridor opening width is very small ($L < 6.0d$) or bay width is very large. For the models with flanges, it appears that γ_f results in a slight overestimation of the moment transferred by flexure, when equivalent column is represented by flange only. In other words, some portion of web needs to be included as part of the column.

6.5.5 Effectiveness of shear reinforcement

The closed vertical stirrups and their arrangement in the slab of models PS3

Table (6.10) : Moments transferred by flexure for the models of main test seires

Model	M_o	M_f	$\frac{M_f}{M_o}$	γ_f eqn (6.11)	$\frac{\gamma_f}{M_f / M_o}$	Main variables
MS4	56.0	27.8	0.50	0.53	1.06	Wall web length 67% of MS7
MS5	57.5	28.0	0.49	0.53	1.08	Corridor opening width
MS6	53.4	31.0	0.58	0.48	0.83	280mm for MS5 400mm for MS6 520mm for MS7
MS7	64.3	30.8	0.48	0.48	1.00	
MS8	64.4	31.5	0.49	0.48	0.98	Gravity load 3 times of MS7
MS9	40.8	30.6	0.75	0.48	0.64	Bay width 1.44 times of MS7
MS10	45.0	27.8	0.62	0.68	1.10	Flange width 300mm for MS10 200mm for MS11 400mm for MS12
MS11	41.7	23.5	0.56	0.65	1.16	
MS12	47.0	29.6	0.63	0.71	1.13	

M_0 = Total experimental unbalanced moment at the onset of steel yielding

M_f = Ultimate flexural capacity of a slab section at a distance d/2 on either side of wall or flange

d = effective depth of tension reinforcement

γ_f = a fraction of unbalanced moment assumed to be transferred by flexure (see eqn 6.11)

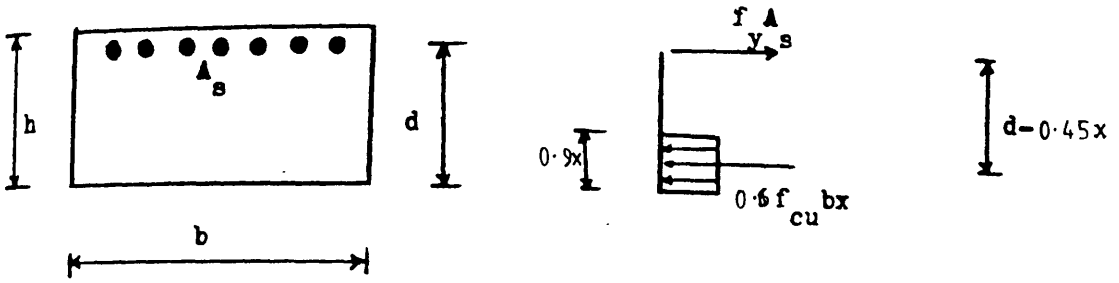

Figure (6.190) : Singly reinforced rectangular section under flexure

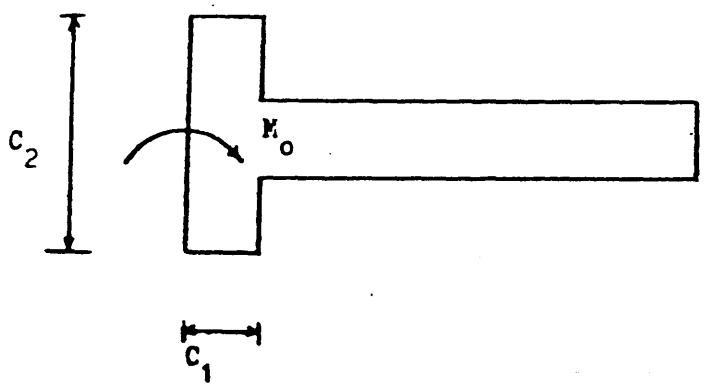

Figure (6.191)

to MS12 were found most effective in resisting punching shear failure (brittle type). In all the cases except model MS4, there was no shear failure in the slab and 'large' ductility was available at the floor slab– shear wall junction. Most of the stirrups around the junction had yielded in most of the models. To check how far this arrangement of stirrup was effective, the efficiency of closed vertical stirrups, λ used in the slab of models PS3 to MS12 was calculated, in line with the current American Code of practice, using the following equation (6.12) :

$$\lambda = \frac{(V_{exp} - 1/2V_c) \times 100}{A_{sv} \cdot f_{yw}} \qquad (6.12)$$

where

V_{exp} = experimental failure load of the model

V_c = shear strength of the junction without stirrup using ACI Code

A_{sv} = total area of shear steel within the critical perimeter (according to ACI Code 318–83)

f_{yw} = characteristic yield strength of stirrup $\leq$ 425 N/mm^2

Table (6.11) lists the shear strength of the junction calculated by ACI Code 318–83 formula without considering the area of closed vertical stirrup within the critical perimeter and percentage of efficiency of shear steel. If all the stirrups within the critical perimeter yielded at failure load, then the stirrups will be called 100% efficient, provided the shear strength calculations by the ACI Code formulae are valid for the models tested in this study. The efficiency of the stirrups used in the models tested in this study, ranges from 51% to 98%. The mean for all 10 models PS3 to MS12 is 71% with a standard deviation of 0.12.

6.6 Comparison of Tested Models with the Models without Shear Reinforcement[23]

6.6.1 Ultimate failure load

For the purpose of making comparison, the dimensions of the models tested in

Table (6.11) : Efficiency of closed vertical stirrups for the models of main test series according to ACI Code 318 - 83

Model	Experimental failure load V_{exp} KN	Shear strength of junction without stirrup V_c KN	Total area of shear steel mm^2	Efficiency λ Eqn.(6.12)	Main variables
PS3	175	82	453	70%	Shear steel
MS4	191	87	685	51%	Wall web length 67% of MS7
MS5	203	63	685	59%	Corridor opening width
MS6	343	161	629	98%	280mm for MS5 400mm for MS6 520mm for MS7
MS7	262	136	585	78%	
MS8	280	150	585	82%	Gravity load 3 times of MS7
MS9	247	146	585	70%	Bay width 1.44 times of MS7
MS10	209	252	283	69%	Flange width 300mm for MS10 200mm for MS11 400mm for MS12
MS11	219	192	396	73%	
MS12	235	262	396	62%	

this study were kept exactly similar to those of models in Reference (23) which were tested without using any shear steel in the slab. In the case of the specimens without shear reinforcement, the cube strength of concrete, f_{cu}, varied from 32 N/mm^2 to 50 N/mm^2 and the yield stress of slab reinforcing bar ranges from 512 N/mm^2 to 573 N/mm^2. In the specimens with the shear reinforcement, the range of f_{cu} was from 33 N/mm^2 to 68 N/mm^2 and that of f_y was from 478 N/mm^2 to 571 N/mm^2. The theoretical design load for both models with or without shear reinforcrment are normalised for the actual cube strength of concrete using the procedure discussed in section 6.5.1.

The normalised design lateral load and experimental failure load for both type of specimens and percentage of strength improved due to shear reinforcement are tabulated in Table (6.12). The values within brackets are for the specimens without shear steel[23]. The provision of shear steel has increased the mean strength of the junction by approximately 41% with standard deviation of 0.30. The improvement of ultimate strength is remarkable for models MS5 and MS6 (about 87% and 79% respectively) where corridor opening width is increased and decreased by 30% respectively from model MS7. The reinforcement ratio which appears in table (6.12) is for all the bars within entire slab width in windward direction.

Due to the variation in the material strengths f_{cu} and f_y in each test model, it is not exactly possible to determine the extent of increase in the strength experimentally. The influence of the variation of concrete strength has been taken into account in the normalisation of design lateral load. The yield stress of bars and their total amount has a marked influence on the strength of the connection as the flexural capacity of the slab depends largely on those values. Since the range of f_y in the specimens with shear reinforcement was lower than those for specimens without shear reinforcement, it can be concluded that the extent of increase in the strength of the floor slab– shear wall connections will be somewhat

larger than what can be gauged from experimental results for all the models except model MS5. Model MS5 had more flexural steel than its counterpart model MT6 and hence the improvement in strength will be lower than that listed in Table (6.12).

6.6.2 Load – Deflection Relationship

In Figures (6.192) and (6.193) the nondimensional curves showing lateral load versus specimens edge displacement are compared for models with and without shear reinforcement and having the same amount of flexural reinforcement. The load–displacement curves indicate very little ductility for the specimens without shear reinforcement. The use of shear reinforcement in the slab has markedly improved the ductility of every models as evident from Figures (6.192) and (6.193). But the use of shear reinforcement in the models did not change the stiffness of the structure. The slight variation in the stiffness may be due to the variation in the material properties of the models.

6.6.3 Strains

Tensile strains in steel in both windward and transverse direction in the slab of models with shear steel are compared with those of models without shear steel in Figures (6.194) to (6.201). The benifit of using shear reinforcement in the slab is readily apparent from the above figures. The reinforcing steel bars have not even yielded in the models without shear steel. Whereas, some of the bars in longitudinal direction in the models with shear steel reached more than three times yield strain before failure. This shows the considerable redistribution of stresses in the adjacent steel bars, causing delay in the ultimate collapse near the junction. Compressive strains in concrete on the bottom surface of the slab of models with shear steel are compared with their counterpatrs for models without shear steel in Figures (6.202) to (6.207). The maximum utilisation of concrete strength is apparent in models where shear steel has been used in the slab.

Table (6.12) : Improvement of ultimate strength due to shear reinforcement. Values without brackets are for the specimens with shear steel and those within brackets are for the specimens without shear steel.

Model No	Percentage of flexural reinforcement	Normalised design load V_{design} KN	Experimental failure load V_{exp} KN	$\frac{V_{exp}}{V_{design}}$	% of strength increased due to shear steel
PS1	1.29	215	219	1.02	
(MT1)	(1.29)	(207)	(175)	(0.85)	20.0
MS4	1.12	220	191	0.87	
(MT3)	(1.29)	(218)	(154)	(0.71)	22.5
MS5	1.35	155	203	1.31	
(MT6)	(1.29)	(152)	(106)	(0.70)	87.1
MS6	1.29	330	343	1.04	
(MT7)	(1.29)	(309)	(178)	(0.58)	79.3
MS7	1.29	240	262	1.09	
(MT2)	(1.29)	(229)	(193)	(0.84)	25.0
MS8	1.29	255	280	1.10	
(MT4)	(1.29)	(200)	(193)	(0.97)	13.4
MS9	0.83	250	247	0.99	
(MT8)	(1.07)	(197)	(164)	(0.83)	19.3

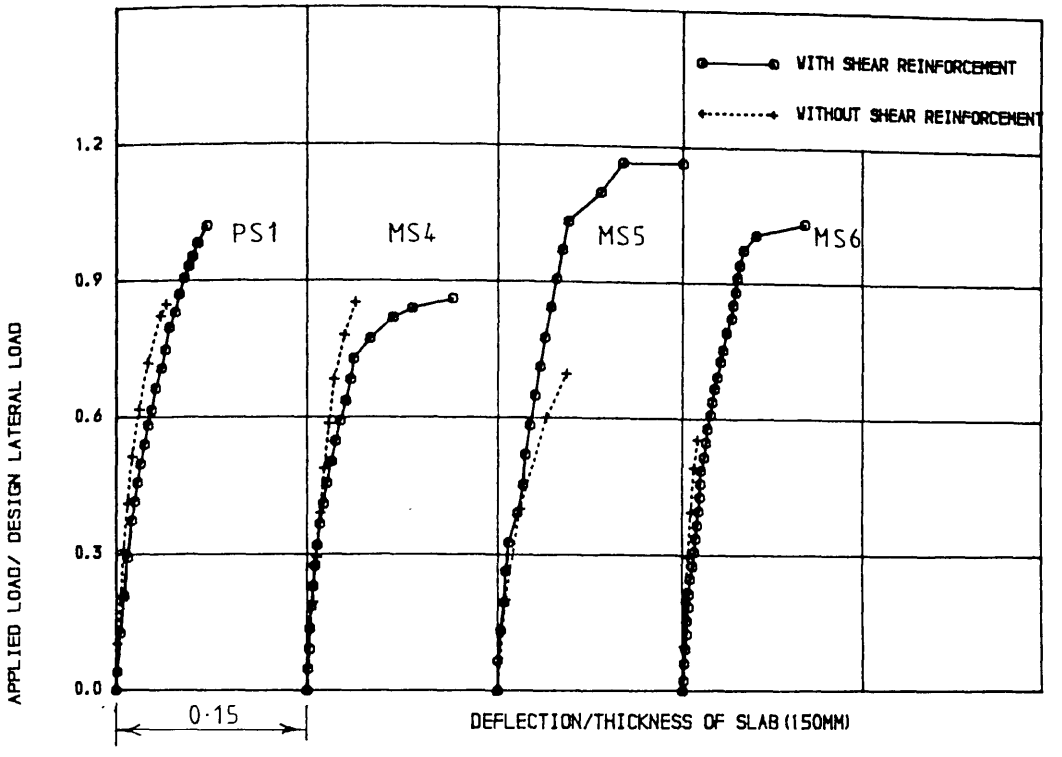

FIGURE (6.192) , LOAD-DEFLECTION CURVES COMPARING SPECIMENS PS1, MS4, MS5 and MS6 WITH SHEAR REINFORCEMENT WITH THE SPECIMENS WITHOUT SHEAR REINFORCEMENT

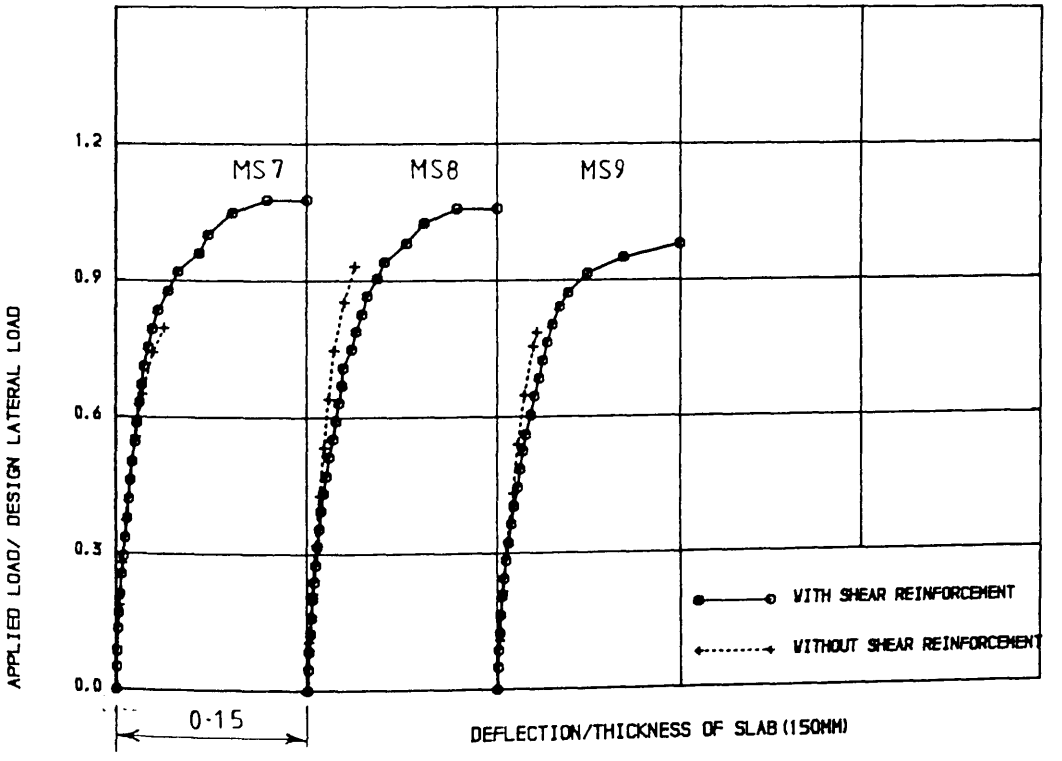

FIGURE (6.193) , LOAD-DEFLECTION CURVES COMPARING SPECIMENS MS7, MS8 and MS9 WITH SHEAR REINFORCEMENT WITH THE SPECIMENS WITHOUT SHEAR REINFORCEMENT

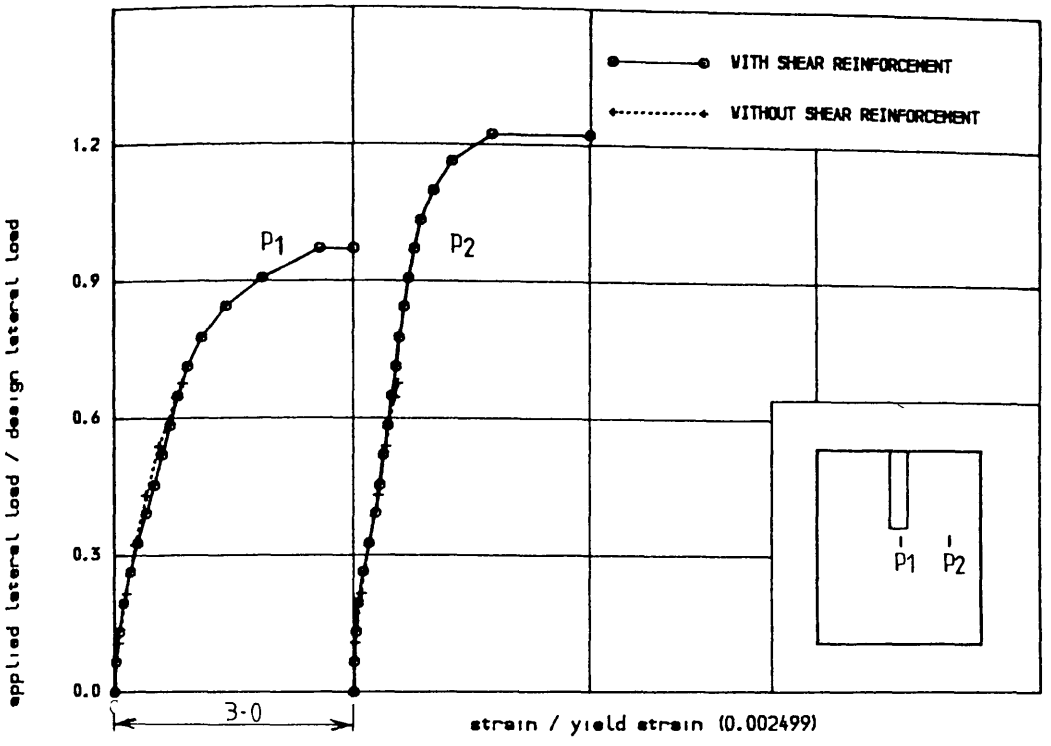

FIGURE (6.194) , COMPARISON OF TENSILE STRAIN IN STEEL IN VINDVARD DIRECTION IN THE SLAB OF MODEL MS5 WITH THAT OF MODEL 'MT6'

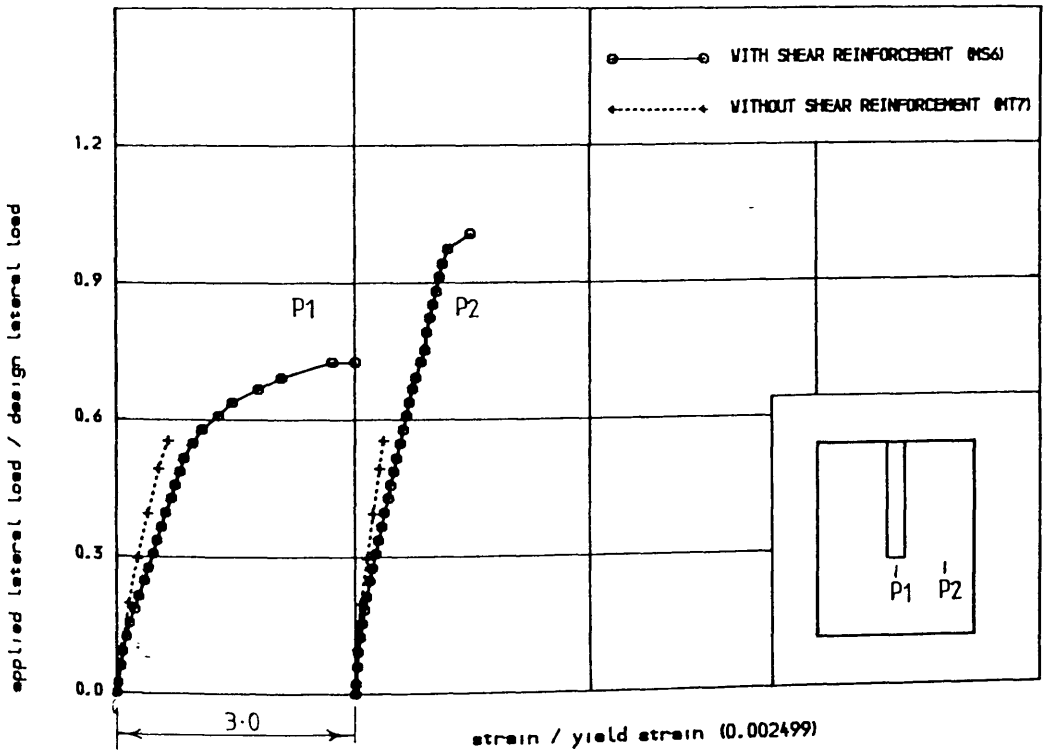

FIGURE (6.195) , COMPARISON OF TENSILE STRAIN IN STEEL IN VINDVARD DIRECTION IN THE SLAB OF MODEL MS6 WITH THAT OF MODEL 'MT7'

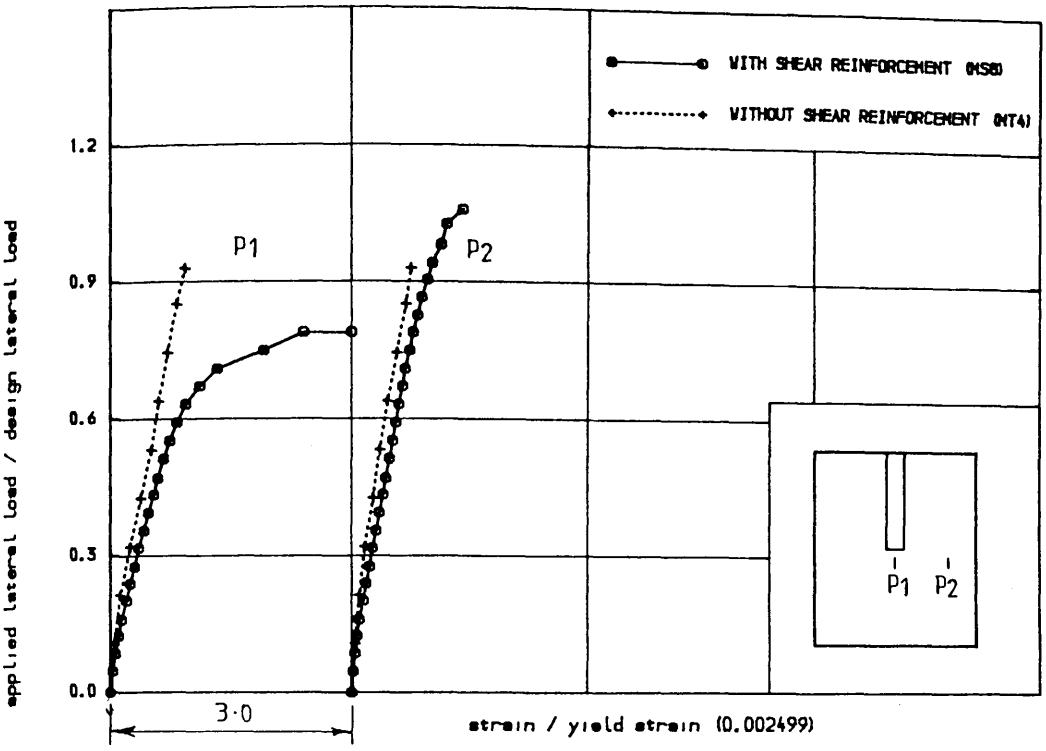

FIGURE (6.196) : COMPARISON OF TENSILE STRAIN IN STEEL IN WINDWARD DIRECTION IN THE SLAB OF MODEL MS8 WITH THAT OF MODEL 'MT4'

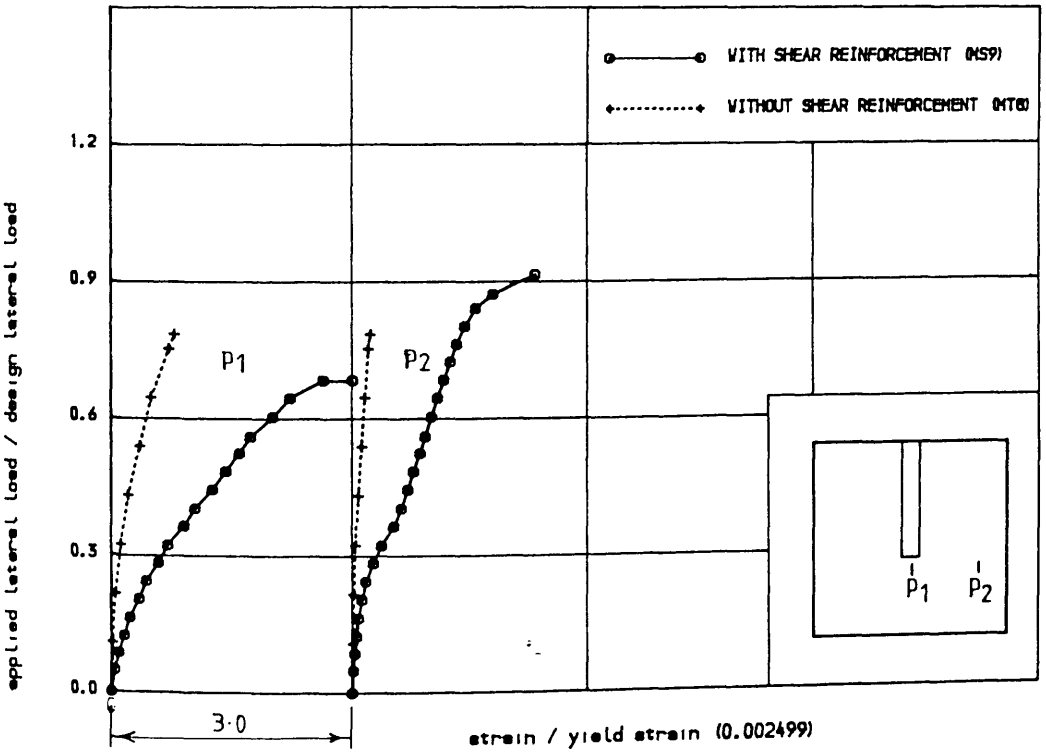

FIGURE (6.197) : COMPARISON OF TENSILE STRAIN IN STEEL IN WINDWARD DIRECTION IN THE SLAB OF MODEL MS9 WITH THAT OF MODEL 'MT8'

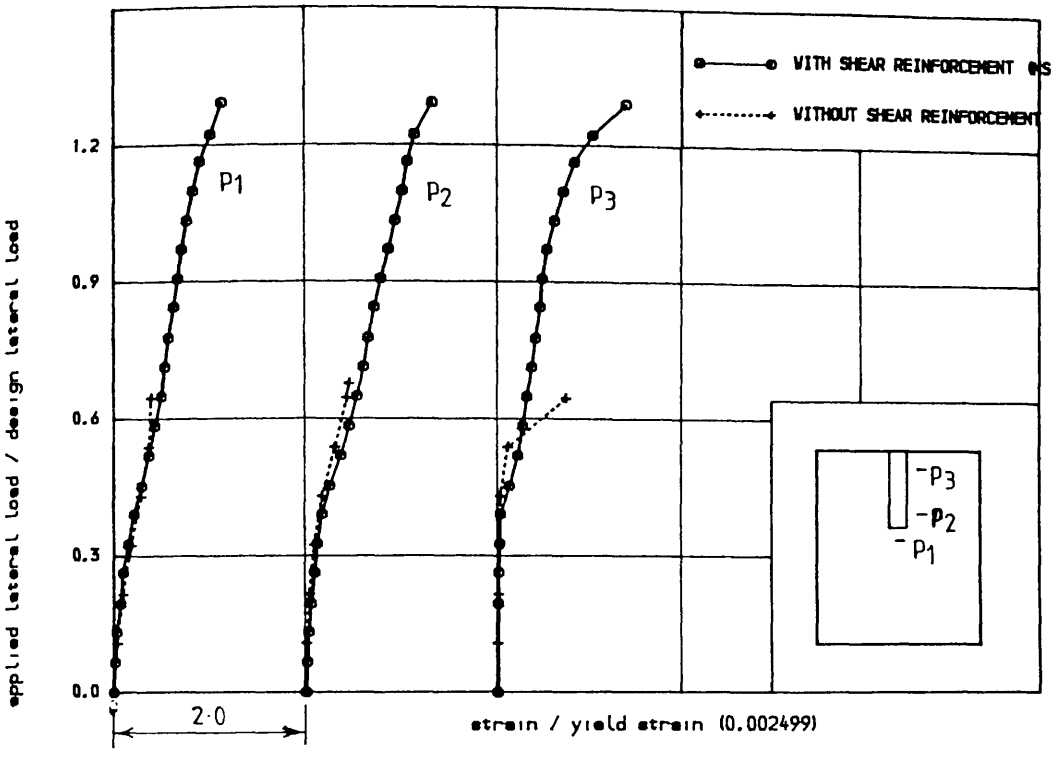

FIGURE (6.198) , COMPARISON OF TENSILE STRAIN IN STEEL IN TRANSVERSE DIRECTION IN THE SLAB OF MODEL MS5 WITH THAT OF MODEL 'MT6'

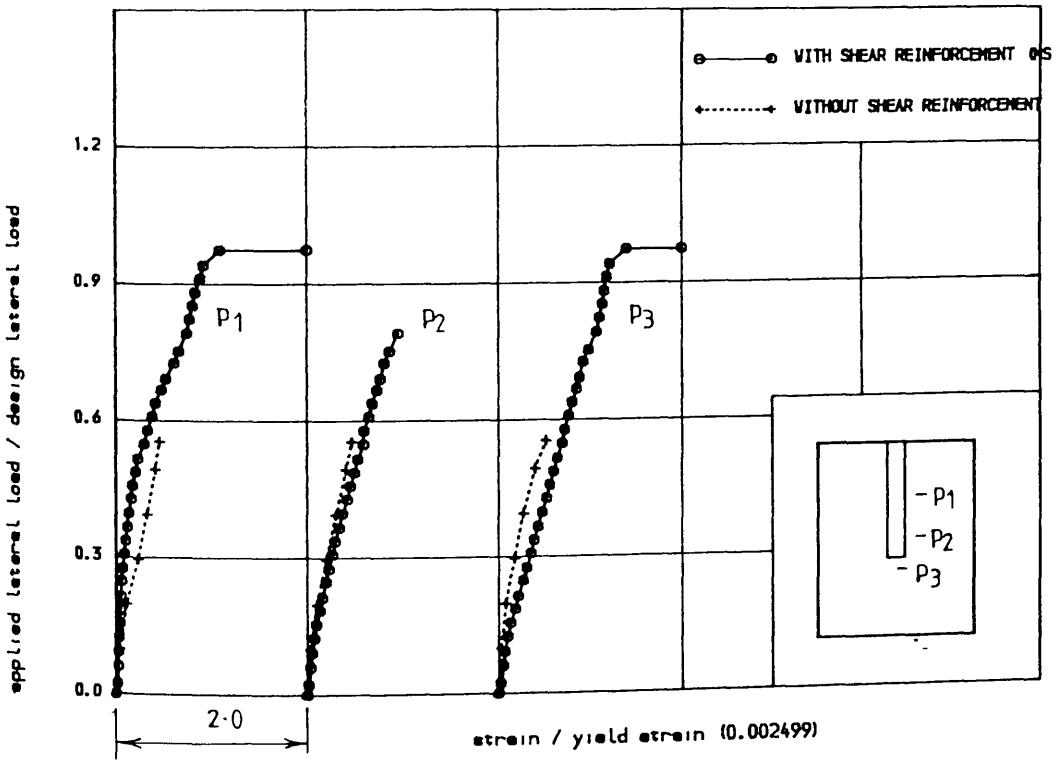

FIGURE (6.199) , COMPARISON OF TENSILE STRAIN IN STEEL IN TRANSVERSE DIRECTION IN THE SLAB OF MODEL MS6 WITH THAT OF MODEL 'MT7'

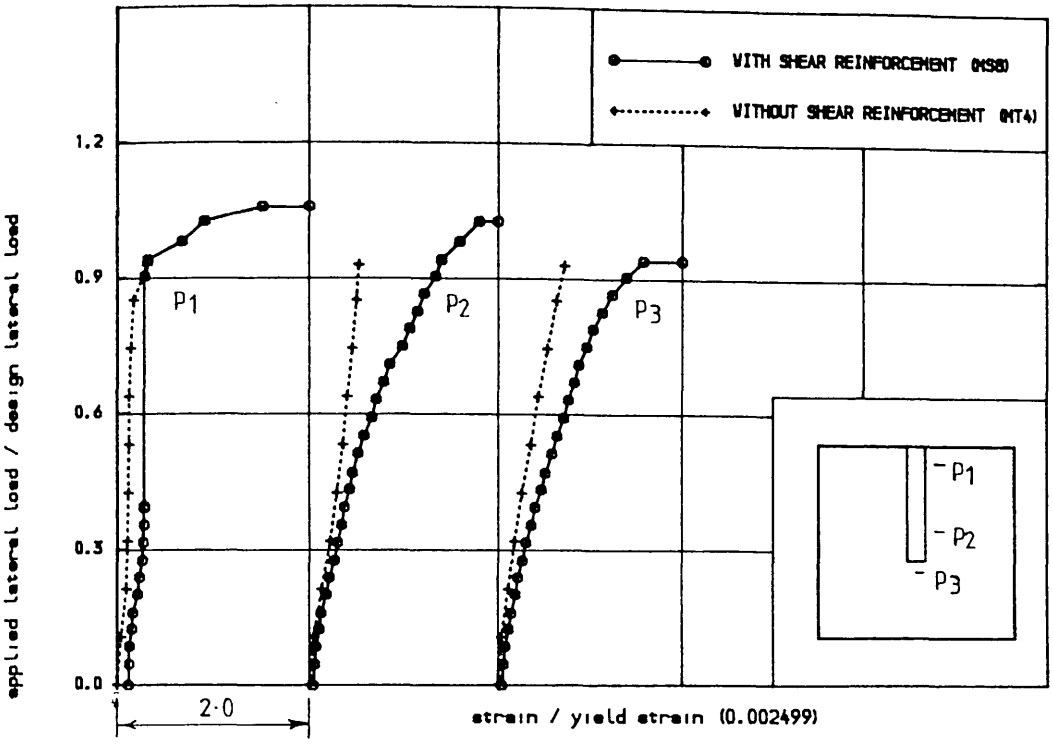

FIGURE (6.200) , COMPARISON OF TENSILE STRAIN IN STEEL IN TRANSVERSE DIRECTION IN THE SLAB OF MODEL MS8 WITH THAT OF MODEL 'MT4'

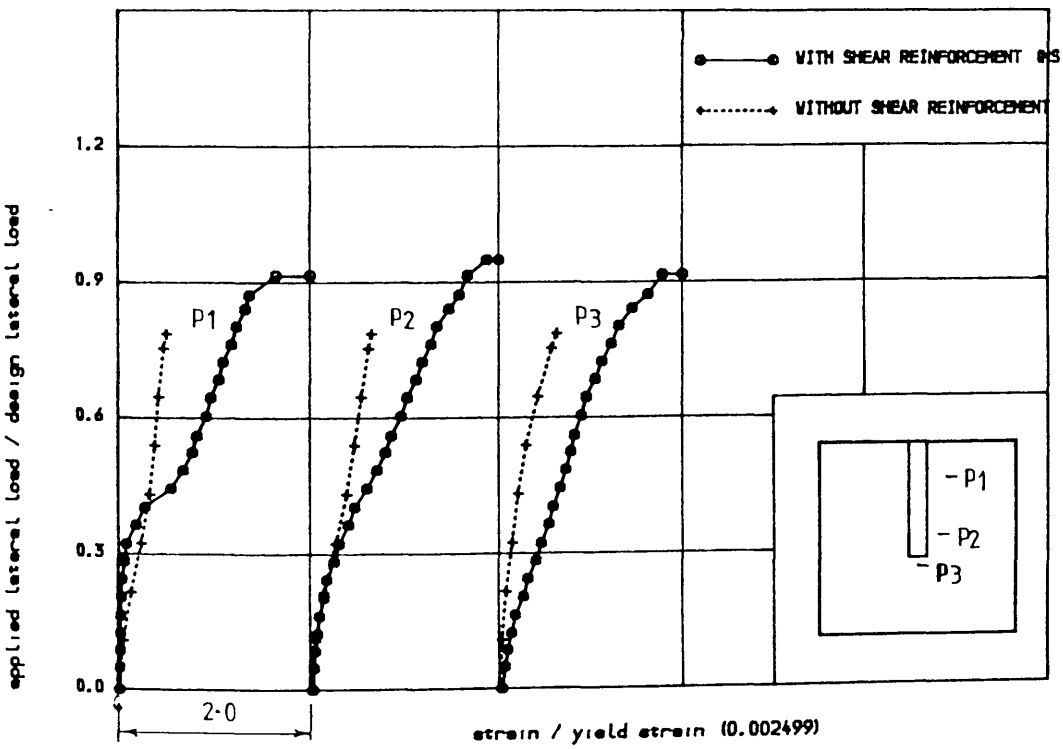

FIGURE (6.201) , COMPARISON OF TENSILE STRAIN IN STEEL IN TRANSVERSE DIRECTION IN THE SLAB OF MODEL MS9 WITH THAT OF MODEL 'MT8'

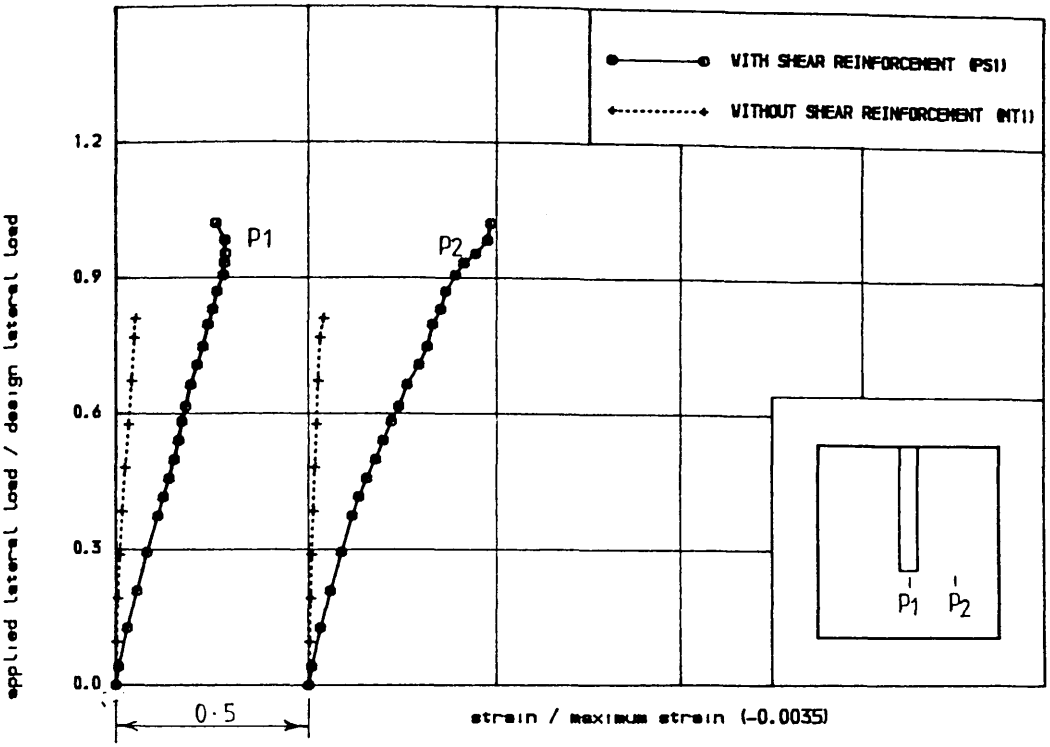

FIGURE (6.202) , COMPARISON OF COMPRESSIVE STRAIN IN CONCRETE IN VINDVARD DIRECTION IN THE SLAB OF MODEL PS1 WITH THAT OF MODEL 'MT1'

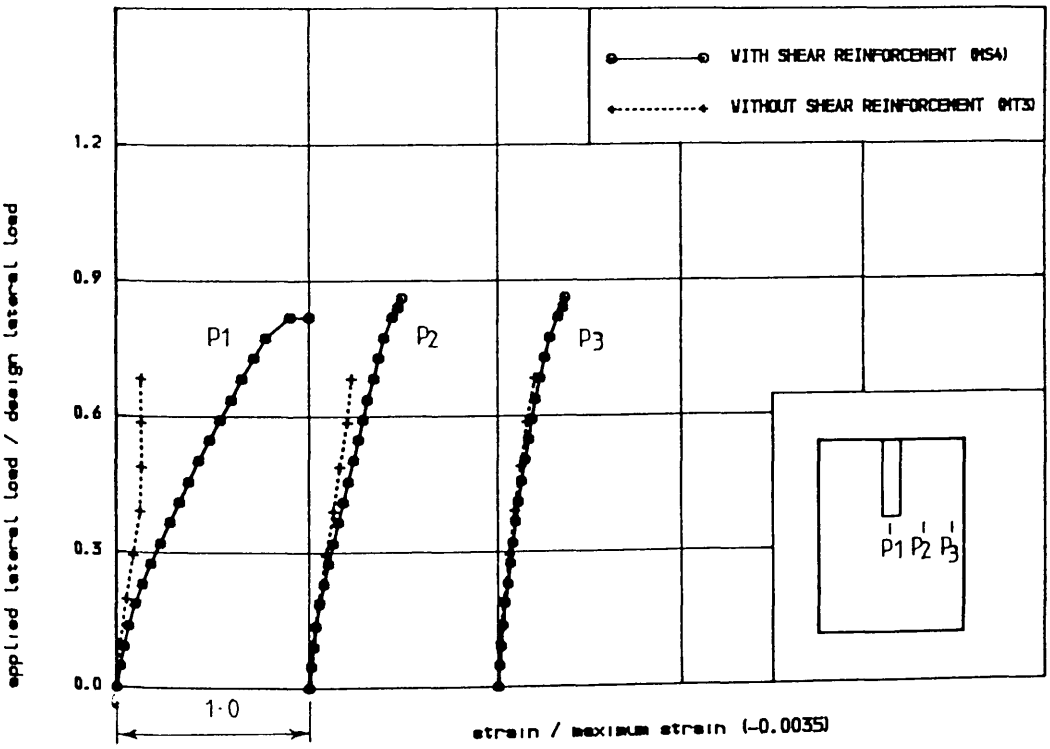

FIGURE (6.203) , COMPARISON OF COMPRESSIVE STRAIN IN CONCRETE IN VINDVARD DIRECTION IN THE SLAB OF MODEL MS4 WITH THAT OF MODEL 'MT3'

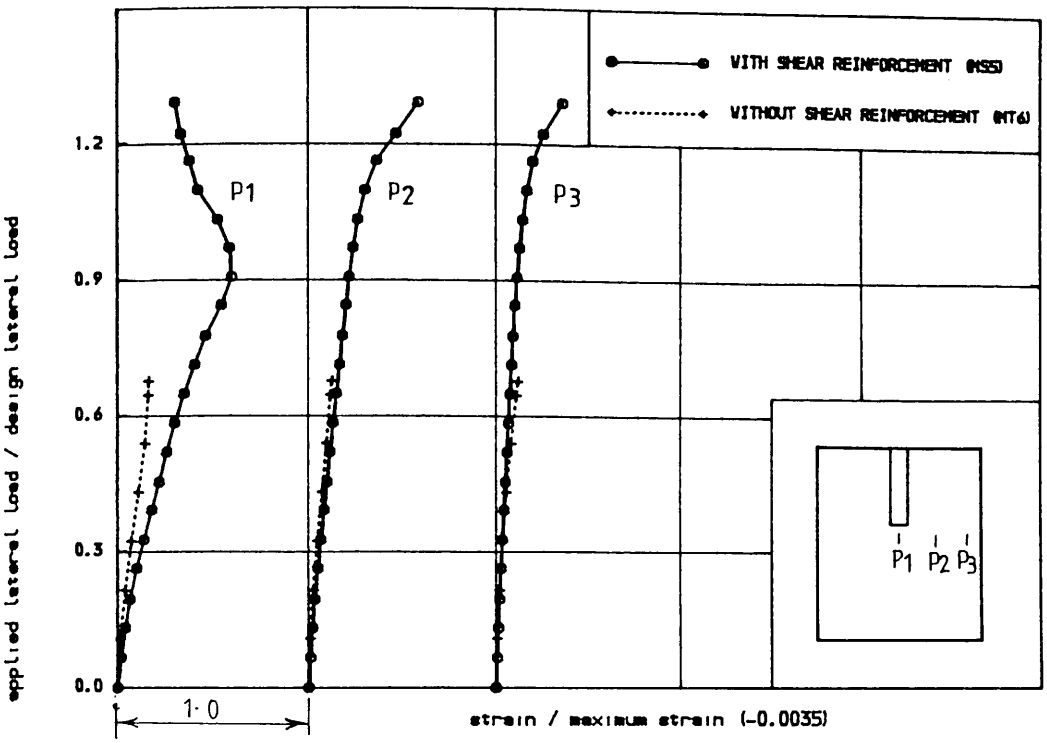

FIGURE (6.204) , COMPARISON OF COMPRESSIVE STRAIN IN CONCRETE IN WINDWARD DIRECTION IN THE SLAB OF MODEL MS5 WITH THAT OF MODEL 'MT6'

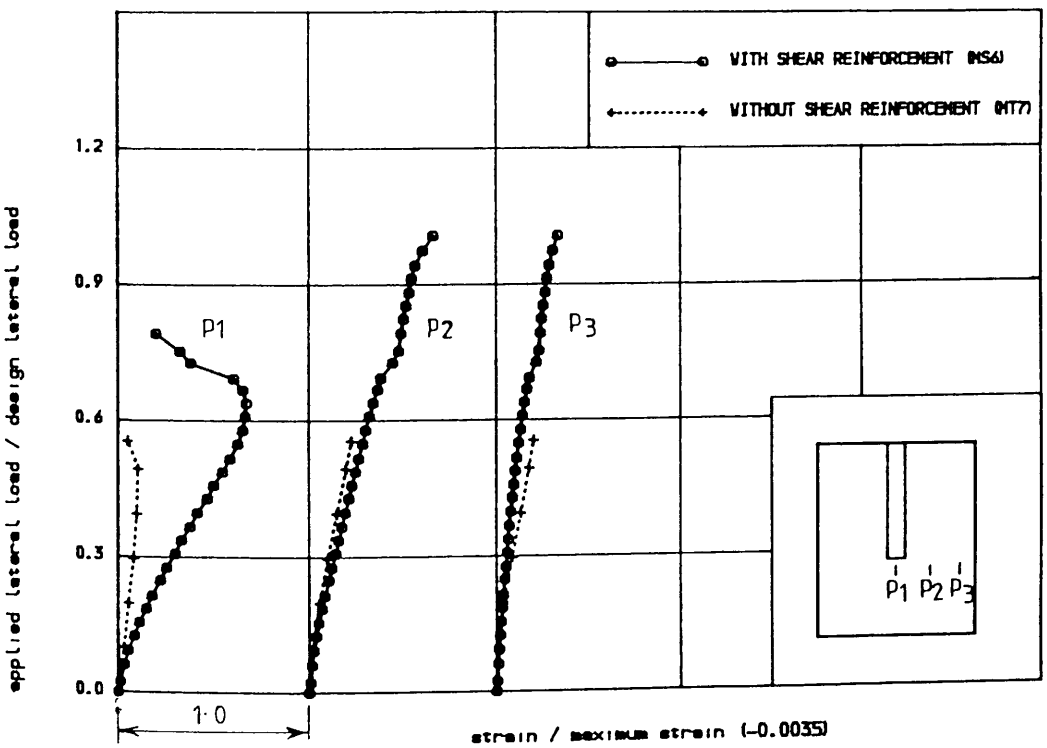

FIGURE (6.205) , COMPARISON OF COMPRESSIVE STRAIN IN CONCRETE IN WINDWARD DIRECTION IN THE SLAB OF MODEL MS6 WITH THAT OF MODEL 'MT7'

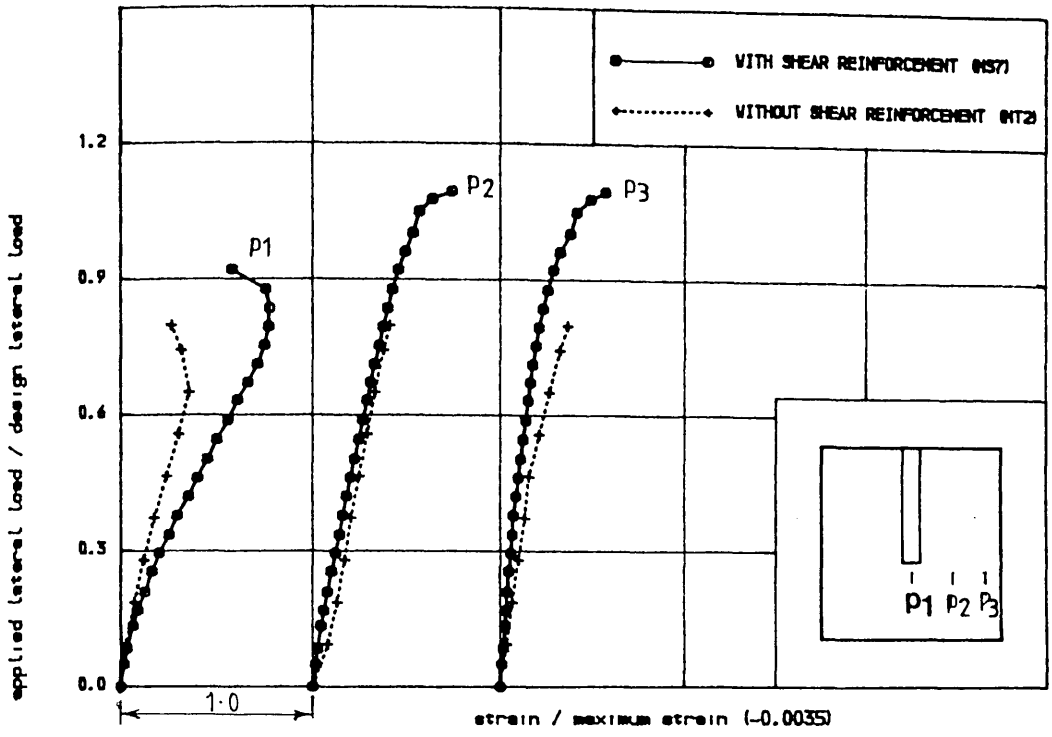

FIGURE (6.206) : COMPARISON OF COMPRESSIVE STRAIN IN CONCRETE IN VINDVARD DIRECTION IN THE SLAB OF MODEL MS7 WITH THAT OF MODEL 'MT2'

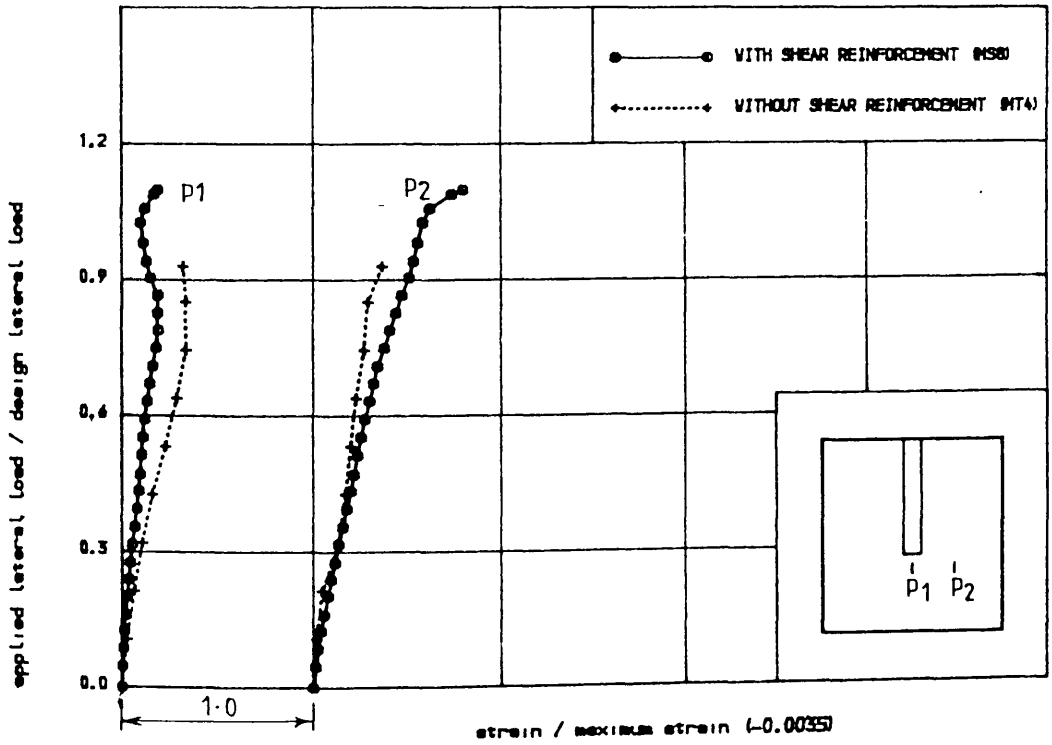

FIGURE (6.207) : COMPARISON OF COMPRESSIVE STRAIN IN CONCRETE IN VINDVARD DIRECTION IN THE SLAB OF MODEL MS8 WITH THAT OF MODEL 'MT4'

CHAPTER SEVEN

THEORETICAL INVESTIGATION

7.1 Introduction

In chapter four, the computer programme used for the nonlinear finite element analysis of reinforced concrete structure was described. In this chapter the nonlinear program is used to carry out the theoretical analysis of the experimental models described in chapter six. The object of this theoretical analysis is :

(a) to build confidence in the accuracy of the results obtained from the three dimensional finite element program. This can be achieved by comparing the theoretical strains, deflections and failure loads with their experimental values.

(b) to obtain a better understanding of stress redistribution and progressive failure of concrete and steel. The redistribution of vertical shear stress components at different stages of loading might assist to understand progressive punching shear failure.

7.2 Nonlinear Analysis

The parameters which have an effect on the numerical solution can be summarised as follows:

(a) Mesh size

(b) Tension stiffening

(c) Tensile strength of concrete

(d) Angle of crack

(e) Shear retention factor of cracked concrete

(f) The norm of convergence tolerance

The influences of some of the above parameters on numerical solution was thoroughly investigated by Elnounu[24] to analyze his experimental models.

All the analysis were carried out using the fixed crack analysis. Six, eight and twelve elements mesh which have 210, 267 and 366 degrees of freedom respectively were used for convergence study. A linear analysis was carried out for the three meshes of Figure (7.1). The average displacement of the nodes on edge EF versus the number of degrees of freedom is plotted in Figure (7.2). The displacement increases about 21% when mesh is refined from six to eight elements but there is only 4.5% change in displacement from eight to twelve elements. Nonlinear analyses were also carried out on model MS7 and it was found that the mesh size has insignificant effect on the strains upto the yield point, but it has a considerable effect on the failure load which decreases about 20% when mesh is refined from six to twelve elements. Keeping in mind cost of computation, the eight element mesh was adopted for acceptable accuracy. But twelve elements mesh were used in model MS9 because of large bay width and in model MS11 because of small flange width.

In the present work, a ceiling of 20 iterations per increment was found sufficient to get convergence using a 10% convergence tolerance for residual forces. Adopting a more accurate tolerance did not show much difference in the behaviour other than increasing the computation cost. Tension stiffening was ignored. The high convergence tolerance with no–tension stiffening model has a considerable advantage over the tension stiffening model in that it requires far less iterations to keep the residual forces within the tolerance and hence less computer time.

Using the eight elements mesh of Figure (7.1), several nonlinear analysis were carried out for model MS7, using constant value of shear retention factor, Beta. Some of the results are presented in Figures (7.3) to (7.7). It is clear from those figures that the strains are not affected by the various values of 'Beta' upto the yield point of the steel; but the failure load is always higher than the experimental value. Elnounu[24] proposed the following equation (7.1) for shear retention factor for the analysis of slab coupled to flanged shear walls.

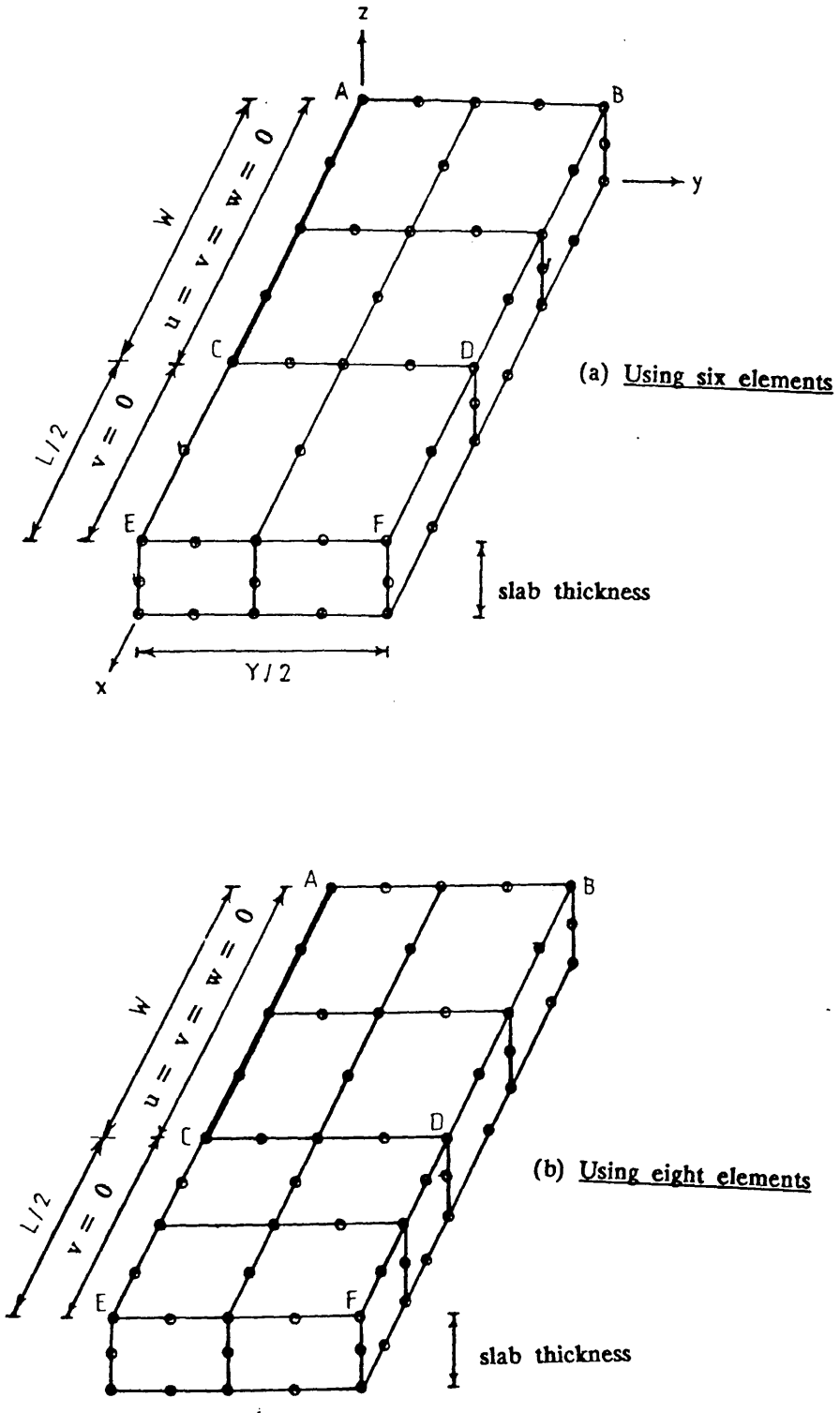

Figure (7.1) : Finite element mesh with boundary conditions.

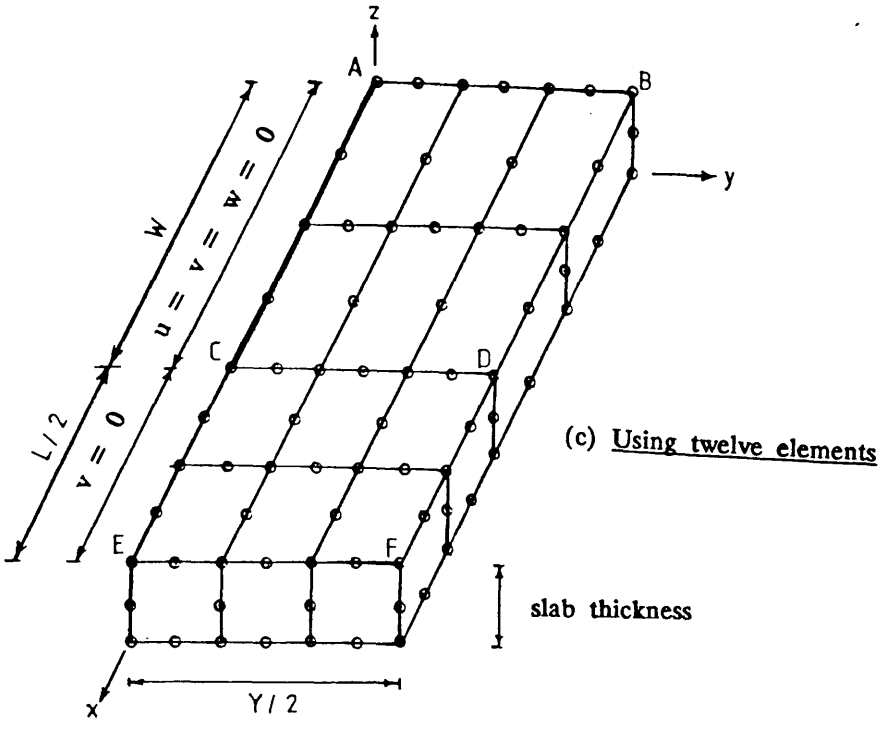

Figure (7.1) : Finite element mesh with boundary conditions.

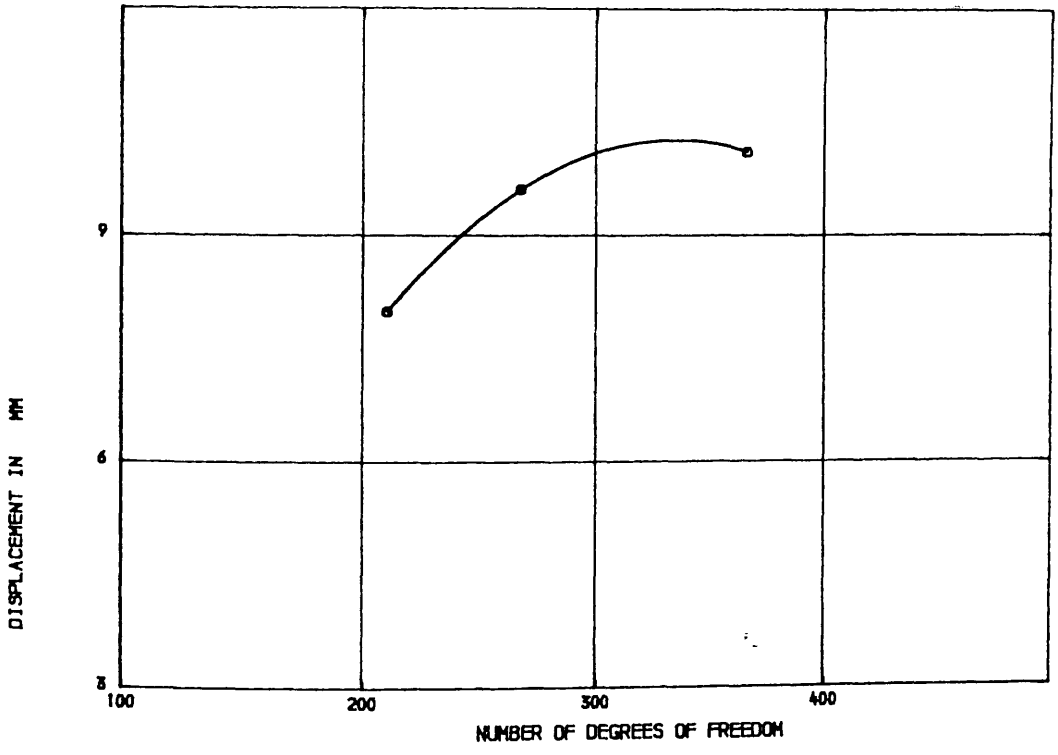

FIGURE (7.2) . EFFECT OF MESH SIZE ON LINEAR DISPLACEMENT AT A LATERAL LOAD EQUALS THE DESIGN LATERAL LOAD

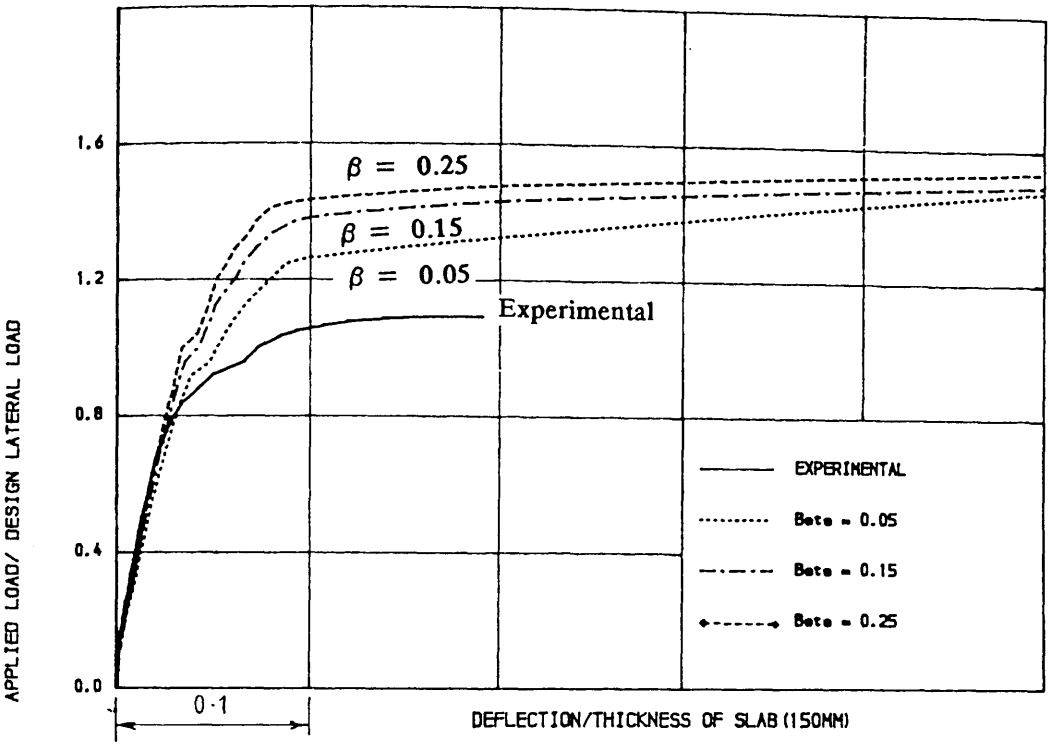

FIGURE (7.3) , EFFECT OF SHEAR RETENTION FACTOR, BETA, ON THE LOAD-DEFLECTION RELATIONSHIP OF MODEL MS7 (Using 8 elements mesh)

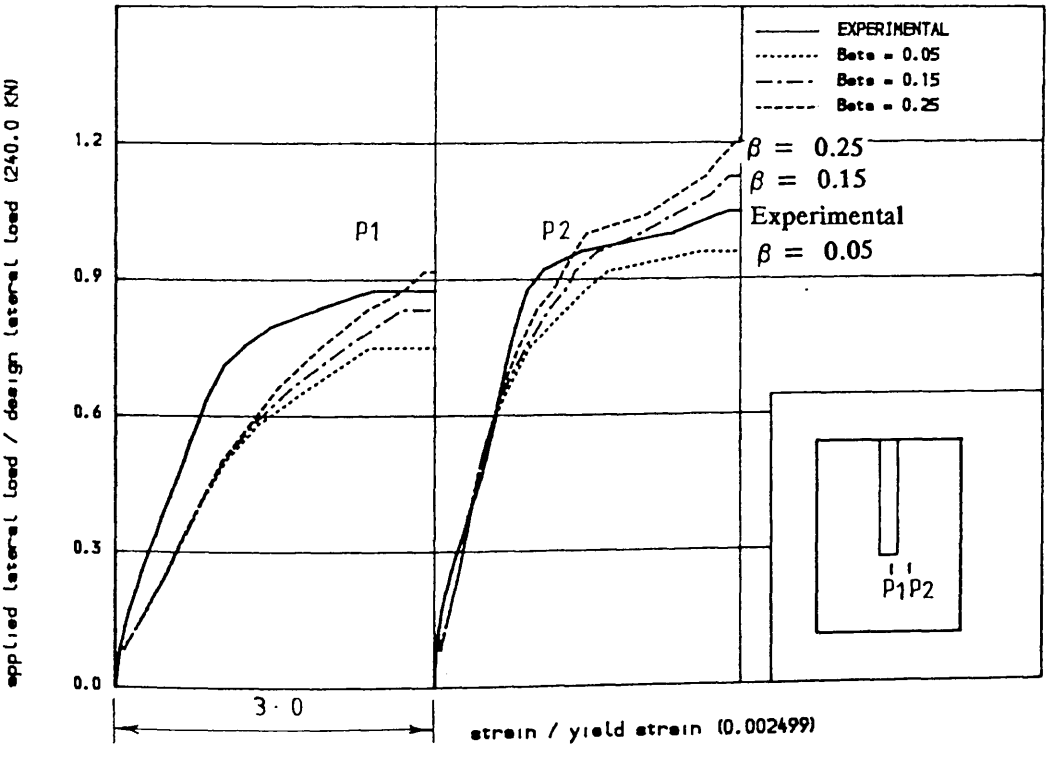

FIGURE (7.4) , EFFECT OF SHEAR RETENTION FACTOR, BETA, ON TENSILE STRAIN IN STEEL IN VINDVARD DIRECTION IN THE SLAB OF MODEL 'MS7'

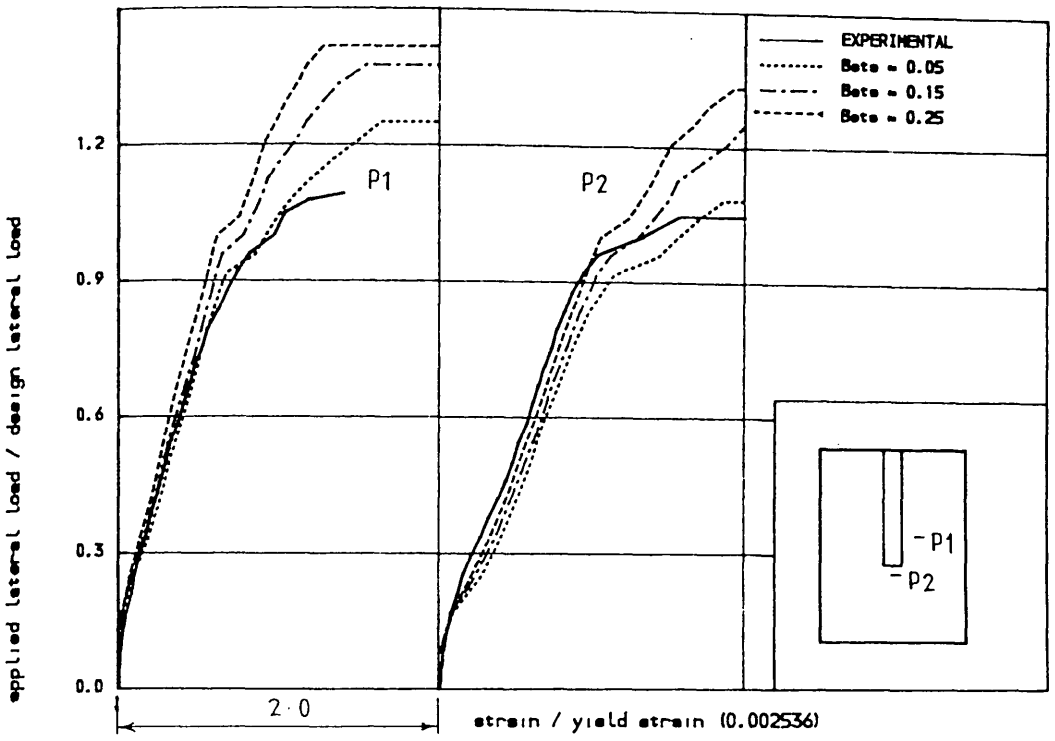

FIGURE (7.5) . EFFECT OF SHEAR RETENTION FACTOR, BETA, ON THE TENSILE STRAIN IN STEEL IN TRANSVERSE DIRECTION IN THE SLAB OF MODEL 'MS7'

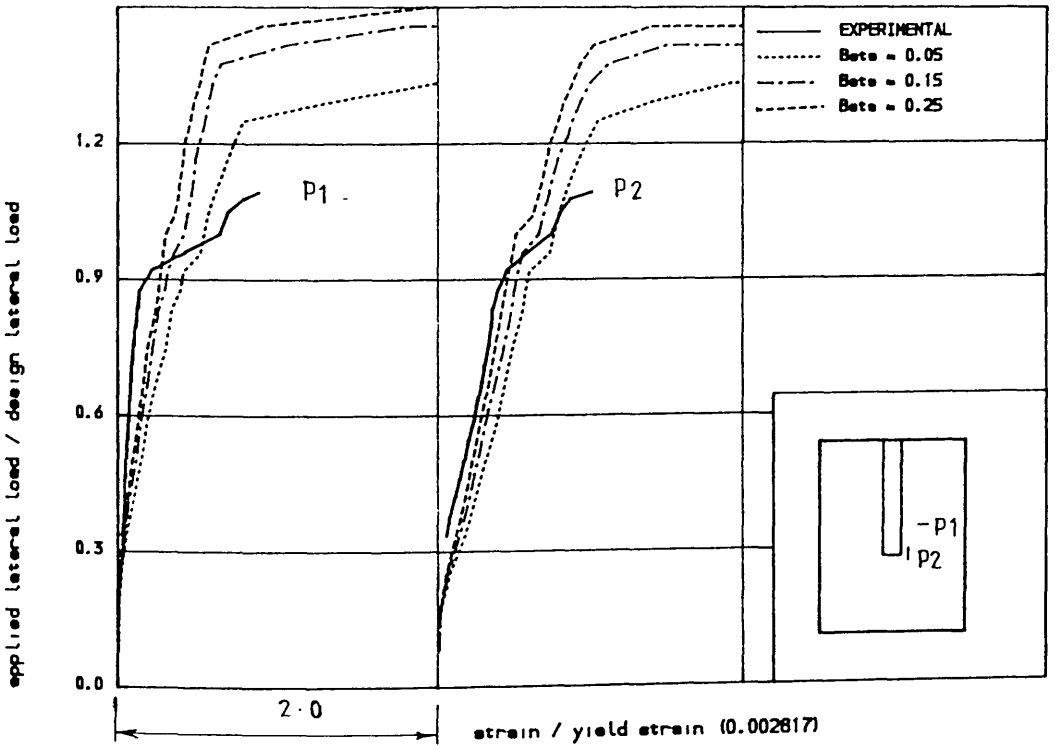

FIGURE (7.6) . EFFECT OF SHEAR RETENTION FACTOR, BETA, ON THE TENSILE STRAIN IN CLOSED VERTICAL STIRRUPS IN THE SLAB OF MODEL 'MS7'

$$\beta = \frac{1.0}{\epsilon_m/\epsilon_{to}} \qquad \text{for} \quad \epsilon_m \geq \epsilon_{to}$$

$$\beta = 1.0 \qquad \text{for} \quad \epsilon_m \leq \epsilon_{to} \tag{7.1}$$

where ϵ_m is the average of the three principal strains at a cracked point, and ϵ_{to} is the cracking tensile strain which was taken as 0.0001. When equation (7.1) was used to analyse the slab coupled with rectangular shear walls, the theoretical failure load was found to be higher than the experimental one. To find a general relationship between the shear retention factor and Z/t_w (the ratio of flange width to wall–web thickness), several nonlinear analysis were performed, varying Z/t_w from 1.0 to 4.0 and using C_1 equal to 0.25, 0.50, 0.75 and 1.0 in the following equations:

$$\beta = \frac{C_1}{\epsilon_m/\epsilon_{to}} \qquad \text{for} \quad \epsilon_m \geq \epsilon_{to}$$

$$\beta = 1.0 \qquad \text{for} \quad \epsilon_m \leq \epsilon_{to} \tag{7.2}$$

From the ratio of V_{exp}/V_{theo}, as shown in Figure (7.8), it was very difficult to express C_1 as a function of Z/t_w. To be on the safe side, equations (7.2) with C_1 = 0.25 were used in all the analyses presented in the rest of this chapter. This value gives the 'best' results for all values of Z/t_w.

7.3 Procedure adopted for the analysis

For reasons of economy, only one half of the symmetric model was considered. In order to minimize the number of elements, the wall was assumed to have a zero thickness. To study the effect of wall thickness in the theoretical analysis, a nonlinear analysis was carried out on model MS7 using the twelve elements mesh. The results are presented in Figure (7.9) for load–deflection relationship and in Figures (7.10) to (7.13) for strains. When compared with the results of zero wall thickness (of eight elements mesh) the analysis (when the wall

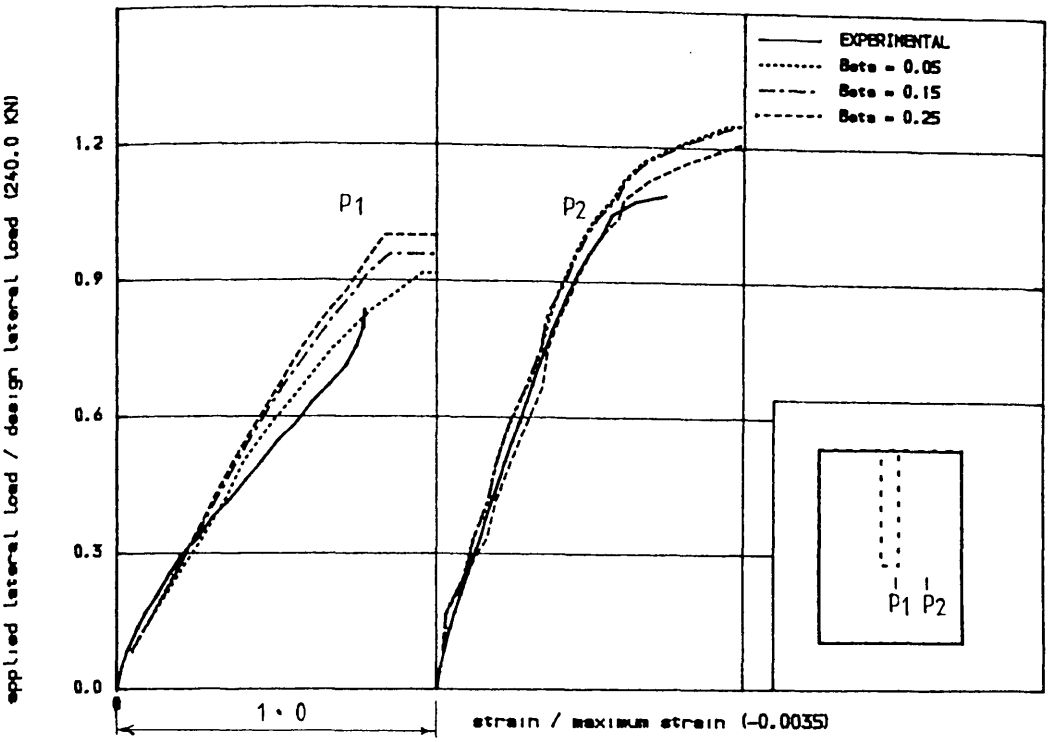

FIGURE (7.7) , EFFECT OF SHEAR RETENTION FACTOR, BETA, ON COMPRESSIVE STRAIN IN CONCRETE IN VINDVARD DIRECTION IN THE SLAB OF MODEL 'MS7'

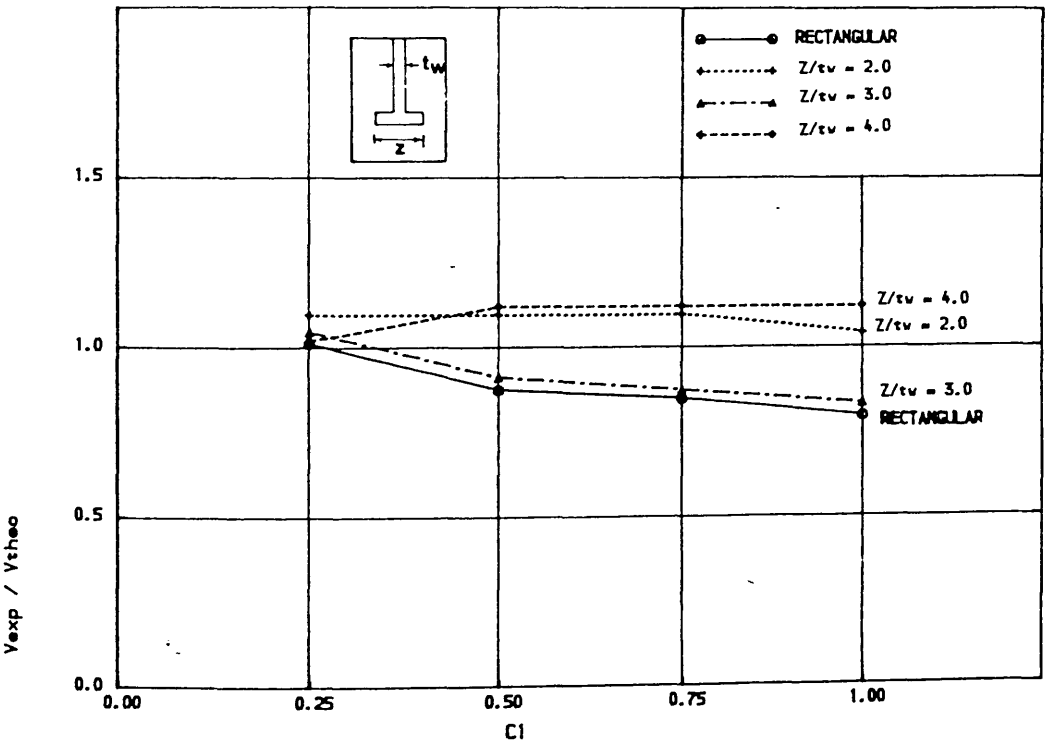

FIGURE (7.8) , CURVES TO GET A RELATIONSHIP BETWEEN THE CONSTANT C1 USED IN EQN. (7.2) AND Z/tv (Z-FLANGE WIDTH, tv-WALL THICKNESS)

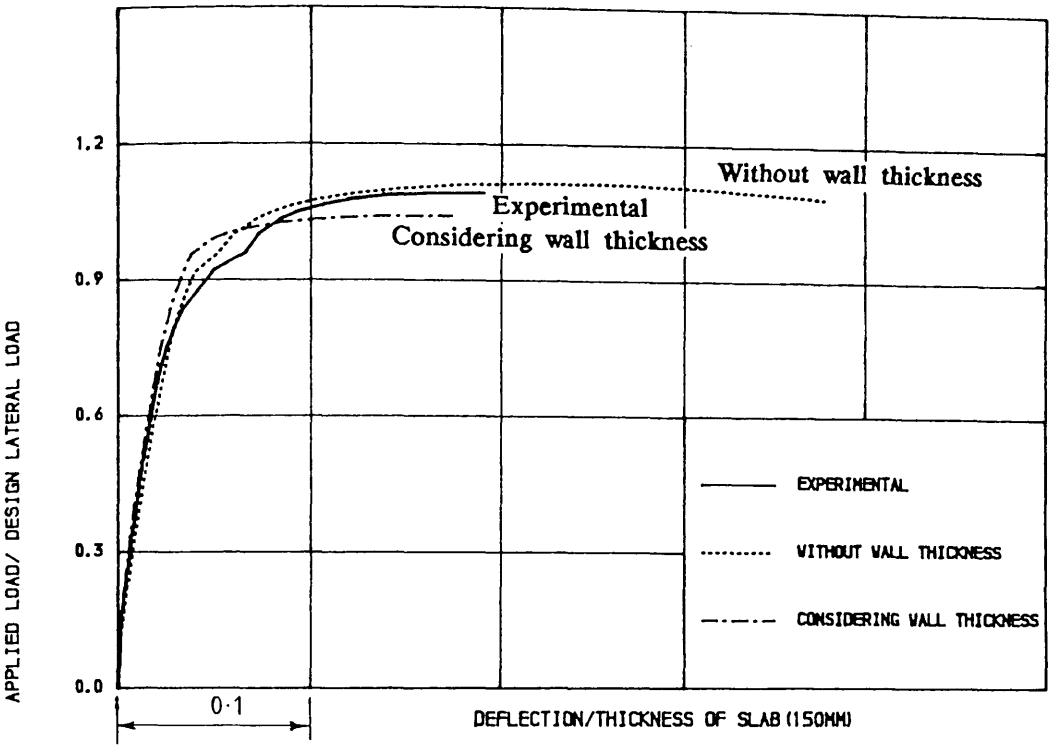

FIGURE (7.9) , EFFECT OF WALL THICKNESS ON LATERAL LOAD-DISPLACEMENT RELATIONS OF MODEL MS7

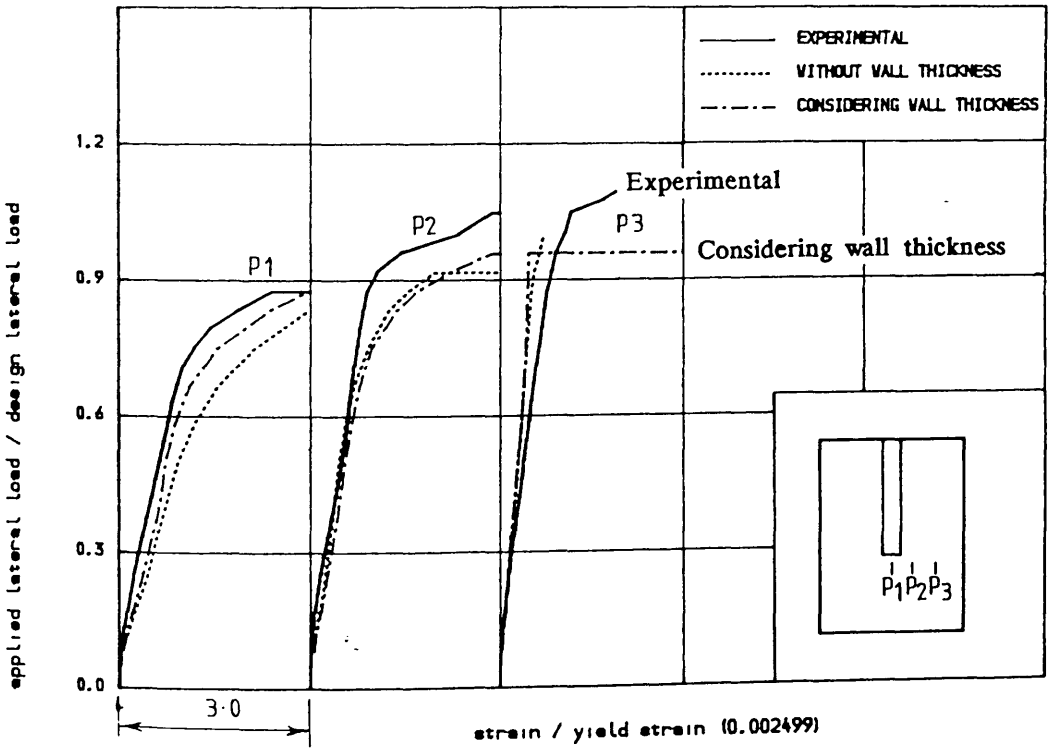

FIGURE (7.10) , EFFECT OF WALL THICKNESS ON TENSILE STRAIN IN STEEL IN WINDWARD DIRECTION IN THE SLAB OF MODEL MS7

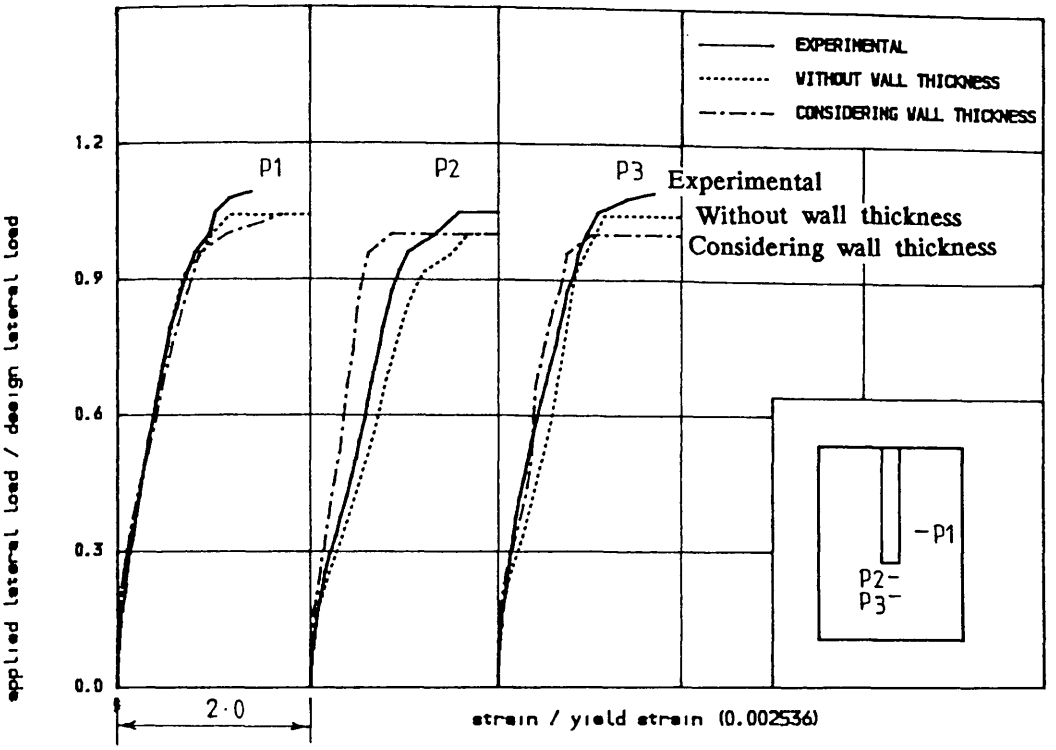

FIGURE (7.11) , EFFECT OF WALL THICKNESS ON TENSILE STRAIN IN STEEL IN TRANSVERSE DIRECTION IN THE SLAB OF MODEL MS7

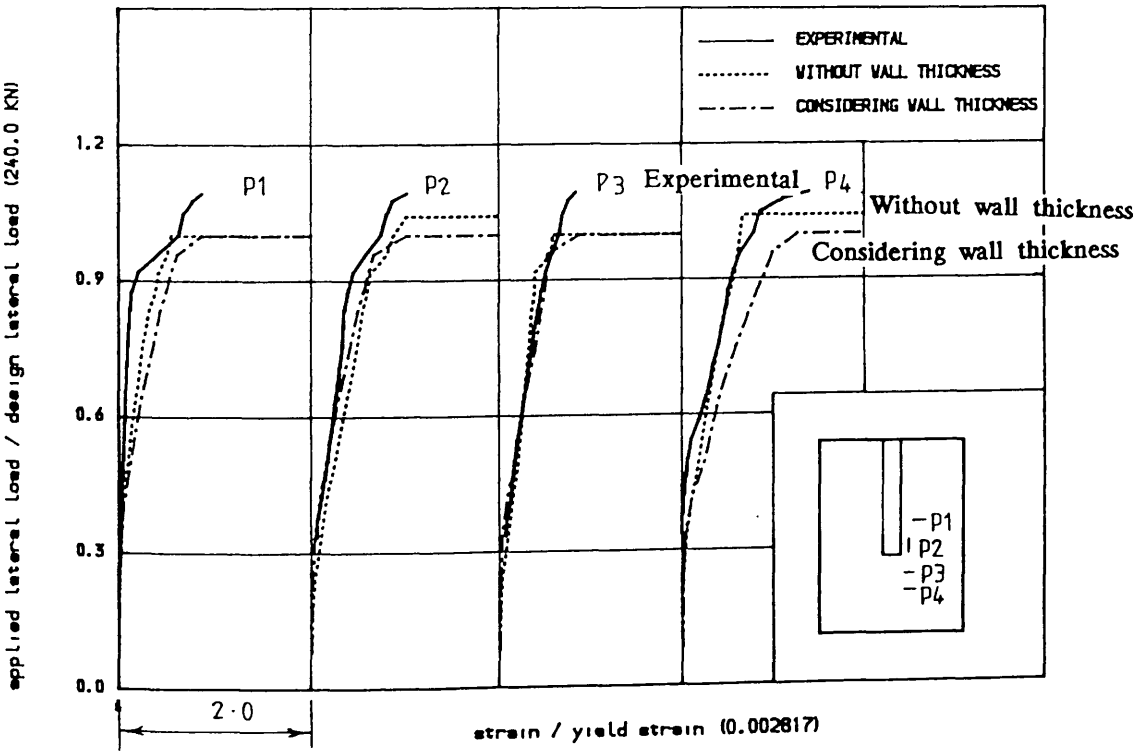

FIGURE (7.12) , EFFECT OF WALL THICKNESS ON TENSILE STRAIN IN CLOSED VERTICAL STIRRUP IN THE SLAB OF MODEL MS7

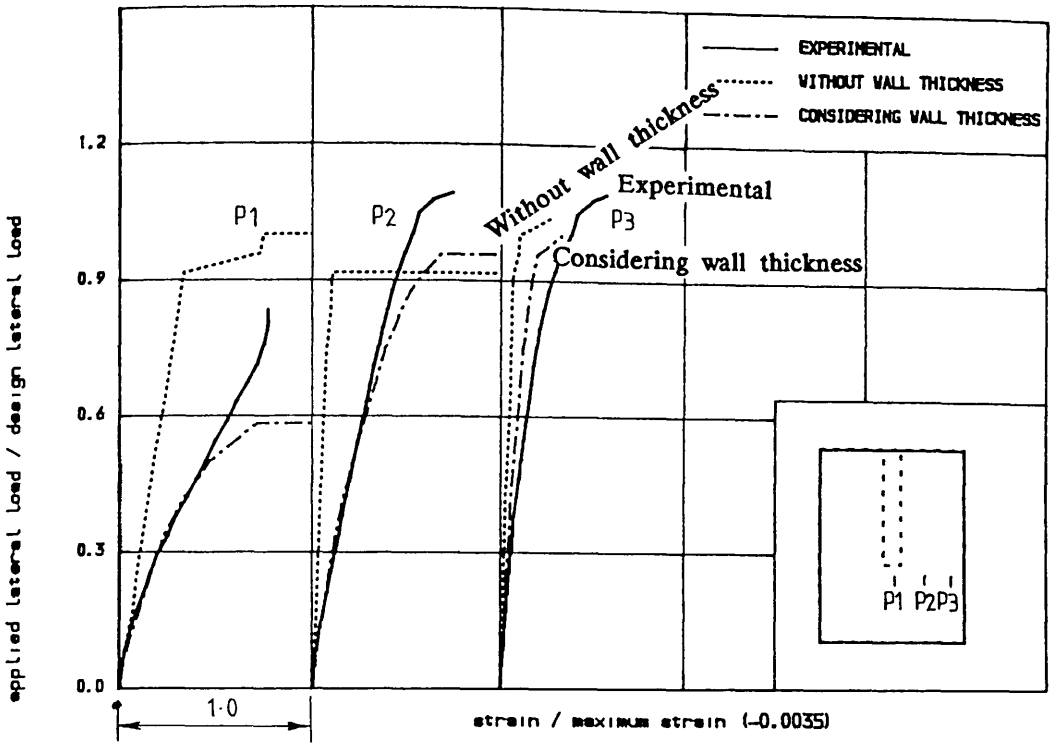

FIGURE (7.13) , EFFECT OF WALL THICKNESS ON COMPRESSIVE STRAIN IN CONCRETE IN WINDWARD DIRECTION IN THE SLAB OF MODEL MS7

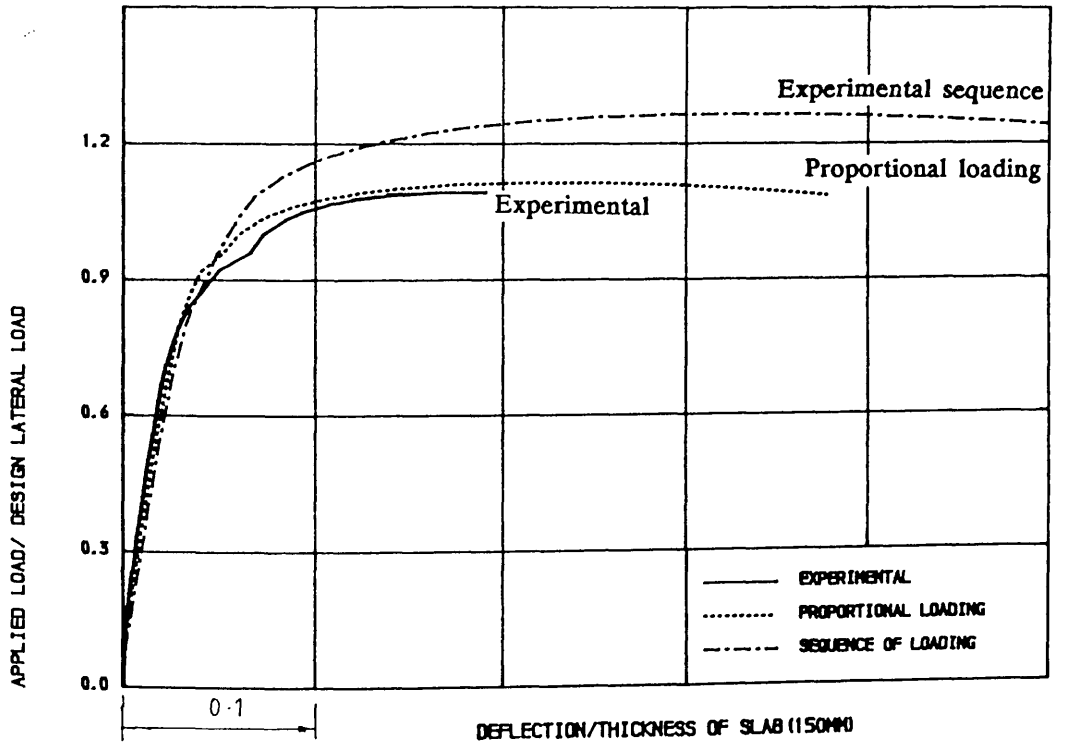

FIGURE (7.14) , EFFECT OF SEQUENCE OF GRAVITY AND LATERAL LOADING IN CONTRAST OF PROPORTIONAL LOADING ON LATERAL LOAD-DISPLACEMENT RELATIONS OF MODEL 'MS7'

thickness is included) shows that the ultimate load of the structure is slightly lower and the stiffness is slightly higher. The prediction of local behaviour is improved as is evident from strain readings in steel and concrete at the points around the wall. As far as computing cost is concerned, analysis with zero wall thickness is preferred because of very insignificant effect on the overall behaviour of the model when the wall thickness is considered.

To duplicate the loading process used in the experiment, the following scheme was followed.

In the first instance, the elastic distribution of the corresponding wind load along the line of contraflexure, required for the prescribed uniform displacement of 0.05 mm was obtained (See Figure 3.15). This distribution was assumed to remain unchanged in the nonlinear analysis. The wind load was thus load controlled. The gravity load was applied during the experiment in the first few increments during which no lateral load was applied. This sequence was duplicated in the theoretical analysis, incorporating the crack opening and closing facility in the programme. Gravity loads, which are applied on edge BDF in Figure (7.1), were assumed to be a uniformly distributed line load.

The sequence of gravity and lateral loading was not followed in the theoretical analysis reported in reference (24) and (44). Instead, proportional gravity and lateral loads were applied such that the ultimate gravity load was achieved together with the experimental lateral load at failure. That assumption did not greatly affect the overall behaviour of the models as evident from Figures (7.14) to (7.17). The failure load is slightly lower (around 5%) for proportional gravity and lateral loading. The local strain behaviour in concrete is improved at the tip of the wall, where early cracking usually occured, but may be closed at a later stage of loading. The sequence of loading in theoretical analysis has insignificant effect on tensile strain in steel upto the yield piont.

It was observed during the experiment that due to the presence of gravity

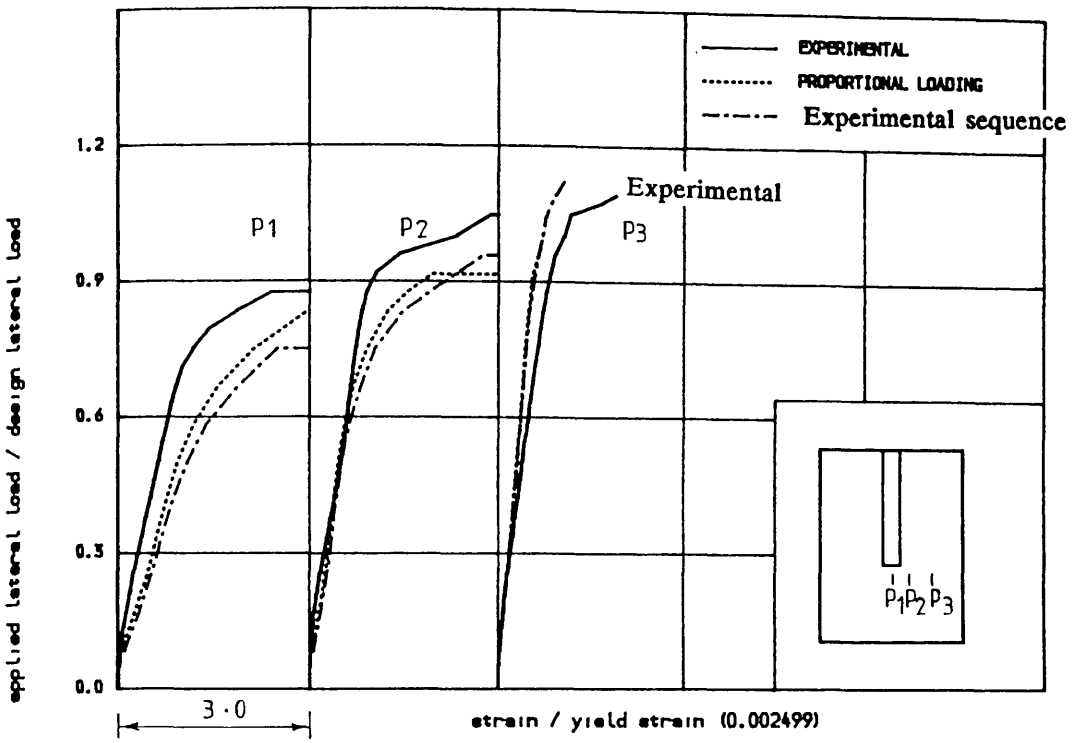

FIGURE (7.15) , EFFECT OF SEQUENCE OF GRAVITY AND LATERAL LOADING ON TENSILE STRAIN IN VINVVARD DIRECTION IN THE SLAB OF MODEL 'MS7'

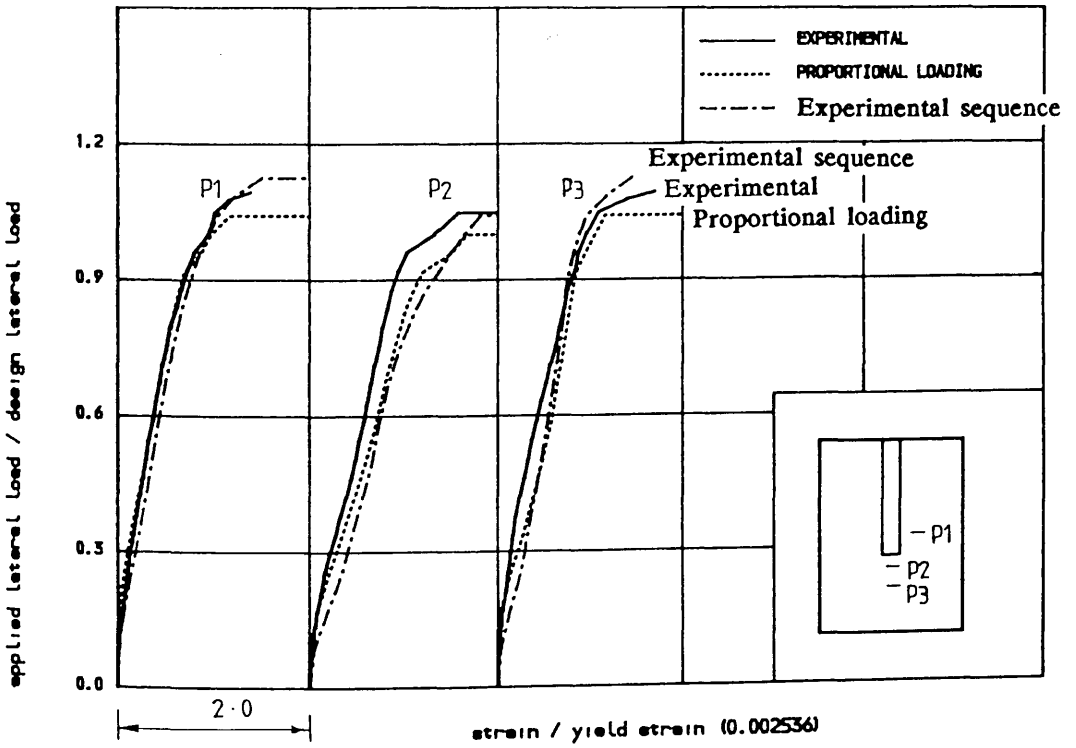

FIGURE (7.16) , EFFECT OF SEQUENCE OF LOADING (FULL GRAVITY LOAD FIRST AND THEN LATERAL LOADING) ON TENSILE STRAIN IN STEEL IN TRANSVERSE DIRECTION , MODEL MS7

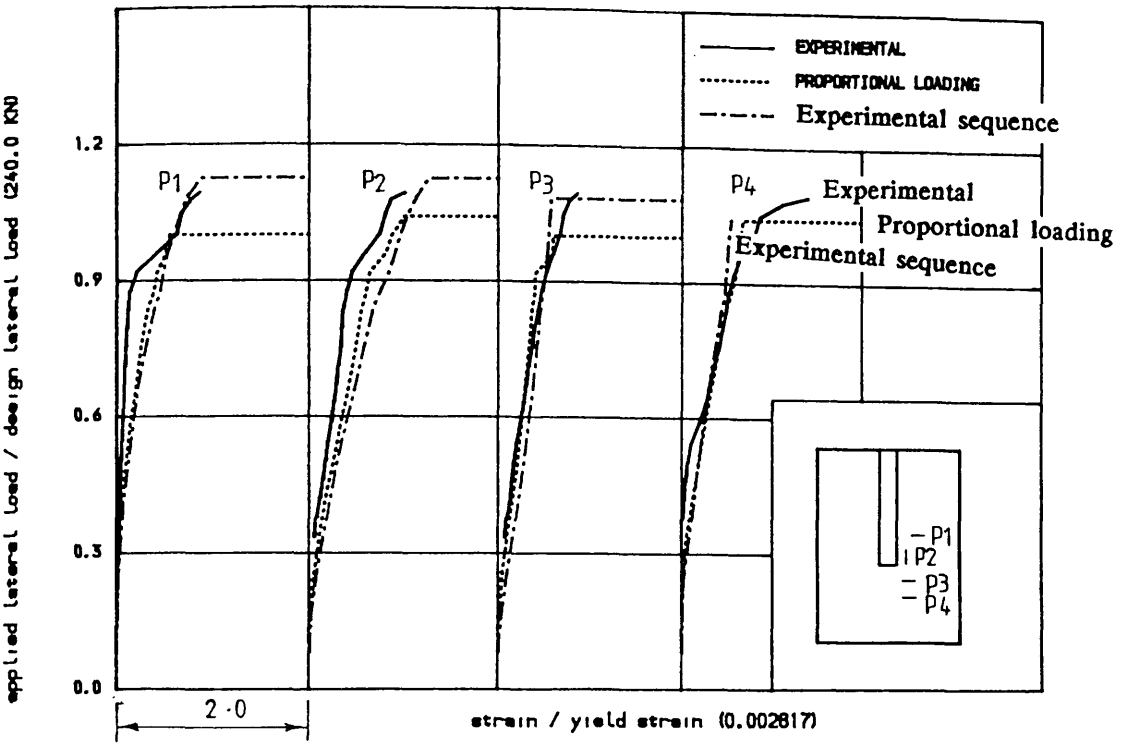

FIGURE (7.17-a) : EFFECT OF SEQUENCE OF LOADING ON TENSILE STRAIN IN CLOSED VERTICAL STIRUP IN THE SLAB OF MODEL MS7

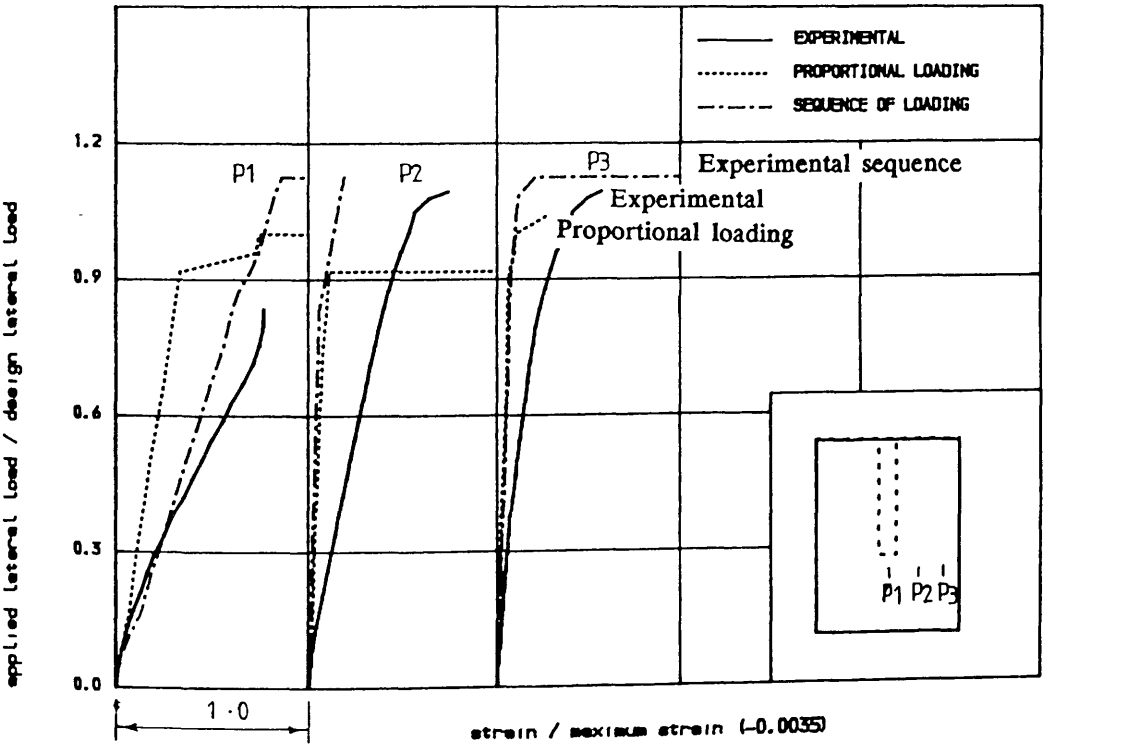

FIGURE (7.17-b) : EFFECT OF SEQUENCE OF LOADING ON COMPRESSIVE STRAIN IN CONCRETE IN LONGITUDINAL DIRECTION IN THE SLAB OF MODEL MS7

loads, the displacement of the line of contraflexure (central line of corridor opening) did not remain constant. The difference, however, was not large even for model MS8 for which the intensity of gravity load was the highest. For this model, the displacement at corner point F (Figure 7.1) was approximately 1.2 times that at central point E. Results from the theoretical analysis exhibited similar behaviour for all the models except for models of flanged width series, viz. MS10, MS11 and MS12. Near the theoretical ultimate load, the displacement at edge F was 1.4, 1.17 and 1.21 times that of central point E respectively.

7.4 Load Displacement Relationship

Curves comparing theoretical load–displacement relationship with their experimental counterpart for all the models are presented in Figures (7.18) to (7.23). In general it can be said that the load–deflection behaviour is predicted with reasonable accuracy, despite the fact that the predicted curves give slightly lower values of displacement than the experimental curve for the same applied load. This difference is considered insignificant because of the difficulties and scatter associated with reinforced concrete behaviour. The fixed crack analysis, used for this theoretical study, also shows a slightly stiffer load–deflection behaviour (see Figure (7.72)) than analysis assuming concrete as a No–tension material. The difference between the experimental and theoretical curves above 60% of design lateral load may be due to the following reasons:

(a) the nonlinear finite element theory does not take into consideration all the factors affecting reinforced concrete behaviour. Bond slip of reinforcement, for instance, is one of such factors; and it is believed that in the absence of bond slip effect, tensile strains in steel will be higher and deflections lower than what they should be when bond slip effect exists. As will be shown later in this chapter, theoretical tensile strains in steel do support this argument.

(b) Correction of experimental displacement at the line of contraflexure due to

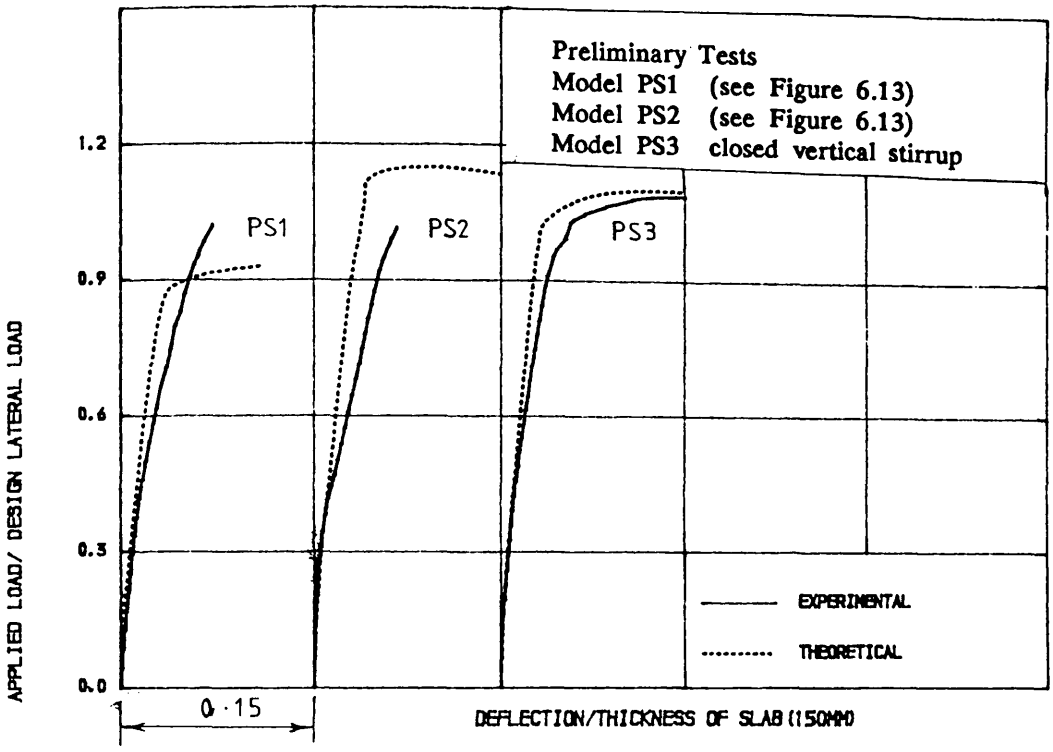

FIGURE (7.18) : LATERAL LOAD-DISPLACEMENT CURVES FOR MODELS OF PRELIMINARY SERIES TO STUDY THE EFFECT OF SHEAR STEEL

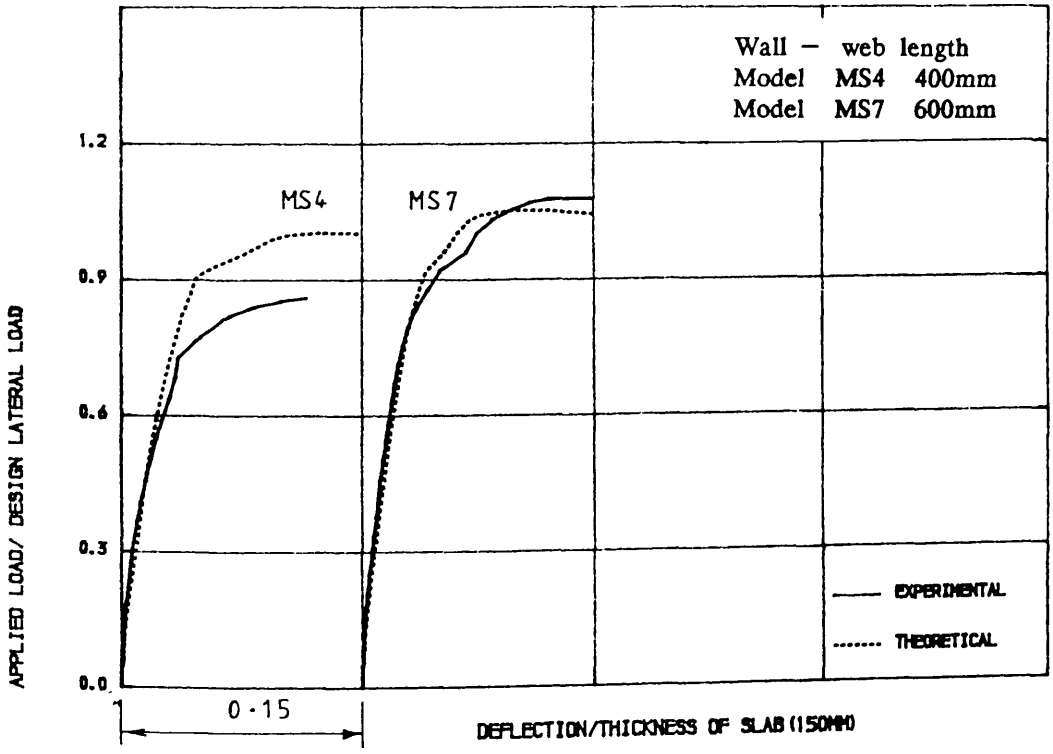

FIGURE (7.19) : LATERAL LOAD-DISPLACEMENT CURVES FOR THE MODELS TO STUDY THE EFFECT OF WALL WEB LENGTH

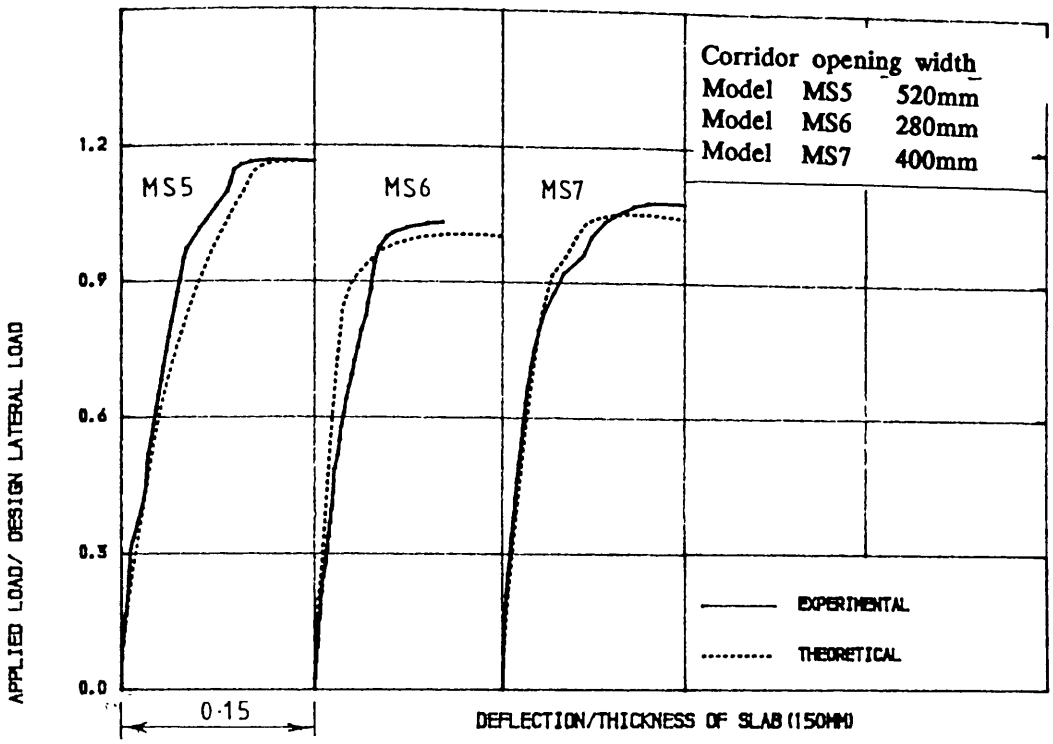

FIGURE (7.20) : LATERAL LOAD - DISPLACEMENT CURVES FOR THE MODELS TO STUDY

THE EFFECT OF CORRIDOR WIDTH

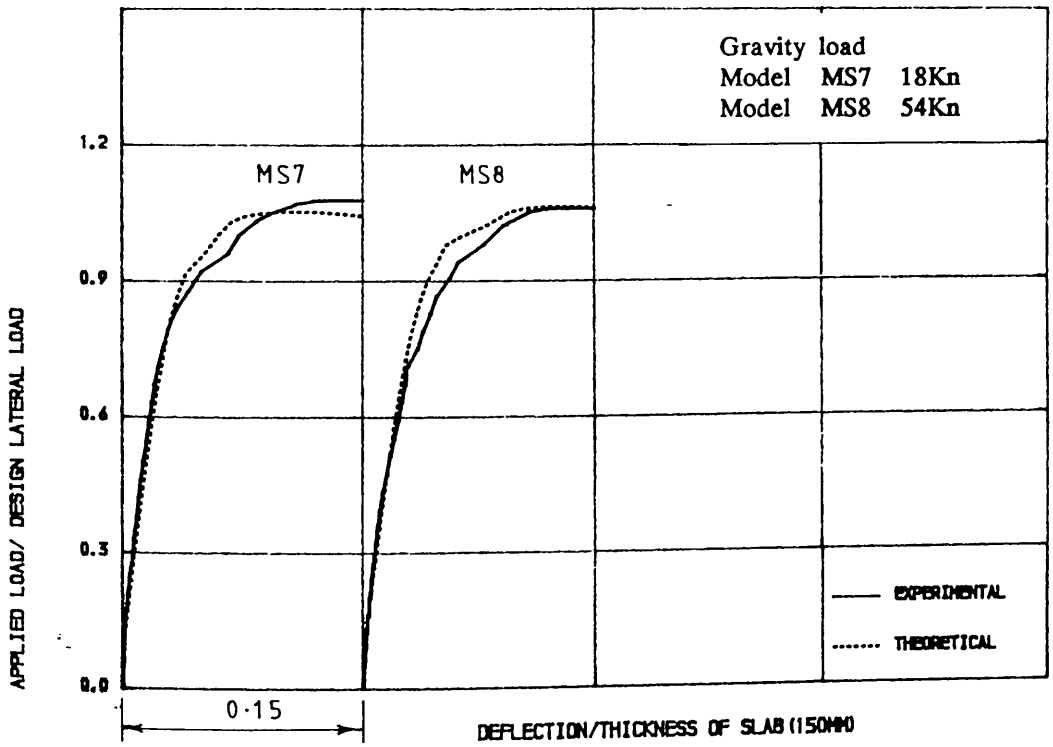

FIGURE (7.21) : LATERAL LOAD - DISPLACEMENT CURVES FOR MODELS TO STUDY

THE EFFECT OF GRAVITY LOAD

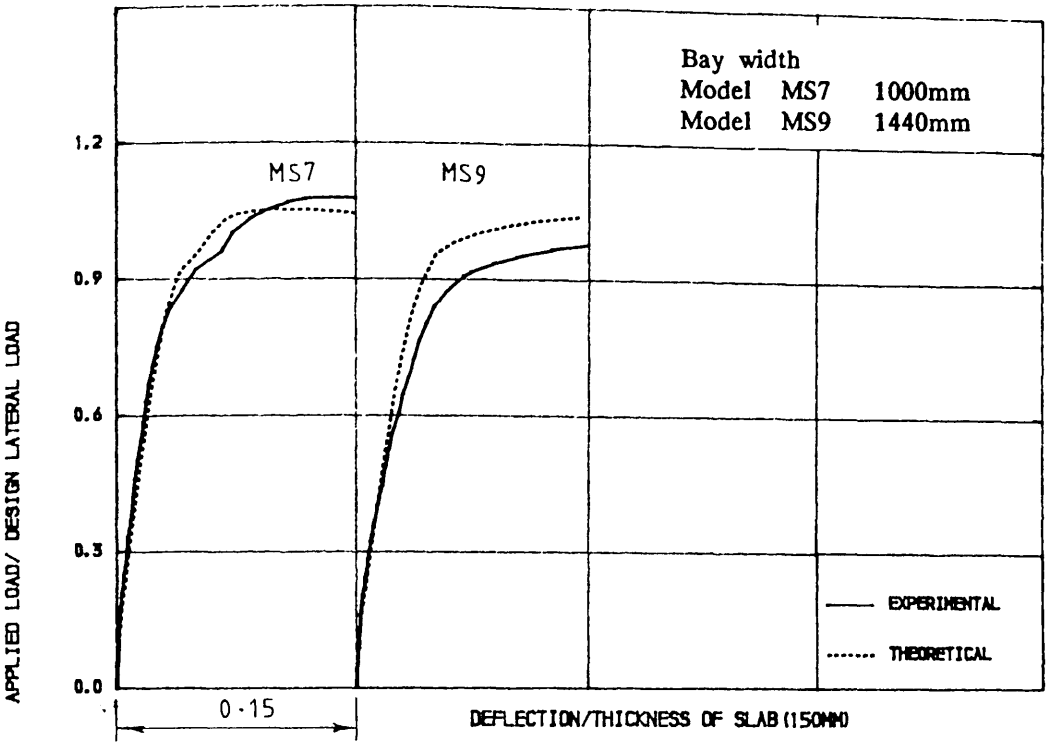

FIGURE (7.22) : LATERAL LOAD - DISPLACEMENT CURVES FOR THE MODELS TO STUDY THE EFFECT OF BAY WIDTH

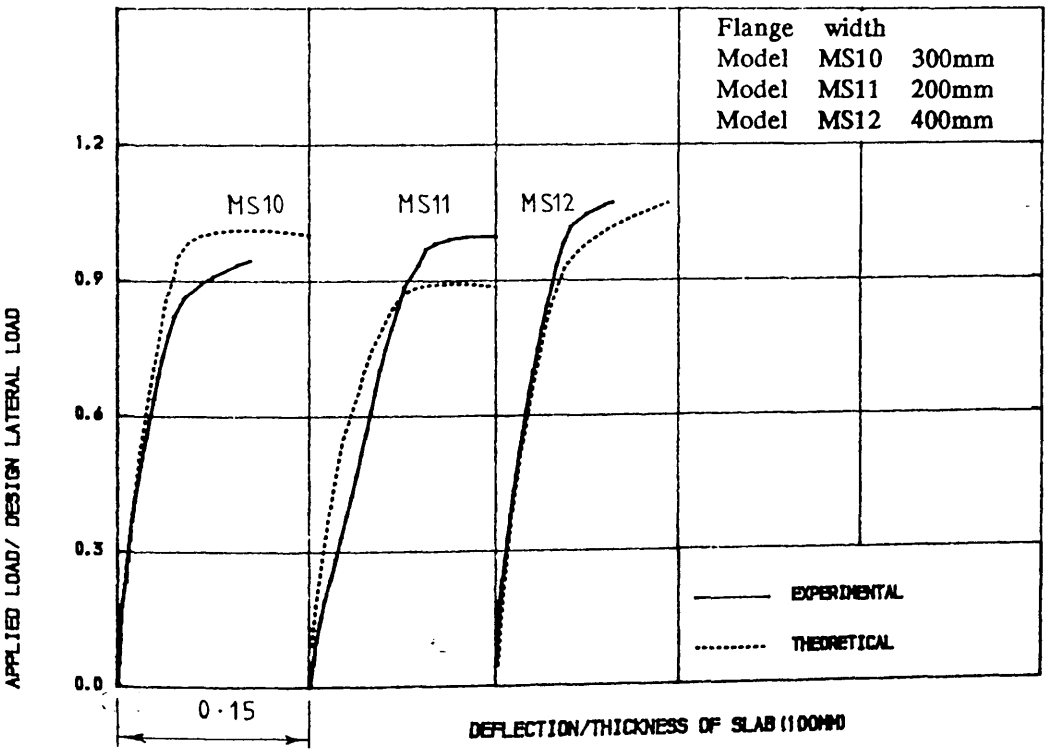

FIGURE (7.23) : LATERAL LOAD - DISPLACEMENT CURVES FOR THE MODELS TO STUDY THE EFFCT OF FLANGE WIDTH

wind loading against wall deformation was assumed to be linearly proportional to L_c (see Figure 6.9) but the variation of strain measured by the strain gauges attached to the wall was found not exactly linear. This may introduce some error in the experimental load–deflection curve.

7.5 Tensile Strain in Steel

Steel strain predictions are examined for both the longitudinal and transverse reinforcement. Care has been taken to choose the Gauss point for strain readings as near as possible to the location of strain gauges in the experiment. Strain in steel in the windward direction, (i.e., x–direction with reference to Figure (7.1)), is presented in Figures (7.24) to (7.35). In general, good agreement is shown at all points. In most of the models, theoretical strains show higher values than experimental one at position P_1 (at the tip of the wall). Very good agreement is found at point P_2 and recorded experimental strain shows slightly higher values than theoretical one at point P_3 (along the edge of the slab).

Theoretical strains in steel in transverse direction, i.e., Y–direction with reference to Figure (7.1), are compared with their experimental values in Figures (7.36) to (7.47) for all the models. The Figures indicate that there is no great inconsistency in the predictions.

The lateral load at which steel yielding was first observed in theoretical analysis is shown in table (7.1) for all the models tested under monotonic loading condition. The average theoretical load at first yield of steel in longitudinal direction for all the models of main test series is equal to 63% of design load with co–efficient of variation 0.12. This value is slightly lower than the average experimental load (66% of design load) at first yield of steel in windward direction. For the models MS4 to MS9 with plane shear walls, the theoretical average load at first yield of steel is 55% of design load (S.D. = 0.03) which is lower than the serviceability limit load (0.625 x design load). The mean ratio of

Table (7.1) : Comparative study of theoretical and experimental lateral load at which steel yielding was first observed, $V_{L.Y}$ as a ratio of the design lateral load, V_{design}

Model	V_{design}	$\frac{V_{L.Y}}{V_{design}}$					
		Longitudinal steel			Transverse steel		
		Experimental	Theoretical	EXP / THEO	Experimental	Theoretical	EXP / THEO
PS1	215.0	0.85	0.750	1.13	-	-	-
PS2	150.0	0.86	0.81	1.06	0.95	1.06	0.90
PS3	155.0	0.72	0.78	0.92	0.94	0.90	1.04
MS4	220.0	0.63	0.58	1.10	0.80	0.92	0.86
MS5	155.0	0.74	0.57	1.30	1.12	0.97	1.15
MS6	330.0	0.55	0.53	1.05	0.78	0.83	0.94
MS7	240.0	0.71	0.57	1.25	0.95	0.84	1.13
MS8	255.0	0.64	0.55	1.16	0.79	0.76	1.04
MS9	250.0	0.41	0.50	0.80	0.65	0.73	0.89
MS10	220.0	0.74	0.86	0.86	0.93	0.87	1.07
MS11	215.0	0.71	0.68	1.04	0.85	0.75	1.14
MS12	215.0	0.79	0.79	1.00	1.08	0.82	1.31
	mean =	0.69	0.66	1.05	0.89	0.86	1.04
	S.D. =	0.12	0.12	0.14	0.13	0.10	0.13

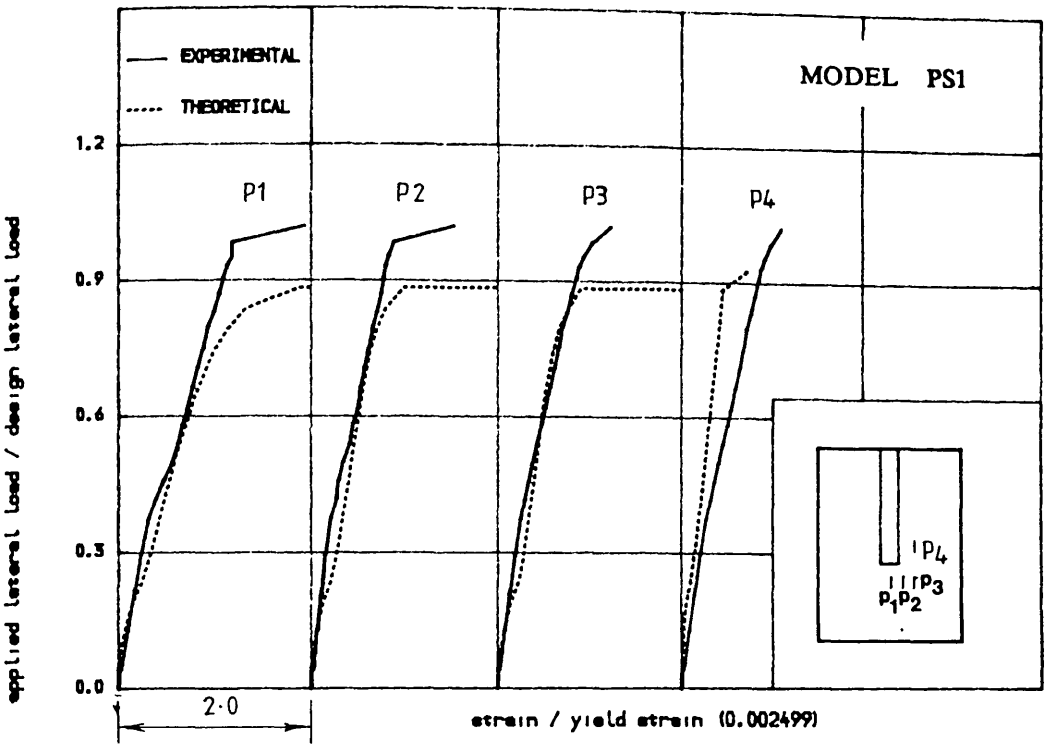

FIGURE (7.24) , TENSILE STRAIN IN STEEL IN VINDVARD DIRECTION ALONG TRANSVERSE SECTION IN THE SLAB OF MODEL PS1

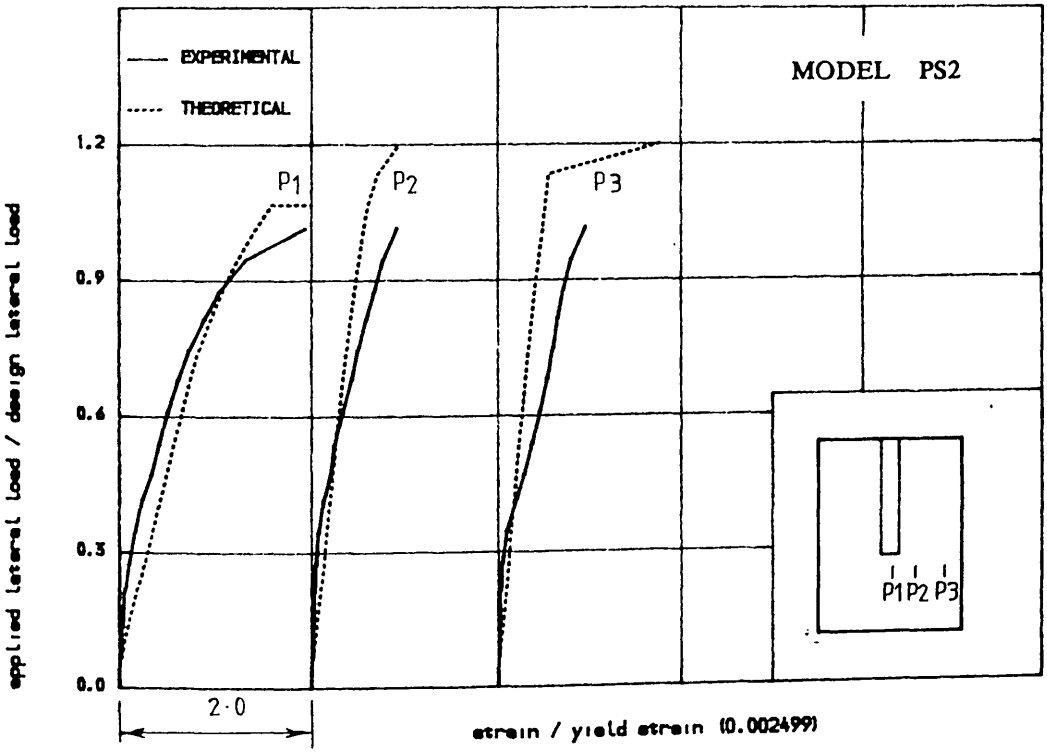

FIGURE (7.25) , TENSILE STRAIN IN STEEL IN VINDVARD DIRECTION ALONG TRANSVERSE SECTION IN THE SLAB OF MODEL PS2

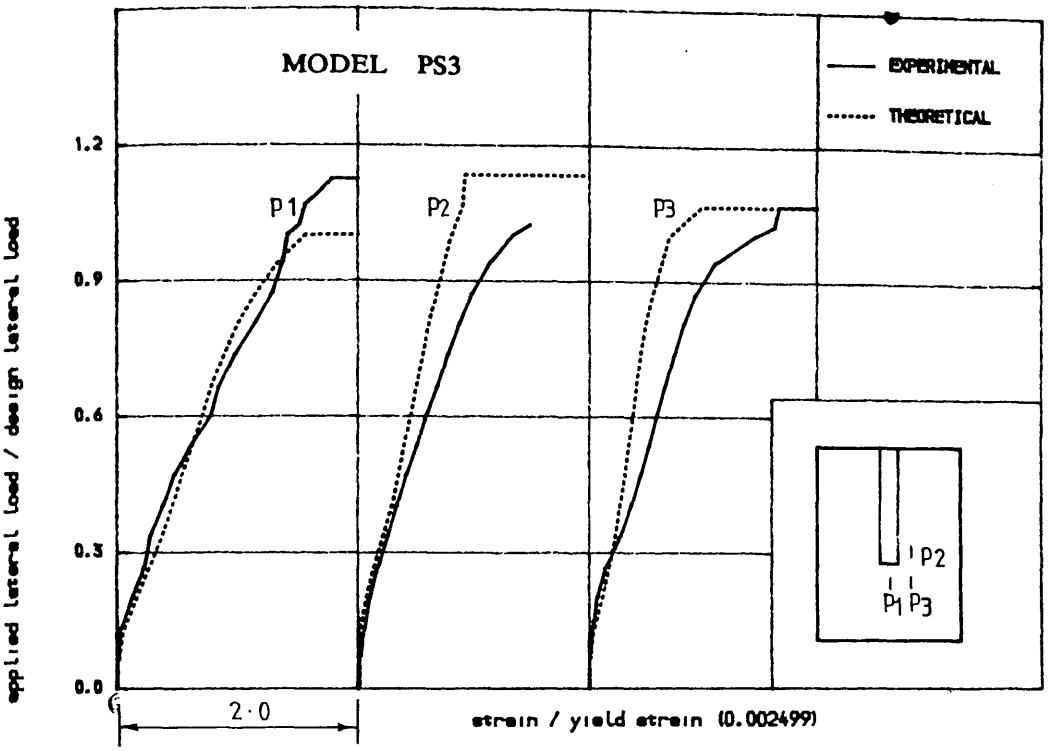

FIGURE (7.26) , TENSILE STRAIN IN STEEL IN VINDVARD DIRECTION ALONG TRANSVERSE SECTION IN THE SLAB OF MODEL PS3

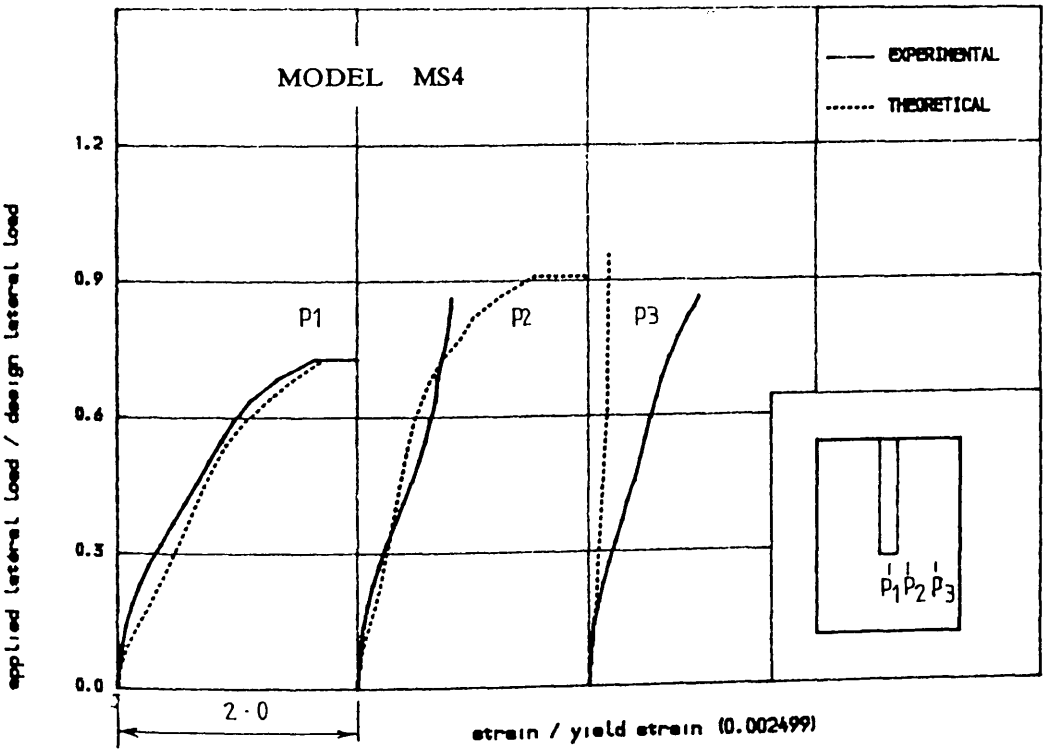

FIGURE (7.27) , TENSILE STRAIN IN STEEL IN VINDVARD DIRECTION ALONG TRANSVERSE SECTION IN THE SLAB OF MODEL MS4

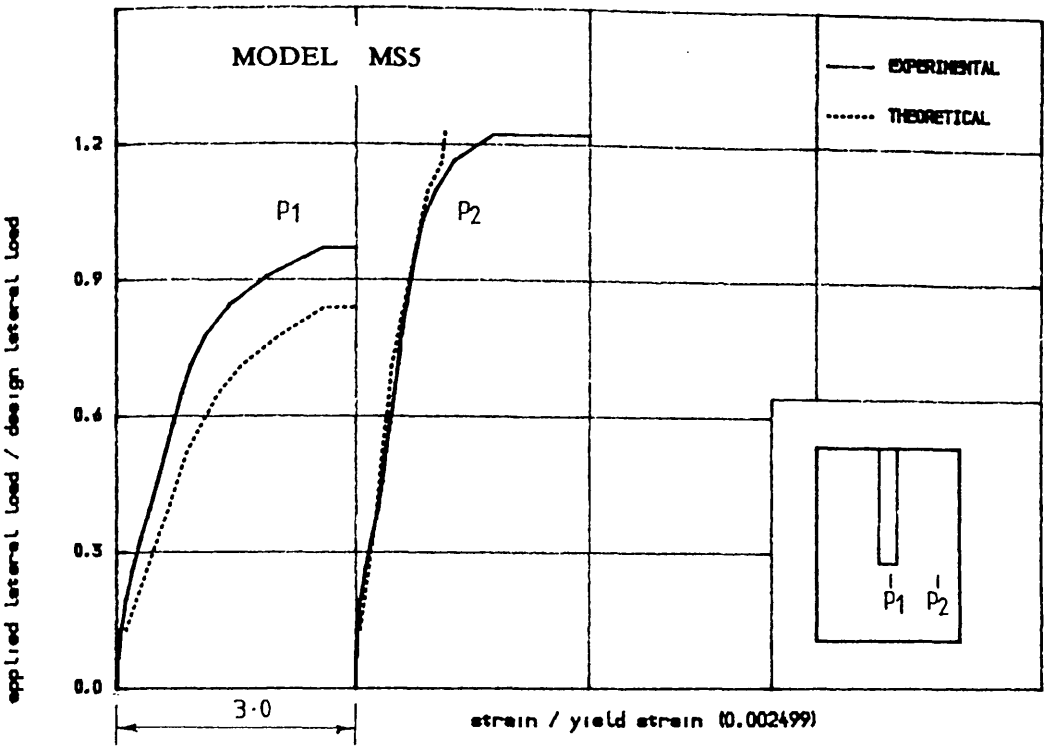

FIGURE (7.28) : TENSILE STRAIN IN STEEL IN WINDWARD DIRECTION ALONG TRANSVERSE SECTION IN THE SLAB OF MODEL MS5

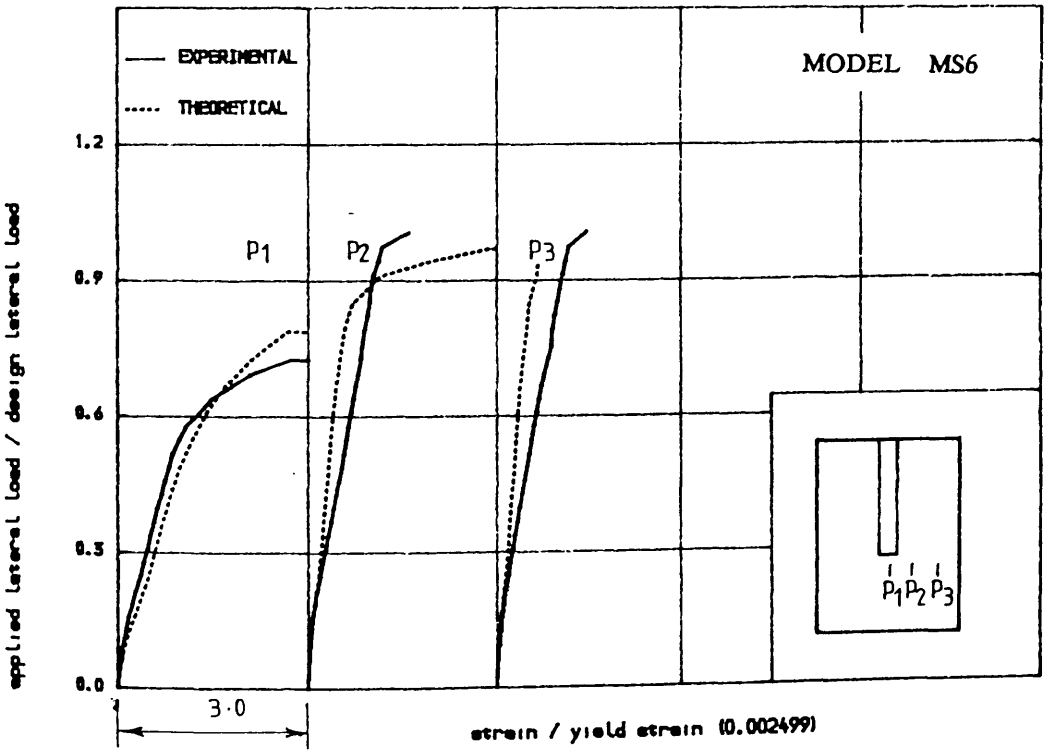

FIGURE (7.29) : TENSILE STRAIN IN STEEL IN WINDWARD DIRECTION ALONG TRANSVERSE SECTION IN THE SLAB OF MODEL MS6

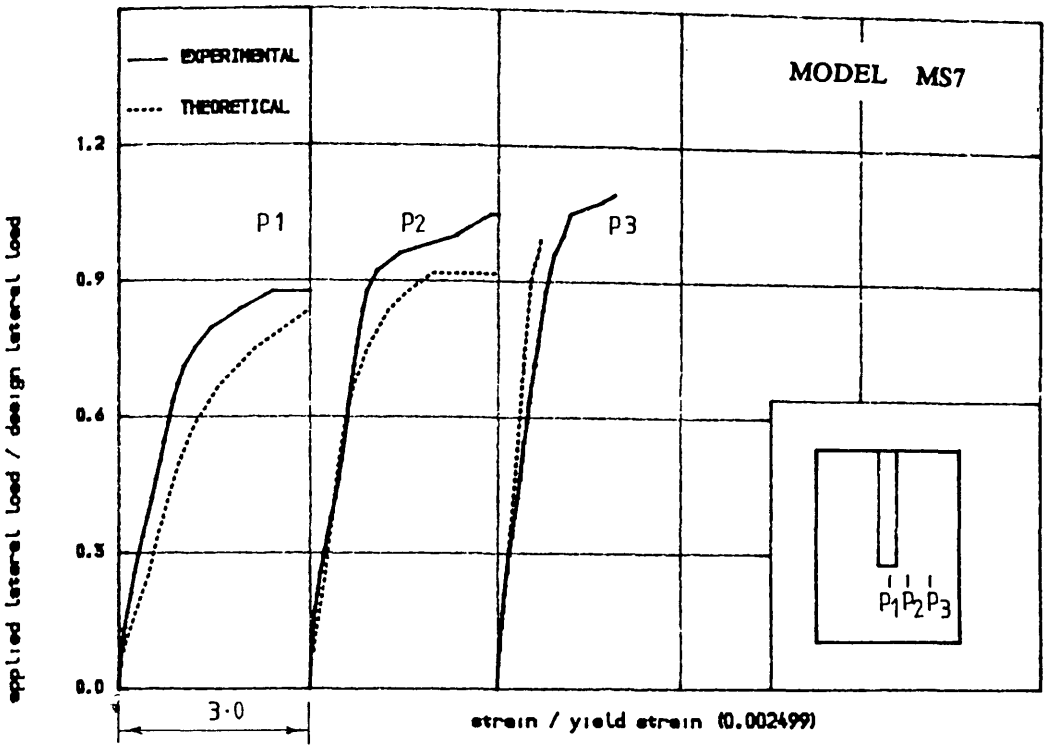

FIGURE (7.30) . TENSILE STRAIN IN STEEL IN WINDWARD DIRECTION ALONG TRANSVERSE SECTION IN THE SLAB OF MODEL MS7

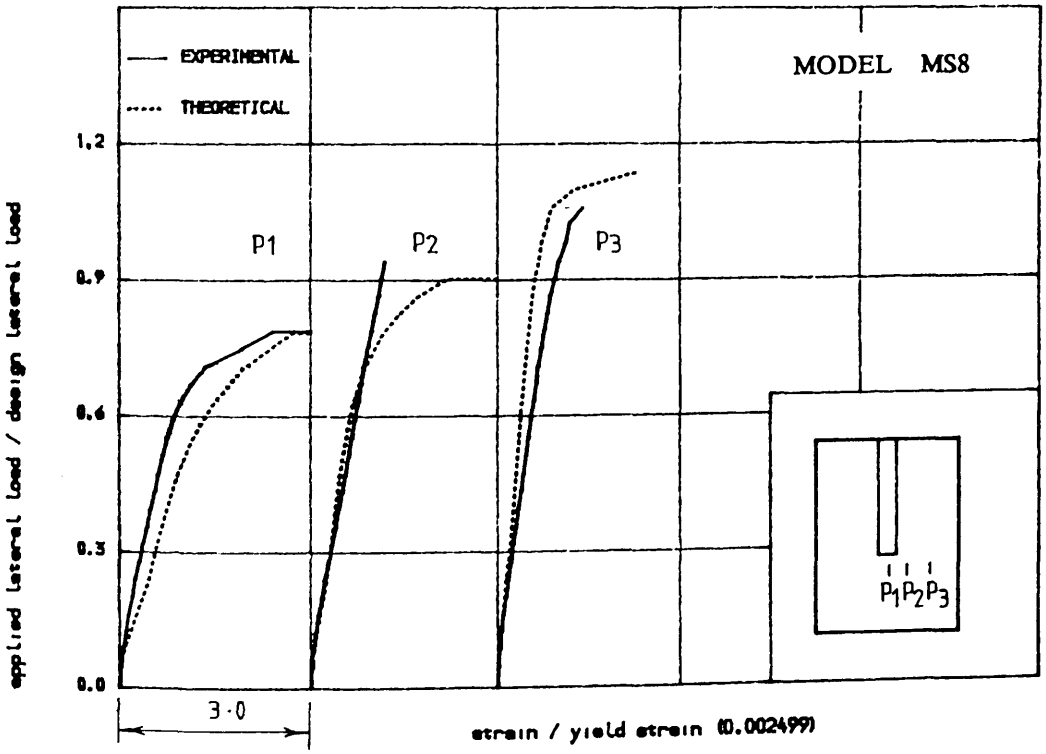

FIGURE (7.31) . TENSILE STRAIN IN STEEL IN WINDWARD DIRECTION ALONG TRANSVERSE SECTION IN THE SLAB OF MODEL MS8

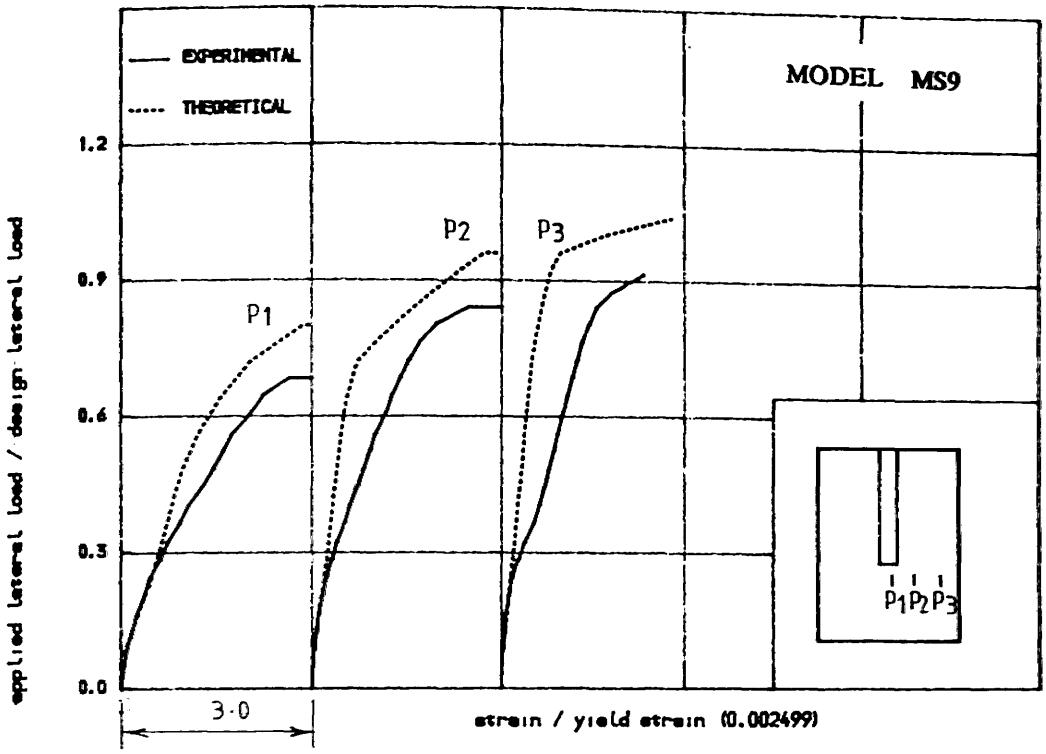

FIGURE (7.32) : TENSILE STRAIN IN STEEL IN VINDVARD DIRECTION ALONG TRANSVERSE SECTION IN THE SLAB OF MODEL MS9

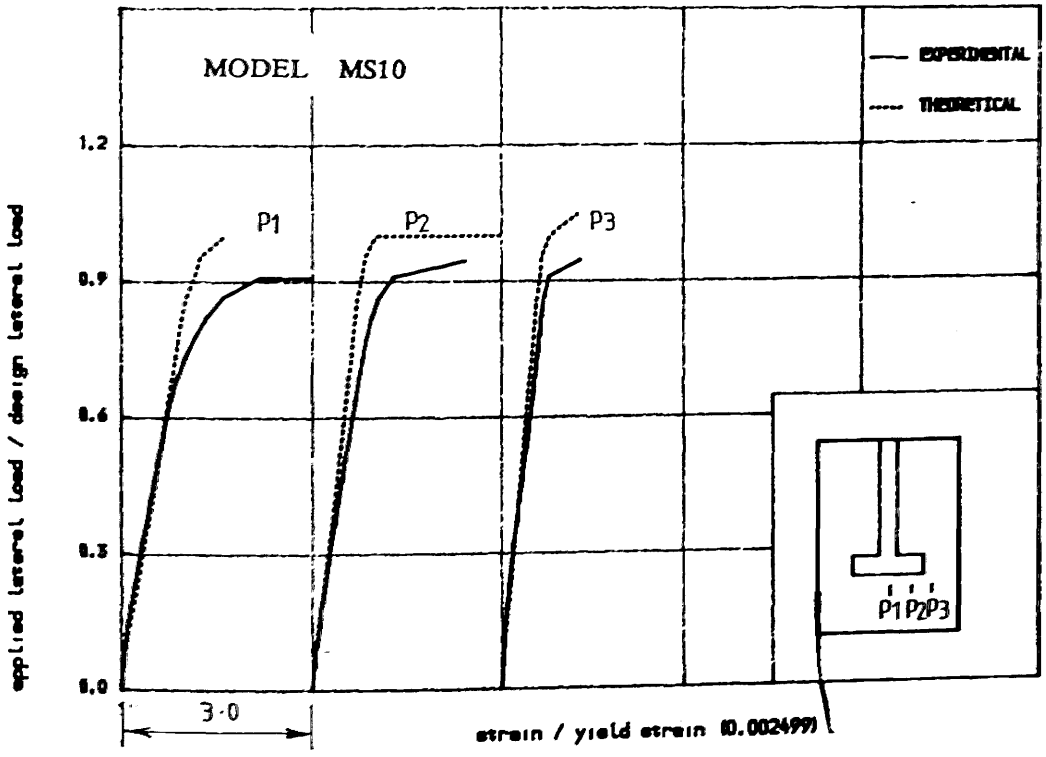

FIGURE (7.33) : TENSILE STRAIN IN STEEL IN VINDVARD DIRECTION ALONG TRANSVERSE SECTION IN THE SLAB OF MODEL MS10

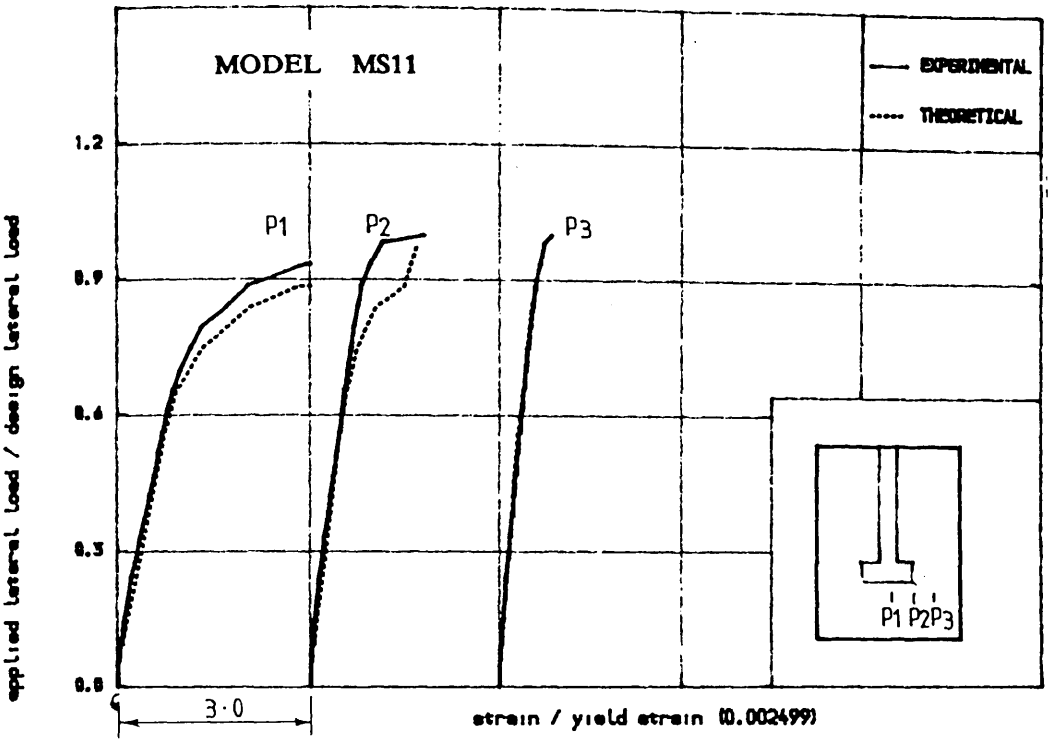

FIGURE (7.34) : TENSILE STRAIN IN STEEL IN WINDWARD DIRECTION ALONG TRANSVERSE SECTION IN THE SLAB OF MODEL MS11

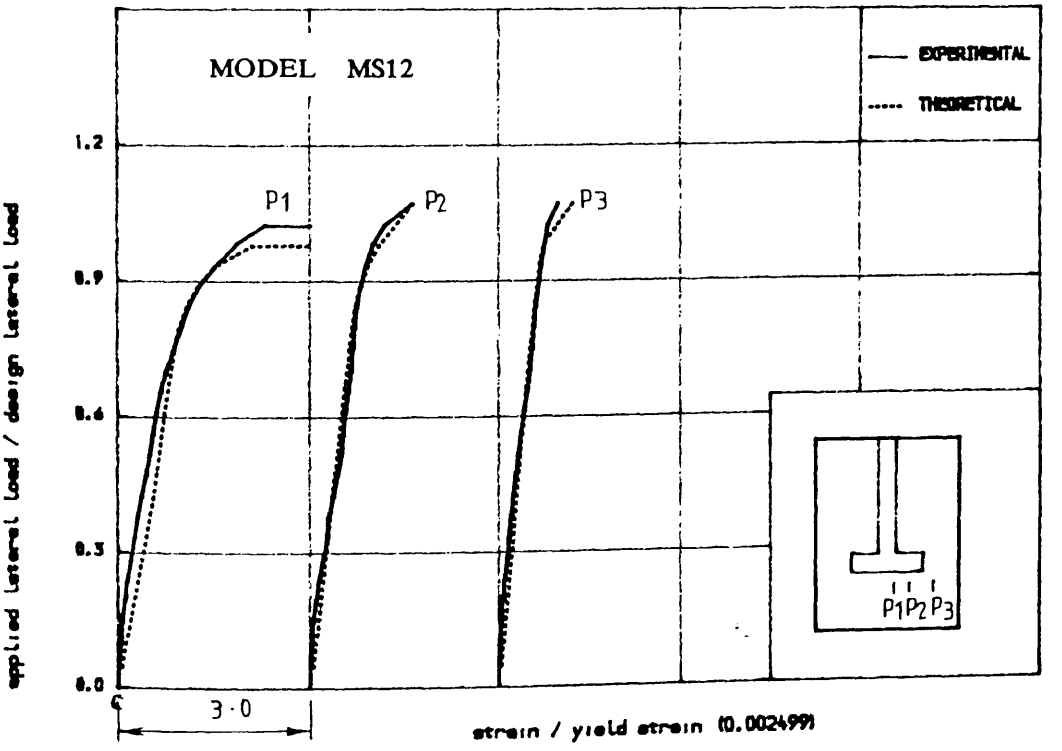

FIGURE (7.35) : TENSILE STRAIN IN STEEL IN WINDWARD DIRECTION ALONG TRANSVERSE SECTION IN THE SLAB OF MODEL MS12

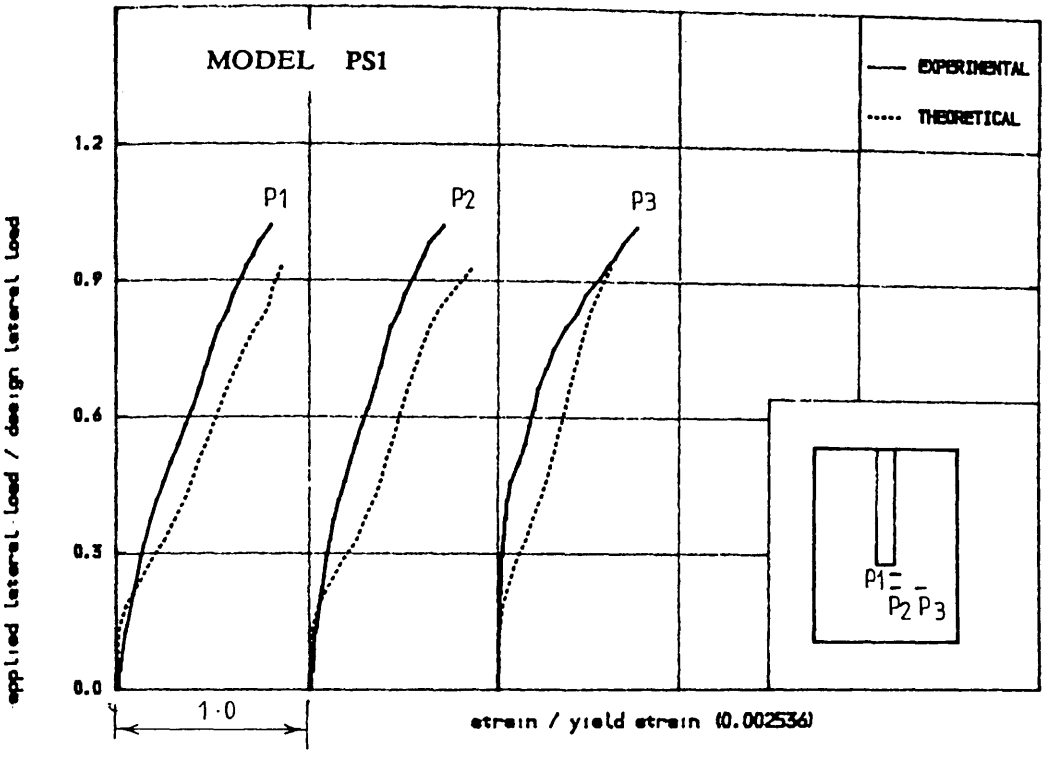

FIGURE (7.36) , TENSILE STRAIN IN STEEL IN TRANSVERSE DIRECTION IN THE SLAB OF MODEL PS1

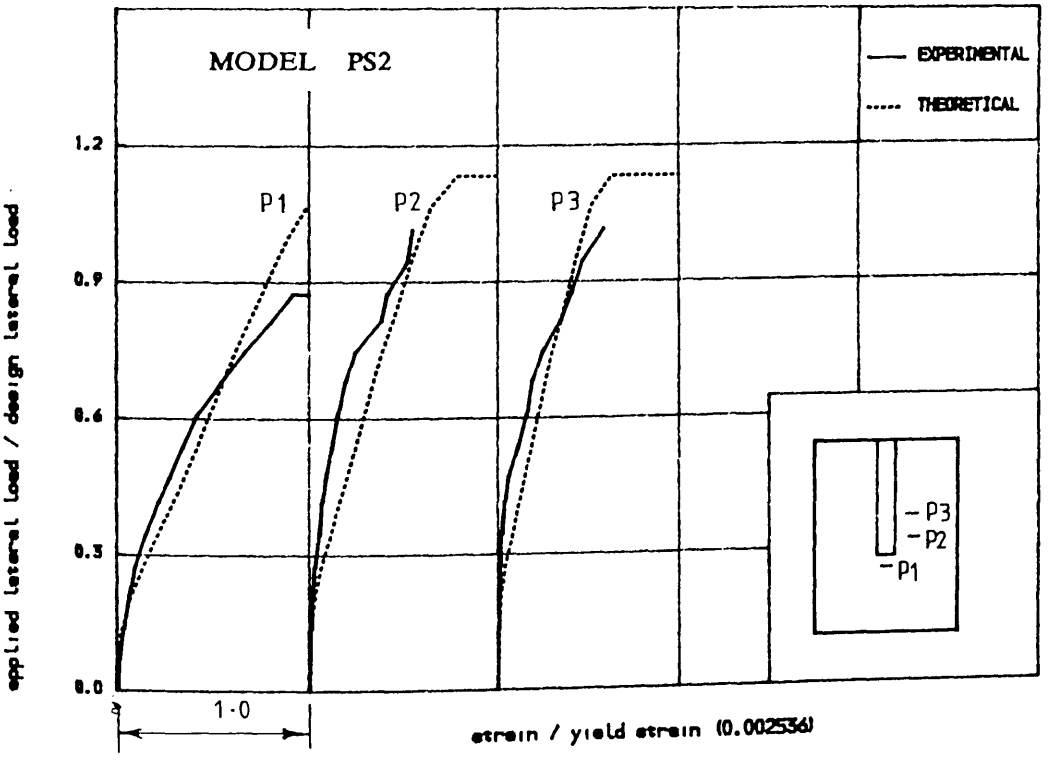

FIGURE (7.37) , TENSILE STRAIN IN STEEL IN TRANSVERSE DIRECTION IN THE SLAB OF MODEL PS2

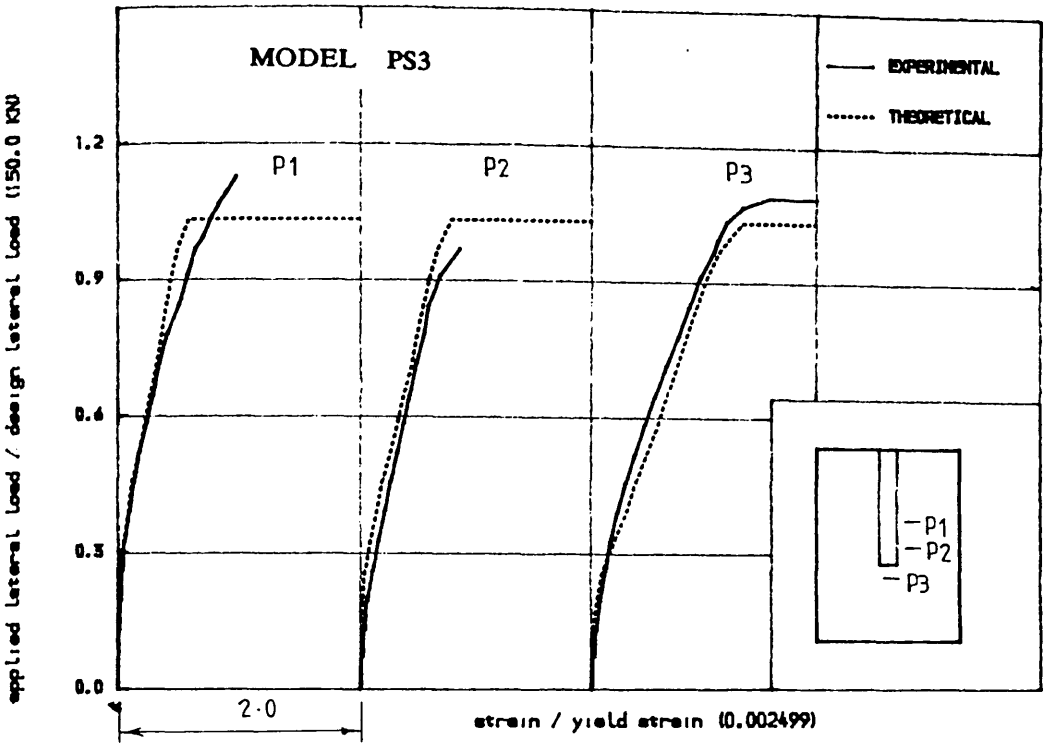

FIGURE (7.38) . TENSILE STRAIN IN STEEL IN TRANSVERSE DIRECTION ALONG VINDVARD SECTION IN THE SLAB OF MODEL PS3

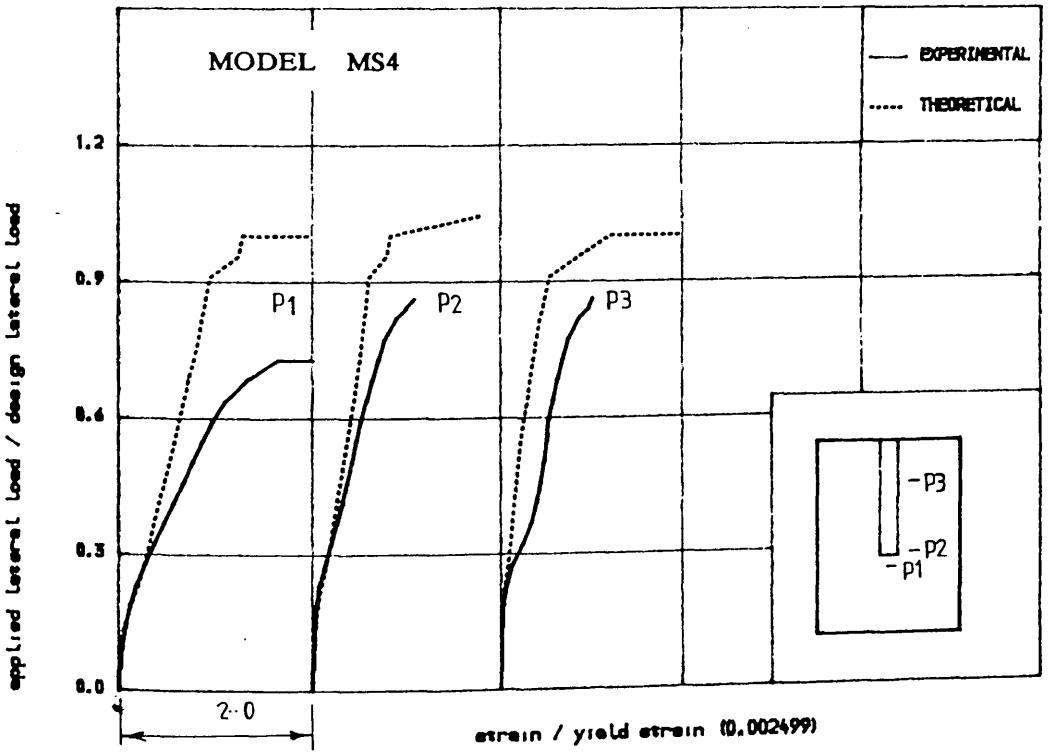

FIGURE (7.39) . TENSILE STRAIN IN STEEL IN TRANSVERSE DIRECTION ALONG VINDVARD SECTION IN THE SLAB OF MODEL MS4

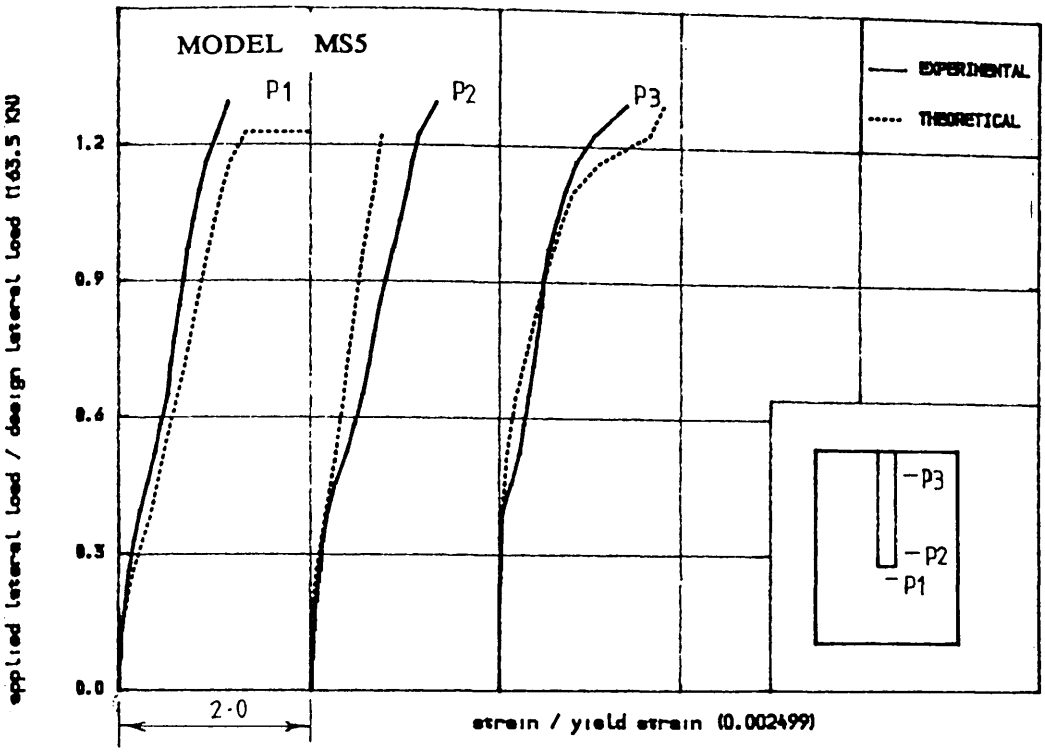

FIGURE (7.40) , TENSILE STRAIN IN STEEL IN TRANSVERSE DIRECTION ALONG VINDVARD SECTION IN THE SLAB OF MODEL MS5

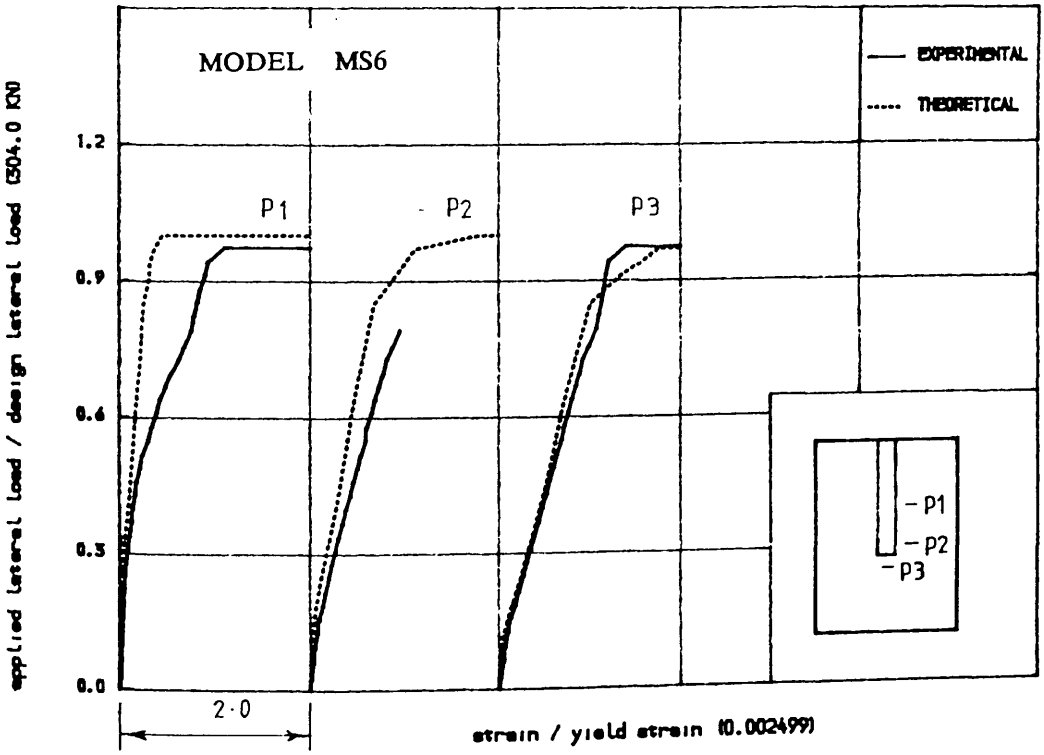

FIGURE (7.41) , TENSILE STRAIN IN STEEL IN TRANSVERSE DIRECTION ALONG VINDVARD SECTION IN THE SLAB OF MODEL MS6

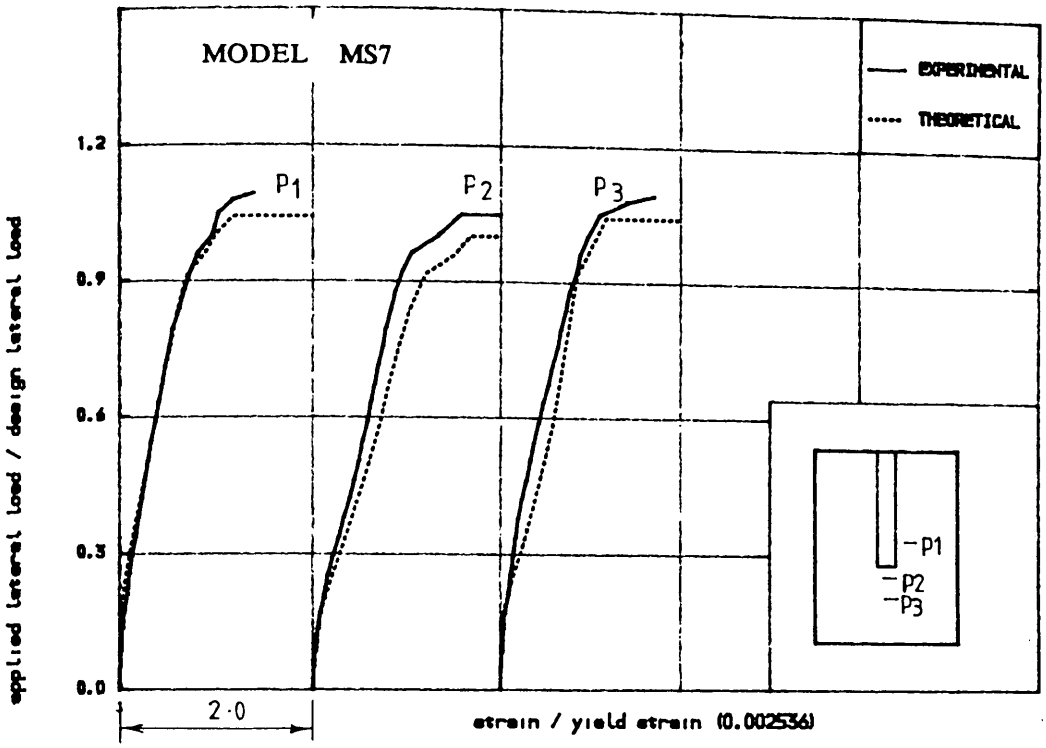

FIGURE (7.42) : TENSILE STRAIN IN STEEL IN TRANSVERSE DIRECTION IN THE SLAB OF MODEL MS7

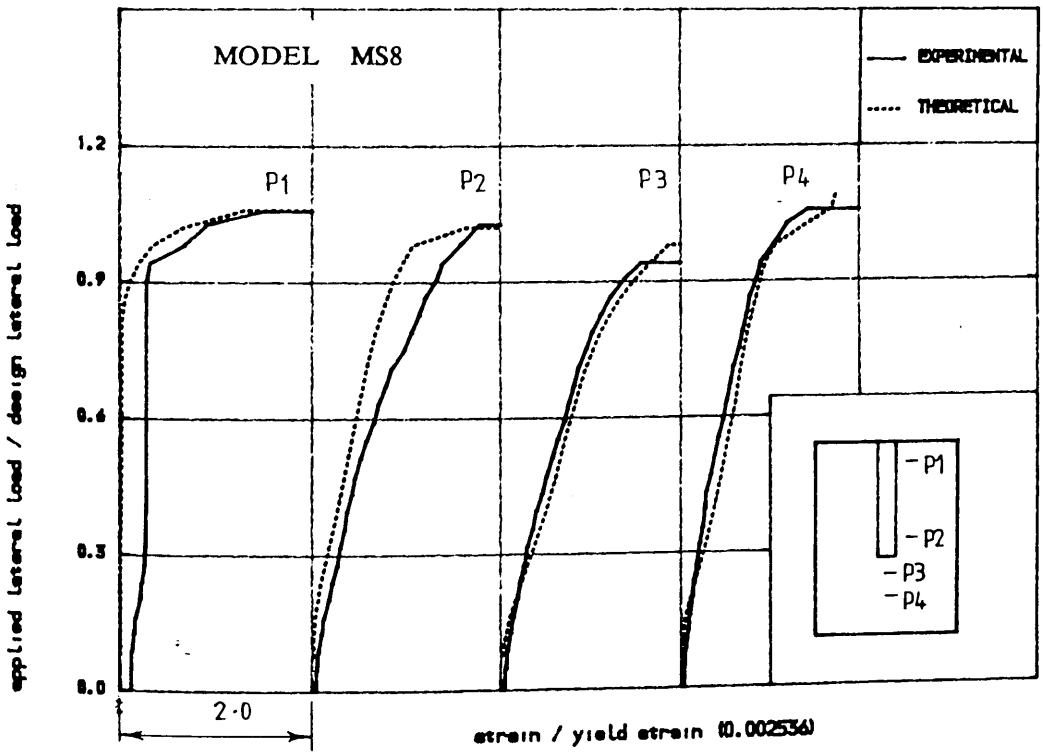

FIGURE (7.44) : TENSILE STRAIN IN STEEL IN TRANSVERSE DIRECTION IN THE SLAB OF MODEL MS8

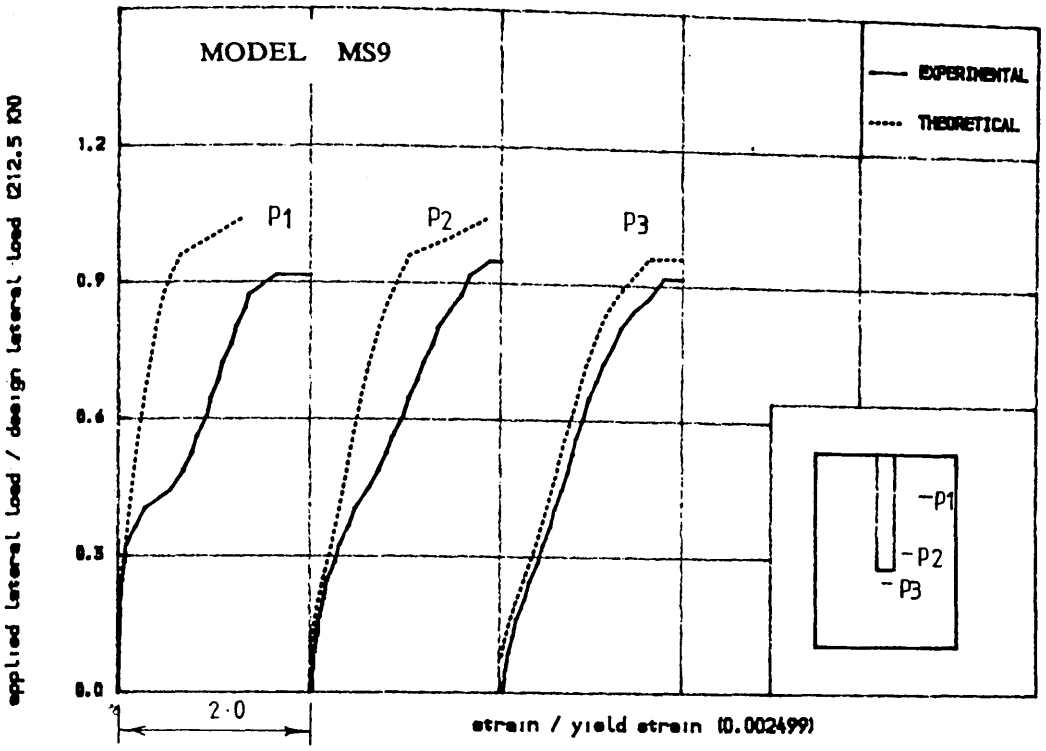

FIGURE (7.44) , TENSILE STRAIN IN STEEL IN TRANSVERSE DIRECTION ALONG VINDWARD SECTION IN THE SLAB OF MODEL MS9

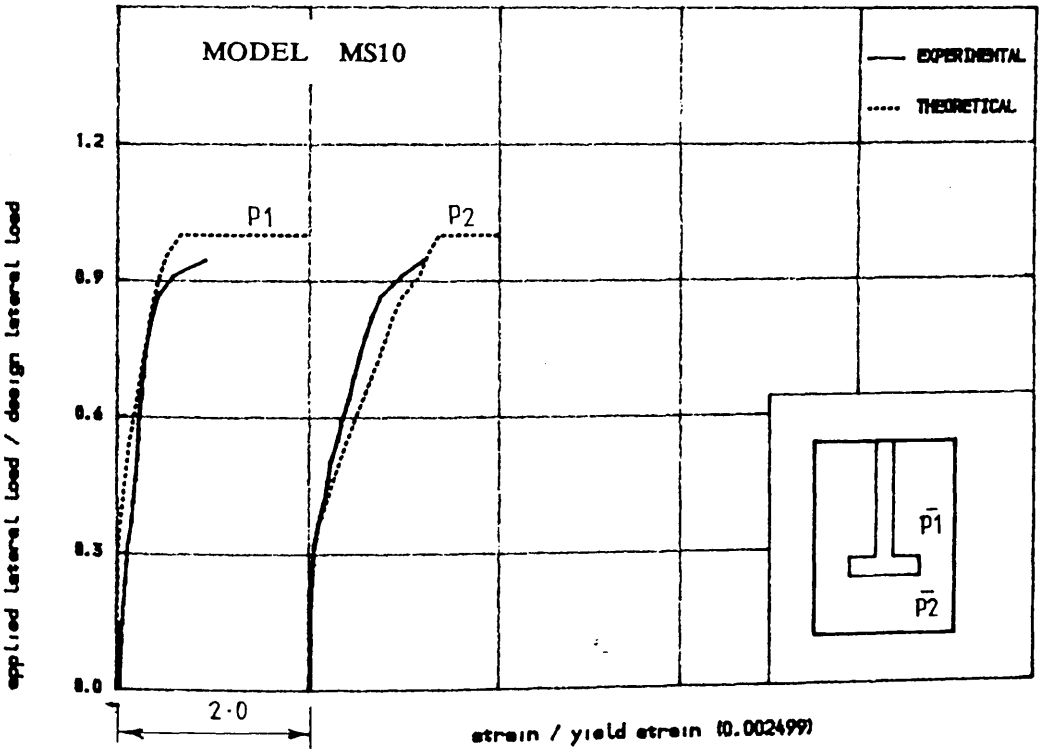

FIGURE (7.45) , TENSILE STRAIN IN STEEL IN TRANSVERSE DIRECTION ALONG VINDWARD SECTION IN THE SLAB OF MODEL MS10

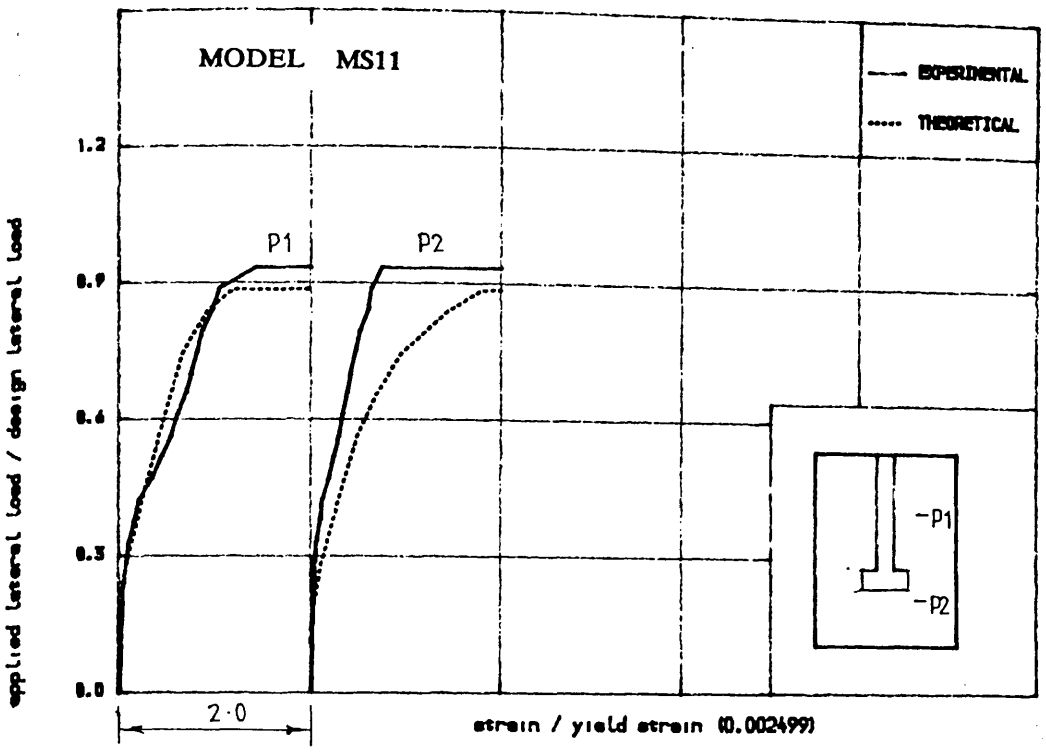

FIGURE (7.46) : TENSILE STRAIN IN STEEL IN TRANSVERSE DIRECTION ALONG VINDVARD SECTION IN THE SLAB OF MODEL MS11

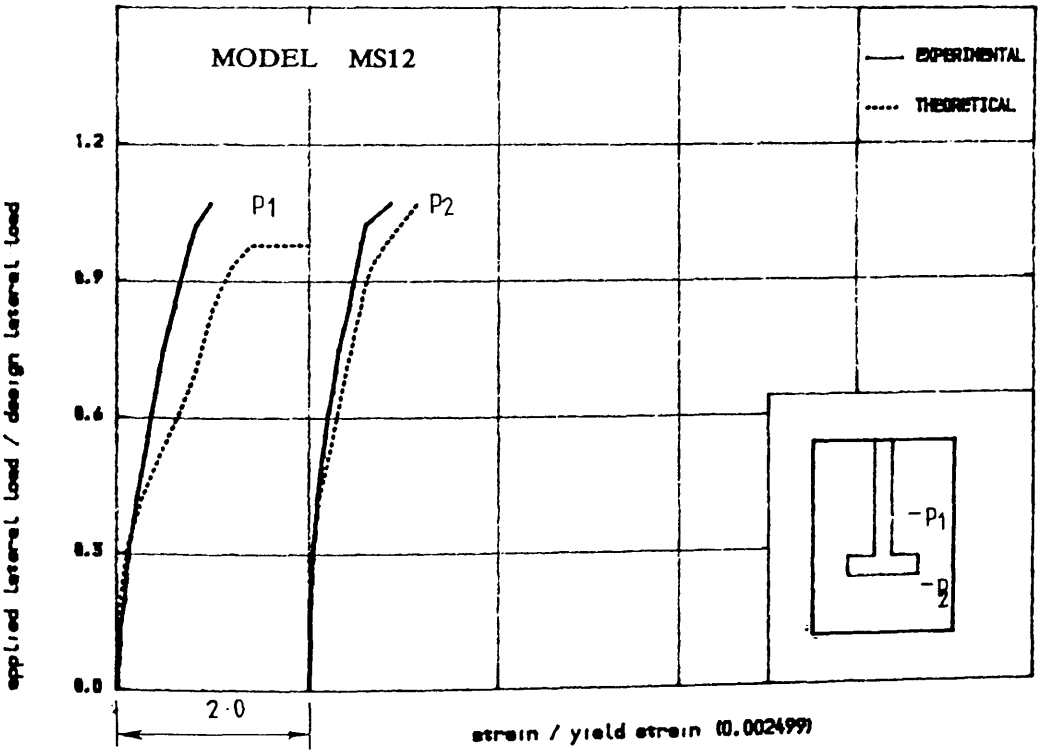

FIGURE (7.47) : TENSILE STRAIN IN STEEL IN TRANSVERSE DIRECTION ALONG VINDVARD SECTION IN THE SLAB OF MODEL MS12

the experimental to the theoretical ($V_{L.y}/V_{design}$) is 1.05 with standard deviation 0.14 for longitudinal steel bars. For transverse steel bars, the mean ratio is 1.045 with co-efficient of variation equals to 0.13.

Figures (7.48) to (7.58) show the comparison of steel strains for closed vertical stirrups for some of the models. Overall the agreement is reasonable.

In some of the Figures, the experimental strain in steel is not shown near the ultimate failure load of the model (see curve for point P2 in Figure 7.31). This was because the strain gauge was damaged. On the other hand, some of the curves (both theoretical and experimental in Figure (7.30)) were intentionally stopped to avoid overlapping when it reached the limit of next vertical line, instead of continuing up to the ultimate failure load.

7.6 Compressive Strain in Concrete

Theoretical compressive strains in concrete in the windward direction are compared with their experimental counterparts in Figures (7.59) to (7.67). These theoretical strains are measured at sampling points located in the compressive side of the slab but at a small distance away from the extreme compressive fibre (in the case of 150 mm slab thickness, this distance was 17 mm) as illustrated in Figure (7.68). But as mentioned in chapter five, strain gauges in the experiments were fixed on the extreme compressive fibre of the slab. Therefore it was expected that the value of such experimental compressive strain measured at the surface will be slightly higher than its theoretical counterpart. This is clear in most of the curves presented in Figures (7.59) to (7.67).

The theoretical values at the extreme fibre of the slab were extrapolated from the three strain values along the depth of the slab, assuming parabolic variation of strain. Figures (7.69) to (7.71) show the comparison between experimental, theoretical and extrapolated strain values. This shows that the proposed finite element analysis predict the compressive strain satisfactorily.

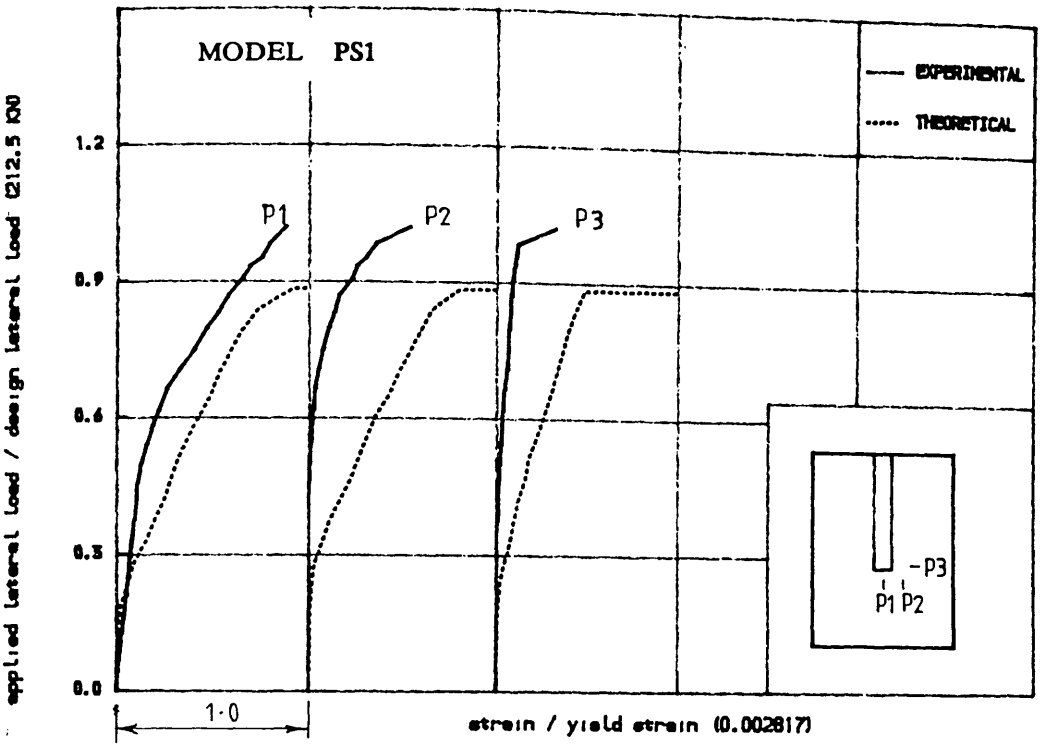

FIGURE (7.48) : STRAIN IN SHEAR STEEL AT DIFFERENT LOCATIONS IN THE SLAB OF MODEL PS1

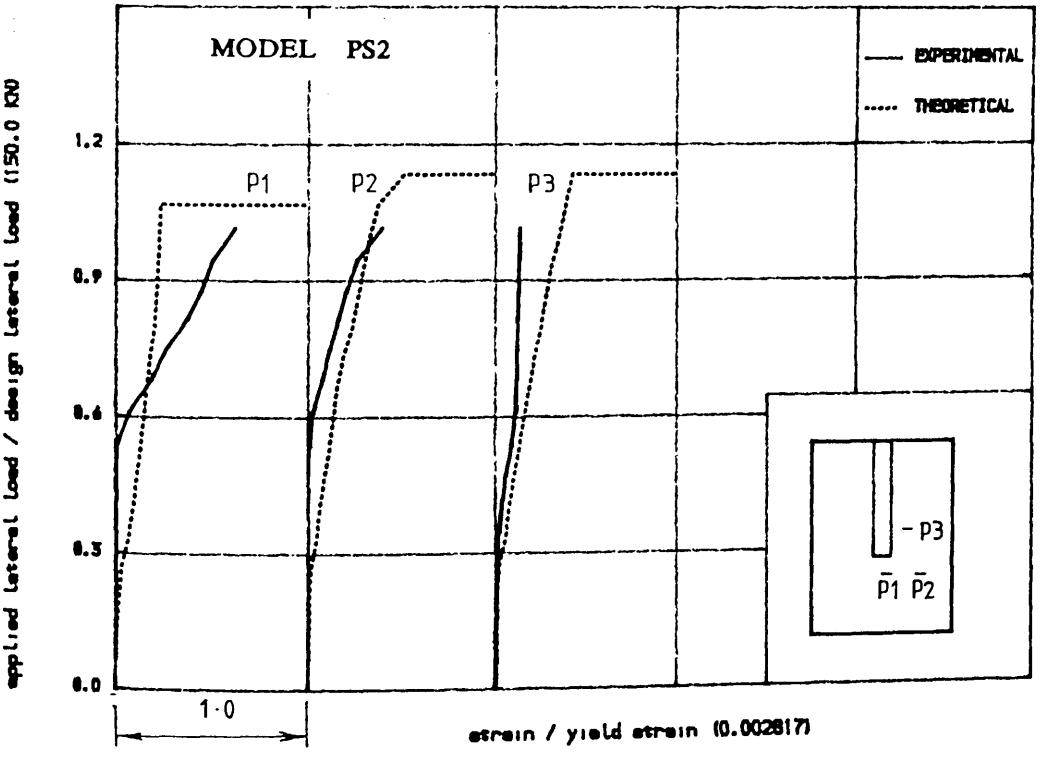

FIGURE (7.49) : STRAIN IN SHEAR STEEL AT DIFFERENT LOCATIONS IN THE SLAB OF MODEL PS2

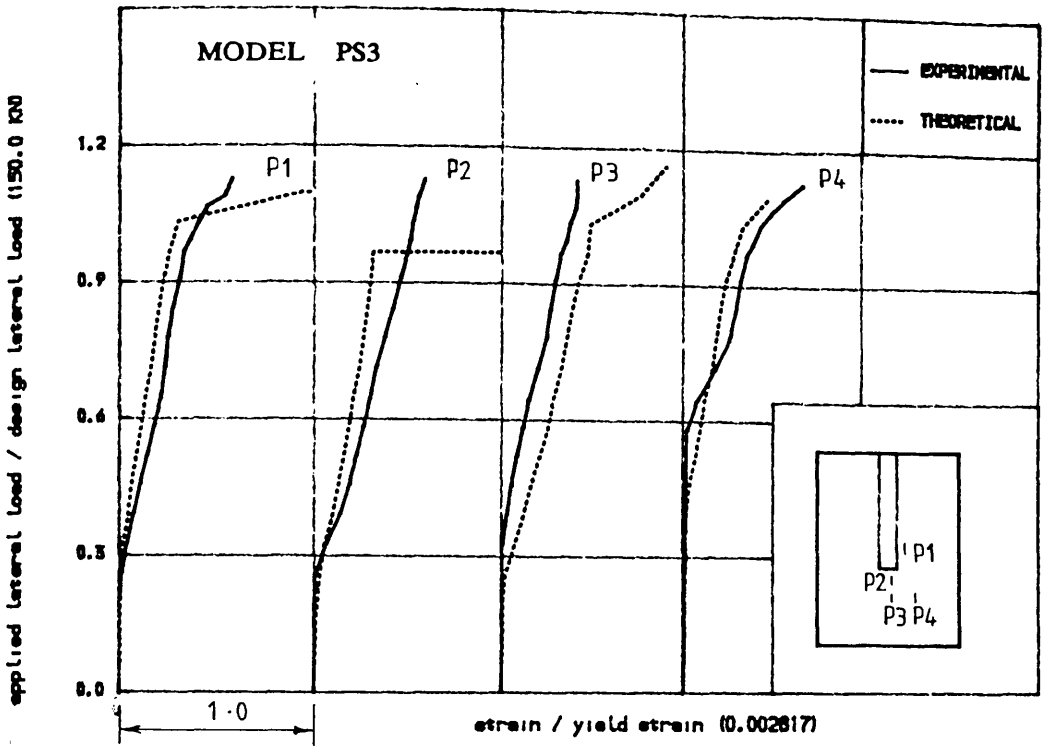

FIGURE (7.50) . STRAIN IN CLOSED VERTICAL STIRUP AT DIFFERENT LOCATIONS IN THE SLAB OF MODEL PS3

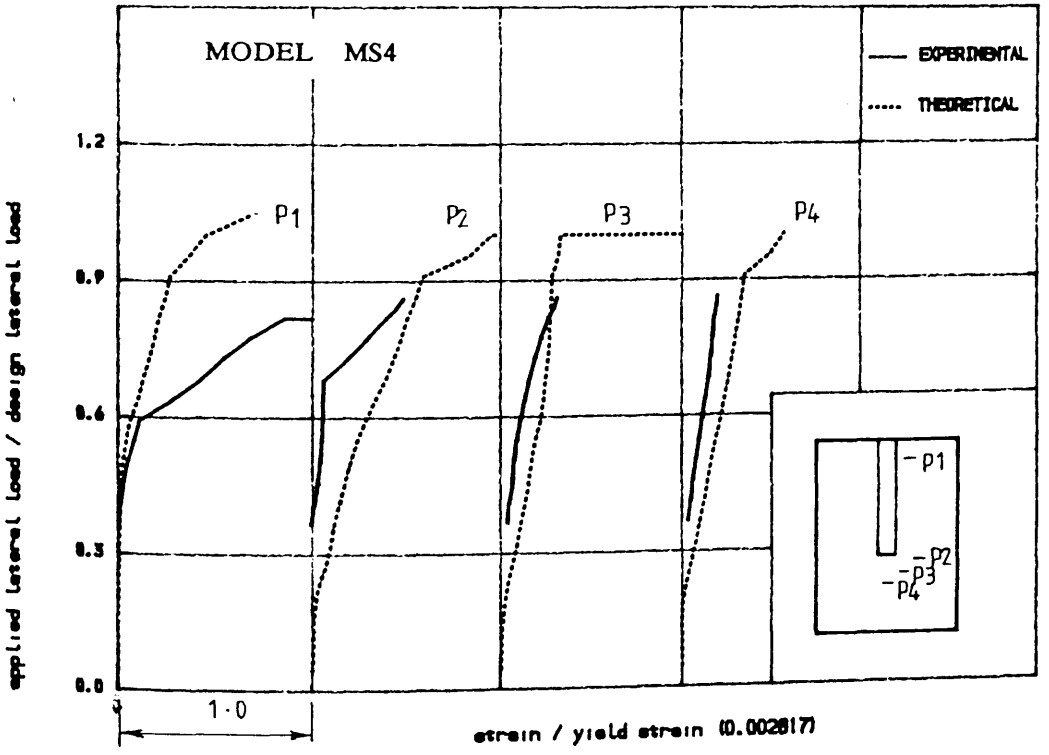

FIGURE (7.51) . STRAIN IN CLOSED VERTICAL STIRUP AT DIFFERENT LOCATIONS IN THE SLAB OF MODEL MS4

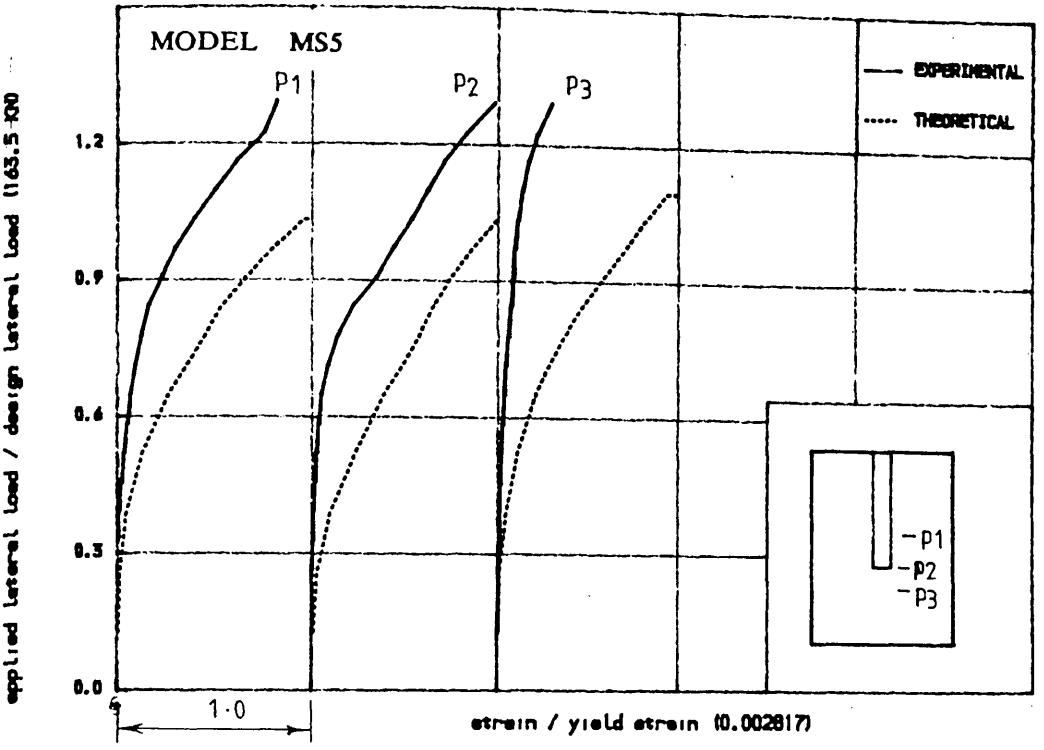

FIGURE (7.52) , TENSILE STRAIN IN CLOSED VERTICAL STIRUP AT DIFFERENT LOCATIONS IN THE SLAB OF MODEL MS5

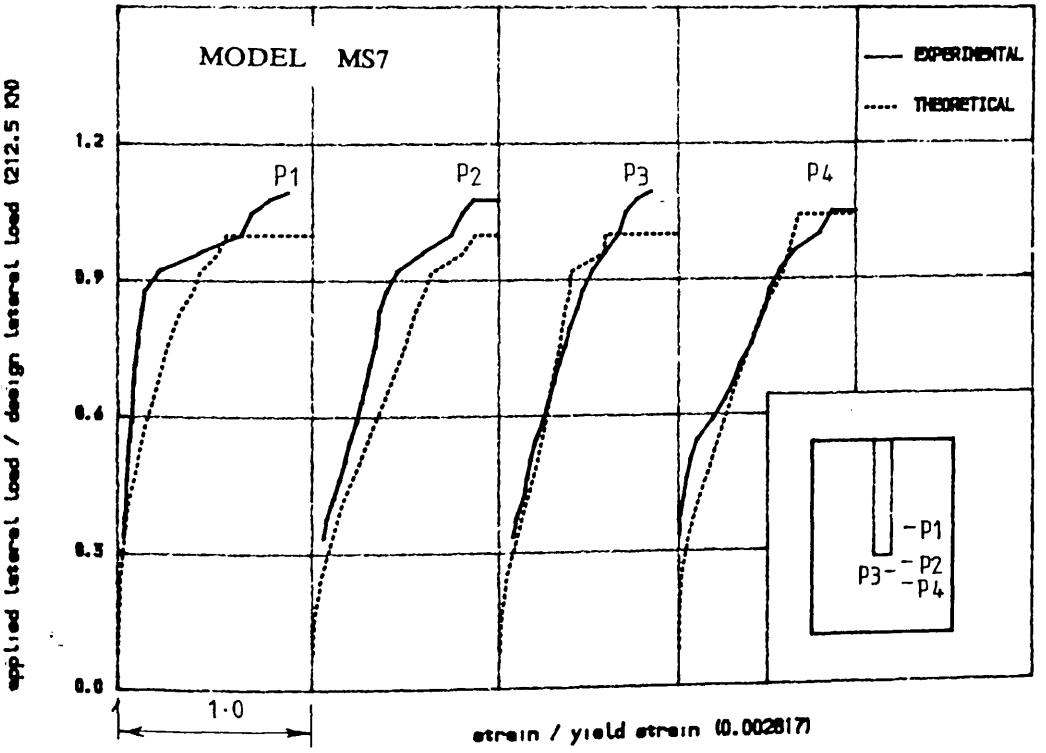

FIGURE (7.53) , STRAIN IN CLOSED VERTICAL STIRUP AT DIFFERENT LOCATIONS IN THE SLAB OF MODEL MS7

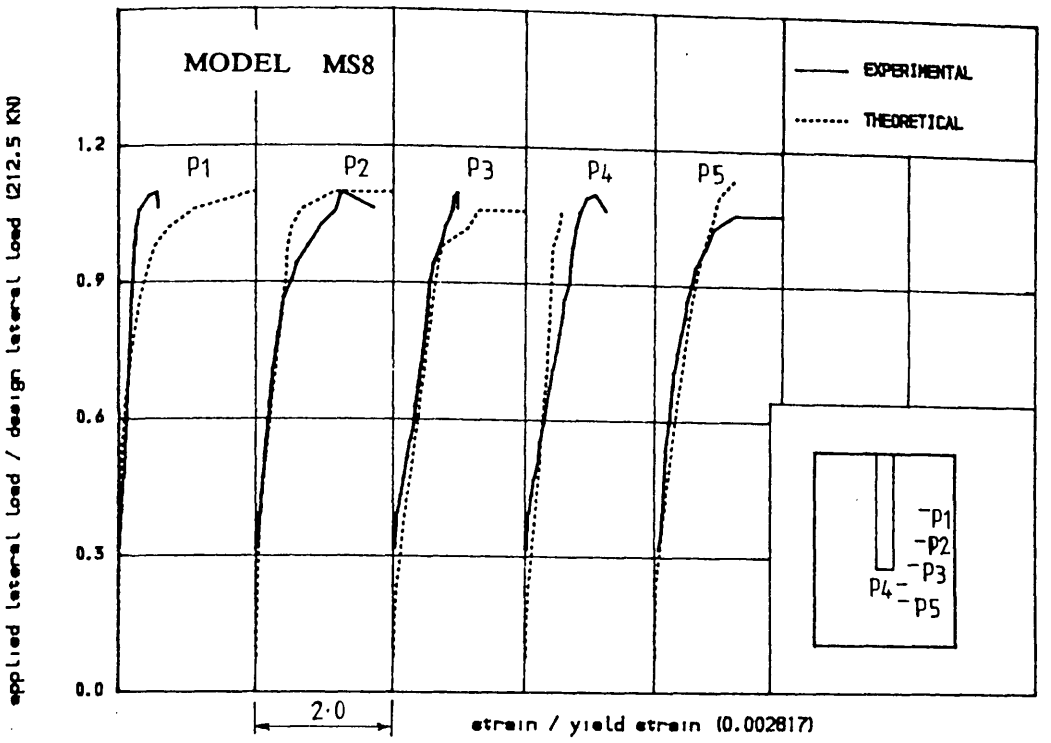

FIGURE (7.54) , STRAIN IN CLOSED VERTICAL STIRRUP AT DIFFERENT LOCATIONS IN THE SLAB OF MODEL MS8

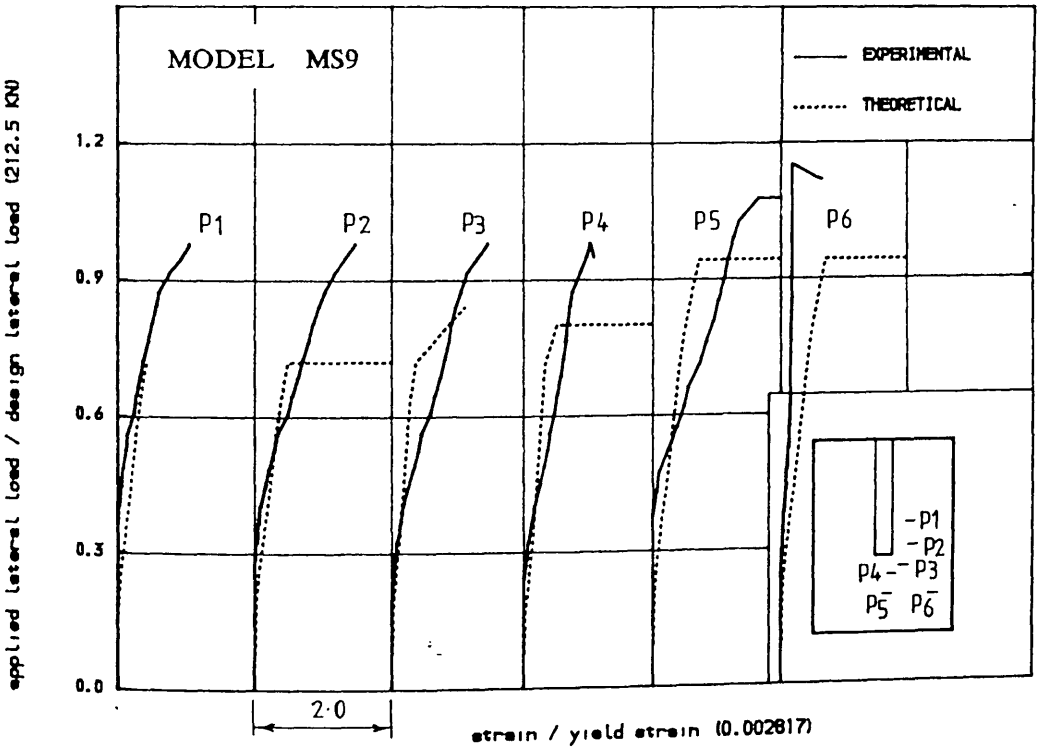

FIGURE (7.55) , TENSILE STRAIN IN CLOSED VERTICAL STIRRUP AT DIFFERENT LOCATIONS IN THE SLAB OF MODEL MS9

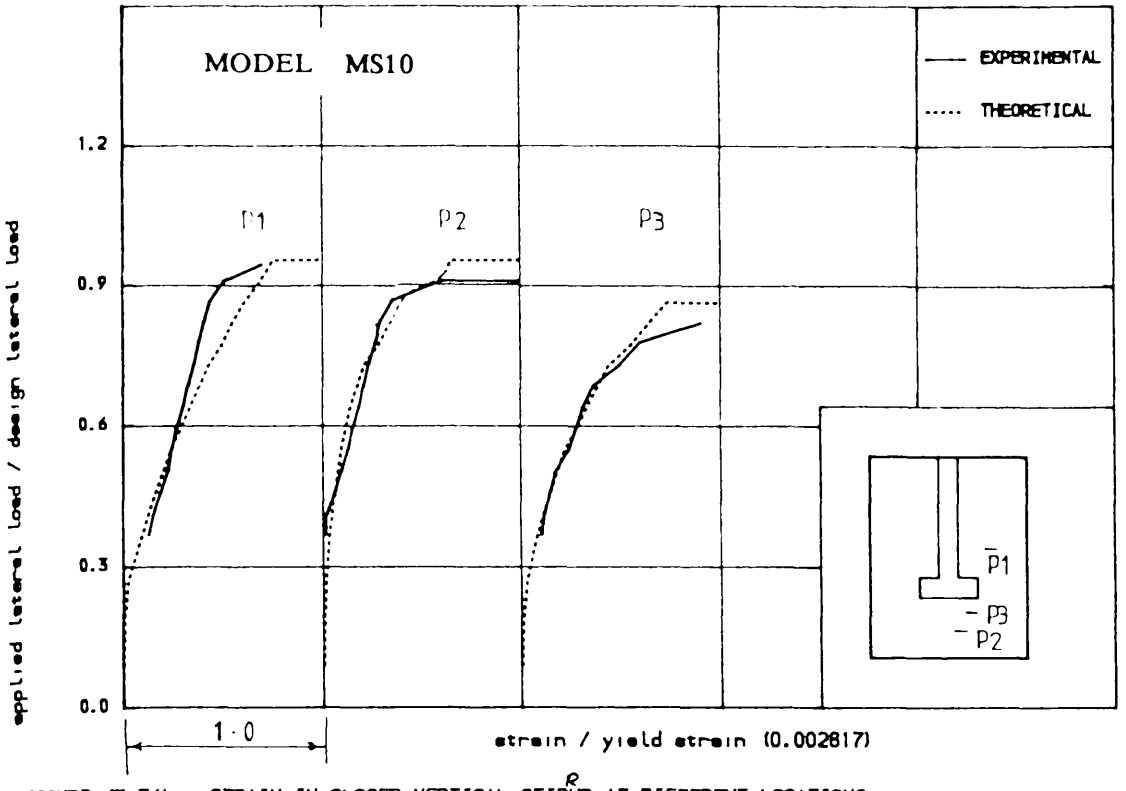

FIGURE (7.56) , STRAIN IN CLOSED VERTICAL STIRRUP AT DIFFERENT LOCATIONS IN THE SLAB OF MODEL MS10

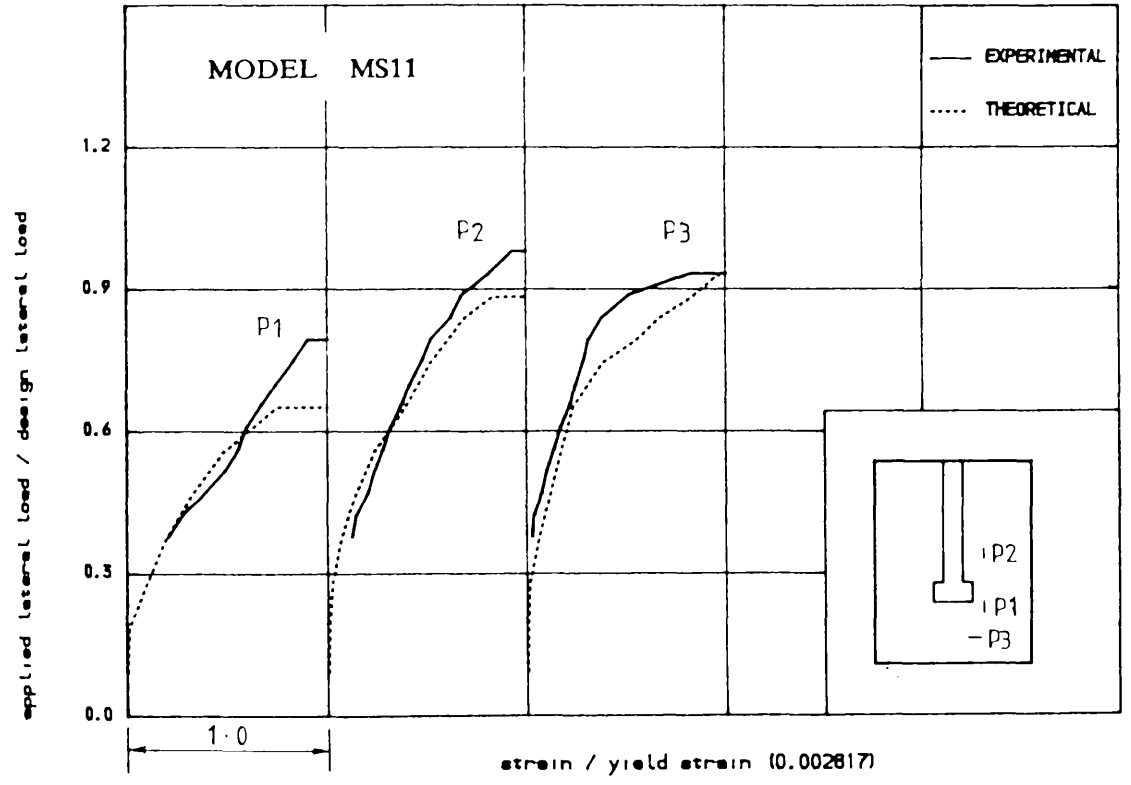

FIGURE (7.57) , STRAIN IN CLOSED VERTICAL STIRRUP AT DIFFERENT LOCATIONS IN THE SLAB OF MODEL MS11

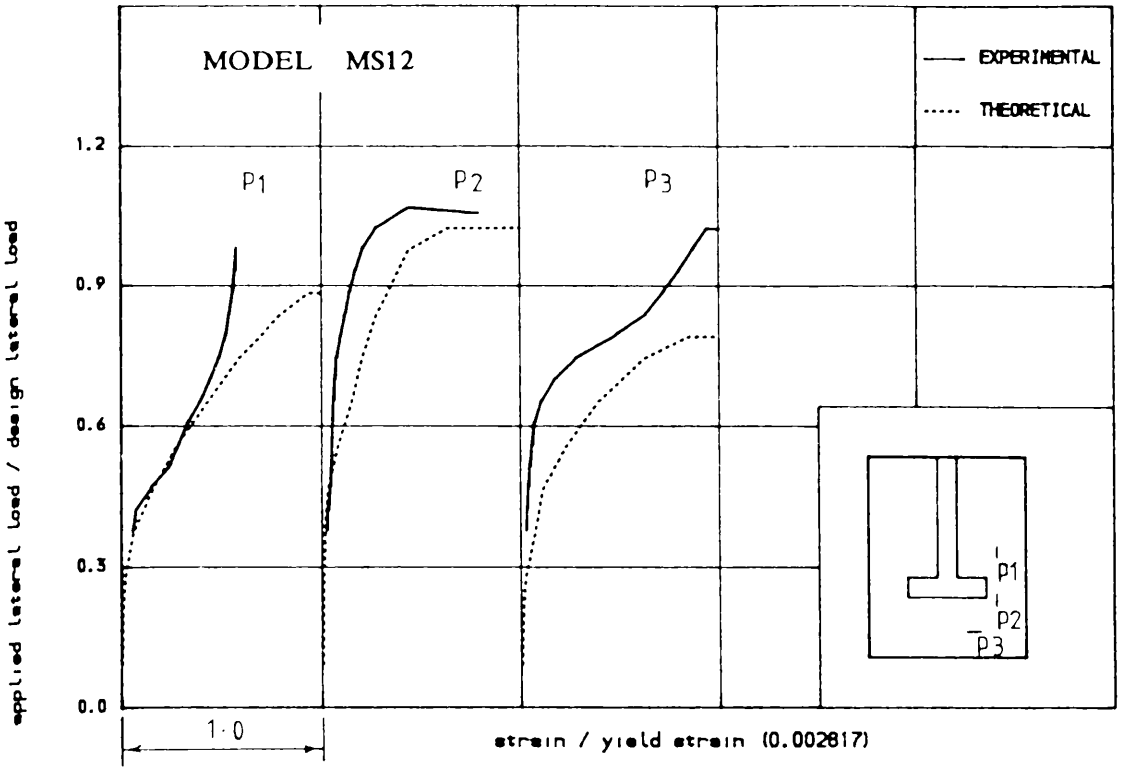

FIGURE (7.58) : STRAIN IN CLOSED VERTICAL STIRRUP AT DIFFERENT LOCATIONS IN THE SLAB OF MODEL MS12

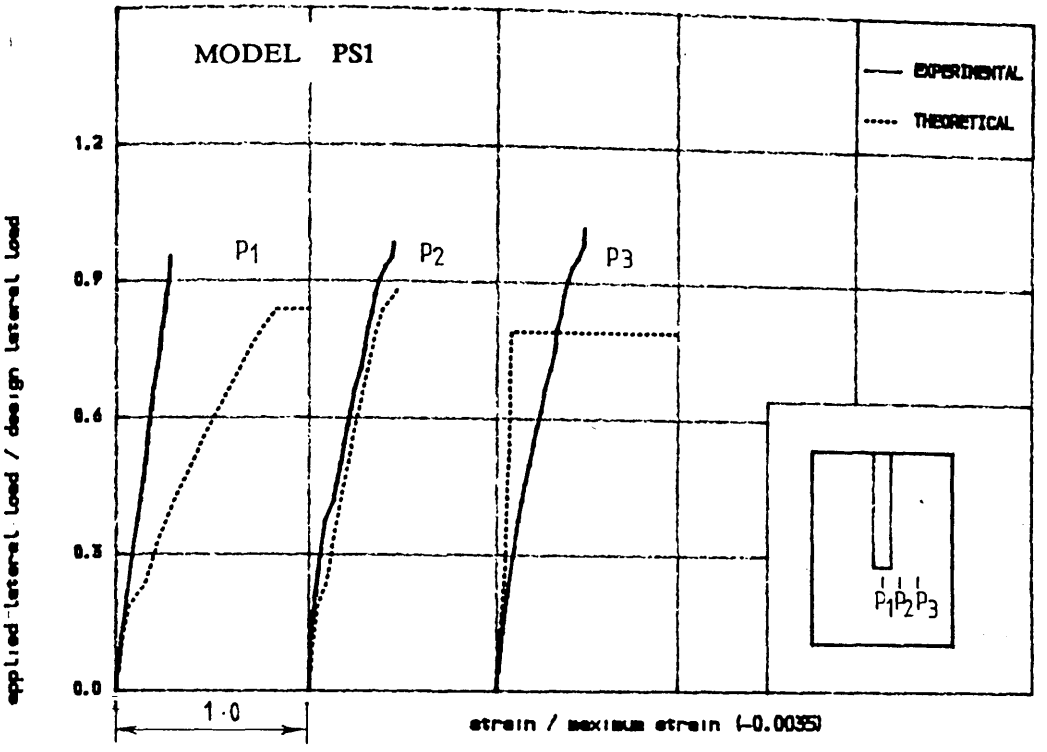

FIGURE (7.59) , COMPRESSIVE STRAIN IN CONCRETE IN VINDVARD DIRECTION IN THE SLAB OF MODEL PS1

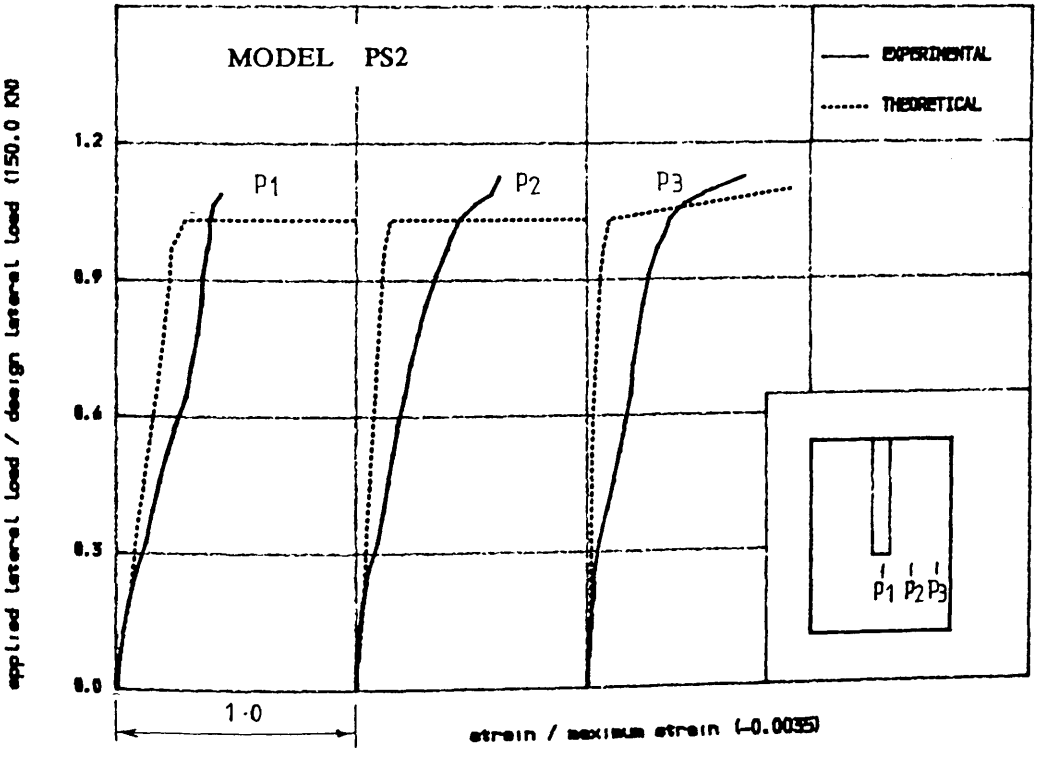

FIGURE (7.60) , COMPRESSIVE STRAIN IN CONCRETE IN VINDVARD DIRECTION IN THE SLAB OF MODEL PS3

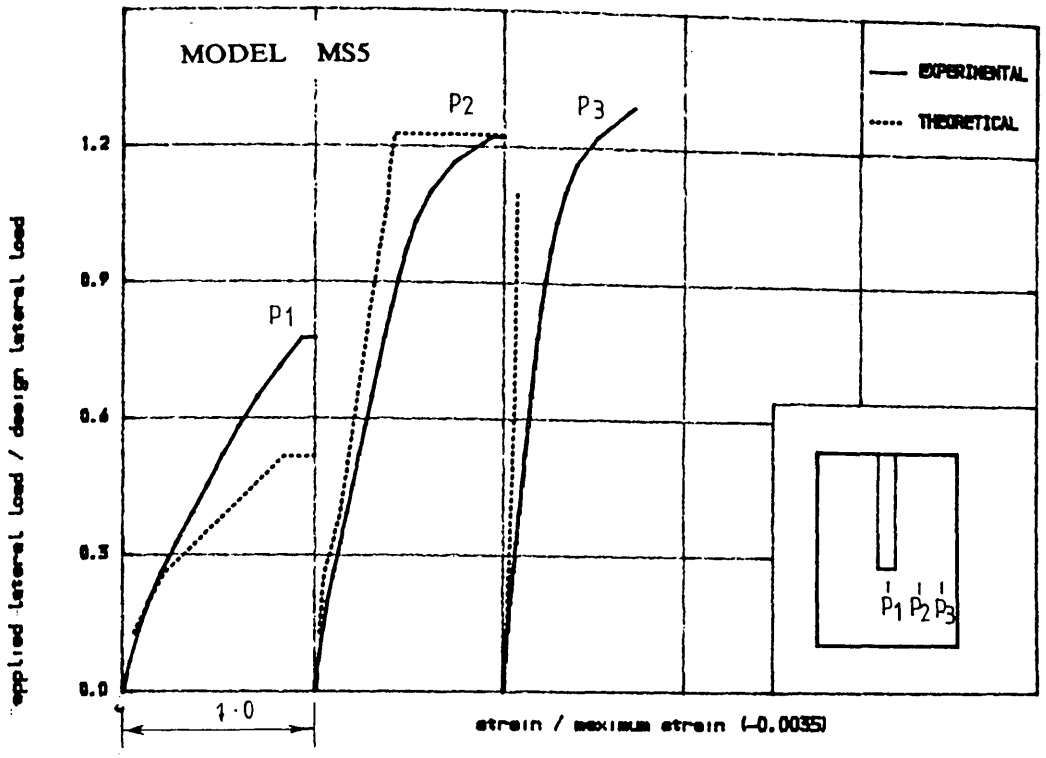

FIGURE (7.61) : COMPRESSIVE STRAIN IN CONCRETE IN VINDWARD DIRECTION IN THE SLAB OF MODEL MS5

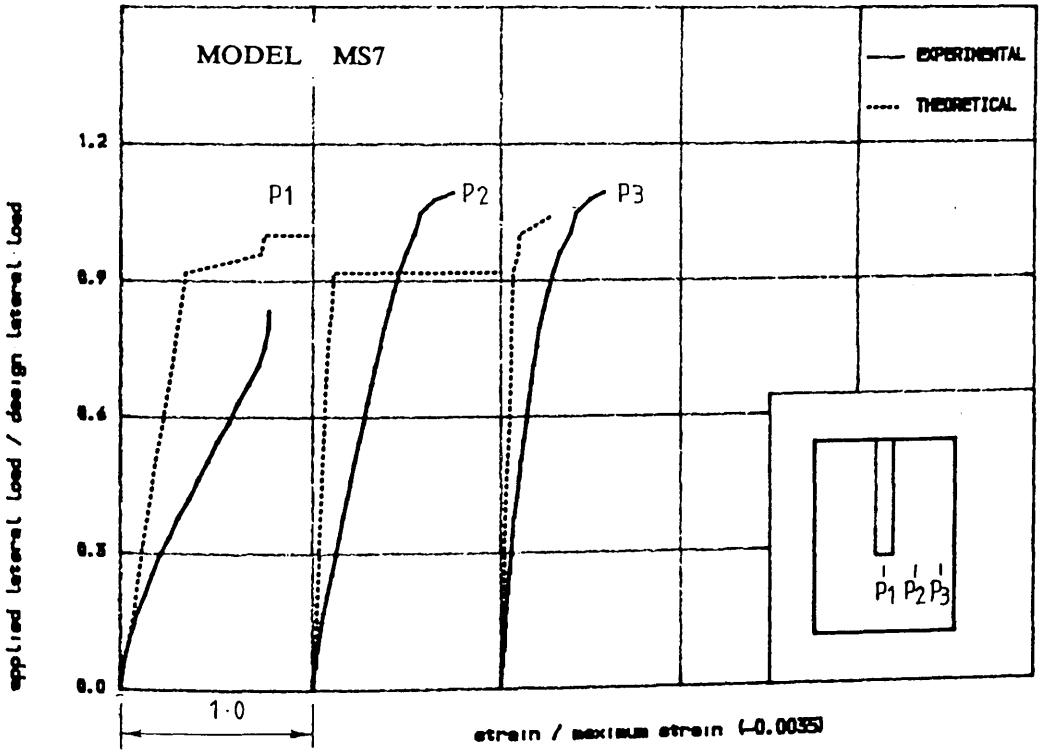

FIGURE (7.62) : COMPRESSIVE STRAIN IN CONCRETE IN VINDWARD DIRECTION IN THE SLAB OF MODEL MS7

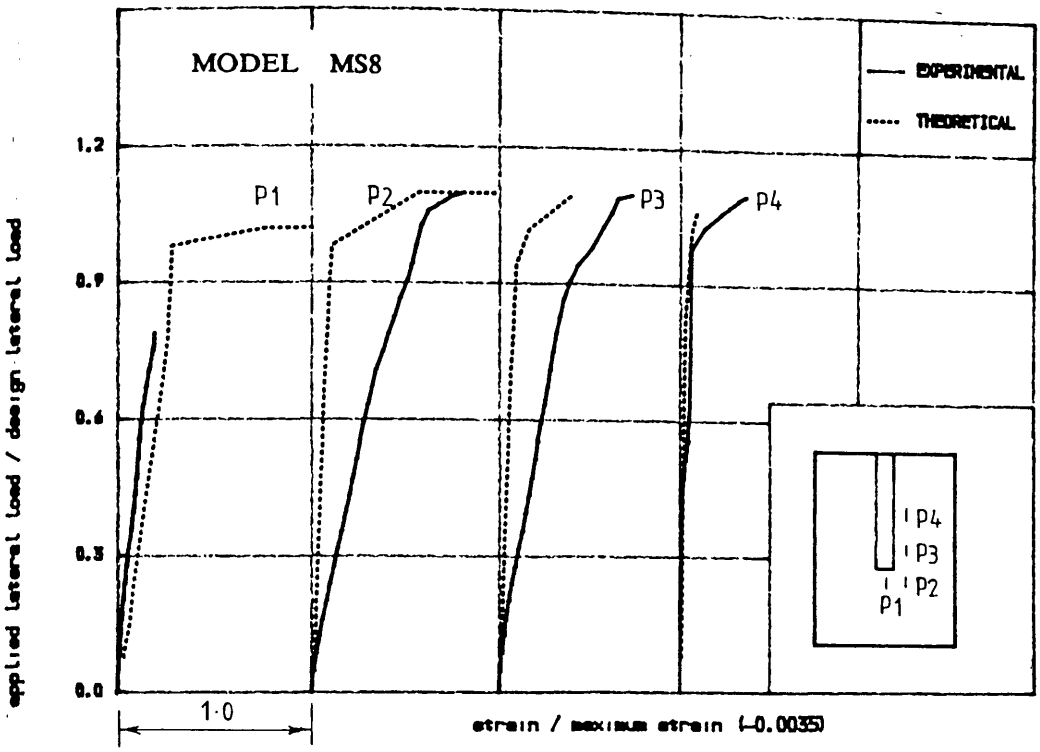

FIGURE (7.63) , COMPRESSIVE STRAIN IN CONCRETE IN WINDWARD DIRECTION IN THE SLAB OF MODEL MS8

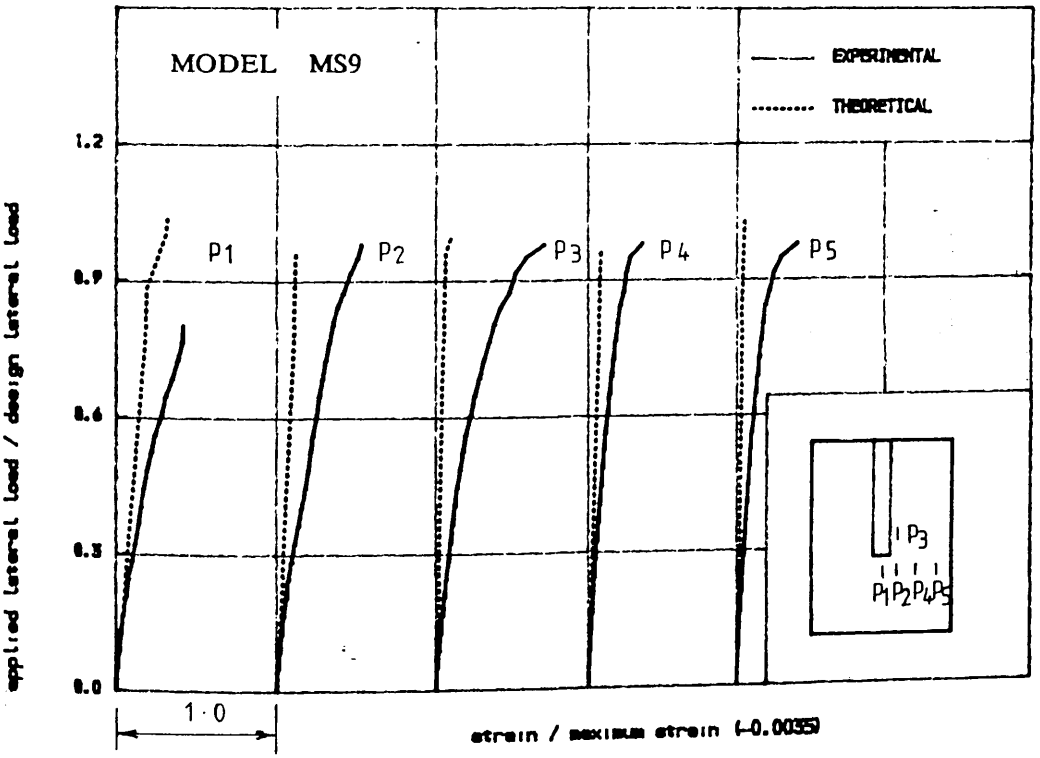

FIGURE (7.64) , COMPRESSIVE STRAIN IN CONCRETE IN WINDWARD DIRECTION IN THE SLAB OF MODEL MS9

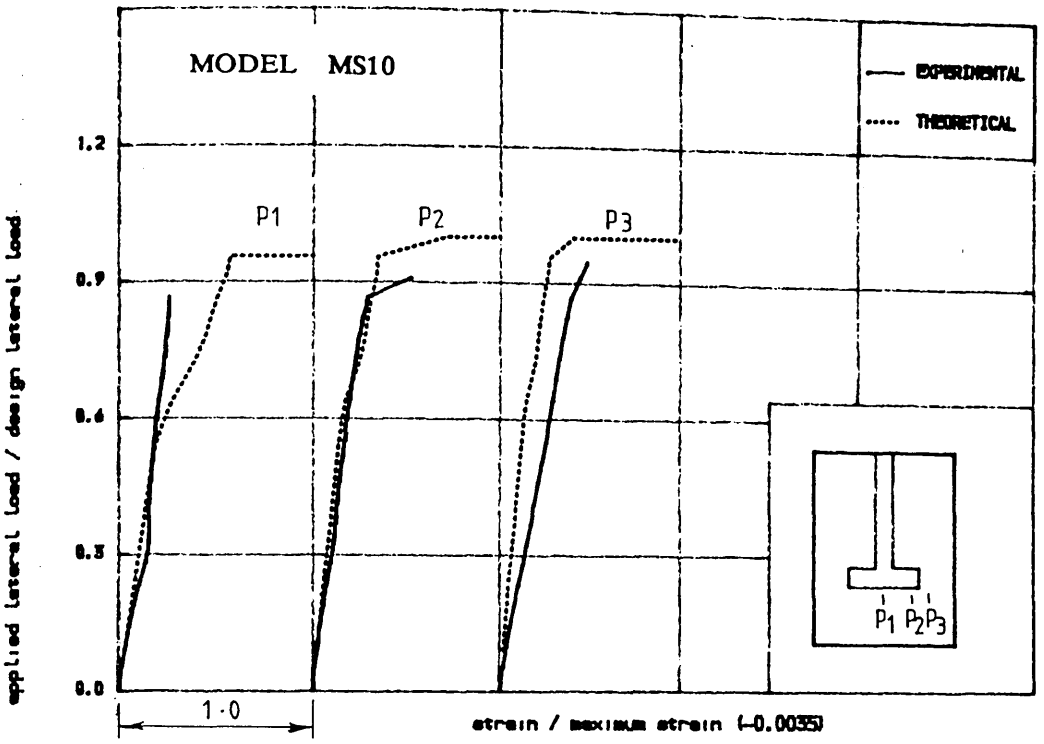

FIGURE (7.65) : COMPRESSIVE STRAIN IN CONCRETE IN WINDWARD DIRECTION IN THE SLAB OF MODEL MS10

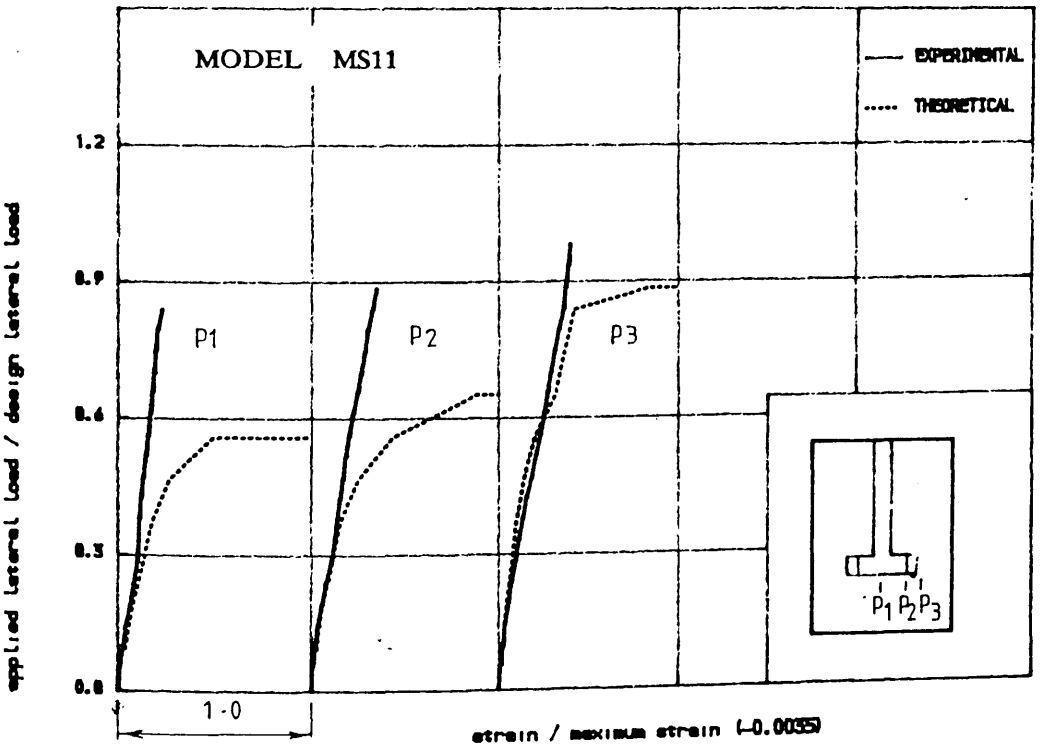

FIGURE (7.66) : COMPRESSIVE STRAIN IN CONCRETE IN WINDWARD DIRECTION IN THE SLAB OF MODEL MS11

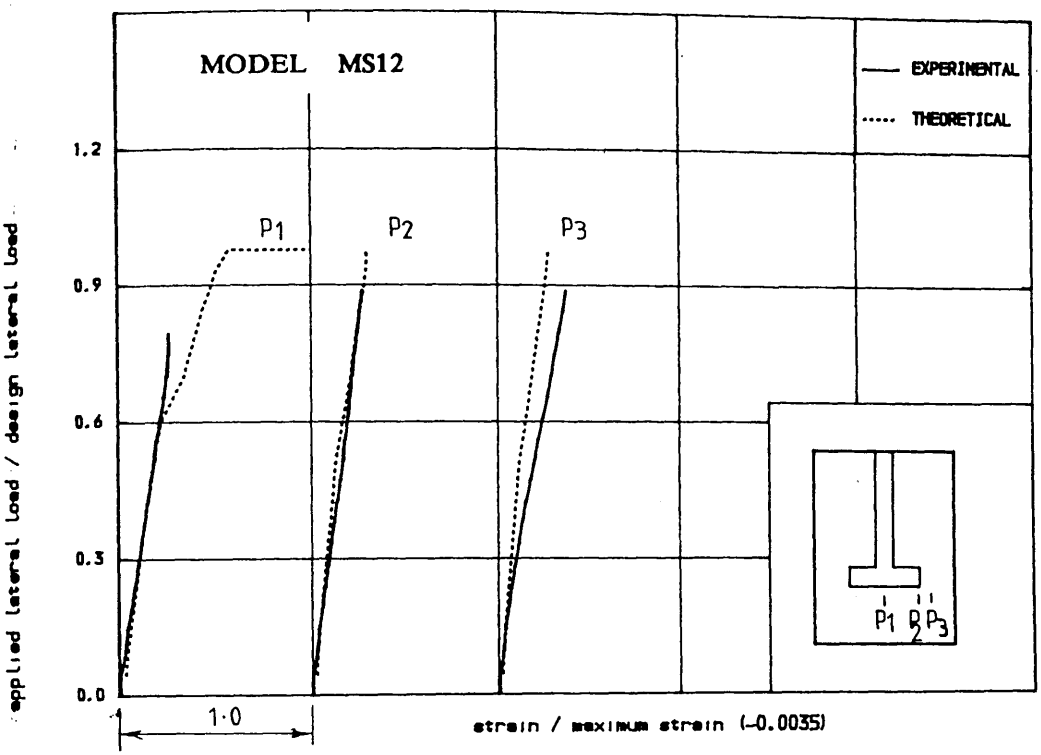

FIGURE (7.67) : COMPRESSIVE STRAIN IN CONCRETE IN WINDWARD DIRECTION IN THE SLAB OF MODEL MS12

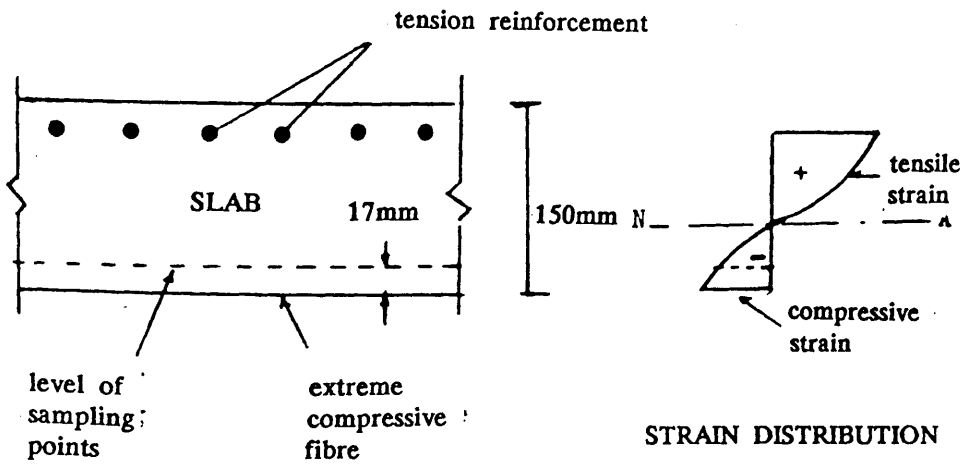

Figure (7.68) : Illustration of compressive strain at theoretical sampling points.

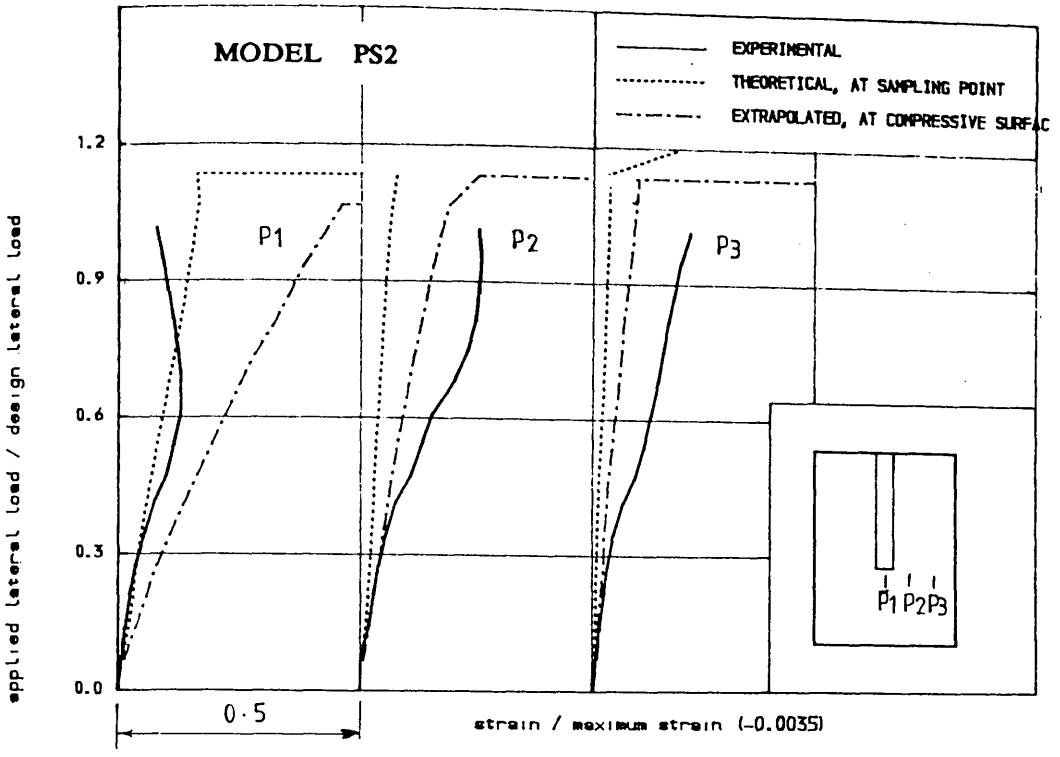

FIGURE (7.69) , COMPRESSIVE STRAIN IN CONCRETE IN WINDWARD DIRECTION IN THE SLAB OF MODEL PS2

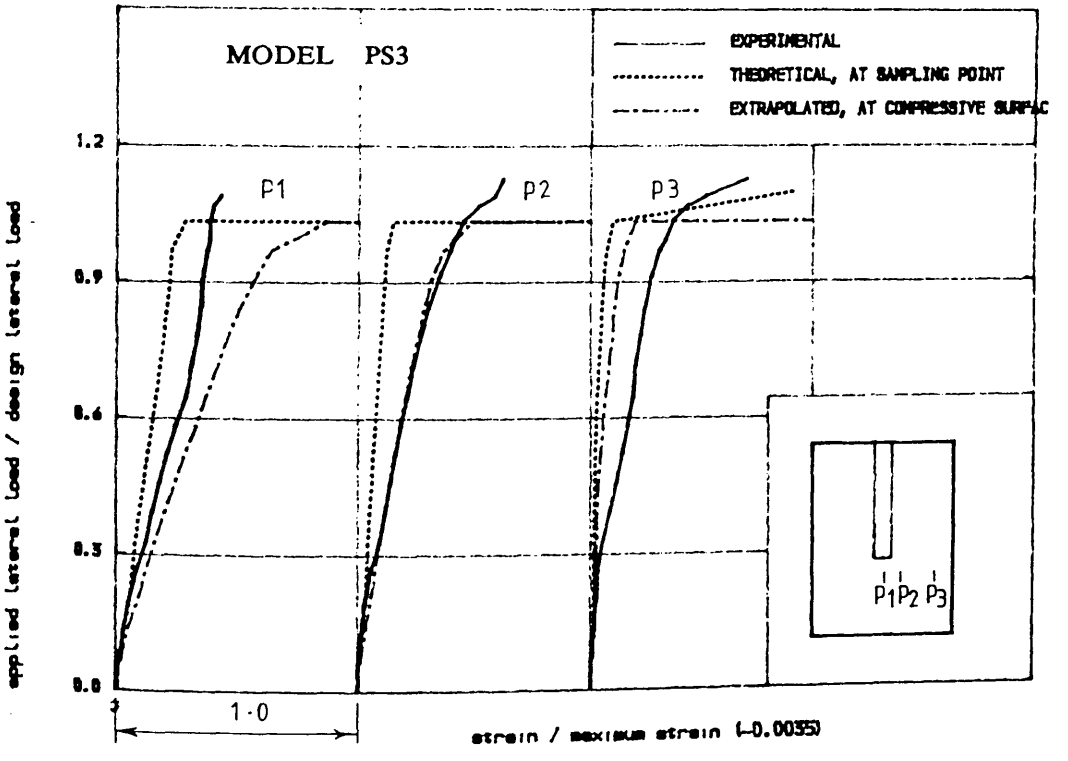

FIGURE (7.70) , COMPRESSIVE STRAIN IN CONCRETE IN WINDWARD DIRECTION IN THE SLAB OF MODEL PS3

7.7 Ultimate Failure Load

During the experiment, failure of the wall–slab connection was assumed to have taken place when punching of slab took place or excessive deflection of slab at the line of contraflexure (i.e., edge EF in Figure 7.1) was observed, accompanied by rapid decrease in lateral load. On the other hand, in theoretical analysis, the second definition which is gradual increase in deflections, can be easily detected as in Figure (7.20); while punching phenomenon can only be known from the very sudden jump in deflection as in models PS1 and PS2 of Figure (7.18).

For all the models tested, the theoretical ultimate load (V_{theo}) is compared with the experimental ultimate load (V_{exp}) in table (7.2). During the test, model MS4 was failed in shear at the back of the slab at 86.6% of design lateral load due to early crushing of the wall, but the theoretical analysis shows flexural type of failure at 102% of design load. So, neglecting the result of this model, the mean ratio of (V_{exp}/V_{theo}) is 1.0 and the standard deviation equals 0.07. From this Table, it can be said therefore that the proposed finite element analysis predicts the failure load satisfactorily.

It is interesting to note that not only the flexural type of failure was successfully predicted (as in Figure 7.20 for models to study the effect of corridor opening width), but also the punching type (as in Figure 7.18 for models PS1 and PS2).

7.8 Concrete as No–Tension Material Analysis

To study the effect of tensile strength of concrete on the predicted behaviour of models, the incremental non–linear analysis were also performed for some of the models considering concrete as a No–tension material.

In the **Fixed Crack analysis**, the crack direction remains fixed and depends on the direction of the principal tensile stress at the loading state when the principal

Table (7.2) : Comparison of failure loads predicted by finite element method with the experimental failure loads

Model	Main Variables	Exper. failure load V_{exp} KN	Theor. failure load V_{theo} KN	$\frac{V_{exp}}{V_{theo}}$	Type of failure Exper.	Theor.
PS1		219.0	200.0	1.10	local	punching
PS2	Shear steel	159.0	180.0	0.89	local	punching
PS3		175.0	180.0	0.97	flexural	Initiated by yielding of steel
MS4	Wall web length 67% of MS7	190.4	220.0	0.87	Initiated by wall crushing & finished by flexure	"
MS5	Corridor opening width	203.0	200.0	1.02	flexural	"
MS6	280mm for MS5 400mm for MS6 520mm for MS7	343.0	330.0	1.04	"	"
MS7		262.0	260.0	1.01	"	"
MS8	Gravity load 3 times of MS7	280.0	280.0	1.00	"	"
MS9	Bay width 1.44 times of MS7	247.0	250.0	0.99	"	"
MS10	Flange width	209.0	220.0	0.95	"	"
MS11	300mm for MS10 200mm for MS11 400mm for MS12	219.0	200.0	1.10	"	"
MS12		235.0	230.0	1.02	"	"
			mean =	1.00		
			S.D. =	0.07		

tensile stress equals the tensile strength of concete. In addition, if there are more than one crack, they are forced to be orthogonal. This procedure involves the modification of the material stiffness matrix to allow for orthotropic properties of concrete after the concrete has cracked. Because of the fact that due to the aggregate interlock, shear stress is permitted on the cracked planes, there is a possibility of tensile stresses building up in directions other than the crack directions. In reinforced concrete, the initial and final crack directions usually do not coincide. So, the assumption of fixed crack directions may involve an error in the analysis.

In the No–Tension analysis, the principal tensile stress is brought back to zero at every stage of analysis. No modification in the material stiffness matrix is involved in this type of analysis, except when the steel yields. In addition the method accords with the assumption normally made in design of not relying on the tensile strength of concrete. As in fixed crack analysis, the convergence tolerance was taken as 10%. The maximum number of iterations was increased from 20 to 40. All other parameters which were tuned for fixed crack analysis were kept the same for this analysis.

The fixed crack analysis and No–tension analysis results of Load–deflection, Load–steel stresses and Load–concrete compressive stresses are shown in Figures (7.72) to (7.82) for some of the models. For No–tension analysis, Figure (7.72) shows that the ultimate loads were slightly higher than the loads obtained by fixed crack analysis for models MS6 and MS7 and for models MS4 and MS5 were found to be exactly equal to that obtained from fixed crack analysis. Fixed crack analysis resulted in slightly stiffer load–deflection curve than that obtained for No–tension analysis.

There is no significant difference between the fixed crack and No–tension analysis results for the load–strain curves for steel in both the longitudinal and transverse directions. Remarkable improvement can be noticed in the load–strain

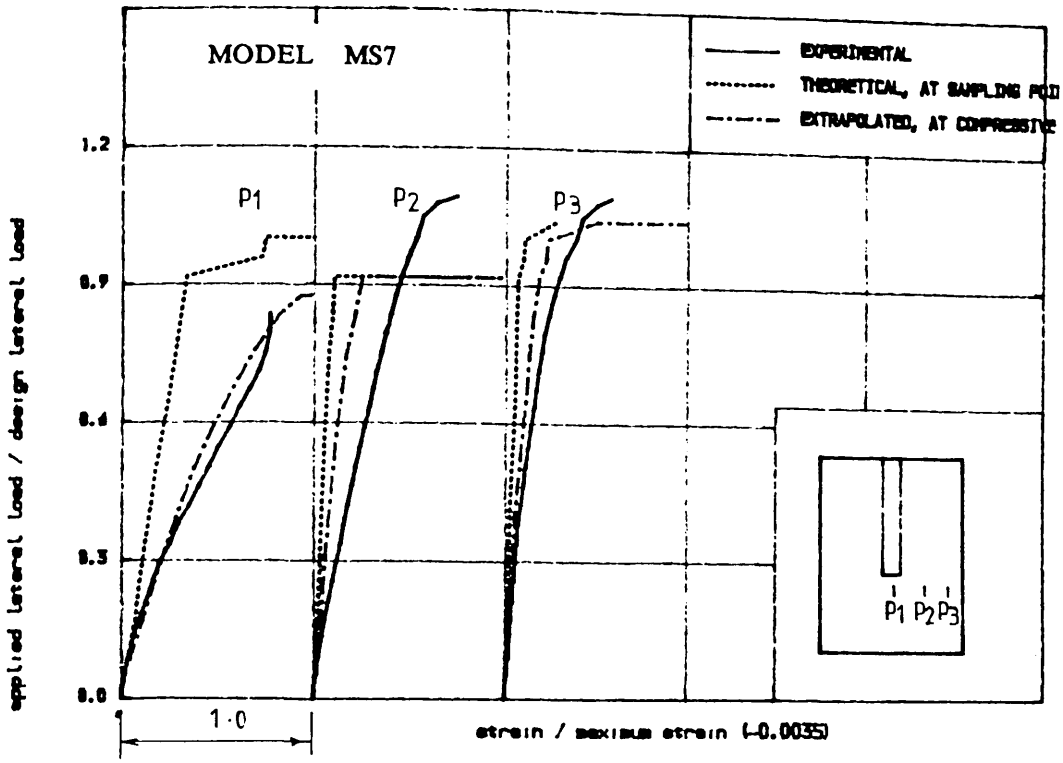

FIGURE (7.71) . COMPRESSIVE STRAIN IN CONCRETE IN WINDWARD DIRECTION IN THE SLAB OF MODEL MS7

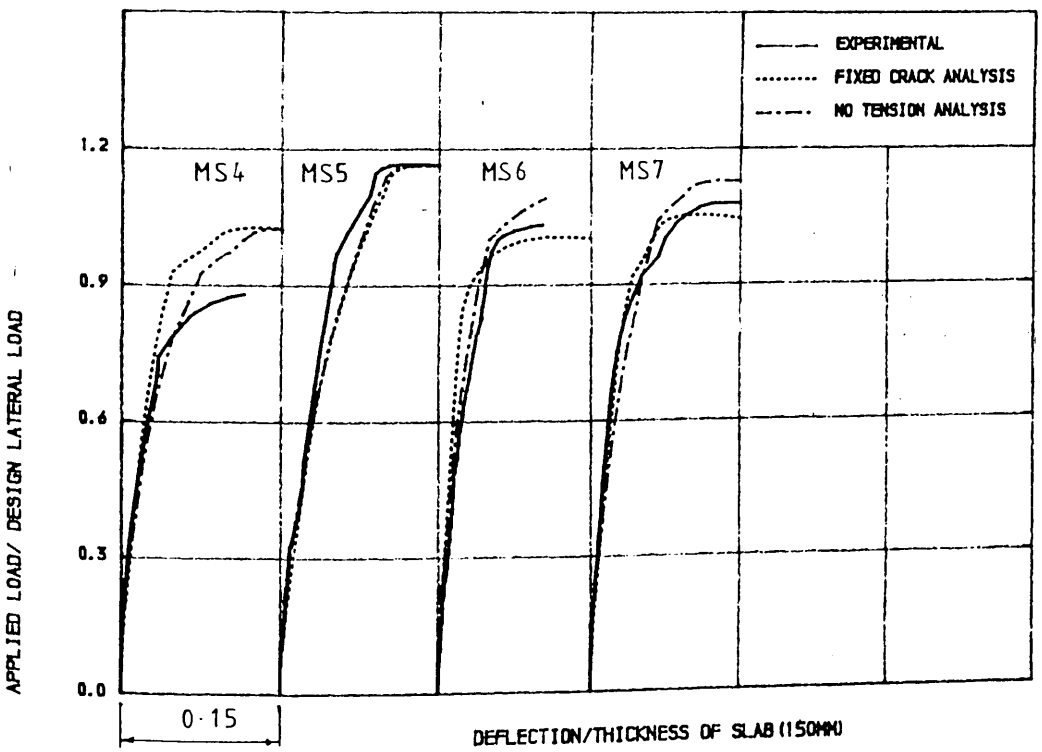

FIGURE (7.72) . COMPARATIVE STUDY OF FIXED CRACK ANALYSIS AND NO TENSION ANALYSIS ON LATERAL LOAD-DISPLACEMENT RELATIONS

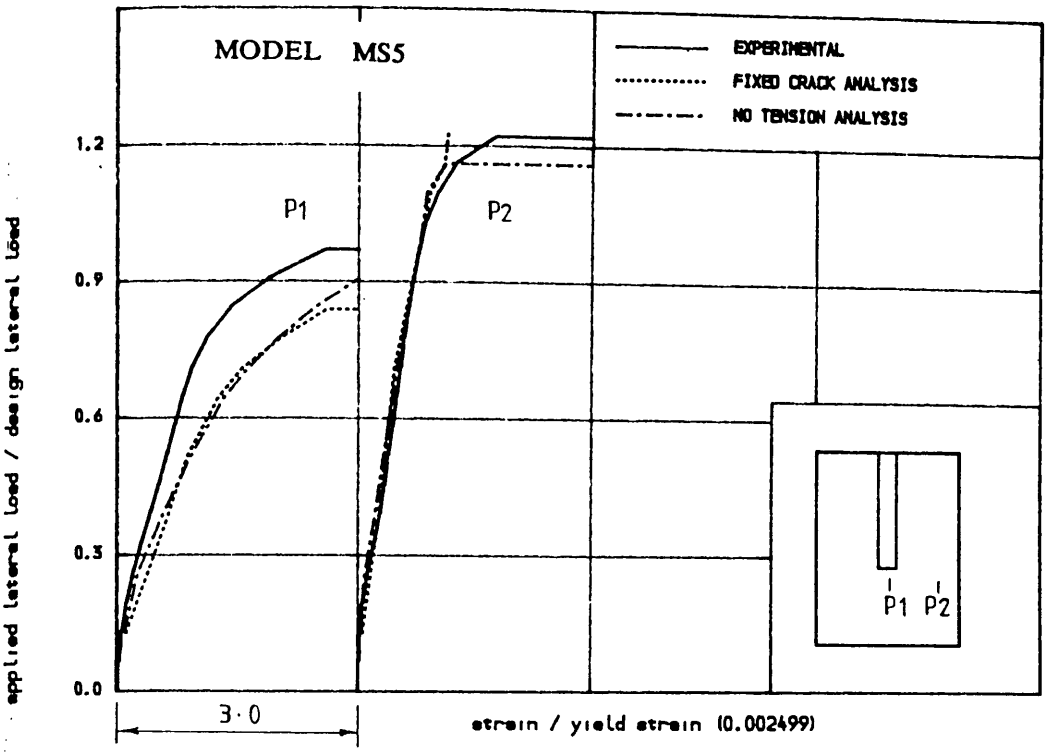

FIGURE (7.73) , TENSILE STRAIN IN STEEL IN VINDVARD DIRECTION ALONG TRANSVERSE SECTION IN THE SLAB OF MODEL MS5

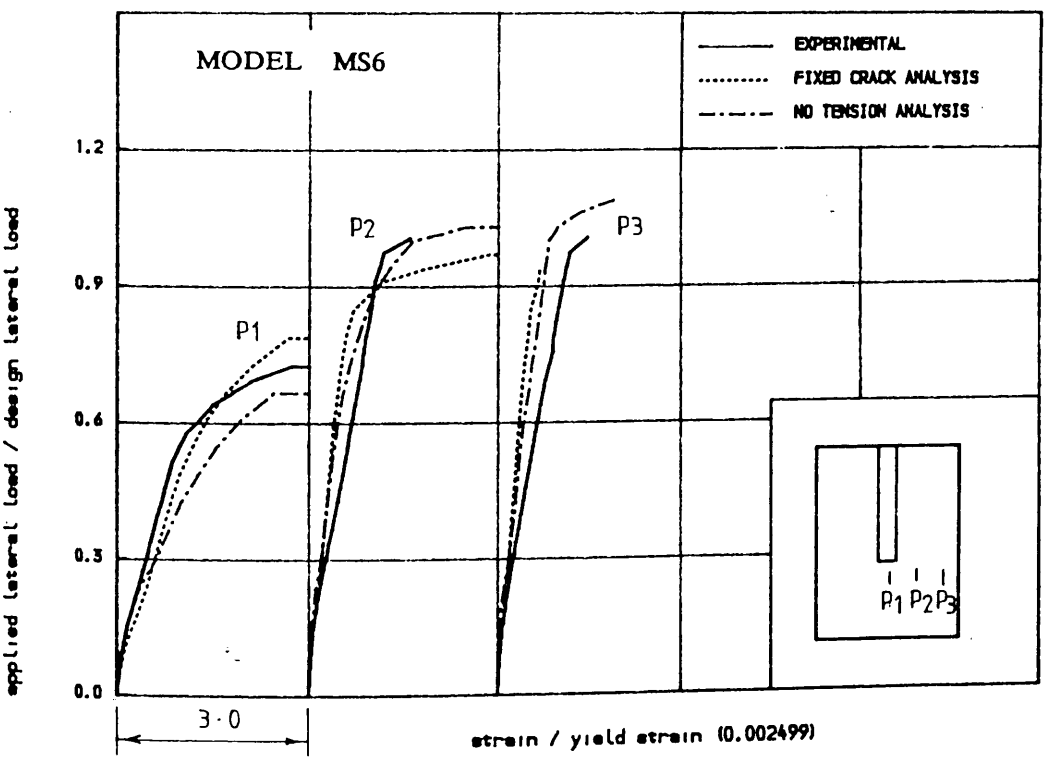

FIGURE (7.74) , TENSILE STRAIN IN STEEL IN VINDVARD DIRECTION ALONG TRANSVERSE SECTION IN THE SLAB OF MODEL MS6

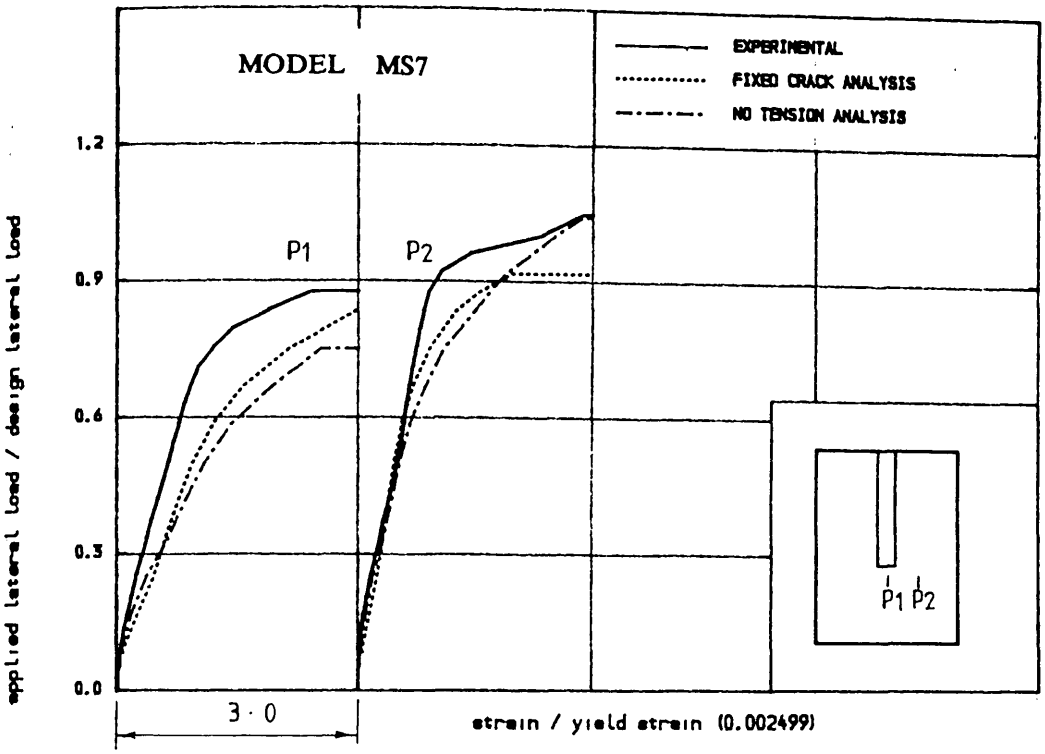

FIGURE (7.75) , COMPARATIVE STUDY OF ANALYSIS ON TENSILE STRAIN IN STEEL IN VINDVARD DIRECTION IN THE SLAB OF MODEL MS7

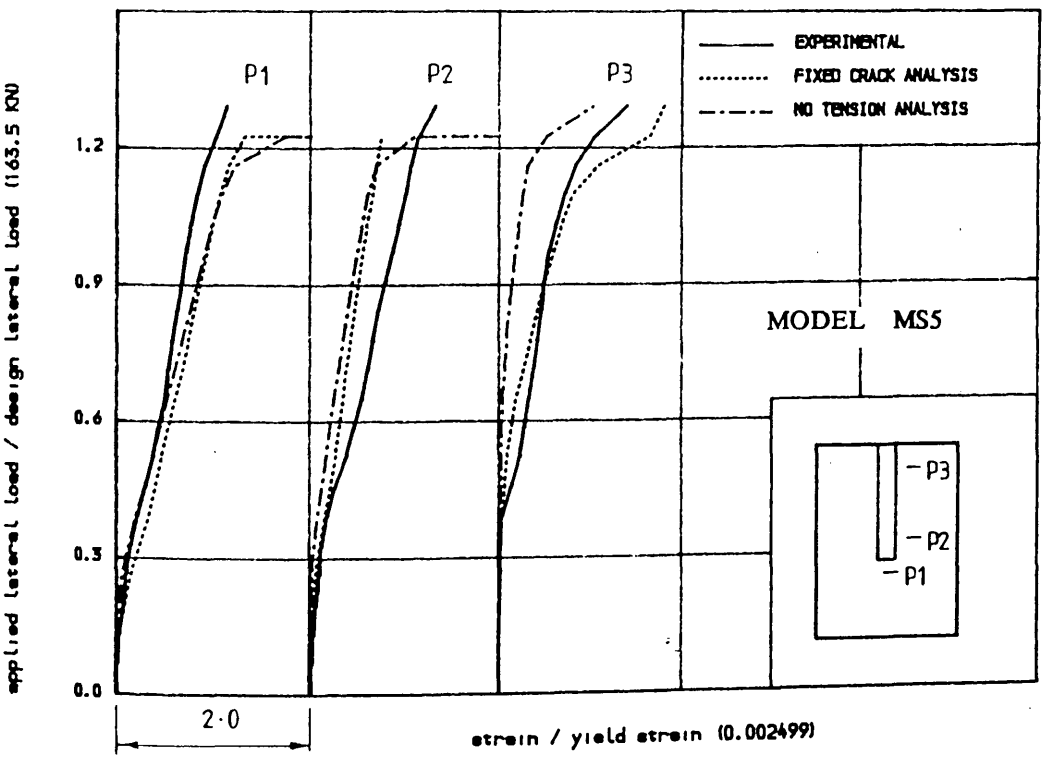

FIGURE (7.76) , TENSILE STRAIN IN STEEL IN TRANSVERSE DIRECTION ALONG VINDVARD SECTION IN THE SLAB OF MODEL MS5

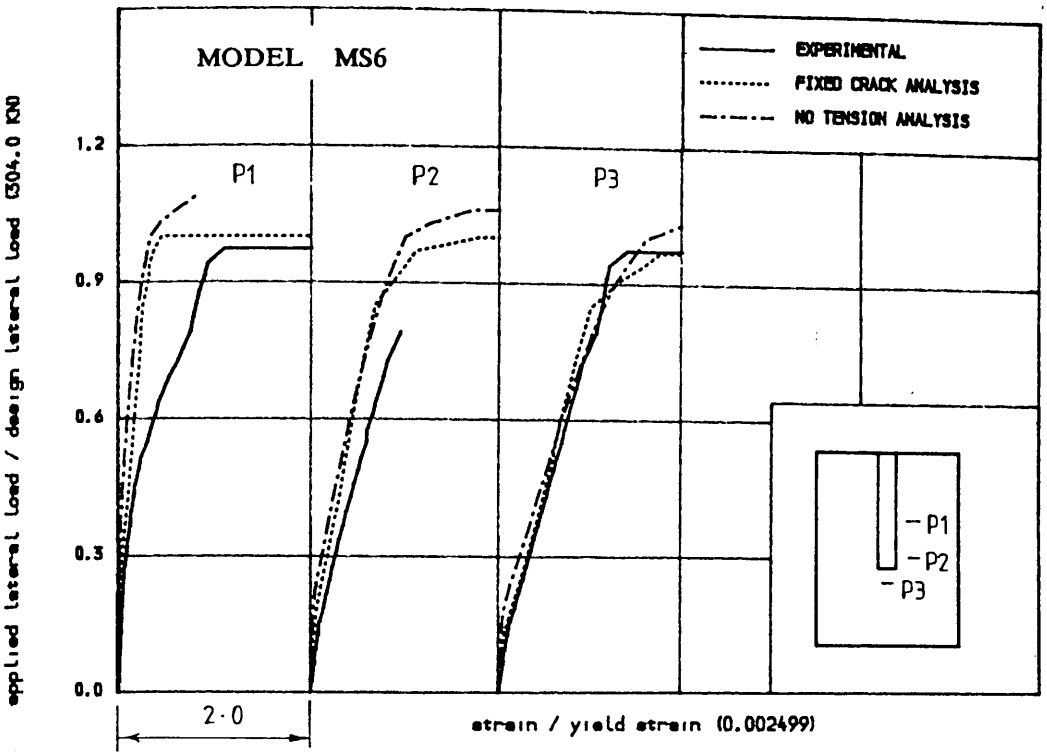

FIGURE (7.77) : TENSILE STRAIN IN STEEL IN TRANSVERSE DIRECTION ALONG VINDWARD SECTION IN THE SLAB OF MODEL MS6

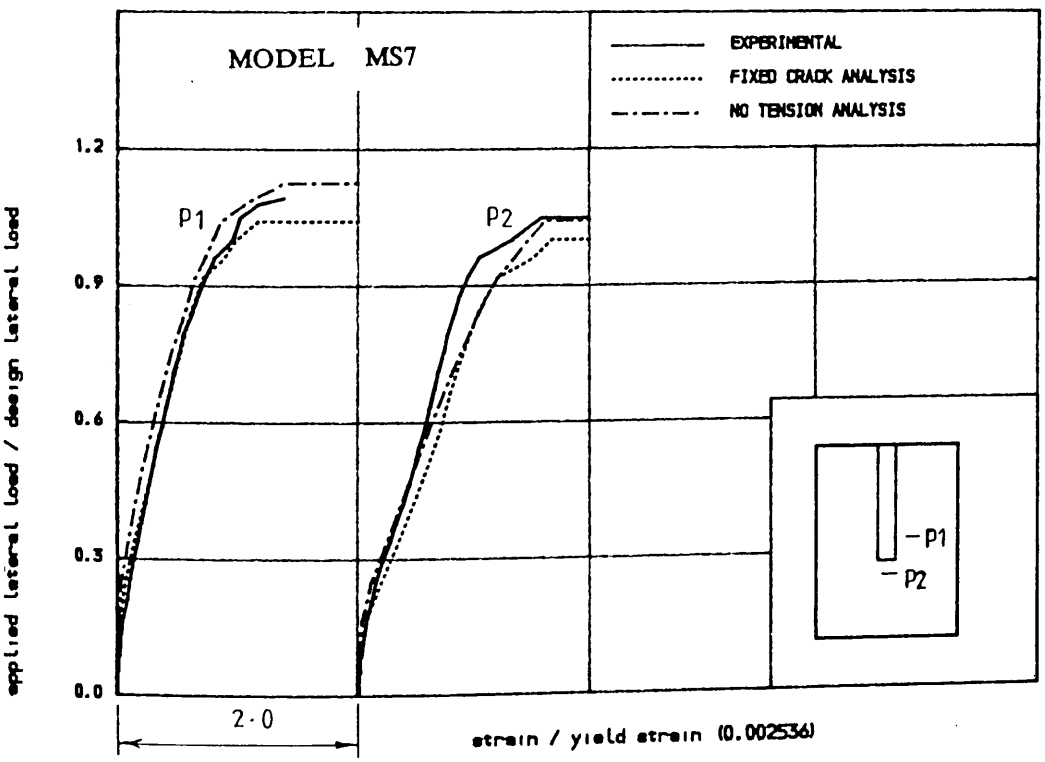

FIGURE (7.78) : COMPARATIVE STUDY OF FIXED CRACK ANALYSIS AND NO TENSION ANALYSIS ON TENSILE STRAIN IN STEEL IN SLAB OF MODEL MS7

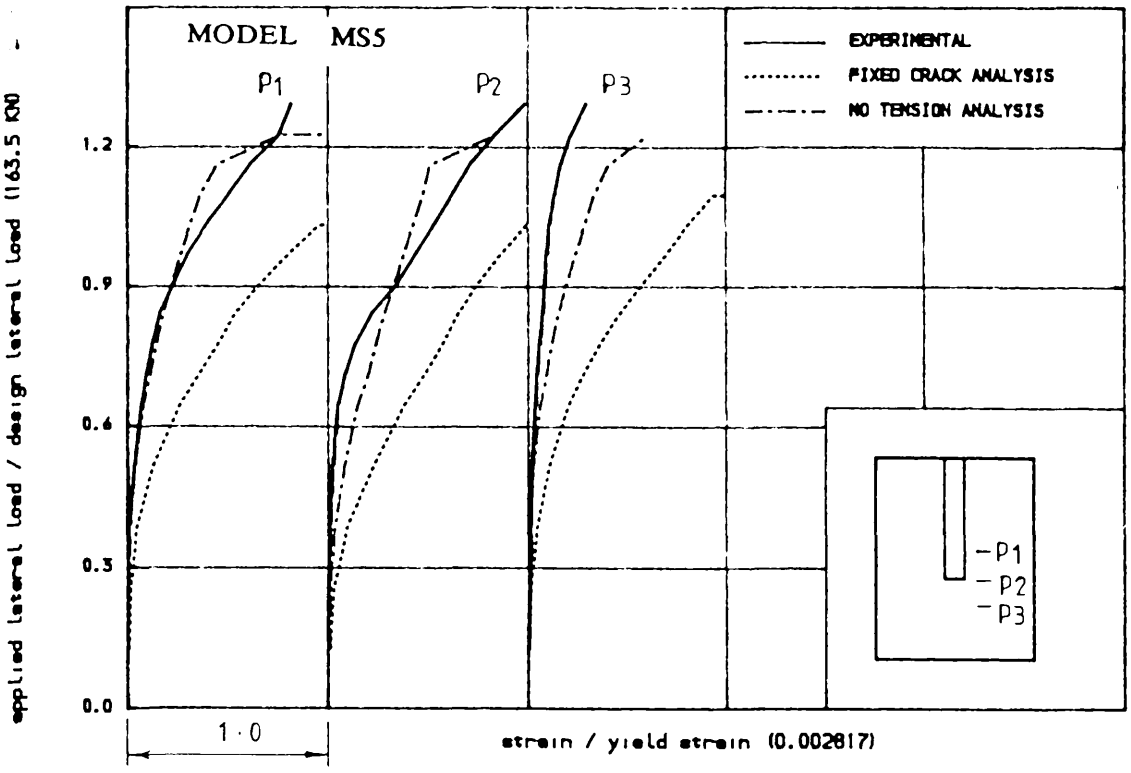

FIGURE (7.79) : TENSILE STRAIN IN CLOSED VERTICAL STIRUP AT DIFFERENT LOCATIONS IN THE SLAB OF MODEL MS5

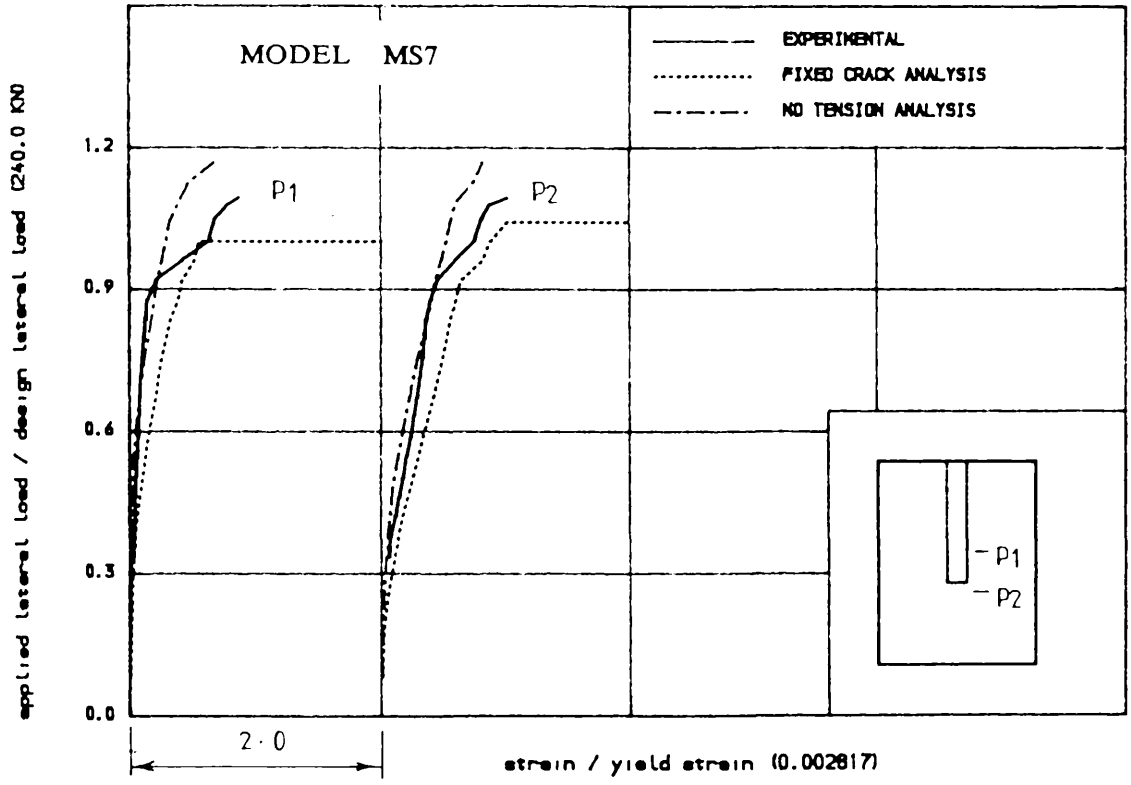

FIGURE (7.80) : CRITICAL STUDY OF FIXED CRACK ANALYSIS AND NO TENSION ANALYSIS ON TENSILE STRAIN IN CLOSED VERTICAL STIRRUP
MODEL MS7

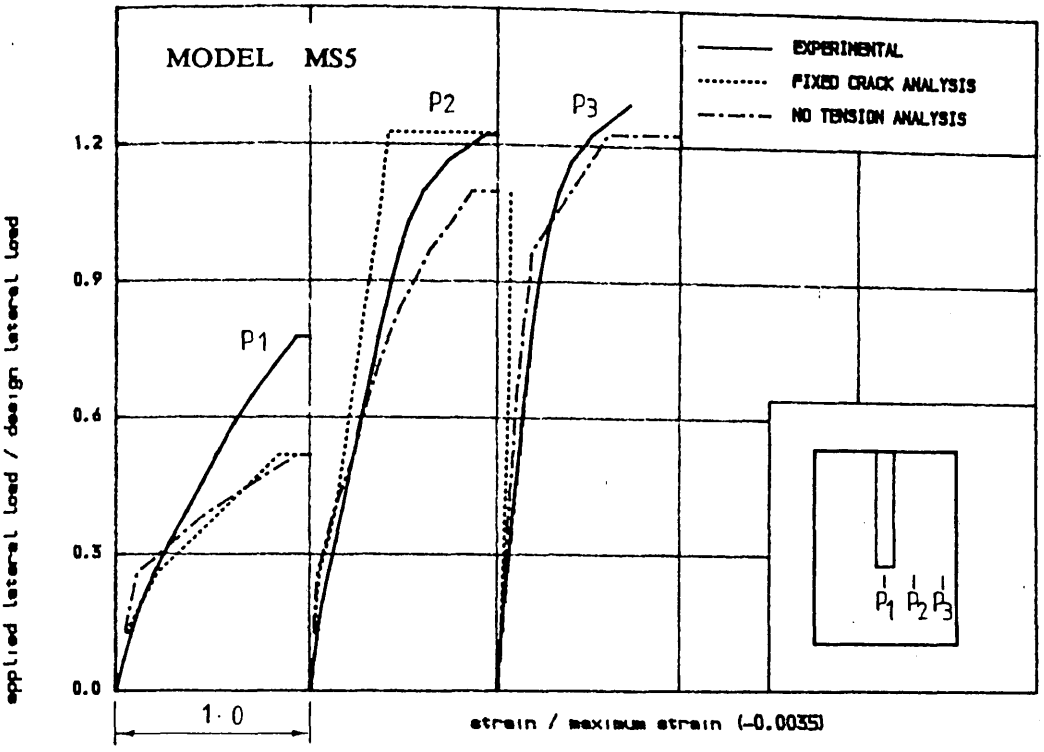

FIGURE (7.81) , COMPRESSIVE STRAIN IN CONCRETE IN WINDWARD DIRECTION IN THE SLAB OF MODEL MS5

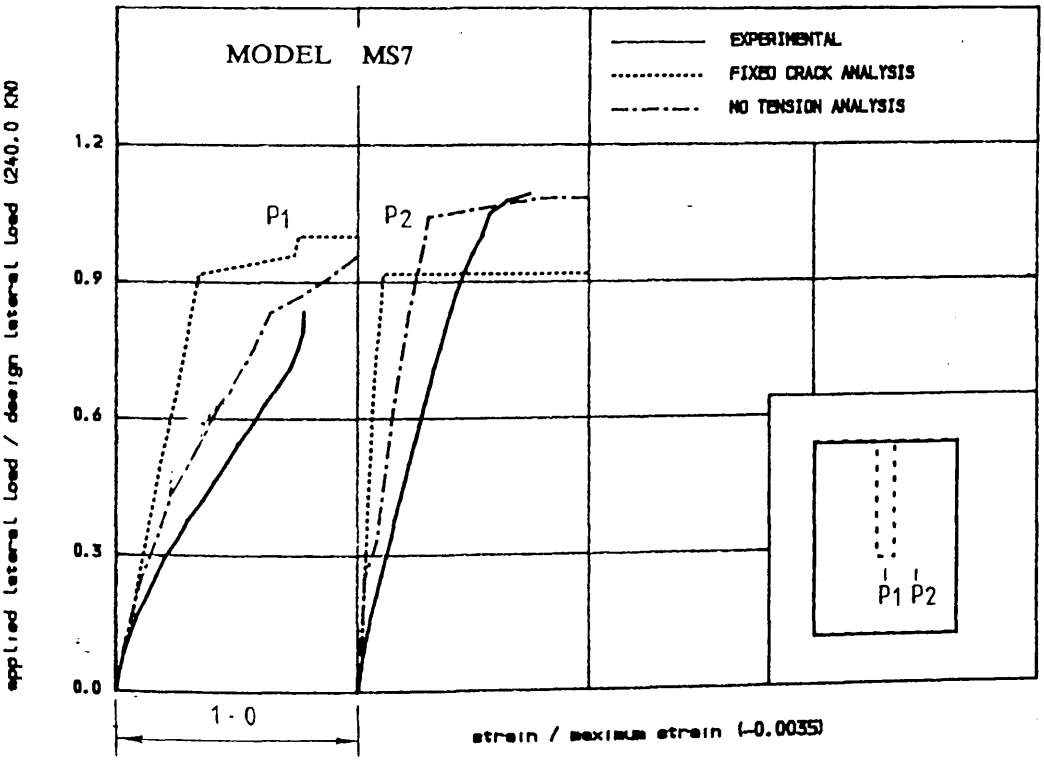

FIGURE (7.82) , COMPARATIVE STUDY OF FIXED CRACK ANALYSIS AND NO TENSION ANALYSIS ON COMPRESSIVE STRAIN IN CONCRETE , MODEL MS7

curves for shear reinforcement (closed vertical stirrup) analysed by No– tension analysis. The contour lines of vertical shear stresses which will be described in next section do support this lower theoretical strains in stirrups in No– tension analysis. This analysis shows better agreement for strains in stirrup with experimental results than fixed crack analysis. Figures (7.81) and (7.82) also show better agreement between experimental and No– tension analysis for the compressive strain in concrete.

7.9 Distribution of Shear Stresses in the Post – Cracking Range

Shear stresses in slab play an important role in the strength of slab– wall connections. The vertical shear stress components (i.e. τ_{yz} and τ_{zx}) are major factors to be considered in predicting the punching failure of the slab. One of the objectives which led to the development of a computer programme for three dimensional non– linear finite element analysis was to include the effect of shear stresses in the assesment of the failure of the junction.

To build confidence in the accuracy of the results obtained from the finite element programme, the distribution of vertical shear stresses τ_{zx} over the depth of the slab at different loading stages is presented in Figure (7.83) for model PS1. Sixteen element mesh with two elements along the depth were considered for that purpose. The figure shows more or less parabolic distribution of shear stress which was as expected.

For some of the models, contours of shear stress were considered to study 'stress distribution pattern' around the wall– slab junction as the loading progressed. Contour lines of vertical shear stresses τ_{zx} and τ_{yz} at the Gauss points in the compressive side of the slab (using eight element mesh with one element along the depth) will be shown. Only half the slab will be shown as in Figure (7.84), where the wall is represented by its centre line AC.

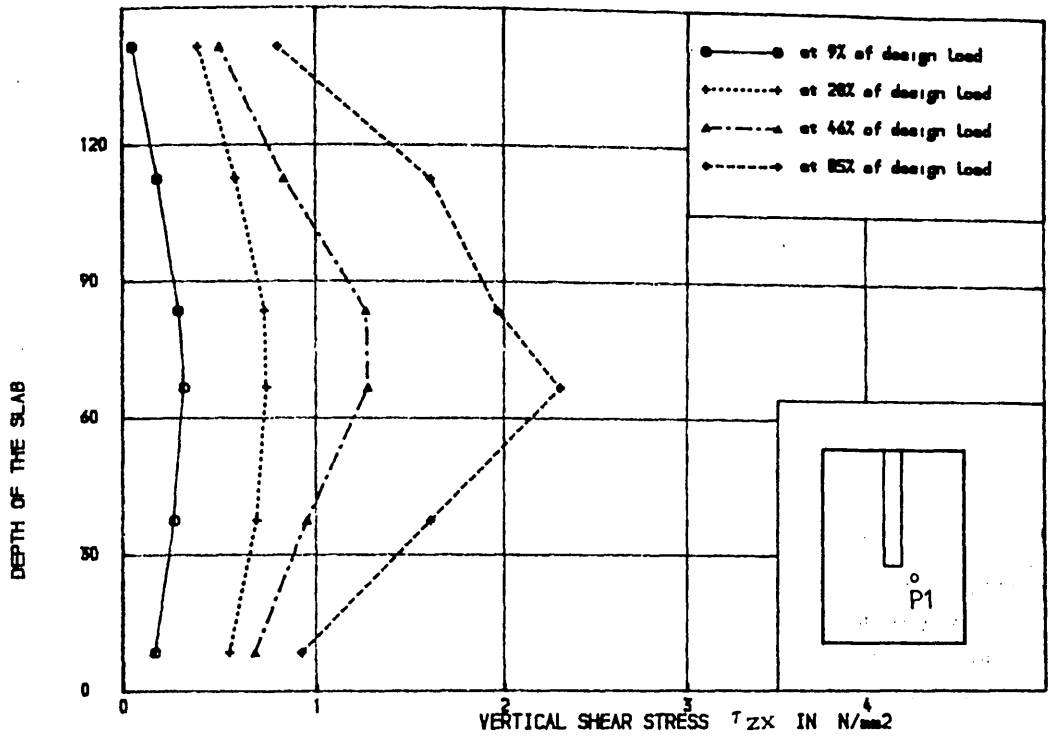

FIGURE (7.83) : VARIATION OF VERTICAL SHEAR STRESS τ_{zx} AT POINT P1 ALONG THE DEPTH OF SLAB OF MODEL 'PS1' AT DIFFERENT STAGES OF LOADING

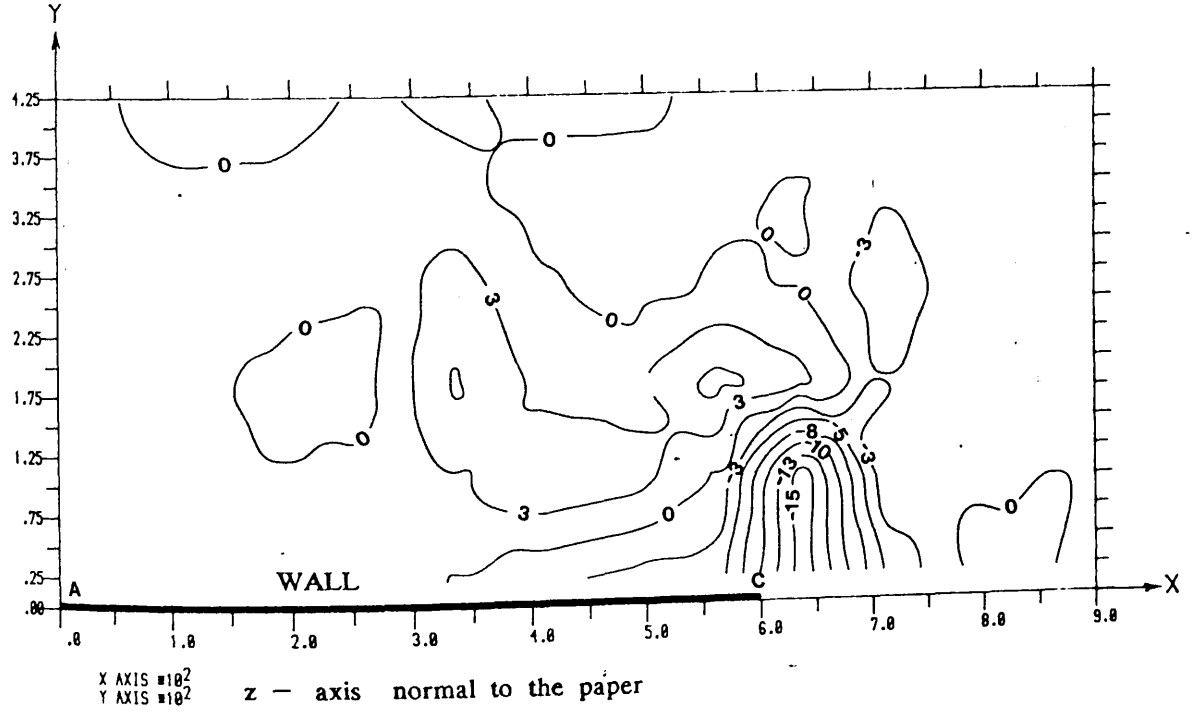

Figure (7.84) : Contour lines of shear stress τ_{zx} (N/mm^2) in the slab of model MS6 without considering any shear steel in the slab and using Fixed crack analysis at a lateral load 0.73 of design load.

Contours of vertical shear stresses obtained by Fixed crack analysis and No– tension analysis are presented in Figures (7.85) to (7.94) for models MS6 and MS7. Contours are also plotted for model MS6 without considering the shear reinforcement in the slab as shown in Figure (7.84). Use of shear reinforcement in the slab changes only a little the distribution of shear stress as shown by contour lines from Figures (7.84) and (7.85). From these figures it is clear that the shear stress distribution pattern obtained by No– tension analysis is completely different from that obtained by fixed crack analysis. The magnitude of verical negative shear stress values in No– tension analysis contours are much lower than those values in fixed crack analysis contours. Contours of some positive shear stresses are found in No– tension analysis at the back of the slab, whereas no such lines were found in fixed crack analysis.

Observing the contour lines by fixed crack analysis of shear stress τ_{zx} in the slab of model MS7 at the three loading stages, it is noticed that the area around the wall nose is found to be highly stressed, which is the critical area for punching failure. Contour lines of τ_{zx} plotted from No– tension analysis show that not only the wall nose is highly stressed but the stresses are redistributed all over the slab. The point of maximum positive shear stress τ_{zx} at the back of the slab, is found at a distance 2d beyond the nose of the wall at all stages of loading. The point of maximum negative shear stress is found in the corridor area at a distance 'd' from the nose of the wall at early stage of loading. At later stage of loading that point comes nearer to the nose of the wall at a distance only d/4.

To illustrate progressive redistribution of shear stress τ_{yz} around the connection, contours of τ_{yz} obtained by fixed crack analysis are shown in Figures (7.93) and (7.94) at two different loading stages. The point of maximum negative shear stress at later loading stage is found to shift from the wall nose towards the slab edge to a point at a distance d/2 from the wall.

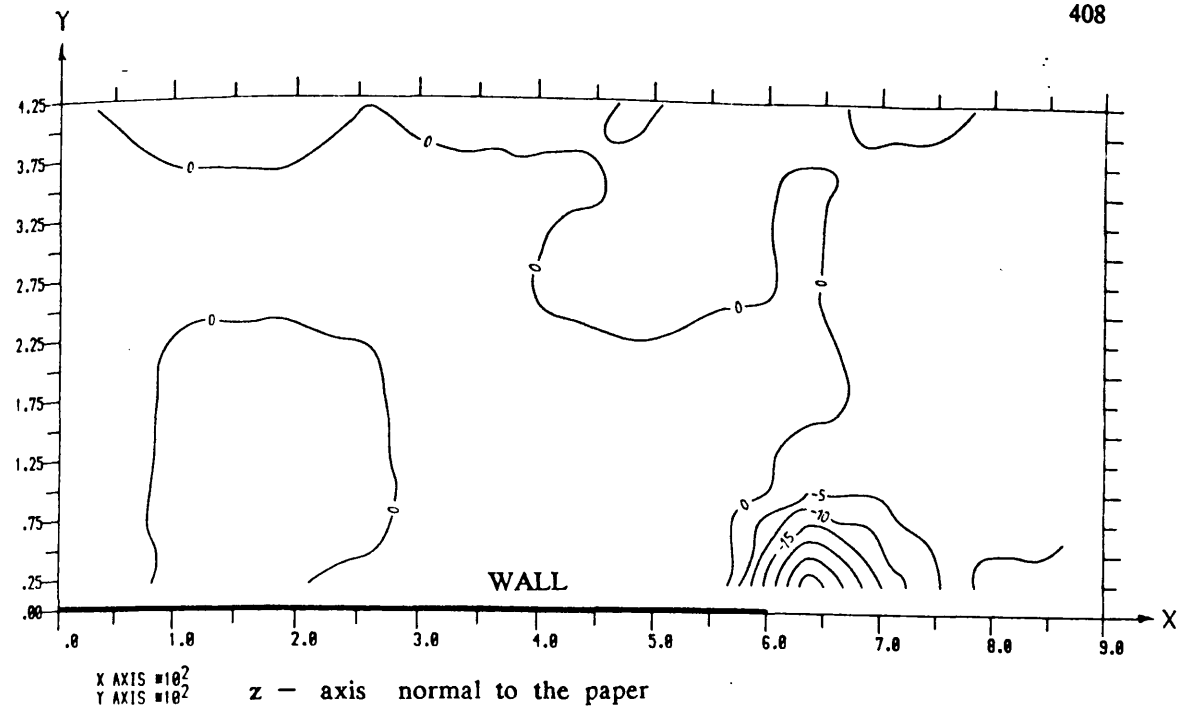

Figure (7.85) : Contour lines of shear stress τ_{zx} (N/mm²) in the slab of model MS6 using Fixed crack analysis at a lateral load 0.73 of design load.

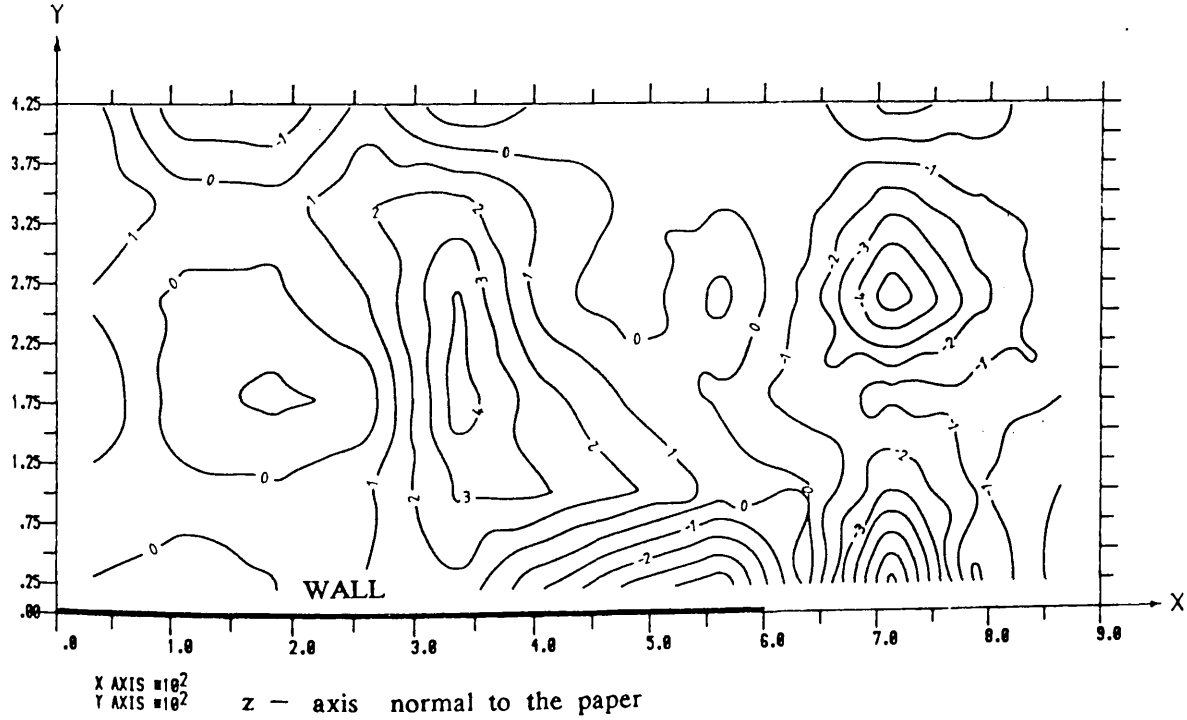

Figure (7.86) : Contour lines of shear stress τ_{zx} (N/mm²) in the slab of model MS6 using No–Tension analysis at a lateral load 0.73 of design load.

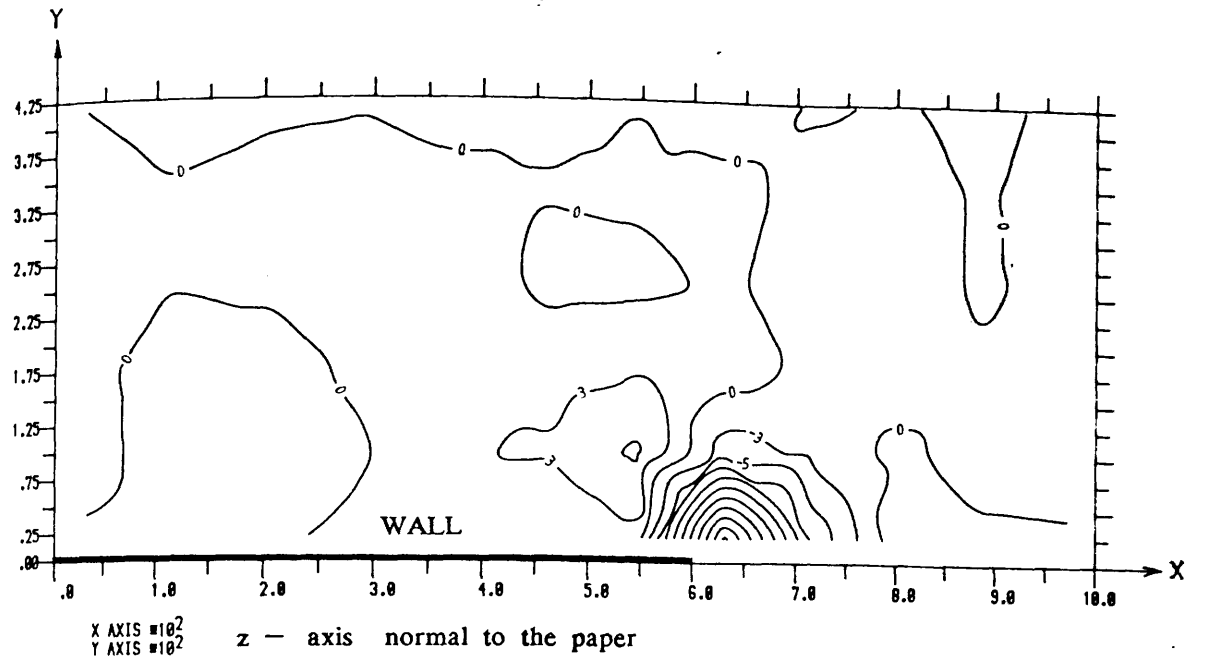

Figure (7.87) : Contour lines of shear stress τ_{zx} (N/mm²) in the slab of model MS7 using Fixed crack analysis at a lateral load 0.58 of design load.

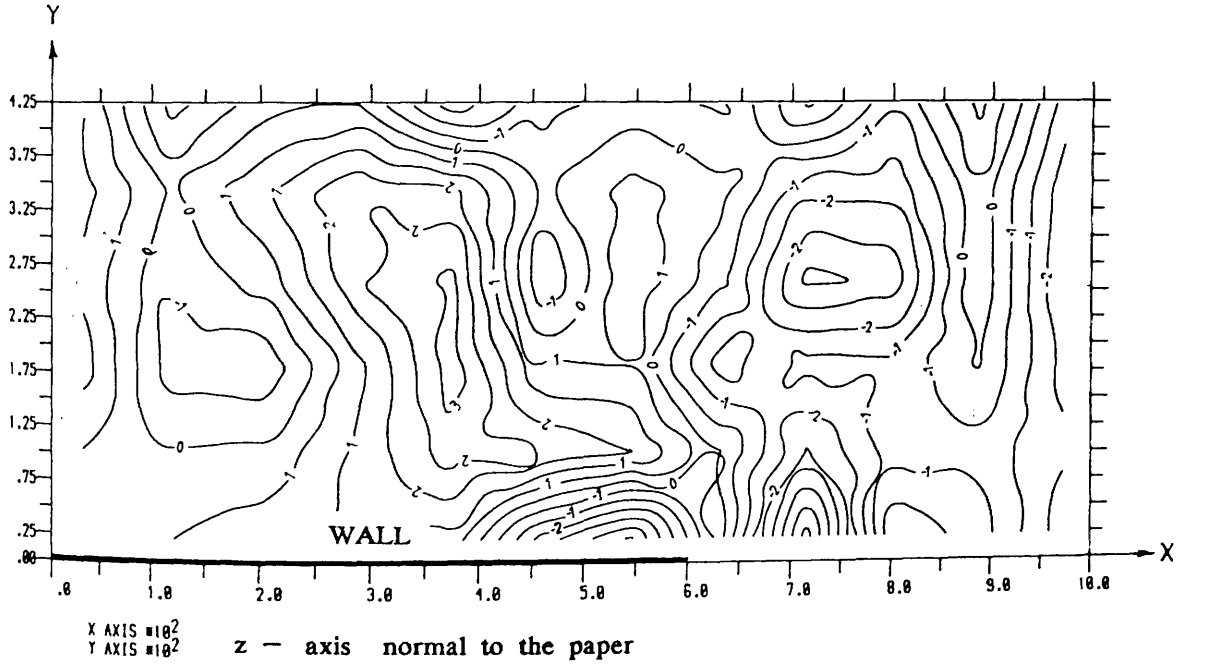

Figure (7.88) : Contour lines of shear stress τ_{zx} (N/mm²) in the slab of model MS7 using No–Tension analysis at a lateral load 0.58 of design load.

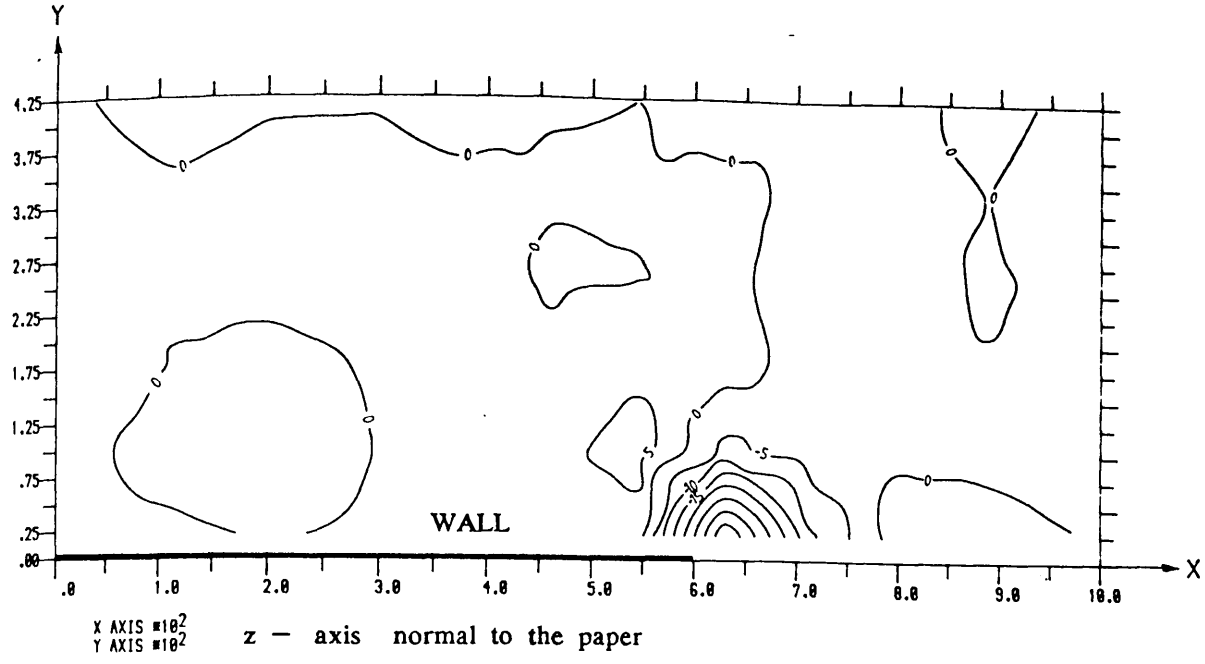

Figure (7.89) : Contour lines of shear stress τ_{zx} (N/mm²) in the slab of model MS7 using Fixed crack analysis at a lateral load 0.83 of design load.

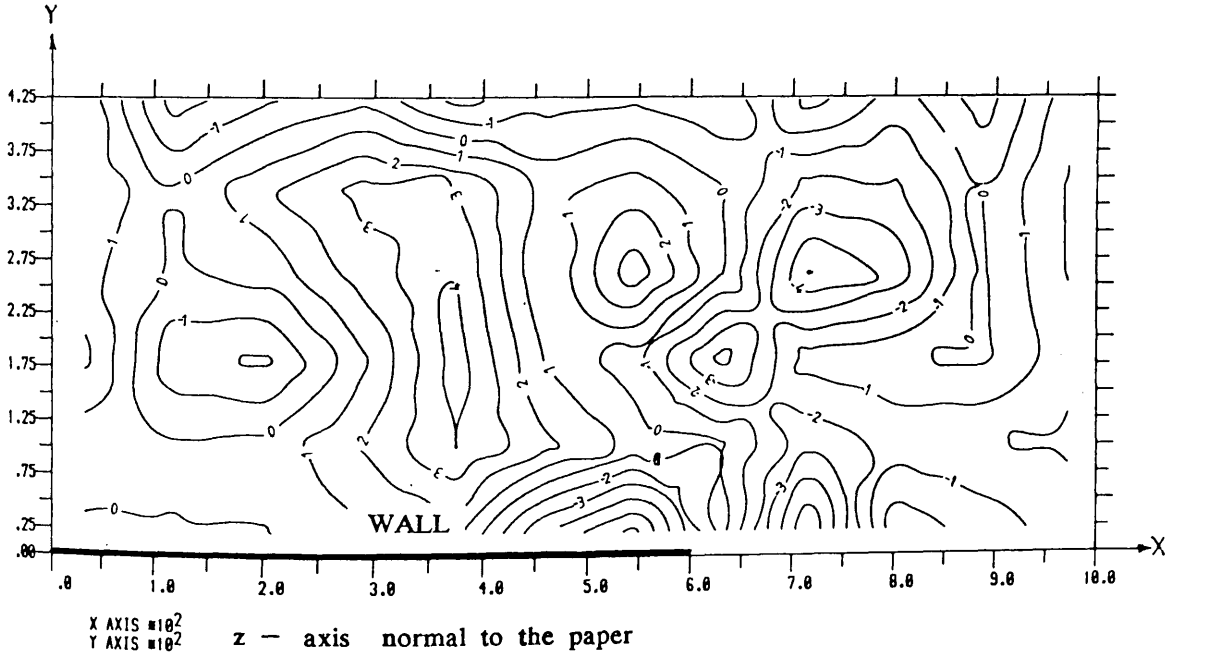

Figure (7.90) : Contour lines of shear stress τ_{zx} (N/mm²) in the slab of model MS7 using No–Tension analysis at a lateral load 0.83 of design load.

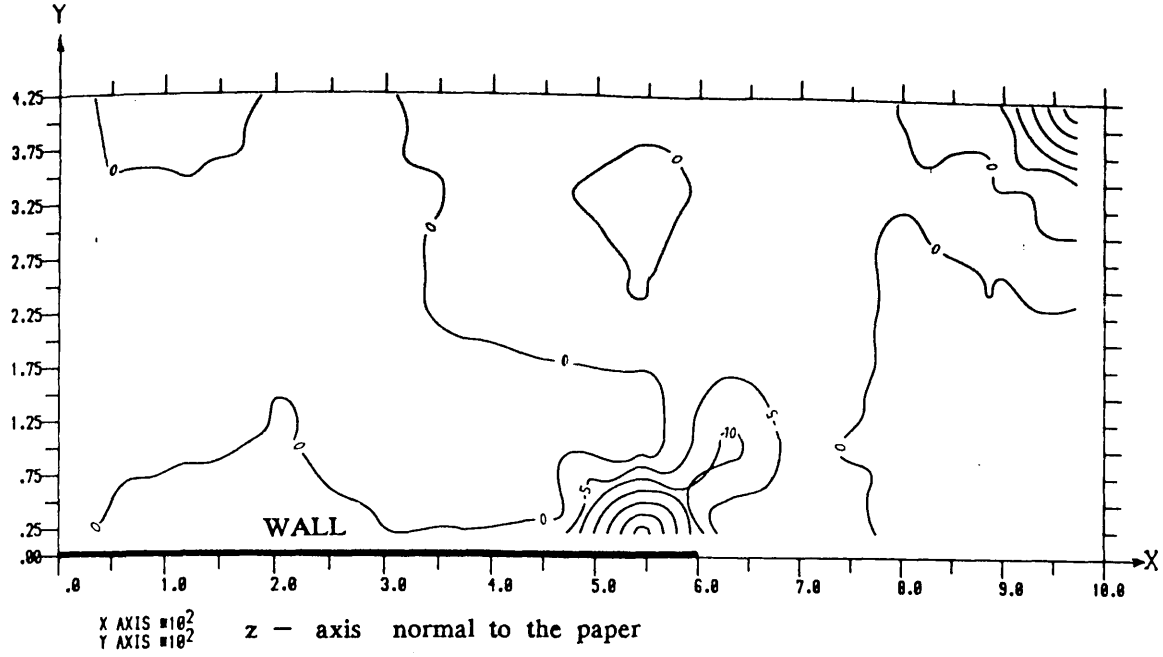

Figure (7.91) : Contour lines of shear stress τ_{zx} (N/mm²) in the slab of model MS7 using Fixed crack analysis at a lateral load 1.04 of design load.

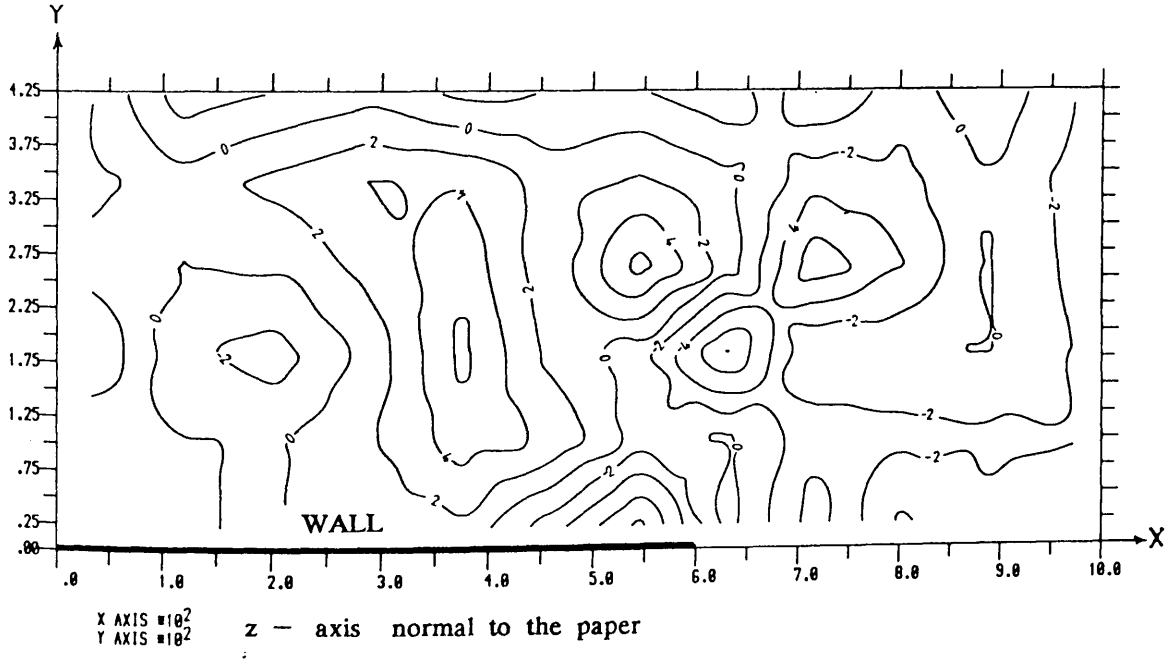

Figure (7.92) : Contour lines of shear stress τ_{zx} (N/mm²) in the slab of model MS7 using No– Tension analysis at a lateral load 1.04 of design load.

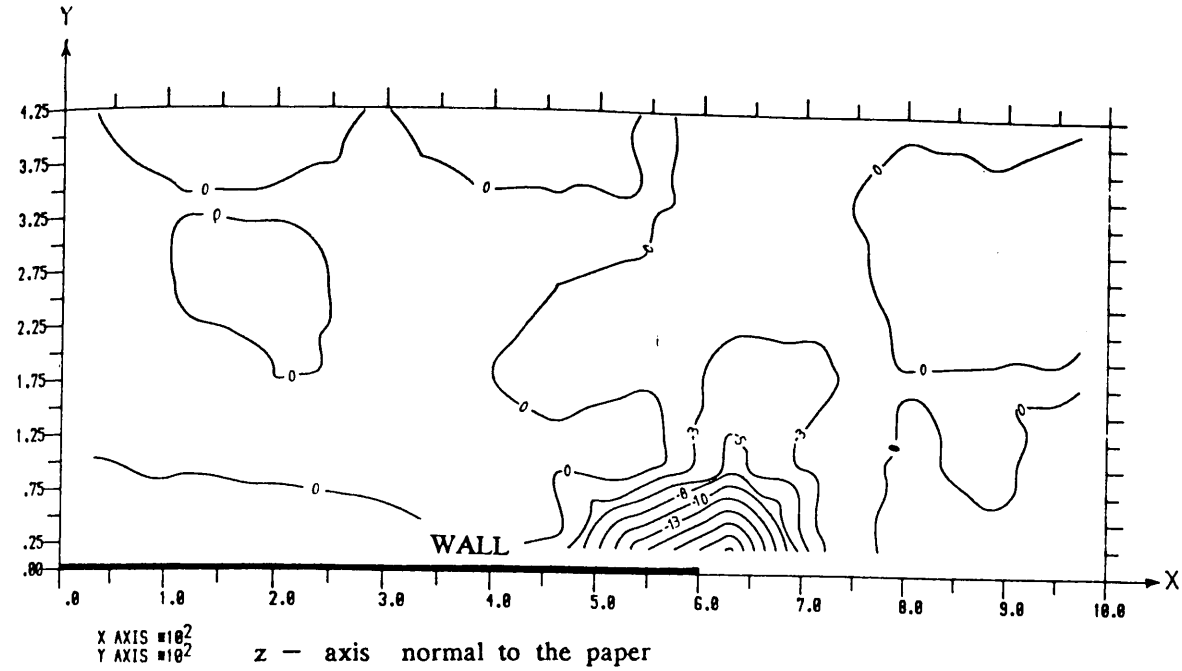

Figure (7.93) : Contour lines of shear stress τ_{yz} (N/mm²) in the slab of model MS7 using Fixed crack analysis at a lateral load 0.83 of design load.

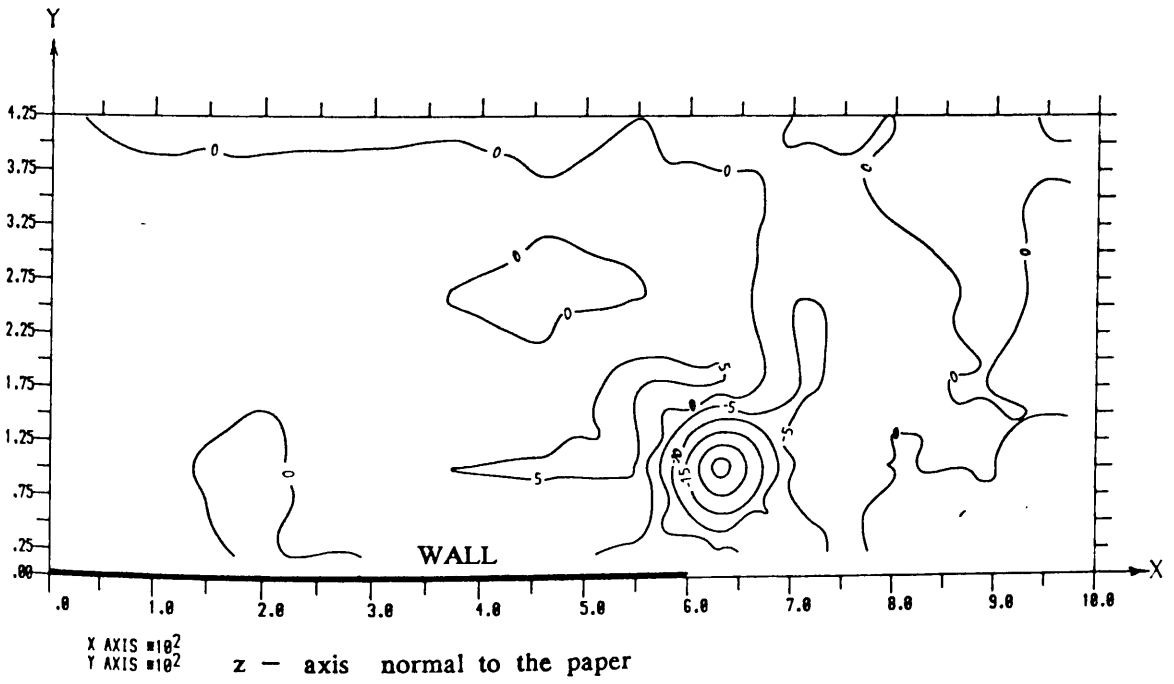

Figure (7.94) : Contour lines of shear stress τ_{yz} (N/mm²) in the slab of model MS7 using Fixed crack analysis at a lateral load 1.04 of design load.

7.10 Theoretical Crack Pattern and the Progress of Failure in Steel and Concrete

In order to compare the crack pattern obtained by theoretical analysis with the experimental one, cracks which occurred in those sampling points located in the tension side of the slab are used. Such crack pattern is obtained for models MS6 and MS7 and may be compared with the experimental one in Figures (7.95) and (7.96). Because only eight elements were used in theoretical analysis, the number of stress sampling points in the tensile region is not large; therefore the resulting crack pattern is crude. But inspite of this crudeness those cracks in Figures (7.95) and (7.96) may be compared satisfactorily with the experimental one.

It has been mentioned in chapter three that the direct design method requires that the steel in slab should yield at sufficient number of points with minimum amount of redistribution of stresses in slab thus converting it into a mechanism. In all the models, local yielding of steel started from a point very close to the wall nose. At ultimate loads in most of the models, the steel in the main direction along the transverse critical section yielded only in two out of four elements. Figure (7.97) shows step by step yielding of longitudinal steel in different elements of the slab of model MS7 as the loading progressed. From this figure it can be observed that the local yielding of the longitudinal steel near the inner edge of the wall started when the applied load was only 58% of the flexural design ultimate load. However the average strain in element No. 5 reached its yield value when the applied load was equal to 69% of deisgn load, while in element No. 6 steel yielded at 95% of design load. Figure (7.98) shows step by step yielding of transverse steel in different elements of the slab of same model MS7 as the loading progressed. From those figures it can be concluded that some redistribution of streeses has taken place before steel in sufficient number of elements yielded. The reason of not yielding the steel of most of the elements even at ultimate failure load was that the area of steel provided in those elements of the slab were

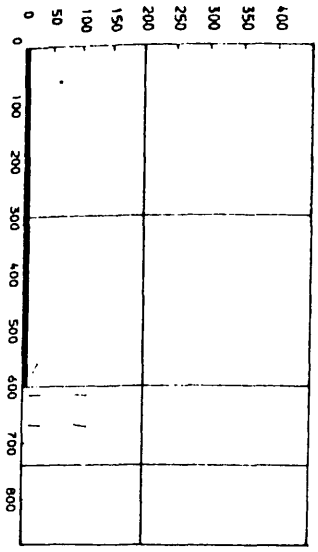

(a) at 6.1%

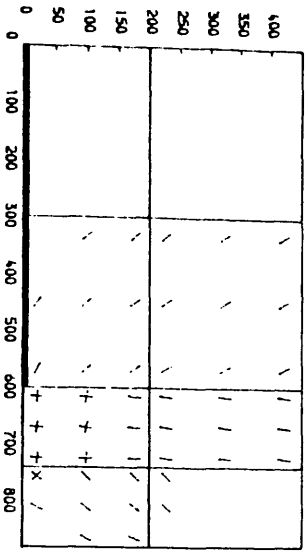

(b) at 12.2%

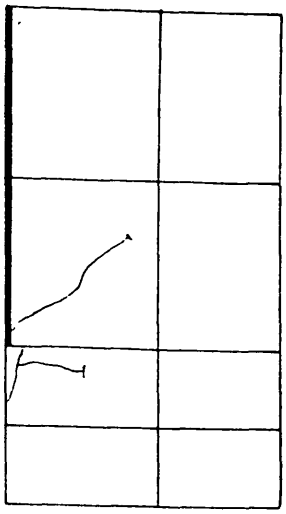

(c) at 20%

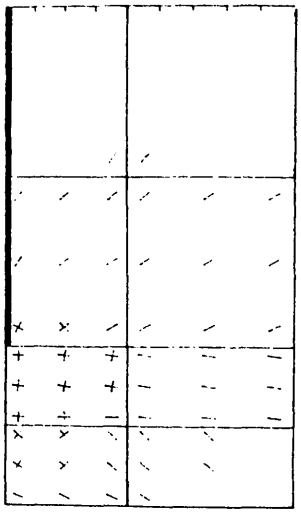

(d) at 18.3%

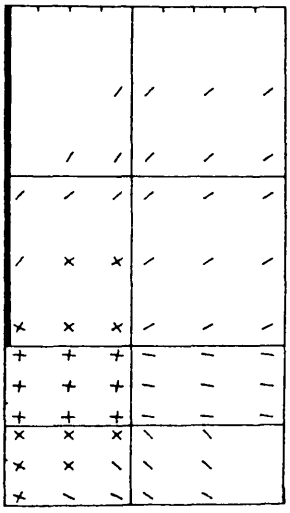

(e) at 24.4%

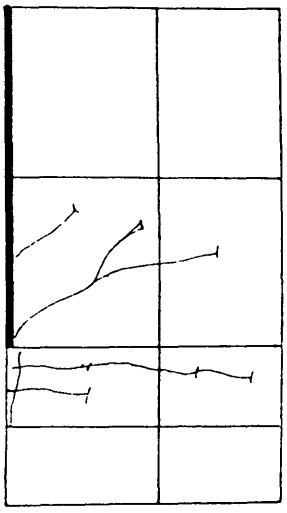

(f) at 27%

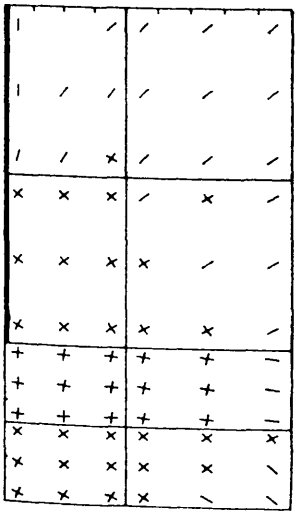

(g) at 60.6%

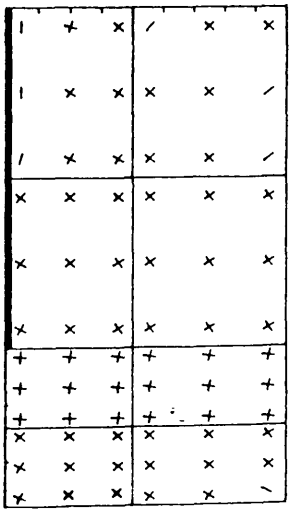

(h) at 97.0%

(i) at failure

| Single crack
+ Double crack

Figure (7.95) : Comparison betwen theoretical and experimental crack patterns in the slab of model 'MS6' at different percentages of design lateral load.

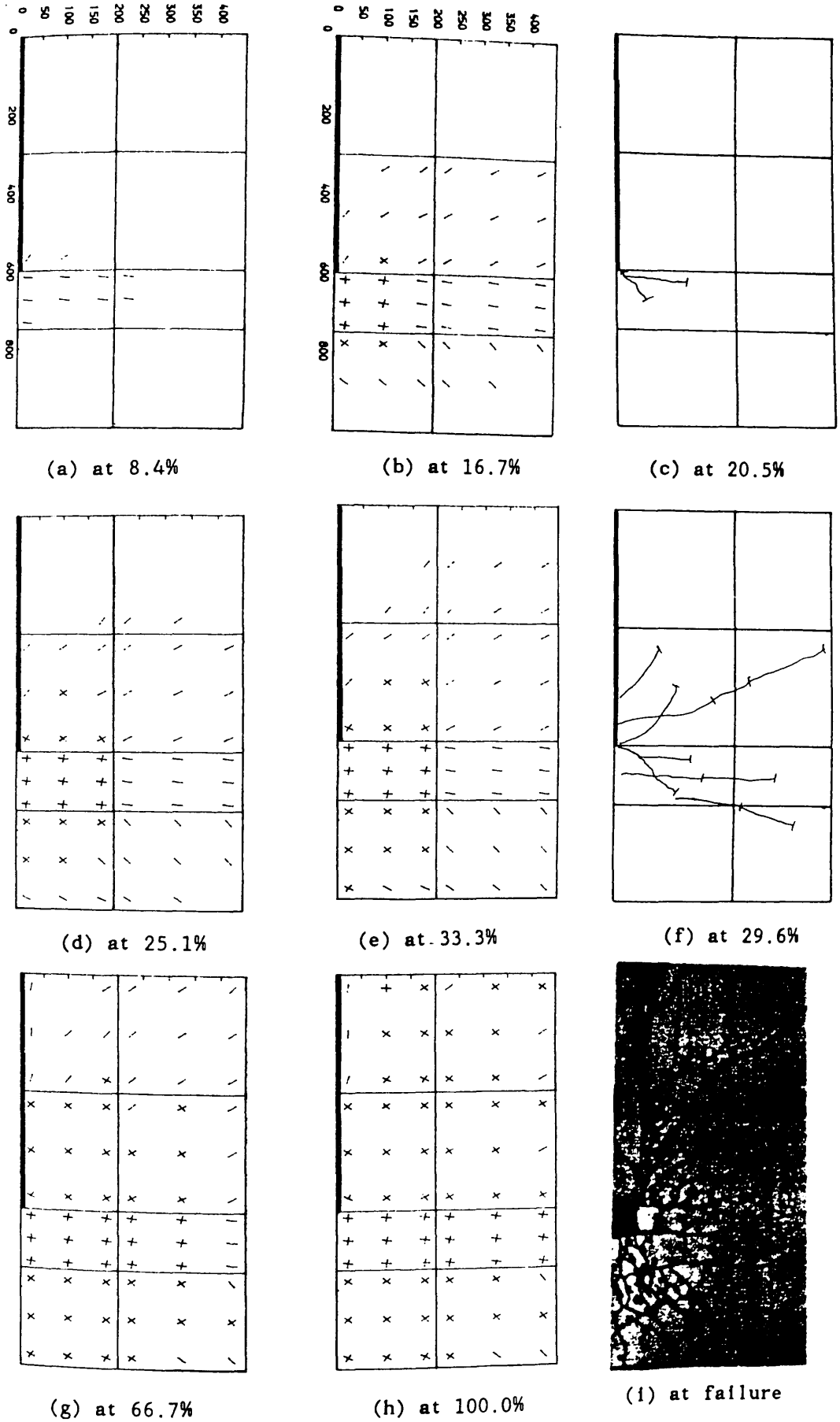

Figure (7.96) : Comparison betwen theoretical and experimental crack patterns in the slab of model 'MS7' at different percentages of design lateral load.

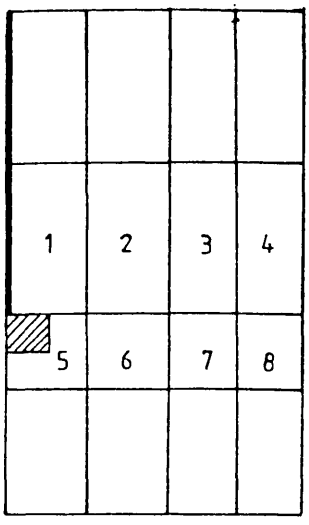

(a) at 58%

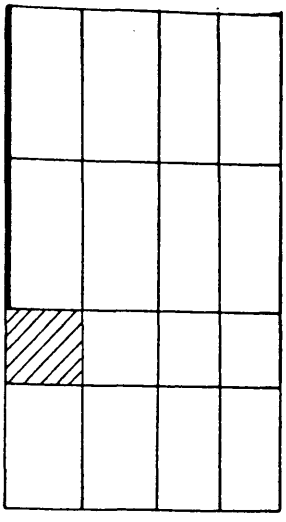

(b) at 69%

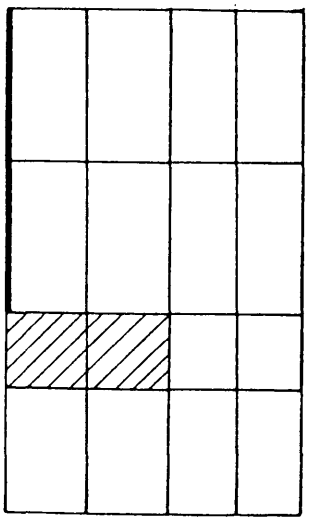

(c) at 91%

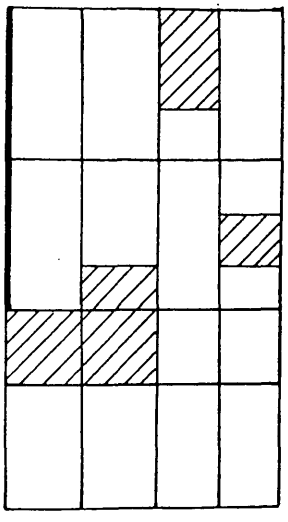

(d) at failure

Figure (7.97) : Step by step yielding of longitudinal steel in different elements of the slab of model 'MS7' at different percentages of design lateral load.

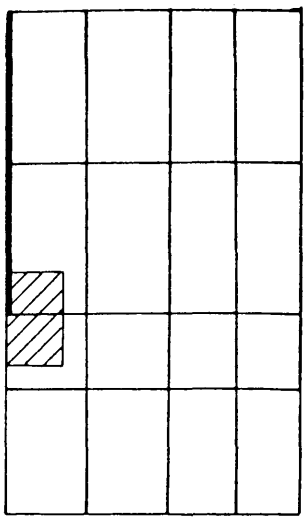

(a) at 82%

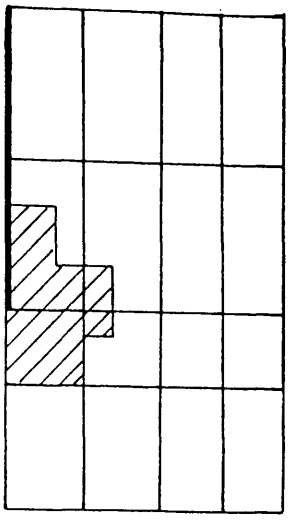

(b) at 96.6%

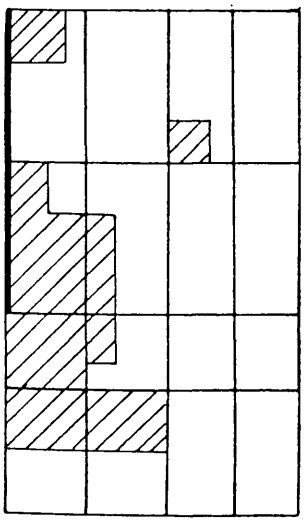

(c) at 105%

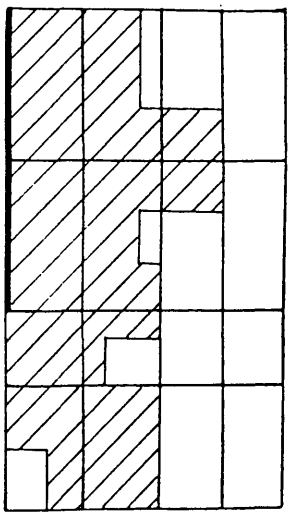

(d) at failure

Figure (7.98) : Step by step yielding of transverse steel in different elements of the slab of model 'MS7' at different percentages of design lateral load.

higher than that required to resist the design lateral load (for example see figure (3.18)).

In order to observe the progress of failure of concrete in the slab, the theoretical results from nonlinear fixed crack analysis were used. In the compressive side of the slab, the region surrounding a Gauss point fails when that gauss point suffers from a crushing situation. As the loading increases, crushing spreads out to other Gauss points in the slab. The sequence of this spreading indicates the progress of failure in concrete. The sequence of that spreading for models MS6, MS12 and MS9 are presented in Figures (7.99) to (7.101) from which it is clear that once the area near the wall fails; failure spreads quickly through the slab indicating the collapse of the slab–wall junction. This progress of failure in concrete can be used in chosing the critical section for the wall–slab connection.

7.11 Development of design equation for predicting Punching shear strength of Shear wall – floor slab connections

7.11.1 General

As noted in chapter two, there is as yet no fully satisfactory and comprehensive theory of punching for slab–wall connections. The proposals made here are therefore empirical. The problem under investigation bears some resemblance to the strength of slab–edge column connections in flat slab structures. The only difference arises from the length of the wall which is much greater than the width of the corresponding column. Code recommendations on the calculation of punching strength of slab–column connections differ in regard to the distance from the column faces to the critical perimeter, and in the expression used to define the limiting value of the stress.

When the perimeter is drawn close to the column the corresponding stresses are very high. If the perimeter is moved outward, the stresses reduce. In BS 8110, the critical section is defined as being at a distance equal to 1.5d, where d is the

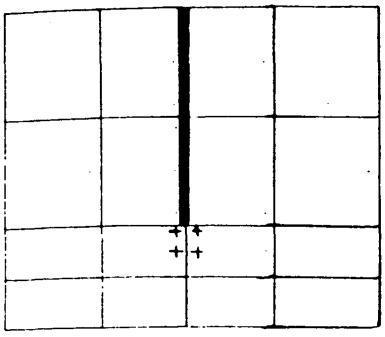

(a) at 26.6%

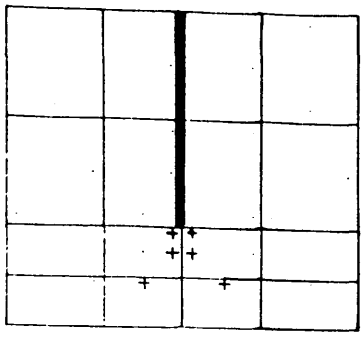

(b) at 80%

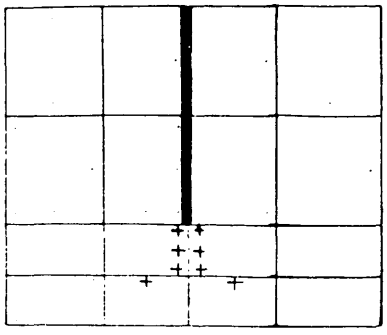

(c) at 86.6%

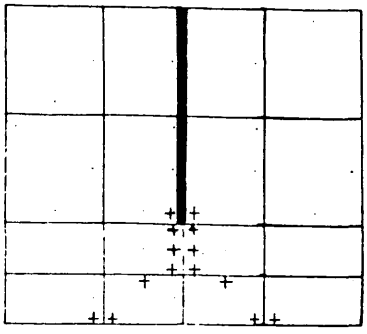

(d) at 96.7%

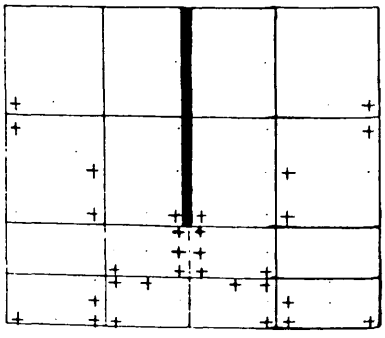

(e) at 100.0%

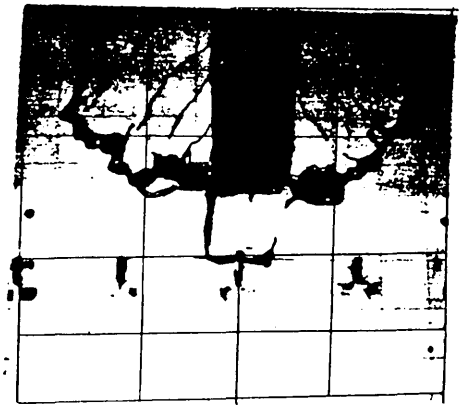

(f) at failure Experimental

Figure (7.99) : Step by step failure in concrete in the compressive side of the slab of model 'MS6' at different percentages of design lateral load.

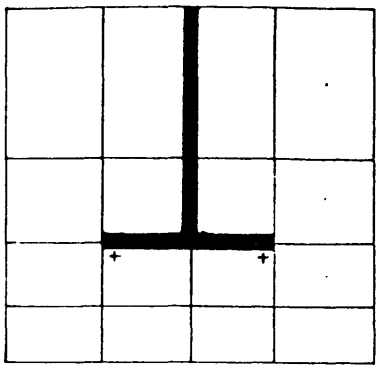

(a) at 57%

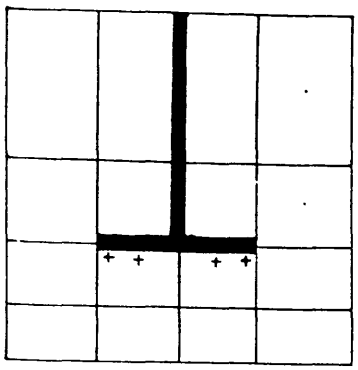

(b) at 85%

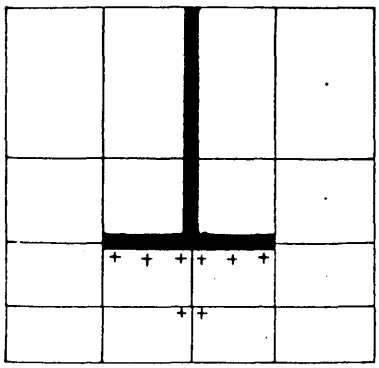

(c) at 95%

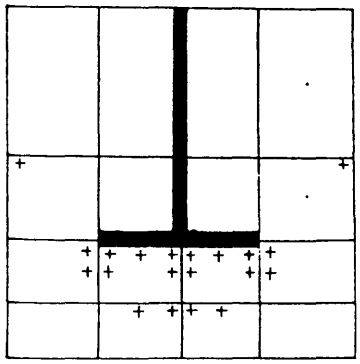

(d) at 100.0%

Theoretical

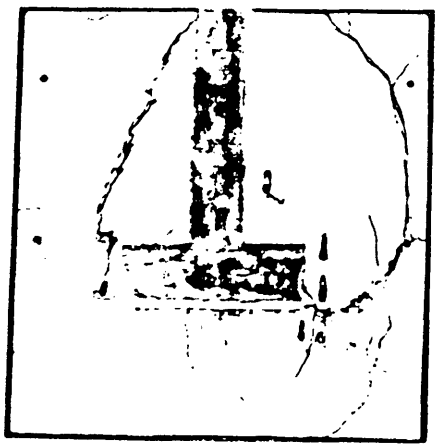

(e) at failure Experimental

Figure (7.100) : Step by step failure in concrete in the compressive side of the slab of model 'MS12' at different percentages of design lateral load.

effective depth of slab. In ACI 318−83, the critical perimeter is located at a distance d/2 from the column faces.

The proposed method is, in fact, based on the shear criteria of failure in which punching is assumed to occur when the shear stress around a critical perimeter reaches a limiting value. The shear capacity is estimated from the product of three terms − a critical area term, a critical shear stress term, and a moment transfer reduction factor.

In proposing the following design method for predicting the punching shear strength, the following considerations were kept in mind :

i) It should show consistent and accurate predictions in relation to the experimental data for all the models with and without flanges with low standard deviation.

ii) It should be simple to use, rather than based on a sophisticated method of analysis.

iii) It should be easily adaptable to cover the use of shear reinforcement (closed vertical stirrups).

7.11.2 Choice of critical punching shear area term

In the experimental investigation reported in References (23) and (24), it was shown that most of the models without shear reinforcement suffered brittle failure by punching shear but models with properly designed shear reinforcement suffered ductile failure as discussed in chapter six.

It was found from the experimental investigation that the critical perimeter for punching failure was at a distance d/2 in the corridor area from the inner edge of the wall, for both plane and flanged shear wall−floor slab connections. For models with plane shear walls, it was suggested that[23] the dimension C_1 of critical

section(see Figure (2.38)) parallel to the wall should be around 3.5 times the thickness of the wall for fully effective critical perimeter. For models with flanged shear walls, the critical section behind the flanges extends at an acute angle to the wall– web. The extent up to which this section extends behind the flange was investigated both experimentally and theoretically by Elnounu [24]. He found that this angle of inclination increases with the flange width.

Based on Elnounu's recommendation, a typical shape of the critical section is shown in Figure (7.102). The thickness of the wall is assumed as flange width for the models with plane walls. The properties of this section are:

Z = flange width for models with T– section shear walls

= equal to wall thickness for plane models

t_f = flange thickness

t_w = web thickness

W = wall web length

d = effective depth of tension reinforcement

$p = Z + d$

$q = t_f + d/2$

$$x/Z = 4.0\ e^{-0.465(Z/tw)} \qquad (7.3)$$

x = distance behind flange up to which the critical section extends,

r = length of inclined portion of the section

$= x^2 + (p - t_w)^2/4$

$$C_1 = [\ q^2 + r(x + 2q)]/[p + 2(q + r)] \qquad (7.4)$$

$C_2 = q + x - C_1$

where C_1 , C_2 determine the location of neutral axis

bp = length of critical perimeter

$= p + 2(r + q)$

A_{cp} = area of critical perimeter

$$= d\ .\ bp \qquad (7.5)$$

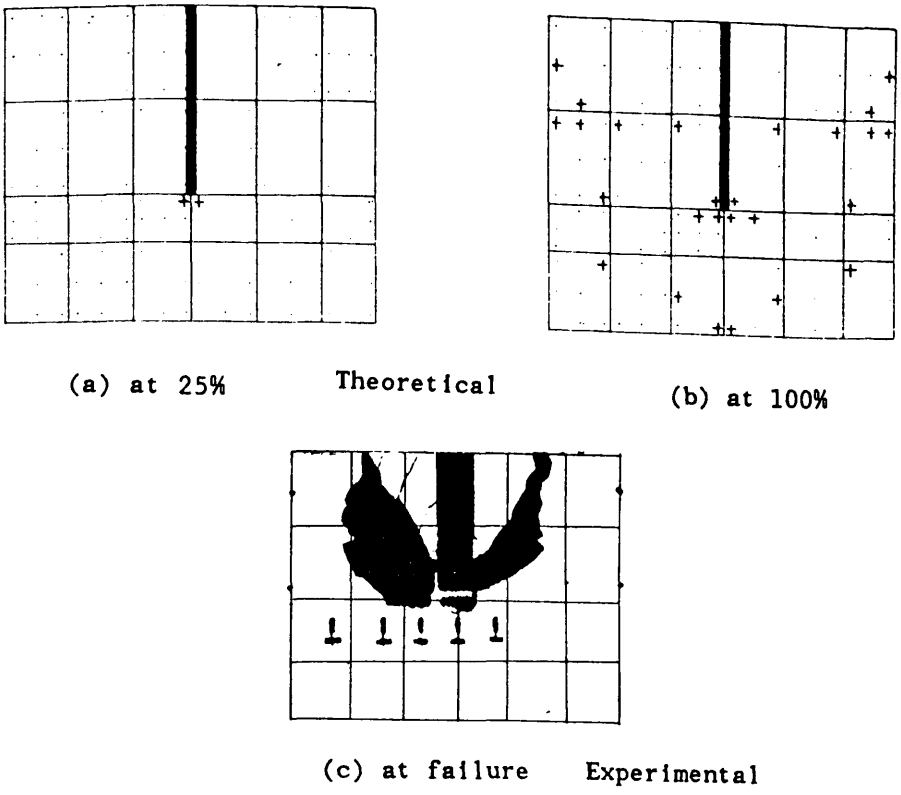

(a) at 25% Theoretical (b) at 100%

(c) at failure Experimental

Figure (7.101) : Step by step failure in concrete in the compressive side of the slab of model 'MS9' at different percentages of design lateral load.

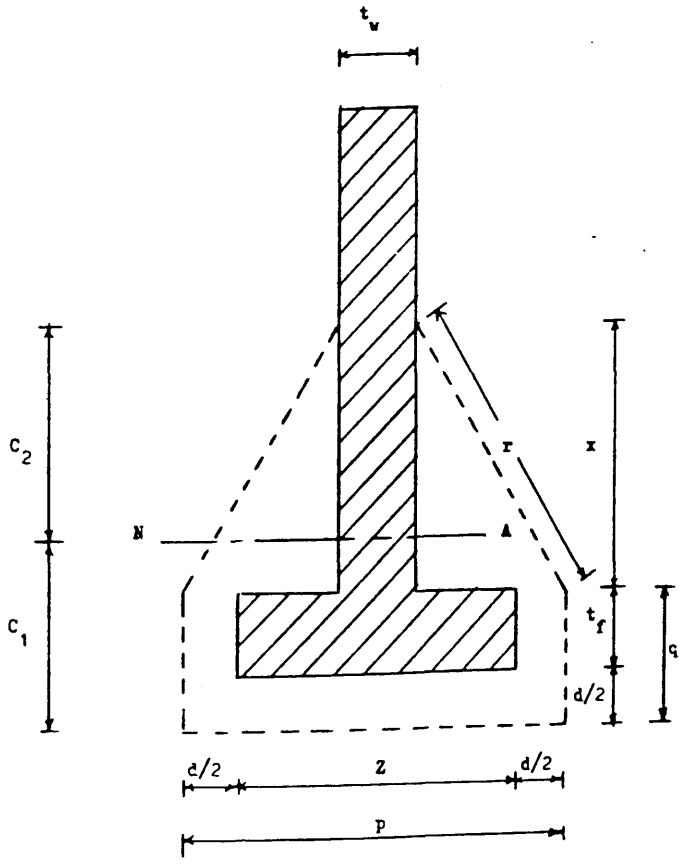

Figure (7.102) : Proposed critical section.

J = similar to the polar moment of inertia

$$= d\, C_1 \left[p\, C_1 + q(C_1 - q/3) + \frac{3xrq(C_1-q)(C_1-2q/3)+2r^2((C_1-q)^3+C_2^3)}{3x(xq+r(C_1-q))} \right] \quad (7.6)$$

7.11.3 Choice of critical shear stress term

In the light of the study presented in chapter two, the shear stress value for critical section in Figure (7.102) was taken as :

$$v_c = 0.3 \left(1 + 2/R_f \right) (f_{cu})^{1/3}$$

where rectangularity factor, $R_f = (x+q)/p \geq 2.0$ (see Figure (7.102))

To incorporate the effect of flexural reinforcement, it was assumed that an increase of every 0.5% in the ratio of flexural steel in the slab above 0.8%, the calculated value of v_c should be increased by 0.05 N/mm^2. Thus

$$v_c = 0.3(1+2/R_f)\, (f_{cu})^{1/3} + 0.1\, (100As/bd - 0.8) \quad (7.7)$$

where values of (100As/bd) are calculated for width (z+3d) and

$$0.8 \leq (100As/bd) \leq 2.0$$

7.11.4 Choice of moment transfer reduction factor

Two approaches are usually adopted for punching shear capacity of slab – column connections transferring shear and unbalanced bending moment. The first approach calculates the increase in shear stress caused by moment transfer (e.g. ACI) and then compares it with the permissible shear value. The second approach calculates the punching capacity for no moment transfer and then applies a reduction factor (e.g. BS 8110). The first approach is followed in this study. The net shear stress around the slab– wall junction is given by :

$$v_c = \frac{V}{A_{cp}} + \frac{K.M\, C_1}{J} \quad (7.8)$$

where $K = 1 - \dfrac{1}{1 + 1/2\sqrt{R_f}}$

$R_f = (x+q)/p$

and all other terms are as defined in section 7.11.2.

For the present study, $M = V\ L/2$. Therefore,

$$V_c = \frac{v_c A_{cp}}{1 + \dfrac{K L}{2} \cdot \dfrac{A_{cp}}{(J/C_1)}} \qquad (7.9)$$

7.11.5 Performance of proposed method

Tables (7.3) and (7.4) compare the predicted punching capacities with the actual failure loads observed in the tests as reported in Reference (23) and (24). Despite the wide ranging nature of the tests, excellent agreement exists between the experimental and calculated values for the models with plane and flanged shear walls, with the average V_{exp}/V_{cal} ratio of 1.07 and 1.02 and co-efficient of correlation of 11.0% and 4.5% respectively. Keeping in mind that no partial safety factors were incorporated, it appears that the proposed method can be used safely with the relevant safety factors.

The figures presented in Table (7.5) also reveal that the proposed method to be more accurate and consistent in its predictions than either the British or the American Code or other proposed methods, when the shear wall is treated as an edge column.

7.11.6 Extension of Proposed method to cover the use of shear reinforcement (closed vertical stirrup)

It was stated in chapter two that when shear reinforcement is placed in the slab, four different modes of failure (see Figure (2.10)) are possible in addition to flexure. When the fracture surface crosses at least some shear reinforcement, the

Table (7.3) : Predicted punching capacities for the models of plane shear wall - floor slab connections in Refernce[23]

Model	Experimental failure load V_{exp} KN	Calculated failure load V_{cal} KN	$\frac{V_{exp}}{V_{cal}}$
MT1	175.5	157.8	1.11
MT2	192.9	174.0	1.10
MT3	154.2	158.0	0.98
MT4	192.8	145.6	1.32
MT5	160.9	145.7	1.10
MT6	105.8	119.4	0.89
MT7	177.8	181.6	0.98
MT8	163.7	144.1	1.14
MT9	147.2	148.1	1.00
MT10	153.3	144.5	1.06
MT11	164.0	146.4	1.12

mean = 1.07

S.D. = 0.11

range = (0.89 - 1.32)

Table (7.4) : Predicted punching capacities for the models of flanged shear wall - floor slab connections in Refernce[24]

Model	Experimental failure load V_{exp} KN	Calculated failure load V_{cal} KN	$\frac{V_{exp}}{V_{cal}}$
MS1	150.0	149.3	1.00
MS2	140.0	149.8	0.94
MS3	150.0	149.0	1.01
MS4	120.0	128.9	0.93
MS5	132.0	130.7	1.01
MS6	130.0	129.2	1.00
MC	140.0	132.9	1.05
MZ1	109.0	105.3	1.04
MZ2	160.0	146.2	1.09
MZ3	148.0	145.4	1.02
MW1	137.0	129.1	1.06
MG1	136.0	125.2	1.09
MG2	140.0	134.7	1.04
MG3	129.0	129.0	1.00

mean = 1.02

S.D. = 0.05

range = (0.93 - 1.09)

codes of practice recommended following equations to calculate the nominal ultimate shear strength for a slab– column connection :

$$\begin{aligned} &\text{BS 8110} && Vn = V_c + V_s \\ &\text{ACI 318–83} && Vn = 1/2\ V_c + V_s \\ &\text{CEB / FIP} && Vn = 1.33\ V_c \end{aligned} \qquad (7.10)$$

where V_c is the punching strength of an otherwise similar slab without shear reinforcement and V_s is the vertical component of the sum of the forces in the shear reinforcement at yield, assumed to work together with concrete. The abscence of reliable data and the lack of information on the efficiency of the various possible forms of shear reinforcement may be appreciated from the divergencies of recent codes.

For slabs with shear reinforcement, ACI Committee 426[5] recommended that the shear stress v_n, on any column face must not exceed the larger of v_c or (1/2 v_c + v_s).

Experimental observation during the test programmee revealed that an increase of about 40% in ultimate strength can be obtained by the use of shear reinforcement in the slab. In addition, the failure mode can be changed from brittle to ductile mode, using shear reinforcement in the slab.

It can be assumed that the presence of closed vertical stirrup has no effect in the critical shear perimeter term and moment transfer reduction factor. The allowable shear stress, v_c, can be increased by 50% by the provision of closed vertical stirrup as required in the slab. So, the punching shear strength of the shear wall – floor slab connection with shear reinforcement in the slab can be calculated from :

$$V = 1.5 * V_{\text{without shear steel}} \qquad (7.11)$$

The design equation (7.11) is applicable only to the models designed according to the procedure given in chapter three of this thesis.

The predicted capacities obtained from equation (7.11) are presented in Table

(7.7) where they compare very favourably with the experimental data. The average V_{exp}/V_{cal} ratio of 1.02 and co-efficient of correlation of 9% confirm the simple changes proposed to cover the use of closed vertical stirrup. This has not led to any loss in the consistency and accuracy of the predictions.

The comparison with the British and American Code predictions summarised in Table (7.6) shows the method to give considerably more realistic estimates of the punching capacity than either of the code methods.

7.11.7 Summary of the proposed method

In order to assist the designers, empirical formulae have been developed to calculate the ultimate shear strength of junctions for both plane and flanged shear wall models. If the designer discovers that the joint is not capable of resisting the design loads, then it is necessary to use shear reinforcement. The amount of shear reinforcement should be calculated and provided in the slab according to the procedure described in chapter three. For the junctions with shear reinforcement in the slab, the ultimate shear strength can be taken as $1.5V_c$, where V_c is given by equation (7.9).

Table (7.5) : Comparison of proposed method (by author) with Code methods and methods proposed by others for the models in Reference (23) & (24) without any shear reinforcement.

Method	Plane shear wall models			Flanged shear wall models		
	mean Vexp/Vcal	Cv(%)	Range	mean Vexp/Vcal	Cv(%)	Range
BS 8110	0.82	13.6	0.59-1.06	0.86	15.4	0.61-1.21
ACI 318-83	1.20	21.0	0.78-1.60	0.71	9.3	0.63-1.02
Elnounu[24]	1.15	12.8	1.00-1.46	1.14	15.8	0.84-1.32
Memon [23]	1.35	15.0	1.20-1.70	not applicable here		
Regan [35]	1.70	19.1	1.43-2.14	not applicable here		
EQ. (7.9)	1.07	11.0	0.89-1.32	1.02	4.5	0.93-1.09

Table (7.6) : Comparison of proposed method with Code methods for the models tested in this study, using shear reinforcement in the slab.

Method	mean V_{exp}/V_{cal}	Cv (%)	Range
EQ. (7.9) (Vn=1.5 Vc)	1.02	9.2	0.85 - 1.14
ACI 318-83 ($Vn=\frac{1}{2}Vc+Vs$)	1.07	16.5	0.88 - 1.42
BS 8110 (Vn=Vc+Vs)	1.61	24.5	1.30 - 2.07

Table (7.7) : Predicted punching capacities for the series of models with shear reinforcement tested in this study.

Model	Experimental failure load V_{exp} KN	Calculated failure load V_{cal} KN	$\frac{V_{exp}}{V_{cal}}$
MS4	190.4	225.0	0.85
MS5	203.0	180.5	1.13
MS6	343.0	304.0	1.13
MS7	262.0	261.5	1.00
MS8	280.0	277.5	1.01
MS9	247.0	267.0	0.93
MS10	209.0	211.5	0.99
MS11	219.0	192.0	1.14
MS12	235.0	232.5	1.01

mean = 1.02

S.D. = 0.09

range = (0.85 - 1.14)

CHAPTER EIGHT

CYCLIC LOADING BEHAVIOUR OF WALL–SLAB CONNECTIONS

8.1 Introduction

Reliable information on strength, failure mode, ductility and energy absorption capacity of reinforced concrete structures is required for the design of important reinforced concrete structures such as nuclear containment structures and prestressed reactor pressure vessels, and shear wall building structures subjected to seismic loading conditions. Many tests [90,91,92,93] have been conducted in various countries on beam – column joints which were designed to respond inelastically to severe earthquake loads. Codified design procedures for such joints have been introduced only in the United States[94] and New Zealand[95]. Paulay and Park in their report[96] summarised the state of the art with respect to the behaviour and design of reinforced concrete beam–column joints in ductile frames for earthquake resistance design.

During an earthquake, there is a possibility of the slab–column connections failing and contributing significantly to the damage of flat–plate structures. The test programme at the University of Washington [39,40] indicated that major damage can readily be avoided by the provision of carefully detailed stirrup reinforcement in the slab. From the literatures survey reported in chapter two, very little is known about the seismic resistance of shear wall – floor slab connections. The deterioration of the load carrying capacity due to reversal of loads and the ductility and the energy absorption that is available at such junctions require a close examination. In this chapter, results are reported of tests on three 'large scale' models MRS13, MRS14 and MRS15 which were tested under combined gravity and reversed lateral loading, "simulating" earthquake effect. The detailed description of the material properties, test equipment and testing procedure used in these tests are given in chapter five.

8.2 Experimental Programme on Cyclic Loading

8.2.1 Model MRS13

The plan and dimension of this model is shown in Figure (8.1). The reinforcement used in the wall is shown in Figure (8.2). The slab of the model was designed to resist 225.0 KN of lateral load acting in the downward direction together with 18.0 KN of gravity load. Figure (8.3) shows the flexural reinforcement layout along with the arrangement of shear reinforcement in the slab. The shear reinforcement in the form of closed vertical stirrup was provided in the slab where the shear stress exceeded allowable concrete shear stress. The flexural reinforcement on both top and bottom faces were identical. This model is similar to the model MS10 which was designed for 220 KN of lateral load and tested under monotonic loading condition. The monotonic failure load of the model MS10 was 209 KN.

A downward load was first applied in increments to the model and two transducers mounted on the slab (see Figure (5.15)) measured the relative rotation between the wall and the cantilever slab. The lateral load versus steel strain curve is shown in Figure (8.3– a). The relative rotation of the slab at the onset of steel yielding as shown in Figure (8.3– b), is termed hereafter as "the yield rotation θ_y". The loading cycle used in testing the model, excluding the initial loading is shown in Figure (8.4). This loading sequence was not intended to simulate any particular earthquake but it was rather regulated by the rotation of the slab with respect to the wall to generate elastic and post– elastic loading history.

Static cyclic loading was used because of the convenience of applying this type of loading. The use of slow reversals of load to represent dynamic loading is thought to be conservative because the strength of concrete and steel increases with the increasing rates of strain.

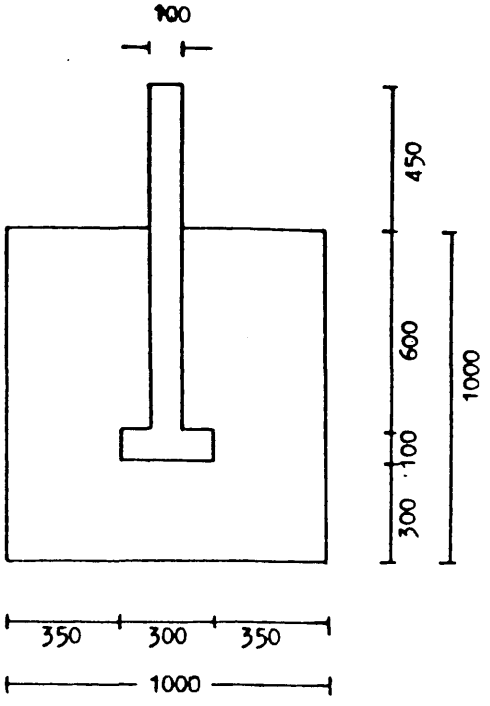

Figure (8.1) : Plan and dimensions of model MRS13

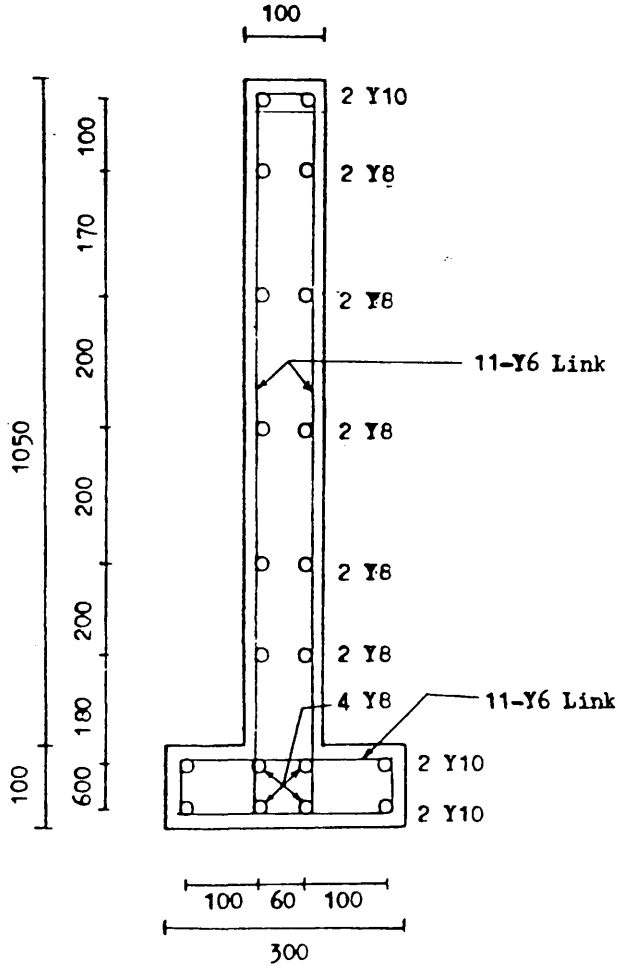

Figure (8.2) : A horizontal section in the wall of model MRS13 showing the reinforcing details

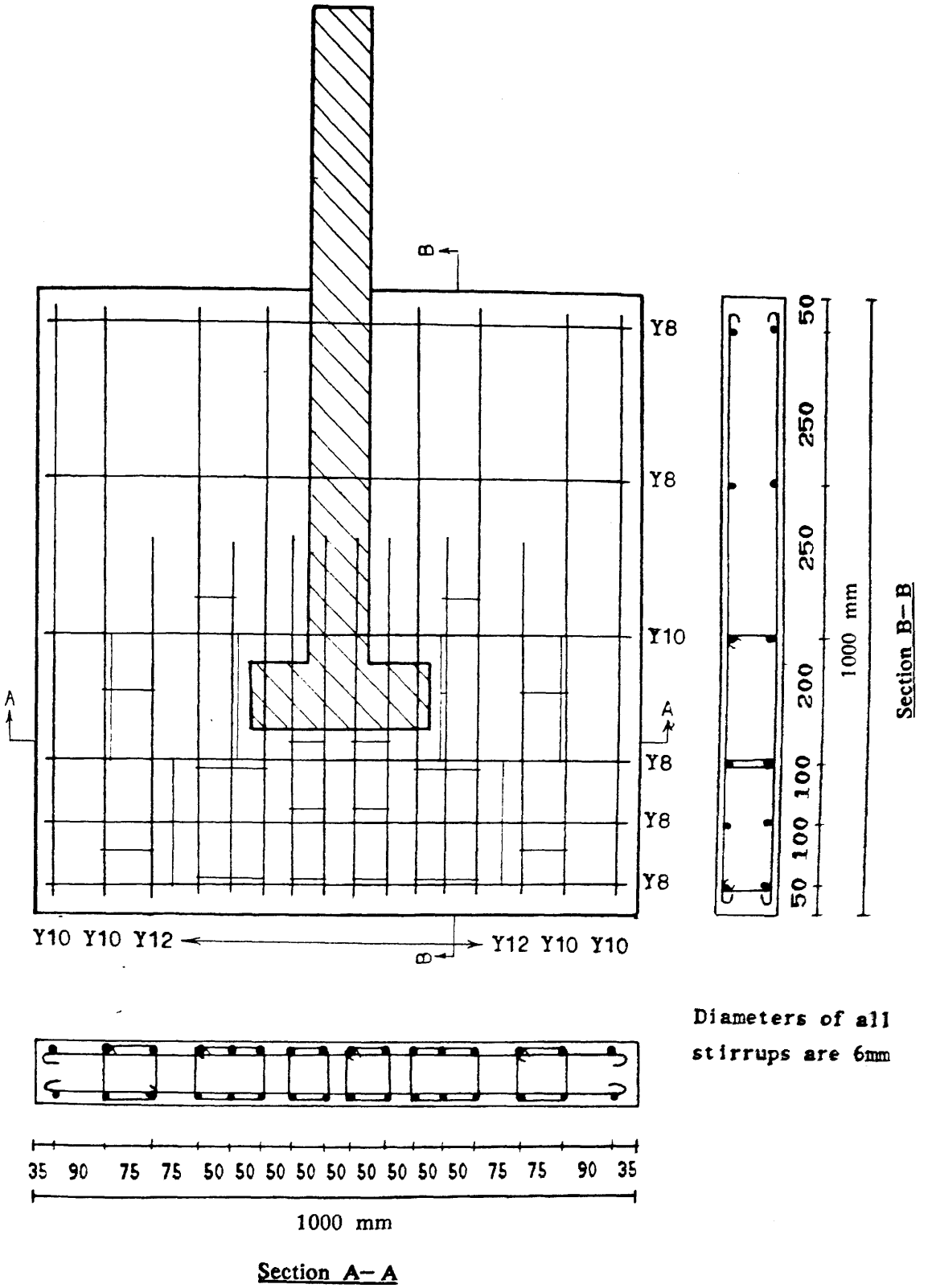

Figure (8.3) : Arrangement of top and bottom reinforcing bars including closed vertical stirrup in the slab of model MRS13 (top and bottom steel bars are identical)

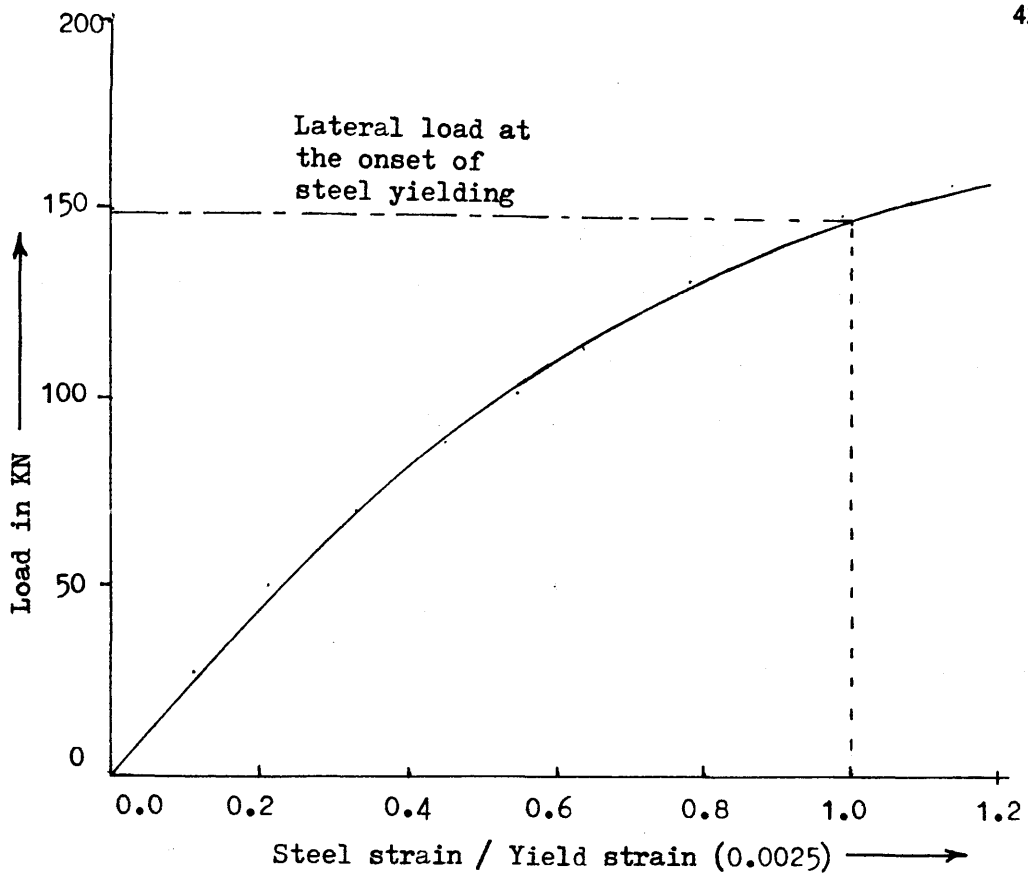

Figure (8.3-a) : Curve showing lateral load versus steel strain measured in the slab of model MRS13

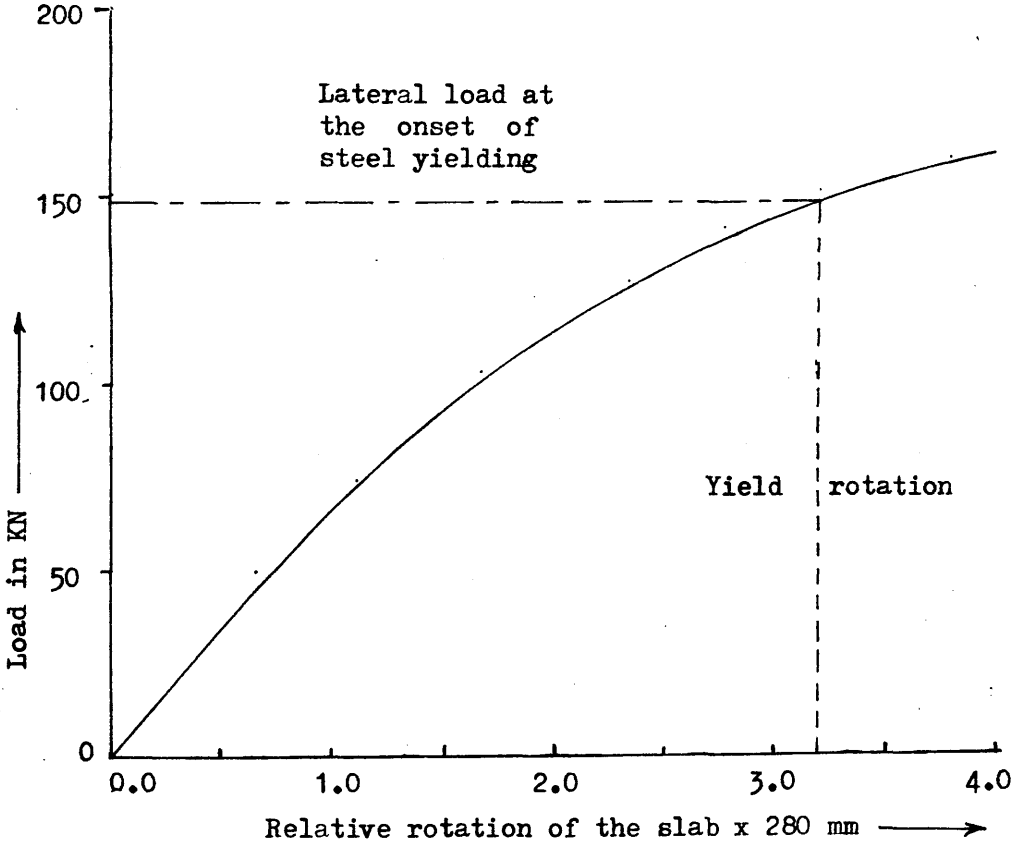

Figure (8.3-b) : Curve showing lateral load versus relaive rotation of the slab of model MRS13

Behaviour of the model

No crack was observed after the ultimate gravity load was applied. At a lateral load of 23% of design load, some cracks parallel to the flange were first observed on the top surface of the slab as shown in Figure (8.5– a). On further loading, earlier cracks extended a little and some new cracks parallel to the flange appeared in the slab as shown in Figure (8.5– b). The final crack patterns of the top and bottom surface of the slab are shown in Figures (8.8) and (8.9). The crack pattern on the top surface is not much different from that of model MS10 (see Figures (6.138) and (8.8) for comparisons) except for some additional cracks on model MRS13 which occurred when top surface was under compression due to upward loading. But the failure line (heavily marked) in this model is different from that of model MS10. Since the bottom surface was also under tension due to upward loading, this surface was also extensively cracked like the top surface. The crack pattern of the bottom surface is not exactly similar to that of top surface but overall similarities can be easily detected.

The load – rotation curve for the slab– wall junction obtained during the loading cycles is shown in Figures (8.6) and (8.7). A lot of problems were encountered in supporting this model while loading in the upward direction. It was found very difficult to apply load in upward direction, when the joint rotation was even less than the yield rotation calculated for downward loading. The model started to rotate at the back edge of the wall 'GH' (see Figure 5.1) and the supporting system (Figure 5.3) was found ineffective in resisting the upward rigid body movement of the model. The wall at the back started crushing due to the concentration of the stresses along line 'GH'. Another hollow beam section was designed and the model was held down by that transverse beam using three 15 mm high strength prestressing strand (Figure 5.4). In the 20th cycle, the model was loaded in the upward direction such that the joint rotation was twice the yield rotation and it was felt that no more upward loading is possible in this model. In

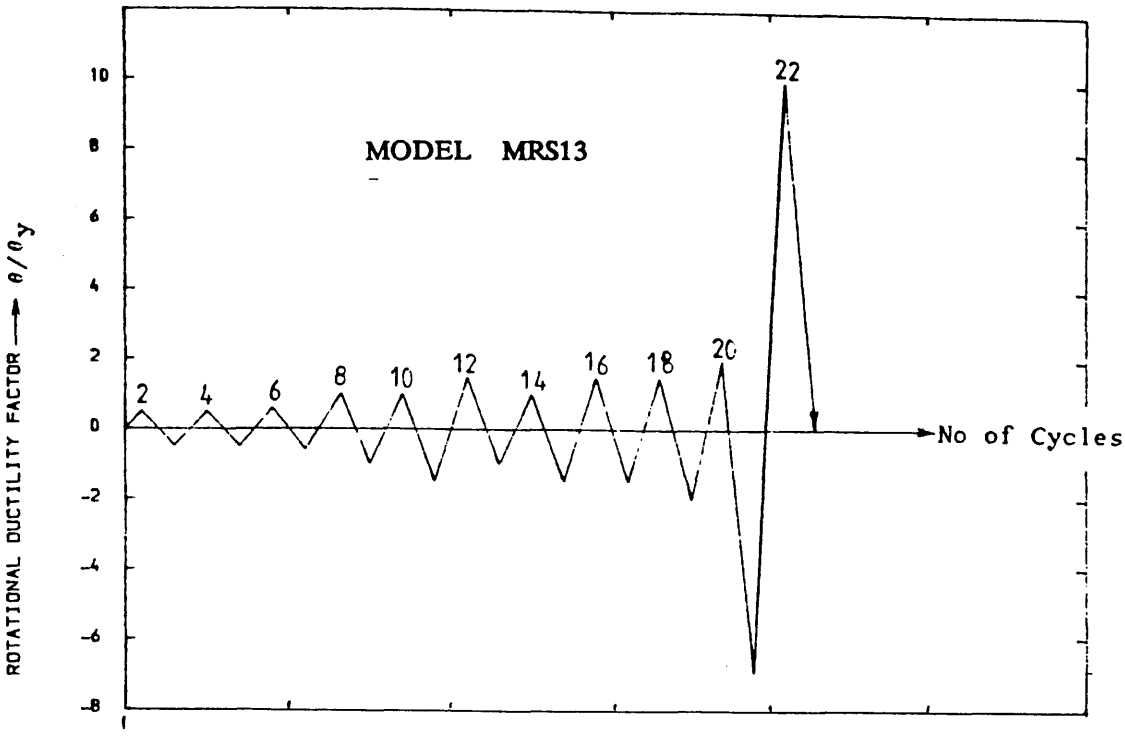

FIGURE (8.4) : LOADING CYCLES USED IN TESTING MODEL MRS13

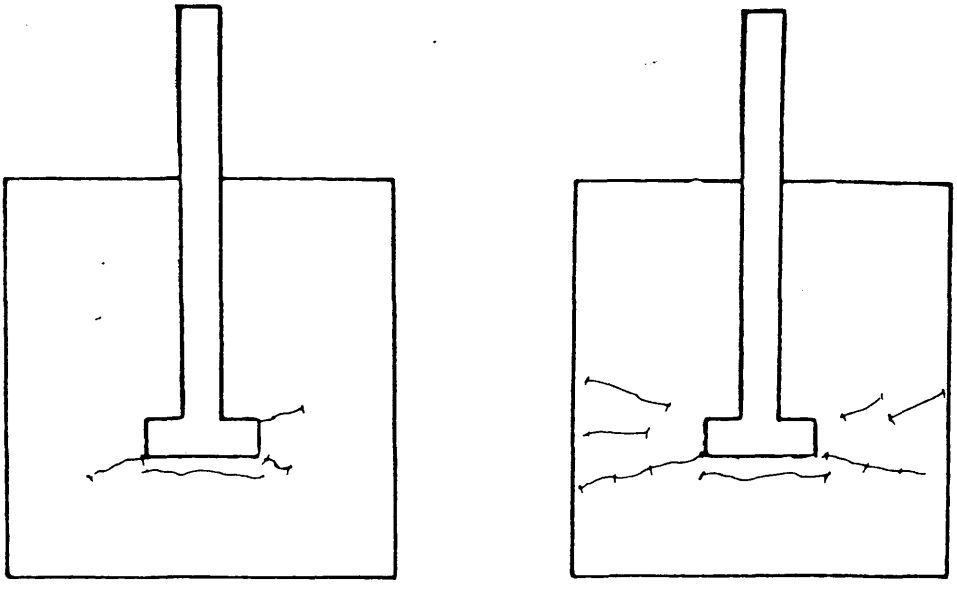

(a) at 23%

(b) at 32%

Figure (8.5) : Cracks initiation during testing of model MRS13 at different percentages of design lateral load.

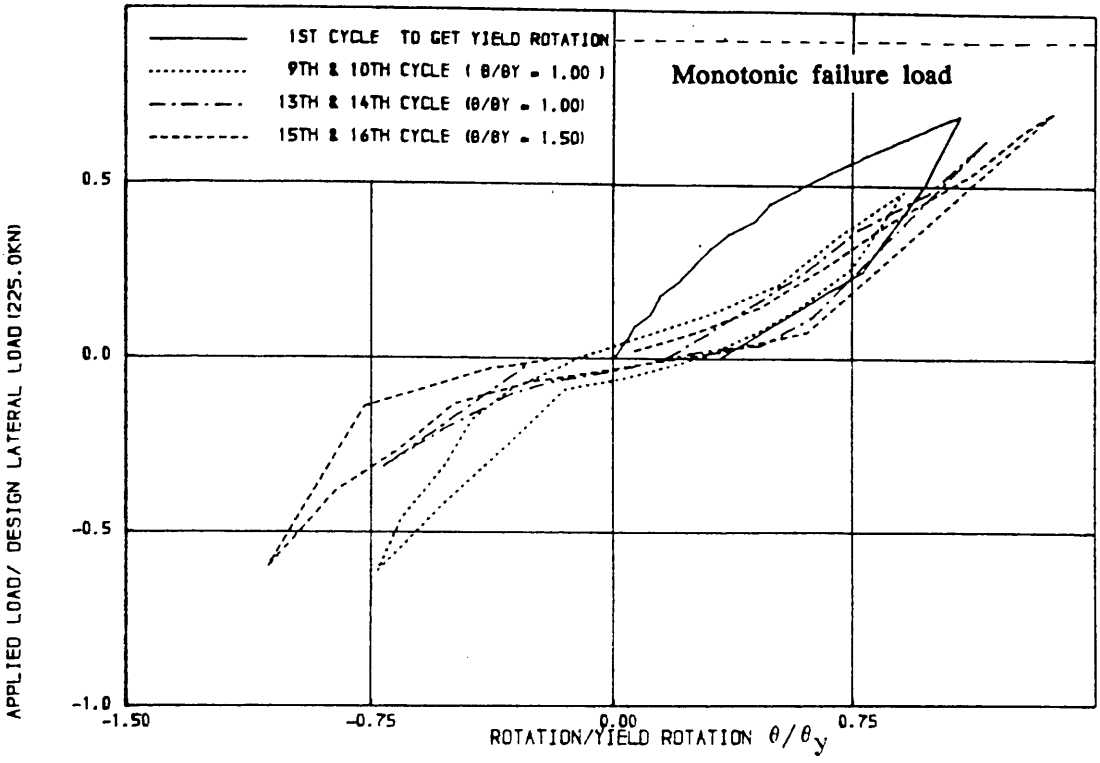

FIGURE (8.6) , RELATIVE ROTATION BETWEEN SHEAR WALL AND FLOOR SLAB FOR MODEL MRS13 AT INITIAL STAGES OF LOADING CYCLE

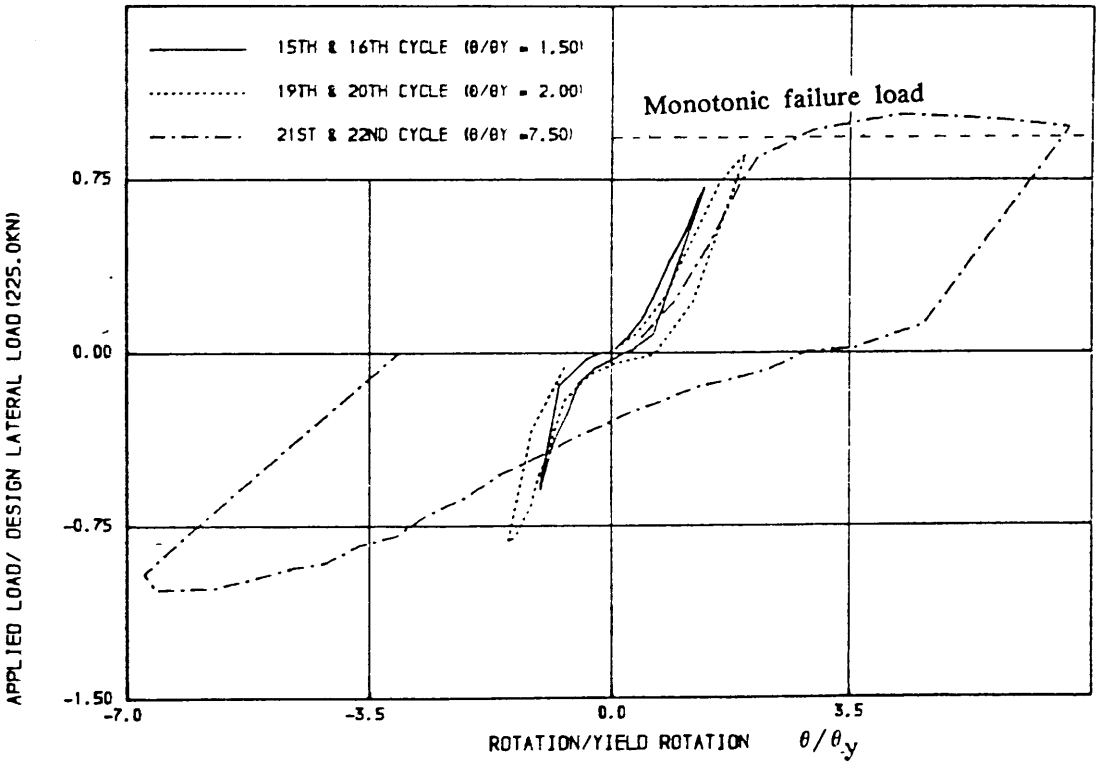

FIGURE (8.7) , RELATIVE ROTATION BETWEEN SHEAR WALL AND FLOOR SLAB FOR MODEL MRS13 AT FINAL STAGES OF LOADING CYCLE

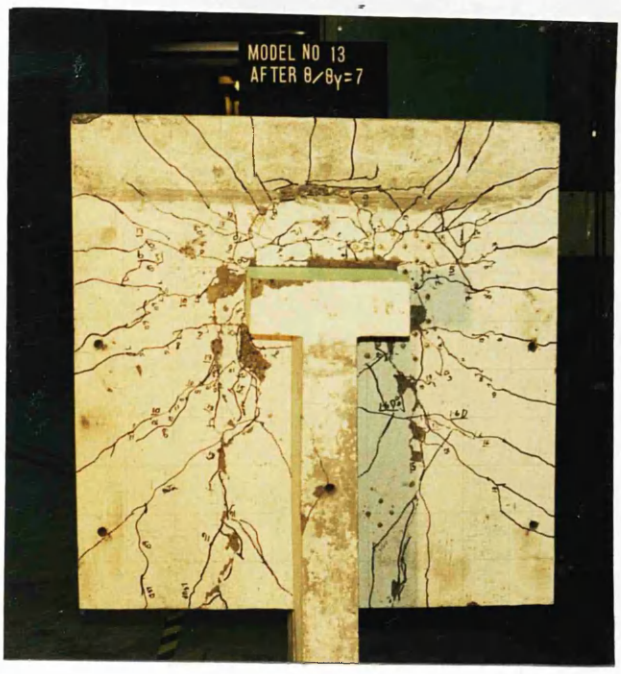

Figure (8.8-a) : Crack pattern on the top surface of the slab of model MRS13

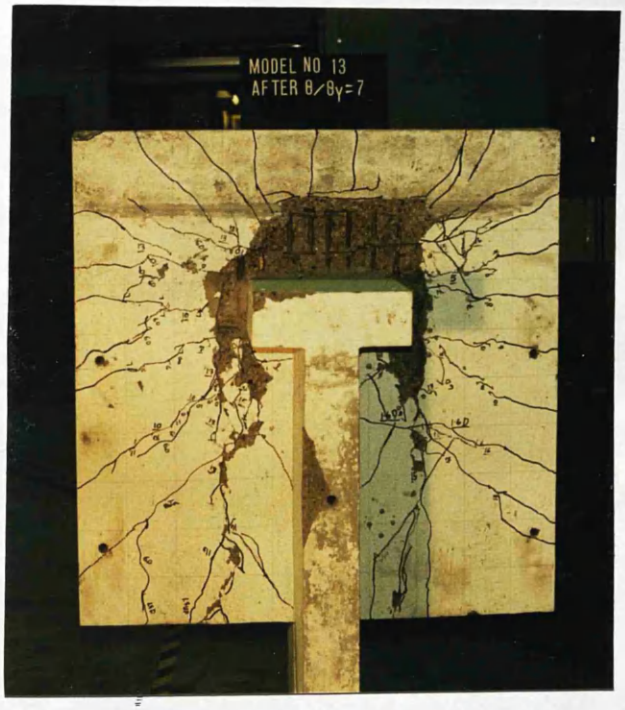

Figure (8.8-b) : Damage visible on the top surface of the slab during testing of model MRS13

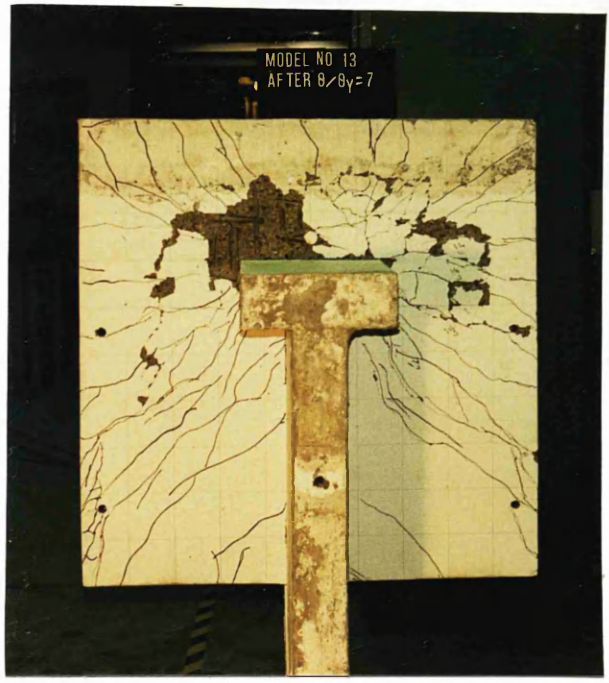

Figure (8.9-a) : Crack pattern on the bottom surface of the slab of model MRS13

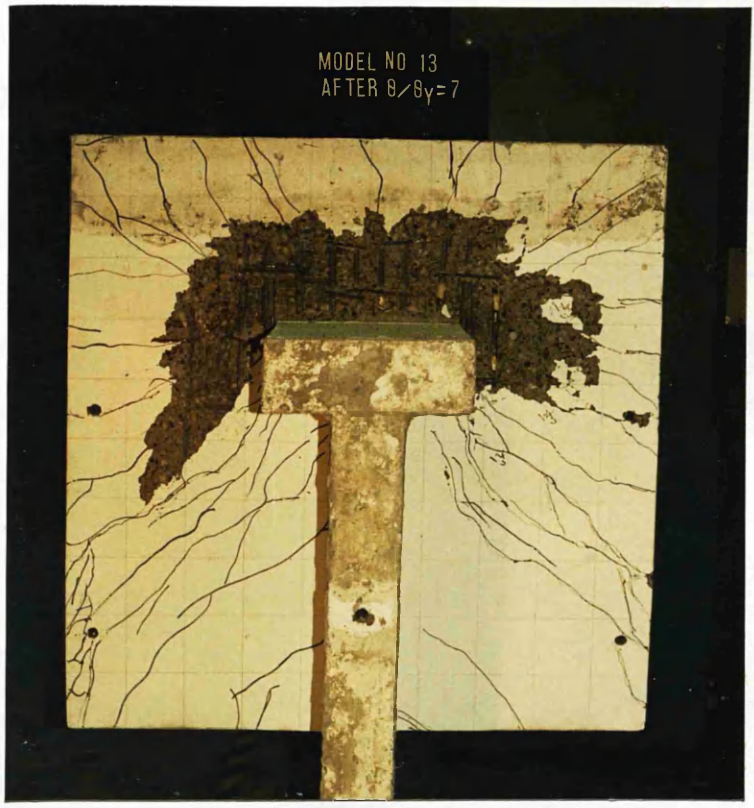

Figure (8.9-b) : Damage visible on the bottom surface of the slab during testing of model MRS13

the 21st cycle, the model was loaded in downward direction and the relative rotation of the slab with respect to the wall was more than 7 times of yield rotation without the specimen failing. It was then decided to apply load again in upward direction and to our surprise, the relative rotation of the slab with respect to the wall was also more than 7 times yield rotation. Though the specimen did not fail, the test was stopped when the ductile behaviour of the joint was demonstrated. Figures (8.10) and (8.11) show the tensile strain in steel in longitudinal and transverse direction under reversed cyclic loading condtions.

8.2.2 Model MRS14

The plan and dimension of the model is shown in Figure (8.12). The wall reinforcement is shown in Figure (8.13). The flexural steel reinforcement in the slab was designed to resist a lateral load equals 220.0 KN as well as an ultimate gravity load of 18.0 KN. The shear reinforcement in the form of closed vertical stirrup was provided in the slab where the shear stress exceeded allowable concrete shear stress. Figure (8.14) shows the main reinforcement layout along with the arrangement of shear reinforcement in the slab. To cater for the reversibility of load, same reinforcement was provided at the bottom of the slab. This model is similar to the model MS7 which was designed for 240 KN of lateral load and tested under monotonic loading condition. The sequence of loading cycles used in testing this model is shown in Figure (8.15). The model was loaded first in downward direction to determine the yield rotation.

Behaviour of the model

No cracks were found after the ultimate gravity load was fully applied. At 23% of design load, two cracks around the nose of the wall were observed. On further loading, at about 36% of design load, the cracks spreaded in the slab as shown in Figure (8.16– b). The overall crack pattern of the top and bottom surface of the model are shown in Figures (8.17) and (8.18). Figures (8.19) and

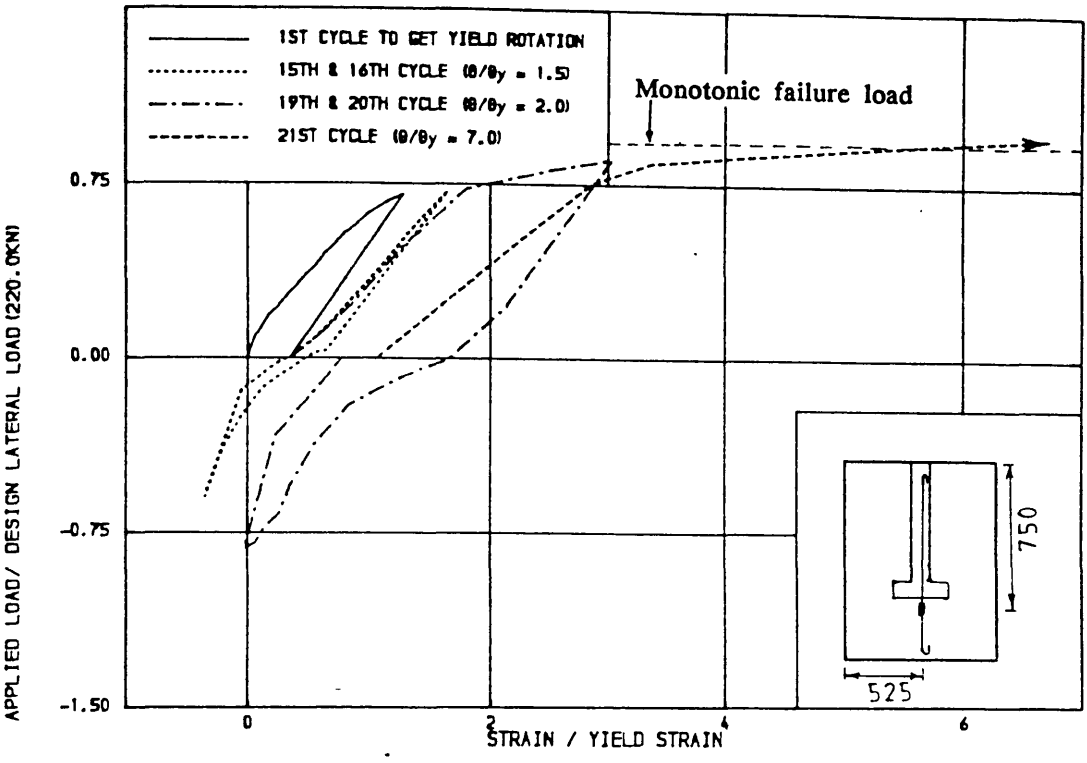

FIGURE (8.10) , TENSILE STRAIN IN STEEL IN LONGIITUDINAL DIRECTION UNDER REVERSE CYCLIC LOADING CONDITIONS IN THE SLAB OF MODEL MRS13

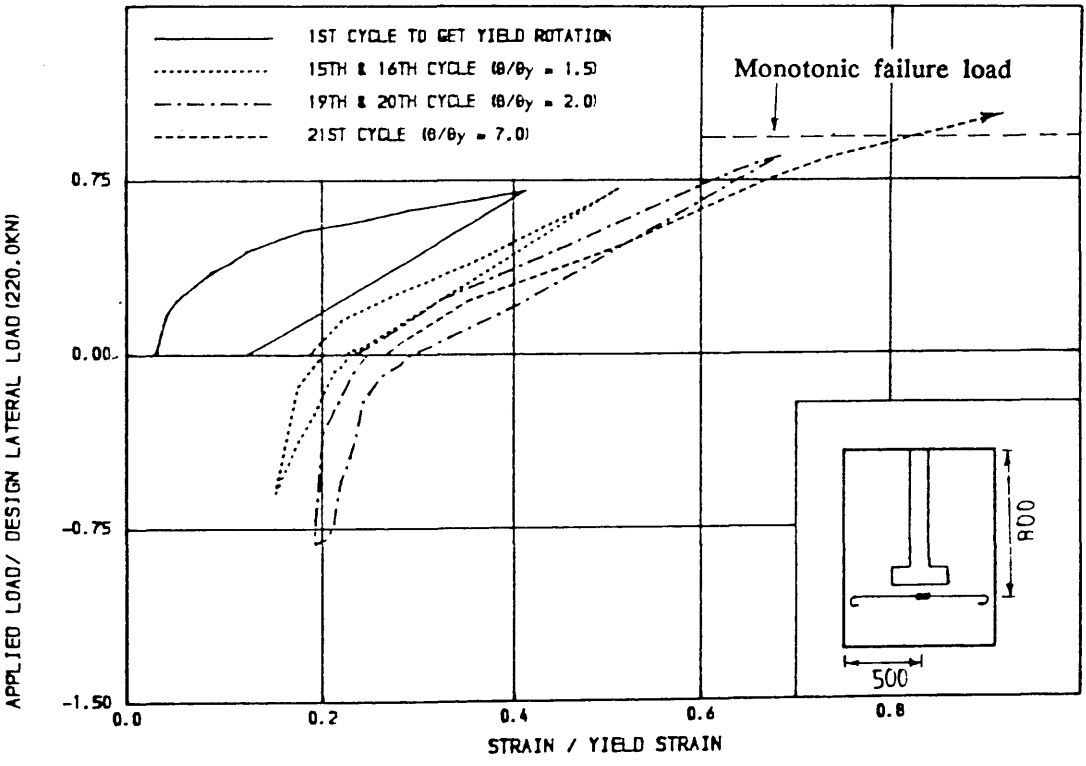

FIGURE (8.11) , TENSILE STRAIN IN STEEL IN TRANSVERSE DIRECTION UNDER REVERSE CYCLIC LOADING CONDITIONS IN THE SLAB OF MODEL MRS13

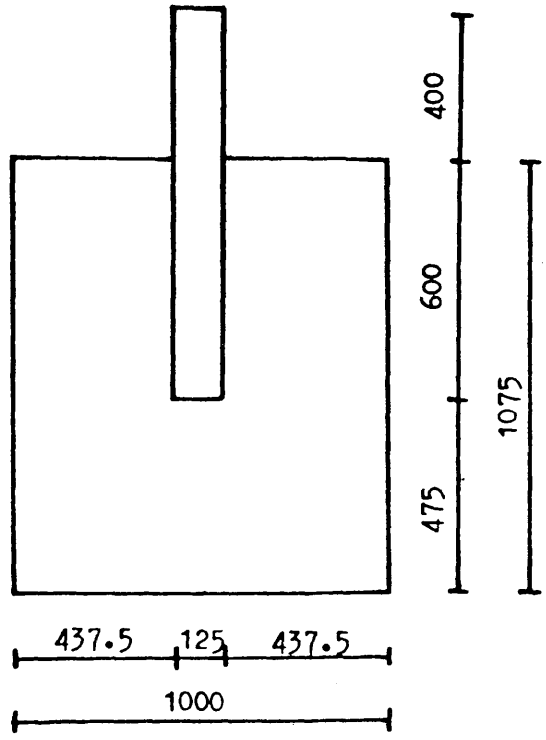

Figure (8.12) : Plan and dimensions of model MRS14

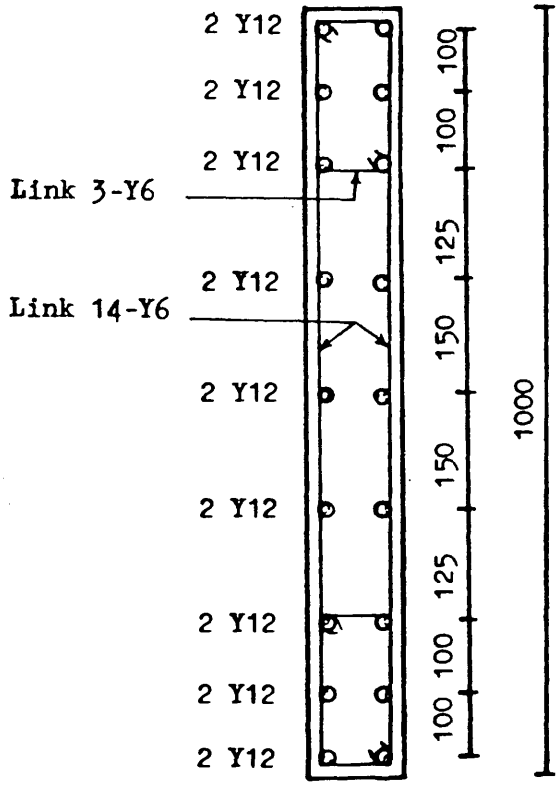

Figure (8.13) : A horizontal section in the wall of model MRS14 showing the reinforcing details

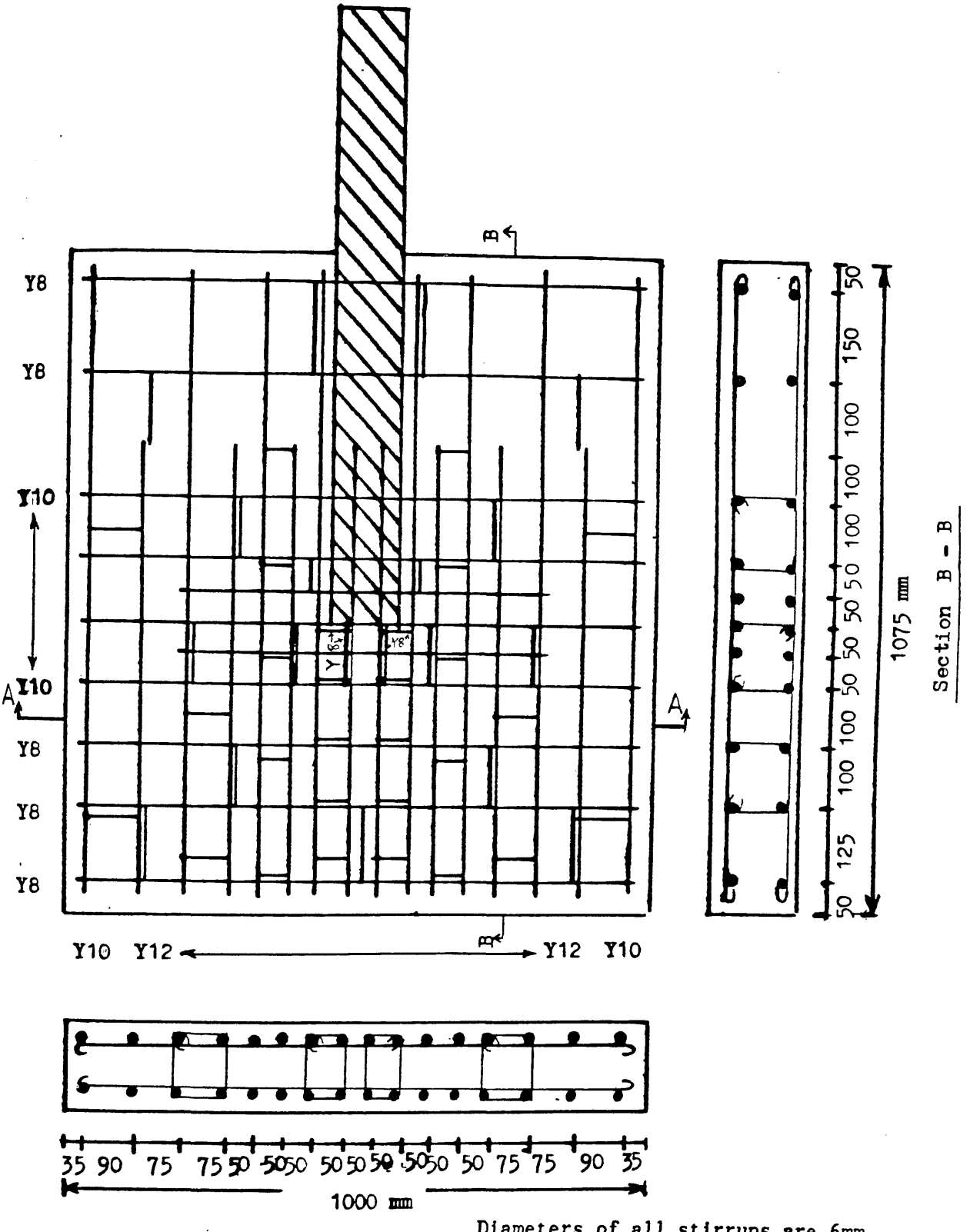

Figure (8.14) : Arrangement of top and bottom reinforcing bars including closed vertical stirrup in the slab of model MRS14 (top and bottom steel bars are identical)

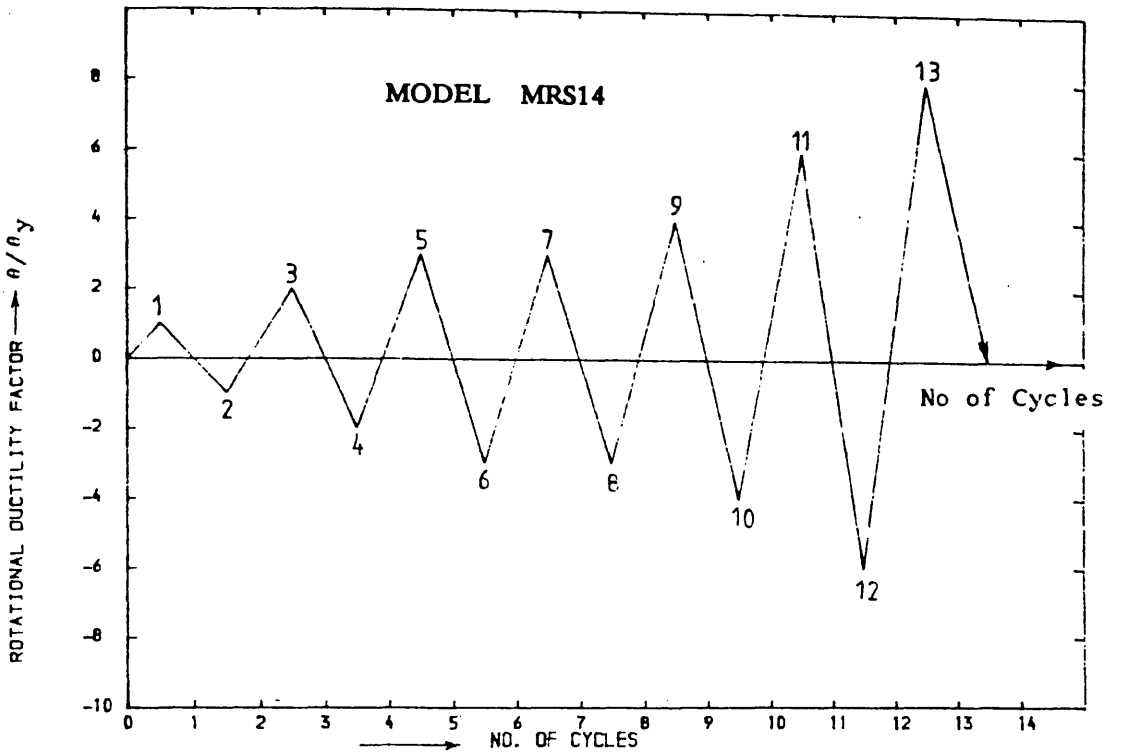

FIGURE (8.15) . LOADING CYCLE USED IN TESTING MODEL MRS14

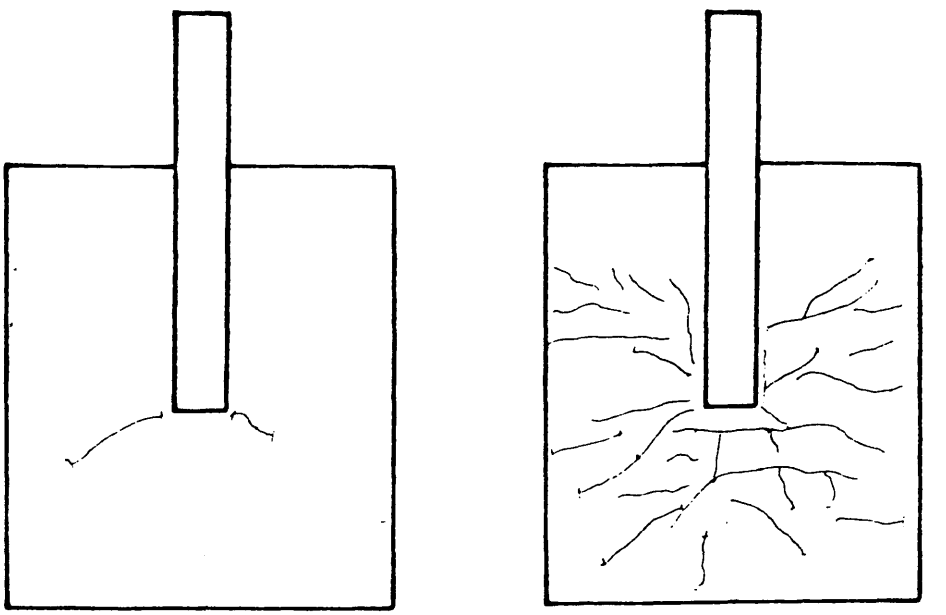

(a) at 23%

(b) at 36%

Figure (8.16) : Cracks initiation during testing of model MRS14 at different percentages of design lateral load

Figure (8.17-a) : Crack pattern on the top surface of the slab of model MRS14

Figure (8.17-b) : Damage visible on the top surface of the slab during testing of model MRS14

Figure (8.18-a) : Crack pattern on the bottom surface of the slab of model MRS14

Figure (8.18-b) : Damage visible on the bottom surface of the slab during testing of model MRS14

(8.20) show the load versus the relative rotation between the slab and the wall measured by transducers mounted on the slab at a distance of 150 mm from the face of the wall. The behaviour of steel on the top face of the slab under reverse cyclic loading condition is shown in Figures (8.21) to (8.23). The longitudinal bar passing through the wall was subjected to large strains. The bar at the edge of the slab was stressed very little.

8.2.3 Model MRS15

The plan and dimension of the model is shown in Figure (8.24). The wall reinforcement is shown in Figure (8.25). The flexural steel reinforcement in the slab was designed to resist a lateral load equals 215.0 KN as well as an ultimate gravity load of 18.0 KN. The shear reinforcement in the form of closed vertical stirrup was provided in the slab where the shear stress exceeded allowable concrete shear stress. Figure (8.26) shows the main reinforcement layout along with the arrangement of shear reinforcement in the slab. To cater for the reversibility of load, same reinforcement was provided at the bottom of the slab. This model is similar in plan to model MS6 which was designed for 330.0 KN and tested under monotonic (only downward) loading condition. The sequence of loading cycles used in testing this model is shown in Figure (8.27).

Behaviour of the model

Cracks were observed for the first time on the top surface of the slab at a lateral load 28% of design load as shown in Figure (8.28–a). All the cracks started from the tip of the wall. Two of them, originating from the wall were inclined towards the sides. On further loading, earlier cracks widened and extended a little and were joined by new cracks. The photographs showing the crack pattern of this model at the end of last cycle are presented in Figures (8.29) and (8.30). Figures (8.31) and (8.32) show the load–rotation curves at initial and final stages of loading cycle. Figures (8.33) and (8.34) show the strain in steel in windward

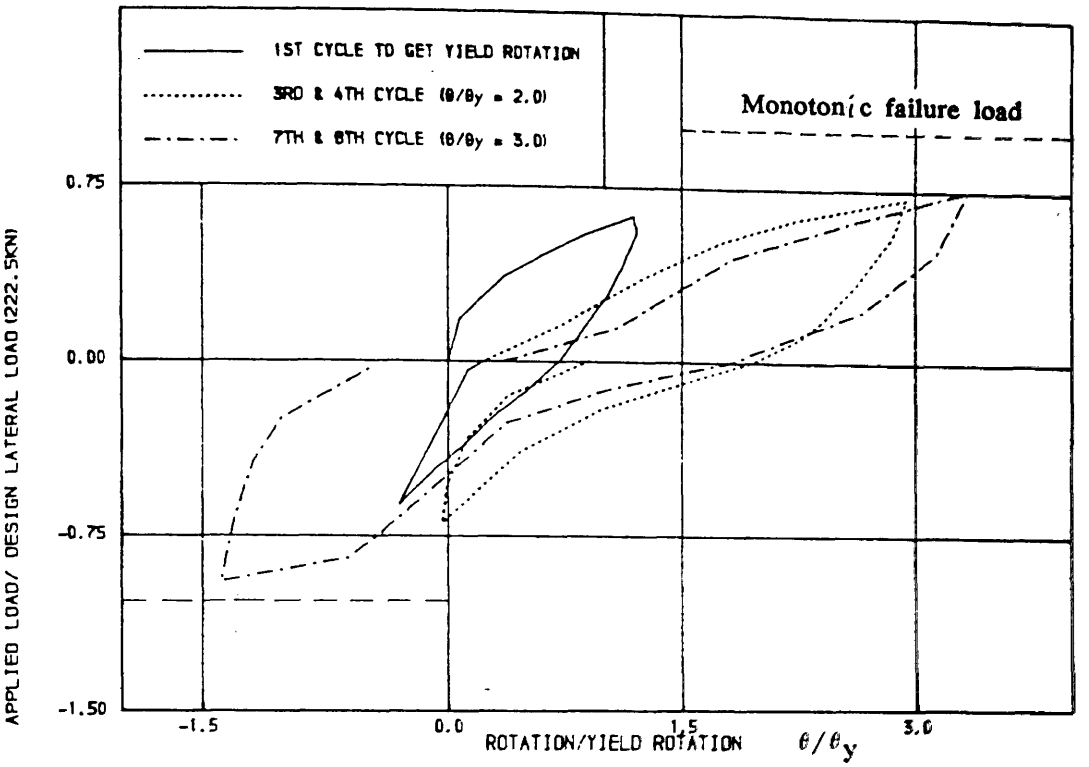

FIGURE (8.19) , RELATIVE ROTATION BETVEEN SHEAR VALL AND FLOOR SLAB FOR MODEL MRS14 AT INITIAL STAGES OF LOADING CYCLE

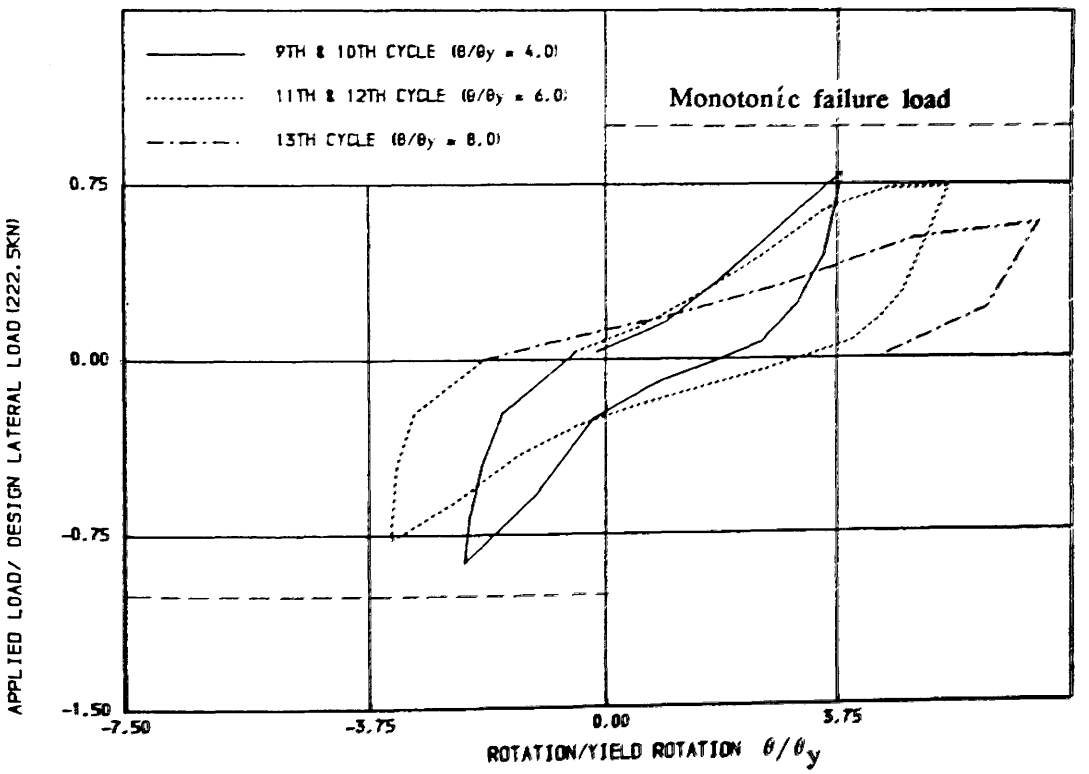

FIGURE (8.20) , RELATIVE ROTATION BETVEEN SHEAR VALL AND FLOOR SLAB FOR MODEL MRS14 AT FINAL STAGES OF LOADING CYCLE

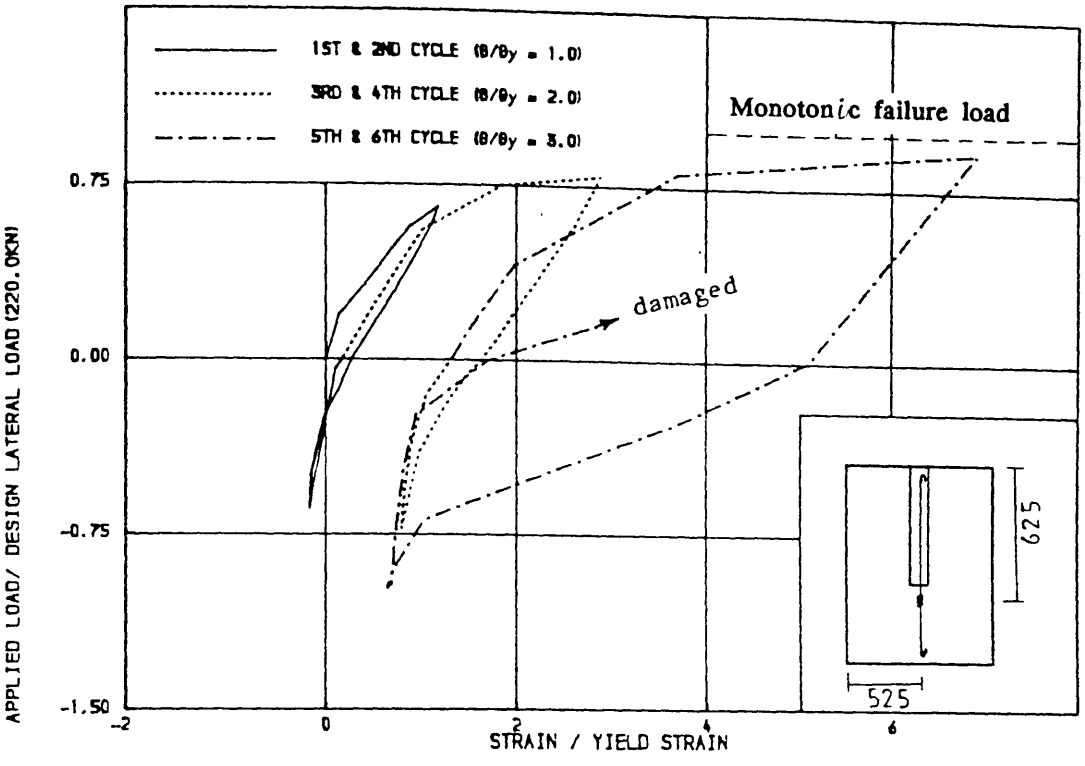

FIGURE (8.21) , TENSILE STRAIN IN LONGITUDINAL STEEL UNDER REVERSED CYCLIC LOADING CONDITIONS IN THE SLAB OF MODEL MRS14

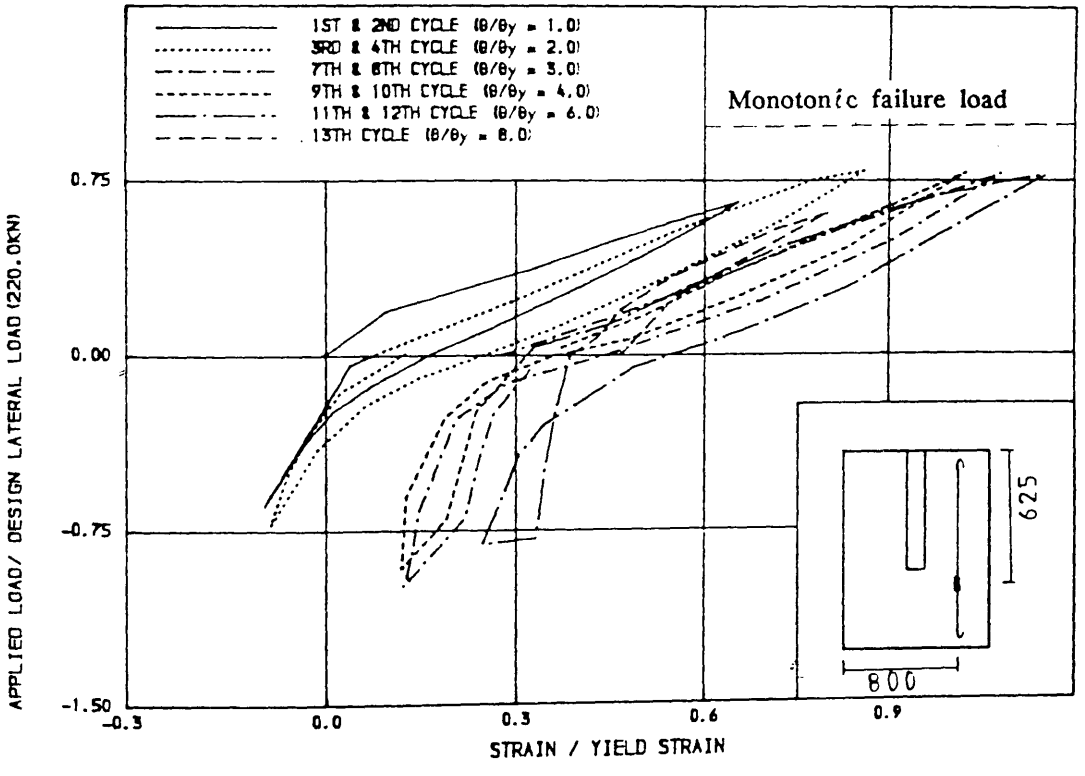

FIGURE (8.22) , TENSILE STRAIN IN STEEL IN LONGITUDINAL DIRECTION UNDER REVERSE CYCLIC LOADING CONDITIONS IN THE SLAB OF MODEL MRS14

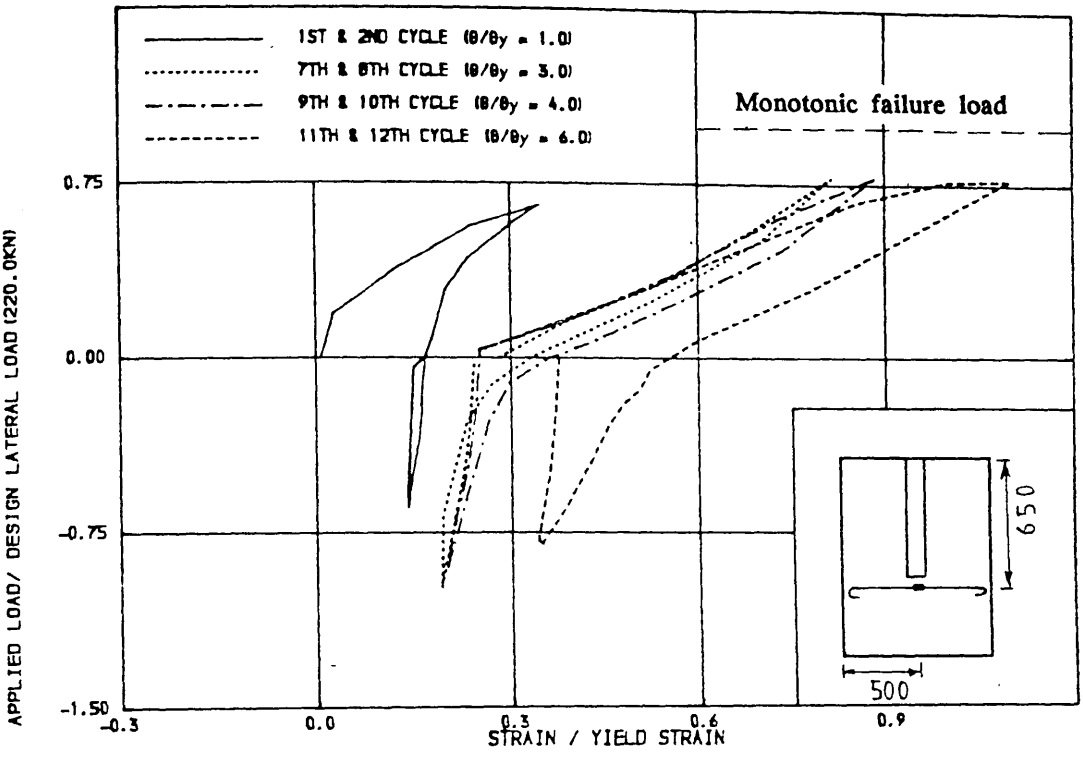

FIGURE (8.23) , TENSILE STRAIN IN STEEL IN TRANSVERSE DIRECTION UNDER REVERSE CYCLIC LOADING CONDITIONS IN THE SLAB OF MODEL MRS14

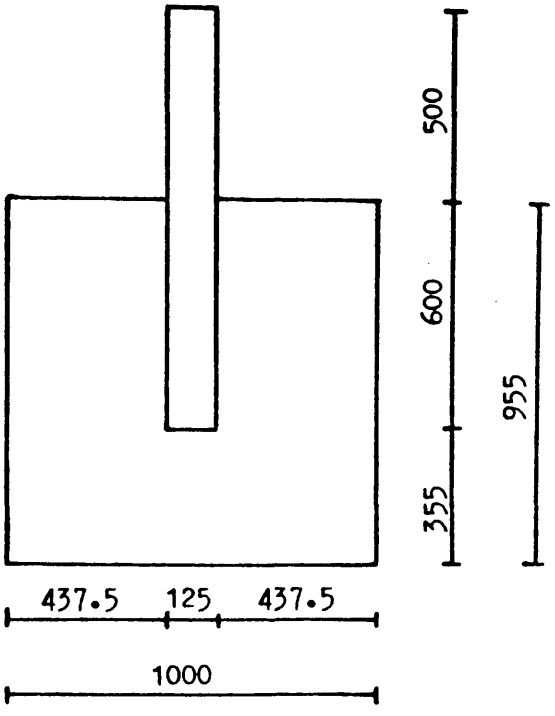

Figure (8.24) : Plan and dimensions of model MRS15

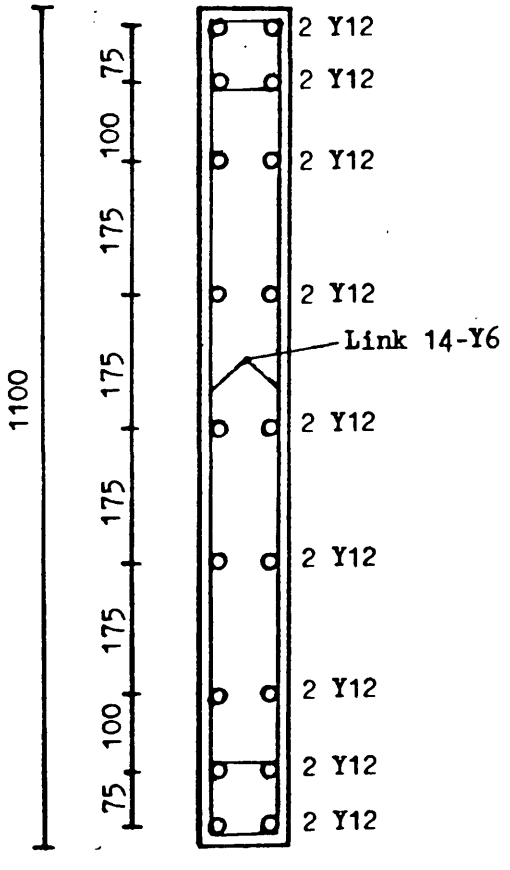

Figure (8.25) : A horizontal section in the wall of model MRS15 showing the reinforcing details

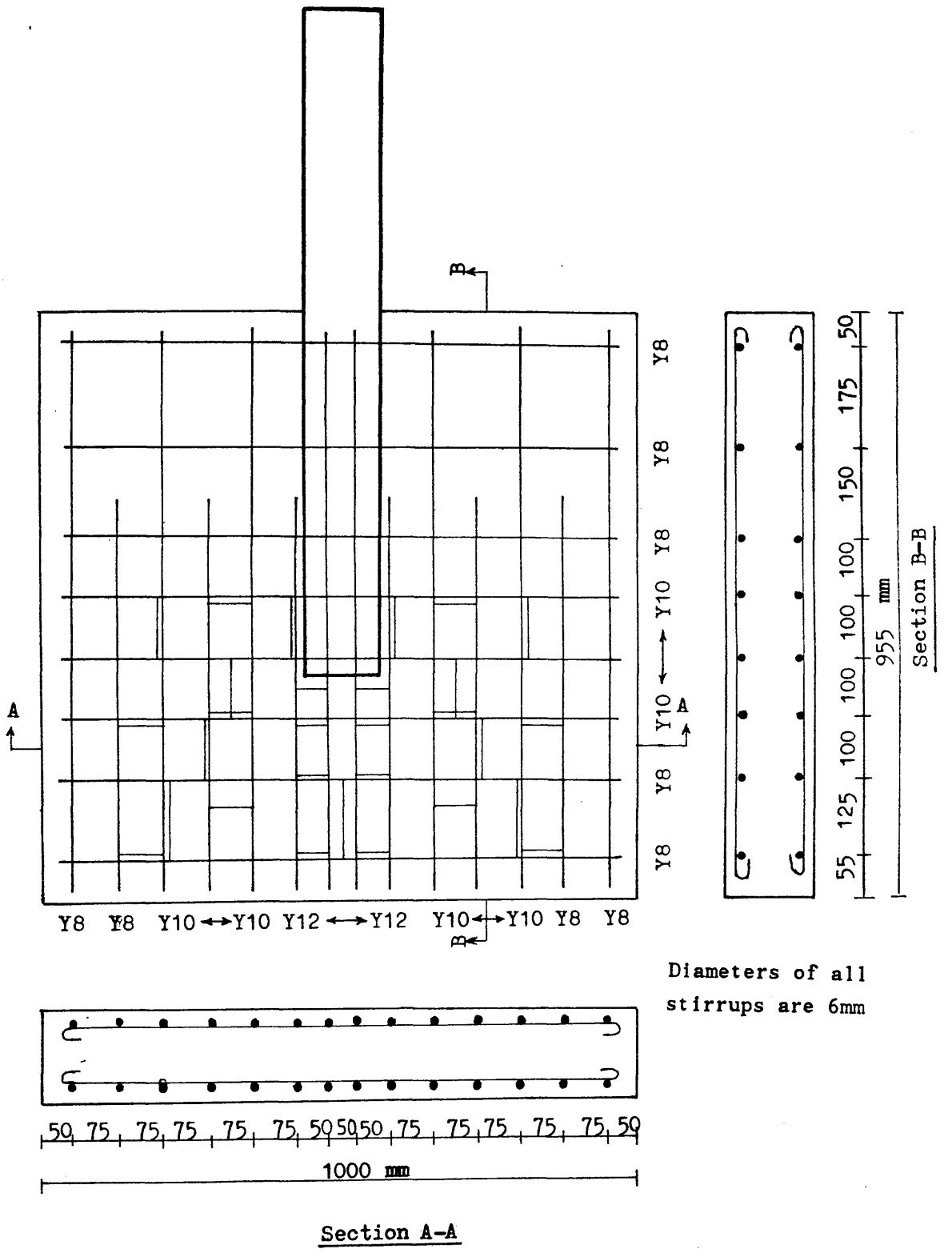

Figure (8.26) : Arrangement of top and bottom reinforcing bars including closed vertical stirrup in the slab of model MRS15 (top and bottom steel bars are identical)

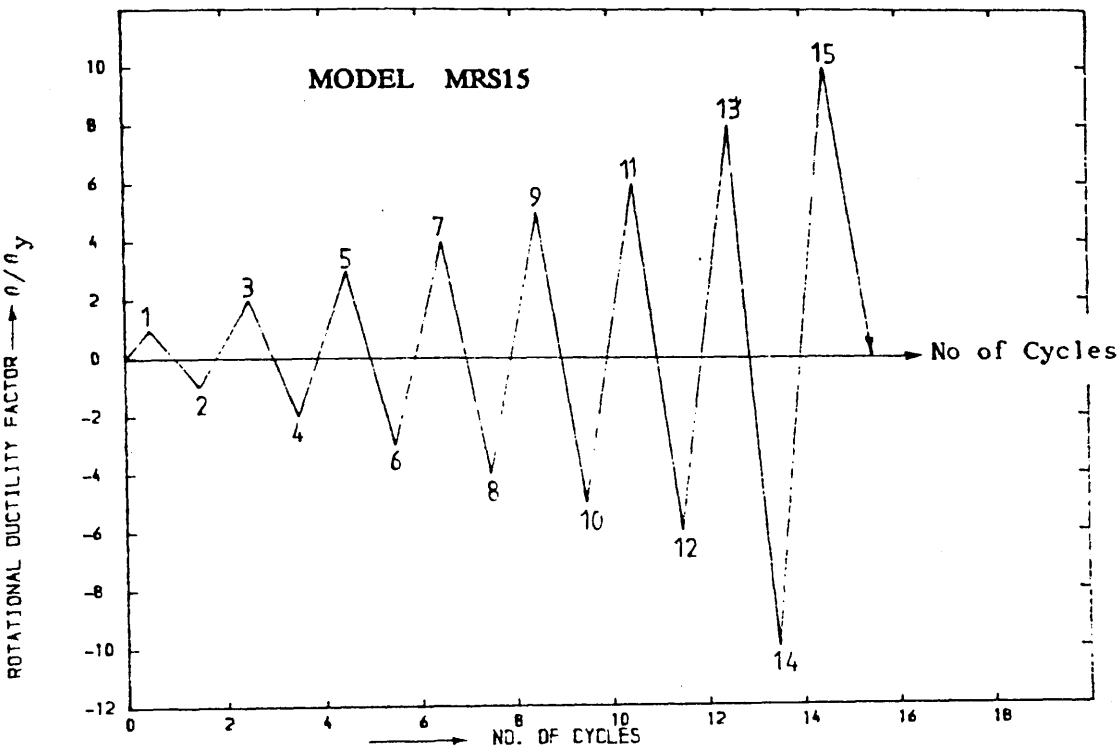

FIGURE (8.27) : LOADING CYCLE USED IN TESTING MODEL MRS'15

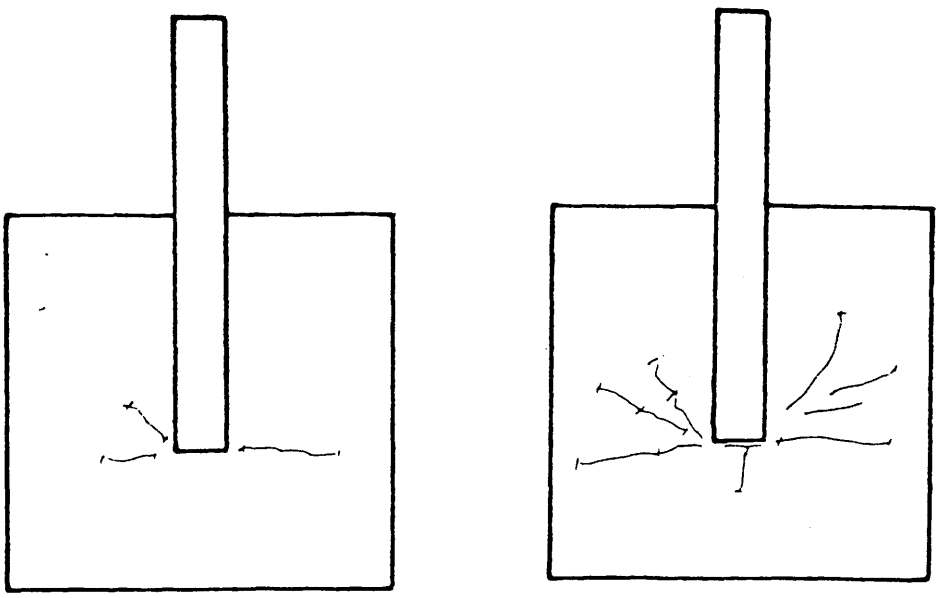

(a) at 24%

(b) at 37%

Figure (8.28) : Cracks initiation during testing of model MRS15 at different percentages of design lateral load

Figure (8.29-a) : Crack pattern on the top surface of the slab of model MRS15

Figure (8.29-b) : Damage visible on the top surface of the slab during testing of model MRS15

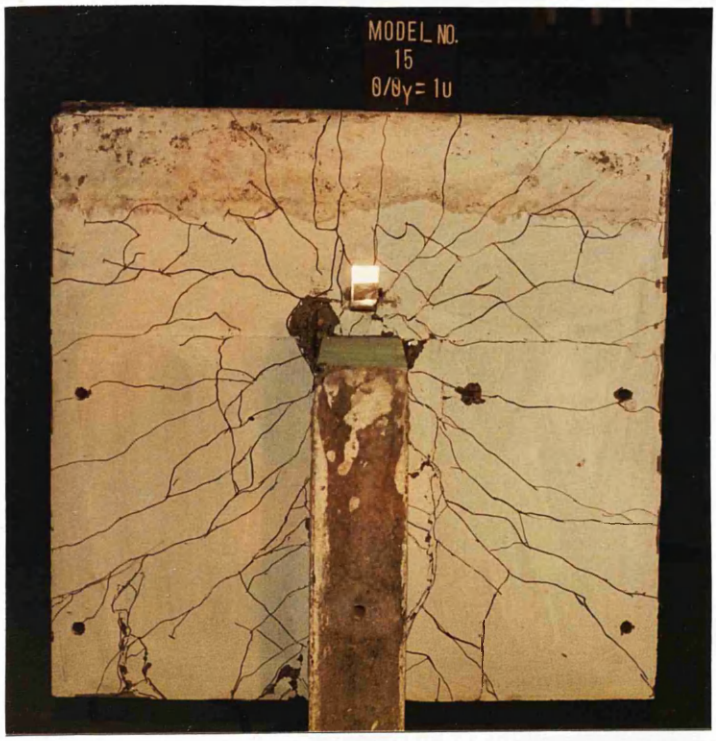

Figure (8.30) : Crack pattern on the bottom surface of the slab of model MRS15

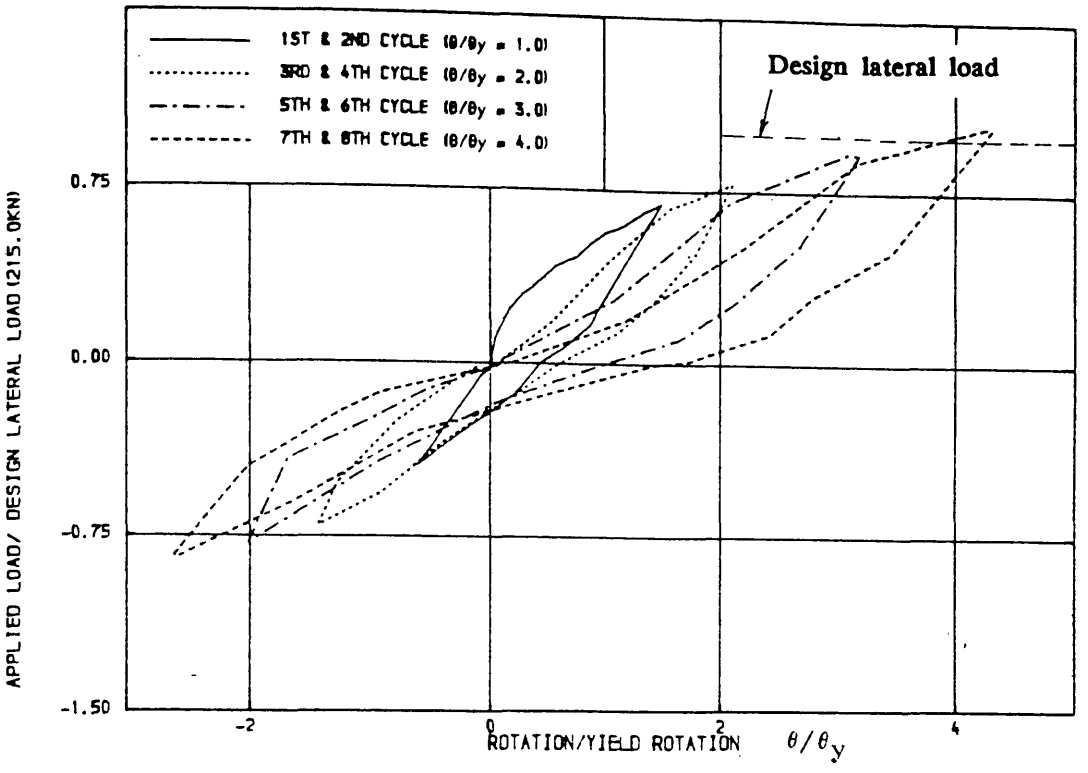

FIGURE (8.31) , RELATIVE ROTATION BETWEEN SHEAR WALL AND FLOOR SLAB FOR MODEL MRS15 AT INITIAL STAGES OF LOADING CYCLE

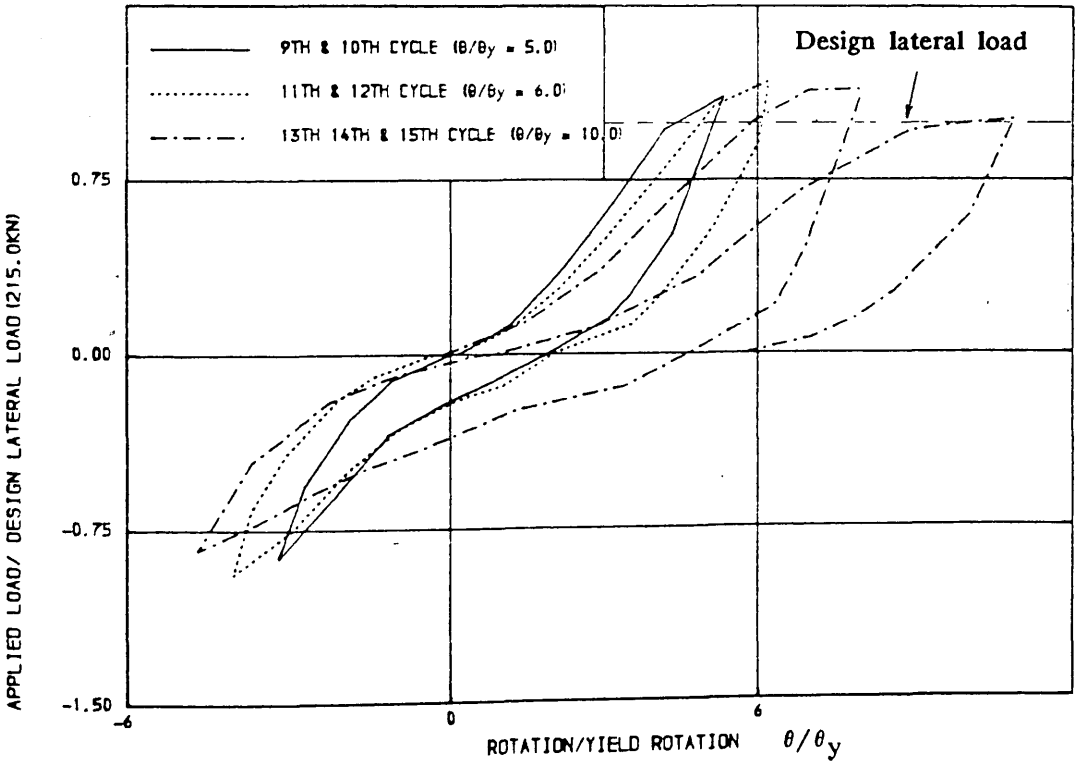

FIGURE (8.32) , RELATIVE ROTATION BETWEEN SHEAR WALL AND FLOOR SLAB FOR MODEL MRS15 AT FINAL STAGES OF LOADING CYCLE

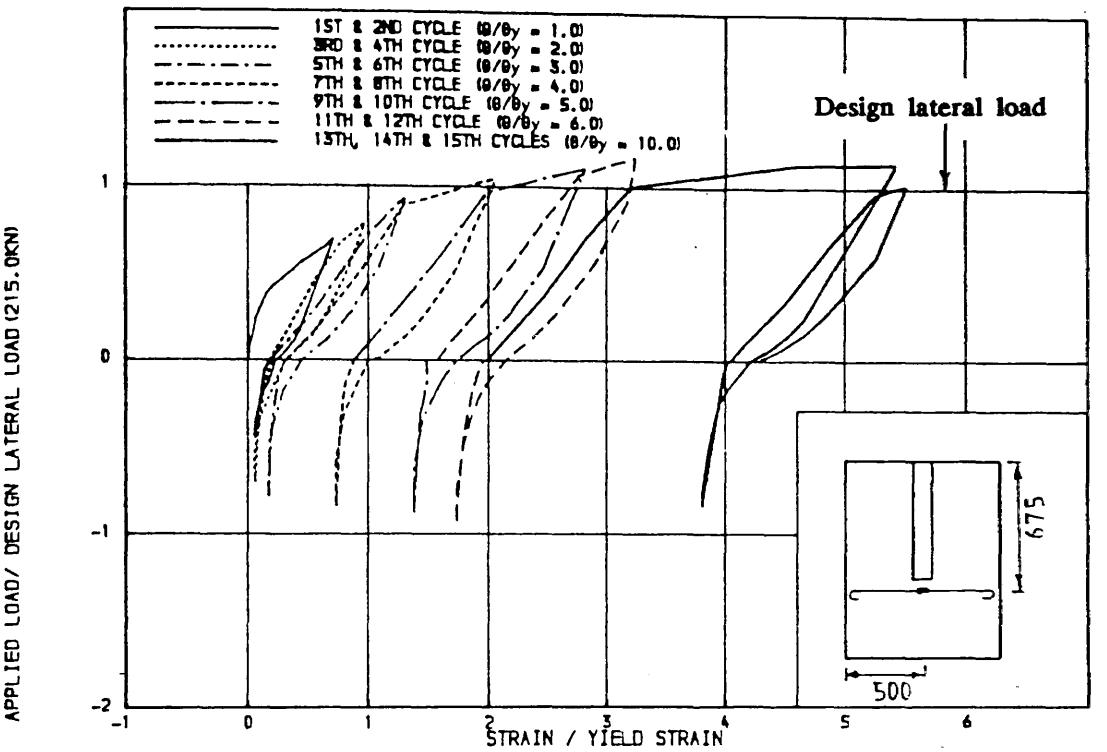

FIGURE (8.33) , TENSILE STRAIN IN STEEL UNDER REVERSE CYCLIC LOADING CONDITIONS

IN THE SLAB OF MODEL MRS15 AT POINT P1 (675.0, 0.0)

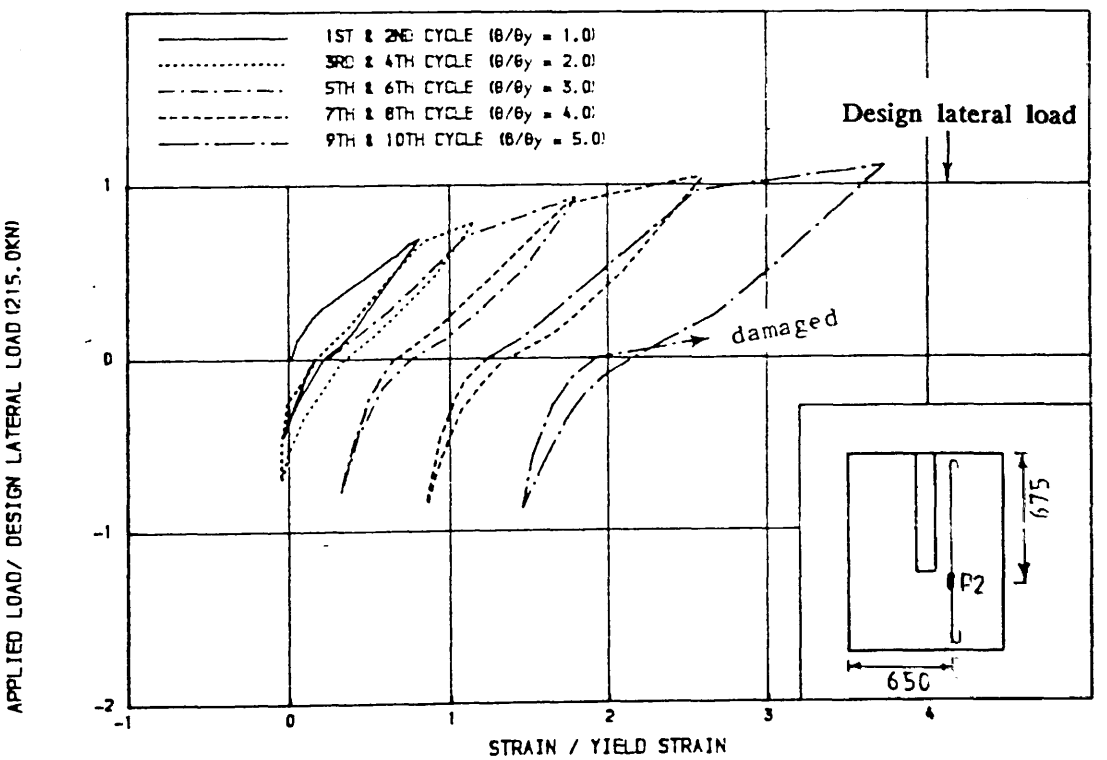

FIGURE (8.34) , TENSILE STRAIN IN STEEL UNDER REVERSE CYCLIC LOADING CONDITIONS

IN THE SLAB OF MODEL MRS15 AT POINT P2 (675.0, 150.0)

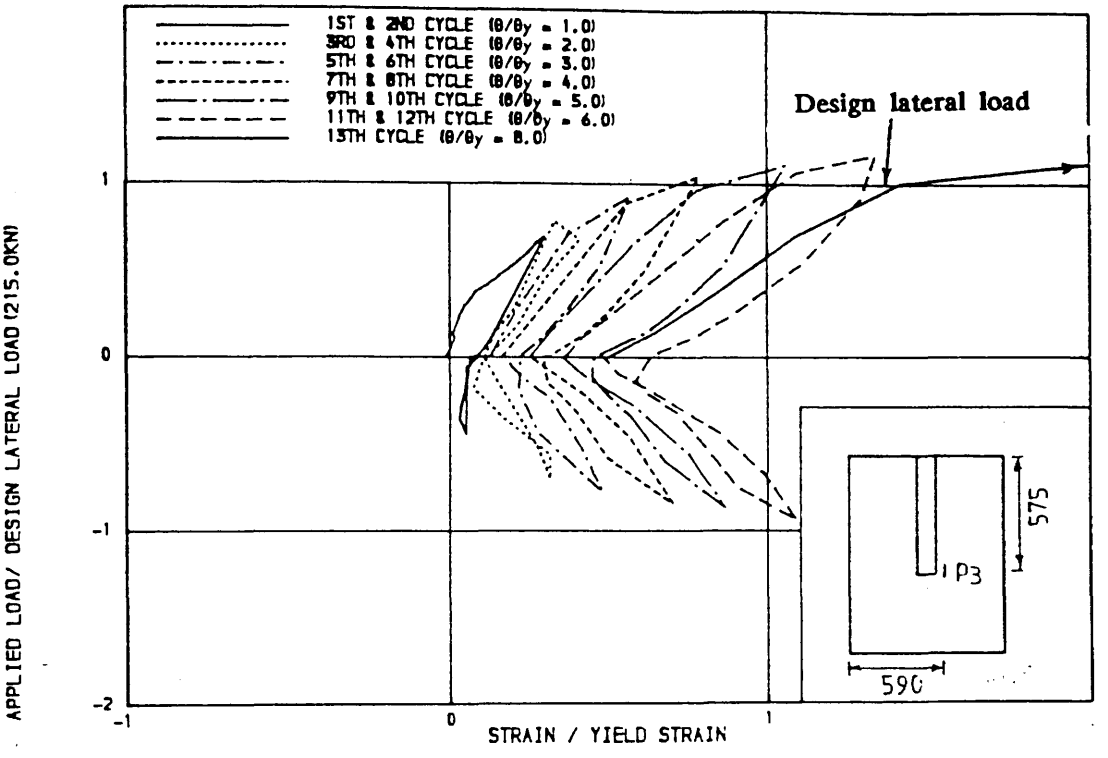

FIGURE (8.35) , TENSILE STRAIN IN VERTICAL STIRRUP UNDER REVERSE CYCLIC LOADING CONDITIONS IN THE SLAB OF MODEL MRS15 AT POINT P3

and transverse direction located on the top face of the slab and subjected to reverse cyclic loading.

8.2.4 Discussion and Analysis of Test Results

8.2.4.1 Criterion for adequate ductility

According to New Zealand Code of practice[95], the criterion for ductile structures or ability for a structure to dissipate energy requires that a specimen should be subjected to a displacement history of at least four complete load cycles, with a displacement amplitude in each direction of loading corresponding to an overall structural displacement ductility, $\mu_d = \pm 4$. It was concluded that[96] a unit satisfying this criterion, is likely to perform satisfactorily in future buildings in New Zealand for which the expected maximum overall displacement ductility demand is of the order of 3 to 5. It was considered that four excursions, each corresponding to the expected maximum ductility demand in each direction of loading during one seismic event, represent sufficiently severe conditions for a ductile unit. Figure (8.36– a) shows this displacement history involving four cycles to $\mu_d = \pm 4$. The imposed cumulative displacement ductility factor for these loading cycles is $4 \times 4 \times 2 = 32$ (Figure 8.36– b). This cumulative displacement ductility factor as an index for the ductile unit should not be misused by evaluating it on the basis of large number of displacement cycles to small ductilities.

The above criteria for ductile units are used here to asses the ductility of the models tested under reversed load. The relative rotation of the slab was monitored in the test instead of its edge displacement and the models MRS13, MRS14 and MRS15 were subjected to a rotation history of several load cycles, with different rotation amplitudes θ/θ_y, in each direction of loading as shown in Figures (8.4), (8.15) and (8.27) respectively. It is seen from Figures (8.36– d), (8.36– e) and (8.36– f) that the specifications implied by Figure (8.36– a) with a cumulative displacement/rotation ductility factor demand of 32 have been satisfied in the last

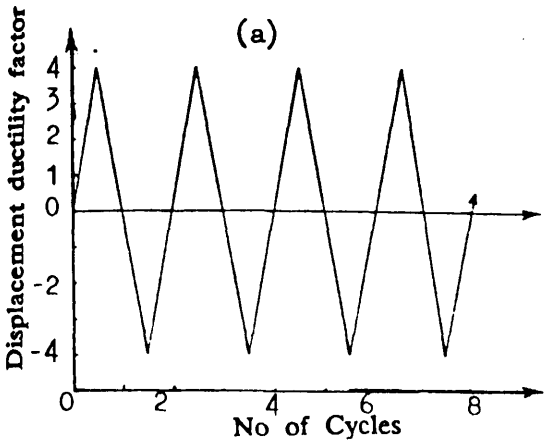

Load histories used for performance test in New Zealand

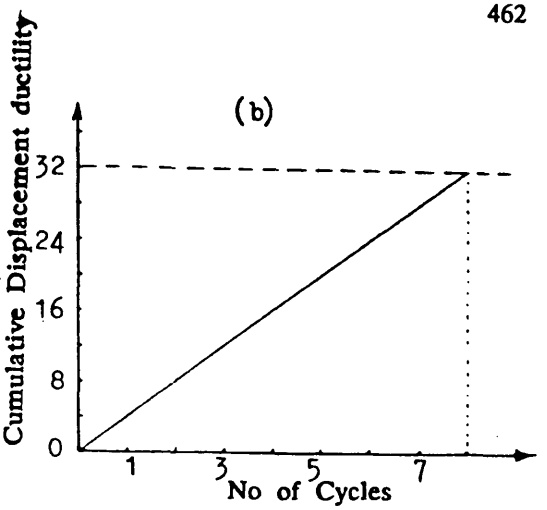

Cumulative displacement ductilities used for performance test

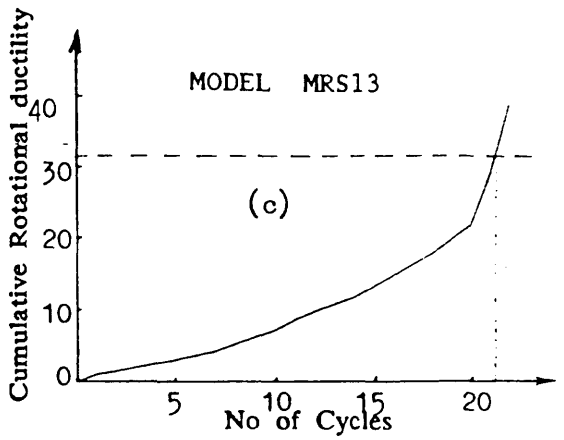

Cumulative rotational ductilities used in testing model MRS13

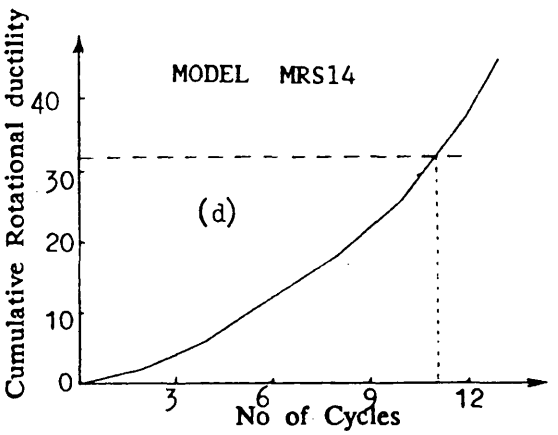

Cumulative rotational ductilities used in testing model MRS14

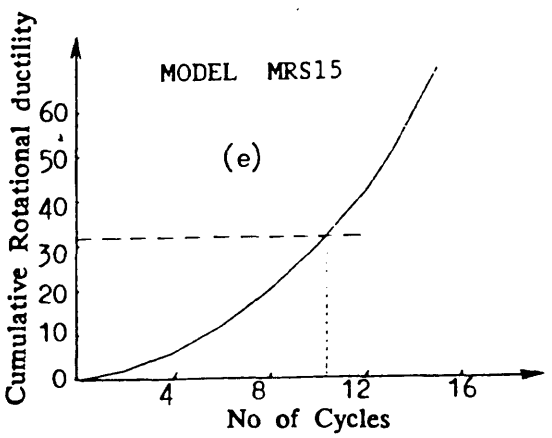

Cumulative rotational ductilities used in testing model MRS15

Figure (8.36)

load cycle for model MRS13, after 11 cycles for model MRS14 and after 10 cycles for model MRS15.

8.2.4.2 Load carrying capacity under reversed load

To satisfy the performance criteria[95] at the end of any test satisfying ductility criterion, the reduction of resistance of the component specimen due to the inflicted damage should not exceed 30% of its design strength. Such a strength reduction of the component should not result in a strength reduction of more than 20% in the entire structural system that is being considered. Figure (8.20) shows that the theoretical design strength of model MRS14 was approached but not exceeded during the test. At a rotational ductility facor, $\mu_d = -3$, (−ve sign indicates loading in upward direction) the maximum load carried by the model was 210.6 KN (95% of the design load). At last load cycle when $\mu_d = -6$, the applied load on the model was 171.9 KN (77% of design load). So the loss in load carrying capacity was 18% of the design load.

Figure (8.32) shows that the theoretical design strength of the model MRS15 was exceeded during the test. During 11th cycle at $\mu_d = +6$, the model sustained peak loads which was about 17% higher than the design strength. The applied load on the model at last load cycle at $\mu_d = +10$ was 218.4 KN (101% of design load). The loss in strength was 16% of design load.

Figure (8.7) shows that the theoretical design strength of the model MRS13 was exceeded in the last loading cycle where $\mu_d = \pm 7.5$. Information about the load carrying capacity is availabe only at $\mu_d = \pm 2$ and at $\mu_d = \pm 7.5$ due to the difficulties encountered in testing this model. Because of the insufficient information it is not possible to calculate the degradation of strength of this model.

8.2.4.3 Stiffness degradation and damping coefficient under reversed load

Seismic response parameter, stiffness of the structure was determined from

lateral load– slab rotation relationship as shown in Figure (8.37–a). The degradation in stiffness (secant) with cycling during the test is shown in Figure (8.38) for models MRS13 to MRS15. For model MRS13, the stiffness at last cycle was about 31% of the stiffness at first yield. For models MRS14 and MRS15, the ratio of the stiffness at last cycle to that at first yield was 25% and 30% respectively.

The damping coefficient, φ, for each completed cycle was calculated from the following equation (8.1) :

$$\varphi = \frac{1}{2\pi} \cdot \frac{(A_1 + A_1')}{(A_2 + A_2')} \qquad (8.1)$$

where A_1 , A_1' , A_2 and A_2' are the areas as shown in Figure (8.37–b). Planimeter was used to measure accurately the above mentioned areas of every completed cycles of the tested models. Average of three measurements was considered. Figure (8.39) shows the effect of number of cycles as well as rotational ductility factor on the damping coefficients of all the models tested. An increase in the damping coefficient with cycling means an increase in the energy absorption of the connection with cycling.

8.3 Constitutive Models for Cyclic Loading

8.3.1 Introduction

Typical behaviour of plain concrete subjected to cyclic uniaxial compressive stress is illustrated in Figure (8.40). The degradation in both stiffness and strength with increasing number of applied cycles are shown. For each cycle of unloading–reloading, a hysteresis loop is observed. The area of this loop (representing energy dissipation) decreases with each successive cycle.

To realistically simulate cyclic response, the model should be capable of accounting for strength degradation, stiffness degradation, and hysteric behaviour

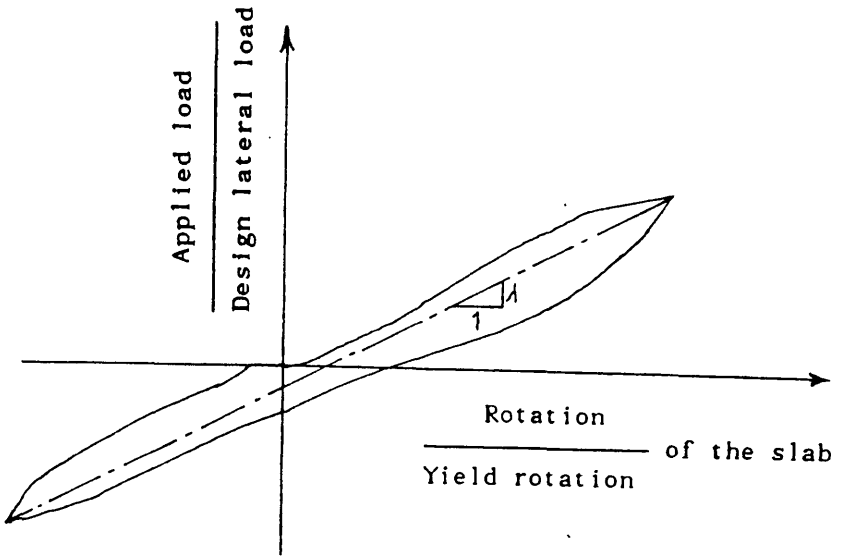

(a) Calculation of stiffness coefficient

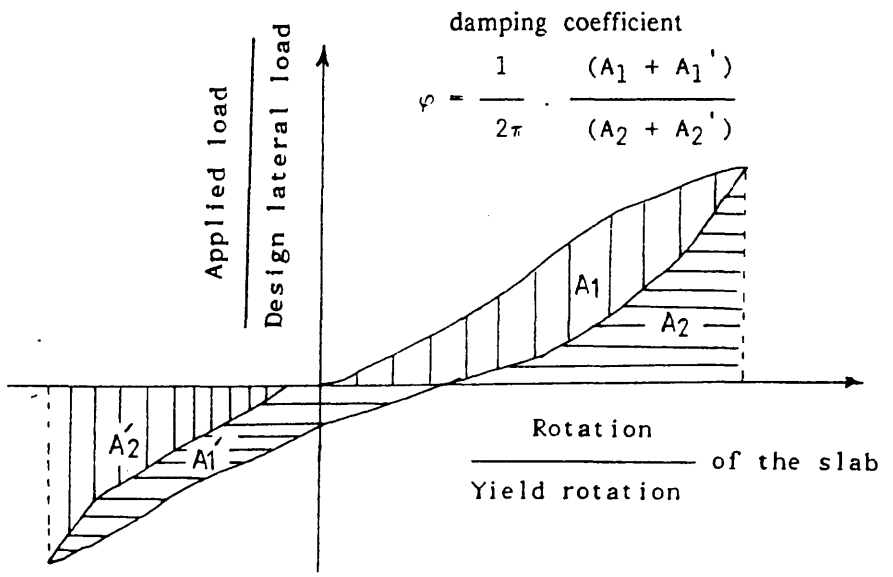

(b) Showing the areas for the calculation of damping coefficient

Figure (8.37) : Seismic response parameters from nondimensionalised Load - Slab rotation (P/P_d - θ/θ_y) cycles

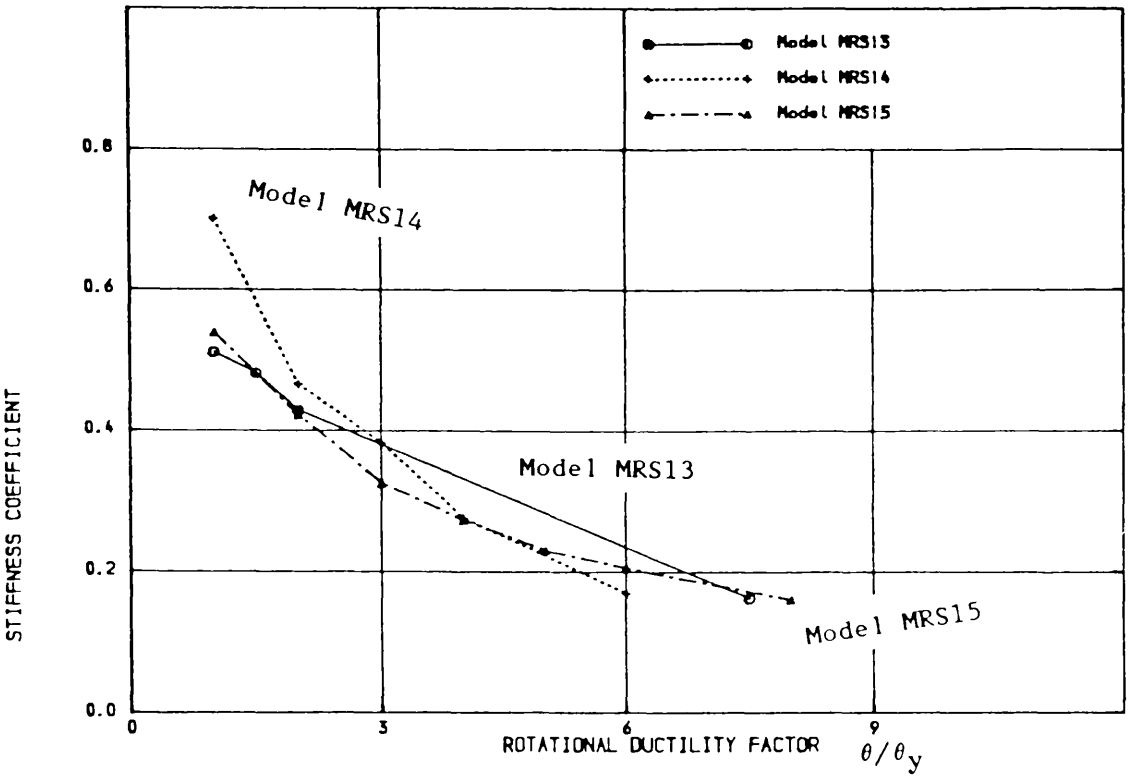

FIGURE (8.38) , EFFECT OF ROTATIONAL DUCTILITY FACTOR ON STIFFNESS CO-EFFICIENT OF THE MODELS TESTED UNDER REVERSED CYCLIC LOADINGS

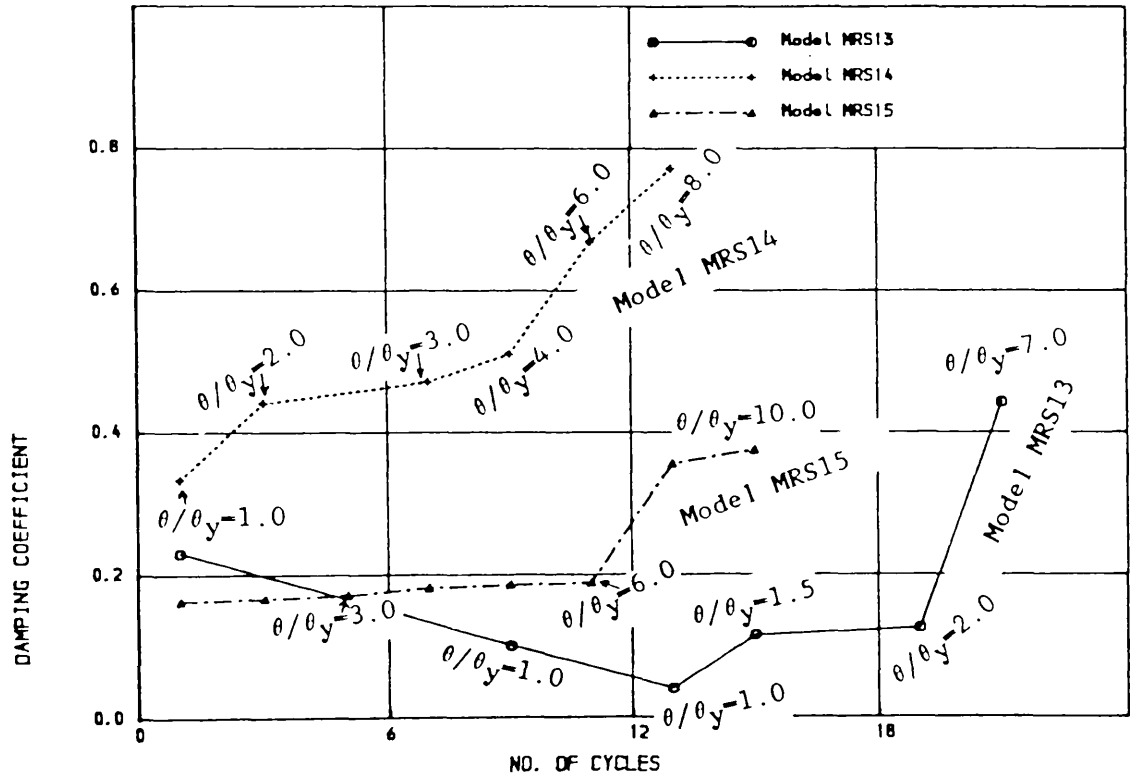

FIGURE (8.39) , EFFECT OF NUMBER OF CYCLES ON THE DAMPING COEFFICIENT OF THE MODELS TESTED UNDER REVERSED CYCLIC LOADINGS

under load cycles. In recent years, considerable interest has developed concerning the multiaxial behaviour of concrete, especially under cyclic loading. This is due to the widespread application of critical reinforced and prestressed concrete structures in which the concrete is multiaxially loaded and in the recognition of the importance of cyclic loads, such as those due to earthquakes or ocean storms. With the development of large digital computers and the advances in numerical techniques, refined analysis of geometrically complex structures are now computationally feasible. However, the capability for numerical prediction of the behaviour of such structures within the nonlinear regime is often limited by the inadequacy of the material models. This is specially true in the presence of load reversals and low–cycle fatigue.

It is well known that, except at very low stress levels, unloading in concrete follows an entirely different path from that followed upon loading. When unloading to the initial state of stress, the strains are not recovered completely and a permanent set of strains (plastic strains) remains. The mathematical models for concrete proposed by Kotsovos et. el. (67,68) as described in details in chapter four are suitable to monotonic loading and can not be applied directly to cyclic loading conditions. In order to model concrete behaviour under cyclic loading conditions, the monotonic models were combined with a loading criterion which is formulated independently from the constitutive relations.

A biaxial orthotopic hypoelastic model was used by Darwin and Pecknold (97) for the analysis of planar reinforced concrete structures. A nonlinear stress–strain law for plain concrete under cyclic biaxial stresses was developed and incorporated into a finite element numerical solution programme. The concept of "equivalent uniaxial strain" was introduced by them (97) to trace the deformation history and to control cyclic behaviour. The orthotropy axes were chosen to coincide with the current principal stress directions, and the strain–dependent tangent moduli were assumed to be functions of the principal stress ratio. Elwi and Murray (98)

generalised the constitutive model for three dimensional (axisymmetric) cases. The model has been used in different applications of finite element analyses to concrete structures. Quite good results have been obtained in most cases[97,99]. It is well known that there is a marked influence of hydrostatic pressure on the behaviour of concrete under triaxial stress states. These behaviours cannot be accounted for by the equivalent uniaxial approach. Thus the model has little validity in three–dimensional situations. It is mainly applicable to planar problems such as beams, panels, and thin shells where the stress state is predominantly biaxial. However, applications of the incremental orthotropic models under general loading histories involving rotation of the principal stress directions have been subjected to strong criticism by Bazant [100], both on physical and theoretical grounds. Because of the orthotropic form of the model, the principal directions of the incremental stresses and strains coincide, and cross effects between incremental normal stresses and shear strains in the principal stress directions are neglected. No explicit loading– unloading criteria are used in these models, so there is ambiguity in the definition of loading and unloading under general loading conditions. A strict loading in one principal stress axis may be accompanied by unloading in the other principal directions.

Fardis et. el.[101] have proposed a simple time–independent, mathematical model for cyclic behaviour of concrete under multiaxial stress conditions. An essential feature of the model is a bounding surface in stress space, which is a function of ϵ_{max}, the maximum compressive strain experienced by the material to the present state. It was encouraged in the paper[101] to implement their model in two– or three– dimensional nonlinear finite element programmes. A brief description of this model is given in the folowing sections.

8.3.2 Cyclic Constitutive Law for Concrete proposed by Fardis et. el.[101]

A simple model was proposed by Fardis et. el. for the time–independent monotonic and cyclic behaviour of concrete. The model uses the concept of a

"bounding surface" in stress space proposed earlier for metals by Dafalias and Popov [102]. The stress point always lies inside or on the bounding surface, and its proximity to the latter determines the value of the tangent plastic modulus. This bounding surface shrinks in stress space as a function of ϵ_{max}, the maximum principal compressive strain ever experienced by the material. Strain components are assumed to be entirely plastic and are computed by superposition of an isotropic component, proportional to the hydrostatic stress increment, and deviatoric and isotropic components, proportional to the octahedral shear stress increment. The plastic modulus for calculation of the latter strain components is a function of the distance of the stress point from the limit surface, measured along the direction of the current stress increment, and of ϵ_{max}. A brief description of the bounding surface and cyclic stress – strain law with its verification against available experimental results will be given in the following sections. The problems encountered in the implementation of this constitutive relationship into the finite element program will also be discussed.

8.3.2.1 Bounding Surface

A pivotal component of the model is a surface in stress space called bounding surface, which for given stress and strain history always encloses the current stress point. For monotonic, nearly proportional loading, the bounding surface is the usual failure surface (defined as the locus of stress points corresponding to ultimate strength) and is almost independent of the strain history. For complicated stress paths involving stress reversals, the bounding surface is a function of the strain history. This is clear from cyclic uniaxial data [103,104] (see Figure (8.40)) which shows that if following several loading–unloading cycles the material reaches an axial strain larger than that at the peak of the monotonic stress–strain curve, then upon subsequent reloading, failure occurs at a stress lower than the uniaxial compressive strength, f'c. Therefore, the bounding surface, which passes through the peak of this latter reloading branch, shrinks during inelastic deformation.

Experimentally it was found that for cyclic loading, the strength of the material depends on the maximum principal compressive strain experienced by the material in the course of loading. This latter strain is denoted here by ϵ_{max}, and is interpreted as the single memory parameter which reflects the effect of previous strain history on the limit surface. Ultrasonic measurements on cyclically loaded uniaxial specimens have shown also that ϵ_{max} is the most appropriate measure of load–induced internal damage(105). For these reasons, the bounding surface (101) was assumed to depend on ϵ_{max} and given by an equation of the form

$$F(\sigma_{ij} , \epsilon_{max}) = 0 \tag{8.2}$$

For given ϵ_{max}, the bounding surface can be described in the three–dimensional Haig–Westergaard principal stress space, and $F(\sigma_{ij}, \epsilon_{max})$ can be considered as a function of stress invariants. The three invariants used are the first stress invariant I_1 and the second and third deviatoric stress invariants J_2 and J_3 where:

$$\begin{aligned} I_1 &= \sigma_{ii} \quad (i = 1,2,3) \\ J_2 &= S_{ij} \cdot S_{ij} / 2 \quad (i,j = 1,2,3) \\ J_3 &= S_{ij} \cdot S_{jk} \cdot S_{ki} \quad (i,j,k = 1,2,3) \end{aligned} \tag{8.3}$$

where $S_{ij} = \sigma_{ij} - \delta_{ij} .I_1/3$ = the deviatoric stress tensor; and δ_{ij} = the Kronecker delta. The three stress invariants I_1, J_2 and J_3 were selected because of their geometrical meaning. The projection of the position vector of the stress point $(\sigma_1,\sigma_2,\sigma_3)$ onto the hydrostatic axis equals $I_1/\sqrt{3}$, where as the distance of $(\sigma_1,\sigma_2,\sigma_3)$ from this latter axis = $\sqrt{2J_2}$. Finally if the stress space is projected on the deviatoric plane, $I_1 = 0$, the angle θ between the projection of the position vector of $(\sigma_I,\sigma_{II},\sigma_{III})$ and the projection of any tensile semiaxis is such that

$$\cos 3\theta = \frac{-3\sqrt{3}\, J_3}{2\, J_2^{\,3/2}} \tag{8.4}$$

After a trial and error procedure, the following equation was chosen for $F(\sigma_{ij}, \epsilon_{max})$ for the bounding surface(101)

$$\frac{\frac{\sqrt{J_2}}{f'_c}}{\frac{I_1}{f'_c} + 0.3}\left(5.3 + \cos 3\theta - \frac{\cos^2 3\theta}{2} + \frac{\cos^3 3\theta}{3}\right) - \frac{4}{7}\sqrt{-1 - 1.35 \ln \cdot \epsilon_{max}} = 0 \qquad (8.5)$$

The above equation (8.5) for the bounding surface applies for combinations of σ_{ij} and ϵ_{max} beyond the peak of the monotonic stress–strain curves, and corresponds to fictitiously high values of ultimate strength for pre–peak values of ϵ_{max} (see Figure 8.40–a). Therefore, it is meaningful to introduce an outerlimit to the bounding surface. This outer limit is selected to be the failure surface obtained in proportional or close to proportional monotonic loading. The monotonic failure surface, serving as an outer limit to the bounding surface in equation (8.5) is given by

$$\left(\frac{I_1}{f'_c} + 0.3\right) - (12 + 11 \cos 3\theta)^{1/6}\left[0.7\left(\frac{\sqrt{J_2}}{f'_c}\right)^2 + 1.85\frac{\sqrt{J_2}}{f'_c}\right] = 0 \qquad (8.6)$$

Therefore, for given ϵ_{max}, the innermost of the two surfaces is considered as the bounding surface from which distances are measured.

8.3.2.2 Incremental Stress–Strain Relation

As mentioned earlier, incremental strain components $d\epsilon_{ij}$ is assumed plastic in this model and decomposed into its deviatoric and volumetric parts

$$d\epsilon_{ij} = de_{ij} + \delta_{ij} \cdot d\epsilon_{kk} / 3 \quad (k = 1,2,3) \qquad (8.7)$$

in which $d\epsilon_{kk}$ = the volumetric strain increment; and δ_{ij} = the Kronecker delta. It was postulated that de_{ij} is caused only by changes in the deviatoric stress tensor,

S_{ij} and the volumetric portion of $d\epsilon_{ij}$ is caused both by isotropic and by deviatoric stress increments.

The deviatoric part of the strain increment, de_{ij}, is proportional to S_{ij}. The proportionality yields

$$\frac{de_{ij}}{S_{ij}} = \frac{d\gamma_o}{\tau_o} \tag{8.8}$$

where the octahedral shear stress and shear strain are defined as $\tau_o = 1/3\ S_{ij} \cdot S_{ij}$ and $\gamma_o = 1/3\ e_{ij} \cdot e_{ij}$ (i,j = 1,2,3). Assuming incremental linearity, we can write

$$d\gamma_o = \frac{d\tau_o}{H} \tag{8.9}$$

where the generalized shear modulus, H depends on σ_{ij} and on the history of strain only through d/d_{max} and ϵ_{max}, where 'd' is the distance of current stress point from the bounding surface (corresponding to compression failure for first loading or reloading and to tension failure for unloading) measured in stress space along the instantaneous loading direction and d_{max} is the value of d at the begining of the current loading process (See Figure 8.41) or at the last stress reversal. A stress reversal is defined as a change in sign of $d\tau_o$. When $d\tau_o = S_{km} \cdot d\sigma_{km} / 3\tau_o$ (k,m = 1,2,3) becomes negative, we have unloading. When $d\tau_o$ becomes positive after being negative we have reloading. If d becomes less than any previously recorded value of d, denoted by d_{min}, then loading beyond that value of d is considered as first loading and not as reloading.

For first loading, H is expressed as

$$H = 16\ f'_c \left(\frac{d}{d_{max} \cdot \epsilon_{max}} \right)^{0.55} \tag{8.10-a}$$

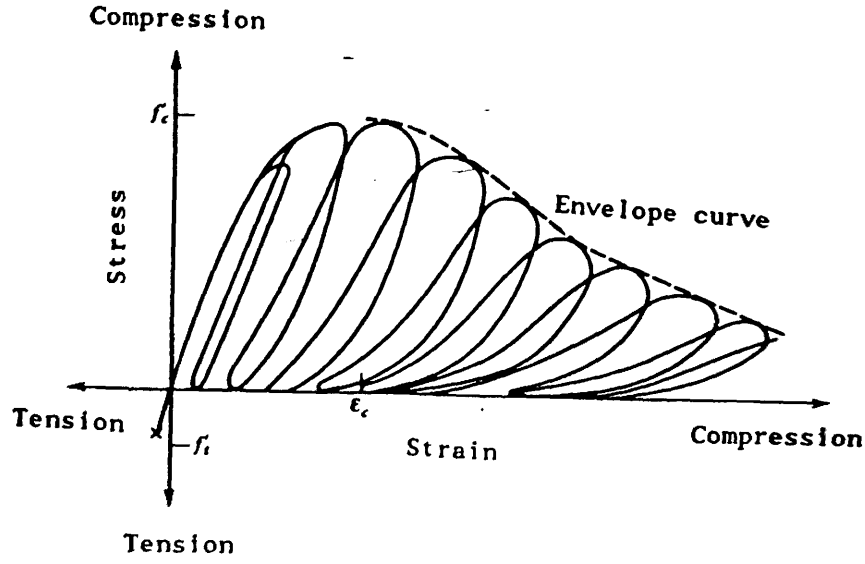

Figure (8.40) : Response of concrete to uniaxial loading (103)

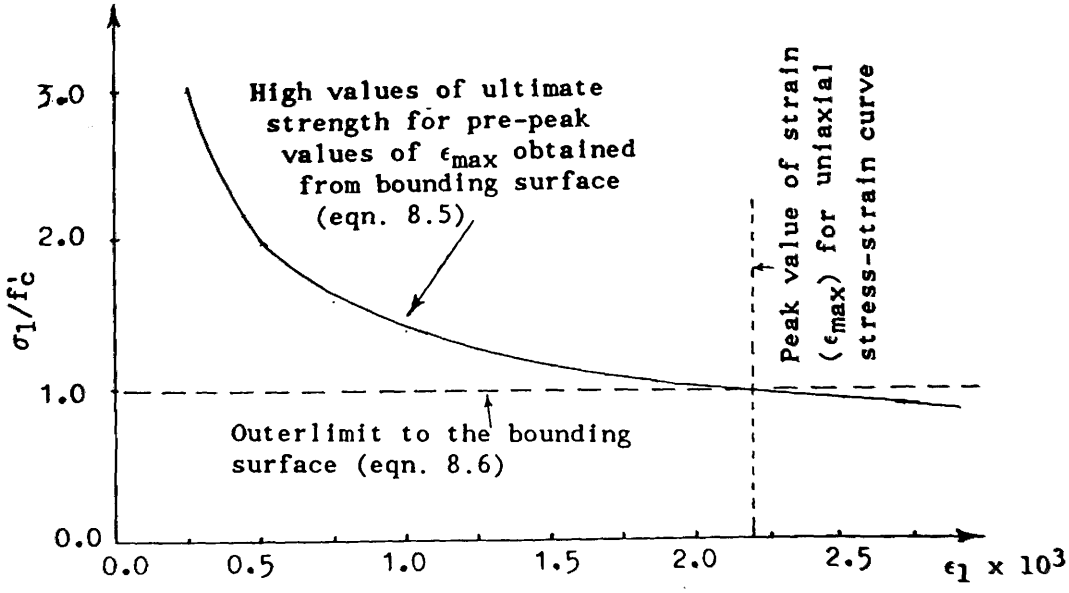

Figure (8.40-a) : Uniaxial stress-strain relationship calculated from bounding surface (eqn. 8.5) and its outer limit (eqn. 8.6)

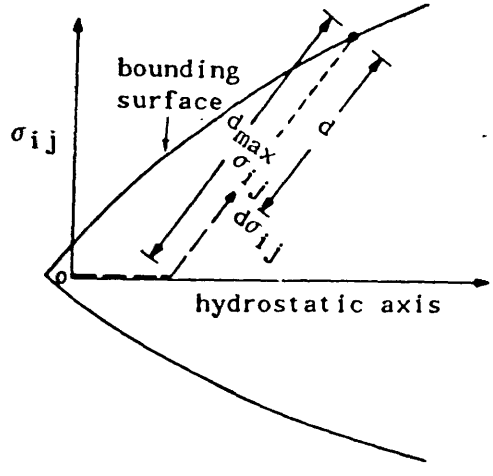

Figure (8.41) : Definition of parameters, d and d_{max} for generalized shear modulus H

For unloading, H is equal to

$$H = 16\, f'_c \left(\frac{d}{d_{max} \cdot \epsilon_{max}} \right) 0.65 \qquad (8.10\text{-b})$$

For reloading, H is equal to

$$H = 3750\, f'_c\, e^{-350\epsilon_{max}} \left[\left(\frac{d}{d_{max}} \right) - 0.75 \left(\frac{d}{d_{max}} \right)^2 \right] \qquad (8.10\text{-c})$$

The portion of the volumetric strain increment $d\epsilon_{kk}$ caused by the isotropic component of $d\epsilon_{ij}$, $\delta_{ij}\, dI_1/3$ is given by

$$d\epsilon_{kk,o} = \frac{dI_1}{3K_t} \qquad (8.11)$$

A simple expression for the tangent modulus K_t was given by

$$K_t = \frac{K_o}{1 + \frac{I_1}{3f'_c}} \qquad (8.12)$$

The initial value of K_t was selected equal to 550 f'c. For cyclic loading, if dI_1 becomes negative (positive) from positive (negative), then we have unloading (reloading). On the basis of hydrostatic tests with unloading, K_t is set equal to K_o during unloading and for reloading upto the maximum previous value of I_1. If loading continues beyond this last maximum value, then K_t is obtained from equation (8.12).

The remaining portion of $d\epsilon_{kk}$ is associated with deviatoric strains. When σ_{ij} is far from the bounding surface, compaction ($d\epsilon_{kk} > 0$) follows any increase in the octahedral shear strain (shear compaction); whereas when the stress point comes close to the bounding surface, an increase in γ_o causes shear dilatancy ($d\epsilon_{kk} < 0$). Assuming incremental linearity we can write

$$d\epsilon_{kk,d} = F_{cd}\, d\gamma_o \quad (k = 1,2,3) \tag{8.13}$$

On the basis of triaxial data with I_1 = constant, the shear compaction dilatancy factor, F_{cd} was selected as

$$F_{cd} = 9.0\,(\epsilon_{max})^{1/4}\,(d/d_{max} - 0.1) \tag{8.14}$$

Combining equations (8.7), (8.9), (8.11) and (8.13) the incremental stress–strain relationship takes the form :

$$d\epsilon_{ij} = \left(\frac{S_{ij}}{\tau_o} + \delta_{ij}\frac{F_{cd}}{3}\right)\frac{d\tau_o}{H} + \delta_{ij}\frac{dI_1}{9K_t} \tag{8.15}$$

By expressing $d\tau_o$ as $\partial\tau_o/\partial\sigma_{km}\, d\sigma_{km}$ (k,m = 1,2,3), equation (8.15) can be written as :

$$d\epsilon_{ij} = \frac{1}{3H\tau_o}\left(\frac{S_{ij}}{\tau_o} + \delta_{ij}\frac{F_{cd}}{3}\right) S_{km}\, d\sigma_{km} + \delta_{ij}\frac{dI_1}{9K_t} \tag{8.16}$$

8.3.2.3 Comparison with test results

Figure (8.42) compares the predictions of stress–strain curves by the proposed cyclic model to typical uniaxial test results. The overall agreement is very good. Since no experimental data are available on the behaviour of plain concrete under biaxial cyclic loading, the model is compared with the experimental monotonic stress–strain curves of Kupfer et el.[57] for various combinations of biaxial compression in Figures (8.43) and (8.44). The part of the curve predicted by the model for first loading match the experimental curves in the major compressive and tensile direction with reasonable accuracy.

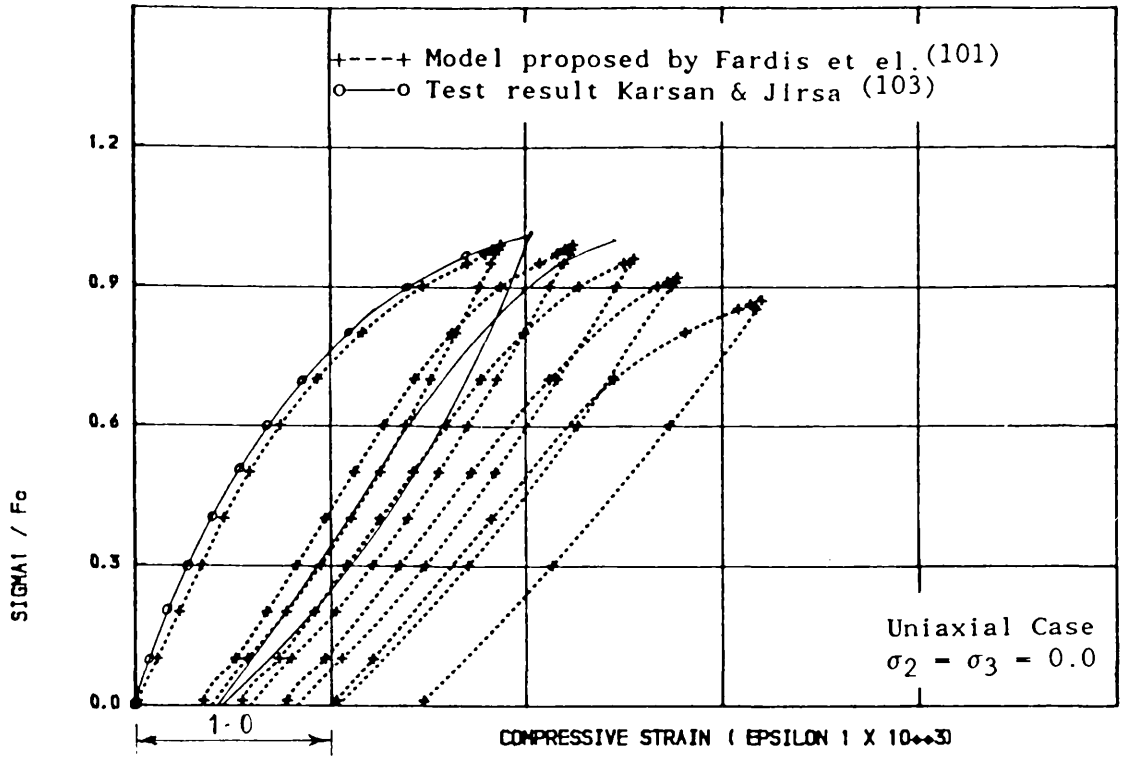

FIGURE (8.42-a) , STRESS-STRAIN RELATIONSHIP OF CONCRETE FOR CYCLIC UNIAXIAL COMPRESSION TEST (SIGMA 2 = SIGMA 3 = 0.0)

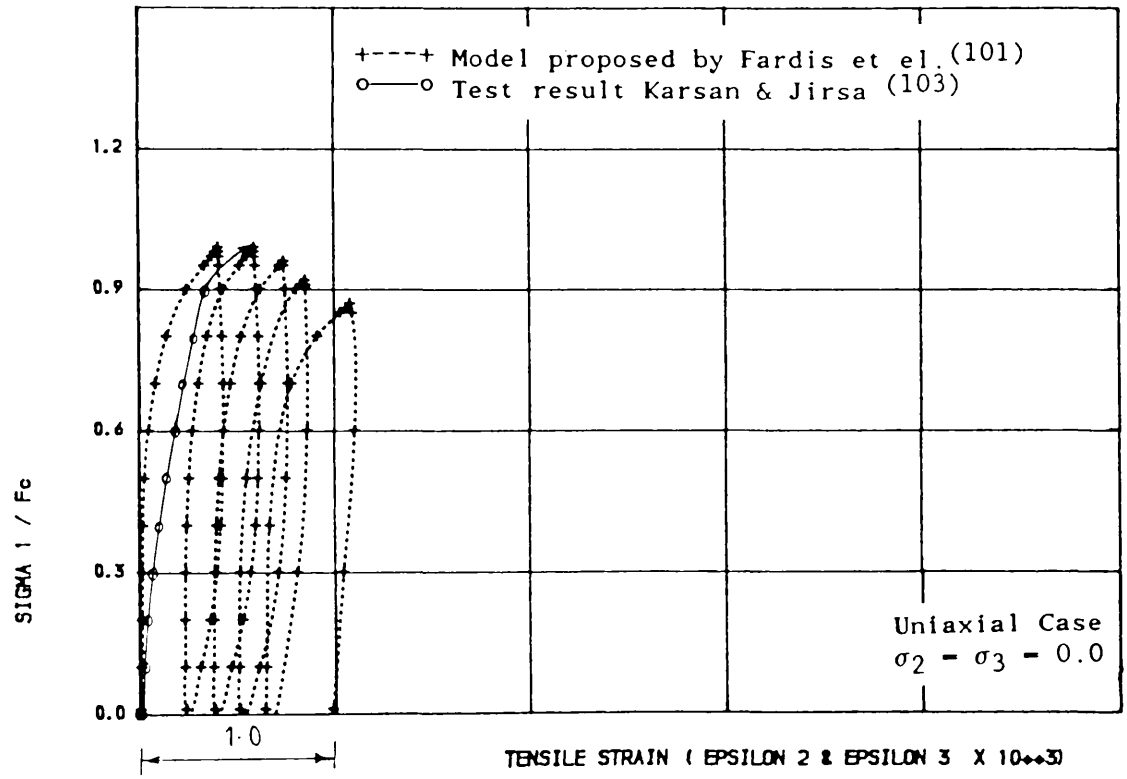

FIGURE (8.42-b) , STRESS-STRAIN RELATIONSHIP OF CONCRETE FOR CYCLIC UNIAXIAL COMPRESSION TEST (SIGMA 2 = SIGMA 3 = 0.0)

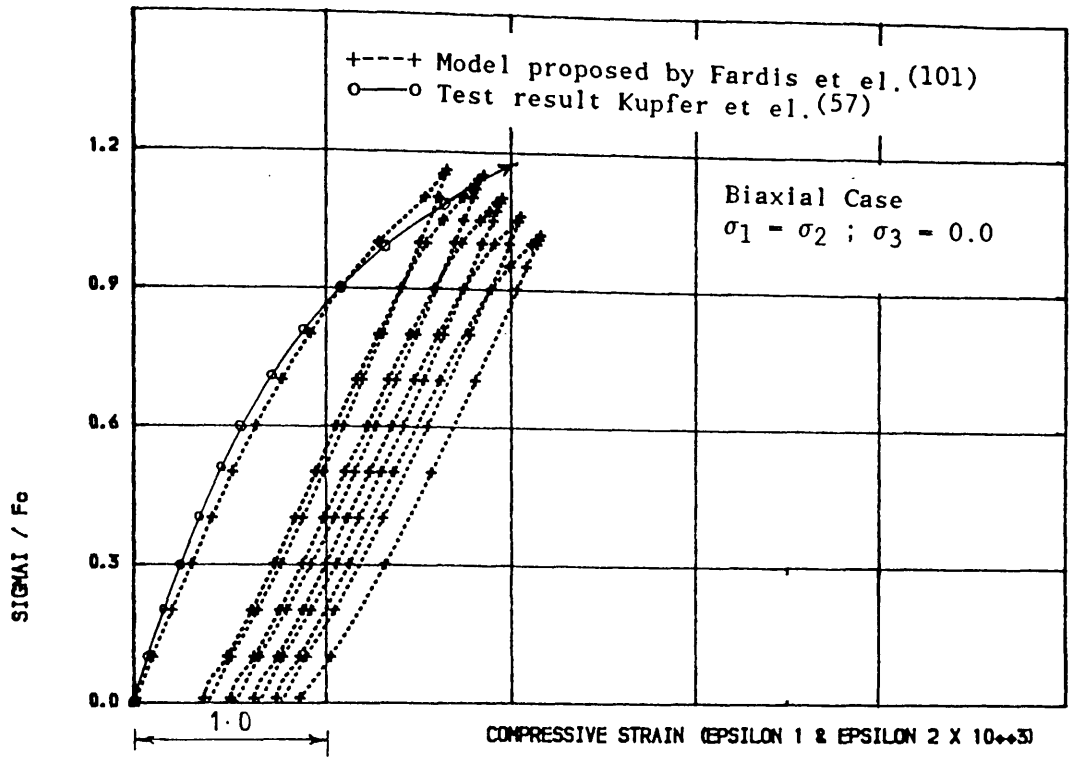

FIGURE (8.43-a) : STRESS - STRAIN RELATIONSHIP OF CONCRETE FOR CYCLIC BIAXIAL COMPRESSION TEST (SIGMA 1 = SIGMA 2)

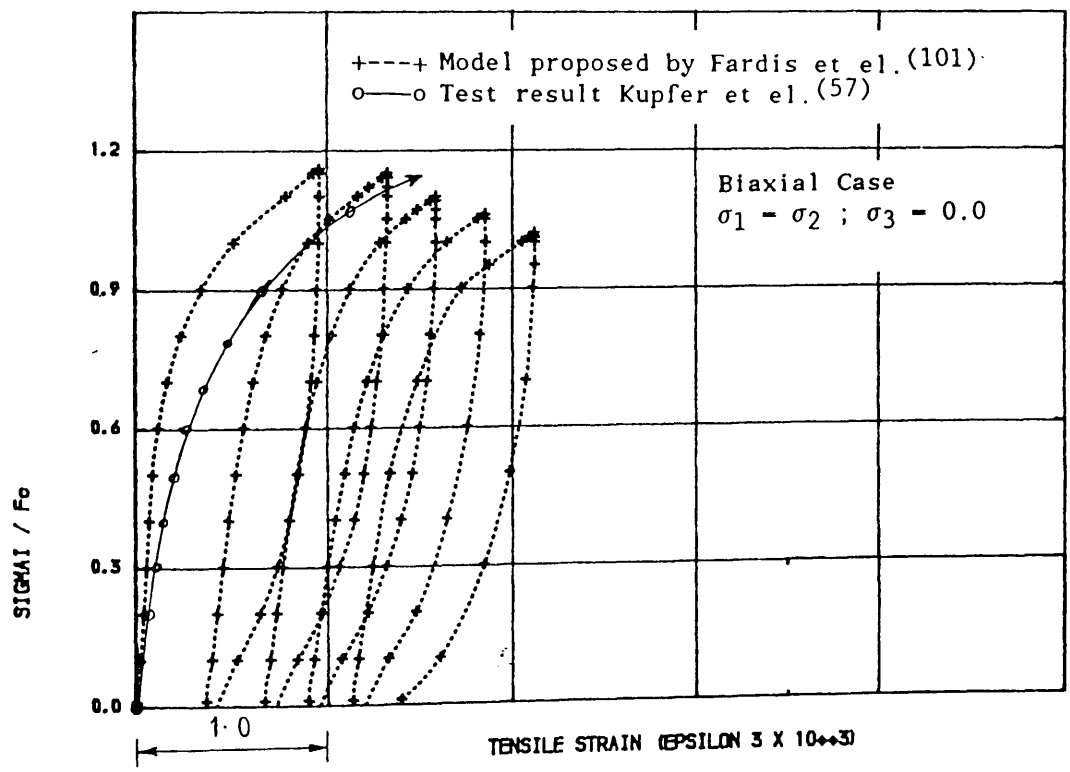

FIGURE (8.43-b) : STRESS - STRAIN RELATIONSHIP OF CONCRETE FOR CYCLIC BIAXIAL COMPRESSION TEST (SIGMA 1 = SIGMA 2)

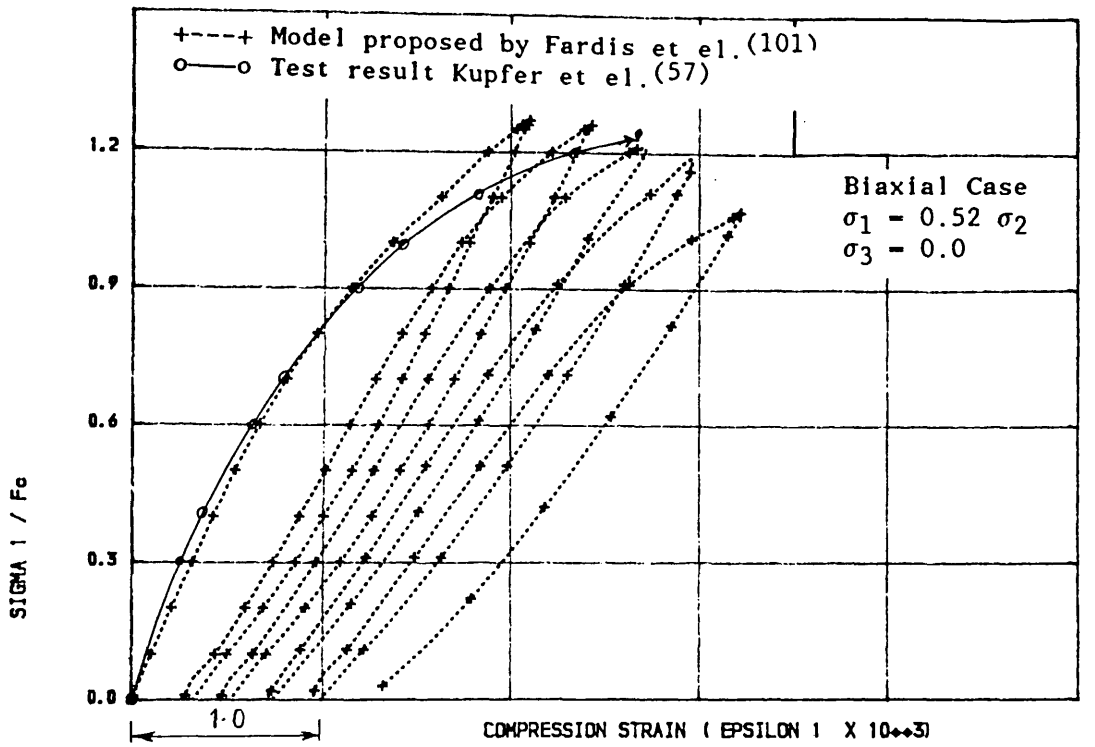

*FIGURE (8.44-a) , STRESS-STRAIN RELATIONSHIP OF CONCRETE FOR CYCLIC BIAXIAL COMPRESSION TEST (SIGMA 2 = 0.52 * SIGMA 1)*

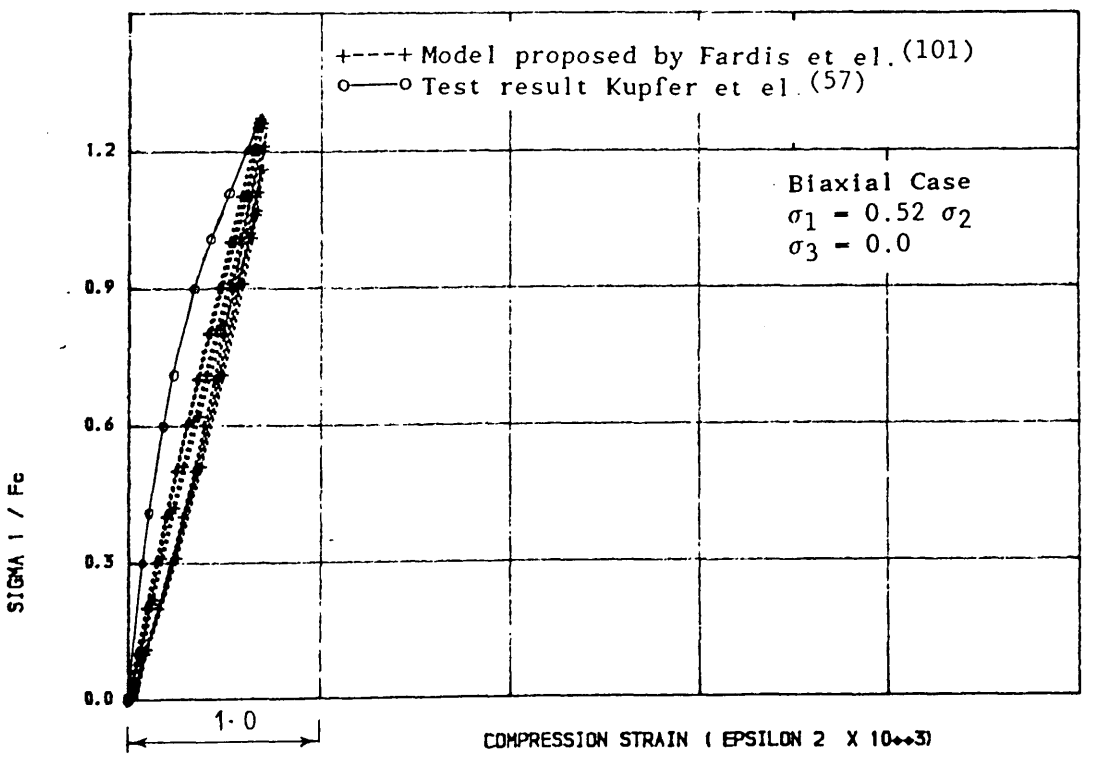

*FIGURE (8.44-b) , STRESS-STRAIN RELATIONSHIP OF CONCRETE FOR CYCLIC BIAXIAL COMPRESSION TEST (SIGMA 2 = 0.52 * SIGMA 1)*

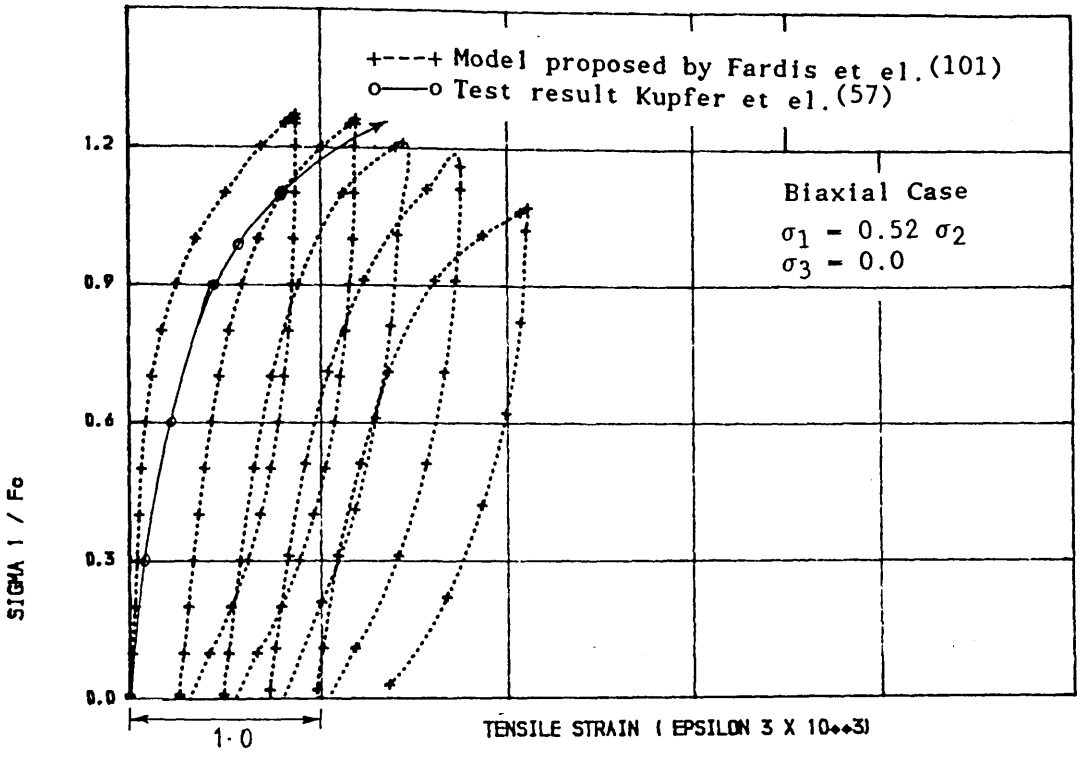

*FIGURE (6.44-c) , STRESS-STRAIN RELATIONSHIP OF CONCRETE FOR CYCLIC BIAXIAL COMPRESSION TEST (SIGMA 2 = 0.52 * SIGMA 1)*

8.3.2.4 Implementation of the Finite Element Programme

The incremental stress – strain relationship of equation (8.16) can be written in matrix form for finite element application as :

$$\{ d\epsilon \} = [C] \{ d\sigma \}$$

where matrix [C] is called the material compliance matrix. To formulate the compliance matrix from equation (8.16) the incremental stress was divided into three parts as follows :

$$d\epsilon_{ij} = \underbrace{\frac{S_{ij}S_{km}\, d\sigma_{km}}{3H\tau_o^2}}_{\text{1st part}} + \underbrace{\delta_{ij}\frac{F_{cd}S_{km}\, d\sigma_{km}}{9\, H\, \tau_o}}_{\text{2nd part}} + \underbrace{\delta_{ij}\frac{dI_1}{9K_t}}_{\text{3rd part}} \quad (k,m = 1,2,3) \quad (8.17)$$

Expanding the first part of equation (8.17) for k,m = 1,2,3, we can write

$$d\epsilon_{ij} = \frac{S_{ij}}{3H\tau_o^2}(S_{11}d\sigma_{11} + S_{22}d\sigma_{22} + S_{33}d\sigma_{33} + S_{12}d\sigma_{12} + S_{23}d\sigma_{23} + S_{31}d\sigma_{31})$$

For triaxial stress conditions, the incremental strain can be related with 1st part of incremental stress as

$$\begin{bmatrix} d\epsilon_{11} \\ d\epsilon_{22} \\ d\epsilon_{33} \\ d\epsilon_{12} \\ d\epsilon_{23} \\ d\epsilon_{31} \end{bmatrix} = [C]^{(1)} \begin{bmatrix} d\sigma_{11} \\ d\sigma_{22} \\ d\sigma_{33} \\ d\sigma_{12} \\ d\sigma_{23} \\ d\sigma_{31} \end{bmatrix}$$

where

$$[C]^{(1)} = \frac{1}{3H\tau_o^2}\begin{bmatrix} s_{11}^2 & s_{11}s_{22} & s_{11}s_{33} & s_{11}s_{12} & s_{11}s_{23} & s_{11}s_{31} \\ s_{11}s_{22} & s_{22}^2 & s_{22}s_{33} & s_{22}s_{12} & s_{22}s_{23} & s_{22}s_{31} \\ s_{11}s_{33} & s_{33}s_{22} & s_{33}^2 & s_{33}s_{12} & s_{33}s_{23} & s_{33}s_{31} \\ s_{11}s_{12} & s_{12}s_{22} & s_{12}s_{33} & s_{12}^2 & s_{12}s_{23} & s_{12}s_{31} \\ s_{11}s_{23} & s_{23}s_{22} & s_{23}s_{33} & s_{23}s_{12} & s_{23}^2 & s_{11}s_{31} \\ s_{11}s_{31} & s_{31}s_{22} & s_{31}s_{33} & s_{31}s_{12} & s_{31}s_{23} & s_{31}^2 \end{bmatrix}$$

Similarly, by expanding the 2nd and 3rd parts of equation (8.17) for k,m = 1,2,3 for triaxial stress conditions, the compliance matrix $[\ C\ ]^{(2)}$ and $[\ C\ ]^{(3)}$ take the form :

$$[C]^{(2)} = \frac{F_{cd}}{9H\tau_o}\begin{bmatrix} s_{11} & s_{22} & s_{33} & s_{12} & s_{23} & s_{31} \\ s_{11} & s_{22} & s_{33} & s_{12} & s_{23} & s_{31} \\ s_{11} & s_{22} & s_{33} & s_{12} & s_{23} & s_{31} \\ 0 & 0 & 0 & 0 & 0 & 0 \\ 0 & 0 & 0 & 0 & 0 & 0 \\ 0 & 0 & 0 & 0 & 0 & 0 \end{bmatrix}$$

Unsymmetric

and

$$[C]^{(3)} = \frac{1}{9\ K_t}\begin{bmatrix} 1 & 1 & 1 & 0 & 0 & 0 \\ 1 & 1 & 1 & 0 & 0 & 0 \\ 1 & 1 & 1 & 0 & 0 & 0 \\ 0 & 0 & 0 & 0 & 0 & 0 \\ 0 & 0 & 0 & 0 & 0 & 0 \\ 0 & 0 & 0 & 0 & 0 & 0 \end{bmatrix}$$

The compliance matrices formulated as above in three parts were added together. In the finite element displacement method, we need the inverse relationship of equation (8.17) where incremental stresses are related to incremental strains by a matrix [D] i.e.,

$$\{ d\sigma \} = [D] \{ d\epsilon \} = [C]^{-1} \{ d\epsilon \}$$

The total [C] matrix was inverted numerically by the standard routines of inversion, e.g., Partitioning method, Gauss – Jordan method, Gauss – elimination method (106) and using standard NAG subroutines F01AAF, F04AEF, F04JDF, F04JGF etc. No unique solution was found for the above matrix. Drucker's material stability theory (107) postulates that a unique inverse of any constitutive relation should always be exist. That is, for any constitutive law $\{\sigma_{ij}\} = [D] \{\epsilon_{ij}\}$ based on an assumed function for strain energy, a unique inverse relation $\{\epsilon_{ij}\} = [D]^{-1} \{\sigma_{ij}\}$ should always be obtained. In the following, the analysis procedure is described with the help of a numerical example.

Let us consider, for example, the total compliance matrix calculated from the constitutive law for Element no. 1, Gauss point 1, of model MRS13

Total Compliance matrix $[C]^T$

$$\begin{bmatrix}
0.466E\text{-}05 & 0.893E\text{-}06 & 0.512E\text{-}05 & -0.149E\text{-}05 & 0.125E\text{-}05 & -0.278E\text{-}06 \\
0.102E\text{-}07 & 0.121E\text{-}04 & -0.146E\text{-}05 & 0.479E\text{-}05 & -0.400E\text{-}05 & 0.892E\text{-}06 \\
0.522E\text{-}05 & -0.466E\text{-}06 & 0.591E\text{-}05 & -0.225E\text{-}05 & 0.188E\text{-}05 & -0.419E\text{-}06 \\
-0.184E\text{-}05 & 0.444E\text{-}05 & -0.260E\text{-}05 & 0.249E\text{-}05 & -0.208E\text{-}05 & 0.463E\text{-}06 \\
0.154E\text{-}05 & -0.371E\text{-}05 & 0.217E\text{-}05 & -0.208E\text{-}05 & 0.174E\text{-}05 & -0.387E\text{-}06 \\
-0.343E\text{-}06 & 0.827E\text{-}06 & -0.484E\text{-}06 & 0.463E\text{-}06 & -0.387E\text{-}06 & 0.862E\text{-}07
\end{bmatrix}$$

for incremental stress level in N/mm^2 $d\sigma_{11} = 0.107$, $d\sigma_{22} = 0.440$, $d\sigma_{33} = 0.0664$, $d\sigma_{12} = 0.132$, $d\sigma_{23} = -0.110$, $d\sigma_{31} = 0.0246$ and incremental strain

$d\epsilon_{11} = 0.540E-06$, $d\epsilon_{22} = 0.727E-05$, $d\epsilon_{33} = -0.275E-06$, $d\epsilon_{12} = 0.533E-05$, $d\epsilon_{23} = -0.445E-05$, $d\epsilon_{31} = 0.992E-06$. The inverse of this matrix obtained by the partitioning method as shown below cannot be accepted as rigidity matrix for the recalculation of stresses (which are found in N/mm^2 $d\sigma_{11} = -208.95$, $d\sigma_{22} = -16.46$, $d\sigma_{33} = -85.41$, $d\sigma_{12} = 58.82$, $d\sigma_{23} = -0.576$, $d\sigma_{31} = -4.2$) from the same above incremental strains.

Inverse of the total Compliance Matrix

$$\begin{bmatrix}
0.173E+12 & -0.187E+11 & -0.154E+12 & -0.456E+07 & 0.954E+07 & 0.371E+08 \\
-0.187E+11 & 0.202E+10 & 0.166E+11 & -0.650E+07 & -0.487E+07 & -0.261E+08 \\
-0.154E+12 & 0.166E+11 & 0.137E+12 & 0.113E+08 & -0.284E+07 & -0.532E+07 \\
-0.563E+07 & -0.745E+07 & 0.127E+08 & 0.226E+08 & -0.915E+06 & -0.506E+07 \\
0.706E+06 & -0.234E+06 & -0.234E+07 & 0.317E+07 & 0.439E+08 & 0.180E+09 \\
0.424E+07 & -0.139E+07 & -0.174E+08 & 0.231E+04 & 0.270E+09 & 0.121E+10
\end{bmatrix}$$

The investigation has showed that the total compliance matrix $[C]^T$ is not symmetrical and this is due to the 2nd part of the incremental stress i.e. due to the contribution from $[C]^{(2)}$. To make the compliance matrix symmetrical (which is true for most of the constitutive models), matrix $[C]^{(2)}$ was modified as

$$[C]^{(2)} = \frac{F_{cd}}{9\,H\,\tau_o}\begin{bmatrix}
S_{11} & \frac{S_{11}+S_{22}}{2} & \frac{S_{11}+S_{33}}{2} & S_{12}/2 & S_{23}/2 & S_{31}/2 \\
\frac{S_{11}+S_{22}}{2} & S_{22} & \frac{S_{22}+S_{33}}{2} & S_{12}/2 & S_{23}/2 & S_{31}/2 \\
\frac{S_{11}+S_{33}}{2} & \frac{S_{22}+S_{33}}{2} & S_{33} & S_{12}/2 & S_{23}/2 & S_{31}/2 \\
S_{12}/2 & S_{23}/2 & S_{33}/2 & 0 & 0 & 0 \\
S_{12}/2 & S_{23}/2 & S_{33}/2 & 0 & 0 & 0 \\
S_{12}/2 & S_{23}/2 & S_{33}/2 & 0 & 0 & 0
\end{bmatrix}$$

With the modified form of $[C]^{(2)}$, the total matrix $[C]^{T}$ was recalculated for the same stress level and for the same sampling point. It was then tried to inverted, but no improvement was noticed from the results as shown below

Modified $[C]^{T}$ matrix

$$\begin{bmatrix} 0.466E\text{-}05 & 0.452E\text{-}06 & 0.517E\text{-}05 & -0.167E\text{-}05 & 0.139E\text{-}05 & -0.310E\text{-}06 \\ 0.452E\text{-}06 & 0.121E\text{-}04 & -0.961E\text{-}06 & 0.462E\text{-}05 & -0.386E\text{-}05 & 0.860E\text{-}06 \\ 0.517E\text{-}05 & -0.961E\text{-}06 & 0.591E\text{-}05 & -0.243E\text{-}05 & 0.203E\text{-}05 & -0.452E\text{-}06 \\ -0.167E\text{-}05 & 0.462E\text{-}05 & -0.243E\text{-}05 & 0.249E\text{-}05 & -0.208E\text{-}05 & 0.463E\text{-}06 \\ 0.139E\text{-}05 & -0.386E\text{-}05 & 0.203E\text{-}05 & -0.208E\text{-}05 & 0.174E\text{-}05 & -0.387E\text{-}06 \\ -0.310E\text{-}06 & 0.860E\text{-}06 & -0.452E\text{-}06 & 0.463E\text{-}06 & -0.387E\text{-}06 & 0.862E\text{-}07 \end{bmatrix}$$

Inverse of the above modified matrix

$$\begin{bmatrix} 0.921E+11 & -0.995E+10 & -0.822E+11 & -0.420E+05 & 0.157E+07 & 0.191E+07 \\ -0.995E+10 & 0.108E+10 & 0.888E+10 & -0.187E+07 & -0.178E+06 & -0.352E+06 \\ -0.822E+11 & 0.888E+10 & 0.733E+11 & 0.193E+07 & -0.142E+07 & -0.419E+07 \\ -0.420E+05 & -0.187E+07 & 0.193E+07 & -0.515E+07 & -0.126E+08 & -0.374E+03 \\ 0.157E+07 & -0.178E+06 & -0.142E+07 & -0.126E+08 & -0.529E+07 & 0.437E+08 \\ 0.191E+07 & -0.352E+06 & -0.419E+07 & -0.374E+03 & 0.437E+08 & 0.196E+09 \end{bmatrix}$$

For further study, the compliance matrix was formulated in the principal directions of S_{ij}. The principal strains were related to the principal stresses by the matrix

$$\begin{bmatrix} 0.1746687E\text{-}04 & -0.5406112E\text{-}05 & -0.1863791E\text{-}06 \\ -0.5406112E\text{-}05 & 0.9299200E\text{-}05 & 0.5943371E\text{-}05 \\ -0.1863791E\text{-}06 & 0.5943371E\text{-}05 & 0.4544529E\text{-}05 \end{bmatrix}$$

The above matrix inverted numerically by the partitioning method. The a_{11} term of the inverted matrix is shown below corresponding to a_{11} of original matrix, where 3 to 7 digits were considered after the decimal point

a_{11} of original matrix	a_{11} of inverted matrix
0.1746687E-04	0.2862996E+11
0.174669E-04	-0.715747E+10
0.17467E-04	-0.86749E+09
0.1747E-04	0.4585E+08
0.175E-04	0.465E+07

This large variation of a_{11} has confirmed that the compliance matrix $[C]^T$ obtained from equation (8.16) proposed by Fardis et el.[101] is nearly singular.

8.3.3 Summary

At any stress level, the compliance matrix for the constitutive law proposed by Fardis et el. was found nearly singular. No unique inverse of the constitutive relation does exist, which violates Drucker's material stability theory. At this stage in the work, it was decided to abandon any further investigation due to lack of time.

Bazant and his co-workers have proposed a series of more sophisticated and very powerful constitutive models [108,109,110], which in principle account for nonlinear cyclic behaviour. Among these models, the most successful in reproducing cyclic behaviour is the model in Reference 109. The incremental plasticity and fracturing (microcracking) theory combines the plastic stress decrements with the fracturing stress decrements, which reflect microcracking, and accounts for internal friction, pressure sensitivity, inelastic dilatancy due to microcracking, strain softening, degradation of elastic moduli due to microcracking, and the hydrostatic

nonlinearity due to pore collapse. Failure envelopes are obtained from the constitutive law as a collection of the peak points of the stress–strain response curves. The jump–kinematic hardening allows for inelastic response during unloading, reloading and cyclic loading and, at the same time, it does not in itsef cause violation of Drucker's postulate. But the model requires a large number of functions and parameters obtained by a nonstandard, optimal–fitting technique. Since the model is incrementally linear, it will be easier to implement into the finite element programme. So the model in Reference 109 can be tried to incorporate into the standard computer programme as a subject of future investigation.

CHAPTER NINE

CONCLUSIONS AND RECOMMENDATIONS

9.1 Conclusions

From the experimental and theoretical investigations carried out in this thesis on the strength and stiffness of the Shear wall – floor slab connections with and without flanges and using shear reinforcement in the slab, the following conclusions can be drawn:

9.1.1 Use of Shear Reinforcement

1 – The mean strength of the junction with shear reinforcement has been increased by approximately 41% over that of models without shear reinforcement.

2 – The use of shear reinforcement in the slab did not change the stiffness of the structure but has markedly improved the ductility of every model as evident from Figures (6.192) and (6.193).

3 – Following the recommendations of ACI Code 318–83 and using equation (6.12), the efficiency of closed vertical stirrups ranges from 51% to 98% for all the models tested. The mean is 71% with S.D. 0.12.

4 – Closed stirrups are suitable as shear reinforcement in earthquake–resistant shear wall structures. They ensure that the wall–slab connection behaves in a ductile fashion when subjected to both monotonic and reverse cyclic loading conditions.

9.1.2 The Experimental Investigation

1 – The strength of the connection may be evaluated following the procedure proposed in section (7.11). The method is found to be quite safe and

consistent when compared with test results (see tables (7.5) and (7.6)).

2 – The critical section for shear is located at a distance d/2 around the flange (where d is the effective depth of tension reinforcement) but behind the flange it is inclined to the web as shown in Figure (7.102).

3 – Recommendations of ACI 318–83 and BS 8110 for the prediction of the strength of slab – edge column connections are unsuitable for estimating the strength of wall–slab connections, assuming shear wall as an edge column.

4 – The average ultimate load for all the models tested monotonically was 1.07 times design load with standard deviation equals 0.09. The adopted design procedure is capable of achieving the required strength of the connection.

5 – Steel did not yield within the service load (0.625 x design load) limit except in models MS6 (with small corridor opening width) and MS9 (with large bay width). The average load at first yield of steel for all the models tested was 66% of the design load.

6 – The degradation of strength due to damage was less than 20% of design strength for all the models tested under reverse cyclic loading conditions.

7 – The stiffness of the structure decreases when the corridor opening width increases, following the relation $K_o = 40.348 + 9388.7 / L$ and $K_{cr} = 14166.0\ (L)^{-1.0571}$; where K_o and K_{cr} are pre and post–cracking stiffness; L is the corridor opening width. The stiffness of the structure increases when flange width increases. This relationship obtained from the test results can be given by the equations $K_o = 0.19432\ (Z)^{1.0532}$ and $K_{cr} = 1.0651\ (Z)^{0.56328}$ where Z is the flange width of the wall. The ratio of the post to pre–cracking stiffness ranges between 27% to 50% for the models of main test series.

8 – The stiffness (secant) of the models at last load cycle (where rotational

ductitlty factor, $\theta/\theta_y > \pm 7.0$) was found 25 to 31% of the stiffness at first yield.

9 – The effect of the percentage of flexural reinforcement (ρ) on the strength of connection corresponds well with CP110. It assumes an increase in the value of critical shear stress of 0.05 N/mm^2 for every increase of 0.5% of the ratio of flexural reinforcement, when $2.0 \geq \rho \geq 0.8$.

9.1.3 The Theoretical Analysis

1 – The three dimensional finite element analysis (described in chapter four) is capable of providing a good prediction of the ultimate failure load and overall behaviour of the models under monotonic loading. The mean ratio of (V_{exp}/V_{theo}) for all the twelve models tested under monotonic loading conditions is 1.0 with standard deviation equals 0.07.

2 – The finite element mesh of Figure (7.1– b) which contained eight elements can be used to analyse the experimental models. The further mesh refinement has little influence on the predicted behaviour, but has a great influence on the cost of analysis (the cost of analysis increases linearly with the increase in the number of elements).

3 – The ultimate failure loads are greatly affected by the value of the shear retention factor. Equations (7.2) are recommended for the evaluation of this factor as a function of strain for all types of models, with and without flanges, with and without shear reinforcement in the slab.

4 – Theoretical analysis considering wall thickness produced lower (around 5%) failure loads, but it was ignored for economical reasons.

5 – The ultimate strength and stiffness of the slab– wall connection obtained from the analysis based on concrete as No– Tension material were found almost identical to the strength and stiffness of the connections obtained from Fixed

crack analysis. No– tension analysis reflected the design assumptions and helped to clarify some of the short– comings of Fixed crack analysis.

6 – The assumption of proportional loading instead of the experimental sequence of gravity and lateral loading, used in theoretical analysis and reported in References (24) and (44), did not greatly affect the overall behaviour of the models.

7 – The cyclic constitutive law proposed by Fardis et el.(101) was found capable of predicting the strength degradation, stiffness degradation and hysteric behaviour of plain concrete under repeated loadings. Unfortunately, the proposed constitutive model was unsuitable for finite element work. Because, at any stress level, the material compliance matrix was found nearly singular. No unique inverse of the constitutive relation does exist, which violates the Drucker's (107) material stability theory.

9.2 Suggestions for Further Research

9.2.1 Experimental Investigations

1 – Some more models should be tested under reversed cyclic loading conditions varying the geometrical parameters like Corridor width, Bay width, Flange width, Wall– web length etc. to study the effect of those parameters on strength degradation, stiffness degradation and hysteric behaviour of slab– wall connections.

2 – Closed vertical stirrups were used as shear reinforcement in the slab. Some other form of shear reinforcement, for example, shear combs can be tried for efficient anchorage and easy installment. The recent paper by Regan(35) could probably form the basis of this work.

9.2.2 Modifications to the Program

1 – A somewhat long–term objective is the inclusion of suitable cyclic constitutive model into the finite element program which can predict with reasonable accuracy the strength and stiffness degradation and the hysteric behaviour of models tested under reversed cyclic loading conditions. The Constitutive model proposed by Bazant [109] can be tried to incorporate into the existing finite element computer program.

2 – The following additions to the present program may be useful :

a – The program requires a fully automatic mesh generator to be incorporated. This will considerably reduce time spent in data preparation.

b – The various plotting routines, which are now separate programs, can also be incorporated in the analysis program.

c – A scheme for the automatically load incrementing will be a useful inclusion for monitoring behaviour near ultimate conditions.

d – As an alternative to the Newton–Raphson method, recent methods of nonlinear techniques such as arc–length methods may be used for economical and more efficient solution.

REFERENCES

1. Rosman R., "Approximate Analysis of Shear Walls Subjected to Lateral Loads," Journal of the American Concrete Institute, Proceedings, Vol.61, No.6, June 1964, PP. 717–734.

2. Tso W. and Mahmoud A., "Effective Width of Coupling Slabs in Shear Wall Buildings", Journal of the Structural Division, ASCE, Vol.103, No.ST3, proceeding Paper 12817, March 1977, PP.573–586.

3. Coull A. and Wong Y. C.,"Bending Stiffness of Floor Slabs in Cross–Wall Structures", Proceedings, Institution of Civil Engineers, Part 2, March 1981, PP.17–35.

4. Hawkins N. M., "Shear Strength of Slabs with Shear Reinforcement", ACI special publication – Shear in Reinforced Concrete – SP 42, Vol.1, Detroit, American Concrete Institute, 1974, PP.785–815.

5. ASCE–ACI Committee 426, "The Shear Strength of Reinforced Concrete Member – Slab", Journal of the Structural Division, ASCE, Vol.100, No.ST8, August 1974, PP.1543–1591.

6. Akiyama H. and Hawkins N. M., "Response of Flat Plate Concrete Structures to Seismic and Wind Forces", Progress report on National Science Foundation Earthquake Hazards Mitigation Program, Grant No. ENN 72–03585, University of Washington, Seattle, July 1984.

7. ACI Committee 318, "Commentary on Building Code Requirements for Reinforced Concrete (ACI 318–63)", Publication SP–10, American Concrete

Institute, Michegan, 1965.

8. Distasio J. and Van Buren M. R., "Transfer of Bending Moment Between Flat Plate Floor and Column", Journal of the American Concrete Institute, Proceedings, Vol.53, No.3, September 1960, PP.299–314.

9. Moe J., "Shearing Strength of Reinforced Concrete Slabs and Footings Under Concentrated Loads", Development Department Bulletin D47, Portland Cement Association, April 1961, 130 PP.

10. Hanson N. W. and Hanson J. M., "Shear and Moment Transfer Between Concrete Slabs and Columns", Journal of the Portland Cement Association, Research and Development Laboratories, Vol.10, No.1, January 1968, PP. 2–16.

11. Regan P.E., "Behaviour of reinforced and prestressed concrete subjected to shear forces, " Paper 7441 S, Proceedings, The Institute of Civil Engineers, Vol. 50, December 1971, pp. 527, Supplement (xvii), pp. 337 – 364.

12. British Standards Institution, "The Structural Use of Concrete", Unified British Code for Structural Use of Concrete in Buildings, CP110, London, 1972.

13. British Standards Institution, "The Structural Use of Concrete", Unified British Code for Structural Use of Concrete in Buildings, BS 8110, London, 1985.

14. Mast P.E., "Stress in Flat Plates Near Columns", Journal of the American Concrete Institute, Vol.67, No.10, October 1970, PP. 761–768.

15. Mast P.E., "Plate Stresses at Columns Near the Free Edge", Journal of the

American Concrete Institute, Vol.67, No.11, November 1967, PP. 109–136.

16. Long A.E., "Punching Failure of Slabs–Transfer of Moment and Shear", Journal of the Structural Division, ASCE, Vol.99, No.ST4, April 1973, pp. 665–685.

17. Long A. E. and Bond D., "Punching Failure Of Reinforced Concrete Slabs", Paper No. 7002, Proceedings of the Institution of Civil Engineers, Vol.37, May 1967, PP. 109–136.

18. Newman K., "Criteria for the behaviour of Plain Concrete under Complex States of Stress", International Conference on Structure of Concrete, Paper F–1, Imperial College, London, England, 1965, pp. 1–27. (Qouted from References 16 & 17)

19. Yamazaki J. and Hawkins N. M., "Shear and Moment Transfer Between Reinforced Concrete Flat Plates and Columns," Report SM 75–2, Department of Civil Engineering, University of Washington, September 1975.

20. Kanoh Y. and Yoshizaki S., "Strength of Slab–column Connections Transferring Shear and Moment", Journal of the American Concrete Institute, March 1979, PP. 461–478.

21. Hawkins N. M., "Shear and Moment Transfer Between Concrete Flat Plates and Columns", Progress Report on National Science Foundation Grant No. 16375, University of Washington, Seattle, Washington, December 1971.

22. Park R. and Gamble W. L., "Reinforced Concrete Slabs" , John Wiley and Sons, New York, 1980. Section 10.3.5. Alternative Beam Analogy Approach

for Interior Connections.

23. Memon M., "Strength and Stiffness of Shear Wall– Floor Slab Connections", Ph. D. Thesis, University of Glasgow, Glasgow, 1984.

24. Elnounu G. F. R., "Design of Shear Wall– Floor Slab Connections",Ph. D. Thesis, University of Glasgow, Glasgow, 1985.

25. Islam S. and Park R., "Tests on Slab– Column Connections With Shear and Unbalanced Flexure", Journal of the Structural Division, ASCE, Vol.102, No.ST3, Proceedings Paper 11972, March 1976, PP. 549– 568.

26. Park R. and Islam S., "Strength of Slab– Column Connections With Shear and Unbalanced Flexure", Journal of the Structural Division, ASCE, Vol.102, No. ST9, Proceeding Paper 12419, September 1976, PP. 1879– 1901.

27. Rangan B. V. and Hall A. S., "Moment and Shear Transfer Between Slab and Edge Column", Journal of the American Concrete Institute, Vol.80, No.3, May– June 1983, PP.183– 191.

28. Hall A. S. and Rangan B. V.,"Forces in the Vicinity of Edge Columns in Flat– Slab Floors", Magazine of Concrete Research, Vol.35, No.122, March 1983, PP. 19– 26.

29. Rangan B. V., "Design of Reinforced Concrete Slabs for Punching Shear", UNICIV Report No. R– 228, The University of New South Wales, Kensington, New Australia, February 1986, 23 PP.

30. Regan P. E., "Behaviour of Reinforced Concrete Flat Slabs", Construction

Industry Research and Information Association, CIRIA Report 89, London, February 1981, 90 PP.

31. Ghali A., Sargious M. A. and Huizer A., "Vertical Prestressing of Flat Plates Around Columns", Shear in Reinforced Concrete, Special Publication SP–42, Vol.2, Detroit, American Concrete Institute, 1974, PP. 905–920.

32. Langhor P. H., Ghali A. and Dilger W. H., "Special Shear Reinforcement for Concrete Flat Plates", Journal of the American Concrete Institute, Proceedings, Vol.73, No.3, March 1976, PP.141–146.

33. Dilger W. H., Elmasri M. Z. and Ghali A., "Flat Plates With Special Shear Reinforcement Subjected to Static and Dynamic Moment Transfer", Journal of the American Concrete Institute, Proceedings, Vol.75, No.10, October 1978, PP. 543–549.

34. Mokhtar A., Ghali A. and Dilger W. H., "Stud Shear Reinforcement for Flat Concrete Plates", Journal of the American Concrete Institute, Proceedings, Vol.82, No.5, September–October 1985, PP. 676–683.

35. Regan P. E., "Shear Combs, Reinforcement Against Punching", The Structural Engineer, Vol. 63B, No.4, December 1985, PP. 76–84.

36. Yamazaki J. and Hawkins N. M., "Behaviour of Concrete Plates Jointed to Columns, "Proceedings, Japan Society of Civil Engineers, No. 292, December 1979, PP. 117–130.

37. Hawkins N. M., Bao A. and Yamazaki J., "Moment Transfer from Concrete Slabs to Columns", a paper obtained by private correspondance, October 1982.

38. Tsuboi Y. and Kawaguchi M., "On Earth quake Resistant Design of Flat Slabs and Concrete Shell Structures", Proceedings of the Second World Conference on Earthquake Engineering, Japan, Vol.3, July 1960, PP. 1693–1708. (Quoted from : Islam S., "Limit design of reinforced concrete slabs–openings and slab–column connections", Ph.D. Thesis, University of Canterbury, Christchurch, New Zealand, 1973.)

39. Hawkins N. M., Mitchell D. and Sheu M. S., "Reversed Cyclic Loading Behaviour of Reinforced Concrete Slab–Column connections", Proceedings, U.S. National Conference on Earthquake Engineering, Ann Arbor, Michigan, U.S.A., June 1975, PP. 306–315. (Quoted from Reference 40)

40. Hawkins N. M., Hanna S. N. and Mitchell D., "The Effects of Shear Reinforcement on Reversed Cyclic Loading Behaviour of Flat Plate Structures", Canadian Journal of Civil Engineering, Vol.2, December 1975, PP. 572–582.

41. Takeda T., Sozen M. A. and Neilson N. M., "Reinforced Concrete Response to Simulated Earthquake", Journal of the Structural Division, ASCE, Vol.96, No.ST12, December 1970, PP.2557–2573.

42. Schwaighofer J. and Collins M. P., "Experimental Study of the Behaviour of Reinforced Concrete Coupling Slabs", Journal of the American Concrete Institute, Proceedings Vol.74, March 1977, PP.123–127.

43. Coull A. and Wong Y. C., "Design of Floor Slabs Coupling Shear Walls", Journal of Structural Engineering, ASCE, Vol.109, No.1, January 1983, PP.109–125.

44. Bhatt P., Memon M. and Bari S., "Strength of Plane Shear Wall–Floor Slab

Junction", Proceedings of the International Symposium on fundamental theory of reinforced and prestressed concrete, September 1986, Nanjing Institute of Technology, Nanjing, China, Vol.3, pp. 541–549, Edited by Ding Dajun.

45. Wood R.H., "The Reinforcement of Slabs in Accordance with a Pre–Determined Field of Moments", Concrete, Feb. 1968, PP. 69–76.

46. Armer G.S.T., Correspondance on "The Reinforcement of Slabs in Accordance with a Pre–Determined Field of Moments", Concrete, Aug. 1968, PP. 319–320.

47. Hago A.W., "Direct Design of Reinforced Concrete Slabs", Ph.D. Thesis, Department of Civil Engineering, University of Glasgow, 1982.

47–a El–hafez L.M.A., "Direct Design of Reinforced Concrete Skew Slabs", Ph.D. Thesis, Department of Civil Engineering, University of Glasgow, 1986.

48. British Standards Institution, "Basic Data for the Design of Buildings, Loading", British Standard Code of Practice CP3, Chapter v, Part II, 1972.

49. Zienkiewicz O.C., "The Finite Element Method", McGraw Hill, 3rd. Edition, 1977.

50. Cook R.D., "Concepts and Applications of Finite Element Analysis", John Wiley & Sons, 1981.

51. Durelli A.J., Phillips E.A. and Tsao C.H., "Analysis of Strees and Strain", McGraw Hill, 1958.

52. Suidan M. and Schnobrich W.C., "Finite Element Analysis of Reinforced Concrete", Journal of the Structural Division, ASCE, Vol. 99, No ST10, October, 1973, pp. 2109–2122.

53. A.S.C.E., "Finite Element Analysis of Reinforced Concrete", State–of–the–Art Report, Newyork, 1982.

54. Zienkiewicz O.C., Owen D.R.J., Phillips D.V. and Nayak G.C., "Finite element methods in the analysis of reactor vessels", Nuclear Engineering and Design, Vol. 20, No. 2, 1972, pp. 507–541.

55. Phillips D.V. and Zienkiewicz O.C., "Finite Element Nonlinear Analysis of Concrete Structures", Proceedings, Institution of Civil Engineers, Vol. 61, Part 2, 1976, pp. 59 – 88.

56. Mohamed M.S., "A Finite Element and Experimental Study of Reinforced Concrete in Torsion", Ph.D. Thesis, University of Glasgow, Glasgow, 1986.

57. Kupfer H.B. and Gerstle K.H., "Behaviour of Concrete under Biaxial Stresses", Journal of Engineering Mechanics Division, ASCE, Vol. 99, No. EM4, August, 1973, pp. 853–866.

58. Gerstle K.H., Linse D.L., Bertacchi P., Kotsovos M.D., Ko H.Y., Newman J.B., Rossi P., Schickert G., Taylor M.A., Traina L.A., Zimmerman R.M., And Bellotti R., "Strength of Concrete Under Multiaxial Stress States", Proceedings, McHenry International Symposium on Concrete and Concrete Structures, Mexico, 1976, American Concrete Institute, pp. 103 – 131.

59. Gerstle K.H., Ashl H., Bellotti R., Bertacchi P., Kotsovos M.D., Ko H.Y.,

Linse D., Newman J.B., Rossi P., Schickert G., Taylor M.A., Traina L.A., Winkler H., and Zimmerman R.M., "Behaviour of Concrete Under Multiaxial Stress States", Journal of Engineering Mechanics Division, ASCE, Vol. 106, No. EM6, December, 1980, pp. 1383–1403.

60. Palaniswamy R. and Shah S.P., "Fracture and Stress–Strain Relation of Concrete Under Triaxial Compression", Journal of Structural Division, ASCE, Vol. 100, No. ST5, May, 1974, pp. 901 – 916.

61. Cedolin L., Crutzen Y.R.J. and Poli S.D., "Triaxial Stress–Strain Relationship for Concrete", Journal of Engineering Mechanics Division, ASCE, Vol. 103, No. EM3, June, 1977, pp. 423 – 439.

62. Ahmed S.H. and Shah S.P., "Complete Triaxial Stress–Strain Curves for Concrete", Journal of Structural Division, ASCE, Vol. 108, NO. ST4, April, 1982, pp. 728–742.

63. Ottosen N.S., "Constitutive Model for Short–Time Loading of Concrete", Journal of Engineering Mechanics Division, ASCE, Vol. 105, No. EM1, February, 1979, pp. 127–141.

64. Ottosen N.S., "A Failure Criterion for Concrete", Journal of Engineering Mechanics Division, ASCE, Vol. 103, No. EM4, August 1977, pp. 527–535.

65. Chen W.F. and Ting E.C., "Constitutive Models for Concrete Structures", Journal of Engineering Mechanics Division, ASCE, Vol. 106, No. EM1, February, 1980,pp. 1–19.

66. Chen W.F., "Plasticity in Reinforced Concrete", McGraw Hill, 1982.

67. Kotsovos M.D. and Newman J.B., "A Mathematical Description of the Deformational Behaviour of Concrete Under Complex Loading", Magazine of Concrete Research, Vol. 31, No. 107, June, 1979, pp. 77–90.

68. Kotsovos M.D., "A Mathematical Description of the Strength Properties of Concrete Under Generalised Stress", Magazine of Concrete Research, Vol. 31, No. 108, September, 1979, pp. 151–158.

69. Kotsovos M.D. and Newman J.B., "Behaviour of Concrete Under Multiaxial Stress", Journal of the American Concrete Institute, September, 1977, pp. 443 – 446.

70. Kotsovos M.D., "Concrete. A Brittle Fracturing Material", Materials and Structures, RILEM, Vol. 17, No. 98, pp. 107–115, 1984.

71. Ngo D. and Scordelis A.C., "Finite Element Analysis of Reinforced Concrete Beams", Journal of the American Concrete Institute, Vol. 64, No. 3, March, 1967, pp. 152–163.

72. Rashid Y.R., "Analysis of Prestressed Concrete Pressure Vessels", Nuclear Engineering And Design, Vol. 7, No. 4, April, 1968, pp. 334–344.

73. Phillips D.V., "Nonlinear Analysis of Structural Concrete by Finite Element Methods", Ph.D. Thesis, University of Wales, Swansea, 1972.

74. Gupta A.K. and Akbar H., "Cracking in Reinforced Concrete Analysis", Journal of Structural Division, ASCE, Vol. 110, No. ST8, August, 1984, pp. 1735–1746.

75. Hand F.R., Pecknold D.A. and Schnobrich W.C., "Nonlinear Layered Analysis of Reinforced Concrete Plates and Shells", Journal of Structural Division, ASCE, Vol. 99, No. ST7, July, 1973, pp. 1491–1505.

76. Al–Manaseer A.A., "A Nonlinear Finite Element Study of Reinforced Concrete Beams", Ph.D. Thesis, Glasgow University, 1983.

77. Al–Mahaidi R.S.H., "Nonlinear Finite Element Analysis of Reinforced Concrete Deep Members", Report No. 79–1, Department of Structural Engineering, Cornell University, January, 1979.

78. Cedolin L. and Poli S.D., "Finite Element Studies of Shear Critical Reinforced Concrete Beams", Journal of Engineering Mechanics Division, ASCE, Vol. 103, No. EM3, June, 1977, pp. 395–410.

79. Duncan W. and Johnarry T., "Further Studies on the Constant Stiffness Method of Nonlinear Analysis of Concrete Structures", Proceedings, Institute of Civil Engineers, Part 2, Vol. 67, 197 ., pp. 951–969.

80. Desai C.S. and Abel J.F., "Introduction to the Finite Element method – A Numerical Method for Engineering Analysis", Van–Nostrand, 1972.

81. Owen D.R.J. and Hinton E., "Finite Elements in Plasticity – Theory and Practice", Pineridge Press, Swansea, 1980.

82. Bathe K.J. and Cimento A.P., "Some Practical Procedures for the solution of Nonlinear Finite Element Equations", Computer Methods in Applied Mechanics and Engineering, Vol. 22, 1980, pp. 59–85.

83. Crisfield M.A., "A Faster Modified Newton Raphson Iteration", Computer Methods in Applied Mechanics and Engineering, Vol. 20, 1979, pp. 267–278.

84. Cope R.J. and Rao P.V., "Nonlinear Finite Element Strategies for Bridge Slabs", in Advanced Mechanics of Reinforced Concrete Structures, IABSE, Delft, 1981, pp. 275–290.

85. Johnarry T., "Elastic–Plastic Analysis of Concrete Structures Using Finite Elements", Ph.D. Thesis, University of Strathclyde, 1979.

86. Irons B.M., "A Frontal Solution Program for Finite Element Analysis", International Journal for Numerical Methods in Engineering, Vol. 2, 1970, pp. 5–32.

87. Hinton E. and Owen D.R.J., "Finite Element Programming", Academic Press, 1977.

88. Khul H., "Strain Gauges ; Theory and Handling", Philips Elektronik Industrie, GmbH – Hamburg, 1982.

89 FLASH Package, GEC 4070 Version Edition 1 April, 1981, Glasgow University.

90. Uzumeri S.M., "Strength and Ductility of Cast–in–place Beam – Column Joints", Reinforced Concrete in Seismic Zones, Publication SP–53, American Concrete Institute, Detroit, 1977, pp. 293–350.

91. Paulay T., Park R. and Priestley M.J.N., "Reinforced Concrete Beam–Column Joints Under Seismic Actions", Journal of the American Concrete Institute,

Proceedings, Vol. 75, No. 11, Nov. 1978, pp. 585–593.

92. Soleimani D., Popov E.P. and Bertero V.V., "Hysteretic Behaviour of Reinforced Concrete Beam – Column Sub–assemblages", Journal of the American Concrete Institute, Proceedings, Vol. 76, No. 11, Nov. 1979, pp. 1179– 1195.

93. Paulay T., Park R. and Birss G.R., " Elastic Beam–Column Joints for Ductile Frames", Proceedings 7th World Conference on Earthquake Engineering, Istanbul, 1980, Vol. 6, pp. 331–338

94. ACI–ASCE Committee 352, "Revised Recommendations for the Design of Beam – Column Joints", Draft No. 11, January 1984, pp. 34.

95. NZS 3101 : 1982, "Code of Practice for the Design of Concrete Structures", Standard Association of New Zealand, Wellington, Part 1, pp. 127, Part 2, pp. 156. (Quoted from Reference 96)

96. Paulay T. and Park R., "Joints in Reinforced Concrete Frames Designed for Earthquake Resistance", Research Report 84–9, Department of Civil Engineering, University of Canterbury, June 1984, pp. 71.

97. Darwin D. and Pecknold D.A., "Inelastic Model for Cyclic Biaxial Loading of Reinforced Concrete", Civil Engineering Studies SRS No. 409, University of Illinois at Urbana–Champaign, Urbana III, July 1974.

98. Elwi A.A. and Murray D.W., "A 3–D Hypoelastic Concrete Constitutive Relationship", Journal of the Engineering Mechanics Divsion, ASCE, Vol. 105, No. EM4, Proceedings paper 14734, August 1979, pp. 623–641.

99. Darwin D. and Pecknold D. A., "Analysis of Cyclic Loading of Plane R/C Structures," Computers and Structures, Vol. 7, 1977, pp. 137–147.

100. Bazant Z. P., "Comment on Orthotropic Models for Concrete and Geomaterials", Journal of Engineering Mechanics Division, ASCE, Vol.109, NO.3, June 1983, pp. 849–865.

101. Fardis M. N., Albie B. and Tassoulas J. L., "Monotonic and Cyclic Constitutive Law for Concrete", Journal of the Engineering Mechanics Division, ASCE, Vol. 109, No. 2, March 1983, pp. 516–536.

102. Dafalias Y. F., and Popov E. P., "Plastic Internal Variables Formalism of Cyclic Plasticity," Journal of Applied Mechanics, Transactions of American Society of Mechanical Engineers, Dec., 1976, pp. 645–651.

103. Karsan E. D. and Jirsa J. O., "Behaviour of Concrete under Compressive Loadings", Journal of the Structural Division, ASCE, Vol. 95, No. ST12, December 1969, pp. 2543–2563.

104. Sinha B.P., Gerstle K.H. and Tulin L.G., "Stress–Strain Relations for Concrete under Cyclic Loading", Journal of the American Concrete Institute, Proceedings, Vol. 61, No. 2, February 1964, pp. 195–211.

105. Spooner D.C. and Dougill J.W., "A Quantatitive Assesment of Damage Sustained in Concrete during Compressive Loading", Magazine of Concrete Research, Vol. 27, No. 92, September 1975, pp. 155–160.

106. Wang P.C., "Numerical and Matrix Methods in Structural Mechanics", John Wiley and Sons, Inc., New York, 1966.

107. Drucker D. C., "A More Fundamental Approach to Plastic Stress–Strain Relations," Proceedings, 1st U.S. National Congress on Applied Mechanics, ASME, 1951, pp. 487–491. (Quoted from : Chen W.F. and Saleeb A.F., "Constitutive equations for Engineering Materials", Volume 1, John Wiley & Sons, Inc., New York, 1982.)

108. Bazant Z. P., and Bhat P. D., "Endochronic Theory of Inelasticity and Failure of Concrete," Journal of the Engineering Mechanics Division, ASCE, Vol. 102, No. EM4, Proc. Paper 12360, Aug., 1976, pp. 701–721.

109. Bazant Z. P., and Kim S. S., "Plastic–Fracturing Theory of Concrete," Journal of the Engineering Mechanics Division, ASCE, Vol. 105, No. EM3, Proc. Paper 14653, June, 1979, pp. 407–428.

110. Bazant Z. P., and Shieh C. L., "Hysteretic Fracturing Endochronic Theory for Concrete," Journal of the Engineering Mechanics Division, ASCE, Vol. 106, No. EM5, Proc. Paper 15781, Oct., 1980, pp. 929–950.

GLASGOW
UNIVERSITY
LIBRARY